

9 Lattice Physics Computations

Dave Knott¹ · Akio Yamamoto²

¹Studsvik Scandpower, Inc., Wilmington, NC, USA

Dave.Knott@studsvik.com

²Graduate School of Engineering, Nagoya University, Nagoya,
Japan

a-yamamoto@nucl.nagoya-u.ac.jp

1	Overview	918
1.1	Introduction	918
1.2	Brief History	920
1.3	Cross Section Library	922
1.4	Entering the Resonance Tables	925
1.4.1	Determining Microscopic Background Cross Sections	925
1.4.2	Resonance Interference Effects	926
1.5	Condensation Scheme	928
1.5.1	Pin-Cell Calculations	929
1.5.2	Coupling Calculation	930
1.6	Assembly Fine-Mesh Transport Calculation	932
1.6.1	The CCCP Method	932
1.6.2	The Method of Characteristics	934
1.7	Fundamental Mode Calculation	935
1.8	Gamma Transport Calculation	937
1.9	Power Distribution Calculation	939
1.10	Burnup Calculation	939
1.11	Edits	940
1.12	Summary	941
2	Cross Section Library	941
2.1	Objective	941
2.2	Choice of Energy Group Structure	943
2.2.1	WIMS 69 Groups	944
2.2.2	XMAS 172 Groups	945
2.2.3	SHEM 281 Groups	946
2.2.4	Other Energy Group Structures	949
2.3	Cross Sections Used in Lattice Physics Computations	952
2.4	Cross Section Processing	954
2.4.1	Generation of Multigroup Cross Section Data	955
2.4.2	Execution Control of NJOY	958
2.4.3	Post-Processing for Cross Section Library	959
2.5	Tabulation and Contents of Cross Section Library	961
2.5.1	General File Format	962

2.5.2	Nuclide Identifiers	962
2.5.3	Dependency of Cross Sections	964
2.5.4	General Data	966
2.5.5	One-Dimensional Data	966
2.5.6	Two-Dimensional Data	968
2.5.7	Burnup-Related Data	968
2.5.8	Gamma Cross Section Library	969
2.6	Summary	969
3	Resonance Treatment	969
3.1	Objective	969
3.2	Effective Cross Sections	970
3.3	Physics of Self-Shielding and Major Resonance Calculations	972
3.3.1	Physics of Self-Shielding	972
3.3.2	Ultrafine Energy Group Calculation	973
3.3.3	Equivalence Theory	973
3.3.4	Subgroup Method	974
3.4	Resonance Self-Shielding in a Homogeneous System	975
3.4.1	Slowing Down of Neutrons in a Homogeneous System	975
3.4.2	Narrow Resonance Approximation	977
3.4.3	Wide Resonance Approximation	980
3.4.4	Intermediate Resonance Approximation	983
3.5	Resonance Self-Shielding in a Heterogeneous Systems	991
3.5.1	Neutron Slowing Down in a Heterogeneous Isolated System	991
3.5.2	Equivalence Theory	997
3.5.3	Various Approximations for Escape Probability	998
3.5.4	Neutron Slowing Down in a Heterogeneous Lattice System	1005
3.5.5	Calculation of the Dancoff Factor and Background Cross Sections	1012
3.5.6	Stamm'lér's Method for a Heterogeneous Lattice System	1020
3.5.7	Potential Limitations of the Equivalence Theory	1023
3.6	Tabulation of Self-Shielding Factors	1026
3.6.1	Cross Section Processing and Effective Cross Sections	1026
3.6.2	Interpolation of Self-Shielding Factor Table	1027
3.7	Ultrafine Group Method	1029
3.7.1	Homogeneous System	1029
3.7.2	Heterogeneous System	1032
3.7.3	Limitations of the Ultrafine Energy Groups Method	1033
3.8	Subgroup Method	1035
3.8.1	General Concept	1035
3.8.2	Direct Approach	1036
3.8.3	Probability Table Approach	1038
3.8.4	Fitting Method	1041
3.8.5	Moment Method	1043
3.8.6	Improvements in the Probability Table Approach	1047
3.9	Other Methods	1047
3.9.1	Tone's Method	1047

3.9.2	The Stoker–Weiss Method and the Space-Dependent Dancoff Method (SDDM)	1051
3.10	Resonance Overlap Effect	1061
3.10.1	Overview	1061
3.10.2	Resonance Interference Factor (RIF) Table	1062
3.10.3	Utilization of an Ultrafine Energy Group Cross Section	1063
3.11	Other Topics in Resonance Calculations	1065
3.11.1	Effective Temperature Used in Resonance Calculation	1065
3.11.2	Temperature Distribution in a Resonance Region	1066
3.11.3	Treatment of Number Density Distribution in a Pellet	1067
3.11.4	Resonance Calculation for Non-Heavy Nuclides	1068
3.11.5	Verification and Validation of Resonance Calculation Model	1068
3.12	Summary	1069
4	<i>Energy Condensation Scheme</i>	1069
4.1	Introduction	1069
4.2	Pin-Cell Spectral Calculations	1070
4.2.1	General Theory	1071
4.2.2	The Method of Collision Probabilities in Slab Geometry	1075
4.2.3	The Method of Collision Probabilities in Cylindrical Geometry	1080
4.2.4	White Boundary Conditions	1085
4.2.5	Buffer Zone	1087
4.2.6	Numerics of the Pin-Cell Spectral Calculation	1088
4.3	Coupling Calculation	1091
4.3.1	The Method of Transmission Probabilities	1092
4.3.2	Numerics of the Coupling Calculation	1094
4.3.3	Solution to the Response Matrix Equations	1097
4.3.4	Geometry of the Coupling Calculation	1099
4.4	Cross Section Condensation	1101
4.5	Sundries	1103
5	<i>Fine-Mesh Assembly Calculation</i>	1104
5.1	Introduction	1104
5.2	General Theory of the Method of Characteristics	1104
5.2.1	Introduction	1104
5.2.2	Solution to the Characteristics Form of the Transport Equation	1105
5.3	Quadrature Sets	1108
5.3.1	Introduction	1108
5.3.2	Azimuthal Angles	1109
5.3.3	Polar Angles	1111
5.4	Geometry Routine	1113
5.4.1	Introduction	1113
5.4.2	Neutron Streaming and Symmetry in Slab Geometry	1114
5.4.3	Ray Tracing in Slab Geometry	1115
5.5	Solution to the Characteristics Equation	1116
5.5.1	Introduction	1116
5.5.2	Initialization of the Flux	1117

5.5.3	Calculating the Source Term	1117
5.5.4	Boundary Conditions	1120
5.5.5	Convergence	1121
5.5.6	Accelerating the Flux Convergence	1123
5.6	Cylindrical Geometry	1125
5.6.1	Introduction	1125
5.6.2	Choosing the Azimuthal Angles of Motion	1127
5.6.3	An Alternative Tracking Approach	1130
5.6.4	Modification to the Characteristics Equation	1133
5.7	Two-Dimensional Geometry	1134
5.8	Mesh Subdivisions for Two-Dimensional Problems	1138
5.8.1	Assigning Material Regions	1138
5.8.2	Meshing	1140
5.8.3	Defining Various Cell Types	1141
5.8.4	Meshing of Control Blade Cells	1144
5.8.5	Final Mesh Layout	1144
5.9	Two-Dimensional Ray Tracing	1145
5.9.1	The Cyclic Tracking Approach	1145
5.9.2	The Macro-Band Approach	1151
5.10	Quadrature Sets for Two-Dimensional LWR Lattice Calculations	1152
5.10.1	Quadratures for Modeling Polar Motion	1152
5.10.2	Quadratures for Modeling Azimuthal Motion	1153
5.11	Acceleration Schemes for Two-Dimensional Calculations	1155
5.11.1	Coarse Mesh Rebalance	1155
5.11.2	Coarse Mesh Finite Difference	1156
5.12	Treating Very Thin Cylindrical Regions	1158
5.13	Final Comments	1160
6	Burnup Calculation	1161
6.1	Objective	1161
6.2	The Physics of Burnup and its Modeling	1162
6.2.1	Phenomena during Burnup	1162
6.2.2	Burnup Chain	1163
6.2.3	Burnup Equation	1170
6.2.4	Burnup, Burnup Time, and Normalization of Neutron Flux	1174
6.3	Numerical Scheme	1176
6.3.1	Potential Causes of Error in a Numerical Solution	1176
6.3.2	General Remarks on Numerical Solutions for the Burnup Equation	1177
6.3.3	The Euler Method	1178
6.3.4	The Runge–Kutta Method	1179
6.3.5	The Matrix Exponential Method	1181
6.3.6	The Matrix Decomposition Method	1183
6.3.7	Bateman Method	1186
6.3.8	The Padé Approximation	1187
6.3.9	The Krylov Subspace Method	1188
6.3.10	Numerical Example	1189
6.3.11	Predictor–Corrector Method	1195

6.3.12	Sub-Step Method	1198
6.3.13	Cooling Calculation.....	1200
6.4	Burnup in Gadolinia-Bearing Fuel.....	1201
6.4.1	Onion-Skin Effect	1202
6.4.2	Asymmetry Effect in Gadolinium Depletion	1204
6.4.3	Various Numerical Techniques for Gadolinium Depletion	1205
6.5	Summary	1207
7	<i>Case Matrix</i>	1207
7.1	Introduction.....	1207
7.2	Cross Section Dependencies in BWRs	1208
7.3	Cross Section Dependencies in PWRs	1218
7.4	Summary	1221
8	<i>Edits</i>	1222
8.1	Nomenclature	1223
8.2	Various Edits	1223
8.3	Neutron Balance	1230
9	<i>Concluding Remarks</i>	1231
	<i>References</i>	1232

Abstract: This chapter presents a detailed description of the elements that comprise a lattice physics code. Lattice physics codes are used to generate cross section data for nodal codes, where the nodal codes are used to model the coupled neutronics and thermal-hydraulics behavior of the entire reactor core during steady state and transient operation. Lattice physics codes analyze axial segments of fuel assemblies, referred to as *lattices*, to determine the detailed spatial and spectral distribution of neutrons and photons across the segment. Once the flux distribution is known, the cross sections can be condensed and homogenized into the structure needed by the nodal code. The nodal code then pieces the various lattices together to construct the various fuel assemblies in the reactor core. This chapter is split into individual sections representing the major pieces of a lattice physics code. ➤ [Section 1](#) presents a general overview of the computational scheme used for a typical lattice physics code (*Knott*). The remaining sections of this chapter are used to describe the major pieces in detail. ➤ [Section 2](#) describes the contents of the cross section library that accompanies a lattice physics code (*Yamamoto*). ➤ [Section 3](#) discusses the various resonance treatments used in lattice physics calculations (*Yamamoto*). ➤ [Section 4](#) describes a method for removing cross section energy detail without sacrificing too much accuracy (*Knott*). ➤ [Section 5](#) describes the fine-mesh transport calculation on the heterogeneous lattice geometry (*Knott*). ➤ [Section 6](#) discusses the burnup calculation (*Yamamoto*). ➤ [Section 7](#) describes some of the details of a typical case matrix (*Knott*), and ➤ [Sect. 8](#) discusses some of the edits that are provided by the lattice physics code (*Knott*). This chapter provides the interested reader with a broad understanding of a typical lattice physics code.

1 Overview

1.1 Introduction

Our primary interest in reactor analysis is to be able to model day-to-day steady state operation of the reactor core, or to model brief periods of time during which the reactor is experiencing some sort of operational transient due to an unexpected insertion or removal of reactivity. Such analyses are performed using a three-dimensional nodal code with thermal–hydraulic feedback. The nodal code models the entire reactor core as a collection of homogeneous prisms, referred to as *nodes*. The nodes are homogeneous in the sense that the material cross sections, used to represent the neutronic properties of the fuel, are constant and there is no geometry detail within a node, such as the explicit representation of fuel pins, guide tubes, or control rods. In other words, everything gets smeared together. A model of a full-sized reactor core will use anywhere from 15,000 to 20,000 nodes. Material cross sections for a node have traditionally been represented by just two energy groups – a fast group typically above 0.625 eV and a thermal group typically below 0.625 eV – although current nodal codes have begun to expand on this number. The material cross sections for a node are obtained from tables generated by a *lattice physics code*. The lattice physics code is used to perform a very detailed neutronic analysis on each unique axial portion of a fuel design, where the characteristics of the fuel might change due to changes in geometry or materials from the surrounding elevations. We refer to these unique axial zones as *lattices*, two of which are illustrated in ➤ [Fig. 1](#). A typical fuel bundle may contain seven or eight different axial zones. This is illustrated in ➤ [Fig. 2](#) for a boiling water reactor (BWR) bundle design, where the panel on the left shows the radial distribution of pin enrichments in the bundle design and the panel on the right shows the axial zoning of each

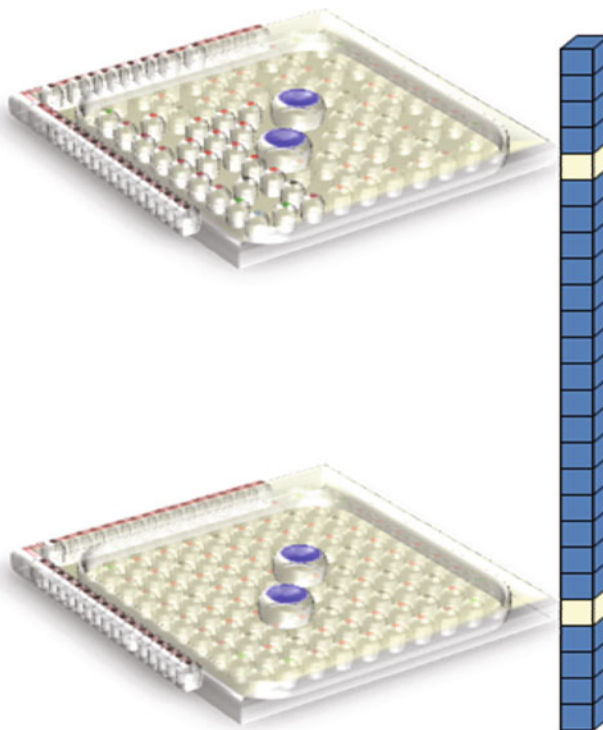


Figure 1
Lattices within homogeneous nodes

of the unique pin types that have been included in the design. In this example, of the 92 fuel pins contained in the bundle design, 13 happen to be unique, differing from each other either in enrichment, burnable absorber content (i.e., Gadolinium mixed into the Uranium fuel pellet), or height. Several pins in the bundle are referred to as part-length rods and span only a portion of the total height of the assembly. The lattice physics code analyses each zone at various snap shots in time (i.e., burnup) and at different core conditions to create tables of homogenized two-group cross sections, which are needed by the nodal code. The collection of cases analyzed to create the tables is referred to as the *case matrix*. The nodal code then interpolates the tables between snap shots to determine the characteristics of the fuel at each specific core elevation, for a given reactor condition. The challenge is to come up with a scheme for the lattice physics code that can accurately reduce the continuous energy raw cross section data for the strongly heterogeneous fuel assembly into a single, homogenized material in two representative energy groups that can be used by the nodal code to produce accurate results.

To create the homogenized, two-group cross sections for each lattice, the lattice physics code needs to calculate an accurate flux distribution in energy and space for the heterogeneous problem. It will then use this flux distribution to spatially and spectrally homogenize the lattice. The main difference between various lattice physics codes in use today is the way in which they go about determining the flux.

**Figure 2**

Panels showing the radial and axial enrichment distribution of pins in a BWR bundle

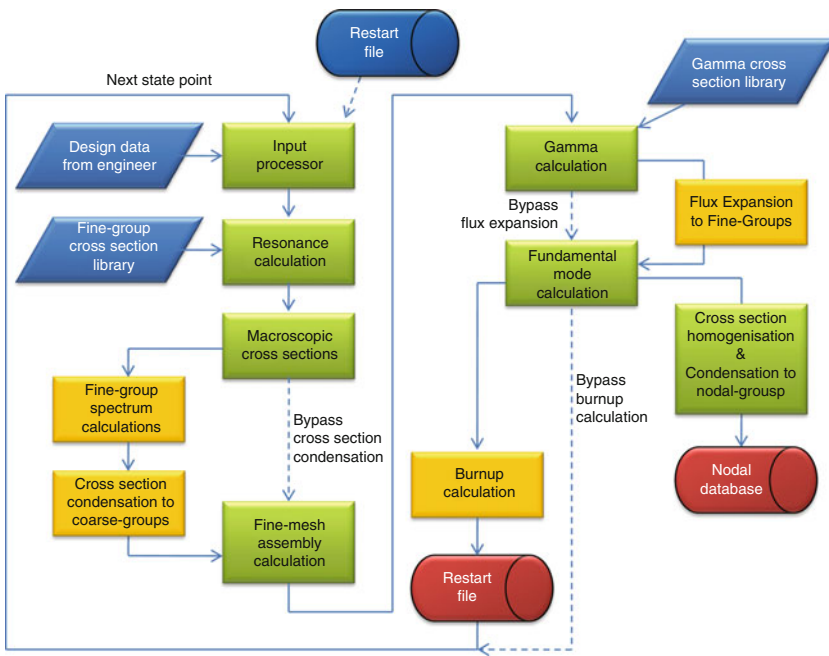
Ideally, the flux distribution in the lattice would be determined by solving the transport equation in the exact geometry of the lattice using continuous energy cross sections, the way a Monte Carlo code might. But because of time constraints, such a calculation is outside the realm of today's design requirements, where thousands of lattice physics calculations are needed to fully functionalize a single fuel design's characteristics. To this end, the calculational scheme within a lattice physics code is intended to reduce the overall computation time without sacrificing too much accuracy.

In this chapter, we will describe the concept of the lattice physics code. The details of the scheme that will be discussed follow the path outlined in [Fig. 3](#). The lattice physics code draws upon many of the topics discussed in other chapters of this handbook, so it provides a nice way of tying many of the topics together. Application to BWR fuel designs are used as examples. Concepts developed to analyze a BWR fuel design can be extended directly to pressurized water reactor (PWR) fuel designs.

1.2 Brief History

In the early days (i.e., late 1950s and early 1960s), the method for analyzing a reactor core consisted of a series of simplistic calculations performed using separate pieces of software that formed a calculational chain. Each piece of software in the chain served a specific purpose and results from one piece of software were used to feed the next piece of software in the chain. The procedure began by calculating a spatially independent fast flux spectrum above 0.625 eV, such as the one generated on a grid of 54 energy groups using the MUFT code (Bohl et al. [1957](#)). The companion thermal flux spectrum below 0.625 eV was generated on a grid of 172 energy groups using the SOFOCATE code (Amster and Suarez [1957](#)). The 0.625 eV energy was used as the thermal cut-off, above which up-scattering effects were neglected. Both MUFT and SOFOCATE were dimensionless codes that simply supplied a general flux spectrum for a given material.

The flux spectrum from the MUFT-SOFOCATE analysis was used to collapse cross sections to a very small number of groups – typically 4. Using the four-group energy structure, a one-dimensional cylindrical pin-cell calculation was performed using the THERMOS code

**Figure 3**

Typical lattice physics calculation scheme

(Honeck 1961). The pin-cell calculation provided representative flux spectrums for the fuel, clad, and coolant regions of the reactor. The flux in the fuel region from the THERMOS pin-cell calculation was passed to a burnup code, such as LEOPARD (Barry 1963), which performed the depletion analysis on selected isotopes. The whole process was very crude by today's standards and offered little in the way of accuracy.

The development of lattice physics codes for reactor analysis began in the mid-1960s with the introduction of WIMS (Winfrith Improved Multigroup Scheme) at Winfrith in the UK (Askew et al. 1966a). The concept gathered all the processes for generating few-group cross section data into a modular collection of software that automated many of the tasks in a systematic fashion, thereby relieving the engineer of a great deal of tedious data transfer and manipulation. But the major evolutionary step was to add a two-dimensional calculation, which analyzed a fuel assembly at a specific elevation. (It should be noted here that the lattice physics code models each lattice as being infinitely tall; i.e., there are no boundaries along the z-axis. This is what we refer to as a two-dimensional problem, i.e., boundaries along two axes.) This two-dimensional calculation provided a way of explicitly capturing the response of each pin due to the influence of its neighbors (other fuel pins, absorber rods, water rods, channel box walls, water gaps, etc.). The original WIMS code provided a framework for research in reactor analysis and could be applied to a very wide range of problems, such as gas-cooled reactors of the Magnox and AGR types that are prevalent in the UK. In the early 1970s, a special version of WIMS was released, LWRWIMS (Fayers et al. 1972), which was streamlined for analyzing light water reactor (LWR) fuel designs. These first versions of WIMS made use of gross approximations at all stages of the

calculational scheme in order to reduce execution time and memory requirements to a manageable level. For LWR analysis, the standard way of determining the flux at the lattice level was based on a few-group diffusion calculation applied to a coarse Cartesian grid.

In the 1970s and early 1980s, a series of lattice physics codes were developed in the Scandinavian countries. These included CASMO (Ahlin and Edenius 1977), CPM (Ahlin and Edenius 1978), and PHOENIX (Stamm'ler 1992). These codes, together with LWRWIMS, the General Electric/Toshiba code TGBLA (Yamamoto et al. 1984), the Combustion Engineering code DIT (Jonsson and Loretz 1991), and the Cadarache code APOLLO (Hoffman et al. 1973), provided a stable platform for LWR lattice physics analysis throughout the 1980s. Most codes were very similar in concept, but differed in detail. All employed significant approximations in order to reduce execution time to a manageable level. However, the newer codes had begun to introduce transport effects into the lattice calculation. Throughout the 1990s, CPM and DIT faded from routine use. During the same period of time, drastic improvements in computer architecture allowed for significant improvements in accuracy in CASMO (CASMO-4 (Knott et al. 1995)), APOLLO (APOLLO-2 (Sanchez et al. 1988)), and the development of HELIOS (Casal et al. 1991). Most lattice physics codes in production use today share many of the ideas from these codes.

The content of this chapter relies heavily on experiences from the development of CASMO-4, LANCER02 (Knott and Wehlage 2007), and AEGIS (Sugimura et al. 2007). When appropriate, deviations from the approaches in these codes are discussed.

1.3 Cross Section Library

The first step in building a lattice physics code is to create an energy group-dependent cross section library. This is our first approximation – that we assume we can accurately represent cross sections over a range of energies using constant values as opposed to point-wise data. The number of energy groups needed and the location of the group boundaries are determined by the lattice physics code's range of application. For example, analysis on mixed-oxide fuel requires different energy detail than does analysis on Uranium-oxide fuel; analysis on fast reactors requires different energy detail than does analysis on thermal reactors; analysis on light water reactors requires different energy detail than does analysis on heavy water reactors, and so on. From the early WIMS days through the 1980s, the cross section libraries associated with production-level lattice physics codes were limited to 100 energy groups or fewer. The original WIMS library contained 69 energy groups (Taubman 1975) and many early lattice physics codes replicated that structure. In the early 1990s, HELIOS was released with a master library containing 190 energy groups, although this group structure was rarely used for analysis. Instead, a smaller library with 35 groups was routinely utilized. Today, it is common for libraries to contain hundreds of energy groups (Rhodes 2009). The more energy groups contained in the library, the more time consuming the analysis becomes. In ➤ 1.5 – and in much more detail in ➤ Sect. 4 – we will discuss the ways of reducing this computational burden.

In addition to determining the energy group structure of the cross section library, it is also necessary to determine the isotopes that will be carried in the library. Not all isotopes need to be included in the library. For instance, deuterium data might only be required if the lattice physics code is going to be applied to heavy water reactor analysis; graphite data might only be required if the lattice physics code is going to be applied to gas-cooled reactors and so on. The number of isotopes included in the library is primarily dictated by the depletion chains that will be solved during the burnup calculation and by the fission products that will be treated explicitly.

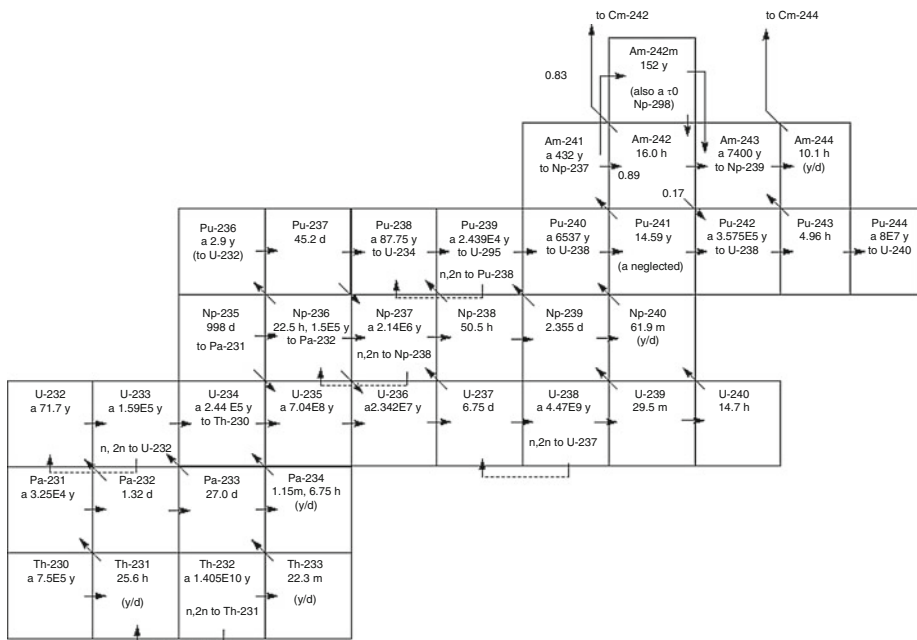


Figure 4
Typical actinide chain

➤ *Figure 4* contains an example of the lower portion of the actinide chain modeled in a typical lattice physics code (Rhodes 2009). In order to model this burnup chain, data for every isotope in the chain would need to be contained in the cross section library, although an exception can be made for the extremely short-lived isotopes (i.e., those isotopes that decay within a matter of minutes). Early libraries typically linearized the depletion chains in order to reduce the computational burden and memory requirements (Stamm'ler and Abbate 1983). In addition, only the most important fission products were modeled explicitly in the library. The fission products that were not modeled explicitly were rolled up into a couple of pseudo isotopes, typically one pseudo isotope for all the slowly saturating fission products and one pseudo isotope for all the non-saturating fission products. The total number of isotopes contained in the early libraries was often limited to 100. Today, it is common practice to include several hundred isotopes in a library and to solve the depletion chains explicitly in their matrix representation (Knott and Wehlage 2007); (Rhodes 2009). ➤ *Section 2* is devoted to a discussion on the cross section library associated with a lattice physics code.

Creation of a multigroup cross section library for a lattice physics code begins with the code that processes the continuous energy cross section data. In the case of the ENDF/B data, the major processing code is NJOY (MacFarlane and Muir 1994a). To create a group-wise library from the continuous energy point-wise data, NJOY must have a flux spectrum with which to combine point-wise data over an energy range,

$$\sigma_x^g = \frac{\int_E^{E+\Delta E} \sigma_x(E) \phi(E) dE}{\int_E^{E+\Delta E} \phi(E) dE} \quad (1)$$

where x is a reaction type (e.g., fission, capture); g is an energy group over the energy interval ΔE ; $\sigma_x(E)$ is the microscopic cross section at energy point E ; and $\phi(E)$ is the flux spectrum used to weigh the continuous energy cross section over the energy interval from E to $E + \Delta E$.

The flux contained in (1) is meant to represent the spectrum found in a typical LWR. Unfortunately, NJOY does not contain the capability of solving the transport equation for a specific flux spectrum. Instead, NJOY contains a couple of options that can be selected to generate an estimate to the true flux found in an LWR. The options available in NJOY assume that the flux behaves as defined by the following expression,

$$\phi(E) \propto \frac{1/E}{\sigma_{t,iso}(E) + \sigma_0} \quad (2)$$

where $\sigma_{t,iso}(E)$ is the microscopic total cross section for the isotope under consideration, iso ; and σ_0 is the microscopic background cross section, which represents the scattering strength of all isotopes in the system other than isotope of interest, iso . In this context, the term *system* refers to the material mixture plus anything else in the immediate vicinity that can contribute to scattering, such as moderator surrounding a fuel pellet. Equation (2) is often referred to as the Bondarenko model based on the narrow resonance (NR) approximation (Lamarch 1972). If possible, group boundaries in the cross section library should be chosen such that results are insensitive to the flux from (2) used to generate the library.

For each isotope containing resonances, NJOY creates a base cross section set at a base temperature (e.g., 300 K), for infinitely dilute conditions by setting σ_0 equal to a very large value (e.g., 10^{10}) in (2). In this context, the term *infinitely dilute* refers to a system in which the background cross section (i.e., the scattering strength of all the other isotopes in the material and surrounding environment) is so large as to render the presence of the resonance absorber unrecognizable. That is, scattering is the dominant process even at resonance energies.

Once the base set of cross sections are generated, NJOY can create correction factors to the infinitely dilute values to account for changes in the cross sections caused by different temperatures and different background cross sections. We will refer to these tables as the *f*-tables, $f(T, \sigma_0)$. When the lattice physics code obtains microscopic cross sections from the cross section library, the code reads the infinitely dilute values and enters the *f*-tables to obtain the appropriate correction factor as a function of temperature and microscopic background cross section,

$$\sigma_{x,iso}^g = \sigma_{x,iso}^g(300 \text{ K}, \infty) \cdot f_{x,iso}^g(T, \sigma_0) \quad (3)$$

Interpolation in the *f*-tables is performed as a quadratic function of the square root of the fuel temperature, $\sqrt{T_f}$, and the logarithm of the microscopic background cross section, $\log(\sigma_0)$. Self-shielded data for each resonance absorber are generated at many different temperatures between 300 and 2,500 K, and at many different background cross section conditions between 10 barns and 10^{10} barns.

In a lattice physics code, the fuel temperature is typically set to a specific value by the user, removing all ambiguity for that particular parameter. The various microscopic background cross sections for the resonance absorbers in the bundle, however, are not obvious and must be determined by the code. If the calculated microscopic background cross section for a particular isotope is incorrect, the lattice physics code will enter the *f*-tables in the wrong location and pick up the wrong cross sections for the resonance region. This introduces a certain amount of error into the analysis, so it becomes very important that the lattice physics code have a way of accurately calculating the background cross section for each material in the fuel assembly.

1.4 Entering the Resonance Tables

1.4.1 Determining Microscopic Background Cross Sections

To calculate a proper *microscopic* background cross section for each isotope in a material mixture, we begin by determining the *macroscopic* background cross section for the system as a whole and then back-out the microscopic contribution for each isotope.

The calculation of a macroscopic background cross section for a system, Σ_0 , can be separated into two contributions: (1) a volume component, Σ_p ; and (2) a surface component, Σ_e (Wigner et al. 1955). That is, $\Sigma_0 = \Sigma_p + \Sigma_e$.

Volume Component

The volume component, Σ_p , accounts for neutrons that are scattered into a resonance energy by the material mixture (i.e., not the moderator). It is calculated in a very straightforward way as the sum of the potential scattering cross sections for all isotopes in the mixture (hence the use of the subscript p for potential),

$$\Sigma_p = \sum_{iso} N_{iso} \sigma_{p,iso} \quad (4)$$

where N_{iso} is the number density for isotope iso ; and $\sigma_{p,iso}$ is the microscopic potential scattering cross section for isotope iso . The potential scattering cross section is energy-independent and represents the forces that act upon a neutron as it moves in or near the nucleus of an atom. It is a function only of the effective scattering radius of the nucleus, which depends on the way in which the different wavelengths of the incident neutron (e.g., *s*-wave, *p*-wave) interact with the target nucleus. The effective scattering radius of each isotope is obtained from the ENDF/B files and the potential scattering cross section is then calculated as $\sigma_{p,iso} = 4\pi R_{0,iso}^2$, where $R_{0,iso}$ is the effective scattering radius of the nuclide.

Surface Component

The surface component, Σ_e , accounts for neutrons that escape the fuel material and are scattered into a resonance energy by the surrounding moderator (hence the use of the subscript e for escape). They are then free to reenter the material, where they may be absorbed. It is the solution to this component that has been studied extensively since the 1960s.

There are many different ways to estimate the contribution from the surface component and different lattice physics codes address it using different approximations. For an isolated fuel pellet, the surface component may be grossly approximated using the Wigner rational expression (Wigner et al. 1955), where a macroscopic escape cross section is expressed as the inverse of the mean chord length for a simple convex body,

$$\Sigma_e = \left(\frac{4V}{S} \right)^{-1} = \frac{1}{2r} \quad (5)$$

In (5), V refers to the volume of the fuel pellet; S refers to the surface area of the pellet; and r is the pellet radius.

The Wigner rational expression is a surprisingly good approximation under certain circumstances. For modern LWR fuel designs, though, the escape cross section calculated using the

Wigner approximation can be in error by far more than is tolerable for the accuracy we desire. Hence, few lattice physics codes rely on the Wigner approximation. Those that do must augment the approximation with a correction factor to produce acceptable results. When this method is chosen, the correction factor is usually determined from a Monte Carlo analysis. ➤ [Section 3](#) is devoted to a thorough description of resonance approximations in lattice physics codes.

For an array of tightly packed fuel pins, such as those in a fuel assembly, some neutrons may escape from one pellet and suffer their first collision in a neighboring pellet rather than in the surrounding moderator. This shadowing effect changes the escape cross section of the isolated pellet and can be taken into account through the use of a Dancoff factor, Γ , and applied to the escape cross section ([Carlvik 1966b](#))

$$\Sigma_0 = \Sigma_p + \Gamma \Sigma_e \quad (6)$$

A detailed description of Dancoff factors is included in ➤ [Sect. 3](#).

For each isotope in the fuel mixture, the associated microscopic background cross section is calculated as

$$\sigma_{0,iso} = \frac{\Sigma_0}{N_{iso}} - \sigma_{p,iso} \quad (7)$$

The microscopic background cross section from (7) is used to enter the resonance tables and obtain the appropriate cross sections for each isotope in each fuel mixture in the lattice.

1.4.2 Resonance Interference Effects

Resonance interference refers to the way in which cross section resonances from one nuclide affect resonance absorption or scattering in another nuclide when multiple resonance absorbers exist in the same fuel mixture. During creation of the cross section library, resonance interference effects were neglected. That is, microscopic cross sections for each isotope in the library were created as if none of the resonances from any of the other isotopes existed. In practice, such a condition will never exist since all LWR fuel consists of several Uranium isotopes and/or Plutonium isotopes – all of which contain many resonances over a wide range of energies. In addition, many major fission products contain large resonances. The presence of the additional resonances will exaggerate the spectral flux dips and change the results when using (1). In lattice physics codes, resonance interference effects between different resonance absorbers in the same material mixture can be taken into account through a separate calculation that determines a resonance interference correction factor to the NJOY-generated cross sections ([Williams 1983; Wehlage 2005](#)).

For this model, a separate ultrafine-group cross section library is utilized that contains tens of thousands of group-wise data points with equal lethargy widths in the resolved resonance energy range from about 40 eV to 10 keV, or possibly even extended up to 100 keV. The narrow resonance (NR) approximation is used to generate a flux spectrum for each resonance absorber in isolation, ϕ_{iso}^u , and a separate flux spectrum for the material mixture as a whole, ϕ_{Mix}^u . Here, u represents the ultrafine-group energy structure. The narrow resonance approximation assumes that the energy lost by a neutron suffering a scattering collision is large compared to the width of a resonance. Under such circumstances, it is unlikely that a neutron will experience more than a single collision within any resonance peak and the neutron is, therefore, somewhat unlikely to be absorbed by a resonance absorber. This approximation tends to be very good for all neutron

energies above 40 eV. Below 40 eV, it is important that the energy group structure of the lattice physics cross section library contains enough detail such that the group-wise cross sections are not strongly shielded.

The ultrafine-group flux for each isotope, ϕ_{iso}^u , and for the material mixture as a whole, ϕ_{Mix}^u , can be described by the following expressions:

$$\phi_{iso}^u = \frac{1/E^u}{\Sigma_{t,iso}^u + \Sigma_0} \quad (8)$$

$$\phi_{Mix}^u = \frac{1/E^u}{\Sigma_{t,Mix}^u + \Sigma_0} \quad (9)$$

where the only difference between (8) and (9) is in the value for the total cross section in the denominator. $\Sigma_{t,iso}^u$ is the ultrafine-group total cross section for isotope iso ; and $\Sigma_{t,Mix}^u$ is the ultrafine-group total cross section for the material mixture as a whole.

Equations (8) and (9) may be solved directly using the macroscopic background cross section for the material mixture, Σ_0 , from (6). The fluxes from (8) are used to create parallel sets of cross sections, in the energy group structure of the lattice physics cross section library, for each individual resonance absorber,

$$\sigma_{x,iso}^g = \frac{\sum_{u \in g} \sigma_x^u \phi_{iso}^u}{\sum_{u \in g} \phi_{iso}^u} \quad (10)$$

And the flux from (9) is used to create cross sections for the material mixture as a whole,

$$\sigma_{x,Mix}^g = \frac{\sum_{u \in g} \sigma_x^u \phi_{Mix}^u}{\sum_{u \in g} \phi_{Mix}^u} \quad (11)$$

where x is the reaction type; iso is a resonance absorber; g is the energy group structure of the lattice physics cross section library; and u is the energy group structure of the ultrafine-group cross section library. Resonance interference correction factors are then calculated as the ratio of (11) to (10),

$$RIF_{x,iso}^g = \frac{\sigma_{x,Mix}^g}{\sigma_{x,iso}^g} \quad (12)$$

and are applied to the cross sections from the lattice physics library,

$$\sigma_{x,iso}^g = \sigma_{x,iso}^g(300\text{ K}, \infty) \cdot f_{x,iso}^g(T, \sigma_0) \cdot RIF_{x,iso}^g \quad (13)$$

RIFs for capture, fission, and elastic scattering cross sections for each major resonance absorber in any material mixture should be calculated. In most cases, the effect of the resonance interference calculation on the results from the lattice physics code is small and serves to basically fine-tune any reactivity coefficients that rely on spectrum hardening effects. A more thorough description of resonance interference effects is contained in [Sect. 3](#).

1.5 Condensation Scheme

Once microscopic cross sections have been obtained from the cross section library and the macroscopic cross sections for each material region in the problem have been created, the lattice physics code is ready to determine the flux distribution throughout the lattice. Solution to the steady state Boltzmann transport equation in the energy group structure of the cross section library is usually supported by modern lattice physics codes, but the calculation is often too time consuming for production-level analysis, where several thousand state points are analyzed to generate nodal cross section data for a single bundle design.

One common approach for reducing execution time to a reasonable level is to condense the cross sections from the energy group structure of the library to a smaller, more manageable energy group structure. When doing this, it is imperative that accuracy is maintained by the smaller cross section set, so an adequate condensation scheme is very important.

HELIOS addressed this issue by performing a single calculation on a generic LWR lattice in the energy group structure of the master cross section library (Casal et al. 1991). The lattice-averaged flux from the reference calculation was then used to condense the entire master cross section library from the fine-group structure (190 groups) into a smaller energy group structure (~35 groups). The smaller library was then used in all production-level analyses without any further condensation. Since the condensation scheme was applied to the microscopic cross sections, the resonance tables (i.e., f -tables) had to be condensed, as well.

CASMO-4 used a different approach (Knott et al. 1995). The cross section library for CASMO-4 contained 70 energy groups and at the beginning of each individual case the code performed a series of calculations in the energy group structure of the library in order to generate a unique condensation spectrum for each different material region of the problem. Macroscopic cross sections for each material region in the problem were condensed from 70-groups to a much smaller group structure, which depended on the type of problem being analyzed, but in general was kept below a dozen energy groups. The approach in LANCER02 is very similar (Knott and Wehlage 2007). The LANCER02 cross section library contains 118 energy groups (or a 190 group library for mixed oxide analysis) and the flux from the condensation scheme is used to collapse macroscopic cross sections to approximately 25 energy groups. The approaches in both CASMO-4 and LANCER02 are based on the scheme described in Knott (1991). This scheme will be described in this chapter.

The condensation scheme in CASMO-4 and LANCER02 consists of a two-step process involving, first, a series of one-dimensional pin-cell calculations and, second, a fast two-dimensional coupling calculation, as illustrated in  Fig. 5. Both calculations could be performed in the energy group structure of the cross section library. An alternative approach would be to perform the coupling calculation in an intermediate energy group structure, somewhere between the fine-group structure of the library and the broad-group structure of the assembly fine-mesh transport solution, in order to reduce execution time even further. Either approach is acceptable, keeping in mind that the level of accuracy used at this stage of the computational scheme will affect the number of energy groups that must be maintained for the assembly fine-mesh transport solution.

In contrast to the two-step approach, CASMO-5 has removed the coupling calculation from the condensation scheme and relies solely on the pin-cell calculations to generate a condensation flux. The lattice physics code AEGIS contains no condensation scheme and performs the assembly fine-mesh transport calculation in the energy group structure of the cross section

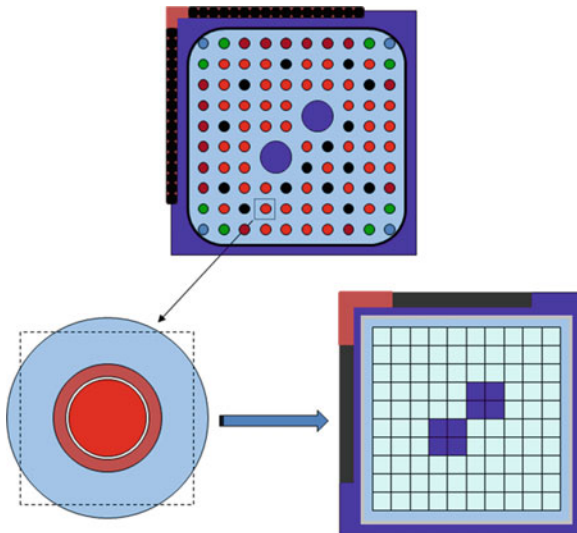


Figure 5
Progression of condensation scheme

library. This is the approach taken for ultimate accuracy, although at the price of a much longer run time.

1.5.1 Pin-Cell Calculations

For the series of one-dimensional pin-cell calculations in the CASMO-4 and LANCER02 condensation scheme, the flux in the system is determined by solving the integral form of the transport equation using the method of collision probabilities (CP). The CP method is ideal for physically small systems containing a small number of mesh. Each pin cell in the lattice – including water rods and vanish locations (i.e., locations above the top of part-length fuel rods) – should take part in its own unique pin-cell calculation. The square coolant region of each cell can be cylindricalized by preserving volume. This converts the two-dimensional nature of the square cell into a one-dimensional problem, where the flux can be determined very rapidly without significantly affecting accuracy. A buffer zone, made up of average fuel and moderator material, can be added to the outside of each cell to help drive the flux across inert pins (e.g., water rods, control rods) and pins containing strong absorbers (e.g., gadolinium, erbium). The system can be represented as a fixed source problem, where the fission spectrum can be used as the neutron source and can be placed in the buffer zone. This helps to facilitate a speedy convergence to the transport solution.

The scalar flux is determined by solving the following integral equation (the derivation of which is presented in detail in [Sect. 4](#)),

$$\phi(\vec{r}_i, E) = \int_{-\infty}^0 Q(\vec{r}_j, E) \cdot T(\vec{r}_j \rightarrow \vec{r}_i, E) \cdot dV_j \quad (14)$$

where $Q(\vec{r}_j, E)$ is the total neutron source in mesh j ; $\phi(\vec{r}_i, E)$ is the scalar flux in mesh i ; and $T(\vec{r}_j \rightarrow \vec{r}_i, E)$ is the first-flight transmission probability of neutrons from mesh j to mesh i , given by the expression

$$T(\vec{r}_j \rightarrow \vec{r}_i, E) = \frac{e^{-\tau(\vec{r}_i - \vec{r}_j, E)}}{4\pi |\vec{r}_i - \vec{r}_j|^2} \quad (15)$$

In order to arrive at the expression for the scalar flux in (14), the source term was assumed to be isotropic. Such an assumption necessitates the use of transport-corrected cross sections in order to account for anisotropic scattering effects. The transport-correction is derived by expanding the scattering kernel using spherical harmonics and keeping only the first two terms. This leads us to the diffusion equations for the scalar flux, ϕ_0^g , and current, ϕ_1^g , and the corresponding definition for the diffusion coefficient

$$D^g = \frac{1/3}{\Sigma_{t_1}^g - \sum \Sigma_{s_1}^{g' \rightarrow g} \left(\phi_1^{g'} / \phi_1^g \right)} \quad (16)$$

The denominator in (16) represents the definition for the transport cross section, which is a function of the ratio of currents in various energy groups. Unfortunately, we do not know the currents in our problem a priori and we are forced to make the assumption that the current-induced scattering of neutrons into an energy group is equal to the current-induced scattering of neutrons out of the energy group,

$$\sum_{g'} \Sigma_{s_1}^{g' \rightarrow g} \phi_1^{g'} \approx \sum_{g'} \Sigma_{s_1}^{g \rightarrow g'} \phi_1^g \quad (17)$$

This is a fair assumption when scattering is the dominant reaction and relatively little neutron absorption is taking place. It is a poor assumption when absorption is the dominant reaction.

From (17) it follows that,

$$\Sigma_{tr}^g = \Sigma_t^g - \sum_{g'} \Sigma_{s_1}^{g \rightarrow g'} = \Sigma_t^g - \Sigma_{s_1}^g \quad (18)$$

which is our definition for the transport cross section. In (18), Σ_t^g is the total cross section in group g ; and $\Sigma_{s_1}^g$ is the first moment to the total scattering cross section in group g . The transport cross section can be created internally from the total cross section and the first moment to the scattering cross section, both of which should be contained in the cross section library.

Specular reflection boundary conditions are used on the outside of the one-dimensional pin-cell geometry to simulate perfect reflection in the square coolant system (i.e., Weiner-Seitz cell).

1.5.2 Coupling Calculation

The solution to the CP equation yields a flux distribution in each region of each pin cell in the energy group structure of the cross section library. This flux distribution is generated without considering the true surroundings of each pin cell (water gaps, water rods, strong absorber pins, control blades, etc.). Before condensing cross sections to a smaller energy group structure, the

fluxes from the one-dimensional pin-cell calculations should be updated to account for the effects on the energy distribution from the surrounding components of the lattice. This can be accomplished by performing a two-dimensional coupling calculation on the entire lattice using a simplified geometry and a simplified solution to the transport equation.

Since this coupling calculation will use a simplified geometry of the lattice, all solutions techniques to the Boltzmann transport equation are viable. At this stage of the calculational scheme, speed is of essence. A very good choice for the two-dimensional coupling calculation is one that solves the integral transport equation using a response matrix (RM) method based on simplified transmission probabilities. In this method, each pin cell is homogenized into an equivalent material set of cross sections using the fluxes from the corresponding one-dimensional pin-cell calculation. Cells are coupled to each other via surface currents, which are assumed to be isotropically distributed in angle and spatially constant along a given cell surface. The equations representing the scalar flux and outward-directed current are, respectively,

$$\phi_I^g = T_{I \leftarrow I}^g Q_I^g V_I + 4 \sum_s T_{I \leftarrow s}^g J_{s,in}^g A_s \quad (19)$$

$$J_{I,out}^g = T_{s \leftarrow I}^g Q_I^g V_I + \sum_{s'} T_{I \leftarrow s'}^g J_{s',in}^g A_{s'} \quad (20)$$

where I represents a spatial mesh, such as an homogenized pin cell; s represents a surface to mesh I ; the T 's are transmission probabilities between volumes and/or surfaces; V represents the volume of mesh I ; and A represents the surface area of surface s . Outward-directed currents from one mesh become the inward-directed currents to the neighboring mesh. The calculation of transmission probabilities will be discussed in [Sect. 4](#).

Following the two-dimensional RM calculation, the energy distribution of neutrons from each one-dimensional pin-cell calculation is updated,

$$\tilde{\phi}_i^g = \phi_i^g \cdot \frac{\phi_I^g V_I}{\sum_{i \in I} \phi_i^g V_i} \quad (21)$$

Fluxes for the surrounding regions of the lattice – channel box wall, water gaps, etc. – are obtained directly from the RM solution. Fluxes for the various regions of a control blade can be obtained from a special series of pin-cell calculations performed on each absorber tube in a control blade and updated with the flux from the RM solution. [Equation \(21\)](#) represents the flux for each material region of the problem that will be used to condense the macroscopic cross sections. The final energy group structure for the two-dimensional assembly transport calculation depends on the accuracy of the condensation scheme, the energy group boundaries in the cross section library, and the types of problems to be analyzed by the lattice physics code.

Today, many lattice physics codes are attempting to move away from cross section condensation and rely solely on solving the fine-mesh transport problem in the energy group structure of the cross section library. Although this approach produces the most accurate solution possible, it is still far too time consuming for a lattice physics code used at a fuel vendor, where millions of lattice calculations must be performed each year in order to support reload core design work. Because of this, the need for a suitable condensation scheme will not go away anytime soon.

[Section 4](#) is devoted to a thorough description of the condensation scheme used in CASMO-4 and LANCER02.

1.6 Assembly Fine-Mesh Transport Calculation

Due to severe heterogeneities present in most modern bundle designs, the final two-dimensional lattice calculation (in the condensed energy group structure if a condensation scheme is employed) should be performed by modeling the lattice in its true geometry. This need renders many solution techniques obsolete due to the complex geometries of LWR fuel designs (cylinders arranged in square arrays, surrounded by channels with partial arcs, etc.). The most feasible techniques are those that solve the integral form of the transport equation. These techniques include the method of collision probabilities (CP) and its current coupling derivatives; the method of characteristics (MoC), and Monte Carlo methods. Monte Carlo methods are far too time consuming when detailed flux tallies in small regions are required, such as those needed for providing the means to solve the depletion chains in fuel pellets. For this reason, we will abandon the idea of using Monte Carlo techniques directly and focus on the other two possibilities.

1.6.1 The CCCP Method

The CP method is an outstanding choice for small problems, such as one-dimensional pin cells. However, because execution times and memory requirements increase with the square of the number of mesh, the straightforward CP method is a very poor choice for large problems, such as full-size lattices. One way around this is to decouple cells and connect them via surface currents, as we did for the coupling calculation in the condensation scheme. This is the approach used for the assembly fine-mesh transport calculation in HELIOS and derivatives thereof. In order to do this, however, an assumption must be made about the distribution of the current in both angle and space as it leaves or enters a cell. Such an assumption will introduce a certain error into the solution, which will manifest itself around cells containing strong absorbers (control rods, control blades, absorber pins, fuel pins containing Gadolinium, etc.). This is highly undesirable for lattice physics code modeling LWR assemblies, since all of the above-mentioned absorbers are present, to some degree, in every assembly design. In addition, anisotropic scattering effects are nearly impossible to model explicitly in the CP method and we are forced to rely solely on transport-corrected cross sections, which tend to be more than adequate for single assembly calculations using perfectly reflective boundary conditions.

The transmission probabilities method used in the first release of HELIOS is referred to as the CCCP method (Current Coupling of the space elements, which are internally treated by collision probabilities (Casal et al. 1991)). It is a method that has since been employed in other lattice physics codes, such as LANCER01 (Azekura et al. 2003) and PARAGON (Ouisloumen et al. 2001). The premise is to perform a very detailed transport solution within a cell, which for fuel pins is made up of the fuel pellet, cladding, and coolant, and possibly including the initial expansion gap between the pellet and the cladding. The surface of each cell is split into multiple regions and a separate current is calculated for each unique region of the surface, as illustrated in  Fig. 6 where each surface has been split in half. This provides a means for modeling spatial changes in the surface current. In the original HELIOS work, the angular distribution of the current is represented using the quadrature used to model neutron transport within the cell: that is, which ever quadrature is used to integrate the collision probabilities within the cell, the same is also used to subdivide the current as it leaves one cell and enters the neighboring cell.

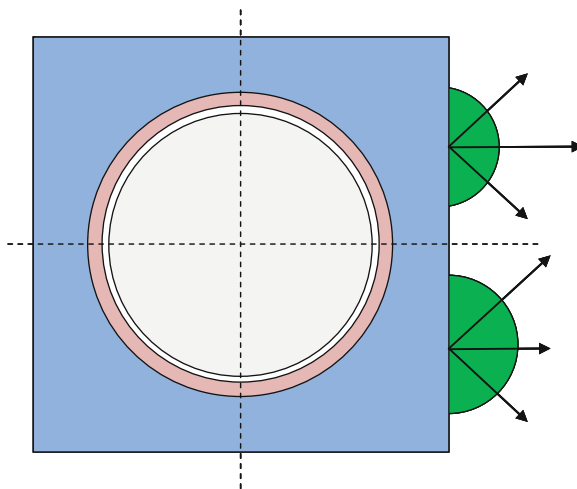


Figure 6
Outward directed currents split along a cell surface

The surface coupling is performed at different polar levels as well as different azimuthal angles, producing a current that can be anisotropic in all directions.

The coupled multigroup equations to be solved are

$$\Sigma_i^g \phi_i^g V_i = \sum_{n,m,l} \Gamma_{nm\rightarrow i}^g J_{nm\rightarrow i}^{-g} A_{nm} + \sum_j P_{j\rightarrow i}^g \sum_{g'} \left(\Sigma_j^{g'\rightarrow g} + \frac{\chi_j^g}{\lambda} v \Sigma_{f,j}^{g'} \right) \phi_j^{g'} V_j \quad (22)$$

$$J_{nm\rightarrow i}^{+g} = \sum_j P_{j\rightarrow nm\rightarrow i}^g \sum_{g'} \left(\Sigma_j^{g'\rightarrow g} + \frac{\chi_j^g}{\lambda} v \Sigma_{f,j}^{g'} \right) \phi_j^{g'} V_j + \sum_{n',m',l'} \Gamma_{n'm'l'\rightarrow nm\rightarrow i}^g J_{n'm'l'}^{-g} A_{n'm'} \quad (23)$$

where $J_{nm\rightarrow i}^{\pm,g}$ is the out-going/in-coming current from/to the cell in group g , through surface segment m , of cell boundary n , in direction l ; ϕ_i^g is the neutron flux in group g , mesh i of the cell; $P_{j\rightarrow i}^g$ is the probability for a neutron emitted in group g , mesh j , to suffer its first collision in mesh i ; $P_{j\rightarrow nm\rightarrow i}^g$ is the probability for a neutron emitted in group g , mesh j , to leave the cell through segment m of node boundary n in directional l ; $\Gamma_{n'm'l'\rightarrow nm\rightarrow i}^g$ is the probability for a neutron in group g , in-coming through segment m' , of cell surface n' , in directional l' , to suffer its first collision in mesh i ; $\Gamma_{n'm'l'\rightarrow nm\rightarrow i}^g$ is the probability for a neutron in group g , in-coming through segment m' ; cell surface n' ; in directional l' , to leave the cell through segment m of cell surface n in directional l ; A_{nm} is the area of segment m of surface n ; V_i is the volume of mesh i ; $\Sigma_i^g, v \Sigma_{f,i}^g, \Sigma_i^{g'\rightarrow g}$ are the macroscopic neutron cross sections in group g , mesh i ; χ_j^g is the fission neutron spectrum in mesh j ; and λ is the neutron multiplication factor.

Ray tracing is used to calculate collision probabilities between mesh within a given cell. The various regions of a cell (e.g., fuel, clad, and coolant) are subdivided further into flat source/flat flux mesh and the collision probabilities are used to redistribute the neutrons between the various mesh of a cell, based on the neutron source distribution in the mesh layout and the neutron current distribution across cell surfaces.

This whole effort is implemented in order to reduce the number of coupled mesh in the CP matrix. In a typical LWR lattice, there may be 5,000 mesh needed to accurately capture the physics of the problem using flat source regions. For a straightforward CP solution, this would require inverting a $5,000 \times 5,000$ matrix for every energy group – a rather daunting task even by today's standards. By decoupling cells from the CP solution, the problem is reduced to a collection of much smaller “mini” CP matrices – one for each cell in the problem (on the order of a couple of hundreds). The size of each mini CP matrix is on the order of 40×40 , except in cells containing fuel pellets with multiple depletion rings, where the mini CP matrix can be as large as 100×100 – still a much more manageable size compared to $5,000 \times 5,000$. The method still suffers from the approximation imposed by coupling cells via currents.

1.6.2 The Method of Characteristics

In contrast to the drawbacks associated with the method of collision probabilities and Monte Carlo methods, the method of characteristics has few drawbacks. Execution times and memory requirements increase linearly with the angular and spatial detail of the problem; the accuracy of the method can be virtually precise – assuming enough angular detail is used and the spatial mesh are small enough and the method can accommodate explicit modeling of anisotropic scattering, if needed. Additionally, the method is relatively simple to implement, compared with other methods.

The method of characteristics was originally introduced into WIMS in the early 1980s as the CACTUS module (Halsall 1980). That first incarnation of the method saw limited success, though, due to memory requirements and limitations in computers of the day. The first serious application in a commercial lattice physics code was introduced into CASMO-4 in the early 1990s, at a time when workstations had progressed to the point where memory was no longer a major issue (although it remained a minor issue for many more years to come). Since then, the method has found widespread use in other lattice physics codes, including a reawakening in WIMS and additional applications in DRAGON (Marleau et al. 1994), AEGIS (Sugimura et al. 2007), LANCER02 (Knott and Wehlage 2007), APOLLO-2 (Masiello et al. 2009), and most ironically HELIOS-2 (Wemple et al. 2008).

The MoC implemented in CASMO-4 and LANCER02 is the most basic of all the characteristic methods and is a direct derivative of the CACTUS module, first proposed by Askew in the 1970s (Askew 1972). The multigroup equation to be solved is the characteristic form of the Boltzmann equation,

$$\frac{d\Phi_{m,i}^G}{ds_m} + \Sigma_{tr,i}^G \Phi_{m,i}^G = Q_{m,i}^G \quad (24)$$

where s_m is a streaming track across a mesh at angle Ω_m ; $\Phi_{m,i}^G$ is the angular flux in direction Ω_m , across mesh i , in energy group G ; and $Q_{m,i}^G$ is the corresponding angular source, which can be calculated using transport-corrected cross sections or can be modeled using anisotropic scattering effects explicitly.

To solve the characteristic equation, streaming tracks are traced over the problem geometry at a number of different angles. Each angle has associated with it a weight, and each track has associated with it a width. Solution to the characteristics equation, in terms of the angular flux, is obtained along streaming rays and is of the form

$$\Phi_{m,i}^G(s_m) = \Phi_{m,i}^G(0)e^{-\Sigma_{tr,i}^G s_m} + \frac{Q_{m,i}^G}{\Sigma_{tr,i}^G}(1 - e^{-\Sigma_{tr,i}^G s_m}) \quad (25)$$

where the source across a mesh is considered constant (i.e., flat source approximation).

The scalar flux for a given mesh is calculated by integrating the angular flux along all streaming tracks that cross the mesh, and integrating over all directions of motion,

$$\phi_i^G = \int_{4\pi} \overline{\Phi}_i^G(\Omega) d\Omega = 4\pi \sum_m \overline{\Phi}_{m,i}^G \omega_m \quad (26)$$

where ω_m is the weight associated with each direction of motion and the average angular flux in a specific direction across a given mesh, $\overline{\Phi}_{m,i}^G$, is obtained from

$$\overline{\Phi}_{m,i}^G = \frac{\sum_k \overline{\Phi}_{m,k,i}^G \cdot s_{m,k,i} \cdot \delta A_m}{\sum_k s_{m,k,i} \cdot \delta A_m} \quad (27)$$

In (27), δA_m is the separation between parallel streaming tracks; $s_{m,k,i}$ is the length of the streaming track crossing mesh i ; and k represents the different streaming tracks that cross mesh i in direction Ω_m . To obtain an expression for the average value of the angular flux along a streaming track, $\overline{\Phi}_{m,k,i}^G$, (25) is integrated along track k , in direction Ω_m , crossing mesh i , and divided by the length of the track,

$$\overline{\Phi}_{m,k,i}^G = \frac{\int_0^{s_{m,k,i}} \Phi_{m,k,i}^G(s') ds'}{\int_0^{s_{m,k,i}} ds'} \quad (28)$$

Solution to the characteristic equation reduces to finding the intersections between rays and mesh boundaries and calculating the angular flux between intersections. The final solution to the equation produces a very detailed, very accurate flux distribution throughout the lattice (in the condensed energy group structure, if a condensation scheme is employed).

Due to its prominence in lattice physics, [Sect. 5](#) is devoted to a thorough description of the method of characteristics as applied to the two-dimensional fine-mesh lattice calculation.

1.7 Fundamental Mode Calculation

The fine-mesh assembly calculation assumes perfect reflection on all surfaces of the bundle. In this way, there are no neutrons leaking into or out of the system. However, the data generated by the lattice physics code will be used in a nodal code to model an entire reactor core and, within the reactor core, there are almost always neutrons leaking into or out of each node in the system. To be consistent with the way in which the nodal cross sections are to be used, the lattice physics code should somehow account for neutron leakage at the assembly level.

Leakage effects can be included in an ad hoc way by performing a buckling calculation on the system. The leakage calculation typically involves solving the fundamental mode equation in the diffusion approximation for the material buckling of the system,

$$\bar{\Sigma}_r^g \Psi^g + B_m^2 \bar{D}^g \Psi^g = \sum_{g' \neq g} \bar{\Sigma}_s^{g' \rightarrow g} \Psi^{g'} + \chi^g \quad (29)$$

where the lattice-averaged diffusion coefficient, \bar{D}^g , is calculated as

$$\bar{D}^g = \frac{1}{3\bar{\Sigma}_{tr}^g} \quad (30)$$

The lattice-averaged removal cross section, $\bar{\Sigma}_r^g$ is calculated as

$$\bar{\Sigma}_r^g = \bar{\Sigma}_{tr}^g - \bar{\Sigma}_s^{g \rightarrow g} \quad (31)$$

and the lattice-averaged cross sections are calculated by volume and flux weighting the cross sections from the various regions of the problem,

$$\bar{\Sigma}_x^g = \frac{\sum_i \bar{\Sigma}_{x,i}^g \phi_i'^g V_i}{\sum_i \phi_i'^g V_i} \quad (32)$$

In (32), x is a reaction type and $\phi_i'^g$ is the MoC flux distribution expanded back to the energy group structure of the cross section library,

$$\phi_i'^g = \tilde{\phi}_i^g \cdot \frac{\phi_i^G}{\sum_{g \in G} \tilde{\phi}_i'^g} \quad (33)$$

To create a lattice-averaged fission spectrum using the averaging technique represented in (32), $\bar{\chi}^g$, the summation should include only the fuel regions in the lattice.

The flux distribution in (33) has been expanded back to the energy group structure of the cross section library in order to more accurately account for leakage effects in the fast energy group range, where the majority of neutron leakage occurs. In (33), $\tilde{\phi}_i^g$ is the condensation flux from (21), and ϕ_i^G is the flux from the broad-group MoC calculation, given by (26).

Equation (27) assumes that the flux has been normalized such that a single absorption occurs in the system, $\sum_g (\bar{\Sigma}_a^g + \bar{D}^g B_m^2) \Psi^g = 1$. The multiplication factor of the system is then calculated from

$$k_{eff} = \sum_g v \bar{\Sigma}_f^g \Psi^g \quad (34)$$

The material buckling is adjusted until $k_{eff} = 1.0$. That is, an initial calculation is performed by setting $B_m^2 = 0$. This reproduces the infinite lattice multiplication factor. Next, a second calculation is performed by setting the buckling to a very small positive value, for example, $B_m^2 = 10^{-6}$. The multiplication factors from the first two calculations are used to extrapolate the buckling value to a new value and the corresponding multiplication factor is calculated using

(34). This process continues until a multiplication factor sufficiently close to unity is obtained (i.e., $|k_{eff} - 1| < 0.00001$). This produces the flux spectrum for a critical system and the expanded flux distribution from the MoC solution is adjusted to account for leakage effects,

$$\phi_i''^g = \phi_i'^g \cdot \frac{\Psi^g \cdot \sum_i V_i}{\sum_i \phi_i'^g V_i} \quad (35)$$

Equation (35) represents the final flux distribution for the lattice. The leakage flux can be used to create the nodal data and to deplete the burnable isotopes in the fuel. We also need the adjoint flux in order to accurately generate nodal kinetics data for the effective delayed neutron fraction, β_{eff}^m , and the prompt neutron lifetime, l_p ,

$$\beta_{eff}^d = \frac{\sum_{iso} \left[\sum_g \beta_{iso}^d \chi_d^g \Psi^{\dagger g} \cdot \sum_g \nu \sigma_{f,iso}^g N_{iso} \Psi^g \right]}{\sum_g \chi^g \Psi^{\dagger g} \cdot \sum_g \nu \Sigma_f^g \Psi^g} \quad (36)$$

$$l_p = \frac{\sum_g \frac{1}{\nu^g} \Psi^{\dagger g} \Psi^g}{\sum_g \chi^g \Psi^{\dagger g} \cdot \sum_g \nu \Sigma_f^g \Psi^g} \quad (37)$$

where the outer summation in (36) is over all isotopes in the fuel and d represents a delayed neutron group.

The adjoint flux is obtained by solving the adjoint to the fundamental mode equation,

$$\Sigma_r^g \Psi^{\dagger g} = \sum_{g' \neq g} \Sigma_s^{g \rightarrow g'} \Psi^{\dagger g'} + \nu \Sigma_f^g \quad (38)$$

where the removal cross section now contains the leakage term

$$\bar{\Sigma}_r^g = \bar{\Sigma}_{tr}^g - \bar{\Sigma}_s^{g \rightarrow g} - B_m^2 \bar{D}^g \quad (39)$$

In this derivation, the spatial component of the adjoint flux is assumed to be equivalent to the spatial component of the forward flux and only the energy distribution of the adjoint flux is assumed to differ from that of the forward flux. This is a very good assumption when there is no spatial leakage explicitly modeled in the system, as is the case for our lattice physics calculations.

1.8 Gamma Transport Calculation

The gamma transport calculation is used to generate a detailed rod-by-rod gamma energy deposition that can be used to determine the gamma heating contribution to the total power distribution. The calculation can also provide a gamma detector response for reactors that contain a gamma TIP (Traversing Incore Probe) system or that use gamma thermometers as a stationary detector system. In BWRs, the detector tube is located in the corner of the lattice that is diagonally opposite to the corner in which the control blade resides.

The gamma transport calculation can be performed using the same computational module as that used to solve the neutron transport problem. Steady state gamma sources are calculated for each region of the lattice in the energy group structure of the accompanying gamma library. The gamma calculation is a fixed source calculation, where the sum of prompt and delayed gamma sources, due to neutron capture and fission, are given by the following expressions:

$$q_{\text{capture}}^g = \sum_g N_{\text{iso}} \sigma_{\text{capture},\text{iso}}^g V_i \phi_i''^g q_{\text{capture},\text{iso}}^g \chi_{\text{capture},\text{iso}}^{g \rightarrow \gamma} \quad (40)$$

$$q_{\text{fission}}^g = q_{\text{fission},\text{iso}} \chi_{\text{fission},\text{iso}}^g \sum_g N_{\text{iso}} \sigma_{\text{fission},\text{iso}}^g V_i \phi_i''^g \quad (41)$$

Here, $q_{\text{capture},\text{iso}}^g$ is the gamma energy (in MeV/fission) released by neutron capture in isotope iso , neutron energy group g ; $q_{\text{fission},\text{iso}}$ is the total gamma energy (in MeV/fission) released through fission in isotope iso ; $\chi_{\text{capture},\text{iso}}^{g \rightarrow \gamma}$ is the gamma spectrum that distributes the energy released from neutron capture in neutron group g , isotope iso , to gamma energy group γ ; $\chi_{\text{fission},\text{iso}}^g$ is the gamma spectrum that distributes the energy released from fission in isotope iso ; $\sigma_{\text{capture},\text{iso}}^g$ and $\sigma_{\text{fission},\text{iso}}^g$ are the gamma microscopic cross sections; V_i is the volume of material region i ; and $\phi_i''^g$ is the neutron flux in material region i , neutron energy group g obtained from (35). The total fixed source in each region of the problem is the sum of (40) and (41).

The gamma transport calculation can use the same geometry and angular detail to solve the transport equation as is used to determine the neutron flux distribution. There is no condensation applied to the gamma cross sections and the flux is determined in the energy group structure of the gamma library. Typical gamma libraries contain no more than a couple of dozen energy groups.

For lattice physics codes based on the MoC, the equation to be solved is (25), where the total fixed source per mesh, i , is given by

$$q_i^\gamma = q_{\text{capture},i}^\gamma + q_{\text{fission},i}^\gamma + \sum_{\gamma'} \Sigma_{s,i}^{\gamma' \rightarrow \gamma} \phi_i^{\gamma'} \quad (42)$$

In (42), $\Sigma_{s,i}^{\gamma' \rightarrow \gamma}$ is the macroscopic gamma scattering cross section. From (42), the isotropic angular source needed in (25) is calculated as $Q_{m,i}^\gamma = q_i^\gamma / 4\pi$, m being the angular direction.

Gamma energy deposition in each unique material region of the lattice is calculated by using the converged gamma fluxes and macroscopic energy deposition cross sections,

$$E_i = \sum_\gamma \Sigma_{e,i}^\gamma V_i \phi_i^\gamma \quad (43)$$

where the energy deposition cross section, $\Sigma_{e,i}^\gamma$, accounts for contributions from the photoelectric effect, pair production, and Compton scattering.

The detector response is defined as the energy deposited to the detector and normalized to the lattice power level. A good approximation for the energy deposition cross section for the detector is to use the value for Fe. The equation for calculating the gamma detector response is given by

$$R = \frac{\sum_\gamma \sigma_{e,\text{Fe}}^\gamma \phi_{\text{DET}}^\gamma}{P} \quad (44)$$

where $\phi_{\text{DET}}^{\gamma}$ is the gamma flux at the location of the detector tube and $\sigma_{e,\text{Fe}}^{\gamma}$ is the microscopic gamma energy deposition cross section for some representative material, for example, Fe. P is the lattice power level, in MeV.

1.9 Power Distribution Calculation

The power generated in a fuel rod is the sum of energy from gamma and beta decay, as well as kinetic energy from fission. The various contributions to the power can be calculated from the following relationships:

Kinetic energy:

$$E_{\text{kinetic}} = \sum_{iso} q_{\text{fission},iso} \sum_i \sum_g N_{iso,i} \sigma_{f,iso,i}^g V_i \phi_i^g \quad (45)$$

Total gamma energy:

$$E_{\gamma} = \sum_i \sum_{\gamma} \Sigma_{e,i}^{\gamma} V_i \phi_i^{\gamma} \quad (46)$$

Beta energy due to capture (a very minor contributor):

$$E_{\beta,i} = \sum_{iso} q_{\beta,iso} \sum_i \sum_g N_{iso,i} \sigma_{a,iso,i}^g V_i \phi_i^g \quad (47)$$

Neutron slowing down:

$$E_{\text{SD},i} = \sum_{iso} \sum_i \sum_g \sum_{g'>g} N_{iso,i} \sigma_{s,iso,i}^{g' \rightarrow g} V_i \phi_i^g \cdot \left(\bar{E}^g - \bar{E}^{g'} \right) \quad (48)$$

where i is a material region; g is a neutron energy group; and γ is a gamma energy group. The microscopic neutron cross sections per isotope are for fission, σ_f^g , absorption, σ_a^g , and scattering, $\sigma_s^{g' \rightarrow g}$. \bar{E}^g is the average energy per neutron group. The summations for i are over all mesh in a specific fuel region.

1.10 Burnup Calculation

The last step of the lattice physics calculation is to determine the change in fuel isotopes over a specified period of time, referred to as a *burnup step*. The equation to be solved is the first-order differential equation of the type (Knott and Wehlage 2007)

$$\begin{aligned} \frac{dN_{iso}}{dt} = & \sum_{iso'} u_{iso,iso'} \lambda_{iso'} N_{iso'} + \sum_{iso'} v_{iso,iso'} \left(\sum_g \sigma_{c,iso'}^g \phi''^g N_{iso'} \right) \\ & + \sum_{iso'} w_{iso,iso'} \left(\sum_g \sigma_{(n,2n),iso'}^g \phi''^g N_{iso'} \right) + \sum_{iso'} \gamma_{iso,iso'} \left(\sum_g \sigma_{f,iso'}^g \phi''^g N_{iso'} \right) \\ & - \left\{ \lambda_{iso} + \left(\sum_g \sigma_{a,iso}^g \phi''^g \right) + \left(\sum_g \sigma_{(n,2n),iso}^g \phi''^g \right) \right\} \cdot N_{iso} \end{aligned} \quad (49)$$

where $\mathbf{u}_{iso,iso'}$, $\mathbf{v}_{iso,iso'}$, $\mathbf{w}_{iso,iso'}$ are branching ratios for decay, neutron capture, and (n, 2n) reactions, respectively; λ_{iso} is the decay constant; $\gamma_{iso,iso'}$ is the fission yield; and ϕ''^g is the flux distribution from (35). The symbols *iso* and *iso'* in (49) represent different isotopes. Equation (49) has a solution of the form

$$N_{iso}(\Delta t) - N_{iso}(0) = (Q - \tilde{\lambda}_{iso} N_{iso}(0)) \frac{(1 - e^{-\tilde{\lambda}_{iso} \cdot \Delta t})}{\tilde{\lambda}_{iso}} \quad (50)$$

where the effective decay constant, $\tilde{\lambda}_{iso}$, is equal to

$$\tilde{\lambda}_{iso} = \lambda_{iso} + \left(\sum_g \sigma_{a,iso}^g \phi''^g \right) + \left(\sum_g \sigma_{n2n,iso}^g \phi''^g \right) \quad (51)$$

and the production term, Q , is assumed constant over a small time interval, Δt .

The analytical solution to (49) can be obtained using a fourth order Runge–Kutta–Gill numerical algorithm for the predictor step, or by several other methods. ➔ Section 6 is devoted to a detailed description of the burnup solution in lattice physics codes.

1.11 Edits

Results from the lattice physics code to the corresponding three-dimensional nodal code are produced in two distinct categories: (1) cross sections that have been condensed and homogenized to represent the characteristics of the entire lattice, and (2) form factors that represent pin-by-pin distributions across the lattice.

The condensed and homogenized cross sections can be created by flux and volume weighting cross sections from every region of the lattice

$$\Sigma_x^h = \frac{\sum_i \sum_{g \in h} \Sigma_{x,i}^g V_i \phi_i''^g}{\sum_i \sum_{g \in h} V_i \phi_i''^g} \quad (52)$$

where x is a reaction type, such as absorption, fission, etc.; the flux, $\phi_i''^g$, includes leakage and is obtained from (35), and h represents the energy group structure of the nodal code, which has commonly been defined as two energy groups with the boundary between the fast and thermal groups at 0.625 eV, although there is some variation to this within the industry.

Form factors typically take the form of a two-dimensional normalized distribution. These factors can represent many physical properties from the lattice calculation, such as a pin-by-pin power distribution, multiple pin-by-pin isotopic distributions, and a pin-by-pin exposure distribution etc. The form factors are usually normalized to an average value of unity with a corresponding scaling factor that is passed to the nodal code. The nodal code can then superimpose the pin-by-pin shape from the lattice physics calculation onto the intra-nodal flux shape. For a more accurate super-positioning, form factors can be broken into individual pieces for each nodal energy group. For instance, the pin-by-pin power distribution can be broken into a fast group distribution and a thermal group distribution before being edited by the lattice physics code. Fast group distributions tend to be fairly flat across the assembly, while thermal group distributions tend to vary significantly from one pin location to another, especially in BWR assemblies.

Along with the form factors, the lattice physics code must also edit surface fluxes, surface currents, and assembly discontinuity factors. These data are used to transfer information about the heterogeneous assembly that would otherwise be lost from the homogeneous cross sections. The surface currents and surface fluxes are used in conjunction with the 2-D form factors in reconstructing the various pin distributions across the node.

Discontinuity factors are used by nodal codes to preserve surface currents from the lattice physics calculation. For a lattice calculation using reflective boundary conditions, the discontinuity factors are defined as

$$\text{DF}_S^h = \frac{\sum_{s \in S} \sum_{g \in h} A_s \psi_s^g}{\bar{\phi}^h} \quad (53)$$

where S is a specific surface of the assembly (north, south, etc.) and s are all the mesh that lie along that surface; A_s are the various surface areas that lie along the assembly surface, S ; ψ_s^g are the scalar fluxes lying along the assembly surface (i.e., the heterogeneous flux); $\bar{\phi}^h$ is the assembly homogeneous flux, and h is the nodal energy group structure. The homogeneous flux is the average flux across the assembly that would be produced by the homogenized cross sections,

$$\bar{\phi}^h = \frac{\sum_i \sum_{g \in h} V_i \phi_i^g}{\sum_i V_i} \quad (54)$$

where the heterogeneous fluxes are those obtained prior to the fundamental mode calculation.

Several parameters commonly edited by a lattice physics code are discussed in [Sect. 8](#).

1.12 Summary

This section has provided an overview of the calculational scheme used for a typical lattice physics code. The remainder of this chapter is devoted to describing, in depth, many of the features mentioned in this overview section. We will concentrate our discussions on methods that are considered to be somewhat current in lattice physics computations. The reader is directed to (Stamm'ler and Abbate 1983) for an in-depth discussion of legacy methods in lattice physics computations.

2 Cross Section Library

2.1 Objective

Various data for nuclear reactions are necessary for lattice physics computations, for example, fission, capture, absorption, scattering, (n , $2n$), and fission spectrum. The typical energy range considered in lattice physics computations ranges from 20 MeV down to 10^{-5} eV – from fast to thermal neutrons. The sources of these nuclear data are evaluated in nuclear data files such as ENDF, JEFF, and JENDL. These nuclear data files are collected for general-purpose utilization and thus contain highly detailed information on cross section data, for example, continuous energy (or “point-wise”) cross section data can be reconstructed from them. They contain cross

sections not only for neutrons but also for other particles, for example, electrons and photons. Covariance data that represent the uncertainty of cross section data are also included for some nuclides. A detailed description of a nuclear data file is, however, far beyond the scope of this section, but can be found in ➤ Chap. 4.

In principle, since a nuclear data file contains “everything,” it can be directly used in lattice physics computations. Such direct utilization of a nuclear data file, however, is not very efficient, for the following reasons:

First, since a nuclear data file is designed for general-purpose utilization, from the viewpoint of lattice physics computations, it contains much excess data. For example, the neutron fission cross section is sometimes classified according to the probability of fission. The inelastic scattering cross sections for different levels are tabulated independently. However, because such detailed classification is not necessary in common lattice physics computations appropriate data preprocessing becomes necessary.

Second, a nuclear data file adopts various formulae to describe the complicated behavior of cross sections, for example, the single and multilevel Bright Wigner and the Rich–Moore formulae used in the resonance peak. With some processing, these data can be used to reconstruct point-wise (or “continuous”) cross sections. The reconstructed point-wise cross sections are discrete (cross sections are given at discrete energy points), but have sufficient resolution to accurately reproduce the original continuous cross sections for nuclides. Since medium-to-heavy nuclides have many resolved resonances, a detailed description of these resonances is necessary. Consequently, for many nuclides, the typical number of energy points for point-wise cross sections ranges from several dozen to several hundred thousand. The reconstruction of a cross section requires considerable computation time, as discussed in ➤ Chap. 4. Furthermore, a great deal of memory is necessary when point-wise cross sections are directly used in lattice physics computations. As the above points make clear, preprocessing of cross sections is both necessary and useful.

What is much needed, then, is a dedicated database for the processed cross sections of various nuclides. In fact, a lattice physics code has its own dedicated cross section database, which is usually called a cross section library. We must note here that the source of cross sections (e.g., ENDF) is called a nuclear data file. The distinctions between a cross section library and cross section file can be confusing, and will be clarified in this section.

Since lattice physics computations are usually carried out in multiple groups (typically, several dozen to a few hundred groups), the number of energy groups in a cross section library is chosen to suit the calculation. A detailed discussion on the number of energy groups and the energy group structure is given in ➤ Sect. 2.2.

The major objective of a lattice physics computation is to provide a set of cross sections for successive core analysis. Therefore, a portion of the cross section data in a nuclear data file is not necessary in lattice computations. In ➤ Sect. 2.3, some typical cross sections used in lattice physics computation will be discussed.

Various processing steps are necessary for the preparation of a cross section library, and nuclear data processing codes are used for this purpose. A general-purpose cross section processing code (e.g., NJOY) and a dedicated post-processing code for library tabulation are commonly used to prepare a cross section library. Though a detailed discussion of nuclear data processing codes is presented in ➤ Chap. 4, a brief discussion that is relevant to cross section library preparation is offered in ➤ Sect. 2.4.

Since numerous data are necessary for cross section data, the methods of tabulation for cross section data are essential for their efficient storage and usage. ➤ Section 2.5 addresses some

key considerations on the tabulation of cross section data, and the structure and contents of a cross section library.

2.2 Choice of Energy Group Structure

The number of energy groups in a cross section library has a significant impact on lattice physics computations from two important points of view, namely, accuracy and computation time. And expectedly, there exists a trade-off between these two parameters. When the number of energy groups is small, the computation time will be short but the accuracy of the calculations might be insufficient. On the other hand, a large number of energy groups can be favorable in terms of accuracy, yet can be impractical due to the long computation time required. If we are to mitigate these contradictions, then the choice of energy group structure becomes crucial. There are two areas in which we can influence this: the number of energy groups, and their structure. We should note that some resonance calculation methods (the subgroup method, and ultrafine energy group calculation) may require a dedicated energy group structure. This topic will be discussed in [Sect. 3](#).

For typical light water reactors, anywhere from several dozen to a few hundred energy groups are adopted in a cross section library used in lattice physics computations. As a general trend, the number of energy groups used in the most recent lattice physics codes is increasing. This is due to improvements in storage capacity, and the higher processing speed of the affordable computers used for production calculations.

As discussed above, a larger number of energy groups allows for a more detailed representation of the energetic behavior of the neutron spectrum, which in turn can be applied with improved accuracy to a wider range of fuel assembly designs. Though the number of energy groups is quite important, the structure of the energy groups is crucial as well. These two factors are strongly interdependent, that is, the number of energy groups depends on the energy group structure, and vice versa.

The choice of an energy group structure is quite difficult. In general, this choice requires that four important physical phenomena in the reactor must be taken into account. The first of these is the generation of fission neutrons in the fast energy range. The second is the slowing down and diffusion of neutrons in the fast to resonance energy range. The third is the resonance absorption, and the final factor is the thermalization of neutrons in the thermal energy range. In order to appropriately incorporate these four phenomena, the energy range of a cross section library is typically divided into three parts: fast, resonance, and thermal regions. The fast range (typically 20 MeV to 10 keV) is usually divided into groups of equal lethargy width to capture the fission, slowing down, and diffusion phenomena. We must note that a sufficiently high upper energy boundary (20 MeV) is important in order to accurately capture an $(n, 2n)$ reaction.

In the resonance energy range (typically 10 keV to 1 eV), the widths of the energy groups should be small when a cross section shows rapid variations in energy, that is, in the resonance region. However, when all the resonances of all nuclides are explicitly taken into account, the energy group structure will be very fine, that is, comparable to point-wise energy groups (a few hundred thousand). From this point of view, the choice of energy group structure also depends on resonance calculation methods, which will be discussed in [Sect. 3](#).

For accurate resonance calculations, the significant resonance peaks should generally be located in the center of the energy group. Since the “significant” resonance depends on the

dominant nuclides appearing in lattice physics computations, it inherently depends on the given type of target reactor. In the case of light water reactor analyses, the first priority is given to major resonances of ^{238}U , and then those of ^{235}U and plutonium isotopes. However, care should also be taken for intermediate weight nuclides such as Fe and Ni, which are important as structural materials. These nuclides also have many resonances in the medium-to-high energy range, and accurate consideration of these resonances is very important, especially for PWR, in which baffle plates or heavy reflectors are made of stainless steel.

The thermal energy range (typically 1 to 10^{-5} eV) is divided into groups of equal lethargy or equal energy width to capture the Maxwell energy distribution of thermal neutrons. Special care must be taken at the boundary of resonance and thermal energy regions, which is usually called the thermal cut-off energy. In the typical thermal energy range, neutron up-scatter, which is caused by the thermal vibration of the nucleolus, is considered through up-scattering cross sections. Therefore, the thermal cut-off energy is set in order to cover the up-scattering effect. In light water reactor analysis, a few electronvolts (eV) is usually sufficient. In the case of graphite-moderated reactors, however, a higher thermal cut-off energy (~ 4 eV) is necessary, due to the greater up-scattering by graphite.

Up-scattering may also pose a challenge in the treatment of resonances at low energy around the thermal cut-off energy. Two issues may need to be addressed for resonance treatment at low energy. The first is the preparation of effective cross sections. In the usual resonance calculations, the neutron slowing down equation is solved from a higher to a lower energy without consideration of up-scattering. By using the neutron spectrum obtained by the neutron slowing down equation, effective cross sections can be evaluated; the effect of up-scattering on the neutron spectrum (and thus on effective cross sections) is therefore not taken into account. Next, many cross section libraries do not have a self-shielding table to evaluate effective cross sections in the thermal energy range, since resonances appear in the epithermal – resonance (i.e., higher than thermal) energy range. Therefore, when large resonances in the thermal energy range have a considerable impact on calculation results, their treatment should be carefully considered. A typical example of such resonances is the giant resonance of ^{240}Pu around 1 eV shown in [Fig. 7](#).

In many cross section libraries for light water reactor analyses, the above resonance is treated by a fine energy group structure around 1 eV, as will be described later. In the following section, the principal energy group structures used in light water reactor analyses are briefly introduced.

2.2.1 WIMS 69 Groups

The 69 group energy structure of WIMS, which is designed for light water reactor analysis, is shown in [Table 1](#) (Askew et al. 1966; WIMS-D/4 2000). The WIMS energy group structure and those derived from it (e.g., 70 energy groups used in CASMO) have been widely used not only in academic investigations, but also for production calculations for light water reactors.

The WIMS library is divided into three parts: fast, resonance, and thermal energy ranges. The fast energy range (10 MeV to 9.118 keV) has 14 groups with an equal lethargy width of 0.5. This structure is selected to capture neutron slowing down and diffusion in the fast energy range, and the fast fission of ^{238}U . The resonance energy range (9.118 keV to 4 eV) is divided into 13 groups. The lethargy width in the resonance energy range is basically 0.5, but several energy boundaries are adjusted in order to put important resonances close to the center of groups. For

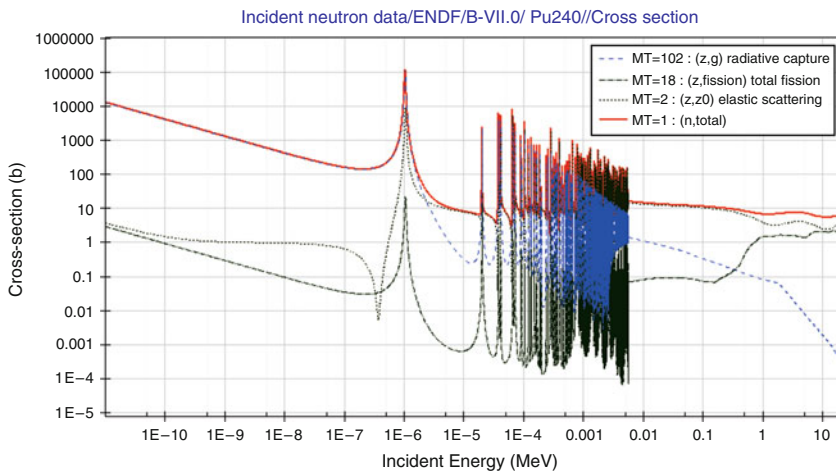


Figure 7

Large resonance of ^{240}Pu around the thermal cut-off energy

example, large resonances of ^{238}U located at 6.7, 20, and 33 eV are included in the 27th group (9.877 – 4.0 eV), 25th group (27.7 – 15.698 eV), and 24th group (48.052 – 27.7 eV), respectively.

A considerable number of energy groups are devoted to the description of the large resonance of ^{240}Pu at 1.0 eV. Since this large resonance is located near the thermal cut-off energy and is affected by thermal up-scattering, it is handled by fine energy discretization, rather than the utilization of a self-shielding table. The approximately 0.02 eV energy mesh is assigned near 1.0 eV. In the preparation of a self-shielding table, slowing down calculations are carried out in a very fine energy group structure, as described in [Sect. 3](#). This slowing down calculation is carried out without consideration of thermal up-scattering, so the utilization of a self-shielding table for resonances below the thermal cut-off energy should be carefully performed.

The thermal energy range is divided into 42 groups, which allows for a detailed description of the Maxwell spectrum of thermal neutrons. We must note that a fine energy mesh is also assigned around 0.3 eV, in which there is a broad resonance of ^{239}Pu .

2.2.2 XMAS 172 Groups

The XMAS 172 group structure is also designed for light water reactor analysis (Sartori [1990](#); Santamarina et al. [2004](#)). Therefore, the XMAS 172 group structure has features similar to those in WIMS 69 groups, for example, fine energy discretization around 1 eV, an energy boundary suitable for large resonances of ^{238}U at low energy. In fact, the XMAS group structure is derived from the WIMS 69 and APOLLO1 99 group structures.

This energy group structure was developed in France and is widely used in light water reactor analyses, particularly in European countries. Since the XMAS group structure has more detailed energy discretization than the WIMS structure, the XMAS group structure can be applied to more generic applications. For example, the XMAS group structure is more suitable for MOX or high burnup fuel analyses, since spectrum variations and resonance absorption by higher plutonium (^{242}Pu) and minor actinides can be taken into account more precisely. In order to accurately consider an (n, 2n) reaction that plays an important part in the burnup

Table 1

WIMS 69 group structure

Group	E_{\max} [eV]	Δu	Group	E_{\max} [eV]	Δu	Group	E_{\max} [eV]	Δu
1	1.000E+07	0.500	24	4.805E+01	0.551	47	5.000E-01	0.223
2	6.066E+06	0.500	25	2.770E+01	0.551	48	4.000E-01	0.134
3	3.679E+06	0.500	26	1.597E+01	0.480	49	3.500E-01	0.090
4	2.231E+06	0.500	27	9.877E+00	0.904	50	3.200E-01	0.065
5	1.353E+06	0.500	28	4.000E+00	0.192	51	3.000E-01	0.069
6	8.210E+05	0.496	29	3.300E+00	0.238	52	2.800E-01	0.113
7	5.000E+05	0.503	30	2.600E+00	0.214	53	2.500E-01	0.128
8	3.025E+05	0.503	31	2.100E+00	0.336	54	2.200E-01	0.201
9	1.830E+05	0.500	32	1.500E+00	0.143	55	1.800E-01	0.251
10	1.110E+05	0.500	33	1.300E+00	0.123	56	1.400E-01	0.336
11	6.734E+04	0.500	34	1.150E+00	0.024	57	1.000E-01	0.223
12	4.085E+04	0.500	35	1.123E+00	0.023	58	8.000E-02	0.177
13	2.478E+04	0.500	36	1.097E+00	0.024	59	6.700E-02	0.144
14	1.503E+04	0.500	37	1.071E+00	0.025	60	5.800E-02	0.148
15	9.118E+03	0.500	38	1.045E+00	0.024	61	5.000E-02	0.174
16	5.530E+03	0.452	39	1.020E+00	0.024	62	4.200E-02	0.182
17	3.519E+03	0.452	40	9.960E-01	0.024	63	3.500E-02	0.154
18	2.239E+03	0.452	41	9.720E-01	0.023	64	3.000E-02	0.182
19	1.425E+03	0.452	42	9.500E-01	0.043	65	2.500E-02	0.223
20	9.069E+02	0.904	43	9.100E-01	0.068	66	2.000E-02	0.288
21	3.673E+02	0.904	44	8.500E-01	0.086	67	1.500E-02	0.405
22	1.487E+02	0.678	45	7.800E-01	0.222	68	1.000E-02	0.693
23	7.550E+01	0.452	46	6.250E-01	0.223	69	5.000E-03	6.215

Δu : lethargy width.

calculation of heavy nuclides, the upper boundary of the energy groups is increased to 20 MeV. The energy group structure of XMAS is shown in [Table 2](#).

2.2.3 SHEM 281 Groups

The SHEM 281 group structure was designed to overcome certain potential deficiencies in the XMAS group structure (Hfaiedh and Santamarina 2005; Hebert and Santamarina 2008). The SHEM group structure is especially designed to avoid the resonance overlap effect among different nuclides. The resonances of major nuclides (heavy nuclides, fission products, structural

Table 2**XMAS 172 group structure**

Group	E_{\max} [eV]	Δu	Group	E_{\max} [eV]	Δu	Group	E_{\max} [eV]	Δu
1	1.964E+07	0.125	59	7.485E+02	0.100	117	1.150E+00	0.022
2	1.733E+07	0.150	60	6.773E+02	0.400	118	1.125E+00	0.014
3	1.492E+07	0.075	61	4.540E+02	0.200	119	1.110E+00	0.012
4	1.384E+07	0.175	62	3.717E+02	0.200	120	1.097E+00	0.024
5	1.162E+07	0.150	63	3.043E+02	0.400	121	1.071E+00	0.025
6	1.000E+07	0.200	64	2.040E+02	0.317	122	1.045E+00	0.010
7	8.187E+06	0.200	65	1.486E+02	0.083	123	1.035E+00	0.015
8	6.703E+06	0.100	66	1.367E+02	0.400	124	1.020E+00	0.024
9	6.065E+06	0.100	67	9.166E+01	0.192	125	9.960E-01	0.010
10	5.488E+06	0.200	68	7.567E+01	0.108	126	9.860E-01	0.014
11	4.493E+06	0.200	69	6.790E+01	0.200	127	9.720E-01	0.023
12	3.679E+06	0.200	70	5.560E+01	0.075	128	9.500E-01	0.021
13	3.012E+06	0.200	71	5.158E+01	0.067	129	9.300E-01	0.022
14	2.466E+06	0.100	72	4.825E+01	0.058	130	9.100E-01	0.057
15	2.231E+06	0.100	73	4.552E+01	0.125	131	8.600E-01	0.012
16	2.019E+06	0.200	74	4.017E+01	0.075	132	8.500E-01	0.073
17	1.653E+06	0.200	75	3.727E+01	0.100	133	7.900E-01	0.013
18	1.353E+06	0.100	76	3.372E+01	0.100	134	7.800E-01	0.101
19	1.225E+06	0.100	77	3.051E+01	0.100	135	7.050E-01	0.120
20	1.108E+06	0.100	78	2.761E+01	0.100	136	6.250E-01	0.146
21	1.003E+06	0.100	79	2.498E+01	0.100	137	5.400E-01	0.077
22	9.072E+05	0.100	80	2.260E+01	0.150	138	5.000E-01	0.030
23	8.209E+05	0.300	81	1.945E+01	0.200	139	4.850E-01	0.113
24	6.081E+05	0.100	82	1.593E+01	0.150	140	4.330E-01	0.079
25	5.502E+05	0.100	83	1.371E+01	0.200	141	4.000E-01	0.023
26	4.979E+05	0.100	84	1.122E+01	0.125	142	3.910E-01	0.111
27	4.505E+05	0.100	85	9.906E+00	0.075	143	3.500E-01	0.090
28	4.076E+05	0.300	86	9.190E+00	0.100	144	3.200E-01	0.017
29	3.020E+05	0.100	87	8.315E+00	0.100	145	3.145E-01	0.047
30	2.732E+05	0.100	88	7.524E+00	0.200	146	3.000E-01	0.069
31	2.472E+05	0.300	89	6.160E+00	0.142	147	2.800E-01	0.121
32	1.832E+05	0.400	90	5.346E+00	0.058	148	2.480E-01	0.120
33	1.228E+05	0.100	91	5.043E+00	0.200	149	2.200E-01	0.152

Table 2 (continued)

Group	E_{\max} [eV]	Δu	Group	E_{\max} [eV]	Δu	Group	E_{\max} [eV]	Δu
34	1.111E+05	0.300	92	4.129E+00	0.032	150	1.890E-01	0.049
35	8.230E+04	0.200	93	4.000E+00	0.168	151	1.800E-01	0.118
36	6.738E+04	0.200	94	3.381E+00	0.024	152	1.600E-01	0.134
37	5.517E+04	0.300	95	3.300E+00	0.176	153	1.400E-01	0.044
38	4.087E+04	0.100	96	2.768E+00	0.017	154	1.340E-01	0.153
39	3.698E+04	0.233	97	2.720E+00	0.045	155	1.150E-01	0.140
40	2.928E+04	0.067	98	2.600E+00	0.019	156	1.000E-01	0.051
41	2.739E+04	0.100	99	2.550E+00	0.077	157	9.500E-02	0.172
42	2.479E+04	0.400	100	2.360E+00	0.103	158	8.000E-02	0.038
43	1.662E+04	0.100	101	2.130E+00	0.014	159	7.700E-02	0.139
44	1.503E+04	0.300	102	2.100E+00	0.039	160	6.700E-02	0.144
45	1.114E+04	0.200	103	2.020E+00	0.046	161	5.800E-02	0.148
46	9.119E+03	0.200	104	1.930E+00	0.048	162	5.000E-02	0.174
47	7.466E+03	0.300	105	1.840E+00	0.047	163	4.200E-02	0.182
48	5.531E+03	0.100	106	1.755E+00	0.050	164	3.500E-02	0.154
49	5.005E+03	0.350	107	1.670E+00	0.049	165	3.000E-02	0.182
50	3.527E+03	0.050	108	1.590E+00	0.058	166	2.500E-02	0.223
51	3.355E+03	0.400	109	1.500E+00	0.017	167	2.000E-02	0.288
52	2.249E+03	0.100	110	1.475E+00	0.021	168	1.500E-02	0.405
53	2.035E+03	0.300	111	1.445E+00	0.053	169	1.000E-02	0.371
54	1.507E+03	0.050	112	1.370E+00	0.024	170	6.900E-03	0.322
55	1.434E+03	0.150	113	1.338E+00	0.028	171	5.000E-03	0.511
56	1.234E+03	0.200	114	1.300E+00	0.051	172	3.000E-03	5.704
57	1.010E+03	0.100	115	1.235E+00	0.054			
58	9.142E+02	0.200	116	1.170E+00	0.017			

Δu : lethargy width.

material nuclides, and burnable nuclides) are treated in different energy groups as much as possible up to 23 eV. The descriptions of slowing down and resonance scattering in coolant and structural material (^{16}O , ^{23}Na , ^{27}Al , ^{56}Fe , ^{58}Ni , and ^{55}Mn) are improved. Threshold reactions such as the inelastic scattering of ^{238}U and fission (1 – 0.1 MeV) are considered in the design of a library structure. Though the number of the energy group is increased (from 172 to 281), it offers higher calculation accuracy than conventional energy group structures. Since the maximum lethargy width in the SHEM structure is less than 0.2 in the slowing down energy region, it is applicable not only to LWR, but also to fast reactors.

The energy group structure of SHEM is shown in Table 3.

2.2.4 Other Energy Group Structures

Looking at recent improvements in cross section libraries, we find an increased number of energy groups in the resonance region. For example, in the latest version of CASMO, resonances in the low-energy ranges (<10 eV) are divided into fine energy groups in which a self-shielding table is not necessary. As a result, the number of energy groups in the cross section library

Table 3
SHEM 281 group structure

Group	Emax [eV]	Δu	Group	Emax [eV]	Δu	Group	Emax [eV]	Δu
1	1.964E+07	0.275	95	2.238E+01	0.010	189	5.320E+00	0.021
2	1.492E+07	0.075	96	2.216E+01	0.007	190	5.210E+00	0.019
3	1.384E+07	0.175	97	2.200E+01	0.014	191	5.110E+00	0.035
4	1.162E+07	0.150	98	2.170E+01	0.010	192	4.933E+00	0.034
5	1.000E+07	0.100	99	2.149E+01	0.007	193	4.768E+00	0.076
6	9.048E+06	0.100	100	2.134E+01	0.005	194	4.420E+00	0.025
7	8.187E+06	0.100	101	2.123E+01	0.004	195	4.310E+00	0.021
8	7.408E+06	0.100	102	2.114E+01	0.004	196	4.220E+00	0.054
9	6.703E+06	0.100	103	2.106E+01	0.004	197	4.000E+00	0.030
10	6.065E+06	0.200	104	2.098E+01	0.010	198	3.882E+00	0.045
11	4.966E+06	0.200	105	2.077E+01	0.004	199	3.712E+00	0.047
12	4.066E+06	0.200	106	2.068E+01	0.004	200	3.543E+00	0.120
13	3.329E+06	0.200	107	2.060E+01	0.004	201	3.142E+00	0.013
14	2.725E+06	0.200	108	2.052E+01	0.005	202	2.884E+00	0.039
15	2.231E+06	0.160	109	2.042E+01	0.007	203	2.775E+00	0.012
16	1.901E+06	0.150	110	2.028E+01	0.010	204	2.741E+00	0.008
17	1.637E+06	0.152	111	2.007E+01	0.024	205	2.720E+00	0.007
18	1.406E+06	0.050	112	1.960E+01	0.011	206	2.700E+00	0.022
19	1.337E+06	0.038	113	1.939E+01	0.010	207	2.640E+00	0.008
20	1.287E+06	0.102	114	1.920E+01	0.006	208	2.620E+00	0.012
21	1.162E+06	0.100	115	1.908E+01	0.060	209	2.590E+00	0.016
22	1.051E+06	0.100	116	1.796E+01	0.011	210	2.550E+00	0.032
23	9.511E+05	0.101	117	1.776E+01	0.011	211	2.470E+00	0.058
24	8.600E+05	0.197	118	1.756E+01	0.006	212	2.330E+00	0.025
25	7.065E+05	0.200	119	1.745E+01	0.036	213	2.273E+00	0.025
26	5.784E+05	0.158	120	1.683E+01	0.017	214	2.217E+00	0.027

Table 3 (continued)

Group	E_{\max} [eV]	Δu	Group	E_{\max} [eV]	Δu	Group	E_{\max} [eV]	Δu
27	4.940E+05	0.080	121	1.655E+01	0.031	215	2.157E+00	0.041
28	4.560E+05	0.100	122	1.605E+01	0.017	216	2.070E+00	0.039
29	4.125E+05	0.072	123	1.578E+01	0.059	217	1.990E+00	0.046
30	3.839E+05	0.180	124	1.487E+01	0.009	218	1.900E+00	0.065
31	3.206E+05	0.180	125	1.473E+01	0.009	219	1.780E+00	0.064
32	2.678E+05	0.152	126	1.460E+01	0.009	220	1.669E+00	0.050
33	2.300E+05	0.165	127	1.447E+01	0.015	221	1.588E+00	0.044
34	1.950E+05	0.167	128	1.425E+01	0.014	222	1.520E+00	0.051
35	1.650E+05	0.164	129	1.405E+01	0.036	223	1.444E+00	0.024
36	1.400E+05	0.131	130	1.355E+01	0.016	224	1.410E+00	0.021
37	1.228E+05	0.060	131	1.333E+01	0.056	225	1.381E+00	0.037
38	1.156E+05	0.200	132	1.260E+01	0.010	226	1.331E+00	0.029
39	9.466E+04	0.140	133	1.247E+01	0.013	227	1.293E+00	0.033
40	8.230E+04	0.200	134	1.231E+01	0.015	228	1.251E+00	0.030
41	6.738E+04	0.200	135	1.213E+01	0.012	229	1.214E+00	0.037
42	5.517E+04	0.100	136	1.198E+01	0.013	230	1.170E+00	0.019
43	4.992E+04	0.200	137	1.182E+01	0.009	231	1.148E+00	0.016
44	4.087E+04	0.100	138	1.171E+01	0.010	232	1.130E+00	0.012
45	3.698E+04	0.100	139	1.159E+01	0.028	233	1.116E+00	0.011
46	3.346E+04	0.133	140	1.127E+01	0.020	234	1.104E+00	0.011
47	2.928E+04	0.067	141	1.105E+01	0.023	235	1.092E+00	0.013
48	2.739E+04	0.048	142	1.080E+01	0.021	236	1.078E+00	0.041
49	2.610E+04	0.043	143	1.058E+01	0.108	237	1.035E+00	0.014
50	2.500E+04	0.097	144	9.500E+00	0.039	238	1.021E+00	0.012
51	2.270E+04	0.200	145	9.140E+00	0.018	239	1.009E+00	0.012
52	1.858E+04	0.137	146	8.980E+00	0.020	240	9.965E-01	0.015
53	1.620E+04	0.084	147	8.800E+00	0.014	241	9.820E-01	0.019
54	1.490E+04	0.091	148	8.674E+00	0.017	242	9.640E-01	0.021
55	1.360E+04	0.200	149	8.524E+00	0.027	243	9.440E-01	0.026
56	1.114E+04	0.200	150	8.300E+00	0.021	244	9.200E-01	0.044
57	9.119E+03	0.200	151	8.130E+00	0.020	245	8.800E-01	0.071
58	7.466E+03	0.200	152	7.970E+00	0.016	246	8.200E-01	0.130
59	6.113E+03	0.200	153	7.840E+00	0.013	247	7.200E-01	0.141
60	5.005E+03	0.200	154	7.740E+00	0.018	248	6.250E-01	0.049

Table 3 (continued)

Group	E_{\max} [eV]	Δu	Group	E_{\max} [eV]	Δu	Group	E_{\max} [eV]	Δu
61	4.097E+03	0.163	155	7.600E+00	0.029	249	5.950E-01	0.070
62	3.481E+03	0.150	156	7.380E+00	0.033	250	5.550E-01	0.065
63	2.996E+03	0.150	157	7.140E+00	0.021	251	5.200E-01	0.091
64	2.579E+03	0.150	158	6.994E+00	0.011	252	4.750E-01	0.096
65	2.220E+03	0.150	159	6.918E+00	0.007	253	4.316E-01	0.101
66	1.910E+03	0.168	160	6.870E+00	0.005	254	3.900E-01	0.100
67	1.614E+03	0.182	161	6.835E+00	0.004	255	3.530E-01	0.083
68	1.345E+03	0.170	162	6.811E+00	0.003	256	3.250E-01	0.064
69	1.135E+03	0.064	163	6.792E+00	0.002	257	3.050E-01	0.086
70	1.065E+03	0.160	164	6.776E+00	0.002	258	2.800E-01	0.094
71	9.075E+02	0.193	165	6.760E+00	0.003	259	2.550E-01	0.098
72	7.485E+02	0.200	166	6.742E+00	0.004	260	2.312E-01	0.098
73	6.128E+02	0.200	167	6.717E+00	0.013	261	2.096E-01	0.098
74	5.017E+02	0.200	168	6.631E+00	0.004	262	1.900E-01	0.160
75	4.108E+02	0.150	169	6.606E+00	0.003	263	1.619E-01	0.160
76	3.536E+02	0.100	170	6.588E+00	0.002	264	1.380E-01	0.140
77	3.199E+02	0.120	171	6.572E+00	0.002	265	1.200E-01	0.140
78	2.838E+02	0.160	172	6.556E+00	0.003	266	1.043E-01	0.150
79	2.418E+02	0.200	173	6.539E+00	0.004	267	8.980E-02	0.160
80	1.980E+02	0.200	174	6.515E+00	0.005	268	7.650E-02	0.160
81	1.621E+02	0.200	175	6.482E+00	0.008	269	6.520E-02	0.161
82	1.327E+02	0.200	176	6.432E+00	0.011	270	5.550E-02	0.160
83	1.086E+02	0.200	177	6.360E+00	0.013	271	4.730E-02	0.160
84	8.895E+01	0.170	178	6.280E+00	0.019	272	4.030E-02	0.158
85	7.505E+01	0.200	179	6.160E+00	0.016	273	3.440E-02	0.160
86	6.144E+01	0.154	180	6.060E+00	0.017	274	2.930E-02	0.161
87	5.267E+01	0.140	181	5.960E+00	0.027	275	2.494E-02	0.220
88	4.579E+01	0.040	182	5.800E+00	0.014	276	2.001E-02	0.300
89	4.400E+01	0.091	183	5.720E+00	0.018	277	1.483E-02	0.350
90	4.017E+01	0.175	184	5.620E+00	0.016	278	1.045E-02	0.380
91	3.372E+01	0.200	185	5.530E+00	0.008	279	7.145E-03	0.450
92	2.761E+01	0.116	186	5.488E+00	0.014	280	4.556E-03	0.600
93	2.459E+01	0.088	187	5.410E+00	0.006	281	2.500E-03	3.124
94	2.252E+01	0.006	188	5.380E+00	0.011			

 Δu : lethargy width.

reaches approximately 600 (Rhodes et al. 2006). Such fine groups are being used in production calculation due to the ongoing improvements in the capacity of affordable computers.

Another energy group structure sometimes used in lattice physics computation is that of so-called ultrafine energy groups (MC^{**}2-2 1999; Ishiguro 1974; Tsuchihashi et al. 1982; Williams et al. 2005; Huria and Ouislomen 2008; Sugimura and Yamamoto 2007). A very fine energy group structure is used in an ultrafine group's spectrum calculation in which resolved resonances are explicitly treated without self-shielding factors. Unfortunately, since the number of energy groups reaches from several thousand to several dozens of thousands, the preparation of an explicit scattering matrix becomes difficult on account of the storage it requires. To overcome this obstacle, a one-dimensional cross section (e.g., absorption, fission, capture, and elastic scattering) is stored in a cross section library. Neutron slowing down is evaluated from slowing down calculations that assume elastic scattering. A more detailed discussion of this will be provided in  Sect. 3.

2.3 Cross Sections Used in Lattice Physics Computations

Various cross sections are used in lattice physics computations. The following cross sections are usually necessary.

Total cross section: A total cross section is necessary for transport calculations in order to obtain neutron spatial distribution. In the principal lattice physics codes, transport-corrected (P0) cross sections are used instead of explicit treatment of anisotropic scattering.

Capture cross section: A capture cross section is necessary for burnup calculations.

Fission cross section: A fission cross section is necessary for burnup calculations as well as pin-power distribution calculations.

Production cross section: A production cross section, which is the product of a fission cross section and the average number of neutrons released per fission, is used in transport calculations to evaluate the reactivity of the fuel assembly.

Absorption cross section: For many nuclides, an absorption cross section can be obtained by the summation of the capture and fission cross sections. However, especially for light nuclides, other reactions may play significant role in neutron absorption. For example, most of the absorption reaction for ¹⁰B is (n, α). Therefore, the absorption cross section should be treated independently from the capture and fission reactions. In lattice physics computations, the absorption cross section is used to evaluate the reactivity of the fuel assembly. Neutron emission reactions other than fission may be considered as absorption cross sections, as described below.

(n, 2n) cross section: This reaction is important both in burnup calculation and in its contribution to reactivity. Since an (n, 2n) reaction increases the number of neutrons, its contribution to reactivity is positive. Note that an (n, 3n) reaction has a similar effect, but has a smaller impact than an (n, 2n) reaction since the cross section of (n, 3n) has a higher threshold energy and is smaller than that of (n, 2n). It is for this reason that in many lattice physics codes, only an (n, 2n) reaction is considered. In order to rigorously incorporate an (n, 2n) reaction, a dedicated treatment that is similar to fission is necessary. Many transport codes, however, do not incorporate the capability of such treatment. Therefore, an (n, 2n) cross section is usually subtracted from the absorption cross section since the “net neutron emission” in an (n, 2n) reaction is one (one absorption, two emissions). This apparently has a positive effect on reactivity. In this simplified treatment, the neutron emission spectrum is disregarded, and emitted neutrons are assumed to have the same energy as the absorbed neutron. When an (n, 3n) reaction is taken into account,

twice the $(n, 3n)$ cross section is subtracted from the absorption cross section. As described in [Figure 2.2](#), since $(n, 2n)$ is a threshold reaction, the upper limit of an energy group in a cross section library is important –20 MeV is necessary in order to accurately incorporate an $(n, 2n)$ reaction.

Scattering cross section: A scattering cross section is treated in matrix form. Though other reactions (e.g., fission) do not have anisotropy on the angular distribution of emitted neutrons, the elastic scattering reaction has considerable anisotropy. This anisotropy on the scattering reaction is expanded by the Legendre functions of the scattering angle. Not just the isotropic (P_0) component of a scattering matrix, but also higher-order anisotropic components (P_1, P_2 , and so on) can be considered. Light nuclides (e.g., hydrogen) have greater anisotropy since the neutrons are scattered in a more forward direction by these nuclides. Since the anisotropic scattering of hydrogen, which is a major nuclide in LWRs, has a large impact on neutron leakage from the core, this effect must be taken into account.

Anisotropic scattering may be explicitly taken into account when the transport calculation module in a lattice physics code has such capability. In fact, the method of characteristics, which is commonly used in the most recent lattice physics codes, can account for anisotropic scattering, though larger memory and longer computation time are required. However, the anisotropic component of a scattering matrix is also approximately taken into account by the transport-corrected total cross section (transport cross section), with a P_0 scattering cross section. When we use the transport-corrected cross section, the self-scattering cross section is also modified to maintain balance in the cross section. Described in more detail, the difference between the total and transport-corrected cross sections is subtracted from the self-scattering cross section.

The effect of anisotropic scattering becomes more important when the angular distribution of the neutron flux is far from isotropic. Since neutron absorption in MOX fuel is much greater than that in UO_2 fuel, the angular distribution of the neutron flux is more anisotropic. The effect of anisotropic scattering therefore becomes more important in MOX fuel analysis.

Another consideration in this regard is the order of anisotropic scattering that should be taken into account. Higher-order anisotropic scattering gives more accurate results, but requires more memory because of the higher-order scattering matrix. In a typical light water reactor analysis, the incorporation of P_1 scattering gives fair results. When up to P_3 components are taken into account, it gives an almost converged result on the treatment of anisotropic scattering. Note that when transport-corrected scattering is used, up to P_1 component is commonly taken into account.

Fission spectrum: Fission spectra are slightly different in each fissionable nuclide, as each fissionable nuclide has an independent fission spectrum. Furthermore, strictly speaking, a given fission spectrum also depends upon the incident neutron energy. In common lattice physics computations, however, such rigorous treatment is not necessary, and an approximate treatment can be applied, as will be described later.

Gamma cross sections: In fission and the successive decays of fission products, many photons (gamma rays) are emitted. The gamma ray plays an important role in the distribution of power in a reactor core since considerable energy (heat) is deposited due to the scattering and absorption of gamma rays. Since the mean free path of a gamma ray is larger than that of typical neutrons, gamma ray “removes” heat from pellet as the form of its energy and releases it at other places. In this sense, a gamma ray “smears” heat generation in a core, which is why this effect is known as gamma smearing. The gamma-smearing effect is important for the accurate evaluation of heat distribution in a fuel assembly.

Table 4Example of energy release per fission of ^{235}U

Form of released energy	MeV	Note
Kinetic energy of fission fragment	168	Heat deposit mainly in pellet
Prompt gamma ray	7	Gammer smearing
Kinetic energy of prompt neutrons	5	Possible heat deposit in moderator
Beta ray originated by decay of fission fragment	8	
Gamma ray originated by decay of fission fragment	7	Gammer smearing
Anti-neutrino	(12)	Cannot be recovered (escapes from reactor)
Gamma ray emitted by capture of fission neutron	3 ~ 12	Gammer smearing
Total	~ 202	

Source: Stacy (2001).

In many cases, the gamma-smearing effect flattens the power distribution in a core, but it may also increase pin-power for pellets with low power density. For example, the power density of a gadolinia-bearing fuel pellet is very low at the beginning of life (BOL) due to the extremely large absorption cross section of gadolinium isotopes. The gamma-smearing effect pushes up the pin-power of a gadolinia-bearing fuel rod at BOL.

Note that gamma smearing is also significant in a reflector that uses medium-heavy nuclides, such as stainless-steel reflectors in advanced type PWRs, and shielding fuel elements in fast breeder reactors. Gamma transport calculation is sometimes carried out to accurately estimate heat deposition by gamma rays. In this case, cross sections for the gamma rays are also necessary. The gamma production cross section is also necessary in order to estimate the gamma source.

Energy release per fission: The value of energy release per fission is not a “cross section,” but is a very important parameter in lattice physics computation, since it defines the normalization condition of the absolute value of neutron flux. Elementary textbooks on reactor physics tell us that the energy release per fission is approximately 200 MeV for ^{235}U . This is not incorrect, but we must be careful how we regard the breakdown of its contents. ➤ [Table 4](#) shows the breakdown of energy release by fission of ^{235}U . Since the energy balance due to fission and successive phenomena is complicated, one needs to be careful when setting values for energy release per fission.

2.4 Cross Section Processing

The source of nuclear data is an evaluated nuclear data file. In order to generate a cross section library for use in lattice physics computations, the processing of nuclear data files is necessary (Marcille and Mills 2003; Yamamoto et al. 2006; Yamamoto and Sugimura 2006). In general, nuclear data processing is divided into two parts. The first part is the generation of

general-purpose multigroup cross section data by a nuclear data processing code. The second part is the editing of cross section data into a suitable format of a lattice physics code. Some detailed description of these processes is presented below.

2.4.1 Generation of Multigroup Cross Section Data

As described before, nuclear data files such as ENDF/B, JEFF, and JENDL are not suitable for direct utilization in lattice physics codes (McLane 2001). Therefore, cross section processing codes are used to generate multigroup cross section data. Many lattice physics codes utilize the NJOY code, which is widely used not only in academia, but also in industry (MacFarlane and Muir 1994b). Though a detailed description of the NJOY code and the theoretical background of cross section processing are given in Chaps. 1 and 4, a brief description of cross section processing is given in this section, with a focus on the preparation of a lattice physics code for a cross section library.

The common nuclear data processing scheme by NJOY is described as follows. The modules of NJOY used in processing are given along with brief descriptions of the outline of processing.

MODER

Since a nuclear data file is given in text format, it is converted to binary format in order to perform rapid input/output during cross section processing.

RECONR

Though the original cross section data is “continuous,” it is energetically discretized for processing. The point-wise cross section data, which accurately reproduces the original continuous cross section data with cross sections at discrete energy grid points, are reconstructed from an original nuclear data file. The accuracy of a reconstructed cross section is determined by the number of energy grid points, and the structure of their point-wise cross sections. In order to reduce the number of energy grid points while retaining accuracy, a dedicated algorithm is used to thin out the energy grid points. In general, grid points are chosen so that the accuracy of the interpolated cross section data satisfies the required tolerance given by the user. The number of grid points of a point-wise cross section may reach a few hundred thousand for heavy nuclides with many resonances. The reconstructed data is written to an intermediate (working) file in the PENDF (point-wise ENDF) format.

BROARDR

The point-wise cross section data are generated at a base temperature (typically room temperature) in RECONR. Cross sections, however, are temperature dependent. Thus, cross section data in the resonance region are broadened by considering the Doppler effect in BROARDR. Specific temperatures are given by users for consideration of the Doppler effect.

THERMR

A cross section in the thermal energy range (~ 4 eV) is created by considering the thermal vibration of the nucleolus. When the chemical binding of a molecule is taken into account (e.g., H in H_2O , D in D_2O , and graphite), $S(\alpha, \beta)$ data, which describe the secondary energy distribution

of a scattered neutron, are also necessary as an input file. The $S(\alpha, \beta)$ data are given as a part of the evaluated nuclear data file.

UNRESR

Multigroup cross section data in the unresolved resonance energy region is given as a function of the background cross sections given in the input data. A narrow resonance approximation is used to evaluate an effective multigroup cross section. The NJOY code provides another approach for the resonance treatment of an unresolved resonance region by PURR. The PURR module can provide a probability table in addition to a self-shielding table for multigroup cross sections. The probability table can be used through the subgroup method, which will be described in [Sect. 3](#).

GROUPR

Since the reconstructed data is “point-wise,” an adequate neutron spectrum is necessary in order to evaluate effective (average) multigroup cross sections. The GROUPR module provides the capability of evaluating the neutron spectrum with the reconstructed point-wise cross sections. Therefore, the present module is highly important in the generation of a multigroup cross section library for lattice physics codes. The GROUPR module provides two different ways to estimate the point-wise neutron spectrum. The first is a very quick, simple approach based on the narrow resonance approximation. In this approach, the neutron flux is simply expressed as

$$\phi(E) = \frac{C(E)}{\sigma_t(E) + \sigma_0} \quad (55)$$

where

$\phi(E)$: neutron flux,

$C(E)$: base spectrum function,

$\sigma_t(E)$: microscopic total cross section of a nuclide,

σ_0 : background cross section.

Note that the theoretical background for resonance calculation will be described in [Sect. 3](#). Since no slowing down calculation is carried out, the generation of a multigroup cross section takes place quite quickly. However, since (55) is based on a narrow resonance approximation, its accuracy is not sufficient for broad resonances that appear in the epithermal energy region, for example, resonance of ^{238}U at 6.7 eV. That said, the above approach is usually satisfactory for the high-energy region in which each resonance is narrow enough, compared to the energy width of neutron slowing down. Note that various options are provided as $C(E)$ in the GROUPR module, that is, $1/E$, fission spectrum $+1/E$, fission spectrum $+1/E + \text{Maxwell}$. A suitable base spectrum function would be preferable for the generation of a cross section library. The base spectrum function can also be given as input data. Therefore, a typical spectrum (e.g., cell average spectrum in the operating condition of light water reactors) can be used. Some sensitivity analyses of the base spectrum function are desirable before the preparation of a cross section library.

The second option is a direct numerical solution of the neutron slowing down equation. In the GROUPR module, the second option can be used for the resolved resonance energy range, and the following equation is usually solved:

$$(\sigma_t(E) + \sigma_0) \phi(E) = \int_E^{E/\alpha} \frac{\sigma_s(E')\phi(E')}{(1-\alpha)E'} dE' + \int_E^{E/\alpha_0} \frac{\sigma_0\phi(E')}{(1-\alpha_0)E'} dE' \quad (56)$$

where

$$\alpha := \left(\frac{A-1}{A+1} \right)^2, \text{ } A \text{ is the relative mass of a nuclide to a neutron,}$$

$$\alpha_0 := \left(\frac{A_0-1}{A_0+1} \right)^2, \text{ } A_0 \text{ is the relative mass of a background nuclide to a neutron,}$$

$\sigma_s(E)$: elastic scattering cross section.

As commonly calculated, hydrogen is assumed as a background nuclide; thus α_0 is set at a very small value (e.g., 10^{-7}). When the mass effect of a moderator is taken into account as the lambda parameter, different A_0 values are used to solve (56). A detailed discussion of this issue will be presented in  Sect. 3.

Though the direct numerical solution of (56) is quite accurate, it may also be time consuming. The computation time depends on the number of points of reconstructed cross sections. In the case of heavy nuclides (e.g., ^{238}U and ^{239}Pu), the number of the reconstructed cross section point may reach a few hundred thousand. Since slowing down calculations are repeatedly carried out for different background cross sections (typically 10–20 different background cross sections for major resonance isotopes), and for different temperatures (typically several temperature points), the computation time needed to process a heavy nuclide may be more than several hours on a modern PC or Workstation.

The obtained effective multigroup cross sections are written into a file in a GENDF (group-wise ENDF) format. The GROUPR module has various options for the energy group structure. The major energy group structures are hardwired in the GROUPR module, for example, WIMS 69 groups and XMAS 172 groups. Of course, an arbitrary energy group structure can be also given for the GROUPR module.

MATXS

The multigroup cross section (GENDF) generated by GROUPR is converted to the MATXS format that can be used in some application codes. Since the MATXS format is versatile, it is useful for many lattice physics codes.

Other Modules

When gamma transport calculations are carried out in a lattice physics code, multigroup cross sections for gamma rays are necessary (Wemple et al. 2008; Mertyurek 2007). In this case, a KERMA (kinetic energy released in material) factor evaluation by the HEATR module, and gamma cross section evaluations by the GAMINR module, are necessary.

The NJOY code can provide a cross section library for the MCNP code, which is a continuous energy Monte Carlo code frequently used for the validation and verification of lattice physics codes. The ACER module is used for the preparation of an MCNP library. When a cross section library for MCNP is generated by the NJOY code and is used for verification, “consistent comparison” between a Monte Carlo code and a lattice physics code can be carried out. Such comparisons (verification and validation) yield rich information regarding the soundness of lattice physics codes.

A cross section library for the widely used lattice physics code WIMS, can be generated through the WIMSR module. Even if direct utilization of the WIMS code is not considered, the output of the WIMSR module provides an invaluable benchmark for a cross section library of

lattice physics codes. As discussed later, the post-processing of NJOY outputs is usually carried out to generate a cross section library of a lattice physics code. Certain aspects of this post-processing are highly complicated, for example, the processing of a fission matrix. Therefore, in order to check the correctness of edited multigroup cross section data, a comparison with the WIMSR output sometimes proves quite useful.

Some Notes on NJOY

The NJOY code is well maintained and is continuously updated with improvements and bug-fixes. These improvements and fixes can be downloaded from the Web site as a collection of patches, and can be applied to the NJOY code by a dedicated update system. The latest version has fewer flaws, and is thus recommended for use. Furthermore, there are various options as input data that are sometimes difficult to use. It is therefore highly recommended that calculation results be verified. A comparison with independent calculations (e.g., continuous energy Monte Carlo calculations) can provide a good means for such verification.

2.4.2 Execution Control of NJOY

In common lattice physics codes, more than a few hundred nuclides may be processed in order to generate a cross section library. When this processing is carried out manually, quality control for the generation of a cross section library becomes difficult. Therefore, a dedicated cross section generation system that automatically generates NJOY inputs and can manage subsequent post-processing steps with minimal user input is often developed and used.

In this section, the cross section library generation system of AELIB, which is a cross section library for the lattice physics code AEGIS, is described as an example (Yamamoto et al. 2006; Yamamoto and Sugimura 2006). A calculation flowchart of the system is shown in  Fig. 8. The NjoyInputMaker code generates input data for NJOY by using short user input that contains the following information:

- Nuclide identification name in AELIB
- Upper energy boundary of resolved energy range
- Potential scattering cross section
- Order of anisotropic scattering
- Temperature points
- Background cross section points

NjoyInputMaker automatically generates not only the input data but also the execution shell. The NJOY code is executed using the automatically generated shell. The calculation result of NJOY is dumped onto a file in the MATXS format. The AELIBEditor code performs post-processing of the NJOY results shown in the next section, and generates AELIB, which is a binary file of a particular format. The details of post-processing will be described in the next section. Note that the AELIBEditor code can generate AELIB not only from the NJOY result, but also from user input data. For example, some fission product nuclides that have a short half-life are defined as “dummy” nuclides with a zero cross section, that is, only decay is considered for these nuclides. In such a case, a zero cross section is given from an input file. Since an ideal nuclide that has a particular multigroup cross section can be defined, a multigroup benchmark calculation, in which a given cross section is used, can easily be performed. Note that using a

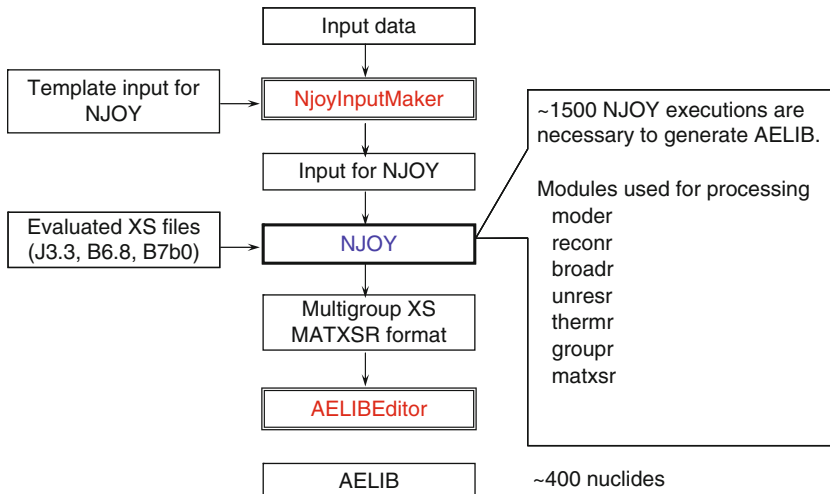


Figure 8
Example of automatic calculation flowchart of NJOY

common PC, it takes approximately two CPU days to generate an entire set of AELIB in which more than 400 nuclides are stored.

2.4.3 Post-Processing for Cross Section Library

The NJOY code can output a multigroup cross section in various formats (e.g., MATXS, WIMS, CCCC, and DTF). These output formats, however, may not be suitable for direct utilization as a cross section library of lattice physics codes. For example, while the MATXS format can be used for very general purposes, it may contain cross sections that are too detailed for lattice physics codes, such as a fission matrix. The WIMS format may require additional data for higher-order anisotropic scattering ($>P1$).

For the reasons given above, many lattice physics codes use their own (dedicated) formats in their cross section library – formats that are suitable for lattice physics computations. In order to generate such a cross section library, post-processing of the NJOY output becomes necessary. A description of post-processing of the MATXS format into a lattice physics code is given below as an example.

Absorption Cross Section

In the MATXS format, various reactions may be tabulated as neutron absorption reactions. However, in lattice physics computations, an absorption cross section is necessary for the neutron transport calculation. Therefore, various neutron absorption reactions are summed in order to obtain an absorption cross section:

$$\sigma_a = \sigma(n, \gamma) + \sigma(n, f) + \sigma(n, p) + \sigma(n, d) + \sigma(n, t) + \sigma(n, \alpha) + \sigma(n, 2\alpha) + \dots - \sigma(n, 2n) - 2\sigma(n, 3n) - 3\sigma(n, 4n) \quad (57)$$

The $(n, 2n)$ cross section is subtracted since its “net emission” of neutrons is 1, that is, “net absorption” is -1 . Similarly, the “net absorptions” for $(n, 3n)$ and $(n, 4n)$ reactions are -2 and -3 , respectively. By using (57), various neutron absorption reactions can be taken into account.

Nu-Value and Fission Spectrum

Energy distribution and the number of released neutrons in fission depend on the incident neutron energy. Therefore, in a nuclear data file, the fission cross sections of major fissionable nuclides are given not only as ordinary (total) fission cross sections, but also in the form of a fission matrix. In the MATXS format, a similar expression is used for the fission cross section. Unfortunately, the transport modules of many lattice physics codes cannot directly handle the fission matrix.

For a fission matrix, the fission neutron is evaluated by

$$f_g = \sum_{g'} \sigma_{f,g' \rightarrow g} \phi_{g'} + \chi_{d,g} \sum_{g'} v_{d,g'} \sigma_{f,g'} \phi_{g'} \quad (58)$$

where

f_g : fission neutrons appeared in group g ,

$\sigma_{f,g' \rightarrow g}$: fission matrix for prompt neutrons, whose incident and emission energy groups are g' and g , respectively,

$\phi_{g'}$: neutron flux of group g' ,

$\chi_{d,g}$: fission spectrum for delayed neutrons,

$v_{d,g}$: number of delayed neutrons per fission,

$\sigma_{f,g}$: (total) fission cross section (MT = 18 in the ENDF format).

However, many lattice physics codes evaluate fission neutrons as follows, since the dependence of fission spectra upon incident neutron energy is fairly minor:

$$f_g = \chi_g \sum_{g'} v_{g'} \sigma_{f,g'} \phi_{g'} \quad (59)$$

In order to fit the fission-related data in the MATXS format into ordinary representation, the following post-processing is carried out for a cross section library of lattice physics codes.

$$\chi_g = \frac{\sum_{g'} \sigma_{f,g' \rightarrow g} \phi_{g'} + \chi_{d,g} \sum_{g'} v_{d,g'} \sigma_{f,g'} \phi_{g'}}{\sum_g \sum_{g'} \sigma_{f,g' \rightarrow g} \phi_{g'} + \sum_{g'} v_{d,g'} \sigma_{f,g'} \phi_{g'}} \quad (60)$$

$$v_g = \frac{\sum_{g'} \sigma_{f,g' \rightarrow g}}{\sigma_{f,g}} + v_{d,g} \quad (61)$$

where

χ_g : fission spectrum for neutrons (including both prompt and delayed),

v_g : number of neutrons per fission (including both prompt and delayed).

Equation (60) indicates that a neutron spectrum is necessary to evaluate the fission spectrum, that is, the fission spectrum depends on the neutron spectrum. However, the neutron spectrum is, of course, unknown during the preparation of the cross section library. Fortunately,

the fission spectrum is not strongly dependent on the neutron spectrum, so we can use a typical neutron spectrum for (60), for example, a cell average neutron spectrum in the operating condition of a typical LWR.

Scattering Matrix

In the MATXS format, various scattering cross sections are independently given as the matrix form. Therefore, these scattering matrixes should be summed up for utilization in lattice physics codes:

$$\begin{aligned}\sigma_{s,g' \rightarrow g} = & \sigma_{el,g' \rightarrow g} + \sigma_{n,2n,g' \rightarrow g} + \sigma_{n,3n,g' \rightarrow g} + \sigma_{n,4n,g' \rightarrow g} + \sigma_{n,n\alpha,g' \rightarrow g} + \sigma_{n,np,g' \rightarrow g} \\ & + \sigma_{n,nd,g' \rightarrow g} + \sigma_{n,nt,g' \rightarrow g} + \sum_i \sigma_{inel,i,g' \rightarrow g} + \sigma_{inel,c,g' \rightarrow g},\end{aligned}\quad (62)$$

where

$\sigma_{s,g' \rightarrow g}$: scattering cross section used for lattice physics computation,

$\sigma_{el,g' \rightarrow g}$: elastic scattering cross section,

$\sigma_{n,2n,g' \rightarrow g}$, $\sigma_{n,3n,g' \rightarrow g}$, $\sigma_{n,4n,g' \rightarrow g}$: (n, 2n) cross section, and so on,

$\sigma_{n,n\alpha,g' \rightarrow g}$, $\sigma_{n,np,g' \rightarrow g}$, $\sigma_{n,nd,g' \rightarrow g}$, $\sigma_{n,nt,g' \rightarrow g}$: (n, n + α) cross section, and so on,

$\sigma_{inel,i,g' \rightarrow g}$: inelastic cross section of i th level,

$\sigma_{inel,c,g' \rightarrow g}$: inelastic cross section of continuous level.

Note that the above treatment is an approximation for (n, 2n) cross sections, and so on, since the “scattering” reaction changes only the energy of an incident neutron and does not affect the number of neutrons. Variations in the number of neutrons through (n, 2n), along with other reactions, are taken into account approximately through modification of the absorption cross section, in which the energy of the incident neutron does not change, as described in “Absorption cross section”. However, the impact of the present approximation is considered negligible, since the total reactivity effect of (n, 2n) and similar reactions are not of a significant degree.

Editing for Cross Section Library

Multiple NJOY calculation results are usually necessary to generate a complete cross section library for an isotope, since variations in temperatures and background cross sections must be taken into account. Furthermore, additional data (e.g., cross section identifiers, names of isotopes, and burnup-related data) may be supplemented by the input data. In order to gather and handle multiple NJOY outputs and fit the cross section data of NJOY outputs into a cross section library format of a lattice physics code, some post-editing is carried out at the end of the post-processing of cross sections.

2.5 Tabulation and Contents of Cross Section Library

The tabulation and contents of a cross section library are very important for utilization by lattice physics codes (Stammler and Abbate 1983; Okumura et al. 2007; Marleau et al. 2000; Hébert et al. 2000). This section provides some practical information on tabulation methods and the contents of a cross section library.

2.5.1 General File Format

Cross section data are stored in a cross section library. There are two approaches to the configuration of a file(s) for a cross section library.

The first approach is an “integrated” cross section library, that is, all cross sections and related data are stored in a file. For example, the WIMS code utilizes one file for a cross section library.

The second approach is an “indexed” cross section library. In this approach, there are two file types in regard to a cross section, that is, an index file and cross sections files. An index file indicates the correspondence between a cross section file and each nuclide and miscellaneous data. A cross section file contains cross sections for a nuclide, that is, each nuclide is stored in an independent file. The MCNP code adopts such a cross section configuration.

There are advantages and disadvantages to both approaches. From the point of view of the integrity of the cross section data, the “integrated” approach is better than the “indexed” approach, since part of the cross section library cannot be replaced. On the other hand, the “indexed” approach is better in terms of flexibility, since the replacement, removal, and addition of cross sections for a particular nuclide(s) are easily accomplished. During routine production calculations, such manipulations are not necessary. However, when research and development works, for example, the incorporation of new burnable absorbers and the adjustment of cross sections to obtain better prediction accuracy, are considered, such flexibility becomes invaluable. The “indexed” approach is also advantageous in the input of cross sections in lattice physics codes, since the nuclides used in the calculation can be read on a “demand-basis.”

The structure of cross section files for the “index” type cross section library is shown in  Fig. 9.

Though the manipulation of many files requires a considerable effort for conventional main-frame computers, it is very easy for the modern Unix, Linux, or Windows operating systems. Many files can quite practically be treated and managed by a directory. If we consider the ongoing progress being made in the computer industry, the second approach, that is, the index-type cross section library, will be more suitable for future lattice physics codes. In this approach, a cross section library is no longer “a file,” but rather, is “a directory.” Note that burnup-related data may also be prepared by an independent file, since the selection of a burnup chain to be used in calculations is easily accomplished.

2.5.2 Nuclide Identifiers

Nuclide identifiers are very important for a lattice physics code since they are the bridge between users and the lattice physics codes. Nuclide identifiers should include the following information:

- Nuclide information (name of element, atomic number, and mass number)
- State of nuclide (ground/meta-stable)
- Fission product or not
- Chemical binding form (e.g., H in H₂O)
- Source of cross section data (e.g., ENDF/B-VII.0)
- Additional information (e.g., adjustment of cross section data)

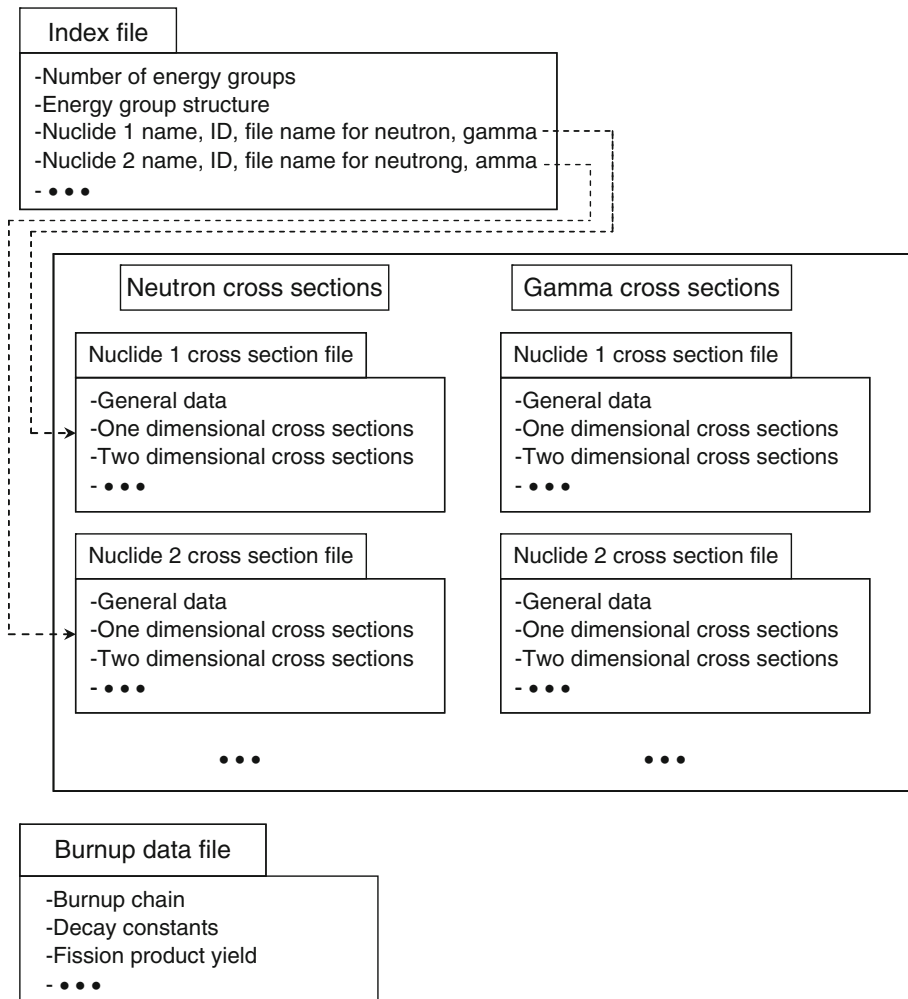


Figure 9
Structure of cross section library ("index" type)

The identifiers can be a string of characters or digits. In conventional lattice physics codes, digits are usually used, for example, “92238” represents ^{238}U . However, when the above information is taken into account, the design of identifiers should be done quite carefully, especially from the viewpoint of extensibility.

Though identifiers based on digits are “computer friendly,” they are not “user friendly.” On the other hand, identifiers based on a string of characters are “user friendly” but are not “computer friendly.” In order to resolve this contradiction, each nuclide can have two identifiers, that is, one consisting of a string of characters, and one of a string of digits. The character identifiers are used in input data, while the digit identifiers are used in the internal calculations of a lattice physics code.

Some nuclides play two roles in lattice physics computations. For example, ^{155}Gd is used as a burnable absorber, but it also appears as a fission product. The number density of ^{155}Gd in a burnable absorber is high, but that of the fission product is low. Therefore, though the self-shielding (resonance) effect of ^{155}Gd in a burnable absorber must be accurately accounted for, the resonance of ^{155}Gd as a fission product may be simply accounted for by assuming an appropriate (fixed) background cross section. Since the scattering matrix of ^{155}Gd as a fission product has a negligible impact from the point of view of neutronics, it may be truncated in a cross section library.

Furthermore, burnable absorber nuclides sometimes have a burnup chain that is independent of that of fission products. In such a case, though the same nuclides (^{155}Gd) appear as both a burnable absorber and fission product, they are considered as different nuclides from the viewpoint of the implementation of lattice physics codes. In order to distinguish “different” ^{155}Gd , different identifiers are necessary for the burnable absorber and fission product. We encounter a similar situation for other nuclides, for example, ^{109}Ag (control rod absorber and fission product), ^{103}Rh (Rh detector and fission product), and Zr (cladding and fission products).

2.5.3 Dependency of Cross Sections

Microscopic cross sections stored in a cross section library are usually dependent on the background cross section and temperature. In a given case, the mass effect of moderator nuclides may be taken into account (a detailed description of the mass effect will be given in [Sect. 3](#)).

In order to account for these dependencies, multiple NJOY calculations are carried out for different calculation conditions (different temperatures and background cross sections). Some typical examples of temperatures and background cross sections used in the NJOY code are shown in [Tables 5](#) and [6](#), respectively.

The temperatures for the major nuclides cover a range from room temperature (293 K) almost to the melting point of UO_2 (2,800 K). The maximum average pellet temperature of light water reactor fuel in a typical nominal operating condition is approximately 1,100 K. Higher temperatures (>1,100 K) are necessary for transient and accident analyses. Hydrogen has more detailed temperature grid points between 300 and 600 K, due to the considerable variation in scattering cross sections in the thermal energy region. For less important nuclides (e.g., fission product with small absorption) less detailed temperature grid points (or even one fixed temperature) can be applied in order to reduce the size of a cross section library with no loss of accuracy.

The grid points for a background cross section cover a range from infinite dilution (10^8 barn) to a fully shielded condition (10 or 1 barn). Dedicated grid points are assigned to ^{238}U since it is a dominant resonance absorber in many currently used reactor fuels. The grid points for ^{238}U have a fine resolution between 10–100 barn, since the typical background cross section for ^{238}U in light water reactor fuel pins is ~50 barn. Since the number densities of other nuclides (e.g., ^{235}U and ^{239}Pu) vary considerably during burnup, their background cross sections should also cover a wide range. For example, a background cross section for ^{235}U in typical UO_2 fuel is ~1,000 barn at beginning of life (BOL), but it increases up to ~5,000 barn at end of life (EOL), since the number density of ^{235}U reduces with burnup. In the case of ^{239}Pu , its background cross

Table 5
Example of temperatures used in the NJOY code

Major nuclides (K)	Hydrogen (K)
293	296
373	350
559	400
748	450
793	500
833	600
963	800
1,273	1,000
1,773	
2,573	

Source: Marcille and Mills (2003).

Table 6
Example of background cross sections used in the NJOY code

^{238}U (barns)	Heavy nuclides (barns)	FP (barns)	Others (barns)
1.00E+08	1.00E+08	1.00E+08	1.00E+08
1.00E+06	1.00E+06	1.00E+06	1.00E+06
1.00E+05	1.00E+05	1.00E+05	1.00E+05
1.00E+04	3.00E+04	1.00E+04	1.00E+04
1.00E+03	1.00E+04	1.00E+03	1.00E+03
3.00E+02	3.00E+03	1.00E+02	1.00E+02
1.00E+02	1.00E+03	1.00E+01	1.00E+01
5.00E+01	3.00E+02		1.00E+00
2.00E+01	1.00E+02		
1.00E+01	1.00E+01		

Source: Marcille and Mills (2003).

section is very large (almost infinite dilution) at BOL, since the number density of ^{239}Pu is very small. At EOL, the background cross section is reduced to approximately several thousands barn due to buildup during burnup.

Due to a current limitation of the NJOY code, the number of background cross sections is limited to less than or equal to 10. When more detailed grid points for a background cross section are necessary, two NJOY executions and the coupling of their results in post-processing becomes necessary.

2.5.4 General Data

When the index file approach is adopted, we have two different files, that is, the index file, and the cross section file for each nuclide. The general data contained in the index file and cross section file are described as follows:

a. Index file

- Numbers of total, fast, and thermal energy groups (note that thermal groups have up-scattering)
- Energy boundaries
- Directory in which cross section files are stored
- Correspondence among name of nuclide (character string identifier), nuclide id (digit identifier), and file name that stores cross section data

b. Cross section file

- Name of nuclide (character string identifier)
- Nuclide id (digit identifier)
- Atomic number, mass number
- Atomic weight (in units of amu is useful for slowing down calculation)
- Number of energy groups
- Fissionable (yes/no)
- Scattering matrix (present/no)
- Upper boundary of resolved resonance range
- Potential scattering cross section
- IR (intermediate resonance) parameter, if necessary
- Energy released per fission
- Kinetic parameters (delayed neutron fraction and decay constant for delayed neutron precursor)
- Number of grid points for temperature
- Number of grid points for background cross section
- Number of grid points for moderator mass effect
- Grid points for temperature
- Grid points for background cross section
- Grid points for moderator mass
- Generation time and date
- Comments
- Others

2.5.5 One-Dimensional Data

In the cross section file for each nuclide, the following one-dimensional cross section data are tabulated:

- Total cross section
- Absorption cross section
- Fission cross section

- Production cross section (number of neutrons released by a fission multiplied by fission cross section)
- $(n, 2n)$ cross section
- Capture cross section
- Fission spectrum
- Neutron source intensity (e.g., by spontaneous fission)
- Other parameters (e.g., $(n, 3n)$, (n, γ) , and so on, if necessary)

Additional parameters may be necessary if a lattice physics code adopts a particular resonance calculation method. When the subgroup method is used, the band cross sections and band probabilities are necessary. Almost continuous energy (point-wise) cross sections are necessary for the ultrafine group calculation method.

The above data are tabulated for each energy group, temperature, background cross section, and moderator mass. Since the volume of data is quite considerable and several elements of the above data are zero, compression of the above data is of practical importance. The following two approaches can be used to reduce data size.

Elimination of Zero Elements

For example, an $(n, 2n)$ cross section has a nontrivial value for energy groups above 1 MeV. In other words, $(n, 2n)$ cross sections are zero for most energy groups. Many nuclides are not fissionable; thus, fission, production cross sections, and the fission spectrum are zero for these nuclides. In order to eliminate the zero elements, the upper and bottom energy groups with significant values are stored with nonzero values between the (stored) upper and bottom energy groups. This approach is adopted in the MATXS format.

Storage of Variations in Cross Sections

Certain one-dimensional cross sections, for example, cross sections in the fast energy range, are insensitive to variations in temperature and background cross section. This means that almost identical cross sections are repeatedly tabulated for different temperatures and background cross sections. In such a case, the difference between cross sections from a base condition (e.g., room temperature and infinite dilution condition) will be zero when variations due to temperature and/or background cross section are considered, as follows:

$$\begin{aligned}\sigma(T, \sigma_0) &= \sigma(T_0, \sigma_{0,\infty}) + (\sigma(T, \sigma_0) - \sigma(T_0, \sigma_{0,\infty})) \\ &= \sigma(T_0, \sigma_{0,\infty}) + \Delta\sigma(T, \sigma_0)\end{aligned}\quad (63)$$

where

$\sigma(T, \sigma_0)$: effective microscopic cross section for temperature T and background cross section σ_0 ,

$\sigma(T_0, \sigma_{0,\infty})$: effective microscopic cross section for temperature T_0 and background cross section $\sigma_{0,\infty}$,

$\Delta\sigma(T, \sigma_0)$: difference of effective microscopic cross section,

T_0 : base temperature, for example, 293 K,

$\sigma_{0,\infty}$: background cross section for infinite dilute condition, for example, 10^8 barn.

Since the zero element of a cross section can be compressed by elimination, as discussed above, consideration through variation of a cross section is effective at reducing the volume of cross section data. The present method is also adopted in the MATXS format.

Reduction of Grid Points for Temperature/Background Cross Sections

For less important nuclides such as minor fission products, full tabulation of the cross sections for all temperatures/background cross sections is not necessary, since they have little impact on the calculation results. For these nuclides, a typical temperature (e.g., that of the operating condition) and background cross section (e.g., average value during burnup) can be used, instead of full tabulation of temperatures/background cross sections.

2.5.6 Two-Dimensional Data

Scattering matrixes for both isotropic component (P0) and anisotropic components are tabulated here. In light water reactor analysis, the transport-corrected total cross section, which considers anisotropic components up to P1, is usually used with acceptable results. However, for fuels with a steep angular flux distribution, an explicit anisotropic scattering calculation is desirable. Higher-order anisotropic scattering matrixes are necessary for such calculations. Several studies have demonstrated that anisotropic scattering up to a P3 component is sufficient for ordinary light water reactor core calculations. Therefore, anisotropic scattering up to P3 components for nuclides with large anisotropic scattering (light nuclides) and reflector materials (e.g., Fe, Ni, and Cr) would be included in the cross section data. For other materials, anisotropic scattering up to a P1 component is sufficient for lattice physics computation. Note that if sensitivity calculations on anisotropic scattering will be carried out, the order of anisotropic scattering in a cross section library should be higher.

Since the size of a scattering matrix is large, the compression of data is crucial. The techniques for one-dimensional cross sections described previously can also be applied to two-dimensional data, that is, scattering matrixes. Furthermore, scattering matrixes for nuclides with a small number density and small cross section (e.g., minor fission products) can be omitted, since the scattering matrix of such nuclides has a negligible impact on reactor physics parameters. This is another reason to provide independent nuclide identifiers for fission products. For example, the number density of ^{155}Gd used as a burnable absorber is high, so its scattering matrix should be explicitly taken into account. However, since the number density of ^{155}Gd as a fission product is small, its scattering matrix can be omitted. Therefore, we can have two different cross section files for ^{155}Gd : one that (for a burnable absorber) contains a scattering matrix, and one that does not.

2.5.7 Burnup-Related Data

For burnup-related data, the following information is necessary:

- Burnup chain (including branching ratio)
- Decay constant for each nuclide
- Yields for fission products

A burnup chain used in a lattice physics code would depend on the purpose of the analysis. Therefore, various burnup chains may be used with the same cross section library. Therefore, burnup-related data might be stored in a file that is independent of the cross section data. More detailed discussion on burnup chains will be presented in ➤ Sect. 6.

2.5.8 Gamma Cross Section Library

In order to evaluate detailed pin-wise energy deposition by gamma rays, a transport calculation of gamma rays is necessary. For such gamma transport calculation, the following data are necessary (Mertyurek 2007):

- Gamma energy released by a photonuclear reaction, mainly (n, γ)
- Gamma spectra of a photonuclear reaction (from neutron group n to gamma group g)
- Gamma energy released by a fission reaction
- Gamma spectra of a fission reaction (to gamma group g)
- Gamma total cross section
- Gamma absorption cross section
- Gamma scattering cross section (isotropic and anisotropic components)
- Energy deposition cross section from gamma

Since gamma cross sections have contents similar to those of neutron cross sections, a similar format for neutron cross sections can be used.

2.6 Summary

In ➤ Sect. 2, a detailed discussion of a cross section library for lattice physics code is provided. Though a cross section library is a crucial part of a lattice physics code, a description of its contents and preparation is rarely found in references. This section will be useful not only for the design and generation of a new cross section library, but also for an understanding of the contents and generation process of a current cross section library.

3 Resonance Treatment

3.1 Objective

All reactor physics calculations are carried out with cross sections. The actual cross-sectional data for each nuclide describe the very detailed (fine) energy structure, typically comprising several hundreds of thousands of energy points for major resonance nuclides. In fact, direct utilization of such ultrafine energy groups in lattice physics computations and subsequent core calculations is so time consuming as to be impractical, even on today's computers. For this reason, the fine energy structures of cross sections, especially in the resonance energy range, are condensed during lattice physics computations, as shown in ➤ Fig. 10. The first step in such energy condensation for cross sections is the resonance calculation. In this context, the resonance calculation is the "sole interface with the real world," since the "actual" cross section

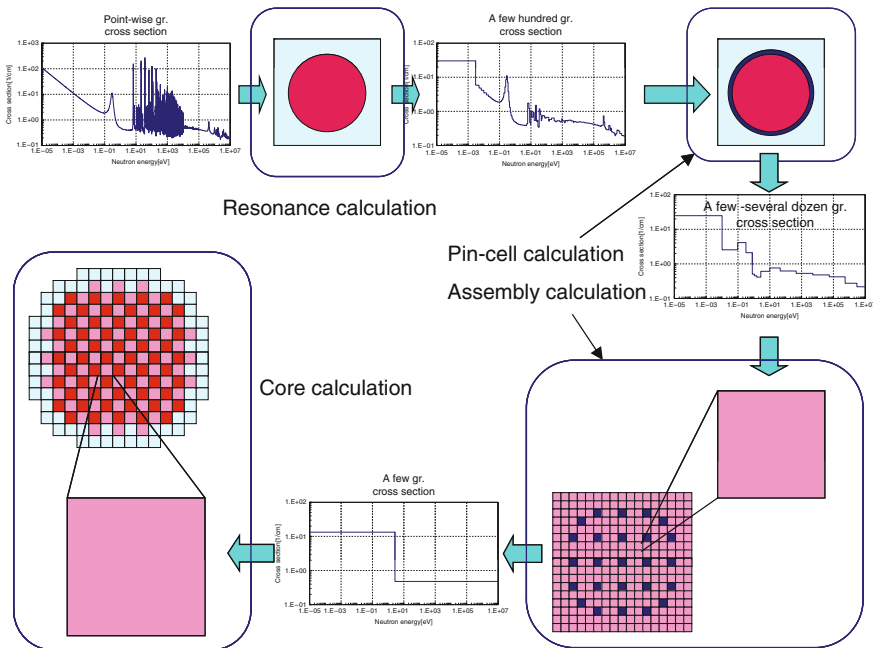


Figure 10
General calculation flow for core analysis

appears only in the resonance calculation, while only the condensed (i.e., artificial) cross sections are used in subsequent calculations. The consequence is that if the resonance calculation were inaccurate, subsequent calculations would be meaningless.

Since the resonance calculation is one of the most difficult and challenging part of reactor physics calculations, significant effort and study have been directed to the development of various innovative calculation methods. A complete review of these resonance calculation methods would, however, require an entire book, and hence, the discussion in [3.2](#) is limited to the major calculation methods being used in current lattice physics codes.

In the following subsection, the concept of an effective cross section is introduced, along with a discussion of the major resonance calculation methods used in current lattice physics codes (Weinberg and Wigner 1958; Dresner 1960; Goldstein and Cohen 1962; Rothenstein 1980; Stamm'ler and Abbate 1983; Rothenstein and Segev 1986; Cullen 1986; Kobayashi 1995; Halsall 1995; Loubiere et al. 1999; Hwang 2003; Reuss and Coste-Delclaux 2003; Hébert 2005b; Karthikeyan and Hébert 2008).

3.2 Effective Cross Sections

The Boltzmann transport equation in continuous energy is given as follows:

$$\vec{\Omega} \cdot \nabla \psi(\vec{r}, E, \vec{\Omega}) + \Sigma_t(\vec{r}, E) \psi(\vec{r}, E, \vec{\Omega}) = Q(\vec{r}, E, \vec{\Omega}) \quad (64)$$

In principle, (64) can be accurately solved with a very fine energy structure, but for the reasons discussed in the previous section, such treatment remains impractical. Thus, the Boltzmann transport equation in a multigroup form is usually used in lattice physics computations:

$$\vec{\Omega} \cdot \nabla \psi_g(\vec{r}, \vec{\Omega}) + \Sigma_{t,g}(\vec{r}, \vec{\Omega}) \psi_g(\vec{r}, \vec{\Omega}) = Q_g(\vec{r}, \vec{\Omega}) \quad (65)$$

With the following definition of a multigroup microscopic cross section, (64) and (65) are consistent.

$$\sigma_g(\vec{r}, \vec{\Omega}) = \frac{\int_{E_g}^{E_{g-1}} dE \sigma(E) \psi(\vec{r}, E, \vec{\Omega})}{\int_{E_g}^{E_{g-1}} dE \psi(\vec{r}, E, \vec{\Omega})} \quad (66)$$

It should be noted that the multigroup cross sections given in (66) is not a common expression since it depends not only on the location, but also on angle. Since neutron transport calculations in a lattice physics code assumes a constant cross section in a small spatial region (e.g., a fuel pellet), the spatially averaged cross section is necessary:

$$\sigma_{i,g}(\vec{\Omega}) \psi_{i,g}(\vec{\Omega}) V_i = \int_{V_i} d\vec{r} \sigma_g(\vec{r}, \vec{\Omega}) \psi_g(\vec{r}, \vec{\Omega}). \quad (67)$$

The cross section expressed in (67) still has angular dependence, which is not usually taken into account in the transport calculations in lattice physics codes. Therefore, the following definition is of practical value for microscopic cross sections in the multigroup neutron transport calculation:

$$\sigma_g(\vec{r}) = \frac{\int_{E_g}^{E_{g-1}} dE \sigma(E) \phi(\vec{r}, E)}{\int_{E_g}^{E_{g-1}} dE \phi(\vec{r}, E)} \quad (68)$$

where $\phi(\vec{r}, E)$ is the total (or scalar) flux, which is defined as

$$\phi(\vec{r}, E) = \int^{4\pi} \psi(\vec{r}, E, \vec{\Omega}) d\vec{\Omega}$$

The cross section given in (68) is called the effective cross section because it can effectively preserve the total reaction rate for the group. The group-wise definition of reaction leads also to scattering matrices for various angular moments. The scattering matrices are not covered in detail here though. It should be noted that detailed information regarding angular flux is implicitly taken into account.

The above discussion clarifies the fact that the essence of the resonance calculation is the energy collapsing and the spatial averaging (homogenization) that uses the detailed angular flux distribution to be obtained by solving (64). The above discussion also suggests a significant contradiction: the detailed angular fluxes used in (66) and (67) are, of course, unknown, since they are exactly what we would like to know. If the exact angular flux were known, the reactor physics calculation would have already been completed with ideal accuracy.

Herein lies the difficulty of the resonance calculation. We need to estimate the neutron flux distribution in a resonance region without a complete knowledge of the entire calculation system, such as a fuel assembly or a reactor core. In this sense, the resonance calculation methods must to a significant degree rely on approximations, which are considered valid from an engineering perspective.

3.3 Physics of Self-Shielding and Major Resonance Calculations

3.3.1 Physics of Self-Shielding

In the resonance energy range, the cross sections of many nuclides (especially heavy nuclides) exhibit a severely varying behavior. Since the peak of a resonance is often quite high, neutrons at the resonance peak energy are often easily absorbed by resonance nuclides. In such a case, the neutron flux also exhibits very complicated energetic behavior due to resonance absorption, as shown in [Fig. 11](#). Since the neutron absorption rate is obtained as a product of the microscopic cross section and the neutron flux, the dip in the neutron flux at a resonance peak reduces absorption at that peak. The resonance peak thus appears to be “energetically” shielded from neutrons around the resonance peak energy. For this reason, the reduction of neutron absorption around the resonance peak by the above mechanism is referred to as the energetic self-shielding effect. It is apparent that the energetic self-shielding effect appears not only in a heterogeneous geometry, but also in a homogeneous geometry, since the slowing down of the neutrons (energetic transport of neutrons) and absorption are the principal physical phenomena behind the energetic self-shielding effect.

There is another important shielding effect related to resonance absorption. In heterogeneous geometry, neutrons that flow from a moderator into a fuel (i.e., into the resonance region) are captured in the peripheral area, as shown in [Fig. 12](#). The neutron flux distribution thus shows a profound depression from the surface to the center part of the fuel near the resonance peak energy. The spatial variation in neutron absorption becomes very large in the resonance energy range due to the large resonance absorption cross section of fuel. This phenomenon is known as the spatial self-shielding effect, since the resonance material “shields” the inflow of neutrons, thus reducing the neutron absorption in the resonance material.

The essence of the resonance calculation is, in other words, the accurate evaluation of the energetic and spatial self-shielding effects in resonance material.

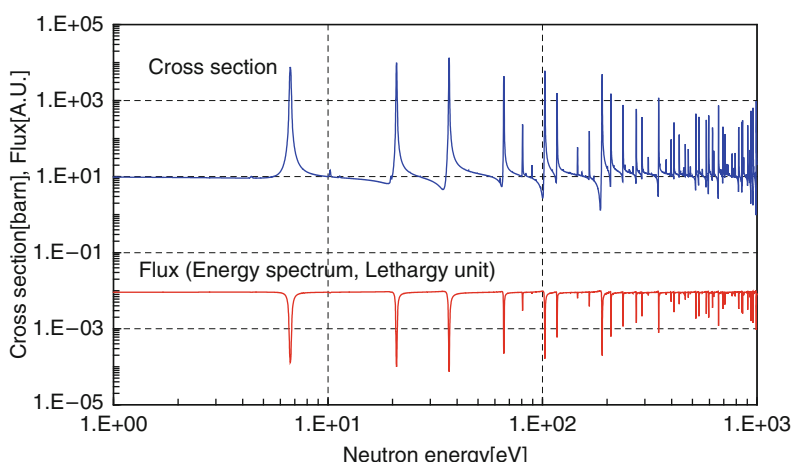


Figure 11

Neutron spectrum obtained by ultra-fine energy groups calculation

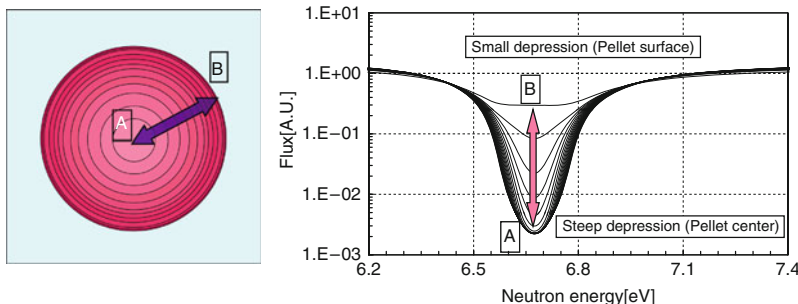


Figure 12
Space dependency of neutron spectrum in a fuel pellet

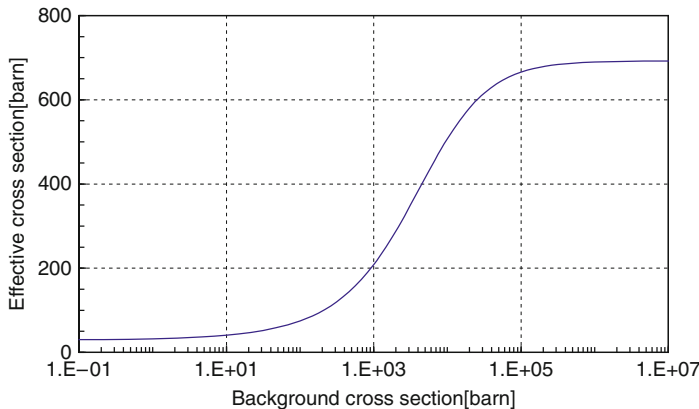
Even though there are various approaches to resonance calculations, they are generally classified into three categories: ultrafine energy group calculation, the equivalence theory, and the subgroup (or multiband) method.

3.3.2 Ultrafine Energy Group Calculation

The ultrafine energy group calculation is a quite simple and direct approach, in which neutron flux distribution (both energetic and spatial) is calculated with very fine energy groups (Ishiguro 1974; Tsuchihashi et al. 1982; Rothenstein et al. 1988; MC^{**} 2-2 1999; Chiba 2003; Sugimura and Yamamoto 2007). In this approach, the effective multigroup cross section is evaluated with a very detailed neutron spectrum distribution, as shown in [Fig. 11](#), and since it is based on first principles, it clearly gives quite accurate, effective cross sections. We must recall, however, the necessity of the resonance calculation. If a neutron transport calculation in very fine energy groups can be carried out, a conventional resonance calculation is not necessary. Currently, the direct practical application of ultrafine energy group calculation is, however, limited to a pin cell or to small multicells, because of the enormous amount of computational resource required for the ultrafine group transport calculation.

3.3.3 Equivalence Theory

The second approach, that is, the equivalence theory, is a historical method that is widely used in current lattice physics codes (Weinberg and Wigner 1958; Dresner 1960; Goldstein and Cohen 1962; Bitelli et al. 1970; Chao and Martinez 1978; Chao et al. 1981; Stamm'lér and Abbate 1983; Rothenstein and Segev 1986; Cullen 1986). In this approach, the neutron escape probability from the fuel (resonance) material is approximated by a rational function of the total cross section of a resonance nuclide. With some additional assumptions, the neutron flux spectrum in a heterogeneous resonance region can be expressed as an analytic formula that is applicable to a homogeneous medium as well. During this derivation, the effect of heterogeneity is taken into account by the macroscopic escape cross section. The escape cross section plays the same role as the background cross section does in the self-shielding effect in a homogeneous system. The notion of escape and background cross sections will be addressed in more detail in [3.4](#) and [3.5](#). Therefore, an effective cross section can be tabulated with a background cross section

**Figure 13**

Effective cross section versus background cross section (^{238}U , 293 K, 6.16–7.52 eV)

(which may include the escape cross section) as an index, as shown in [Fig. 13](#). Consequently, the effective cross sections in homogeneous and heterogeneous configurations will be the same if they have the same background cross sections. In this sense, the treatment of homogeneous and heterogeneous geometries is unified through the background cross section. In other words, the spatial self-shielding effect (captured by the escape cross section) and the energetic self-shielding effect (captured by the background cross section) are unified.

Though the equivalence theory offers a very simple and effective approach to resonance calculation, one must remember that it incorporates many approximations that are implicitly used. Therefore, the application of the equivalence theory is inherently limited to simple configurations, such as an isolated pin cell or regular lattices. Very heterogeneous geometries with complicated resonance material distribution require a more sophisticated approach.

3.3.4 Subgroup Method

The previous approach, the subgroup method, provides a calculation route that offers a compromise, by using a correlation between the neutron flux and the resonance cross section shown in [Fig. 11](#) (Nikoleav et al. 1971; Levitt 1972; Cullen 1986). Generally speaking, neutron flux is inversely proportional to the macroscopic total cross section of a resonance material. This dynamic suggests that neutron energy groups would be subdivided not by the order of energy (the conventional approach), but by the magnitude of the cross section, as shown in [Fig. 14](#). When neutron energy groups are defined according to the magnitude of the cross section, the variations in neutron flux in a subdivided energy group will be smaller than those in a conventional subdivision, since the variation of the cross section (and thus that of the neutron flux) in a sub-energy group is smaller. The dependence of the effective cross section in each subgroup on a shielding condition (in the equivalence theory, on a background cross section) is clearly weaker, and it is this condition, which guarantees the robustness of the subgroup method. Although a very fine energy group structure is necessary in the ultrafine energy group calculation, a few subgroups within a conventional group offer high accuracy, which makes the subgroup method computationally efficient.

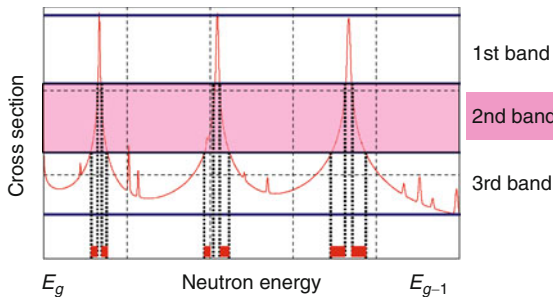


Figure 14
Concept of the subgroup method

The above discussion describes the concept of the subgroup method, in which the energy group structure in each subgroup is explicitly defined. In other words, all energy points are explicitly classified into corresponding subgroups. However, the subgroup method currently used in lattice physics codes does not have such an explicit energy group structure. Each subgroup is probabilistically defined in terms of its band probability and the corresponding band cross sections. The band probability and band cross sections are chosen to be independent of the self-shielding condition (i.e., the background cross section in the equivalence theory). Since each band does not have an explicit energy range, direct application of the current subgroup method is difficult when the shape of the cross section of a nuclide is different in each resonance region. The radial temperature distribution in a pellet poses just such a situation, since the shape of a cross section in a resonance energy range depends on the temperature, due to the Doppler effect. Furthermore, since the common subgroup method relies on the narrow resonance approximation that will be presented in the [3.4](#), its accuracy might be limited.

The advantages and disadvantages of the three major resonance calculation methods are summarized in [Table 7](#). This table suggests that there is no method of “last resort,” so the choice of a resonance calculation method greatly depends on the design concept of a given lattice physics code.

In the following subsection, the theoretical basis of the resonance calculation methods will be described. Beginning with the resonance theory in a homogeneous medium, the discussion is then extended to heterogeneous geometries.

3.4 Resonance Self-Shielding in a Homogeneous System (Dresner 1960; Rothenstein and Segev 1986; Cullen 1986)

3.4.1 Slowing Down of Neutrons in a Homogeneous System

In a homogeneous system, where the neutron flux is isotropic, the Boltzmann transport equation can be written as follows:

$$\Sigma_t(E)\phi(E) = \int_0^\infty \Sigma_s(E' \rightarrow E)\phi(E')dE' + \frac{\chi(E)}{k_{eff}} \int_0^\infty v\Sigma_f(E')\phi(E') dE' \quad (69)$$

Table 7**Advantages and disadvantages of the major resonance calculation methods**

Methods	Advantages	Disadvantages
Equivalence theory	Simple Fast	Inability to treat space-dependent resonance shielding Inability to treat complicated geometry Limited accuracy due to assumptions for simplification Inability to treat the resonance interference effect
Subgroup method	Reasonably accurate Applicable to general geometry	Longer computation time than the equivalence theory Inability to treat temperature distribution Inability to treat resonance interference effect
Ultrafine group method	Accurate Applicable to general geometry Ability to treat resonance interference effect	Longer computation time and larger memory storage Impractical for large system (e.g., a fuel assembly)

where

 $\Sigma_t(E)$: macroscopic total cross section, $\Sigma_s(E' \rightarrow E)$: macroscopic scattering cross section, $\nu\Sigma_f(E)$: macroscopic production cross section, $\chi(E)$: fission spectrum, $\phi(E)$: scalar flux, and k_{eff} : k -effective.

In the resonance region (e.g., 1 eV–10 keV and 10–300 keV for the resolved and unresolved resonance energy ranges, respectively, for ^{238}U), fission neutrons can be neglected, and elastic scattering is the dominant mechanism for the slowing down of neutrons. Under these assumptions, (69) can be simplified into

$$\left(\sum_k N_k \sigma_{t,k}(E) \right) \phi(E) = \sum_k \frac{1}{1 - \alpha_k} \int_E^{E/\alpha_k} N_k \sigma_{s,k}(E') \phi(E') \frac{dE'}{E'} \quad (70)$$

where

 $\sigma_{t,k}(E')$: microscopic total cross section of nuclide k , $\sigma_{s,k}(E')$: microscopic elastic scattering cross section of nuclide k , $\phi(E)$: total (scalar) neutron flux, and $\alpha_k = \left(\frac{A-1}{A+1} \right)^2$ when A is the atomic mass in atomic mass units (amu).

If a material is a pure scatterer that consists of a single nuclide, (70) becomes

$$N_k \sigma_{t,k}(E) \phi(E) = \frac{1}{1 - \alpha_k} \int_E^{E/\alpha_k} N_k \sigma_{t,k}(E') \phi(E') \frac{dE'}{E'} \quad (71)$$

It is easily confirmed that the solution to (71) is given by

$$\phi(E) = \frac{C}{N_k \sigma_{t,k}(E) E} \quad (72)$$

where

C: a constant that is defined by the source intensity.

Equation (72) suggests that the asymptotic neutron spectrum in a pure scatter is inversely proportional to the macroscopic total cross section and the neutron energy. In fact, in an LWR lattice, the overall behavior of the neutron spectrum in the resonance region is approximately given by $1/E$ even with absorption, since the moderator (H_2O) is almost a pure scatterer in the resonance energy region.

Unfortunately, the analytic solution to the equation for the slowing down of neutrons can be derived only under a very limited condition. Additional approximations will thus be necessary as a basis for further derivation. In the following sections, we discuss the major approximations that are behind the resonance calculations of many lattice physics codes.

3.4.2 Narrow Resonance Approximation

First, let us assume that the homogeneous material is composed of a resonance nuclide and other (nonresonant) nuclides. Even though the material may contain multiple resonance nuclides, the narrow resonance (NR) approximation to be discussed below will be valid when there is no coincident resonance overlap among nuclides (which will be discussed in more detail in a later section). Now, assume that the energy dependence of cross sections for nonresonant nuclides is assumed to be constant, with no absorption, that is, their total cross sections are equal to the potential scattering cross sections ($\sigma_{t,k} = \sigma_{s,k} = \sigma_{p,k}$). This assumption can be justified by the fact that this potential scattering, which is independent of the incident neutron energy, is dominant for nonresonant nuclides in the resonance energy range. With this assumption, (70) becomes as follows:

$$\left(N_r \sigma_{t,r}(E) + \sum_{k \neq r} N_k \sigma_{p,k} \right) \phi(E) = \frac{1}{1 - \alpha_r} \int_E^{E/\alpha_r} N_r \sigma_{s,r}(E') \phi(E') \frac{dE'}{E'} + \sum_{k \neq r} \frac{1}{1 - \alpha_k} \int_E^{E/\alpha_k} N_k \sigma_{p,k} \phi(E') \frac{dE'}{E'} \quad (73)$$

where the subscript r denotes a resonance nuclide.

It should be noted again that (73) assumes that only a resonance nuclide has energy dependence on cross sections, that is, other nuclides have a constant total and scattering cross sections. As discussed later, this simplification (which neglects the resonance overlap effect) is one of the weaknesses of this resonance calculation method. In actual fuel, a fuel material could have a

very diverse composition due to burnup (through the generation of minor actinides and fission products, which have many distinct resonances) and/or its initial mixed loading (e.g., MOX fuel, which includes both uranium and plutonium isotopes).

Unfortunately, the right-hand side of (73) contains an unknown function of energy E' , that is, neutron flux. Therefore, some assumptions are necessary in order to analytically solve (73).

For the purpose of further simplification, the resonance width of nuclide r is assumed to be narrow compared to the slowing down width. This means that most neutrons that appear near the resonance peak energy come from outside of the resonance peak (i.e., the nonresonant energy range) due to much higher energies. Furthermore, from (72), we see that the neutron spectrum in the nonresonant part is assumed to be proportional to $1/E$, since the energy dependence of the total cross section in the nonresonant part is fairly flat. Though the neutron spectrum around the resonance peak does not have a $1/E$ shape, its contribution to the integration of the energy is small because of the narrow resonance width. With these assumptions, the second term in the right-hand side of (73) can be reduced into the following:

$$\begin{aligned} \sum_{k \neq r} \frac{1}{1 - \alpha_k} \int_E^{E/\alpha_k} N_k \sigma_{p,k} \phi(E') \frac{dE'}{E'} &= \sum_{k \neq r} \frac{N_k \sigma_{p,k}}{1 - \alpha_k} \int_E^{E/\alpha_k} \phi(E') \frac{dE'}{E'} \\ &\approx \sum_{k \neq r} \frac{N_k \sigma_{p,k}}{1 - \alpha_k} \int_E^{E/\alpha_k} \frac{1}{E'} \frac{dE'}{E'} \\ &= \sum_{k \neq r} N_k \sigma_{p,k} \frac{1}{E} \end{aligned} \quad (74)$$

Note that the proportional constant C in (72) has been taken arbitrarily as 1 for normalization of the flux such that $E\phi(E) = 1$ above the resonance.

Next, we will estimate the first term in the right-hand side of (73). For this estimation, two additional approximations are introduced. The scattering cross section of a resonant nuclide in the nonresonant part is considered as a constant, since it is dominated by the potential scattering in this energy range. Furthermore, the shape of the neutron spectrum is approximated by $1/E$, as are the treatments for other nuclides. Using these assumptions, we have

$$\begin{aligned} \frac{1}{1 - \alpha_r} \int_E^{E/\alpha_r} N_r \sigma_{s,r}(E') \phi(E') \frac{dE'}{E'} &\approx \frac{N_r \sigma_{p,r}}{1 - \alpha_r} \int_E^{E/\alpha_r} \phi(E') \frac{dE'}{E'} \\ &\approx \frac{N_r \sigma_{p,r}}{1 - \alpha_r} \int_E^{E/\alpha_r} \frac{1}{E'} \frac{dE'}{E'} = N_r \sigma_{p,r} \frac{1}{E} \end{aligned} \quad (75)$$

By substituting (74) and (75) into (73), we obtain the following equation:

$$\left(N_r \sigma_{t,r}(E) + \sum_{k \neq r} N_k \sigma_{p,k} \right) \phi(E) = \frac{N_r \sigma_{p,r} + \sum_{k \neq r} N_k \sigma_{p,k}}{E} \quad (76)$$

Finally, the energy dependence of the neutron flux is given by

$$\begin{aligned} \phi(E) &= \frac{N_r \sigma_{p,r} + \sum_{k \neq r} N_k \sigma_{p,k}}{N_r \sigma_{t,r}(E) + \sum_{k \neq r} N_k \sigma_{p,k}} \frac{1}{E} \\ &= \frac{\sigma_{p,r} + \sigma_0}{\sigma_{t,r}(E) + \sigma_0} \frac{1}{E} \end{aligned} \quad (77)$$

In (77), the background cross section (σ_0), is defined as

$$\sigma_0 = \left(\sum_{k \neq r} N_k \sigma_{p,k} \right) / N_r \quad (78)$$

Equation (77) is the analytic form for the energy dependence of the neutron flux obtained by the narrow resonance (NR) approximation. Note that the absolute value of the neutron flux is not necessary in the resonance calculation, since the neutron flux is used as the weighting function. Though (72) is limited to a pure scatter, (77) is an extension that accounts for absorption, and can thus be used in the case of general homogeneity.

The background cross section defined by (78) is a fictitious microscopic cross section that determines the depression of the neutron flux at resonance peak energy. When the background cross section is very small, the energetic neutron flux behavior given by (77) approaches that in (72), in which the contribution of scattering from other nuclides is not considered. In this case, the neutron flux is inversely proportional to the microscopic total cross section of the resonance nuclide. Note that the variation due to the $1/E$ part is much smoother than that in the microscopic cross section. On the contrary, when the background cross section is very large, the neutron flux given by (77) approaches $1/E$, which is an asymptotic neutron spectrum in which no absorption is considered, that is, the scattering of other nonresonant nuclides dictates the spectrum. The actual neutron flux variation will be between the two extreme cases above, and would be interpolated by the background cross section.

The background cross section plays a very important role in resonance calculation theory, as will be described later.

During the derivation of (77), many assumptions were used. It is worthwhile to summarize the assumptions used in the NR approximation:

- No resonance overlap is considered.
- Nonresonant nuclides have constant scattering cross sections, which are dominated by the potential scattering.
- The resonant nuclide has a constant scattering cross section above the resonance, which is dominated by the potential scattering.
- The slowing down of neutrons is dominated by elastic scattering.
- The energy dependence of the neutron flux in the nonresonant part is asymptotic ($1/E$ shape).
- The neutron source within the resonance energy range is dominated by scattered neutrons coming from outside of the resonance peak. In other words, the resonance peak is so narrow compared to the average energy loss of neutrons due to elastic scattering.
- The source of neutron scattering is calculated by the asymptotic $1/E$ spectrum.

Though the above assumptions help to greatly simplify the expression of the energy dependence of the neutron flux, some of them may be a source of significant error. Since a resonance peak is assumed to be narrow, the NR approximation is more appropriate for a higher energy region in which the resonance is narrower than the slowing down width, in a relative sense. On the other hand, the accuracy of the NR approximation diminishes for broad resonances in the epithermal energy region (e.g., the resonance of ^{238}U at 6.7 eV). The accuracy of the NR approximation will be discussed later in more detail.

3.4.3 Wide Resonance Approximation

The first term in the right-hand side of (73) can be simplified by another assumption, namely the assumption that a resonant nuclide has infinite mass. This means that the width of the resonance peak is “wide” compared to the average energy loss due to scattering. In this regard, this approximation is called the wide resonance (WR) approximation, or the wide resonance infinite (mass) absorber (WRIA) approximation. When the mass of a nuclide is infinite, no energy loss is expected in the elastic scattering reaction. This physical observation suggests that the first term in (73), which is the energy integral of an in-scatter neutron by the resonant nuclide, is equal to the out-scatter reaction at energy E , that is,

$$\begin{aligned} \lim_{\alpha_r \rightarrow 1} \frac{1}{1 - \alpha_r} \int_E^{E/\alpha_r} N_r \sigma_{s,r}(E') \phi(E') \frac{dE'}{E'} &\approx \lim_{\alpha_r \rightarrow 1} \frac{1}{1 - \alpha_r} N_r \sigma_{s,r}(E) \phi(E) \int_E^{E/\alpha_r} \frac{dE'}{E'} \\ &= N_r \sigma_{s,r}(E) \phi(E) \lim_{\alpha_r \rightarrow 1} \frac{1}{1 - \alpha_r} \ln\left(\frac{1}{\alpha_r}\right) \\ &= N_r \sigma_{s,r}(E) \phi(E) \lim_{\alpha_r \rightarrow 1} \frac{-\ln \alpha_r}{1 - \alpha_r} \\ &= N_r \sigma_{s,r}(E) \phi(E) \end{aligned} \quad (79)$$

Here, the energy dependence of the scattering cross section and the neutron flux is assumed to be constant within the narrow integration range, $E/\alpha_r \sim E$. By substituting (79) into (73) and applying the NR approximation for nonresonant nuclides, we obtain

$$\left(N_r \sigma_{t,r}(E) + \sum_{k \neq r} N_k \sigma_{p,k} \right) \phi(E) = N_r \sigma_{s,r}(E) \phi(E) + \frac{\sum_{k \neq r} N_k \sigma_{p,k}}{E} \quad (80)$$

Since $\sigma_{a,r}(E) = \sigma_{t,r}(E) - \sigma_{s,r}(E)$, (80) is rewritten as

$$\left(N_r \sigma_{a,r}(E) + \sum_{k \neq r} N_k \sigma_{p,k} \right) \phi(E) = \frac{\sum_{k \neq r} N_k \sigma_{p,k}}{E} \quad (81)$$

The final form of flux, is then

$$\begin{aligned} \phi(E) &= \frac{\sum_{k \neq r} N_k \sigma_{p,k}}{N_r \sigma_{a,r}(E) + \sum_{k \neq r} N_k \sigma_{p,k}} \frac{1}{E} \\ &= \frac{\sigma_0}{\sigma_{a,r}(E) + \sigma_0} \frac{1}{E} \end{aligned} \quad (82)$$

where $\sigma_0 = \left(\sum_{k \neq r} N_k \sigma_{p,k} \right) / N_r$.

Note that the narrow resonance approximation is still applied to the nonresonant nuclides to derive (82). Therefore, the above derivation is sometimes called the WR–NR approximation, which means that the WR approximation is applied to the resonant nuclide, while the NR approximation is applied to the nonresonant nuclides. In this context, the above approximation

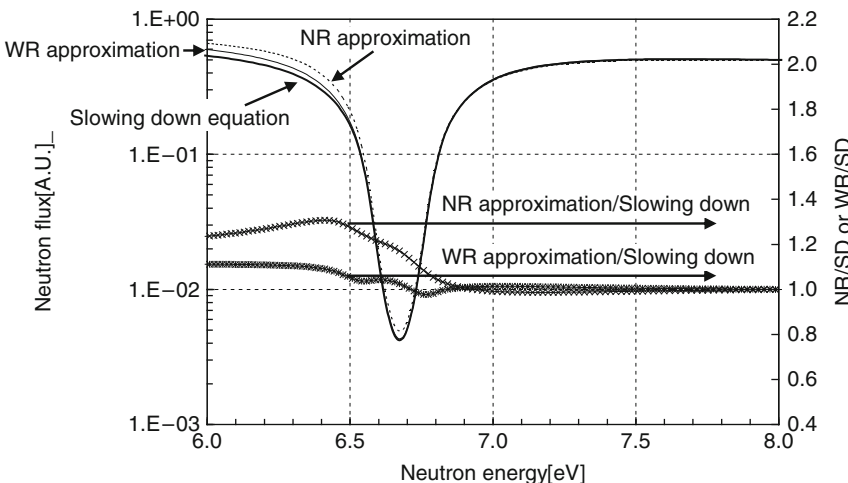


Figure 15

Neutron fluxes $\phi(E)$ obtained by the NR, WR approximations, and the numerical solution of the slowing down equation (SD) (homogeneous mixture of ^{238}U and hydrogen, 293 K, $\sigma_0 = 50$ barn)

is also referred to as the narrow resonance infinite mass (NRIM) approximation. The above assumption is justified by the fact that the energy loss from the slowing down by nonresonant nuclides (e.g., hydrogen) is generally much larger than the width of a resonance peak.

A comparison of (77) and (82) provides useful insight into the energy dependence of the neutron flux at the resonance peak. In fact, when the scattering reaction of the resonant nuclide is neglected (i.e., $\sigma_{p,r}$ and $\sigma_{s,r}(E)$ are zero), (77) and (82) become identical. This observation is adequate, since the scattering reaction of a resonant nuclide is essentially “neglected” in the WR approximation. Due to the assumptions in the WR approximation, it is more appropriate to treat broad resonances appearing in the epithermal-low energy range.

Figure 15 shows neutron spectra in a homogeneous mixture of ^{238}U and hydrogen around 7 eV, as obtained by different methods. The background cross section (σ_0) is 50 barn and the temperature is 293 K. The neutron flux is normalized at 8 eV. The ratios of the two approximated results to the reference are also shown. The reference result is obtained by the numerical solution of the slowing down equation, and the two approximate solutions (the NR and WR approximations) are also depicted in Fig. 15. Since the resonance of ^{238}U at 6.7 eV is located in a lower energy region and is relatively wide, the WR approximation is in better agreement with the reference solution.

Differences in the neutron spectrum affect the effective cross section during energy condensation. Tables 8 and 9 show a comparison of the effective microscopic capture cross sections of ^{238}U and ^{235}U obtained by the NR and WR approximations, and offer an accurate slowing down equation. Table 8 indicates that the NR approximation gives higher accuracy than the WR approximation in the higher energy range, while the WR approximation works better in the lower energy range. In comparison with ^{238}U shown in Table 8, the capture cross section of ^{235}U shown in Table 9 is accurately calculated by both the NR and WR

Table 8

Comparison of the effective microscopic capture cross section of ^{238}U obtained through the numerical solution of the slowing down equation (SD), and the narrow resonance (NR) and the wide resonance (WR) approximations (background cross section = 50 barn, 293 K, homogeneous mixture of ^{238}U and hydrogen; values are in barn)

Group number (XMAS 172 group)	Upper energy [eV]	Calculation method			Difference [%]	
		S.D.	N.R.	W.R.	(N.R.-S.D.)/S.D.	(W.R.-S.D.)/S.D.
45	1.11E+04	0.649	0.648	0.661	-0.19	1.80
46	9.12E+03	0.592	0.592	0.640	-0.03	7.97
47	7.47E+03	0.730	0.730	0.817	0.00	11.93
48	5.53E+03	0.776	0.773	0.838	-0.33	7.97
49	5.00E+03	0.736	0.734	0.875	-0.24	18.93
50	3.53E+03	0.749	0.747	1.020	-0.24	36.13
51	3.35E+03	0.940	0.937	1.229	-0.28	30.75
52	2.25E+03	0.745	0.746	1.027	0.17	37.82
53	2.03E+03	0.878	0.873	1.385	-0.54	57.77
54	1.51E+03	0.663	0.665	0.946	0.32	42.73
55	1.43E+03	0.999	0.983	1.406	-1.63	40.76
56	1.23E+03	1.334	1.322	1.833	-0.91	37.44
57	1.01E+03	1.084	1.064	2.159	-1.89	99.18
58	9.14E+02	1.289	1.261	1.750	-2.23	35.73
59	7.49E+02	1.390	1.374	1.685	-1.11	21.22
60	6.77E+02	1.323	1.291	1.855	-2.44	40.20
61	4.54E+02	1.397	1.374	1.502	-1.65	7.50
62	3.72E+02	0.751	0.680	1.143	-9.45	52.19
63	3.04E+02	1.814	1.654	2.297	-8.78	26.65
64	2.04E+02	1.567	1.262	2.184	-19.49	39.33
65	1.49E+02	1.287	1.289	1.217	0.15	-5.44
66	1.37E+02	2.757	2.085	3.304	-24.38	19.84
67	9.17E+01	2.129	2.103	1.993	-1.23	-6.38
68	7.57E+01	0.370	0.363	0.373	-1.87	0.84
69	6.79E+01	4.700	3.599	4.845	-23.43	3.09
70	5.56E+01	0.101	0.101	0.101	0.00	0.00
71	5.16E+01	0.144	0.144	0.144	-0.04	-0.01
72	4.83E+01	0.173	0.173	0.173	-0.06	0.01
73	4.55E+01	0.516	0.512	0.517	-0.82	0.20
74	4.02E+01	5.747	5.296	6.111	-7.85	6.32

Table 8 (continued)

Group number (XMAS 172 group)	Upper energy [eV]	Calculation method			Difference [%]	
		S.D.	N.R.	W.R.	(N.R.-S.D.)/S.D.	(W.R.-S.D.)/S.D.
75	3.73E+01	25.430	16.285	25.851	-35.96	1.66
76	3.37E+01	0.874	0.881	0.874	0.78	0.03
77	3.05E+01	0.398	0.399	0.398	0.08	0.00
78	2.76E+01	0.459	0.459	0.459	-0.03	0.00
79	2.50E+01	1.151	1.143	1.153	-0.64	0.17
80	2.26E+01	27.522	24.430	26.354	-11.23	-4.24
81	1.95E+01	1.175	1.193	1.175	1.56	0.04
82	1.59E+01	0.349	0.349	0.349	0.05	-0.01
83	1.37E+01	0.342	0.342	0.342	-0.07	0.00
84	1.12E+01	0.849	0.850	0.847	0.11	-0.24
85	9.91E+00	0.507	0.507	0.507	-0.01	0.00
86	9.19E+00	0.866	0.866	0.867	-0.04	0.02
87	8.32E+00	2.403	2.400	2.404	-0.12	0.08
88	7.52E+00	45.674	48.196	45.455	5.52	-0.48
89	6.16E+00	5.218	5.259	5.212	0.80	-0.12
90	5.35E+00	1.903	1.903	1.903	0.02	-0.01
91	5.04E+00	1.215	1.216	1.215	0.03	-0.02
92	4.13E+00	0.783	0.783	0.783	0.00	0.00

Background cross section = 50 barn, 293 K, homogeneous mixture of ^{238}U and hydrogen; values are in barn.

approximations, since the background cross section (1,000 barn, which is typical for ^{235}U in an LWR lattice) is much larger than that of ^{238}U in this calculation, and the peak of the resonance cross section is smaller and narrower than ^{238}U . Note that the typical peak values of the resonance cross sections are 10,000 barns and 1,000 barns for the microscopic total cross sections of ^{238}U and ^{235}U , respectively. In the case of a more shielded condition, the difference between the NR and WR approximations will be larger for ^{235}U .

3.4.4 Intermediate Resonance Approximation

Concept

The NR and WR approximations give the two limiting conditions in neutron slowing down for a resonant nuclide. Actual resonance peaks, however, appear to have an “intermediate” resonance width, which would be a blend of the “narrow” and “wide” ones. The intermediate resonance (IR) approximation offers a compromise approach for resonances of intermediate width (Sehgal and Goldstein 1966; Goldstein 1967; Ishiguro 1968; Ishiguro and Takano 1969).

Table 9

Comparison of the effective capture cross section of ^{235}U obtained through the numerical solution of the slowing down equation (SD), the narrow resonance approximation (NR), and the wide resonance approximation (WR)

Group number (XMAS 172 group)	Upper energy [eV]	Calculation method			Difference [%]	
		S.D.	N.R.	W.R.	(N.R. – S.D.)/ S.D.	(W.R. – S.D.)/S.D.
45	1.11E+04	1.063	1.063	1.063	0.00	0.00
46	9.12E+03	1.216	1.216	1.216	0.00	0.00
47	7.47E+03	1.261	1.261	1.261	0.00	0.00
48	5.53E+03	1.246	1.246	1.246	0.00	0.00
49	5.00E+03	1.458	1.458	1.458	0.01	0.00
50	3.53E+03	1.667	1.667	1.667	0.00	0.00
51	3.35E+03	1.825	1.825	1.825	0.00	0.00
52	2.25E+03	3.948	3.948	3.950	0.00	0.04
53	2.03E+03	3.292	3.292	3.293	-0.01	0.03
54	1.51E+03	2.801	2.801	2.802	0.00	0.04
55	1.43E+03	3.460	3.460	3.462	-0.02	0.04
56	1.23E+03	4.392	4.392	4.395	0.00	0.06
57	1.01E+03	5.085	5.084	5.088	-0.01	0.06
58	9.14E+02	4.505	4.505	4.507	-0.01	0.03
59	7.49E+02	4.798	4.796	4.806	-0.04	0.17
60	6.77E+02	5.226	5.225	5.232	-0.02	0.12
61	4.54E+02	5.069	5.069	5.073	-0.01	0.06
62	3.72E+02	7.121	7.120	7.128	-0.02	0.09
63	3.04E+02	8.422	8.423	8.449	0.01	0.32
64	2.04E+02	10.840	10.837	10.861	-0.03	0.20
65	1.49E+02	10.432	10.427	10.440	-0.05	0.07
66	1.37E+02	12.841	12.834	12.855	-0.06	0.11
67	9.17E+01	12.150	12.128	12.162	-0.17	0.10
68	7.57E+01	11.336	11.322	11.323	-0.12	-0.11
69	6.79E+01	13.380	13.381	13.394	0.01	0.11
70	5.56E+01	18.998	18.985	19.001	-0.07	0.02
71	5.16E+01	31.862	31.845	31.854	-0.05	-0.02
72	4.83E+01	15.778	15.768	15.763	-0.07	-0.09
73	4.55E+01	20.648	20.639	20.653	-0.04	0.02
74	4.02E+01	18.433	18.380	18.408	-0.29	-0.13

Table 9 (continued)

Group number (XMAS 172 group)	Upper energy [eV]	Calculation method			Difference [%]	
		S.D.	N.R.	W.R.	(N.R. – S.D.) / S.D.	(W.R. – S.D.) / S.D.
75	3.73E+01	38.266	38.331	38.328	0.17	0.16
76	3.37E+01	37.883	37.813	37.856	-0.18	-0.07
77	3.05E+01	9.621	9.622	9.621	0.01	0.00
78	2.76E+01	6.655	6.653	6.652	-0.03	-0.04
79	2.50E+01	41.271	41.293	41.279	0.05	0.02
80	2.26E+01	28.951	28.899	28.927	-0.18	-0.08
81	1.95E+01	33.076	32.867	32.933	-0.63	-0.43
82	1.59E+01	14.145	14.135	14.134	-0.07	-0.08
83	1.37E+01	66.431	66.467	66.524	0.05	0.14
84	1.12E+01	6.232	6.233	6.234	0.02	0.03
85	9.91E+00	17.173	17.189	17.186	0.09	0.08
86	9.19E+00	63.474	63.361	63.344	-0.18	-0.21
87	8.32E+00	4.426	4.427	4.426	0.01	0.00
88	7.52E+00	56.860	57.016	56.963	0.27	0.18
89	6.16E+00	5.579	5.578	5.577	-0.02	-0.05
90	5.35E+00	3.515	3.515	3.515	0.00	0.00
91	5.04E+00	21.761	21.734	21.716	-0.13	-0.21
92	4.13E+00	2.133	2.133	2.133	0.00	0.00

Background cross section = 1,000 barn, 293 K, homogeneous mixture of ^{235}U and hydrogen; values are in barn.

The discussion in [3.4.3](#) clarifies that the difference between the NR and WR approximations can be found in their differing treatment of the scattering cross section of a resonant nuclide. In other words, the scattering cross section of a resonant nuclide is fully incorporated in the NR approximation, but is completely neglected in the WR approximation. This observation naturally provides for an intermediate approach, that is, only a part of the scattering cross section of a resonant nuclide is taken into account:

$$\begin{aligned} \phi(E) &= \frac{\lambda N_r \sigma_{p,r} + \sum_{k \neq r} N_k \sigma_{p,k}}{N_r \sigma_{a,r}(E) + \lambda N_r \sigma_{p,r} + \sum_{k \neq r} N_k \sigma_{p,k}} \frac{1}{E} \\ &= \frac{\lambda \sigma_{p,r} + \sigma_0}{\sigma_{a,r}(E) + \lambda \sigma_{p,r} + \sigma_0} \frac{1}{E} \end{aligned} \quad (83)$$

where λ is the IR parameter. The NR and WR approximations correspond to $\lambda = 1$ and $\lambda = 0$, respectively. By choosing an appropriate IR parameter, (83) gives better accuracy for resonances of intermediate width.

Historically, the IR parameter was introduced to provide an analytical expression for the energy dependence of the neutron flux at resonances of intermediate width. However, in the practical world of lattice physics computing, slowing down calculations are carried out by the numerical solution of (70) during the stage of cross section libraries; we can thus accurately evaluate the energy dependence of the neutron flux even for resonances of intermediate width. In this sense, an analytical expression for the energetic behavior of neutron flux is no longer necessary in order to evaluate the effective cross section.

In spite of the above description, the IR parameter still plays a very important role in today's lattice physics computation. In the slowing down calculations, the "effective" width of a resonance depends not only on the actual width of the resonance peak, but also on the average increment of lethargy (average energy loss) in the collision between a neutron and a target nuclide.

Let us assume a resonance peak. This resonance peak is "narrow" when hydrogen is used as a moderator nuclide. The same resonance peak, however, would be "wide" when a neutron loses its energy due to collisions with a heavier nuclide (e.g., oxygen, uranium). This discussion suggests that the width of resonance effectively depends also on the mass of the moderator nuclide. The IR parameter can be used to correct the mass effect of a moderator nuclide. ➤ [Table 10](#) shows the effective capture cross sections of ^{238}U in the 172 XMAS groups when various nuclides are assumed as moderator. This result was obtained through a numerical solution of the slowing down equation. The background cross section in ➤ [Table 10](#), which influences the magnitude of the self-shielding effect, is assumed to be 50 barns.

➤ [Table 10](#) clearly indicates that the mass of the moderator nuclide has a significant impact on the effective cross sections even if the background cross section is the same. The actual dependence of the effective cross section on the mass of the moderator nuclide is somewhat complicated, as can be seen in this table. However, heavy nuclides generally contribute less to the background cross section than do light nuclides such as hydrogen, since the energy loss of a neutron through a collision is much smaller and also the IR factor is small for resonant nuclides. Since the variation in the effective cross section in ➤ [Table 10](#) comes from the superficial "relative width" of a resonance peak, it would be adequately captured by the IR parameter. In order to apply the IR parameter to all nuclides, (83) is extended as follows:

$$\phi(E) = \frac{\lambda_r \sigma_{p,r} + \sigma_0}{\sigma_{a,r}(E) + \lambda_r \sigma_{p,r} + \sigma_0} \frac{1}{E} \quad (84)$$

$$\sigma_0 = \left(\sum_{k \neq r} \lambda_k N_k \sigma_{s,k} \right) / N_r \quad (85)$$

where λ_r and λ_k are the IR parameters for resonance nuclide r and the non-resonance nuclide k , respectively. [Equation \(84\)](#) indicates that the scattering of all nuclides is taken into account with use of the IR parameter, that is, the "effective" scattering cross section is used through $\lambda_k \sigma_{s,k}$. When nuclide k is hydrogen, $\lambda_k = 1$, while $\lambda_k < 1$ for other nuclides. In general, the value of the IR parameter becomes smaller when the mass of a nuclide becomes heavier.

Table 10

Moderator mass effect on effective microscopic capture cross section of ^{238}U . Hydrogen, oxygen, and uranium are considered as the moderator nuclides

Group number (XMAS 172 group)	Upper energy [eV]	Moderator nuclide			Difference [%]	
		H	^{16}O	^{238}U	$(^{16}\text{O}-\text{H})/\text{H}$	$(^{238}\text{U}-\text{H})/\text{H}$
45	1.11E+04	0.649	0.649	0.652	0.03	0.40
46	9.12E+03	0.594	0.594	0.596	0.03	0.38
47	7.47E+03	0.732	0.731	0.726	-0.06	-0.79
48	5.53E+03	0.779	0.779	0.778	0.01	-0.06
49	5.00E+03	0.738	0.738	0.740	0.03	0.34
50	3.53E+03	0.754	0.754	0.749	-0.07	-0.73
51	3.35E+03	0.943	0.942	0.934	-0.11	-1.00
52	2.25E+03	0.748	0.747	0.750	-0.12	0.20
53	2.03E+03	0.881	0.881	0.877	-0.07	-0.54
54	1.51E+03	0.666	0.665	0.664	-0.10	-0.23
55	1.43E+03	1.003	1.003	0.999	-0.08	-0.44
56	1.23E+03	1.341	1.340	1.329	-0.07	-0.91
57	1.01E+03	1.091	1.087	1.053	-0.30	-3.50
58	9.14E+02	1.296	1.297	1.300	0.04	0.29
59	7.49E+02	1.406	1.402	1.375	-0.32	-2.21
60	6.77E+02	1.331	1.329	1.295	-0.12	-2.72
61	4.54E+02	1.406	1.405	1.402	-0.08	-0.33
62	3.72E+02	0.755	0.752	0.696	-0.38	-7.77
63	3.04E+02	1.826	1.814	1.703	-0.65	-6.76
64	2.04E+02	1.577	1.571	1.375	-0.37	-12.80
65	1.49E+02	1.294	1.317	1.422	1.83	9.91
66	1.37E+02	2.791	2.752	1.882	-1.41	-32.57
67	9.17E+01	2.137	2.113	2.116	-1.14	-0.99
68	7.57E+01	0.371	0.369	0.359	-0.56	-3.30
69	6.79E+01	4.747	4.930	7.026	3.84	47.99
70	5.56E+01	0.101	0.101	0.101	0.01	0.01
71	5.16E+01	0.144	0.144	0.144	0.00	-0.09
72	4.83E+01	0.173	0.173	0.173	-0.03	-0.13
73	4.55E+01	0.517	0.516	0.507	-0.08	-1.91
74	4.02E+01	5.799	5.731	4.711	-1.16	-18.76
75	3.73E+01	25.817	27.635	51.450	7.04	99.29

Table 10 (continued)

Group number (XMAS 172 group)	Upper energy [eV]	Moderator nuclide			Difference [%]	
		H	^{16}O	^{238}U	$(^{16}O-H)/H$	$(^{238}U-H)/H$
76	3.37E+01	0.873	0.885	0.898	1.40	2.89
77	3.05E+01	0.398	0.398	0.399	-0.13	0.31
78	2.76E+01	0.459	0.459	0.458	-0.03	-0.13
79	2.50E+01	1.154	1.152	1.119	-0.11	-3.04
80	2.26E+01	27.675	27.550	13.338	-0.45	-51.81
81	1.95E+01	1.172	1.237	1.309	5.53	11.64
82	1.59E+01	0.349	0.350	0.351	0.17	0.43
83	1.37E+01	0.343	0.342	0.339	-0.09	-1.09
84	1.12E+01	0.849	0.848	0.829	-0.11	-2.40
85	9.91E+00	0.508	0.507	0.506	-0.02	-0.22
86	9.19E+00	0.868	0.867	0.859	-0.08	-1.07
87	8.32E+00	2.411	2.405	2.299	-0.23	-4.64
88	7.52E+00	45.716	42.732	12.215	-6.53	-73.28
89	6.16E+00	5.207	5.686	6.598	9.19	26.71
90	5.35E+00	1.905	1.896	1.919	-0.49	0.71
91	5.04E+00	1.216	1.220	1.238	0.31	1.75
92	4.13E+00	0.783	0.783	0.784	0.00	0.05

Background cross section = 50 barn, 293 K, edited in 172 XMAS groups.

Numerical Procedure

A detailed procedure to evaluate the IR parameter is presented below (MacFarlane and Muir 1994a):

- Case 1: Perform the slowing down calculation with a homogeneous mixture of hydrogen and a resonance nuclide (e.g., ^{238}U). The composition of the homogeneous mixture is adjusted to give a typical background cross section for a resonance nuclide. For example, in the case of ^{238}U in a light water reactor lattice, 50 barn may be used. The evaluated effective cross section is σ_{Case1} .
- Case 2: Perform another slowing down calculation with a homogeneous mixture of hydrogen and the resonance nuclide used in Case 1. The composition of the homogeneous mixture is slightly changed from that in Case 1 so that the background cross section for the resonance nuclide is increased slightly. If the background cross section cannot be directly specified in the slowing down calculation, the number density of the moderator nuclide is adjusted. In Case 2, for example, 55 barn is used, a number density that is 10% more than that in Case 1. The evaluated effective cross section is σ_{Case2} .
- Case 3: Perform the third slowing down calculation with a homogeneous mixture of another moderator nuclide (e.g., oxygen) and the resonance nuclide used in Case 1. The composition of the homogeneous mixture is adjusted to give the same background cross section as in Case 2. Since the (potential) scattering cross section is different among nuclides, the

Table 11

IR parameter for the microscopic absorption cross section of ^{238}U in 172-groups XMAS energy structure

Group number (XMAS172)	Upper energy [eV]	a = 16 Background XS (barn)			a = 40 Background XS (barn)			a = 238 Background XS (barn)		
		50	1,000	10,000	50	1,000	10,000	50	1,000	10,000
57	1.01E+03	0.995	0.997	0.998	0.990	0.993	0.994	0.897	0.949	0.956
60	6.77E+02	0.998	0.999	0.999	0.997	0.999	0.999	0.899	0.942	0.946
63	3.04E+02	0.991	0.994	0.994	0.980	0.987	0.987	0.764	0.872	0.890
64	2.04E+02	0.965	0.983	0.990	0.916	0.951	0.968	0.494	0.704	0.808
66	1.37E+02	0.970	0.988	0.990	0.919	0.968	0.975	0.357	0.715	0.793
69	6.79E+01	1.000	1.000	1.000	0.992	0.982	0.985	0.328	0.682	0.776
75	3.73E+01	1.000	1.000	1.000	1.000	1.000	1.000	0.191	0.466	0.648
80	2.26E+01	0.986	0.993	0.994	0.949	0.983	0.984	0.148	0.415	0.591
88	7.52E+00	0.872	0.977	0.988	0.654	0.938	0.969	0.043	0.198	0.348

293 K; a represents the mass number; Lower energy for group 88 is 6.16 eV.

composition of the homogeneous mixture is changed accordingly from that in Case 2. In the case of oxygen, the potential scattering cross section is approximately 3.9 barn, while that of hydrogen is 20.5 barn. Thus, the number density of oxygen in Case 3 will be $20.5/3.9 \approx 5.25$ times larger than that of hydrogen in Case 2. The evaluated effective cross section is $\sigma_{\text{Case}3}$. When the NJOY code is used, one can arbitrarily set the mass of the admixed moderator. Therefore, we can easily perform Case 3 in the NJOY code, as will be described later (MacFarlane and Muir 1994a).

- Compute the IR parameter by

$$\lambda = \frac{\sigma_{\text{Case}3} - \sigma_{\text{Case}1}}{\sigma_{\text{Case}2} - \sigma_{\text{Case}1}} \quad (86)$$

In (86), the variation in the effective cross section and that of the background cross section is assumed to have a linear relationship. This treatment is justified since the background cross section and the effective cross section has smooth correlation as shown in Fig. 22 and variation of the background cross section is very small in the above calculation.

Examples of evaluation results of the IR parameter for the ^{238}U and ^{235}U absorption cross section are shown in Tables 11 and 12, respectively. In both tables, the 172-group XMAS-type energy group structure is assumed. In the 88th group (7.52 eV–6.16 eV), which includes the large resonance of ^{238}U , the IR parameters for oxygen ($a = 16$), light nuclides ($a = 40$), and uranium ($a = 238$) are approximately 0.87, 0.65, and 0.04, respectively, when the background cross section is 50 barn. This result clearly shows the significance of the IR parameter in the resonance calculation.

Table 12 provides other interesting observations. The IR parameters for ^{235}U are clearly different from those for ^{238}U . For example, the IR parameters of the ^{235}U absorption cross section for oxygen, light nuclide, and uranium are 1.0, 0.77, and 0.15, respectively, in the 88th group. Since the width of the resonance peak for ^{235}U is generally narrower than that for ^{238}U , the IR

Table 12

IR parameter for the microscopic absorption cross section of ^{235}U in 172-groups XMAS energy structure

Group number (XMAS172)	Upper energy [eV]	a= 16 Background XS (barn)			a= 40 Background XS (barn)			a= 238 Background XS (barn)		
		50	1,000	10,000	50	1,000	10,000	50	1,000	10,000
62	3.72E+02	0.999	0.996	1.000	0.980	0.979	1.000	0.926	0.925	0.923
63	3.04E+02	0.952	0.972	0.975	0.932	0.961	0.963	0.824	0.869	0.877
64	2.04E+02	0.992	0.997	0.988	0.995	0.999	1.000	0.814	0.867	0.866
66	1.37E+02	1.000	1.000	1.000	1.000	1.000	1.000	0.911	0.917	0.918
67	9.17E+01	1.000	1.000	1.000	1.000	1.000	1.000	0.669	0.718	0.739
68	7.57E+01	1.000	1.000	1.000	1.000	1.000	1.000	0.922	0.924	0.927
69	6.79E+01	0.955	0.960	0.964	0.811	0.873	0.885	0.430	0.526	0.554
70	5.56E+01	0.958	0.988	0.990	1.000	1.000	1.000	0.629	0.692	0.711
71	5.16E+01	1.000	1.000	1.000	0.958	0.933	0.929	0.767	0.784	0.797
75	3.73E+01	0.956	0.970	0.972	0.981	0.973	0.976	0.183	0.461	0.540
79	2.50E+01	0.989	0.987	0.988	0.915	0.941	0.947	0.747	0.711	0.712
81	1.95E+01	0.990	1.000	1.000	0.954	0.955	0.968	0.350	0.443	0.522
83	1.37E+01	0.974	0.985	0.986	0.990	0.961	0.967	0.370	0.485	0.537
86	9.19E+00	1.000	1.000	1.000	1.000	1.000	1.000	0.331	0.327	0.374
88	7.52E+00	1.000	1.000	1.000	0.775	0.874	0.889	0.154	0.287	0.333

293 K; a represents mass number; Lower energy for group 88 is 6.16 eV.

parameter becomes larger than that of ^{238}U . The systematic estimation of the IR parameter clarifies that the IR parameter depends not only on the resonance nuclide, but also on the magnitude of the background cross section, the temperature, and the energy range (energy group).

The above observation highlights a conflict with (84), which is commonly used in many lattice physics codes. In that equation, the IR parameter is assumed to be a constant that is inherent to each moderator nuclide, that is, the dependency of the IR parameter on various other parameters (temperature, background cross section, and energy range) cannot be directly incorporated. This is a limitation of the conventional IR method, in which only one IR parameter is considered for each nuclide.

We should therefore choose an appropriate IR parameter for each nuclide. First, since ^{238}U is a dominant resonance absorber in light water reactor calculations, ^{238}U can be assumed as a typical resonance absorber. For the background cross section, a typical value for ^{238}U (e.g., 50 barn) can be assumed. For the energy range, the major resonance of ^{238}U in 6.7 eV is considered a typical resonance. Fortunately, temperature has less impact on the IR parameter, since hot operating conditions will be used in the evaluation of the IR parameter.

Some additional discussion related to the IR parameter will be useful. In today's lattice physics codes, the tabulation of an effective cross section (more generally, a cross section library) is performed through a nuclear data processing code such as NJOY (MacFarlane and Muir 1994a). In NJOY, the mass of a moderator nuclide and its background cross section are given

independently through user input. The former is given as the $\alpha = \left(\frac{A-1}{A+1}\right)^2$ parameter for the admixed moderator, and the latter is given by a combination of the fraction of the admixed moderator cross section γ and the background cross section σ_0 . Note that the cross section of the admixed moderator is given by $\gamma\sigma_0$. The remaining part, that is, $(1 - \gamma)\sigma_0$, is generally assumed to be hydrogen.

In conventional lattice physics codes, the mass effect of the moderator is treated through the above approach, that is, correction by the IR parameter. However, when we can freely draw a blueprint of a cross section library for a lattice physics code, the mass effect of the moderator can be incorporated by a correction table that is similar to a self-shielding factor table. In this case, the library has a correction table for each nuclide, which gives the correction factor of the effective cross section for various masses of the moderator. Although the size of such a library will be larger than that of the current one, one can expect it to yield a more accurate treatment. Such a consideration becomes especially useful when lattice physics codes are applied to non-LWRs, for example, heavy water reactors, graphite reactors, and fast reactors.

3.5 Resonance Self-Shielding in a Heterogeneous Systems

3.5.1 Neutron Slowing Down in a Heterogeneous Isolated System

Formulation of Neutron Slowing Down Equation

In this subsection, we will discuss resonance self-shielding in a heterogeneous system (Dirac 1943; Weinberg and Wigner 1958; Dresner 1960; Rosenstein 1960; Goldstein and Cohen 1962; Stamm'ler and Abbate 1983; Rothenstein and Segev 1986). Since various difficulties arise in the treatment of a heterogeneous system, we will start with an isolated system, in which there is an isolated lump of resonance material in a large moderator. A fuel rod in a large moderator region, for example, is an isolated system.

Since it is necessary to know the energy dependence of the neutron spectrum in detail in order to evaluate the effect of resonance shielding, we will consider the neutron slowing down equation in an isolated heterogeneous system:

$$\begin{aligned} \Sigma_{t,f}(E)\phi_f(E)V_f &= P_{f \rightarrow f}(E)V_f \int_0^{\infty} dE' \Sigma_{s,f}(E' \rightarrow E)\phi_f(E') \\ &\quad + P_{m \rightarrow f}(E)V_m \int_0^{\infty} dE' \Sigma_{s,m}(E' \rightarrow E)\phi_m(E') \end{aligned} \quad (87)$$

where

$\Sigma_{t,f}(E)$: macroscopic total cross section in fuel,

$\Sigma_{s,f}(E' \rightarrow E)$: macroscopic scattering cross section in fuel,

$\Sigma_{s,m}(E' \rightarrow E)$: macroscopic scattering cross section in moderator,

$\phi_f(E), \phi_m(E')$: neutron fluxes in fuel and moderator, respectively,

V_f, V_m : volumes of fuel and moderator, respectively, and

$P_{f \rightarrow f}(E), P_{m \rightarrow f}(E)$: fuel-to-fuel, and moderator-to-fuel collision probabilities, respectively.

Space dependent neutron transport can be described in various ways, for example, the discrete-ordinates method, or the method of characteristics. However, the collision probability method is well suited to describe the neutron balance in fuel and moderator regions, since in a simple system, analytical approaches with some approximations can be applied to collision probabilities.

The approximations involved for the collision probability calculation have a crucial meaning in the equivalence theory, as will be discussed later.

If we assume that the neutron slowing down is dominated by elastic scattering, the right-hand side of (87) can be written as

$$\begin{aligned}\Sigma_{t,f}(E)\phi_f(E)V_f &= P_{f \rightarrow f}(E)V_f \sum_{k \in f} \int_E^{E/\alpha_k} \frac{dE' N_k \sigma_{es,k}(E') \phi_f(E')}{(1 - \alpha_k)E'} \\ &\quad + P_{m \rightarrow f}(E)V_m \sum_{k \in m} \int_E^{E/\alpha_k} \frac{dE' N_k \sigma_{es,k}(E') \phi_m(E')}{(1 - \alpha_k)E'}\end{aligned}\quad (88)$$

where k is a nuclide index.

When the NR approximation discussed in [3.4.2](#) is applied to the right-hand side of (88), it becomes

$$\Sigma_{t,f}(E)\phi_f(E)V_f = \frac{1}{E} (P_{f \rightarrow f}(E)V_f \Sigma_{p,f} + P_{m \rightarrow f}(E)V_m \Sigma_{p,m}) \quad (89)$$

where

$\Sigma_{p,f}$: macroscopic potential scattering cross section of fuel, and

$\Sigma_{p,m}$: macroscopic potential scattering cross section of moderator.

In an isolated system, the fuel-to-fuel collision probability can be written as the fuel-to-moderator collision probability

$$P_{f \rightarrow f}(E) = 1 - P_{f \rightarrow m}(E) \quad (90)$$

where

$P_{f \rightarrow m}(E)$: fuel-to-moderator collision probability.

[Equation \(90\)](#) can be derived from the normalization condition of collision probability, that is, the sum of the collision probabilities for fuel-to-fuel, and fuel-to-moderator, is unity. By substituting (90) into (89), we obtain

$$\Sigma_{t,f}(E)\phi_f(E)V_f = \frac{1}{E} ((1 - P_{f \rightarrow m}(E)) V_f \Sigma_{p,f} + P_{m \rightarrow f}(E)V_m \Sigma_{p,m}) \quad (91)$$

Reciprocity Theorem

Two different collision probabilities now appear in (91). A further simplification can be made to derive the analytic form for the energy dependence of the neutron spectrum in the fuel region. Next, we will consider the reciprocity theorem

$$P_{m \rightarrow f}(E)V_m \Sigma_{p,m} = P_{f \rightarrow m}(E)V_f \Sigma_{t,f}(E) \quad (92)$$

In (92), the total cross section of the moderator is assumed to be equal to the potential scattering cross section, which is energy independent.

An intuitive understanding of (92) is as follows. [Equation \(92\)](#) is rewritten as

$$\frac{P_{m \rightarrow f}(E)}{V_f \Sigma_{t,f}(E)} = \frac{P_{f \rightarrow m}(E)}{V_m \Sigma_{p,m}} \quad (93)$$

Since $P_{m \rightarrow f}(E)$ is the collision probability from moderator to fuel, it is proportional to the attenuation between moderator and fuel, the fuel volume, and the total cross section of the fuel. Therefore, $P_{m \rightarrow f}(E)/(V_f \Sigma_{t,f}(E))$ represents the attenuation between moderator and fuel. A similar consideration of $P_{f \rightarrow m}(E)$ yields $P_{f \rightarrow m}(E)(V_m \Sigma_{p,m})$ that is the attenuation between fuel and moderator. Since the neutron attenuation between two points does not have directional dependence (i.e., attenuation from A to B is equivalent to attenuation from B to A), we achieve the equality of (93). Note that $\Sigma_{p,m}$ and $\Sigma_{t,m}$ are assumed to be equal in the above discussion.

By substituting (92) into (91), we obtain

$$\phi_f(E) = \frac{1}{E} \left((1 - P_{f \rightarrow m}(E)) \frac{\Sigma_{p,f}}{\Sigma_{t,f}(E)} + P_{f \rightarrow m}(E) \right) \quad (94)$$

If an accurate value for the fuel-to-moderator collision probability $P_{f \rightarrow m}(E)$ is known, the accurate energy dependence of the neutron flux can be evaluated using (94). A detailed numerical calculation for $P_{f \rightarrow m}(E)$ would give, of course, an accurate result, but such numerical calculation would require considerable computation time. An approximate analytic expression for $P_{f \rightarrow m}(E)$ is therefore needed for an efficient evaluation of the energy dependence of the neutron flux. This approach yields an important by-product: the concept of equivalence between heterogeneous and homogeneous systems, which will be discussed later.

Estimation of Escape Probability and Average Chord Length

In an isolated system, the collision probability from the fuel-to-moderator region is equivalent to the neutron escape probability from the fuel, $P_e(E)$, which is defined by the probability that a neutron born in the fuel region will escape from the fuel without a collision in the fuel, and will suffer its first collision in the moderator.

The escape probability of a neutron, which is flying in direction $\vec{\Omega}$, and whose distance to the fuel lump surface is s , is given by $\exp(-\Sigma_{t,f}(E)s)$. Since the small volume around the neutron is expressed as $(\vec{n} \cdot \vec{\Omega}) dS ds$, the volume average of the escape probability for direction $\vec{\Omega}$ is given by

$$\begin{aligned} P_e(E, \vec{\Omega}) &= \frac{1}{V_f} \int_S (\vec{n} \cdot \vec{\Omega}) dS \int_0^l \exp(-\Sigma_{t,f}(E)s) ds \\ &= \frac{1}{\Sigma_{t,f}(E)V_f} \int_S (\vec{n} \cdot \vec{\Omega}) dS \{1 - \exp(-\Sigma_{t,f}(E)l)\} \end{aligned} \quad (95)$$

where

$\vec{\Omega}$: neutron flight direction,

\vec{n} : normal vector to surface,

S : surface area of a fuel lump,

l : track length of neutron in a fuel lump (chord length), and

s : coordinate along neutron flight direction.

Note that the integration of (95) is carried out for $\vec{n} \cdot \vec{\Omega} > 0$.

The physical meaning of (95) can be explained by Fig. 16.

Since $P_e(E, \vec{\Omega})$ depends on $\vec{\Omega}$, the average on $\vec{\Omega}$ is considered in order to obtain the final form of $P_e(E)$, that is,

$$P_e(E) = \frac{1}{4\pi} \int_{\vec{n} \cdot \vec{\Omega} > 0} P_e(E, \vec{\Omega}) d\vec{\Omega} \quad (96)$$

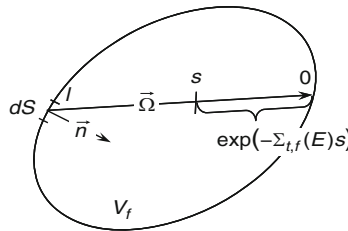


Figure 16
Calculation of escape probability

Using (95) and (96), the escape probability from an isolated fuel lump is given as follows:

$$\begin{aligned} P_e(E) &= \frac{1}{4\pi V_f} \int_{\vec{n} \cdot \vec{\Omega} > 0} d\vec{\Omega} \int_S (\vec{n} \cdot \vec{\Omega}) dS \int_0^l \exp(-\Sigma_{t,f}(E)s) ds \\ &= \frac{1}{4\pi \Sigma_{t,f}(E) V_f} \int_{\vec{n} \cdot \vec{\Omega} > 0} d\vec{\Omega} \int_S dS (\vec{n} \cdot \vec{\Omega}) \{1 - \exp(-\Sigma_{t,f}(E)l)\} \end{aligned} \quad (97)$$

In order to obtain a detailed form of (97), the distribution function of chord length l , which also depends on $\vec{\Omega}$, is necessary. The distribution function of the chord length is given as follows (Dirac 1943):

$$f(l)dl = \frac{\int_l^{l+dl} d\vec{\Omega} \int_S dS (\vec{n} \cdot \vec{\Omega})}{\int_{\vec{n} \cdot \vec{\Omega} > 0} d\vec{\Omega} \int_S dS (\vec{n} \cdot \vec{\Omega})} \quad (98)$$

The value of $f(l)dl$ represents the probability of the chord length's appearance between l and $l + dl$. **Figure 16** presents $(\vec{n} \cdot \vec{\Omega})dS$ as the weight of a chord, whose direction is $\vec{\Omega}$, and which cuts the surface area of dS . As a result, the numerator of (98) shows the summation of the weights of chords whose lengths are between l and $l + dl$, and the denominator shows the summation of the weight of all chords.

The denominator of (98) can be rewritten as follows:

$$\begin{aligned} \int_{\vec{n} \cdot \vec{\Omega} > 0} d\vec{\Omega} \int_S dS (\vec{n} \cdot \vec{\Omega}) &= \int_{\cos \theta > 0} d\vec{\Omega} \int_S dS \cos \theta = \int_0^1 \mu d\vec{\Omega} \int_S dS \\ &= \int_0^1 2\pi \mu d\mu \int_S dS = \pi S \end{aligned} \quad (99)$$

where

$$\begin{aligned} \mu &= \cos \theta, \\ d\vec{\Omega} &= \cos \theta d\theta \int_0^{2\pi} d\varphi = 2\pi d\mu. \end{aligned}$$

The average chord length \bar{l} is given by

$$\bar{l} = \int_0^\infty l f(l) dl \quad (100)$$

Table 13**Parameters for resonance calculation in simple heterogeneous geometry**

Geometry	Surface area	Volume	Average chord length
Slab (H : width of slab)	$2S$	SH	$2H$
Cylinder (R : radius)	$2\pi R$	πR^2	$2R$
Hollow cylinder*	$2\pi(R+r)$	$\pi(R^2 - r^2)$	$2(R-r)$
Sphere (R : radius)	$4\pi R^2$	$4\pi R^3/3$	$4R/3$

*Void is assumed for hollow part. Inner radius is r .

By substituting (98) and (99) into (100), we obtain

$$\bar{l} = \frac{1}{\pi S} \int_{4\pi} d\vec{\Omega} \int_S dS l(\vec{n} \cdot \vec{\Omega}) = \frac{1}{\pi S} \int_{4\pi} d\vec{\Omega} V = \frac{V \cdot 4\pi}{\pi S} = \frac{4V}{S} \quad (101)$$

Note that the following relationship is used in the above derivation:

$$\int_S dS l(\vec{n} \cdot \vec{\Omega}) = V \quad (102)$$

A chord in a lump and its nearby volume constitutes a small “cylinder,” whose bottom area and height are dS and $l(\vec{n} \cdot \vec{\Omega})$, respectively. Thus, $dS l(\vec{n} \cdot \vec{\Omega})$ indicates the volume of the small cylinder in which a chord is contained. Therefore, the integration of the volume of each small cylinder gives the total volume of a lump.

Equation (101) suggests that the average chord length is given by the volume and the surface area of a lump. Typical average chord lengths using simple geometry, which frequently appear in lattice physics computations, are summarized in **Table 13**.

Using (98), (99), and (101), (98) can be rewritten as

$$\int_l^{l+dl} d\vec{\Omega} \int_S dS (\vec{n} \cdot \vec{\Omega}) = \pi S \cdot f(l) dl = \frac{4\pi V}{\bar{l}} f(l) dl \quad (103)$$

By substituting (103) into (97), we obtain

$$\begin{aligned} P_e(E) &= \frac{1}{4\pi \Sigma_{t,f}(E) V_f} \int_{\vec{n} \cdot \vec{\Omega} > 0} d\vec{\Omega} \int_S dS (\vec{n} \cdot \vec{\Omega}) \{1 - \exp(-\Sigma_{t,f}(E)l)\} \\ &= \frac{1}{4\pi \Sigma_{t,f}(E) V_f} \int_0^\infty \int_l^{l+dl} d\vec{\Omega} \int_S dS (\vec{n} \cdot \vec{\Omega}) \{1 - \exp(-\Sigma_{t,f}(E)l)\} \\ &= \frac{1}{4\pi \Sigma_{t,f}(E) V_f} \int_0^\infty \frac{4\pi V_f}{\bar{l}} f(l) dl \{1 - \exp(-\Sigma_{t,f}(E)l)\} \\ &= \frac{1}{\Sigma_{t,f}(E) \bar{l}} \int_0^\infty dl f(l) \{1 - \exp(-\Sigma_{t,f}(E)l)\} \end{aligned} \quad (104)$$

When the actual form of the chord distribution function is known, an analytic form of the escape probability can be derived. Though the actual chord distribution function depends on the shape of the fuel lump, we assume it is given by the following:

$$f(l) dl = \frac{1}{\bar{l}} \exp(-l/\bar{l}) dl \quad (105)$$

[Equation \(105\)](#) indicates the probability of a longer chord existing exponentially decreases as the length of the chord increases (Sauer 1963). Such a distribution is, clearly, a poor approximation for many shapes. The form of [\(105\)](#) remains important, however, if we are to derive the equivalence between heterogeneous and homogeneous systems.

By substituting [\(105\)](#) into [\(104\)](#), we obtain

$$\begin{aligned} P_e(E) &= \frac{1}{\Sigma_{t,f}(E)\bar{l}} \int_0^\infty dl f(l) \{1 - \exp(-\Sigma_{t,f}(E)l)\} \\ &= \frac{1}{\Sigma_{t,f}(E)\bar{l}} \int_0^\infty dl \frac{1}{\bar{l}} \exp(-l/\bar{l}) \{1 - \exp(-\Sigma_{t,f}(E)l)\} \\ &= \frac{1}{\Sigma_{t,f}(E)\bar{l} + 1} \end{aligned} \quad (106)$$

[Equation \(106\)](#) is Wigner's rational approximation for the escape probability (Weinberg and Wigner 1958). [Equation \(106\)](#) suggests that the escape probability from a lump, which has a great optical thickness $\Sigma_{t,f}(E)\bar{l}$, becomes smaller. This is the case for a large total cross section and/or large average chord length. On the contrary, when the optical thickness of a lump is small, the escape probability approaches unity. Such a situation can be observed in a small lump with a small total cross section. We see then, that Wigner's rational approximation satisfies our intuitive sense of the physical properties of the escape probability. In fact, Wigner's rational approximation gives an accurate value for the black limit (infinite $\Sigma_{t,f}(E)\bar{l}$, $P_e(E) = 0$) and the white limit (zero $\Sigma_{t,f}(E)\bar{l}$, $P_e(E) = 1$).

Approximations of Neutron Spectrum in a Heterogeneous System

By approximating the escape probability using the rational approximation in [\(106\)](#), we can derive the “equivalence” between heterogeneous and homogeneous systems, as follows.

[Equation \(94\)](#) is rewritten as follows:

$$\begin{aligned} \phi_f(E) &= \frac{1}{E} \left((1 - P_{f \rightarrow m}(E)) \frac{\Sigma_{p,f}}{\Sigma_{t,f}(E)} + P_{f \rightarrow m}(E) \right) \\ &= \frac{1}{E} \left((1 - P_e(E)) \frac{\Sigma_{p,f}}{\Sigma_{t,f}(E)} + P_e(E) \right) \end{aligned} \quad (107)$$

By substituting [\(106\)](#) into [\(107\)](#), we can derive the following equation:

$$\begin{aligned} \phi_f(E) &= \frac{1}{E} \left(\left(1 - \frac{1}{\Sigma_{t,f}(E)\bar{l} + 1} \right) \frac{\Sigma_{p,f}}{\Sigma_{t,f}(E)} + \frac{1}{\Sigma_{t,f}(E)\bar{l} + 1} \right) \\ &= \frac{1}{E} \frac{\Sigma_{p,f}\bar{l} + 1}{\Sigma_{t,f}(E)\bar{l} + 1} \\ &= \frac{1}{E} \frac{\Sigma_{p,f} + 1/\bar{l}}{\Sigma_{t,f}(E) + 1/\bar{l}} \end{aligned}$$

$$\begin{aligned}
 &= \frac{1}{E} \frac{\Sigma_{p,f} + \Sigma_e}{\Sigma_{t,f}(E) + \Sigma_e} \\
 &= \frac{1}{E} \frac{N_r(\sigma_{p,r} + \sigma_{0,f}) + \Sigma_e}{N_r(\sigma_{t,r}(E) + \sigma_{0,f}) + \Sigma_e} \\
 &= \frac{1}{E} \frac{\sigma_{p,r} + (\sigma_{0,f} + \Sigma_e/N_r)}{\sigma_{t,r}(E) + (\sigma_{0,f} + \Sigma_e/N_r)}
 \end{aligned} \tag{108}$$

where

Σ_e : macroscopic escape cross section,

N_r : number density of the resonance nuclide,

$\sigma_{p,r}$: potential scattering cross section of the resonance nuclide, and

$\sigma_{0,f} = \sum_{k \neq r} N_k \sigma_{s,k} / N_r$: background cross section for the resonance nuclide.

The escape cross section is defined by the inverse of the average chord length ($\Sigma_e = 1/\bar{l}$). When the average chord length is small, the escape cross section becomes large, and vice versa. This suggests that the escape cross section is related to the escape probability from a fuel lump.

Various assumptions are used to derive the above equivalence between heterogeneous and homogeneous systems. They are summarized as follows:

- No resonance overlap is considered.
- Nonresonant nuclide has a constant scattering cross section.
- Resonant nuclide has a constant scattering cross section.
- Neutron slowing down is dominated by elastic scattering.
- Energy dependence of neutron flux at nonresonant part is asymptotic ($1/E$).
- Use of narrow resonance (NR) approximation for neutron slowing down source.
- The escape probability from a lump is approximated by Wigner's rational approximation, that is, (106).

The accuracy of (108) thus depends on the validity of the above assumptions. The approximation for the escape probability, particularly, has a significant impact on the equivalence theory.

3.5.2 Equivalence Theory

When we compare (77) and (108), an apparent similarity can be found. Indeed, by adding the escape cross section to both the numerator and the denominator of (77), we can derive (108). The physical interpretation of this relationship is given as follows.

When a fuel lump has a large escape probability (i.e., an optically thin lump), neutrons entering from the moderator can easily reach everywhere in the fuel lump. This means that the energy dependence (depression) of the neutron flux at the resonance peak is mitigated by the incoming neutrons from the moderator. In other words, neutrons in a fuel lump with a large escape probability will likely experience a collision in the moderator, so that the depression of the neutron flux in the fuel becomes smaller. This effect is captured through the escape cross section. This is analogous to our discussion of the background cross section given by (78). In the previous discussion of a homogeneous system, we noted that the depression of the neutron flux at the resonance peak is mitigated by the background cross section.

The above discussion is the essence of the equivalence theory between heterogeneous and homogeneous systems, that is, the energy dependence of neutron flux can be approximated in the same analytic form by a different argument, σ_0 or $\sigma_{0,f} + \Sigma_e/N_r$.

To sum up, the background cross section with the NR approximation is given by

In a homogeneous system:

$$\sigma_{0,r} = \sum_{k \neq r} N_k \sigma_{p,k} / N_r = \sum_{k \neq r} N_k \sigma_{s,k} / N_r \quad (109)$$

In a heterogeneous system:

$$\sigma_{0,r} = \sigma_{0,f} + \Sigma_e / N_r = \sum_{k \neq r} N_k \sigma_{s,k} / N_r + \Sigma_e / N_r \quad (110)$$

In other words, the effect of heterogeneity on the energy dependence of the neutron flux is represented by the fictitious escape cross section, which is equivalent to, and has the same effect as, the background cross section. Therefore, when the effective cross sections are tabulated for various background cross sections, the result can be used not only for a homogeneous system, but also for a heterogeneous system. From the viewpoint of cross section preparation, this equivalence significantly reduces the size of the tabulation table for effective cross sections. If the equivalence is not used, the effective cross sections for various heterogeneous systems will be tabulated independently. The tabulation of effective cross sections will be discussed in more detail in [3.6](#).

The distribution function of the chord length given by [\(105\)](#) is chosen in order to derive an analytic form of neutron flux that is consistent with that of a homogeneous system. This is a key point of the equivalence theory. In this context, other expressions for the escape probability can be used in the framework of the equivalence theory, as is discussed in [3.5.3](#).

3.5.3 Various Approximations for Escape Probability

Incorporation of the Bell Factor

In [3.5.1](#), the escape probability from a fuel lump was approximated by Wigner's rational approximation of [\(106\)](#) in order to achieve equivalence between heterogeneous and homogeneous systems. Though Wigner's rational approximation reflects our intuition regarding the behavior of the escape probability, better approximations can be used ([Levine 1963](#); [Carlvik 1967](#); [Chiarella and Keane 1969](#); [Mizuta 1970](#); [Stamm'ler and Abbate 1983](#); [Hébert and Marleau 1991](#)). One of the improved rational approximations involves a correction by the Bell factor, as follows:

$$P_e(E) = \frac{a_B}{\Sigma_{t,f}(E)\bar{l} + a_B} = \frac{a_B \Sigma_e}{\Sigma_{t,f}(E) + a_B \Sigma_e} \quad (111)$$

where

a_B : the Bell factor.

The escape probability, $P_e(E)$, is a function of the total cross section and the shape of the fuel lump (i.e., the average chord length). Therefore, when the escape probability is evaluated by

an accurate method (e.g., numerical calculation by the collision probability method), the Bell factor can be evaluated by

$$a_B = \frac{P_e}{1 - P_e} \Sigma_{t,f} \bar{l} \quad (112)$$

In a typical situation that appears in LWR lattice physics computations, $a_B = 1.1\text{--}1.4$ gives adequate results (Levine 1963). By substituting (111) into (107), we obtain

$$\phi_f(E) = \frac{1}{E} \frac{\sigma_{p,r} + (\sigma_{0,f} + a_B \Sigma_e / N_r)}{\sigma_{t,r}(E) + (\sigma_{0,f} + a_B \Sigma_e / N_r)} \quad (113)$$

A comparison of (113) and (108) clarifies the merit of (111). In fact, the escape cross section is modified from Σ_e to $a_B \Sigma_e$ in (113). In other words, the escape probability (which is equivalent to the neutron inflow effect) is underestimated in Wigner's rational approximation as it is conventionally used, as given by (106).

Though the Bell factor is considered as an adjustment parameter, its range of validity can be mathematically derived as follows. When the value of $\Sigma_{t,f}(E) \bar{l}$ is small, (104) is approximated by the Taylor series expansion

$$\begin{aligned} P_e(E) &= \frac{1}{\Sigma_{t,f}(E) \bar{l}} \int_0^\infty dl f(l) \{1 - \exp(-\Sigma_{t,f}(E)l)\} \\ &\approx \frac{1}{\Sigma_{t,f}(E) \bar{l}} \int_0^\infty dl f(l) \left[1 - \left\{1 - \Sigma_{t,f}(E)l + (\Sigma_{t,f}(E)l)^2/2\right\}\right] \\ &= \frac{1}{\bar{l}} \int_0^\infty dl f(l) l - \frac{1}{2} \frac{\Sigma_{t,f}(E)}{\bar{l}} \int_0^\infty dl f(l) l^2 \\ &= 1 - \frac{1}{2} \Sigma_{t,f}(E) \frac{\bar{l}^2}{\bar{l}} \\ &\approx \frac{1}{1 + \frac{1}{2} \Sigma_{t,f}(E) \frac{\bar{l}^2}{\bar{l}}} \\ &= \frac{a_B}{\Sigma_{t,f}(E) \bar{l} + a_B} \end{aligned} \quad (114)$$

where

$$a_B = 2 \frac{(\bar{l})^2}{\bar{l}^2}.$$

The Schwarz inequality is established for arbitrary function $f(l)$.

$$\int l^2 f(l) dl > \left\{ \int l f(l) dl \right\}^2 \quad (115)$$

From (115), we have the following relationship:

$$\bar{l}^2 > (\bar{l})^2 \quad (116)$$

Therefore,

$$a_B = 2 \frac{(\bar{l})^2}{\bar{l}^2} < 2 \quad (117)$$

Utilization of the Bell factor increases the accuracy of the escape probability, which can be rigorously reproduced for a particular energy point (i.e., particular fuel cross section) by choosing an appropriate value for the Bell factor. However, such rigorous reproduction of the escape probability for all energy ranges (i.e., for various fuel cross sections) is impossible, so it still includes an error factor that has the potential to impact resonance calculations.

N-Terms Rational Approximations

Further improvement of the escape probability can be achieved by using the summation form of the rational approximations. In order to derive this approximation, the distribution function of the chord length is approximated by a summation of the exponential functions

$$f(l)dl = \sum_{n=1}^N c_n \exp(-d_n l) dl \quad (118)$$

By substituting (118) into (104), we obtain

$$\begin{aligned} P_e(E) &= \frac{1}{\Sigma_{t,f}(E)\bar{l}} \int_0^\infty dl \sum_{n=1}^N c_n \exp(-d_n l) \{1 - \exp(-\Sigma_{t,f}(E)l)\} \\ &= \frac{1}{\Sigma_{t,f}(E)\bar{l}} \sum_{n=1}^N c_n \int_0^\infty dl \exp(-d_n l) \{1 - \exp(-\Sigma_{t,f}(E)l)\} \\ &= \sum_{n=1}^N \frac{c_n/d_n}{\Sigma_{t,f}(E)\bar{l} + d_n\bar{l}} \\ &= \sum_{n=1}^N \frac{b_n a_n}{\Sigma_{t,f}(E)\bar{l} + a_n} \end{aligned} \quad (119)$$

where

$$\begin{aligned} a_n &= d_n \bar{l}, \\ b_n a_n &= c_n/d_n. \end{aligned}$$

For a very small optical length, (119) can be reduced into

$$P_e(E) = \lim_{\Sigma_{t,f}(E)\bar{l} \rightarrow 0} \sum_{n=1}^N \frac{b_n a_n}{\Sigma_{t,f}(E)\bar{l} + a_n} = \sum_{n=1}^N b_n \quad (120)$$

Since $P_e(E)$ should be approaching unity for a very small optical length, we obtain the normalization condition as follows:

$$\sum_{n=1}^N b_n = 1 \quad (121)$$

Wigner's rational approximation of (106) gives an accurate result for an escape probability with a large $\Sigma_{t,f}(E)\bar{l}$. In order to be consistent with the derivatives of (106) when there is large $\Sigma_{t,f}(E)\bar{l}$, the following constraint on the coefficients of (119) should be satisfied:

$$\sum_{n=1}^N b_n a_n = 1 \quad (122)$$

Note that (122) is an additional constraint, and may not necessarily be satisfied. For example, (111) and (124) do not satisfy (122).

Equation (119) is considered as a superposition of the rational approximations with the Bell factor, that is, a_n and b_n are the Bell factor for each rational approximation and the corresponding weight of each term.

Carlvik's Two-Term Rational Approximation

A well-known approximation for the escape probability for the cylindrical geometry in (119) is given by Carlvik et al. (Carlvik 1967; Stamm'ler and Abbate 1983):

$$P_e(E) = 2 \frac{2}{\Sigma_{t,f}(E)\bar{l} + 2} - \frac{3}{\Sigma_{t,f}(E)\bar{l} + 3} \quad (123)$$

For slab geometry, Roman gives the following (Stamm'ler and Abbate 1983):

$$P_e(E) = 1.1 \frac{1.4}{\Sigma_{t,f}(E)\bar{l} + 1.4} - 0.1 \frac{5.4}{\Sigma_{t,f}(E)\bar{l} + 5.4} \quad (124)$$

The three term rational approximation is also considered to increase the accuracy of the escape probability from a fuel lump (Hébert and Marleau 1991).

By substituting (119) into (107), we obtain

$$\begin{aligned} \phi_f(E) &= \frac{1}{E} \left((1 - P_e(E)) \frac{\Sigma_{p,f}}{\Sigma_{t,f}(E)} + P_e(E) \right) \\ &= \frac{1}{E} \left(\left(1 - \sum_{n=1}^N \frac{b_n a_n}{\Sigma_{t,f}(E)\bar{l} + a_n} \right) \frac{\Sigma_{p,f}}{\Sigma_{t,f}(E)} + \sum_{n=1}^N \frac{b_n a_n}{\Sigma_{t,f}(E)\bar{l} + a_n} \right) \\ &= \frac{1}{E} \left(\left(\sum_{n=1}^N b_n - \sum_{n=1}^N \frac{b_n a_n}{\Sigma_{t,f}(E)\bar{l} + a_n} \right) \frac{\Sigma_{p,f}}{\Sigma_{t,f}(E)} + \sum_{n=1}^N \frac{b_n a_n}{\Sigma_{t,f}(E)\bar{l} + a_n} \right) \\ &= \frac{1}{E} \left(\sum_{n=1}^N b_n \frac{\Sigma_{t,f}(E)\bar{l}}{\Sigma_{t,f}(E)\bar{l} + a_n} \frac{\Sigma_{p,f}}{\Sigma_{t,f}(E)} + \sum_{n=1}^N \frac{b_n a_n}{\Sigma_{t,f}(E)\bar{l} + a_n} \right) \\ &= \frac{1}{E} \sum_{n=1}^N b_n \frac{\Sigma_{p,f}\bar{l} + a_n}{\Sigma_{t,f}(E)\bar{l} + a_n} \\ &= \frac{1}{E} \sum_{n=1}^N b_n \frac{\sigma_{p,r} + \sigma_{0,f} + a_n/\bar{l}/N_r}{\sigma_{t,r}(E) + \sigma_{0,f} + a_n/\bar{l}/N_r} \\ &= \frac{1}{E} \sum_{n=1}^N b_n \frac{\sigma_{p,r} + \sigma_{0,f} + a_n \Sigma_e / N_r}{\sigma_{t,r}(E) + \sigma_{0,f} + a_n \Sigma_e / N_r} \\ &= \frac{1}{E} \sum_{n=1}^N b_n \frac{\sigma_{p,r} + \sigma_{0,n}}{\sigma_{t,r}(E) + \sigma_{0,n}} \end{aligned} \quad (125)$$

where

$$\sigma_{0,n} = \sigma_{0,f} + a_n \Sigma_e / N_r.$$

Evaluation of the Effective Cross Section from N-Term Rational Approximation

Equation (125) is given by the superposition of (113). Though the background cross section for each term in (125) is given by $\sigma_{0,n} = \sigma_{0,f} + a_n \Sigma_e / N_r$, it cannot be directly applied to the interpolation of effective cross sections, due to the superposition of several terms. In this case, the equivalent background cross section for (125) is given as follows:

$$\begin{aligned} \sigma_{g,x} &= \frac{\int_{E_g}^{E_{g-1}} dE \sigma_x(E) \phi_f(E)}{\int_{E_g}^{E_{g-1}} dE \phi_f(E)} \\ &= \frac{\int_{E_g}^{E_{g-1}} dE \sigma_x(E) \frac{1}{E} \sum_{n=1}^N b_n \frac{\sigma_{p,r} + \sigma_{0,n}}{\sigma_{t,r}(E) + \sigma_{0,n}}}{\int_{E_g}^{E_{g-1}} dE \frac{1}{E} \sum_{m=1}^N b_m \frac{\sigma_{p,r} + \sigma_{0,m}}{\sigma_{t,r}(E) + \sigma_{0,m}}} \\ &= \sum_{n=1}^N b_n \frac{\int_{E_g}^{E_{g-1}} dE \sigma_x(E) \frac{1}{E} \frac{\sigma_{p,r} + \sigma_{0,n}}{\sigma_{t,r}(E) + \sigma_{0,n}}}{\int_{E_g}^{E_{g-1}} dE \frac{1}{E} \frac{\sigma_{p,r} + \sigma_{0,n}}{\sigma_{t,r}(E) + \sigma_{0,n}}} - \frac{\int_{E_g}^{E_{g-1}} dE \frac{1}{E} \frac{\sigma_{p,r} + \sigma_{0,n}}{\sigma_{t,r}(E) + \sigma_{0,n}}}{\int_{E_g}^{E_{g-1}} dE \frac{1}{E} \sum_{m=1}^N b_m \frac{\sigma_{p,r} + \sigma_{0,m}}{\sigma_{t,r}(E) + \sigma_{0,m}}} \end{aligned} \quad (126)$$

In order to simplify (126), we can use the following relationship:

$$\sigma_{g,x,n} = \frac{\int_{E_g}^{E_{g-1}} dE \sigma_x(E) \phi_n(E)}{\int_{E_g}^{E_{g-1}} dE \phi_n(E)} = \frac{\int_{E_g}^{E_{g-1}} dE \sigma_x(E) \frac{1}{E} \frac{\sigma_{p,r} + \sigma_{0,n}}{\sigma_{t,r}(E) + \sigma_{0,n}}}{\int_{E_g}^{E_{g-1}} dE \frac{1}{E} \frac{\sigma_{p,r} + \sigma_{0,n}}{\sigma_{t,r}(E) + \sigma_{0,n}}} \quad (127)$$

In (127), $\sigma_{g,x,n}$ is a effective cross section whose background cross section is given by $\sigma_{0,n}$.

Next, we use the following relationship:

$$\begin{aligned} \sigma_{g,a,n} &= \frac{\int_{E_g}^{E_{g-1}} dE \sigma_{a,r}(E) \phi_n(E)}{\int_{E_g}^{E_{g-1}} dE \phi_n(E)} = \frac{\int_{E_g}^{E_{g-1}} dE \frac{1}{E} \sigma_{a,r}(E) \frac{\sigma_{p,r} + \sigma_{0,n}}{\sigma_{t,r}(E) + \sigma_{0,n}}}{\int_{E_g}^{E_{g-1}} dE \frac{1}{E} \frac{\sigma_{p,r} + \sigma_{0,n}}{\sigma_{t,r}(E) + \sigma_{0,n}}} \\ &= \frac{\int_{E_g}^{E_{g-1}} dE \frac{1}{E} \sigma_{a,r}(E) \frac{\sigma_{p,r} + \sigma_{0,n}}{\sigma_{t,r}(E) + \sigma_{0,n}}}{\int_{E_g}^{E_{g-1}} dE \frac{1}{E} \frac{\sigma_{p,r} + \sigma_{a,r}(E) - \sigma_{a,r}(E) + \sigma_{0,n}}{\sigma_{t,r}(E) + \sigma_{0,n}}} \\ &= \frac{\int_{E_g}^{E_{g-1}} dE \frac{1}{E} \sigma_{a,r}(E) \frac{\sigma_{p,r} + \sigma_{0,n}}{\sigma_{t,r}(E) + \sigma_{0,n}}}{\int_{E_g}^{E_{g-1}} dE \frac{1}{E} - \int_{E_g}^{E_{g-1}} dE \frac{1}{E} \sigma_{a,r}(E) \frac{\sigma_{p,r} + \sigma_{0,n}}{\sigma_{t,r}(E) + \sigma_{0,n}} \frac{1}{\sigma_{p,r} + \sigma_{0,n}}} \\ &= \frac{\int_{E_g}^{E_{g-1}} dE \frac{1}{E} \sigma_{a,r}(E) \frac{\sigma_{p,r} + \sigma_{0,n}}{\sigma_{t,r}(E) + \sigma_{0,n}}}{\int_{E_g}^{E_{g-1}} dE \frac{1}{E} - \frac{1}{\sigma_{p,r} + \sigma_{0,n}} \int_{E_g}^{E_{g-1}} dE \frac{1}{E} \sigma_{a,r}(E) \frac{\sigma_{p,r} + \sigma_{0,n}}{\sigma_{t,r}(E) + \sigma_{0,n}}} \end{aligned} \quad (128)$$

From (128), we have

$$\int_{E_g}^{E_{g-1}} dE \frac{1}{E} \sigma_{a,r}(E) \frac{\sigma_{p,r} + \sigma_{0,n}}{\sigma_{t,r}(E) + \sigma_{0,n}} \left/ \int_{E_g}^{E_{g-1}} dE \frac{1}{E} \right. = \frac{\sigma_{g,a,n}}{1 + \frac{\sigma_{g,a,n}}{\sigma_{p,r} + \sigma_{0,n}}} \quad (129)$$

By using (129), we can derive the following equation:

$$\begin{aligned} & \frac{\int_{E_g}^{E_{g-1}} dE \frac{1}{E} \frac{\sigma_{p,r} + \sigma_{0,n}}{\sigma_{t,r}(E) + \sigma_{0,n}}}{\int_{E_g}^{E_{g-1}} dE \frac{1}{E} \sum_{m=1}^N b_m \frac{\sigma_{p,r} + \sigma_{0,m}}{\sigma_{t,r}(E) + \sigma_{0,m}}} \\ &= \frac{\int_{E_g}^{E_{g-1}} dE \frac{1}{E} \frac{\sigma_{p,r} + \sigma_{0,n}}{\sigma_{t,r}(E) + \sigma_{0,n}}}{\sum_{m=1}^N b_m \int_{E_g}^{E_{g-1}} dE \frac{1}{E} \frac{\sigma_{p,r} + \sigma_{0,m}}{\sigma_{t,r}(E) + \sigma_{0,m}}} \\ &= \frac{\int_{E_g}^{E_{g-1}} dE \frac{1}{E} \frac{\sigma_{p,r} + \sigma_{a,r}(E) - \sigma_{a,r}(E) + \sigma_{0,n}}{\sigma_{t,r}(E) + \sigma_{0,n}}}{\sum_{m=1}^N b_m \int_{E_g}^{E_{g-1}} dE \frac{1}{E} \frac{\sigma_{p,r} + \sigma_{a,r}(E) - \sigma_{a,r}(E) + \sigma_{0,m}}{\sigma_{t,r}(E) + \sigma_{0,m}}} \\ &= \frac{\int_{E_g}^{E_{g-1}} dE \frac{1}{E} - \int_{E_g}^{E_{g-1}} dE \frac{1}{E} \sigma_{a,r}(E) \frac{\sigma_{p,r} + \sigma_{0,n}}{\sigma_{t,r}(E) + \sigma_{0,n}} \frac{1}{\sigma_{p,r} + \sigma_{0,n}}}{\sum_{m=1}^N b_m \left(\int_{E_g}^{E_{g-1}} dE \frac{1}{E} - \int_{E_g}^{E_{g-1}} dE \frac{1}{E} \sigma_{a,r}(E) \frac{\sigma_{p,r} + \sigma_{0,m}}{\sigma_{t,r}(E) + \sigma_{0,m}} \frac{1}{\sigma_{p,r} + \sigma_{0,m}} \right)} \\ &= \frac{1 - \frac{1}{\sigma_{p,r} + \sigma_{0,n}} \int_{E_g}^{E_{g-1}} dE \frac{1}{E} \sigma_{a,r}(E) \frac{\sigma_{p,r} + \sigma_{0,n}}{\sigma_{t,r}(E) + \sigma_{0,n}} \left/ \int_{E_g}^{E_{g-1}} dE \frac{1}{E} \right.}{\sum_{m=1}^N b_m \left(1 - \frac{1}{\sigma_{p,r} + \sigma_{0,m}} \int_{E_g}^{E_{g-1}} dE \frac{1}{E} \sigma_{a,r}(E) \frac{\sigma_{p,r} + \sigma_{0,m}}{\sigma_{t,r}(E) + \sigma_{0,m}} \left/ \int_{E_g}^{E_{g-1}} dE \frac{1}{E} \right. \right)} \\ &= \frac{1 - \frac{1}{\sigma_{p,r} + \sigma_{0,n}} \frac{\sigma_{g,a,n}}{1 + \sigma_{g,a,n}/(\sigma_{p,r} + \sigma_{0,n})}}{\sum_{m=1}^N b_m \left(1 - \frac{1}{\sigma_{p,r} + \sigma_{0,m}} \frac{\sigma_{g,a,m}}{1 + \sigma_{g,a,m}/(\sigma_{p,r} + \sigma_{0,m})} \right)} \\ &= \frac{f_n}{\sum_{m=1}^N b_m f_m} \end{aligned} \quad (130)$$

where

$$f_n = \frac{\sigma_{p,r} + \sigma_{0,n}}{\sigma_{p,r} + \sigma_{0,n} + \sigma_{g,a,n}}.$$

Finally, by using (127) and (130), (126) is rewritten as follows:

$$\sigma_{g,x} = \frac{\sum_{n=1}^N w_n \sigma_{g,x,n}}{\sum_{n=1}^N w_n} \quad (131)$$

where

$$w_n = b_n f_n.$$

Resonance Integral and Effective Cross Section

When the resonance integral is tabulated in a cross section library, the following relationship can be used (Stamm'lér et al. 1973):

$$\begin{aligned}
 \sigma_{g,x} &= \frac{\int_{E_g}^{E_{g-1}} dE \sigma_x(E) \phi_f(E)}{\int_{E_g}^{E_{g-1}} dE \phi_f(E)} \\
 &= \frac{\int_{E_g}^{E_{g-1}} dE \sigma_x(E) \frac{1}{E} \sum_{n=1}^N b_n \frac{\sigma_{p,r} + \sigma_{0,n}}{\sigma_{t,r}(E) + \sigma_{0,n}}}{\int_{E_g}^{E_{g-1}} dE \frac{1}{E} \sum_{n=1}^N b_n \frac{\sigma_{p,r} + \sigma_{0,n}}{\sigma_{t,r}(E) + \sigma_{0,n}}} \\
 &= \frac{\sum_{n=1}^N b_n \int_{E_g}^{E_{g-1}} dE \sigma_x(E) \frac{1}{E} \frac{\sigma_{p,r} + \sigma_{0,n}}{\sigma_{t,r}(E) + \sigma_{0,n}}}{\sum_{n=1}^N b_n \int_{E_g}^{E_{g-1}} dE \frac{1}{E} \frac{\sigma_{p,r} + \sigma_{0,n}}{\sigma_{t,r}(E) + \sigma_{0,n}}} \\
 &= \frac{\sum_{n=1}^N b_n \left(\int_{E_g}^{E_{g-1}} (dE/E) \right) \cdot I_{g,x}(\sigma_{0,n})}{\sum_{n=1}^N b_n \int_{E_g}^{E_{g-1}} dE \frac{1}{E} \left(1 - \frac{\sigma_{a,r}(E)}{\sigma_{t,r}(E) + \sigma_{0,n}} \right)} \\
 &= \frac{\sum_{n=1}^N b_n \left(\int_{E_g}^{E_{g-1}} (dE/E) \right) \cdot I_{g,x}(\sigma_{0,n})}{\sum_{n=1}^N b_n \left(\int_{E_g}^{E_{g-1}} (dE/E) \right) - \sum_{n=1}^N b_n \int_{E_g}^{E_{g-1}} dE \sigma_{a,r}(E) \frac{1}{E} \frac{\sigma_{p,r} + \sigma_{0,n}}{\sigma_{t,r}(E) + \sigma_{0,n}} \frac{1}{\sigma_{p,r} + \sigma_{0,n}}} \\
 &= \frac{\sum_{n=1}^N b_n \left(\int_{E_g}^{E_{g-1}} (dE/E) \right) \cdot I_{g,x}(\sigma_{0,n})}{\left(\int_{E_g}^{E_{g-1}} (dE/E) \right) - \sum_{n=1}^N b_n \left(\int_{E_g}^{E_{g-1}} (dE/E) \right) \cdot I_{g,a}(\sigma_{0,n}) / (\sigma_{p,r} + \sigma_{0,n})} \\
 &= \frac{\sum_{n=1}^N b_n I_{g,x}(\sigma_{0,n})}{1 - \sum_{n=1}^N b_n I_{g,a}(\sigma_{0,n}) / (\sigma_{p,r} + \sigma_{0,n})}
 \end{aligned} \tag{132}$$

where $I_{g,x}$ is the resonance integral per unit lethargy width as defined by

$$I_{g,x}(\sigma_{0,n}) = \frac{\int_{E_g}^{E_{g-1}} dE \sigma_x(E) \phi_n(E)}{\int_{E_g}^{E_{g-1}} dE \frac{1}{E}} \approx \frac{\int_{E_g}^{E_{g-1}} dE \sigma_x(E) \left(\frac{1}{E} \frac{\sigma_{p,r} + \sigma_{0,n}}{\sigma_{t,r}(E) + \sigma_{0,n}} \right)}{\int_{E_g}^{E_{g-1}} dE \frac{1}{E}}$$

The resonance integral, which is the energy integration of the reaction rate that is defined by $\int_{E_g}^{E_{g-1}} dE \sigma_x(E) \phi(E)$, is used instead of the effective cross section in the resonance calculation of

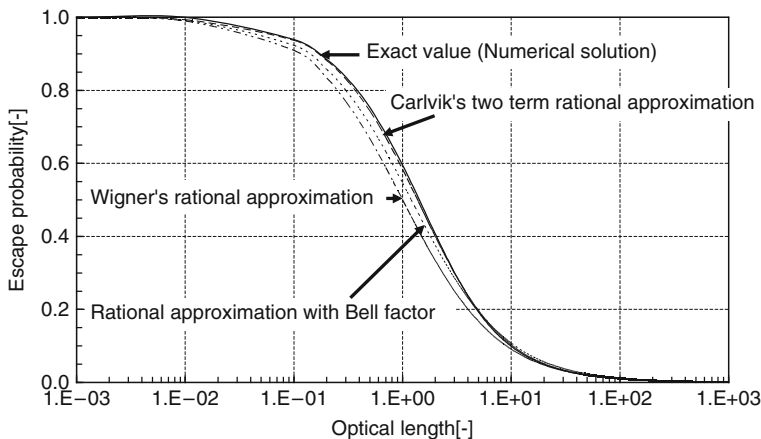


Figure 17

Comparison of various approximations for the escape probability from an infinite cylinder. The horizontal axis shows the average optical length of an infinite cylinder, that is, diameter multiplied by the macroscopic total cross section

some lattice physics codes, for example, the WIMS code. The resonance integral and the effective cross section can be converted into each other using (181), and can thus be considered as almost “equivalent” quantities. As a shortcut for (132), the following can be used as an “equivalent” background cross section:

$$\bar{\sigma}_0 = \left(\sum_{n=1}^N b_n \sqrt{\sigma_{0,n}} \right)^2 \quad (133)$$

The above relationship is justified, since the resonance integral has a strong correlation with the square root of the background cross section for the practical value of background cross sections, as will be discussed in [Sect. 3.6.3](#) with reference to [Fig. 22](#).

We have thus far described three different approximations for the escape probability. [Figures 17](#) and [18](#) show the accuracy of these approximations for an infinite cylindrical fuel lump. Carlvik’s two-term rational approximation of (123) clearly gives better results than the others, and Wigner’s approximation with the Bell factor is the next best. Wigner’s rational approximation as conventionally used gives accurate results for the white and the black limits, but shows a considerable discrepancy at a medium optical thickness, which is mainly the case in common LWR lattice calculations.

3.5.4 Neutron Slowing Down in a Heterogeneous Lattice System

Formulation of Slowing Down Equation in Lattice System

In [Sect. 3.5.1](#), we discussed the energy dependence of the neutron flux in an isolated fuel lump, in which a neutron escaping from one fuel lump never enters other fuel lumps. In an actual fuel assembly, however, many fuel rods are packed in one assembly, so that neutrons that escape from one fuel rod do in fact enter other fuel rods. In this case, the “effective” escape

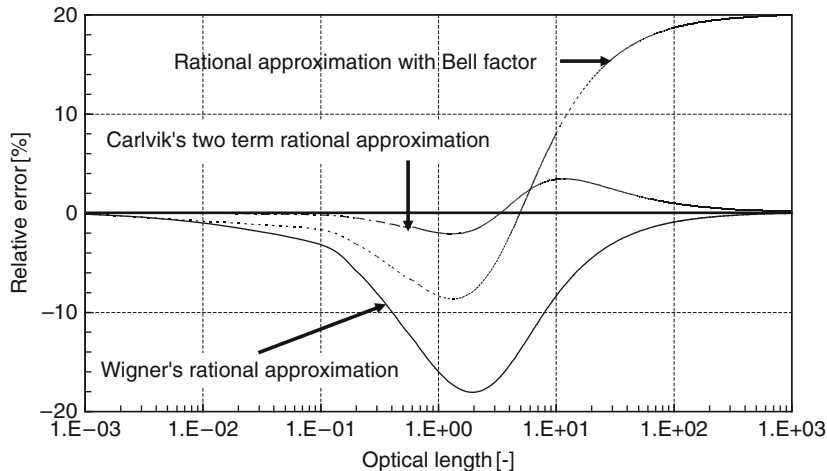


Figure 18

Accuracy of various approximations for the escape probability from an infinite cylinder. The horizontal axis shows the average optical length of the infinite cylinder, that is, the diameter multiplied by the macroscopic total cross section

from a fuel is reduced, so the energy dependence of the neutron flux is affected (Dresner 1960; Rosenstein 1960).

Let us consider an ideal fuel assembly in which the fuel rods are very tightly packed. If there is no gap between fuel pellets (i.e., no moderator and cladding in a fuel assembly), the energy dependence of the neutron flux will be identical to that in a homogeneous system composed of only fuel material. This suggests that the energy dependence of the neutron flux can be roughly expressed as an intermediate dynamic between that found in isolated heterogeneous and homogeneous systems.

The equivalence theory gives a unified description of the energy dependence of the neutron flux in isolated and homogeneous systems. From (108), the neutron flux in an isolated fuel lump is expressed as

$$\phi_f(E) = \frac{1}{E} \frac{\sigma_{p,r} + (\sigma_{0,f} + \Sigma_e/N_r)}{\sigma_{t,r}(E) + (\sigma_{0,f} + \Sigma_e/N_r)} \quad (134)$$

When the escape cross section Σ_e becomes zero, (134) is reduced into that in the homogeneous system given by (77). That is, (134), which is based on the equivalence theory, can express the neutron flux in both heterogeneous and homogeneous systems. We can therefore expect that the neutron flux in a heterogeneous lattice system can also be described in the framework of the equivalence theory, if we adjust the escape cross section. The final goal of this subsection, then, is to derive a definition of the escape cross section in lattice systems.

In the following part, we first discuss a regular lattice system, which consists of an infinite regular array of fuel rods. A regular lattice system, however, does not apply to actual fuel assemblies because they contain many irregularities, for example, guide and instrumentation thimbles in PWR, water channels, gap water, and part length rods in BWR. Such irregularities

have, of course, an impact on neutron flux. Treatment to account for these irregularities will be also discussed later in this subsection.

We begin with the neutron balance equation for a heterogeneous system:

$$\Sigma_{t,f}(E)\phi_f(E)V_f = \sum_j P_{j \rightarrow f}(E)V_j \int_0^\infty dE' \Sigma_{s,j}(E' \rightarrow E) \phi_j(E') \quad (135)$$

where

j : region number in a heterogeneous system, which includes the fuel in question, the moderator, and other fuels.

Recalling the derivation of (89), (135) can be transformed with the NR approximation into the following:

$$\phi_f(E) = \frac{1}{E} \sum_j \frac{P_{j \rightarrow f}(E)V_j \Sigma_{p,j}}{\Sigma_{t,f}(E)V_f} \quad (136)$$

We then consider (137) and (138), which are the normalization conditions of the collision probabilities, and the reciprocity theorem discussed in (92), respectively

$$\sum_{j \neq m} P_{f \rightarrow j}(E) = 1 - P_{f \rightarrow m}(E) \quad (137)$$

$$P_{j \rightarrow f}(E)V_j \Sigma_{t,j}(E) = P_{f \rightarrow j}(E)V_f \Sigma_{t,f}(E) \quad (138)$$

In an actual system composed of multiple regions, m in (137) includes not only the moderator, but also other regions, with the exception of fuel (e.g., cladding). By substituting (137) and (138) into (136), (136) can be rewritten as follows:

$$\begin{aligned} \phi_f(E) &= \frac{1}{E} \sum_j \frac{P_{j \rightarrow f}(E)V_j \Sigma_{p,j}}{\Sigma_{t,f}(E)V_f} \\ &= \frac{1}{E} \sum_j \frac{P_{f \rightarrow j}(E)V_f \Sigma_{t,f}(E)}{\Sigma_{t,j}(E)} \frac{\Sigma_{p,j}}{\Sigma_{t,f}(E)V_f} \\ &= \frac{1}{E} \sum_j \frac{P_{f \rightarrow j}(E)\Sigma_{p,j}}{\Sigma_{t,j}(E)} \\ &= \frac{1}{E} \left(\sum_{j \neq m} \frac{P_{f \rightarrow j}(E)\Sigma_{p,j}}{\Sigma_{t,j}(E)} + \frac{P_{f \rightarrow m}(E)\Sigma_{p,m}}{\Sigma_{t,m}(E)} \right) \\ &\approx \frac{1}{E} \left(\frac{\Sigma_{p,f}}{\Sigma_{t,f}(E)} \sum_{j \neq m} P_{f \rightarrow j}(E) + P_{f \rightarrow m}(E) \right) \\ &= \frac{1}{E} \left((1 - P_{f \rightarrow m}(E)) \frac{\Sigma_{p,f}}{\Sigma_{t,f}(E)} + P_{f \rightarrow m}(E) \right) \end{aligned} \quad (139)$$

In the above derivation, we applied an important assumption, namely, that the macroscopic total cross sections in the fuel regions are spatially constant. This assumption is justified because identical or similar compositions are used in an LWR fuel assembly. However, the above assumption could introduce a crucial error for fuel assemblies of various compositions. Furthermore, no absorption is assumed for the moderator region; that is, the total cross section and the (potential) scattering cross section are identical in the moderator region. Also, the scattering reaction is dominated by the potential scattering, which has an energetically constant cross section.

Dancoff Correction or Dancoff Factor

When (139) and (94) are compared, we can find that they have an identical form, that is, the neutron fluxes in both isolated and lattice systems can be described by a unified analytical form. Note that the above discussion assumes the same composition of fuel, but the regularity of the lattice is not assumed. In this context, (139) can be applied to irregular and general arrangements of heterogeneous fuel.

In the case of an isolated system, the collision probability from the fuel to the moderator is evaluated as the escape probability from the fuel, and is approximated by the rational approximation in order to derive the equivalence between heterogeneous and homogeneous systems. Thus, a similar approach will be useful for (139).

In a lattice system, the number of neutrons entering a fuel region decreases, since part of the neutrons in the moderator region is absorbed into “other” fuels. In other words, other fuels make “shadows” for the fuel we consider. In order to consider the shadowing effect in a lattice system, the Dancoff correction C is used (Stamm’ler and Abbate 1983; Sugimura and Yamamoto 2006):

$$C = \frac{I_0 - I}{I_0} \quad (140)$$

where

I_0 : number of neutrons entering the fuel region in an isolated system,

I : number of neutrons entering the fuel region in question in a lattice system.

When the number of entering neutrons is the same in both isolated and lattice systems, the Dancoff correction is zero ($I = I_0$). On the contrary, when the number of neutrons from the moderator region is fully shadowed, that is, $I = 0$, the Dancoff correction is 1. Thus, the Dancoff correction represents the degree of the shadowing effect by other fuel rods.

The Dancoff correction can also be defined in terms of the reduction of the escape probability. That is, some of the neutrons escaping from a fuel may have their next collision in other fuels. On the contrary, in the case of an isolated fuel (with a convex shape), all neutrons escaping from a fuel have their next collision in the moderator. Thus, the “effective” neutron escape probability from a fuel is reduced in lattice geometry.

Dancoff Correction and Collision Probability in the Moderator

When the thickness of the moderator is l , the un-collided probability between fuels is given by $\exp(-\Sigma_{t,m} l)$. Here l is defined by the distance between one fuel from which a neutron escapes, and another fuel in which the neutron has a collision. Thus, the Dancoff correction is given by the following equation:

$$C = \frac{\int_{\vec{n} \cdot \vec{\Omega} > 0} d\vec{\Omega} \int_S dS (\vec{n} \cdot \vec{\Omega}) \exp(-\Sigma_{t,m} l)}{\int_{\vec{n} \cdot \vec{\Omega} > 0} d\vec{\Omega} \int_S dS (\vec{n} \cdot \vec{\Omega})} \quad (141)$$

In the case of isolated geometry, the Dancoff correction is zero, since $\exp(-\Sigma_{t,m} l)$ is zero for infinite l . When the isotropic neutron source is uniformly distributed, (140) and (141) give identical results, which can be proved through selected formulations (Kobayashi 1995). Since approximations for (141) can be derived more easily than those for (140), in the following discussion we will consider (141). Note that (140) is used for the neutron current method and the

enhanced neutron current method, which are suitable for the evaluation of the Dancoff correction in complicated and large geometries (Sugimura and Yamamoto 2006; Yamamoto 2009). Explanations of these methods will be given later.

In order to discuss the characteristics of the Dancoff correction, an approximate expression for the Dancoff correction will be derived, though it is not used in actual lattice physics calculations. We now consider the chord length distribution in the moderator region, $f(l)dl$, which is a concept similar to the escape probability from a fuel discussed in ➤ 3.5.1. With the chord distribution function, the Dancoff correction is given by

$$C = \int_0^\infty dl f(l) \exp(-\Sigma_{t,m} l) \quad (142)$$

Equation (142) indicates that the Dancoff correction is given by the average of probability that there will not be a collision with the moderator. In some lattice physics computations, the Dancoff factor D is also used:

$$\begin{aligned} D &= 1 - C = 1 - \int_0^\infty dl f(l) \exp(-\Sigma_{t,m} l) \\ &= \int_0^\infty dl f(l) - \int_0^\infty dl f(l) \exp(-\Sigma_{t,m} l) \\ &= \int_0^\infty dl f(l) \{1 - \exp(-\Sigma_{t,m} l)\} \end{aligned} \quad (143)$$

In order to incorporate the Dancoff correction into the equivalence theory, approximations similar to those used for the escape probability from fuel are applied to the Dancoff correction. First, the chord length distribution is approximated by the exponential function, which is used for the escape probability from fuel, that is, (105):

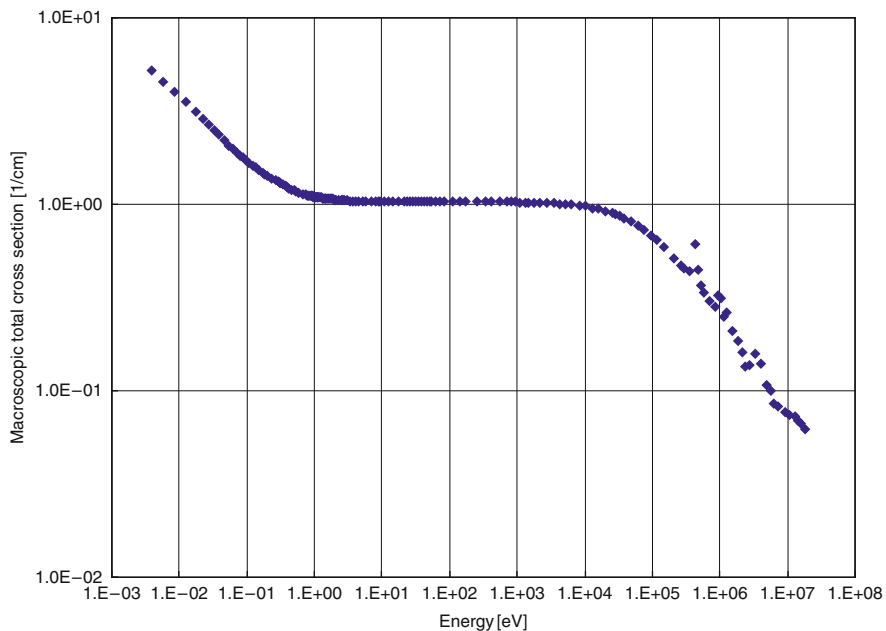
$$f(l)dl = \begin{cases} 0 & (l < l_m) \\ \frac{1}{\bar{l} - l_m} \exp\left\{-(l - l_m)/(\bar{l} - l_m)\right\} d(l - l_m) & (l \geq l_m) \end{cases} \quad (144)$$

where l_m is the minimum thickness of the moderator between two fuels. From the definition, the chord length function is zero for $l < l_m$. Therefore, the chord length distribution for the moderator is defined by the parallel translation of the chord length distribution for a fuel region, which is given by (105). By substituting (144) into (142), we obtain

$$\begin{aligned} C &= \int_0^\infty dl f(l) \exp(-\Sigma_{t,m} l) \\ &= \int_{l_m}^\infty \frac{1}{\bar{l} - l_m} \exp\left\{-(l - l_m)/(\bar{l} - l_m)\right\} \exp(-\Sigma_{t,m} l) d(l - l_m) \\ &= \frac{\exp(-\Sigma_{t,m} l_m)}{\Sigma_{t,m} \cdot (\bar{l} - l_m) + 1} \end{aligned} \quad (145)$$

(145), particularly, becomes Wigner's rational approximation for the escape probability from the moderator when $l_m = 0$:

$$C = \frac{1}{\Sigma_{t,m} \bar{l} + 1}. \quad (146)$$

**Figure 19**

Example of the macroscopic cross section of light water (under typical LWR operating conditions)

Note that the moderator region among the fuel is “isolated” when $l_m = 0$. In this case, (146) gives the escape probability for an isolated “moderator” lump. A corresponding equation for a fuel is given by (106). From the perspective of its physical meaning, the Dancoff correction is similar to that of the escape probability from fuel, that is, the escape probability from the moderator. However, since the total cross section of the moderator is fairly constant in the resonance energy range, as shown in Fig. 19, the Dancoff correction is incorporated in the equivalence theory as an independent energy constant. It depends only on the chord length distribution of the moderator region and the total cross section of the moderator, and does not depend on the fuel cross section.

Dancoff Correction and Escape Probability for an Isolated Fuel Lump

When the angular distribution of neutrons entering from the moderator region into the fuel is isotropic, the collision probability from the fuel to the moderator in a lattice system is expressed as follows (Kobayashi 1995):

$$P_{f \rightarrow m}(E) = \frac{(1 - C)P_e(E)}{1 - (1 - \Sigma_{t,f}(E)\bar{l}P_e(E))C} \quad (147)$$

where

$P_{f \rightarrow m}(E)$: collision probability from the fuel to the moderator in a lattice system, and
 $P_e(E)$: escape probability from the fuel (i.e., collision probability from the fuel to the moderator in an isolated system).

When Wigner's rational approximation with the Bell factor is applied to (147), we obtain

$$\begin{aligned}
 P_{f \rightarrow m}(E) &= \frac{(1-C)P_e(E)}{1 - (1 - \Sigma_{t,f}(E)\bar{l}P_e(E))C} \\
 &= \frac{(1-C) \cdot \frac{a_B}{\Sigma_{t,f}(E)\bar{l} + a_B}}{1 - \left(1 - \Sigma_{t,f}(E)\bar{l} \cdot \frac{a_B}{\Sigma_{t,f}(E)\bar{l} + a_B}\right)C} \\
 &= \frac{g(C, a_B)}{\Sigma_{t,f}(E)\bar{l} + g(C, a_B)}
 \end{aligned} \tag{148}$$

where

$$g(C, a_B) = \frac{(1-C)a_B}{1 + C(a_B - 1)} \tag{149}$$

By comparing (111) and (148), we have the following relationship:

$$\frac{\bar{l}^{iso}}{\bar{l}^{lat}} = \frac{4V}{S^{iso}} \frac{S^{lat}}{4V} = \frac{S^{lat}}{S^{iso}} = \frac{\Sigma_e^{lat}}{\Sigma_e^{iso}} = \frac{g(C, a_B)/\bar{l}}{a_B/\bar{l}} = \frac{(1-C)}{1 + C(a_B - 1)} \tag{150}$$

Therefore, the “effective” surface area of the fuel from which the inflow of neutrons is reduced in the lattice system due to the shadowing effect of other fuels. In the case of Wigner's rational approximation ($a_B = 1$):

$$\frac{S^{lat}}{S^{iso}} = (1 - C) \tag{151}$$

Thus, the Dancoff correction directly shows the reduction in the effective surface area of the fuel in the lattice system.

Equivalence Theory in Lattice System

By substituting (148) into (139), we obtain

$$\begin{aligned}
 \phi_f(E) &= \frac{1}{E} \left((1 - P_{f \rightarrow m}(E)) \frac{\Sigma_{p,f}}{\Sigma_{t,f}(E)} + P_{f \rightarrow m}(E) \right) \\
 &= \frac{1}{E} \left(\left(1 - \frac{g(C, a_B)}{\Sigma_{t,f}(E)\bar{l} + g(C, a_B)}\right) \frac{\Sigma_{p,f}}{\Sigma_{t,f}(E)} + \frac{g(C, a_B)}{\Sigma_{t,f}(E)\bar{l} + g(C, a_B)} \right) \\
 &= \frac{1}{E} \frac{\Sigma_{p,f}\bar{l} + g(C, a_B)}{\Sigma_{t,f}(E)\bar{l} + g(C, a_B)} \\
 &= \frac{1}{E} \frac{\Sigma_{p,f} + g(C, a_B)/\bar{l}}{\Sigma_{t,f}(E) + g(C, a_B)/\bar{l}} \\
 &= \frac{1}{E} \frac{\Sigma_{p,f} + g(C, a_B)\Sigma_e}{\Sigma_{t,f}(E) + g(C, a_B)\Sigma_e}
 \end{aligned}$$

$$\begin{aligned}
&= \frac{1}{E} \frac{N_r(\sigma_{p,r} + \sigma_{0,f}) + g(C, a_B)\Sigma_e}{N_r(\sigma_{t,r}(E) + \sigma_{0,f}) + g(C, a_B)\Sigma_e} \\
&= \frac{1}{E} \frac{\sigma_{p,r} + (\sigma_{0,f} + g(C, a_B)\Sigma_e/N_r)}{\sigma_{t,r}(E) + (\sigma_{0,f} + g(C, a_B)\Sigma_e/N_r)}
\end{aligned} \tag{152}$$

If we invoke the relevant discussion of the equivalence theory, the background cross section for nuclide r is given by

$$\sigma_{0,r} = \sigma_{0,f} + g(C, a_B)\Sigma_e/N_r \tag{153}$$

When (113) and (153) are compared, the background cross section in a lattice system becomes smaller than that in an isolated system, since $g(C, a_B) \leq a_B$. In a lattice system, the self-shielding effect is larger than it is in an isolated system, as was discussed previously. Equation (153) represents this physical phenomenon. When $a_B = 1$, the background cross section is given by

$$\sigma_{0,r} = \sigma_{0,f} + D\Sigma_e/N_r \tag{154}$$

In the case of an isolated system ($D = 1$), the background cross section for nuclide r given by (154) is equivalent to (110), which was originally derived for an isolated system.

3.5.5 Calculation of the Dancoff Factor and Background Cross Sections

Calculation of Dancoff Factor Using the Collision Probability Method

Once the Dancoff correction has been calculated, we can estimate the background cross section in a lattice geometry, as shown in (154). Though various analytical methods have been developed for the estimation of the Dancoff correction in simple geometries (i.e., slab, cylinder), the following numerical procedure with the collision probability method is actually used in today's lattice physics codes. We will now consider the value of $\Sigma_{t,f}(E)\bar{l}P_{f \rightarrow m}(E)$, whose detailed analytic form is derived from (147)

$$\Sigma_{t,f}(E)\bar{l}P_{f \rightarrow m}(E) = \Sigma_{t,f}(E) \frac{(1-C)\bar{l}P_e(E)}{1 - (1 - \Sigma_{t,f}(E)\bar{l}P_e(E))C} \tag{155}$$

In conventional equivalence theory, we treat a fuel as black, that is, the total cross section of a fuel is very large. By applying this assumption, we obtain

$$\begin{aligned}
\lim_{\Sigma_{t,f}(E) \rightarrow \infty} \Sigma_{t,f}(E)\bar{l}P_{f \rightarrow m}(E) &= \lim_{\Sigma_{t,f}(E) \rightarrow \infty} \frac{\Sigma_{t,f}(E)\bar{l}(1-C)P_e(E)}{1 - C + \Sigma_{t,f}(E)\bar{l}P_e(E)C} \\
&= \lim_{\Sigma_{t,f}(E) \rightarrow \infty} \frac{(1-C)P_e(E)}{(1-C)/(\Sigma_{t,f}(E)\bar{l}) + P_e(E)C} \\
&= \lim_{\Sigma_{t,f}(E) \rightarrow \infty} \frac{(1-C)P_e(E)}{P_e(E)C} = \frac{(1-C)}{C}
\end{aligned} \tag{156}$$

where

$$\bar{l} = 4V/S.$$

In actual numerical computations, the total cross section of a fuel region is set at a sufficiently large value (e.g., 10^5 cm^{-1}), and then the collision probability from a fuel to the moderator is calculated (Tsuehihashi et al. 1982; Stamm'ler and Abbate 1983; Ishiguro 1985). Once the collision probability from a fuel to the moderator is obtained, the Dancoff correction is evaluated by (156). Note that the chord length is calculated by the volume and surface area of the fuel region, that is, $\bar{l} = 4V/S$, as given in (101). Once the Dancoff correction is obtained, we can easily evaluate the background cross section, which is used for the calculation of effective cross sections.

The above derivation also represents a potential source of error in the Dancoff correction method. For example, let us consider a fuel pellet that is annularly subdivided into multiple regions. Such a subdivision is usually used for a Gadolinia-bearing fuel pellet. The Dancoff correction for the inner region of a subdivided fuel pellet is clearly unity, since the collision probability from the inner region of the fuel to the moderator approaches zero, due to the large total cross section in a pellet. In other words, neutrons cannot “escape” from the inner region of the fuel to the moderator at resonance peak energy, because they always experience collisions in the outer regions of the fuel pellet, which have a very large total cross section. When the Dancoff correction is unity ($C = 1$ or $D = 0$), the background cross section becomes identical to that of a homogeneous system. The above discussion suggests that spatial dependent self-shielding cannot be directly handled by the Dancoff correction given by (156), which represents a major drawback of the conventional equivalence theory.

That said, the above discussion of the Dancoff correction also shows the advantage it offers. The Dancoff correction does not depend on the composition (cross section) of a fuel; it is calculated by the geometry and the cross section of the moderator. Variations in the cross section in the moderator region are very smooth, especially in the resonance energy range, as shown in ➤ Fig. 19. The calculation of the Dancoff correction is thus greatly simplified, and once the Dancoff correction is obtained (with a representative moderator cross section), it can be used for all resonance energy groups.

In the equivalence theory, the heterogeneity effect for a fuel region is incorporated through the escape cross section, and the property of a moderator is taken into account through the Dancoff correction. The escape cross section and the Dancoff correction are both constants. In reality, interaction takes place between the fuel and moderator regions through the “communication” of neutrons, that is, the neutron spectrum in each region is affected by the spectrum in the other region. In the equivalence theory, this situation is simplified, and the effects of the moderator, and of other fuels on the neutron spectrum, are treated independently through the escape cross section, and the Dancoff correction, respectively. Such simplicity contributes greatly to the success of the equivalence theory in conventional resonance calculations. Again, however, it should be noted that such simplification could restrict the application of the Dancoff correction.

Neutron Current Method for Dancoff Correction Calculation

In the following part of this subsection, two numerical methods to evaluate the Dancoff correction and the background cross section are introduced, that is, the neutron current method and the enhanced neutron current method (Sugimura and Yamamoto 2006; Yamamoto 2008, 2009). In conventional equivalence theory, the heterogeneous effect (the Dancoff correction) is evaluated by the collision probability method, as was previously discussed. Though the collision probability method is very efficient for a simple geometry, its applicability to large and

complicated geometries is quite limited due to its computational inefficiency. For example, a collision probability calculation of an LWR fuel assembly still requires considerable computation time, even with the latest computers. For this reason, direct calculation of the Dancoff correction for a large geometry using the collision probability method would be limited by the computation time it requires.

Recently, the method of characteristics has been widely used for neutron transport calculations in lattice physics computations. The neutron current and the enhanced neutron current methods utilize the method of characteristics, rather than the collision probability method, to evaluate the Dancoff correction and the background cross section in a heterogeneous geometry (Sugimura and Yamamoto 2006; Yamamoto 2008, 2009). Using these methods, the Dancoff correction and the background cross section in a large and complicated geometry, such as that of an LWR fuel assembly, can be easily calculated.

The neutron current method and the enhanced neutron current method are based on the approximations used in the equivalence theory, that is, the NR approximation, the rational approximation for the escape probability, and the black-limit approximation of a fuel lump. Thus, they are mathematically equivalent to the equivalence theory used in current lattice physics codes. In other words, the accuracy of these methods is the same as that of the conventional equivalence theory. Though many lattice physics codes utilize collision probability methods for the evaluation of the Dancoff correction in a simple geometry, in a large geometry (even in an entire LWR core) the Dancoff correction is easily calculated by the neutron current and the enhanced neutron current methods.

The original definition of the Dancoff correction is given by the reduction of the incoming neutron current into fuel regions, as shown in (140). In the neutron current method, the Dancoff correction is calculated by the neutron flux in the fuel region as follows:

$$C = \frac{\phi_0 - \phi}{\phi_0} \quad (157)$$

where

ϕ_0 : neutron flux of fuel region at isolated system, and

ϕ : neutron flux of fuel region at lattice system.

When we assume that there is no neutron (slowing down) source in a fuel region, and that the fuel is purely an absorber material with a very large absorption cross section, the average neutron flux in a fuel region will be proportional to the incoming neutron current into the fuel. In such a case, (157) can be rewritten as follows:

$$C = \frac{I_0 - I}{I_0} = \frac{\phi_0 - \phi}{\phi_0} \quad (158)$$

Since the transport codes used in lattice physics computations have the capability to estimate the neutron flux in each region, the definition of the Dancoff correction given by (157) is useful, and is easily adopted in current lattice physics codes. That is, when a lattice physics code utilizes the method of characteristics for transport calculations, the transport module can be directly used for estimation of the Dancoff correction.

A detailed discussion of the validity of (158) is given as follows. For the sake of simplicity, we will consider a fuel-moderator two-region system.

Recalling (94), the energy dependence of the neutron flux in an isolated fuel lump is given by

$$\phi_f(E) = \frac{1}{E} \left((1 - P_{f \rightarrow m}(E)) \frac{\Sigma_{p,f}}{\Sigma_{t,f}(E)} + P_{f \rightarrow m}(E) \right) \quad (159)$$

With (139), that in a lattice system is

$$\phi_f(E) = \frac{1}{E} \left((1 - P_{F \rightarrow M}(E)) \frac{\Sigma_{p,f}}{\Sigma_{t,f}(E)} + P_{F \rightarrow M}(E) \right) \quad (160)$$

Note that the fuel and moderator regions in a lattice system are indicated by F and M , respectively, to distinguish them from those in an isolated system (f and m). When the black-limit approximation is applied to the fuel region, (159) can be simplified as follows:

$$\begin{aligned} \phi_0 &= \lim_{\Sigma_{t,f}(E) \rightarrow \infty} \phi_f(E) \\ &= \lim_{\Sigma_{t,f}(E) \rightarrow \infty} \frac{1}{E} \left((1 - P_{f \rightarrow m}(E)) \frac{\Sigma_{p,f}}{\Sigma_{t,f}(E)} + P_{f \rightarrow m}(E) \right) \\ &= \frac{1}{E} \lim_{\Sigma_{t,f}(E) \rightarrow \infty} P_{f \rightarrow m}(E) \\ &= \frac{1}{E} \left(1 - \lim_{\Sigma_{t,f}(E) \rightarrow \infty} P_{f \rightarrow f}(E) \right) \end{aligned} \quad (161)$$

Note that the normalization condition for collision probability, that is, $P_{f \rightarrow m}(E) = 1 - P_{f \rightarrow f}(E)$, is used. Similarly, for the lattice system

$$\begin{aligned} \phi &= \lim_{\Sigma_{t,f}(E) \rightarrow \infty} \phi_F(E) \\ &= \lim_{\Sigma_{t,f}(E) \rightarrow \infty} \frac{1}{E} \left((1 - P_{F \rightarrow M}(E)) \frac{\Sigma_{p,f}}{\Sigma_{t,f}(E)} + P_{F \rightarrow M}(E) \right) \\ &= \frac{1}{E} \lim_{\Sigma_{t,f}(E) \rightarrow \infty} P_{F \rightarrow M}(E) \\ &= \frac{1}{E} \left(1 - \lim_{\Sigma_{t,f}(E) \rightarrow \infty} P_{F \rightarrow F}(E) - \lim_{\Sigma_{t,f}(E) \rightarrow \infty} P_{F \rightarrow F'}(E) \right) \end{aligned} \quad (162)$$

where

$P_{F \rightarrow M}(E) = \sum_{j \neq F, F'} P_{F \rightarrow j}(E)$: collision probability from fuel F to other regions, except for fuel (F and F'), and

$P_{F \rightarrow F'}(E) = \sum_{j=F'} P_{F \rightarrow j}(E)$: collision probability from fuel F to other fuels F' (fuel F is not included in fuel F').

Here, the relationship $P_{F \rightarrow M}(E) = 1 - P_{F \rightarrow F}(E) - P_{F \rightarrow F'}(E)$ is used.

By substituting (161) and (162) into (157), we obtain

$$\begin{aligned}
 C &= \frac{\phi_0 - \phi}{\phi_0} \\
 &= \frac{\frac{1}{E} \left(1 - \lim_{\Sigma_{t,f}(E) \rightarrow \infty} P_{f \rightarrow f}(E) \right) - \frac{1}{E} \left(1 - \lim_{\Sigma_{t,f}(E) \rightarrow \infty} P_{F \rightarrow F}(E) - \lim_{\Sigma_{t,f}(E) \rightarrow \infty} P_{F \rightarrow F'}(E) \right)}{\frac{1}{E} \left(1 - \lim_{\Sigma_{t,f}(E) \rightarrow \infty} P_{f \rightarrow f}(E) \right)} \\
 &= \frac{\lim_{\Sigma_{t,f}(E) \rightarrow \infty} P_{F \rightarrow F}(E) - \lim_{\Sigma_{t,f}(E) \rightarrow \infty} P_{f \rightarrow f}(E) + \lim_{\Sigma_{t,f}(E) \rightarrow \infty} P_{F \rightarrow F'}(E)}{1 - \lim_{\Sigma_{t,f}(E) \rightarrow \infty} P_{f \rightarrow f}(E)} \\
 &= \frac{\lim_{\Sigma_{t,f}(E) \rightarrow \infty} P_{F \rightarrow F'}(E)}{1 - \lim_{\Sigma_{t,f}(E) \rightarrow \infty} P_{F \rightarrow F}(E)}
 \end{aligned} \tag{163}$$

Note that the fuel-to-fuel self-collision probabilities are identical in both isolated and lattice systems (i.e., $P_{f \rightarrow f}(E) = P_{F \rightarrow F}(E)$), since the fuel-to-fuel self-collision probabilities depend only upon the property of the fuel lump we are considering.

The original definition of the Dancoff correction states that a fraction of the neutrons escaping from a fuel lump suffer their first collision in other fuel lumps. The numerator and denominator of (163) represent the collision probability in other fuel lumps, and the escape probability from the fuel we are considering. Thus (163), which is derived from an analytic expression of the neutron flux, is mathematically identical to that of the original definition of the Dancoff correction. The above discussion can easily be extended to more complicated systems with more than two materials.

In the actual numerical computation of the Dancoff factor, the following procedure is followed:

- a. The total cross section of each material in the system, except for the fuel, is set to be equivalent to the value of the potential scattering cross section of each material. No scattering is assumed (scattering cross section is set at zero), so the total and absorption cross sections are identical for each material.
- b. The neutron source intensity of each material in the system, except for the fuel, is set to be equivalent to the value of the potential scattering cross section (the NR approximation).
- c. The total cross section of the fuel is set to be sufficiently large, for example, 10^5 cm^{-1} . No scattering is assumed (scattering cross section is set at zero), so the total and the absorption cross sections are identical, in terms of fuel.
- d. The neutron source intensity in the fuel is set at zero.
- e. Perform a one-group fixed-source neutron transport calculation in an isolated system, in which the fuel lump in question is put in a sufficiently large moderator.
- f. Evaluate the neutron flux in the fuel region obtained in step (e).
- g. Perform a one-group fixed-source neutron transport calculation in a lattice system.
- h. Evaluate the neutron flux in the fuel region obtained in step (g).
- i. Evaluate the Dancoff correction by (157).

Using the neutron current method, the Dancoff correction can be evaluated not only for a fuel, but for other resonance materials as well. For example, zirconium isotopes, which are used

in cladding, channel boxes and water rods, have resonances, so that appropriate self-shielding should be taken into account. Since cladding, channel boxes and water rods form a complicated geometry in a BWR fuel assembly, it becomes quite difficult to calculate the Dancoff correction accurately. However, the neutron current method offers an easy way to evaluate the Dancoff correction for zirconium isotopes in a complicated geometry.

An example of the calculation results of the Dancoff factors D ($D = 1 - C$) for fuel pins is shown in Fig. 20, which represents a typical setting of a fuel assembly adjacent to a baffle plate in a PWR (Sugimura and Yamamoto 2006). The Dancoff factor depends on the position of the fuel rod, and it becomes large for fuel rods that are adjacent to a baffle plate. Since the same resonance material (uranium) does not exist in the baffle and reflector regions, neutrons from the baffle-reflector region are not “shadowed.” Thus, the Dancoff factor becomes large; that is, the Dancoff correction becomes small in the region near the baffle-reflector. Furthermore, the Dancoff factors obtained by the neutron current method are consistent with those obtained by the conventional collision probability method.

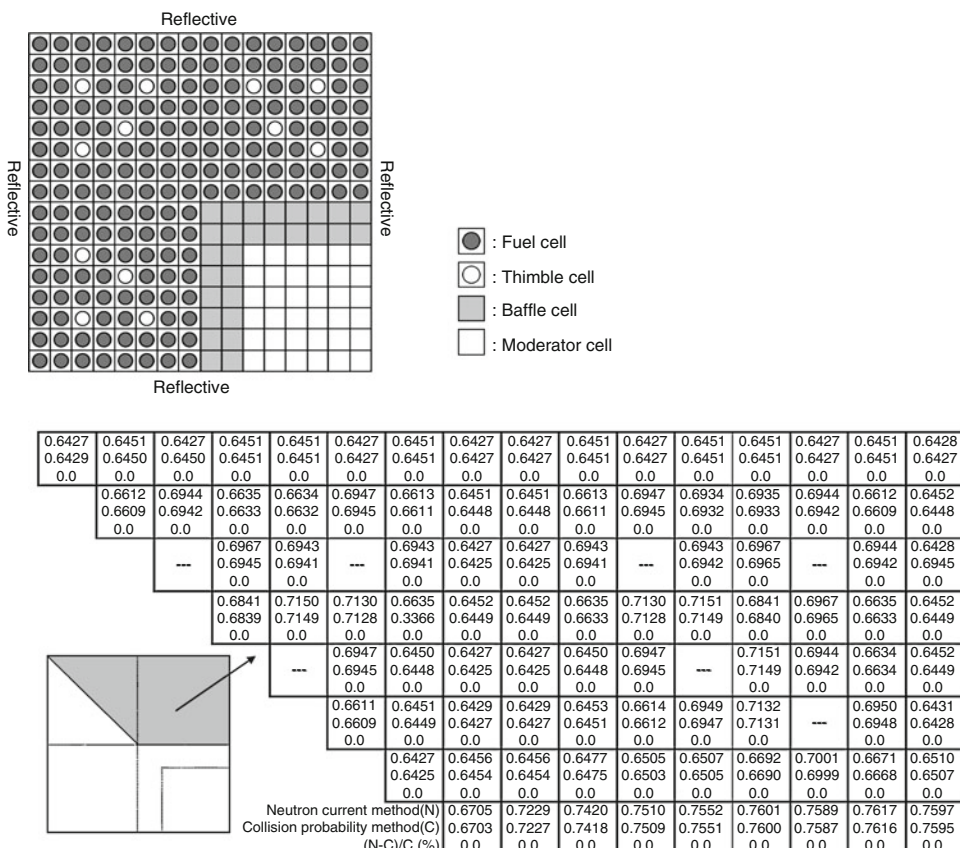


Figure 20

Example of Dancoff factors in a large and complicated geometry

Enhanced Neutron Current Method for Background Cross Section Evaluation

In the neutron current method, two transport calculations are needed to evaluate the Dancoff correction in isolated and lattice systems. The enhanced neutron current method offers a simpler way to calculate the background cross section; one fixed-source transport calculation in one group is sufficient to evaluate the background cross section, including the heterogeneous effect (Yamamoto 2008, 2009). In the enhanced neutron current method, the total reaction rate of fuel region $\Sigma_{t,f}(E)\phi_f(E)$ is considered. By using (152), we obtain

$$\Sigma_{t,f}(E)\phi_f(E) = \Sigma_{t,f}(E) \frac{\Sigma_{p,f} + g(C, a_B)\Sigma_e}{\Sigma_{t,f}(E) + g(C, a_B)\Sigma_e} \quad (164)$$

Note that the term $1/E$ is omitted since its variation is much smoother than that due to the resonance peak, and the source intensity can be adjusted. That is, the source intensity due to slowing down by the potential scattering is considered to be $\Sigma_{p,f}$, instead of $\Sigma_{p,f}/E$.

When the black-limit approximation is applied to the fuel, (164) can be reduced as follows:

$$\begin{aligned} \lim_{\Sigma_{t,f}(E) \rightarrow \infty} \Sigma_{t,f}(E)\phi_f(E) &= \lim_{\Sigma_{t,f}(E) \rightarrow \infty} \Sigma_{t,f}(E) \frac{\Sigma_{p,f} + g(C, a_B)\Sigma_e}{\Sigma_{t,f}(E) + g(C, a_B)\Sigma_e} \\ &= \Sigma_{p,f} + g(C, a_B)\Sigma_e \\ &= N_r(\sigma_{p,r} + \sigma_{0,f}) + g(C, a_B)\Sigma_e \\ &= N_r\sigma_{p,r} + N_r(\sigma_{0,f} + g(C, a_B)\Sigma_e/N_r) \end{aligned} \quad (165)$$

By using (165), we can derive the background cross section, including the heterogeneous effect, as follows:

$$\begin{aligned} \sigma_0 &= \sigma_{0,f} + g(C, a_B)\Sigma_e/N_r \\ &= \frac{\lim_{\Sigma_{t,f}(E) \rightarrow \infty} \Sigma_{t,f}(E)\phi_f(E) - N_r\sigma_{p,r}}{N_r} \\ &= \frac{\lim_{\Sigma_{t,f}(E) \rightarrow \infty} \Sigma_{t,f}(E)\phi_f(E)}{N_r} - \sigma_{p,r} \end{aligned} \quad (166)$$

In lattice geometry, the Dancoff correction can also be derived using (166), that is,

$$g(C, a_B) = \frac{\lim_{\Sigma_{t,f}(E) \rightarrow \infty} \Sigma_{t,f}(E)\phi_f(E) - N_r\sigma_{p,r} - N_r\sigma_{0,f}}{\Sigma_e} \quad (167)$$

The value of $\lim_{\Sigma_{t,f}(E) \rightarrow \infty} \Sigma_{t,f}(E)\phi_f(E)$, which is the total reaction rate, can be evaluated by means of a transport calculation by using the method of characteristics. The escape cross section is given by $S/(4V)$. The number density and the potential scattering cross sections are known values. Therefore, the right-hand side of (167) can be evaluated. When the Bell factor is unity, $g(C, a_B)$ becomes the Dancoff factor $D(D = 1 - C)$, from the definition of $g(C, a_B)$ given by (149).

The actual calculation procedure of the enhanced neutron current method is as follows:

- a. The total cross sections of a material in the system, except for the fuel, are set to be equivalent to the potential scattering cross section. No scattering is assumed, so the total and absorption cross sections are identical in these materials.
- b. The neutron source intensities of the materials in the system (including the fuel region) are set to be equivalent to the potential scattering cross section (the NR approximation).
- c. The total cross section of the fuel is set to be sufficiently large, for example, 10^5 cm^{-1} . No scattering is assumed, so the total and the absorption cross sections in the fuel are identical.
- d. Perform a one-group fixed-source neutron transport calculation in the lattice system.
- e. Evaluate the total reaction rate $\Sigma_{t,f}(E)\phi_f(E)$ in each fuel region.
- f. Evaluate the background cross section by (166). The Dancoff factor can be evaluated by (167) with the Bell factor $a_B = 1$, if necessary.

The enhanced neutron current method gives a different background cross section for each fuel rod, which reflects the spatial source distribution in the moderator region, and the spatial variation of the neutron inflow to the fuels. In this method, the shadowing effect from the other fuel rods is naturally taken into account.

Since the fuel region is considered as a completely black material, that is, all fuels are treated as being made of the same material with a very large absorption cross section, the difference in fuel cross sections among fuel rods cannot be taken into account in this method. In this context, the enhanced neutron current method is consistent with the conventional equivalence theory, with Wigner's rational approximation and the Dancoff correction. Therefore, the enhanced neutron current method cannot be applied to self-shielding calculations in which the grayness of a fuel must be taken into account, for example, calculation of the space-dependent effective cross section in a pellet.

One may consider the possibility of applying the N -term rational approximation in the derivation of the enhanced neutron current method. However, since the accuracy of Wigner's rational approximation is the same as that of the N -term rational approximation, the accuracy of the enhanced neutron current method cannot be improved by incorporation of the N -term rational approximation. The following formulation will clarify this discussion.

First, by recalling the discussion for (119) and (148), we assume that the fuel-to-moderator collision probability can be expressed by the following rational approximation:

$$P_{f \rightarrow m}(E) = \sum_{n=1}^N \frac{g(C, a_B)b_n a_n}{\Sigma_{t,f}(E)\bar{l} + g(C, a_B)a_n} \quad (168)$$

By substituting (168) into (139) and using (121), we obtain

$$\phi_f(E) = \frac{1}{E} \sum_{n=1}^N b_n \frac{\Sigma_{p,f} + g(C, a_B)a_n \Sigma_e}{\Sigma_{t,f}(E) + g(C, a_B)a_n \Sigma_e} \quad (169)$$

Therefore, the total reaction rate is given by

$$\begin{aligned}
 \lim_{\Sigma_{t,f}(E) \rightarrow \infty} \Sigma_{t,f}(E) \phi_f(E) &= \lim_{\Sigma_{t,f}(E) \rightarrow \infty} \Sigma_{t,f}(E) \sum_{n=1}^N b_n \frac{\Sigma_{p,f} + g(C, a_B) a_n \Sigma_e}{\Sigma_{t,f}(E) + g(C, a_B) a_n \Sigma_e} \\
 &= \sum_{n=1}^N b_n \lim_{\Sigma_{t,f}(E) \rightarrow \infty} \Sigma_{t,f}(E) \frac{\Sigma_{p,f} + g(C, a_B) a_n \Sigma_e}{\Sigma_{t,f}(E) + g(C, a_B) a_n \Sigma_e} \\
 &= \sum_{n=1}^N b_n \{ \Sigma_{p,f} + g(C, a_B) a_n \Sigma_e \} \\
 &= \sum_{n=1}^N b_n \Sigma_{p,f} + \sum_{n=1}^N b_n g(C, a_B) a_n \Sigma_e \\
 &= \Sigma_{p,f} \sum_{n=1}^N b_n + g(C, a_B) \Sigma_e \sum_{n=1}^N b_n a_n \\
 &= \Sigma_{p,f} + g(C, a_B) \Sigma_e
 \end{aligned} \tag{170}$$

Equation (170) indicates that the total reaction rate is the same as that in (165), which is derived with the one-term rational approximation. In other words, the obtained background cross section is independent of the number of terms in the rational approximation. This is to be expected, since the behavior of the N -term rational approximation converges with that of the one-term rational approximation at the black limit.

In the enhanced neutron current method, the black limit is assumed for evaluation of the background cross section. However, it can be extended to include the “grayness” of the fuel by including the total reaction rate obtained by the moderate magnitude of the total cross sections, that is, a_n and b_n is determined by the least square fitting of $\Sigma_{t,f}(E) \phi_f(E) = \Sigma_{t,f}(E) \sum_{n=1}^N b_n \frac{\Sigma_{p,f} + g(C, a_B) a_n \Sigma_e}{\Sigma_{t,f}(E) + g(C, a_B) a_n \Sigma_e}$. This approach is a generalization of Hébert and Marleau (1991), in which the collision probability method is used (Koike et al. 2010).

3.5.6 Stamm'ler's Method for a Heterogeneous Lattice System

In 3.5.5, the lattice effect was considered in terms of the Dancoff correction, and the escape probability from a fuel lump in a lattice system was corrected (reduced) by applying the Dancoff correction.

There is another approach to treating the lattice effect in the equivalence theory, which is discussed in detail by Stamm'ler et al. and is currently being adopted in major lattice physics codes, such as CASMO, WIMS, and PHOENIX (Stamm'ler and Abbate 1983). In this subsection, Stamm'ler's treatment of the lattice effect will be briefly reviewed.

In an infinite lattice system, the collision probability from region I to J is assumed to be expressed by

$$p_{IJ} = p_{ij} + p_{ib} R p_{bj} + p_{ib} R p_{bb} R p_{bj} + p_{ib} R p_{bb} R p_{bb} R p_{bj} + \dots \tag{171}$$

where

p_{IJ} : collision probability from region I to J in a lattice system,

p_{ij} : collision probability from i to j in an isolated system,

p_{bb} : transmission probability of a neutron from cell boundary b to another cell boundary b ,

p_{ib} : transmission probability of a neutron born in region i to reach cell boundary b ,

p_{bj} : collision probability that a neutron entering cell boundary b will suffer its first collision in region j , and

R : reflection probability at cell boundary b .

In (171), several paths from region I to J in the lattice system are taken into account, so that the collision probability becomes larger than it is in an isolated system. The first term of the right-hand side of (171) is the direct collision from region i to j inside a cell. The second term represents a collision from region i to the cell boundary, then from the cell boundary to region j in another cell. The third term represents a collision from region i to the cell boundary, then from the cell boundary to another cell boundary (transmission of the cell), and finally from the cell boundary to region j . When a neutron is passing through a cell boundary, the reflection probability is taken into account by considering the neutron reflection at the fuel assembly boundary. When a fuel assembly becomes large, the reflection probability approaches unity, since most of the fuel cells are not adjacent to the assembly boundary.

Equation (171) can be transformed as follows:

$$p_{IJ} = p_{ij} + \frac{Rp_{ib}p_{bj}}{1 - Rp_{bb}} \quad (172)$$

By incorporating several physical considerations, whose details are given by Stamm'ler and Abbate (1983), we obtain the following formula:

$$p_{FF} = p_{ff} + \frac{x(1 - p_{ff})^2}{x(1 - p_{ff}) + A + B} \quad (173)$$

where

$$x = \frac{4V_f}{S_f} \Sigma_{t,f}$$

$$A = \frac{S_b}{S_f t_{fb}^2} \gamma_b^0$$

$$B = \frac{S_b}{S_f t_{fb}^2} \frac{f(1-g)}{1-f(1-g)}$$

S_b : surface area of cell boundary,

S_f : surface area of fuel lump (pellet),

V_f : volume of fuel lump,

t_{fb} : transmission probability that neutrons leaving a fuel surface with cosine angular distribution will reach the cell boundary,

γ_b^0 : blackness of a cell when the total cross section of the fuel is zero,

f : ratio of assembly surface area to that of the sum of all cell surface areas,

g : first-flight reflection probability across the gap between fuel assemblies.

Note that $B = 0$ in the case of an infinite regular lattice, that is, pin cell geometry.

In contrast to the Dancoff correction, this method naturally incorporates the energy dependence of the shadowing effect among fuel rods. The relationship between the Dancoff factor and Stamm'ler's method is shown as follows:

$$D = \lim_{\Sigma_{t,f} \rightarrow \infty} \frac{1 - p_{FF}}{1 - p_{ff}} = 1 - \frac{1}{1 + A + B} \quad (174)$$

Therefore, the Dancoff correction method is considered to be an asymptotic case with a black-limit approximation.

Next, we will try to express (173) with a rational approximation in order to derive an equivalence relationship. For an isolated fuel lump with a cylindrical shape, we can apply Carlvik's two-term rational approximation, as defined by (123):

$$P_e(E) = 1 - P_{ff}(E) = 2 \frac{2}{\Sigma_{t,f}(E)\bar{l} + 2} - \frac{3}{\Sigma_{t,f}(E)\bar{l} + 3} \quad (175)$$

Substituting (175) into (173), and after some algebra, we obtain

$$p_e^{lat} = 1 - p_{FF} = \beta_1 \frac{\alpha_1}{x + \alpha_1} + \beta_2 \frac{\alpha_2}{x + \alpha_2} \quad (176)$$

where

$$\begin{aligned} \alpha_{1,2} &= \frac{(5C + 6) \mp \sqrt{C^2 + 36C + 36}}{2(C + 1)} \\ C &= A + B \\ \beta_1 &= \frac{C' - \alpha_1}{\alpha_2 - \alpha_1} \\ \beta_2 &= 1 - \beta_1 \\ C' &= \frac{4C + 6}{C + 1} \end{aligned}$$

By substituting (176) into (139) we obtain

$$\phi_f(E) = \frac{1}{E} \sum_{n=1}^2 \beta_n \frac{\sigma_{p,r} + \sigma_{0,n}}{\sigma_{t,r}(E) + \sigma_{0,n}} \quad (177)$$

where

$$\sigma_{0,n} = \sigma_{0,f} + \alpha_n \Sigma_e / N_r$$

Now we have a form identical to that in (125). Therefore, with (131), (132), or (133), we can derive the effective cross section using Stamm'ler's method.

The advantages and disadvantages of Stamm'ler's method are summarized as follows:

- Energy dependence of the shadowing effect for a regular lattice is taken into account approximately.
- Boundary effect of a fuel assembly is taken into account approximately using an average.
- Approximate treatment of the assembly boundary effect.

- Rational approximation for the escape probability.
- This method only yields the effective cross section for an “average pin cell” in a fuel assembly. Effective cross sections that are position-dependent due to lattice irregularity (e.g., gap water, water holes, or water rods) cannot be evaluated. The Dancoff correction is still needed to evaluate such effects.

3.5.7 Potential Limitations of the Equivalence Theory

In [3.5](#), the equivalence theory for resonance calculations, which is widely used for current lattice physics computations, is discussed. In the explanation of each method, several crucial approximations used in the equivalence theory were pointed out (Mizuta [1970](#)). Since these approximations largely determine the accuracy and applicability of the equivalence theory, a review of the approximations used in the equivalence theory is most useful. They are summarized as follows:

1. No resonance overlap is considered.

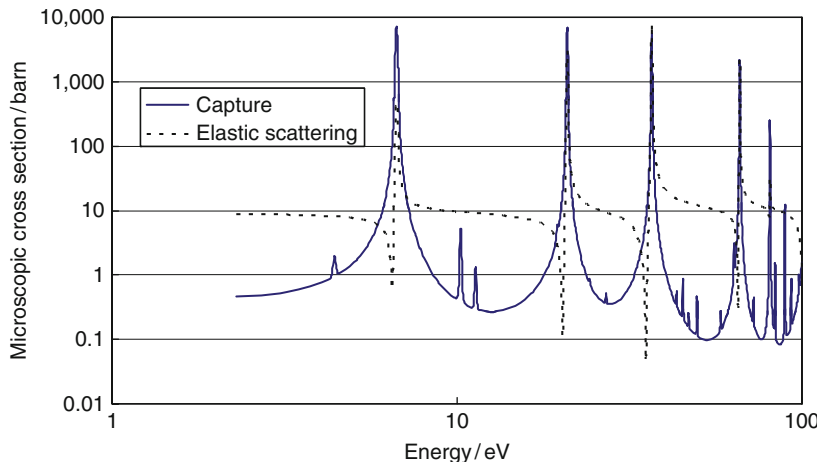
In the neutron slowing down calculation, the cross section variation is considered only for a resonance isotope, and the scattering cross section is assumed to be constant and dominated by the potential scattering, which is independent of energy. Since various nuclides exist in fuel, especially in a burnt fuel, coincident overlaps among resonance peaks of different nuclides are inevitable. The effect of such resonance overlap has an impact on the energy dependence of the neutron flux. In the preparation of a cross section library, the slowing down calculation for an ultrafine energy group structure is usually carried out with point-wise cross sections. The slowing down calculation is numerically carried out with a resonance nuclide and an energetically constant background cross section. In a common multigroup cross section library, therefore, the resonance overlap effect is not taken into account. The resonance overlap effect will be discussed in more detail in [3.10](#), since it has a considerable impact on effective cross section evaluation.

2. Nonresonant nuclide has a constant scattering cross section.

In an LWR lattice, the major contributors to the slowing down of neutrons are hydrogen and oxygen. In the resonance energy range, these nuclides have fairly constant cross sections, so this assumption is appropriate. Note that in the preparation of a cross section, a constant background cross section is assumed in the slowing down calculation.

3. Resonant nuclide has a constant scattering cross section.

In reality, the scattering cross section of a resonance nuclide in the resonance energy range is not constant, and sometimes has peaks of the scattering cross section (resonance scattering), as shown in [Fig. 21](#). Though the constant scattering cross section is assumed in the NR, WR, and IR approximations, the explicit energy dependence of the scattering cross section of a resonance nuclide is taken into account in the slowing down calculation in cross section library preparation. This inconsistency would be a source of error in the equivalence theory.

**Figure 21**

Microscopic capture and elastic scattering cross sections of ^{238}U (ENDF/B-VII, 300 K)

4. Neutron slowing down is dominated by elastic scattering.

In the resonance energy range, this assumption is appropriate. However, we should take care that neutron slowing down due to elastic scattering does not incorporate the thermal vibration of the target nuclides. If the thermal vibration is taken into account, the energy dependence of the neutron flux will be changed. This simplification (no thermal vibration in the slowing down calculation in the resonance energy range) could be a source of error not only for the equivalence theory, but also for other resonance calculation methods, including the continuous-energy Monte Carlo method (Lee et al. 2009).

5. Energy dependence of the neutron flux in the nonresonant part is asymptotic.

In the equivalence theory, the energy dependence of the neutron flux in the nonresonant part is assumed to be asymptotic ($1/E$). However, in cross section library preparation, the neutron slowing down calculation is usually explicitly carried out for a resonance nuclide with a constant background cross section. In reality, therefore, the energy dependence of the neutron flux in the nonresonant part is not assumed to be asymptotic. This inconsistency would be a cause of error in the equivalence theory.

6. The NR, WR, and IR approximations.

In cross section library preparation, hydrogen is usually used as a background nuclide. Therefore, when the moderator in a system consists of only hydrogen, the homogeneous term in the background cross section (except for the escape cross section) will not be a source of error. However, since various nuclides exist in a system, the slowing down of neutrons by these nuclides should be accurately taken into account in an actual situation. In this context, both the NR and WR approximations will be a source of error, since these methods incorporate approximations to evaluate the source of the slowing down. The IR approximation offers an adjustment

factor for various nuclides with a heavier mass. As discussed in [3.4.4](#), the conventional IR approximation, which utilizes one IR parameter for a nuclide, is still a source of error since one IR parameter cannot be applied to all self-shielding situations.

7. Escape probability from a fuel lump.

In the equivalence theory, the escape probability from a fuel lump is approximated by the rational approximation to derive the equivalence between homogeneous and heterogeneous systems. However, since the rational approximation cannot rigorously reproduce the escape probability from a fuel lump for all fuel cross section values, it is a source of error in the equivalence theory.

8. Dependence of the Dancoff correction on the moderator cross section.

The Dancoff correction depends on the cross section of the moderator, which is theoretically energy dependent. However, in actual lattice physics computations, the Dancoff correction is usually assumed to be constant throughout the resonance energy range. Though the cross section of the moderator is fairly flat in this energy range, this assumption could be a source of error.

9. The same fuel material (cross section) for all fuel.

The lattice effect, that is, the shadowing effect by other fuels, is incorporated through the Dancoff correction or Stamm'ler's method. These methods are based on the assumption that all fuels in the system consist of the same material (cross section). However, various fuel materials are used in a single fuel assembly, and different types of fuel assemblies may be loaded into adjacent positions in a core. The shadowing effect that is evaluated using the above assumption may not be accurate.

10. Spatially constant cross section in fuel and moderator.

In the evaluation of the escape probability from a fuel lump, the cross section in a fuel lump is assumed to be spatially constant. This situation captures a fuel pellet well, before burnup. However, once a fuel pellet experiences burnup, the fuel composition has a spatial variation due to the gradient of flux in the fuel pellet and the space-dependent resonance shielding effect. For example, ^{239}Pu is generally produced on the pellet surface due to the spatially self-shielding effect of ^{238}U . Therefore, this assumption might be a source of error in the equivalence theory. Fortunately, as several studies have confirmed, the spatial average treatment does not have a significant impact on the accuracy of resonance calculations (Rothenstein et al. [1988](#); Stoker and Weiss [1996](#)).

11. Black approximation in the Dancoff correction evaluation.

In the evaluation of the Dancoff correction, a fuel lump is assumed to be black, that is, is assumed to behave as a completely absorbent material. This is a source of error in the capture of the lattice effect. For example, let us consider the resonance shielding of ^{239}Pu in a UO_2 pellet. In the beginning of life, the number density of ^{239}Pu is small. In this situation, the self-shielding of ^{239}Pu is not black, that is, it is in an intermediate, diluted (or "gray") condition. However, in the estimation of the Dancoff correction, the entire nuclide is assumed to be black, and could thus be a source of error. The Dancoff correction for a resonance nuclide with a low concentration would therefore be overestimated, since the resonance nuclide is assumed to be completely black, that is, is assumed to have a very large macroscopic cross section.

3.6 Tabulation of Self-Shielding Factors

3.6.1 Cross Section Processing and Effective Cross Sections

In the framework of the equivalence theory, multigroup cross sections are prepared by solving the slowing down equation in a homogeneous medium, as was discussed in [Sect. 2](#). A number of cross section processing codes, such as NJOY, are used for cross section preparation. Cross section processing codes perform slowing down calculations for various background cross sections and temperature conditions, since the self-shielding effect significantly depends on these parameters. Finally, cross section processing codes output the relationship among the background cross section, the temperature, and the effective cross section. These parameters are tabulated in the cross section library of lattice physics codes.

In a typical cross section library, the effective cross sections are not directly tabulated as a function of the background cross section and temperature. Instead, the base cross section for the reference temperature (e.g., 293 K) and infinite background cross section (e.g., 10^{10} barn), and their ratios to the base cross sections for other temperatures and background cross sections, are tabulated in a cross section library (Abagyan et al. [1980](#)). The ratio is the self-shielding factor, which is defined as

$$f(\sigma_0, T) = \frac{\sigma(\sigma_0, T)}{\sigma(\sigma_0^{\text{inf}}, T_{\text{ref}})} \quad (178)$$

where

$f(\sigma_0, T)$: self-shielding factor for the background cross section (σ_0) and temperature (T);
 $\sigma(\sigma_0^{\text{inf}}, T_{\text{ref}})$: base cross section and σ_0^{inf} is a sufficiently large background cross section, for example, 10^{10} barn, and T_{ref} is a reference temperature, for example, room temperature; and
 $\sigma(\sigma_0, T)$: effective cross section at the background cross section (σ_0) and temperature (T).

The shielded cross section is reconstructed as

$$\sigma(\sigma_0, T) = \sigma(\sigma_0^{\text{inf}}, T_{\text{ref}}) f(\sigma_0, T) \quad (179)$$

A cross section library that tabulates the reference cross sections and the shielding factors is referred to as a Bondarenko-type cross section library.

Another choice is the tabulation of the base cross section at a reference condition and the deviation of a cross section from the base cross section. The design of the MATXS format, for example, was based on this concept (Macfarlane and Muir [1994a](#)). In this case, the shielded cross section is reconstructed by

$$\sigma(\sigma_0, T) = \sigma(\sigma_0^{\text{inf}}, T_{\text{ref}}) + \Delta\sigma(\sigma_0, T) \quad (180)$$

where $\Delta\sigma(\sigma_0, T)$: difference of effective cross section at the background cross section (σ_0) and temperature (T).

When a cross section does not have resonance, the difference of the cross section in (180) will be zero at the same temperature. Therefore, we can naturally compress the size of a cross section library by truncating (or compressing) the zero values in the self-shielding factor table. This explains the superiority of the MATXS format.

The resonance integral given in (132) can be also used instead of the effective cross section. The resonance integral is converted into the effective cross section as follows:

$$\sigma_{g,x} = \frac{I_{g,x}(\sigma_0, T)}{1 - I_{g,a}(\sigma_0, T)/(\sigma_{p,r} + \sigma_0)} \quad (181)$$

where

$\sigma_{g,x}$: effective cross section of reaction type x ,

$I_{g,x}(\sigma_0, T)$: resonance integral of reaction type x for background cross section (σ_0) and temperature T ,

$I_{g,a}(\sigma_0, T)$: resonance integral of absorption reaction for background cross section (σ_0), and temperature T ,

σ_0 : background cross section, and

$\sigma_{p,r}$: potential scattering cross section of the resonance nuclide.

In the case of the N -term rational approximation, (132) is used to obtain the effective cross section.

3.6.2 Interpolation of Self-Shielding Factor Table

Since the self-shielding factor table is tabulated for discrete values of background cross sections and temperatures, interpolation is necessary in order to obtain an effective cross section for a desired background cross section and temperature.

Since the range of the background cross section is very wide (typically $10\text{--}10^{10}$ barn), linear interpolation is not a suitable approach. The grid point for the background cross section is often chosen as the equal interval on a logarithmic axis. In fact, the dependence of an effective cross section on the background cross section is expressed as a reasonably smooth function when the background cross section is expressed on a logarithmic axis, as shown in  Fig. 22.

Therefore, interpolation by the background cross section should be performed on a logarithmic basis. A higher-order polynomial function could be used to increase the accuracy of the interpolation. However, an unphysical polynomial dip would degrade the accuracy of the interpolation when the grid points of the background cross section are not appropriate and/or the variation in the effective cross sections is steep.

Though the accuracy of linear interpolation on a log-log scale is generally lower than that of a higher-order polynomial, the method of linear interpolation is more robust. Therefore, one should carefully check the validity of the cross section interpolation method when it is implemented in a lattice physics code. In general, the reproducibility of the effective cross section should be checked against various background cross sections and temperatures, including the intervals between tabulation points.

When the property of the neutron spectrum is taken into account, the following formula will be also suitable for interpolation:

$$\sigma_{g,x}(\sigma_0) = \sigma_{g,x}(\sigma_0 = \infty) \cdot \frac{\sigma_0^{-1} + a - \sigma_0 b}{\sigma_0^{-1} + c - \sigma_0 d} \quad (182)$$

where

a, b, c, d : parameters for interpolation.

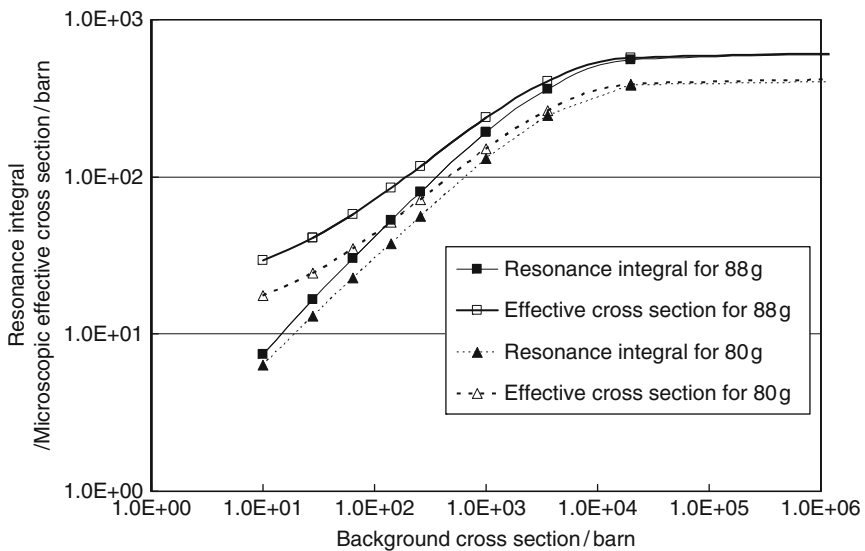


Figure 22

Variations in the resonance integral and effective cross section (absorption) of ^{238}U at 900 K, for 80 g (22.6–19.45 eV) and 88 g (7.52–6.16 eV) of 172 XMAS group structure

Equation (182) was originally derived for subgroup cross sections (to be described later) based on the NR approximation for neutron flux in a resonance peak (Yamamoto 2003, 2004).

In the original derivation, the four coefficients in (182) were analytically derived. In the actual interpolation procedure, however, the coefficients in (182) (a , b , c , and d) can be evaluated by the tabulated data set for the background cross section and the effective cross section. Since (182) well reproduces the behavior of the effective cross section for a wide range of background cross sections, (182) offers an accurate approach to interpolation.

Examples of a number of interpolation schemes are shown below:

$$RI(\sigma_0) = a + b\sqrt{\sigma_0} \quad (183)$$

$$\sigma_{eff}(\sigma_0)/\sigma_{eff}(\sigma_0 = \infty) = \sqrt{\sigma_0} \exp[-f\sigma_0] \quad (184)$$

$$\sigma_{eff}(\sigma_0)/\sigma_{eff}(\sigma_0 = \infty) = 1 + a(\tan h(b \ln[\sigma_0] + c) - 1) \quad (185)$$

$$\sigma_{eff}(\sigma_0)/\sigma_{eff}(\sigma_0 = \infty) = \sqrt{(a + \sigma_0)/(a + b + \sigma_0)} \quad (186)$$

$$RI(\sigma_0)/RI(\sigma_0 = \infty) = (\sigma_0/(a + \sigma_0))^b. \quad (187)$$

Equations (183)–(185) are used in the WIMS (Askew et al. 1966), EPRICELL, and IDX (Kidmon 1975) codes, respectively, and (186) and (187) have been proposed by Segev (1975, 1981).

When the resonance integral is used, the root of the background cross section can be used as an interpolation variable, since the resonance integral has a strong linear relationship with the root of the background cross section, as discussed in (133).

The effective cross section is generally a very smooth function of temperature. It can be therefore be interpolated by a quadratic polynomial, or by a combination of constant, root, and linear terms of temperature in Kelvin. Since the resonance integral has a strong correlation with the root of temperature in Kelvin, it could be interpolated with the root of temperature in Kelvin. However, for more accurate interpolation, the root and linear terms of temperature in Kelvin are both necessary.

Interpolation of the self-shielding factor table may dominate the accuracy of the effective cross section. One should therefore be careful in the choice and application of an interpolation scheme, and the accuracy of the interpolation should be confirmed though comparison with other interpolation schemes and/or integration tests of a lattice physics code. For example, variations in the assembly k -infinity should show a smooth dependence on the variations in fuel temperature. Similarly, the assembly k -infinity should be a smooth function of the number density of a resonance absorber. Some anomalies in the calculated k -infinity could signify inappropriate interpolation of the effective cross section.

Finally, it should be noted that, taking into account the advances in affordable PCs, the fine grid points of the background cross section and temperature in a cross section library are recommended, rather than utilization of a sophisticated interpolation scheme.

3.7 Ultrafine Group Method

3.7.1 Homogeneous System

In a homogeneous system, the Boltzmann transport equation shown in (64) can be simplified as follows:

$$\Sigma_t(E)\phi(E) = \int_0^\infty dE' \Sigma_s(E' \rightarrow E)\phi(E') + \chi(E) \int_0^\infty dE' v\Sigma_f(E')\phi(E') \quad (188)$$

The scattering term, that is, the first term of the right-hand side of (188), can be reduced as follows when the elastic scattering is dominant:

$$\begin{aligned} \int_0^\infty dE' \Sigma_s(E' \rightarrow E)\phi(E') &= \int_0^\infty dE' \Sigma_{es}(E') P(E' \rightarrow E)\phi(E') \\ &= \sum_k \int_E^{E/\alpha_k} \frac{dE' N_k \sigma_{es,k}(E') \phi(E')}{(1 - \alpha_k) E'} \end{aligned} \quad (189)$$

In the ultrafine group method, the fission source in (188) can be approximated as a fixed source, which is assumed to be independent of neutron flux. In this case, since the absolute value of the fixed source can be arbitrarily set, the sum of the fission source is set at unity, that is, $\int_0^\infty dE' v\Sigma_f(E')\phi(E') = 1$. Finally, (188) is rewritten as follows:

$$\Sigma_t(E)\phi(E) = \sum_k \int_E^{E/\alpha_k} \frac{dE' N_k \sigma_{es,k}(E') \phi(E')}{(1 - \alpha_k) E'} + \chi(E) \quad (190)$$

Unfortunately, (190) cannot be analytically solved, except for the particular case ($\alpha_k = 0, \sigma_{es,k} = \text{const.}$). A numerical solution, however, can be easily obtained by means of sufficient energy discretization (Ishiguro 1974; Tsuchihashi et al. 1982; Rothenstein et al. 1988; Macfarlane and Muir 1994a; Kobayashi 1995; MC** 2-2 1999; Hazama et al. 2006; Sugimura and Yamamoto 2007).

When the variations in the cross sections and neutron flux in an energy range (energy group) is assumed to be constant, (190) can be converted into a multigroup form as follows:

$$\Sigma_{t,fg}\phi_{fg} = \sum_k \sum_{fg'} \frac{\Sigma_{es,k,fg'}\phi_{fg'}\Delta E_{fg'}}{(1-\alpha_k)\bar{E}_{fg'}} + \chi_{fg} \quad (191)$$

where

$$\begin{aligned} fg &= \{ E \mid E_{fg} \leq E \leq E_{fg-1} \} \\ \Delta E_{fg} &= E_{fg-1} - E_{fg} \\ \bar{E}_{fg} &= \sqrt{E_{fg}E_{fg-1}} \\ fg' &= \{ E_{fg'} \mid \bar{E}_{fg} \leq E_{fg'} \leq \bar{E}_{fg}/\alpha_k \} \end{aligned}$$

In (191), neutron flux is defined as the average value in a group, and is different from that in a common multigroup equation (integrated value in a group). It should be again noted that the width of an energy group should be narrow enough to neglect variations in the cross section and the neutron flux inside a group. The typical width of this ultrafine energy group is $\Delta U_{fg} = \ln(E_{fg}/E_{fg-1}) = 0.0002 \sim 0.001$, which is sufficiently narrower than that of the energy loss of elastic scattering by a heavy nuclide (e.g., 0.0168 for ^{238}U) and the widths of the major resonance peaks (Ishiguro 1974).

Equation (191) can be solved by the following procedure. The neutron flux for the first group is given by

$$\phi_1 = \frac{\chi_1}{\Sigma_{t,1}} \quad (192)$$

For the second group

$$\phi_2 = \frac{1}{\Sigma_{t,2}} \left(\sum_k \frac{\Sigma_{es,k,1}\phi_1\Delta E_1}{(1-\alpha_k)\bar{E}_1} + \chi_2 \right) \quad (193)$$

For the third group

$$\phi_3 = \frac{1}{\Sigma_{t,3}} \left(\sum_k \left(\frac{\Sigma_{es,k,1}\phi_1\Delta E_1}{(1-\alpha_k)\bar{E}_1} + \frac{\Sigma_{es,k,2}\phi_2\Delta E_2}{(1-\alpha_k)\bar{E}_2} \right) + \chi_3 \right) \quad (194)$$

By repeating the above procedure, the neutron fluxes for successive energy groups can be recursively solved unless up-scattering is taken into account.

Note that the removal cross section, which is defined by

$$\Sigma_{r,fg} = \Sigma_{t,fg} - \frac{\Sigma_{es,k,fg}\Delta E_{fg}}{(1-\alpha_k)\bar{E}_{fg}} \quad (195)$$

could be used in (192)–(194) in order to be consistent with (191). However, the second term in the right-hand side of (195), which represents self-scattering, is sufficiently small in the ultrafine energy group structure. Thus, direct utilization of the total cross section is justified.

Direct implementation of the above procedure entails considerable computation cost, since the summation of the slowing down source that appears in the right-hand side of (192)–(194) will be large, especially when a material contains hydrogen, whose α_k is nearly zero. For this reason, several numerical techniques can be applied.

The slowing down source terms for group fg and $fg - 1$ are given as follows:

$$S_{fg} = \sum_k \sum_{fg' = fg'_{k,fg}}^{fg-1} \frac{\Sigma_{es,k,fg'} \phi_{fg'} \Delta E_{fg'}}{(1 - \alpha_k) \overline{E}_{fg'}} \quad (196)$$

$$S_{fg-1} = \sum_k \sum_{fg' = fg'_{k,fg-1}}^{fg-2} \frac{\Sigma_{es,k,fg'} \phi_{fg'} \Delta E_{fg'}}{(1 - \alpha_k) \overline{E}_{fg'}} \quad (197)$$

where

$fg'_{k,fg}$: upper energy group from which neutrons are down-scattered into fg , for nuclide k ,
 $fg'_{k,fg-1}$: upper energy group from which neutrons are down-scattered into $fg - 1$, for nuclide k .

By subtracting (196) and (197), we obtain

$$\begin{aligned} S_{fg} - S_{fg-1} &= \sum_k \sum_{fg' = fg'_{k,fg}}^{fg-1} \frac{\Sigma_{es,k,fg'} \phi_{fg'} \Delta E_{fg'}}{(1 - \alpha_k) \overline{E}_{fg'}} - \sum_k \sum_{fg' = fg'_{k,fg-1}}^{fg-2} \frac{\Sigma_{es,k,fg'} \phi_{fg'} \Delta E_{fg'}}{(1 - \alpha_k) \overline{E}_{fg'}} \\ &= \sum_k \sum_{fg' = fg'_{k,fg}}^{fg-2} \frac{\Sigma_{es,k,fg'} \phi_{fg'} \Delta E_{fg'}}{(1 - \alpha_k) \overline{E}_{fg'}} + \sum_k \frac{\Sigma_{es,k,fg-1} \phi_{fg-1} \Delta E_{fg-1}}{(1 - \alpha_k) \overline{E}_{fg-1}} \\ &\quad - \sum_k \sum_{fg' = fg'_{k,fg}}^{fg-2} \frac{\Sigma_{es,k,fg'} \phi_{fg'} \Delta E_{fg'}}{(1 - \alpha_k) \overline{E}_{fg'}} - \sum_k \sum_{fg' = fg'_{k,fg-1}}^{fg'_{k,fg}-1} \frac{\Sigma_{es,k,fg'} \phi_{fg'} \Delta E_{fg'}}{(1 - \alpha_k) \overline{E}_{fg'}} \\ &= \sum_k \frac{\Sigma_{es,k,fg-1} \phi_{fg-1} \Delta E_{fg-1}}{(1 - \alpha_k) \overline{E}_{fg-1}} - \sum_k \sum_{fg' = fg'_{k,fg-1}}^{fg'_{k,fg}-1} \frac{\Sigma_{es,k,fg'} \phi_{fg'} \Delta E_{fg'}}{(1 - \alpha_k) \overline{E}_{fg'}} \quad (198) \end{aligned}$$

Equation (198) indicates that the slowing down source of group fg can be calculated by adding the contribution from group $fg - 1$ (the first term in the right-hand side of (198)), and subtracting the contributions of $fg'_{k,fg-1} \leq fg' \leq fg'_{k,fg} - 1$ (the second term in the right-hand side of (198)) from the slowing down source of group $fg - 1$. Since the number of energy groups that satisfies $fg'_{k,fg-1} \leq fg' \leq fg'_{k,fg} - 1$ is small, the computational load for estimating the slowing down source is significantly reduced.

Finally, (191) can be rewritten as follows:

$$\Sigma_{t,fg} \phi_{fg} = S_{fg-1} + \sum_k \frac{\Sigma_{es,k,fg-1} \phi_{fg-1} \Delta E_{fg-1}}{(1 - \alpha_k) \overline{E}_{fg-1}} - \sum_k \sum_{fg' = fg'_{k,fg-1}}^{fg'_{k,fg}-1} \frac{\Sigma_{es,k,fg'} \phi_{fg'} \Delta E_{fg'}}{(1 - \alpha_k) \overline{E}_{fg'}} + \chi_{fg} \quad (199)$$

The number of nuclides can reach several hundred for a burnt pellet, in which there are many heavy and fission product nuclides. In such a case, the computational load for the right-hand side of (199) would be heavy. In order to reduce this load, the nuclides can be categorized by their atomic mass, since slowing down due to elastic scattering depends on atomic mass. For example, in a typical LWR analysis, zirconium and uranium can be considered as representative nuclides for cladding, fission products, and heavy nuclides, in addition to hydrogen and oxygen (Sugimura and Yamamoto 2007).

The above numerical solution is used to solve the neutron slowing down equation in a homogeneous system, and is used in major codes such as NJOY. Furthermore, (199) is also used to evaluate the neutron slowing down source in the heterogeneous calculation that will be discussed in the next subsection.

Once the neutron flux in each energy group is obtained, the effective cross section is given by (200), which is the common definition

$$\sigma_g = \frac{\sum_{fg \in g} \Delta E_{fg} \sigma_{fg} \phi_{fg}}{\sum_{fg \in g} \Delta E_{fg} \phi_{fg}} \quad (200)$$

3.7.2 Heterogeneous System

In a heterogeneous system, the neutron slowing down equation is given by (201), when the collision probability is used for the transport kernel.

$$\Sigma_{t,i}(E) \phi_i(E) V_i = \sum_j P_{j \rightarrow i}(E) V_j \left(\begin{array}{l} \int_0^\infty dE' \Sigma_{s,j}(E' \rightarrow E) \phi_j(E') \\ + \chi_j(E) \int_0^\infty dE' v \Sigma_{f,j}(E') \phi_j(E') \end{array} \right) \quad (201)$$

By applying the same approximations (multigroup and fixed source) used in [Sect. 3.7.1](#), we obtain

$$\Sigma_{t,f,fg} \phi_{f,fg} V_f = \sum_j P_{j \rightarrow f,fg} V_j (\Sigma_{s,fg} + \chi_{j,fg}) \quad (202)$$

When the collision probability in each group is evaluated, (202) can be easily solved. Since (202) contains neutron transport in space, its application is practically limited to a small system, such as a pin cell. Since (202) is a common multigroup form of the transport equation, other transport theories, for example, the discrete-ordinate method or the method of characteristics, can be used. However, the collision probability method is a practical choice due to its superiority for a small system, as discussed in [Sect. 4](#).

Even if a small system is considered, estimation of the collision probability for each group may require considerable computational effort, since in ultrafine energy group calculations, the typical number of energy groups ranges from some tens of thousand to a hundred thousand. Since the collision probability calculation in a one-dimensional system (e.g., cylinder) is quite rapid, a cylindrical approximation with a white boundary condition is a practical choice for an ultrafine energy group calculation in a heterogeneous system.

However, since typical LWR lattices adopt a square shape, a cylindrical approximation would introduce considerable error to the evaluation of neutron flux. Since estimation of the collision probability in a general two-dimensional geometry requires the numerical integration of angle and space with a ray-tracing method, its direct implementation becomes impractical due to the longer computation time required. Collision probabilities are therefore pre-tabulated for various cross sections in each region, and the collision probabilities in each group are obtained by an interpolation of the table (Ishiguro 1974). Though such table interpolation offers a simple, practical approach to the estimation of collision probability, its application is practically limited to a small system, in which there are just a few regions.

The number of regions in a heterogeneous system is, of course, larger than that in a homogeneous system. Thus, evaluations of the slowing down sources for all regions require a longer

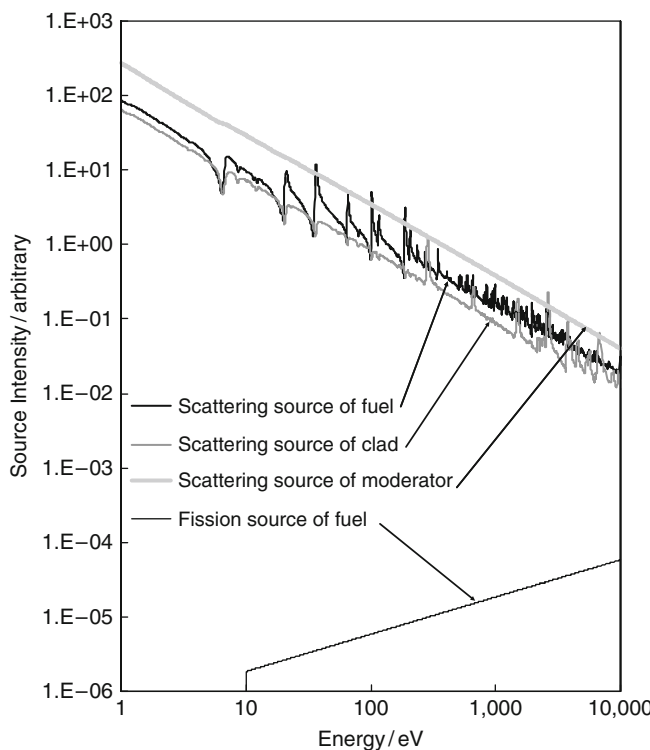


Figure 23

Typical neutron slowing down source in an LWR cell. Note that the fission source is assigned above 10 eV

computation time. Some typical slowing down sources and neutron fluxes in an LWR cell are shown in [Figs. 23](#) and [24](#). These figures suggest that the neutron source in the moderator region is fairly close to $1/E$, in which the NR approximation is well established for the neutron slowing down source. Therefore, the neutron source in the moderator region can be given $1/E$ as a fixed source, and no slowing down calculation would be carried out for the moderator region. Such an approximation not only gives good results, but also considerably reduces the computation time required (Sugimura and Yamamoto [2007](#)).

3.7.3 Limitations of the Ultrafine Energy Groups Method

The approximations used in the ultrafine energy groups method are summarized as follows:

- Neutron slowing down is dominated by elastic scattering.
- Fission source is treated as a fixed source.
- Cross section and neutron flux are assumed to be constant in a group.
- Thermal up-scattering is not taken into account.

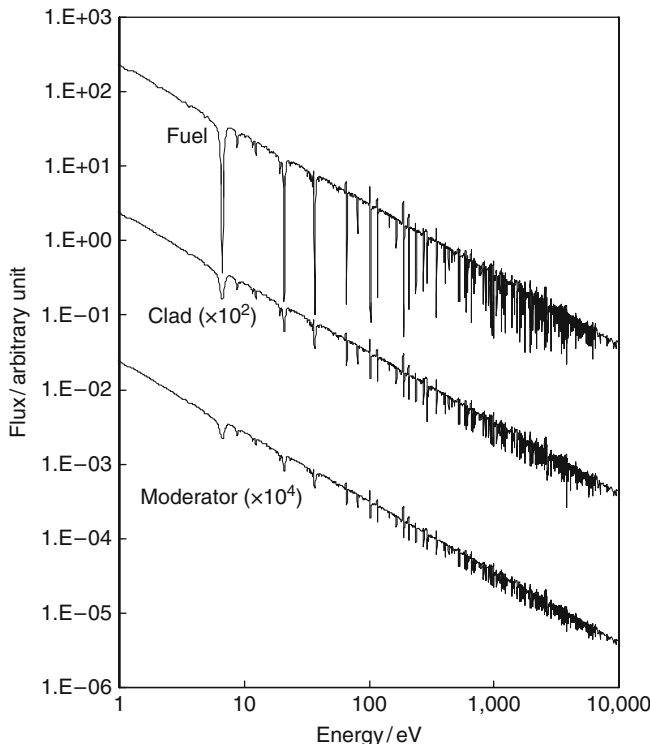


Figure 24
Typical neutron fluxes in an LWR cell

For a heterogeneous system, the following additional approximations would be taken into account, which are common in typical transport calculations:

- Angular/spatial discretization, and
- Treatment of anisotropic scattering.

The above assumptions usually have small impact on common lattice physics computations for an LWR, if sufficient considerations are taken into account. The ultrafine group method thus offers much greater accuracy than the equivalence theory, and can also overcome a number of deficiencies of that theory (NR/WR/IR approximations, escape probability approximations, resonance overlap, and so on). In fact, the result of the ultrafine group method is usually comparable to that of the continuous-energy Monte Carlo method. The largest and most crucial drawback of this method is its applicability to a large geometry, for example, its direct application to an entire fuel assembly will require hours of calculation with a modern PC, which would be prohibitive in production lattice physics computations. Therefore, the ultrafine group method would be coupled with other resonance calculation methods in order to reinforce its weak points. For example, the ultrafine group calculation can be carried out in a homogeneous system to correct the resonance overlap effect, or it can be carried out in pin cell geometry, with

the position dependency corrected by the conventional equivalence theory with the Dancoff factor (Sugimura and Yamamoto 2007).

3.8 Subgroup Method

3.8.1 General Concept

In the subgroup method, an energy group is subdivided into several subgroups in order to accurately consider variations in the cross section within a group. Since the subgroup method can accurately calculate the effective cross section even if the number of the subgroups in an energy group is a few to several, some lattice physics codes (e.g., APOLLO, WIMS, and HELIOS) incorporate the subgroup method for evaluation of the effective cross section (Nikoleav et al. 1971, 1973; Levitt 1972; Sinitsa and Nikoleav 1973; Cullen 1974, 1986; Ribon 1986; Halsall 1995; Hébert 1998; Loubiere et al. 1999; Yamamoto and Takeda 2000; Sublet and Ribon 2002; Hébert and Coste 2002; Yamamoto 2003, 2004; Hébert 2004, 2005a; Chiba and Unesaki 2006; Yamamoto and Takeda 2006).

The basic concept of the subgroup method is as follows. Variations in neutron flux mainly depend on the magnitude of the cross section, as described in the resonance theory for a homogeneous system, for example, (77). Therefore, when a group is divided into several subgroups according to the magnitude of the cross section, the variations in the neutron flux in a subgroup would be smaller than that in the original group structure. The concept of the subgroup method based on the above explanation is shown in  Fig. 14.

A subgroup structure defined by the above approach has one distinguishing feature: the energy range for a subgroup is no longer contiguous as in the conventional multigroup method. Direct utilization of this physical concept in a resonance calculation is referred to as the direct approach. Though the direct approach yields a clear and intuitive insight into the subgroup method, it also has drawbacks. The most significant drawback is that the subgroup averaged cross section still has dependency on the background cross section, though its dependency on the background cross section is much smaller than that of the effective cross section as defined in a conventional multigroup structure.

On account of this deficiency, the direct approach is not widely used in present day lattice physics codes. Instead of the direct approach, the concept of the probability table method is widely used in practical applications. In this approach, the cross sections of subgroups and their weights (corresponding to the energy group width of each subgroup in the direct method) are chosen so that they are independent of the background cross section. In the probability table approach, the parameters for subgroups (their cross sections and weights) become nonphysical, and no longer have corresponding distinguishing energy ranges as in the direct method.

Though the concept of the probability table is widely used in lattice physics computations, we will discuss the direct approach first, since an intuitive physical understanding of the direct approach is much easier than the probability table approach. An explanation of the probability table approach will be provided after we discuss the direct approach. Two separate methods to generate the probability table are also discussed in this subsection.

3.8.2 Direct Approach

The neutron transport equation for the “direct” subgroup approach is obtained by the energy integration of the following transport equation for a subgroup sg :

$$\vec{\Omega} \cdot \nabla \psi(\vec{r}, E, \vec{\Omega}) + \Sigma_t(\vec{r}, E, \vec{\Omega})\psi(\vec{r}, E, \vec{\Omega}) = Q(\vec{r}, E, \vec{\Omega}) \quad (203)$$

We obtain

$$\vec{\Omega} \cdot \nabla \psi_{sg}(\vec{r}, \vec{\Omega}) + \Sigma_{t,sg}(\vec{r})\psi_{sg}(\vec{r}, \vec{\Omega}) = Q_{sg}(\vec{r}) \quad (204)$$

Cross section for subgroup sg is given as follows:

$$\sigma_{sg}(\vec{r}) = \frac{\int_{sg} dE \sigma(E) \phi(\vec{r}, E)}{\int_{sg} dE \phi(\vec{r}, E)} \quad (205)$$

Note that the angular dependence of the neutron source and of the effective cross section in sg is neglected for the sake of simplicity. Such simplification is also used for conventional effective cross sections in a multigroup energy structure. The effective cross section for a conventional multigroup structure is obtained with the neutron scalar flux of subgroup sg , which is obtained as a solution of (204)

$$\sigma_g(\vec{r}) = \frac{\sum_{sg \in g} \sigma_{sg}(\vec{r}) \phi_{sg}(\vec{r})}{\sum_{sg \in g} \phi_{sg}(\vec{r})} \quad (206)$$

In the equivalence theory, the spatial distribution of the neutron flux is evaluated approximately by the escape probability from a fuel lump. In contrast to the equivalence theory, the spatial distribution of the neutron flux is evaluated by the explicit transport calculation in each subgroup. Therefore, the subgroup method can give more accurate results than the equivalence theory. Furthermore, application of the conventional equivalence theory is limited to the average value of a fuel lump, and the spatial distribution of the self-shielding effect cannot be evaluated, since it relies on the escape probability from a fuel lump. The subgroup method can, however, be applied to more general conditions, which include the spatial distribution of the self-shielding effect.

When a subgroup structure is sufficiently fine, variations in the cross section and neutron spectrum in a subgroup can be neglected. Under such conditions, the subgroup method will be consistent with the ultrafine group method. That said, the essential usefulness of the subgroup method is due to the high accuracy that can be obtained even with a small number of subgroups. In this context, the subgroup method is considered as a resonance calculation method that is different from the ultrafine group method.

The effectiveness of the subgroup method depends on the accuracy or appropriateness of the subgroup parameters when a small (i.e., practical) number of subgroups is used in calculations. Since a cross section in a subgroup depends on the neutron spectrum in a subgroup, its evaluation is important. In the direct approach, we have the freedom to choose the energy group structure for subgroups, so we should find a better energy group structure for a subgroup. The neutron flux is approximately inversely proportional to the magnitude of the cross section. Therefore, a subgroup structure, which is defined by the magnitude of the cross section and has discrete ranges, as shown in  Fig. 14, is clearly better than the conventional approach

(sequential division of energy range), since variations in the cross section in a group (and thus variations in the neutron flux in a group) are smaller than those in a conventional group structure with a contiguous energy range.

The subgroup cross section becomes independent of the background cross section (or the shielding condition) when the resonance cross section has a “step shape,” that is, the cross section in each subgroup is constant. In reality, however, we cannot neglect variations in the cross section in a subgroup, so the subgroup cross section inevitably has dependency on the neutron spectrum. Therefore, in the direct approach of the subgroup method, the subgroup cross section is evaluated by

$$\sigma_{sg}(\sigma_0) = \frac{\int_{sg} dE \sigma(E) \phi(E, \sigma_0)}{\int_{sg} dE \phi(E, \sigma_0)}$$

$$sg = \{ E | \sigma_{sg,min} \leq \sigma(E) \leq \sigma_{sg,max} \} \quad (207)$$

where

σ_{sg} : subgroup cross section in subgroup sg.

$\phi(E, \sigma_0)$ is obtained by solving a slowing down equation in a homogeneous system composed of hydrogen and the resonance nuclide in question. By performing slowing down calculations for different background cross sections, we can tabulate the dependency of subgroup cross sections on the background cross sections. Once the background cross section in a heterogeneous geometry is evaluated, the subgroup cross section can be obtained through interpolation of the pre-tabulated data. This approach is the same as in the conventional equivalence method, but provides better accuracy, since the sensitivity (variation) of the subgroup cross section on the background cross section is smaller. However, since the above approach still relies on the equivalence between homogeneous and heterogeneous systems, it presents a potential source of error.

When the direct approach of the subgroup method is applied to a general geometry, the evaluation of the background cross section becomes difficult, especially in the evaluation of the space-dependent effective cross section. Since the equivalence theory relies on the rational approximation for the neutron escape probability from a fuel lump, it cannot directly treat the inner regions of a resonance lump. In fact, the heterogeneous term in the background cross section for the inner region of a fuel lump will be zero, since the Dancoff correction becomes unity in such a case. The inner region of a fuel lump is surrounded by fuels, which in a Dancoff factor evaluation are black; thus, the Dancoff correction is unity for such inner regions. In other words, the appropriate derivation of the background cross section for general geometry is difficult, which is why application of the direct approach of the subgroup method has been limited (Yamamoto 2003).

A recent study, however, presents the possible resolution of this issue by using the effective cross section as an index of the self-shielding condition. In this approach, the following procedures are used to evaluate the effective cross section in a general heterogeneous system (Yamamoto et al. 2009a, b):

1. Tabulate the subgroup and the effective cross sections, which are defined by (205) and (206), respectively, versus the background cross section. The subgroup and effective cross sections are evaluated through slowing down calculations in a homogeneous system with various background cross sections.

2. Perform a transport calculation using the tabulated subgroup cross sections. For the first iteration, the subgroup cross sections with an infinite-dilution condition can be used as a starting point.
3. Evaluate the effective cross section by (206) with the subgroup neutron flux obtained in (2).
4. A corresponding background cross section that reproduces the effective cross section obtained in (3) is then estimated from the tabulated data.
5. Update the subgroup cross sections with the background cross section obtained in (4).
6. Repeat (2)–(5) until convergence; a few iterations are sufficient to obtain converged results.

By using the above approach, the evaluation of the background cross section, which is a difficult step in the application of the direct approach of the subgroup method, can be avoided. The above procedure can thus be a practical way to apply the direct approach of the subgroup method in general geometry.

3.8.3 Probability Table Approach

In the direct approach of the subgroup method, the energy group structure for each subgroup is explicitly specified. Contrary to this, in the probability table approach, the energy group structure is not explicitly defined (Levitt 1972; Cullen 1974, 1986; Ribon 1986; Halsall 1995; Hébert 1998; Sublet and Ribon 2002; Hébert and Coste 2002; Hébert 2005a; Chiba and Unesaki 2006). In the mathematical context, it is considered as a utilization of the Lebesgue integration, that is, the integration of neutron spectrum $f(E)$ into energy is converted to that on a cross section

$$\int_{E_g}^{E_{g-1}} dE f(E) = \int_{\sigma_{\min,g}}^{\sigma_{\max,g}} d\sigma f(\sigma) p(\sigma) \quad (208)$$

where

σ : cross section,

$f(E)$: neutron spectrum (dependence of neutron flux on energy),

$f(\sigma)$: neutron spectrum (dependence of neutron flux on cross section),

$p(\sigma)$: probability that cross section in group g is σ ,

$\sigma_{\min,g}$: minimum value of cross section in group g ,

$\sigma_{\max,g}$: maximum value of cross section in group g .

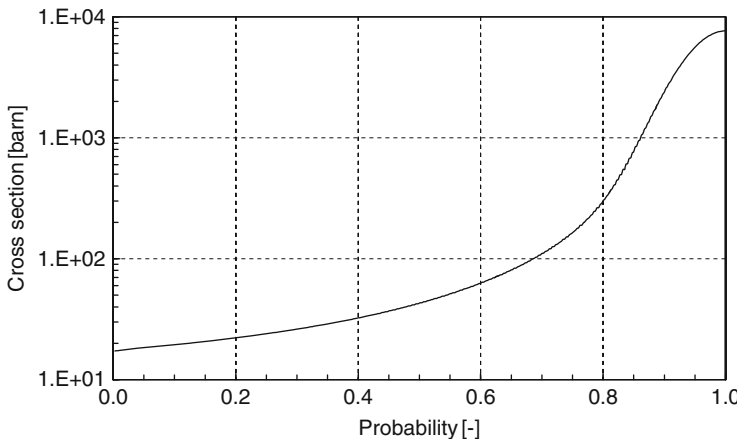
Note that $f(\sigma)$ and $f(E)$ represent the same physical quantity but have different formulas. Variations in $f(\sigma)$ are much smoother than those of $f(E)$ since the neutron spectrum is a smooth function of the magnitude of the cross section. Recalling the NR approximation, the neutron flux is expressed as

$$f(\sigma) = \frac{\sigma_0}{\sigma(E) + \sigma_0} \quad (209)$$

which is a smooth function of the cross section (σ) of a resonant nuclide.

In (209), the $1/E$ dependence is omitted since variations in neutron flux due to $1/E$ are not very large. The probability density function for the cross section, $p(\sigma)$, is also a smooth function of the cross section. An example of $p(\sigma)$ is shown in  Fig. 25.

The above discussion suggests that the integration in the right-hand side of (208) is easier than that in the left-hand side, since the behavior of the integrand is much smoother. Coarse discretization can therefore be used in the integration of the right-hand side of (208).



■ **Figure 25**

Cumulative probability density function of cross section for ^{238}U (88 group in the 172-group XMAS structure (7.52–6.16 eV), in which there is a large resonance of ^{238}U)

By adopting the concept of the probability density of the cross section, we can define a set of subgroup cross sections and their associated weights that are independent of the background cross section, that is, generalized subgroup cross sections and weights can be derived. Since these parameters are independent of the magnitude of self-shielding, they can be used in any configuration, including the space-dependent self-shielding in a fuel lump, which is difficult to handle using the conventional direct approach of the subgroup method.

The above approach, however, also has a significant drawback. By adopting the integration procedure on the cross section, energy-dependent information is lost. That is, each subgroup defined by the probability table method has no physical energy group structure. This creates difficulty in the treatment of the temperature distribution in a configuration. The shape of a resonance cross section depends on temperature, due to the Doppler broadening effect, as shown in ▶ Fig. 26.

When there is temperature distribution in a system, we have different sets of subgroup cross sections and their associated probabilities (weights), even for a nuclide. However, since the implicit energy group structure for each subgroup is different, direct utilization of subgroup parameters with different temperatures cannot be justified in transport calculations. Let us assume two different multigroup cross section sets with totally different energy group structures, but with the same number of energy groups. We can perform a transport calculation that simultaneously uses these two multigroup cross section sets, since the number of energy groups is the same. However, such calculation is, clearly, meaningless. Because direct application of the probability table method for a temperature-dependent problem causes the above inconsistency, care must be taken.

We now consider a set of subgroup cross sections and their associated probabilities, σ_{sg} and p_{sg} . Note that σ_{sg} is constant in a subgroup. Intuitive interpretation of the probability is the fraction of the energy range of the corresponding subgroup within an energy group. When the probability is larger, the corresponding subgroup occupies a larger fraction in an energy group. The subgroup cross section physically represents the average cross section in a subgroup.

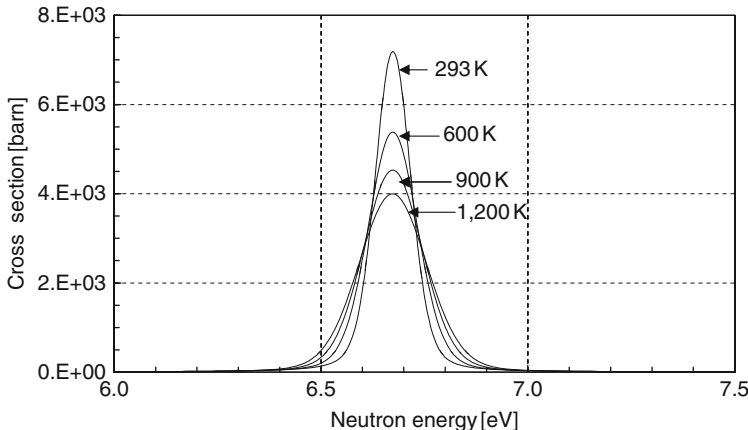


Figure 26
Variations in a ^{238}U capture cross section due to Doppler broadening

However, it must again be remembered that each subgroup has no explicit energy range, and thus these remain abstract and rather mathematical properties.

With the subgroup parameters (subgroup cross sections and probabilities), we have the following equations:

$$\int_{E_g}^{E_{g-1}} dE f(E) = \int_{\sigma_{\min,g}}^{\sigma_{\max,g}} d\sigma f(\sigma) p(\sigma) = \sum_{sg \in g} f_{sg} p_{sg} \quad (210)$$

$$\sum_{sg \in g} p_{sg} = 1 \quad (211)$$

where

$$f_{sg} = f(\sigma_{sg})$$

Equation (210) means that the neutron flux can be integrated through a quadrature set, whose quadrature points and associated weights are σ_{sg} and p_{sg} , respectively. Under this assumption, the effective cross section can be obtained by

$$\sigma_g = \frac{\int_{E_g}^{E_{g-1}} dE \sigma(E) \phi(E)}{\int_{E_g}^{E_{g-1}} dE \phi(E)} = \frac{\int_{\sigma_{\min,g}}^{\sigma_{\max,g}} d\sigma \sigma \phi(\sigma) p(\sigma)}{\int_{\sigma_{\min,g}}^{\sigma_{\max,g}} d\sigma \phi(\sigma) p(\sigma)} = \frac{\sum_{sg \in g} \sigma_{sg} \phi_{sg} p_{sg}}{\sum_{sg \in g} \phi_{sg} p_{sg}} \quad (212)$$

Once the subgroup parameters, that is, σ_{sg} and p_{sg} are known, we can evaluate the effective cross section through the neutron flux for subgroup ϕ_{sg} , which is obtained by a transport calculation for each subgroup. A set of subgroup parameters is called a probability table, which is obtained by a number of numerical calculations that will be discussed later.

Since subgroup parameters are chosen to be independent of the background cross section, they can in principle be used in any configuration. Such flexibility is the advantage of the probability method. However, as discussed previously, an explicit energy group structure cannot be

defined (or is lost) in the derivation of the subgroup cross section. Therefore, application of this method to a problem with temperature distribution is limited.

The fitting and the moment methods are major approaches to the derivation of subgroup parameters. From a historical point of view, they represent the origin of the subgroup method. A more intuitive approach, that is, the direct approach discussed [3.8.2](#), was devised as a physical interpretation of the subgroup method based on the probability table approach.

3.8.4 Fitting Method

The fitting method is a numerical calculation procedure to derive a set of probability tables used in the subgroup method (Nikoleav et al. 1971; Levitt 1972). In the following, we will discuss the derivation based on the NR approximation.

When the NR approximation for the neutron flux is applied to the formulation of the subgroup cross section, we obtain the following equation:

$$\sigma_{t,sg}(\sigma_0) = \frac{\int_{sg} dE \sigma_t(E) \phi(E, \sigma_0)}{\int_{sg} dE \phi(E, \sigma_0)} = \frac{\int_{sg} dE \sigma_t(E) \frac{1}{\sigma_t(E) + \sigma_0}}{\int_{sg} dE \frac{1}{\sigma_t(E) + \sigma_0}} \quad (213)$$

The band probability is defined by the width of the energy range for each subgroup, as follows:

$$p_{sg} = \frac{\int_{sg} dE}{\int_g dE} \quad (214)$$

The numerator in (213) can be written as follows:

$$\begin{aligned} \int_{sg} dE \sigma_t(E) \frac{1}{\sigma_t(E) + \sigma_0} &= \int_{sg} dE \frac{\sigma_t(E) + \sigma_0 - \sigma_0}{\sigma_t(E) + \sigma_0} \\ &= \int_{sg} dE - \sigma_0 \int_{sg} dE \frac{1}{\sigma_t(E) + \sigma_0} \end{aligned} \quad (215)$$

By substituting (214) and (215) into (213), we obtain the following:

$$\begin{aligned} \sigma_{t,sg}(\sigma_0) &= \frac{\int_{sg} dE - \sigma_0 \int_{sg} dE \frac{1}{\sigma_t(E) + \sigma_0}}{\int_{sg} dE \frac{1}{\sigma_t(E) + \sigma_0}} \\ &= \frac{p_{sg} \int_g dE}{\int_{sg} dE \frac{1}{\sigma_t(E) + \sigma_0}} - \sigma_0 \end{aligned} \quad (216)$$

From (216), we have the following relationship:

$$\int_{sg} dE \frac{1}{\sigma_t(E) + \sigma_0} = \frac{p_{sg} \int_g dE}{\sigma_{t,sg}(\sigma_0) + \sigma_0} \quad (217)$$

By substituting (214) and (217) into (215), we obtain

$$\begin{aligned} \int_{sg} dE \sigma_t(E) \frac{1}{\sigma_t(E) + \sigma_0} &= p_{sg} \int_g dE - \sigma_0 \frac{p_{sg} \int_g dE}{\sigma_{t,sg}(\sigma_0) + \sigma_0} \\ &= \frac{\sigma_{t,sg}(\sigma_0) p_{sg} \int_g dE}{\sigma_{t,sg}(\sigma_0) + \sigma_0} \end{aligned} \quad (218)$$

With (213), (217) and (218), the total cross section is given as follows:

$$\begin{aligned} \sigma_{t,g}(\sigma_0) &= \frac{\int_{E_g}^{E_{g-1}} dE \sigma_t(E) \frac{1}{\sigma_t(E) + \sigma_0}}{\int_{E_g}^{E_{g-1}} dE \frac{1}{\sigma_t(E) + \sigma_0}} \\ &= \frac{\sum_{sg \in g} \int_{sg} dE \sigma_t(E) \frac{1}{\sigma_t(E) + \sigma_0}}{\sum_{sg \in g} \int_{sg} dE \frac{1}{\sigma_t(E) + \sigma_0}} \\ &= \frac{\sum_{sg \in g} \frac{\sigma_{t,sg}(\sigma_0) p_{sg} \int_g dE}{\sigma_{t,sg}(\sigma_0) + \sigma_0}}{\sum_{sg \in g} \frac{p_{sg} \int_g dE}{\sigma_{t,sg}(\sigma_0) + \sigma_0}} \\ &= \frac{\sum_{sg \in g} \frac{\sigma_{t,sg}(\sigma_0) p_{sg}}{\sigma_{t,sg}(\sigma_0) + \sigma_0}}{\sum_{sg \in g} \frac{p_{sg}}{\sigma_{t,sg}(\sigma_0) + \sigma_0}} \end{aligned} \quad (219)$$

In (219), the subgroup cross section has dependency on the background cross section. However, we assume that the subgroup cross sections are independent of the background cross section, so the effective cross section is defined as

$$\sigma_{t,g}(\sigma_0) = \frac{\sum_{sg \in g} \frac{\sigma_{t,sg} p_{sg}}{\sigma_{t,sg} + \sigma_0}}{\sum_{sg \in g} \frac{p_{sg}}{\sigma_{t,sg} + \sigma_0}} \quad (220)$$

In the fitting method, the subgroup parameters (a set of subgroup cross sections and associated probabilities) are chosen to satisfy (220) through a fitting procedure. When the number of subgroup is N , we have $2N$ unknowns for the subgroup cross sections and the probabilities. The normalization condition for the probabilities can be used as a constraint.

$$\sum_{sg \in g} p_{sg} = 1 \quad (221)$$

In addition, we should consider at least $2N - 1$ relations between the background cross section and the effective cross section in order to complete a set of equations with which to estimate

unknowns:

$$\sigma_{t,g}(\sigma_{0,l}) = \frac{\sum_{sg \in g} \frac{\sigma_{t,sg} p_{sg}}{\sigma_{t,sg} + \sigma_{0,l}}}{\sum_{sg \in g} \frac{p_{sg}}{\sigma_{t,sg} + \sigma_{0,l}}} \quad (l = 1, 2, \dots, 2N - 1) \quad (222)$$

We can use more than $2N - 1$ relations for the background cross section and the effective cross section. In this case, the subgroup parameters are evaluated through the least square fitting. Therefore, this approach is usually called the fitting method.

In principle, there is not a general set of subgroup parameters that is independent of the background cross section. Therefore, even if we use the fitted subgroup parameters, the effective cross section cannot be exactly reproduced for every background cross section. This is a shortcoming of the fitting method. Furthermore, when the number of subgroups increases, the fitting procedure used for (222) sometimes runs into numerical difficulties and may provide a nonphysical solution for the subgroup parameters, for example, negative and/or imaginary probabilities and subgroup cross sections.

Despite this deficiency, the fitting method remains a major approach to the derivation of subgroup cross sections since it gives the “general” subgroup parameters that can be used for any geometry, and estimation of the effective cross section in general geometry becomes easy once the subgroup is obtained. Furthermore, in the fitting method, the band probabilities and subgroup cross sections are chosen to reproduce the effective multigroup cross section, which in a homogeneous system, is usually generated through an accurate numerical solution of the slowing down equation (ultrafine group calculation). In this context, the fitting method can implicitly incorporate the “slowing down” effect, which is obtained by the ultrafine group calculation.

3.8.5 Moment Method

The moment method is another approach to estimating subgroup parameters (Ribon 1986; Hébert and Coste 2002; Hébert 2005a). In this method, we use the following “moment” of a cross section:

$$M_{t,n} = \frac{\int_{E_g}^{E_{g-1}} dE \sigma_t(E)^n}{\int_{E_g}^{E_{g-1}} dE} \quad (223)$$

where n is the order of a moment. Using the probability density function of the cross section and applying the integration with a cross section, (223) can be rewritten as follows:

$$\begin{aligned} M_{t,n} &= \frac{\int_{E_g}^{E_{g-1}} dE \sigma_t(E)^n}{\int_{E_g}^{E_{g-1}} dE} = \frac{\int_{\sigma_{t,\min,g}}^{\sigma_{t,\max,g}} d\sigma_t \sigma_t^n p(\sigma_t)}{\int_{\sigma_{t,\min,g}}^{\sigma_{t,\max,g}} d\sigma_t p(\sigma_t)} \\ &\approx \frac{\sum_{sg \in g} \int_{\sigma_{t,\min,g}}^{\sigma_{t,\max,g}} d\sigma_t \sigma_t^n \delta(\sigma_t - \sigma_{t,sg}) p_{sg}}{\sum_{sg \in g} \int_{\sigma_{t,\min,g}}^{\sigma_{t,\max,g}} d\sigma_t \delta(\sigma_t - \sigma_{t,sg}) p_{sg}} \\ &= \frac{\sum_{sg \in g} \sigma_{t,sg}^n p_{sg}}{\sum_{sg \in g} p_{sg}} = \sum_{sg \in g} \sigma_{t,sg}^n p_{sg} \end{aligned} \quad (224)$$

The moment of a cross section using the subgroup parameters is given by

$$m_{t,n} = \sum_{sg \in g} \sigma_{t,sg}^n p_{sg} \quad (225)$$

In the moment method, we also have $2N$ unknowns for the subgroup cross sections and probabilities, just as in the fitting method. Since the normalization condition for probability is also used in the moment method, we should consider the $2N - 1$ constraints for different moments:

$$\sum_{sg \in g} p_{sg} = 1 \quad (226)$$

$$\frac{\int_{E_g}^{E_{g-1}} dE \sigma_t(E)^n}{\int_{E_g}^{E_{g-1}} dE} = \sum_{sg \in g} \sigma_{t,sg}^n p_{sg} \quad (n = I + 1, I + 2, \dots, I + 2N - 1, I : \text{integer}) \quad (227)$$

When $n = 0$, (227) is reduced to (226). By solving (226) and (227), (i.e., $\sum_{sg \in g} p_{sg} = 1$ and $M_{t,n} = m_{t,n}$), we can obtain the subgroup parameters. However, (226) and (227) require the solution of the n th degree equation, which would be difficult to obtain. In the following part, a numerical procedure for the evaluation of subgroup parameters using the Pade approximation, as proposed by Ribon et al. is described (Ribon 1986).

First, in the case of $I = 0$, we define a polynomial of order $2N - 1$, which contains the moments of a cross section in its coefficients:

$$F(z) = \sum_{n=0}^{\infty} m_{t,n} z^n = \sum_{n=0}^{2N-1} m_{t,n} z^n + r(z^{2N}) \quad (228)$$

where $r(z^{2N})$ indicates a residual term.

When the value of z is chosen to satisfy $\sigma_{t,sg} z < 1$, (228) can be rewritten as follows:

$$\begin{aligned} F(z) &= \sum_{n=0}^{2N-1} m_{t,n} z^n + r(z^{2N}) \\ &= \sum_{n=0}^{2N-1} \sum_{sg \in g} \sigma_{t,sg}^n p_{sg} z^n + r(z^{2N}) \\ &= \sum_{sg \in g} p_{sg} \sum_{n=0}^{2N-1} (\sigma_{t,sg} z)^n + r(z^{2N}) \\ &= \sum_{sg \in g} p_{sg} \frac{1}{1 - \sigma_{t,sg} z} + r'(z^{2N}) \end{aligned} \quad (229)$$

$F(z)$ can be also expressed by $M_{t,n}$ since $m_{t,n}$ should reproduce $M_{t,n}$, that is, $M_{t,n} = m_{t,n}$. Using the Pade approximation, $F(z)$ can be written as follows:

$$F(z) = \sum_{n=0}^{2N-1} M_{t,n} z^n + R(z^{2N}) = \frac{\sum_{n=0}^{N-1} a_n z^n}{\sum_{n=0}^N b_n z^n} + R'(z^{2N}) \quad (230)$$

where $R(z^{2N})$ is a residual term, which is slightly different from $r(z^{2N})$.

Note that the summation of the polynomial order in the numerator and denominator of the Pade approximation should be $2N - 1$, in order to approximate a polynomial of order $2N - 1$. Thus, the order of polynomials for the numerator and denominator in (230) is chosen to be $N - 1$ and N , respectively ($N - 1 + N = 2N - 1$). In the Pade approximation, the coefficients in (230) can be determined by the following set of $2N$ linear equations:

$$\begin{aligned} a_n &= \sum_{m=0}^n M_{t,n-m} b_m \quad (n = 0, 1, \dots, N-1) \\ 0 &= \sum_{m=0}^N M_{t,N+n-m} b_m \quad (n = 0, 1, \dots, N-1) \end{aligned} \quad (231)$$

where

$$b_0 = 1$$

Once we know the coefficients of a_n and b_n , (230) can be transformed into the following:

$$\begin{aligned} F(z) &= \frac{\sum_{n=0}^{N-1} a_n z^n}{\sum_{n=0}^N b_n z^n} + R'(z^{2N}) = \frac{\sum_{n=0}^{N-1} a_n z^n}{1 + \sum_{n=1}^N b_n z^n} + R'(z^{2N}) \\ &= \frac{\sum_{n=0}^{N-1} a_n z^n}{\prod_{n=1}^N \left(1 - \frac{z}{z_n}\right)} + R'(z^{2N}) = \sum_{n=1}^N \frac{\omega_n}{1 - \frac{z}{z_n}} + R'(z^{2N}) \end{aligned} \quad (232)$$

where

ω_n : a coefficient defined by a_n and b_n .

In (232), the denominator is factorized with the roots of $1 + \sum_{n=0}^N b_n z^n = 0$, expressed by z_n . By comparing (229) and (232), we find that the subgroup cross section is given by

$$\sigma_{t,sg=n} = \frac{1}{z_n} \quad (234)$$

Therefore, the subgroup cross section can be evaluated using the roots of $1 + \sum_{n=0}^N b_n z^n = 0$. Once we have the subgroup cross sections, the associated probabilities are calculated by

$$M_{t,n} = m_{t,n} = \sum_{sg \in g} \sigma_{t,sg}^n p_{sg} \quad (n = 1, 2, \dots, N) \quad (235)$$

The moments for other cross sections (except for the total cross section) are defined by

$$M_{x,n} = \frac{\int_{E_g}^{E_{g-1}} dE \sigma_x(E) \sigma_t(E)^n}{\int_{E_g}^{E_{g-1}} dE} \quad (236)$$

$$m_{x,n} = \sum_{sg \in g} \sigma_{x,sg} \sigma_{t,sg}^n p_{sg} \quad (237)$$

When the values of $\sigma_{t,sg}$ and p_{sg} are known, the moments for other cross sections can be derived by equating (236) and (237), that is,

$$M_{x,n} = m_{x,n} \quad (238)$$

In the above derivation, the moments of the cross sections with an integer order are preserved. The above procedure is generally used in the moment method. However, it could also be extended to non-integer moments (Chiba and Unesaki 2006). Let us consider an effective cross section based on the NR approximation:

$$\sigma_{x,g}(\sigma_0) = \frac{\int_{E_g}^{E_{g-1}} dE \sigma_x(E) \frac{1}{\sigma_t(E) + \sigma_0}}{\int_{E_g}^{E_{g-1}} dE \frac{1}{\sigma_t(E) + \sigma_0}} \quad (239)$$

By considering very small and large values for the background cross section, we have the following expressions for the infinite-dilute and fully shielded conditions:

$$\begin{aligned} \sigma_{x,g}(\sigma_0 = \infty) &= \frac{\int_{E_g}^{E_{g-1}} dE \sigma_x(E)}{\int_{E_g}^{E_{g-1}} dE} = \frac{\int_{E_g}^{E_{g-1}} dE \sigma_x(E) \sigma_t(E)^0}{\int_{E_g}^{E_{g-1}} dE \sigma_t(E)^0} \\ &= \frac{M_{x,0}}{M_{t,0}} \end{aligned} \quad (240)$$

$$\begin{aligned} \sigma_{x,g}(\sigma_0 = 0) &= \frac{\int_{E_g}^{E_{g-1}} dE \sigma_x(E) \frac{1}{\sigma_t(E)}}{\int_{E_g}^{E_{g-1}} dE \frac{1}{\sigma_t(E)}} = \frac{\int_{E_g}^{E_{g-1}} dE \sigma_x(E) \sigma_t(E)^{-1}}{\int_{E_g}^{E_{g-1}} dE \sigma_t(E)^{-1}} \\ &= \frac{M_{x,-1}}{M_{t,-1}} \end{aligned} \quad (241)$$

In the above equations, the asymptotic neutron flux ($1/E$) is assumed to be unity. Equations (240) and (241) suggest that an effective cross section for a particular background cross section may be given by an interpolation of n :

$$\sigma_{x,g}(\sigma_0) = \frac{M_{x,n}}{M_{t,n}} \quad (242)$$

in which $-1 \leq n \leq 0$, since all shielded conditions appear between two extreme conditions, that is, the infinite-dilute ($n = 0$) and the fully shielded ($n = -1$) conditions.

The above discussion justifies the preservation of the cross section moments of a non-integer order. A previous study also indicates that the accuracy of the effective cross sections in a homogeneous geometry is improved by preservation of the non-integer moments of the cross sections (Chiba and Unesaki 2006).

In the conventional moment method, which preserves the integer moments of cross sections, no distinct physical properties are directly taken into account during the derivation process. On the contrary, in the non-integer approach, neutron flux behavior is partly (at least in the infinite-dilute and the fully shielded conditions) taken into account in the generation process of the subgroup cross sections. Thus, the accuracy of the subgroup parameters derived by the preservation of non-integer moments becomes higher.

3.8.6 Improvements in the Probability Table Approach

Various efforts are still being made to improve the probability table approach. Some of the issues addressed by these improvements are introduced below.

In general, subgroup parameters are generated with the slowing down calculation in a homogeneous system. However, the subgroup parameters generated in a homogeneous system may not exactly reproduce the effective cross section in a heterogeneous system. Therefore, the generation of subgroup parameters using the slowing down calculation in a heterogeneous geometry is proposed, in order to increase the accuracy of the actual calculation results in a heterogeneous fuel assembly (Joo et al. 2009).

Direct application of the probability table approach for nonuniform temperature problems poses difficulties, as was discussed earlier. However, because nonuniform temperature distribution appears in actual reactor core analyses, a countermeasure to this is important. Several methods have thus far been proposed to address this issue (Joo et al. 2005; Wemple et al. 2007).

Resonance overlap (or interference), which will be discussed in ➤ 3.10, may also have an impact on the calculation accuracy of the subgroup method. This topic has also been investigated by several researchers (Hébert 2004).

3.9 Other Methods

3.9.1 Tone's Method

In fast reactor calculations, a resonance calculation based on Tone's method is sometimes used (Tone 1975). In this method, a resonance absorber is not approximated as black, the escape probability from a fuel lump is directly evaluated by the collision probability method, and the rational approximation in the equivalence theory is not explicitly used. Therefore, the background cross section for a general heterogeneous geometry can be evaluated with approximated treatment of the space-dependent self-shielding effect.

Recalling (136), the neutron flux in region i can be calculated by considering the contribution of neutron sources in other regions:

$$\phi_i(E) = \frac{1}{E} \sum_j \frac{P_{j \rightarrow i}(E) V_j \Sigma_{p,j}}{\Sigma_{t,i}(E) V_i} \quad (243)$$

Note that the NR approximation is used for the neutron slowing down source in each region. In Tone's method, we introduce the following key approximation:

$$\frac{P_{j \rightarrow i}(E)}{\Sigma_{t,i}(E)} = \alpha_i(E) \frac{P_{j \rightarrow i,g}}{\Sigma_{t,i,g}} \quad (244)$$

where g denotes a group averaged property. For example, the collision probability $P_{j \rightarrow i,g}$ is the group average collision probability, which is obtained by a set of multigroup cross sections. Equation (244) indicates that the fine energy dependency of the collision probability inside an energy group relies only on target region i . In reality, the energy dependence of the collision probability relies not only on region i , but on other regions as well, including the source region. In other words, with the exception of region i , cross sections are assumed to be energetically

constant in an energy group. In a more physical interpretation, a resonance nuclide in question is not included (or can be neglected) in other regions, in the evaluation of the background cross section. This is a major assumption in Tone's method that represents a potential cause of error.

By substituting (244) into (243), we obtain

$$\phi_i(E) = \frac{1}{E} \alpha_i(E) \sum_j \frac{P_{j \rightarrow i,g} V_j \Sigma_{p,j}}{\Sigma_{t,i,g} V_i} \quad (245)$$

In addition to the above equation, the reciprocity theorem and the normalization condition for collision probabilities are also taken into account:

$$P_{j \rightarrow i}(E) V_j \Sigma_{t,j}(E) = P_{i \rightarrow j}(E) V_i \Sigma_{t,i}(E) \quad (246)$$

$$\sum_j P_{i \rightarrow j}(E) = 1 \quad (247)$$

Equation (247) can be transformed as follows, by substituting (244) and (246) into (247):

$$\begin{aligned} 1 &= \sum_j P_{i \rightarrow j}(E) \\ &= \sum_j \frac{P_{j \rightarrow i}(E) V_j \Sigma_{t,j}(E)}{V_i \Sigma_{t,i}(E)} \\ &= \sum_j \alpha_i(E) \frac{P_{j \rightarrow i,g}}{\Sigma_{t,i,g}} \frac{V_j \Sigma_{t,j}(E)}{V_i} \\ &= \alpha_i(E) \frac{1}{\Sigma_{t,i,g} V_i} \sum_j P_{j \rightarrow i,g} V_j \Sigma_{t,j}(E) \end{aligned} \quad (248)$$

Finally, using (248), α is expressed as follows:

$$\alpha_i(E) = \frac{\Sigma_{t,i,g} V_i}{\sum_j P_{j \rightarrow i,g} V_j \Sigma_{t,j}(E)} \quad (249)$$

By substituting (249) into (245), we obtain:

$$\begin{aligned} \phi_i(E) &= \frac{1}{E} \alpha_i(E) \sum_j \frac{P_{j \rightarrow i,g} V_j \Sigma_{p,j}}{\Sigma_{t,i,g} V_i} \\ &= \frac{1}{E} \frac{\Sigma_{t,i,g} V_i}{\sum_j P_{j \rightarrow i,g} V_j \Sigma_{t,j}(E)} \sum_j \frac{P_{j \rightarrow i,g} V_j \Sigma_{p,j}}{\Sigma_{t,i,g} V_i} \\ &= \frac{1}{E} \frac{\sum_j P_{j \rightarrow i,g} V_j \Sigma_{p,j}}{\sum_j P_{j \rightarrow i,g} V_j \Sigma_{t,j}(E)} \end{aligned}$$

$$\begin{aligned}
&\approx \frac{1}{E} \frac{\sum_j P_{j \rightarrow i,g} V_j \cdot \left(N_{r,j} \sigma_{p,r} + \sum_{k \neq r} N_{k,j} \sigma_{p,k} \right)}{\sum_j P_{j \rightarrow i,g} V_j \cdot \left(N_{r,j} \sigma_{t,r}(E) + \sum_{k \neq r} N_{k,j} \sigma_{p,k} \right)} \\
&= \frac{1}{E} \frac{\sigma_{p,r} \sum_j P_{j \rightarrow i,g} V_j N_{r,j} + \sum_j P_{j \rightarrow i,g} V_j \sum_{k \neq r} N_{k,j} \sigma_{p,k}}{\sigma_{t,r}(E) \sum_j P_{j \rightarrow i,g} V_j N_{r,j} + \sum_j P_{j \rightarrow i,g} V_j \sum_{k \neq r} N_{k,j} \sigma_{p,k}} \\
&= \frac{1}{E} \frac{\sigma_{p,r} + \left(\sum_j P_{j \rightarrow i,g} V_j \sum_{k \neq r} N_{k,j} \sigma_{p,k} \right) / \left(\sum_j P_{j \rightarrow i,g} V_j N_{r,j} \right)}{\sigma_{t,r}(E) + \left(\sum_j P_{j \rightarrow i,g} V_j \sum_{k \neq r} N_{k,j} \sigma_{p,k} \right) / \left(\sum_j P_{j \rightarrow i,g} V_j N_{r,j} \right)} \\
&= \frac{1}{E} \frac{\sigma_{p,r} + \sigma_0}{\sigma_{t,r}(E) + \sigma_0}
\end{aligned} \tag{250}$$

where

$$\sigma_0 = \frac{\sum_j \sum_{k \neq r} P_{j \rightarrow i,g} V_j N_{k,j} \sigma_{p,k}}{\sum_j P_{j \rightarrow i,g} V_j N_{r,j}} \tag{251}$$

We assume that with the exception of a resonance nuclide, cross sections are approximated by a constant potential scattering cross section.

[Equation \(251\)](#) indicates that the background cross section is obtained by the collision probabilities among regions, volume, number densities, and potential cross sections. Since collision probabilities depend on the effective cross sections, which in turn depend on the background cross sections, an iteration calculation procedure is necessary, which is as follows:

1. Assume initial background cross sections for resonance nuclides. They can be evaluated using the conventional equivalence method with the Dancoff correction.
2. Evaluate the effective cross sections of resonance nuclides using the conventional equivalence theory.
3. Evaluate group-wise collision probability using the effective cross section evaluated in (2).
4. Update the background cross section using (251).
5. Repeat (2)–(4) until convergence. A few iterations are usually sufficient to obtain the converged result.

Tone's method seeks to incorporate actual collision probabilities among regions through the approximation of (244). Therefore, it is more applicable to general geometry than the conventional equivalence method. Furthermore, since only the definition of the background cross section is changed, it has a closer affinity to the conventional equivalence method than to the subgroup method.

An example of a performance comparison between the subgroup and Tone's methods in a fast reactor fuel assembly is shown in [Fig. 27](#) (Chiba 2003). The fuel assembly used for the comparison is shown on the left side of [Fig. 27](#), in which there are 169 fuel pins. The effective microscopic capture cross section of ^{238}U in each fuel rod is evaluated at 300 K. JENDL3.2 is used throughout the comparison. The number of energy groups (70 groups) and the energy group structure used in this comparison, is the same as in JSF-3-3.2R. The moment method is

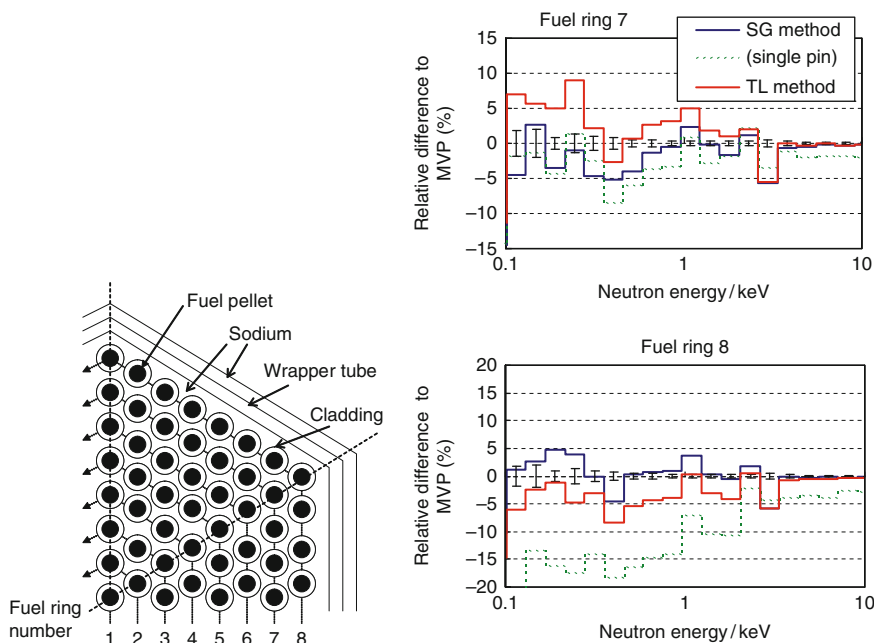


Figure 27

Schematic view of fast reactor fuel assembly, and the difference between effective cross sections obtained by the subgroup method and Tone's method (SG; subgroup, TL; table lookup by Tone's method) (Chiba 2003)

used to generate the subgroup parameters in the subgroup method. The number of subgroups is set at less than or equal to five.

The wrapper tube and sodium in the peripheral region of the assembly create position dependency on the effective cross sections in a fuel assembly. That is, the effective cross sections in the outer ring of the fuel assembly become larger, since ^{238}U is not included in the wrapper tube and sodium, and they act as a neutron source of heavy nuclides in the resonance energy region. In fast reactor calculations, this effect is called the double heterogeneity effect: pellet, cladding, and coolant for the primary and fuel rods, and wrapper and sodium for the secondary heterogeneity.

In order to verify the significance of the position dependency, the subgroup method is also applied to a single pin-cell geometry, which does not consider the wrapper tube and sodium in the peripheral region.

A comparison of the effective cross section for ^{238}U is shown on the right side of Fig. 27. The reference result is obtained by the continuous-energy Monte Carlo code, MVP. In this comparison, the subgroup method gives better accuracy than Tone's method. In the outermost fuel ring (ring 8), the double heterogeneity effect exerts a considerable effect on the effective cross sections, so such an effect must be accurately taken into account. Since BWR fuel assembly also has a similar structure (channel box with gap water around the fuel assembly), the position dependency of the effective cross section is also important.

The above results suggest that the subgroup method gives better accuracy than Tone's method. In this context, Tone's method can be considered as a simple and reasonably accurate resonance calculation method that can be applied to general geometry. Due to this feature, some lattice physics codes adopt this method as the resonance calculation method.

The advantages and disadvantages of Tone's method are summarized as follows:

- Contributions to a background cross section from other regions are taken into account approximately through region-wise and group-wise collision probabilities.
- Its affinity to the conventional equivalence theory is high. Cross section libraries and self-shielding factors prepared for the conventional method with equivalence theory can be directly used in Tone's method.
- The “gray regions” from the viewpoint of the resonance calculation can be approximately treated. Thus the space-dependent self-shielding effect in a fuel lump could be evaluated approximately.
- The NR approximation is used. Note that this method is primarily intended for fast reactor calculations, in which the NR approximation displays a high degree of accuracy. In this context, this method can be accurately applied to resonances in a higher energy range in LWR calculations, in which the NR approximation is valid.
- The energy dependence of collision probabilities among regions are approximated using (244).
- Iteration calculations are required for effective cross sections, in which calculation of the collision probabilities is included, though only a few iterations are needed to obtain converged results. If one's initial rough predictions for effective cross sections is reasonably good, no iteration may be necessary.

3.9.2 The Stoker–Weiss Method and the Space-Dependent Dancoff Method (SDDM)

The Stoker–Weiss Method

The Stoker–Weiss method is another approach to estimating the space-dependent self-shielding effect for the annular regions of a cylindrical fuel rod (Stoker and Weiss 1996; Matsumoto et al. 2005; Matsumoto et al. 2006). This method derives an approximate expression of the escape probability from the annular regions in a fuel pellet not only for an outer ring, but for the inner rings as well.

From a practical point of view, the space-dependent self-shielding effect is important because

- Larger resonance capture of ^{238}U on the pellet surface area causes a higher plutonium buildup in the outer region of a fuel pellet.
- The power distribution inside a pellet is significantly affected by the plutonium buildup and power distribution as the outer region becomes higher at middle to end of life. Consequently, burnup on the pellet surface becomes higher than that of the pellet average, which has an impact on the fission gas release from a pellet, which could be a one of the mechanical limitations of a fuel rod.
- The temperature distribution in a pellet is influenced by the power distribution inside it, for example, the pellet centerline and the average temperature.

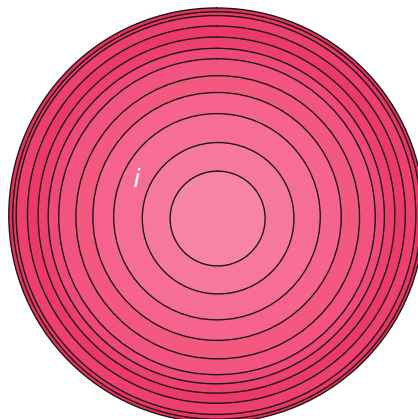


Figure 28
Annular subdivisions of a fuel pellet

Therefore, a simple method to estimate the self-shielding effect inside a pellet is important, mainly for the mechanical evaluation of a fuel rod and a fuel assembly.

From the viewpoint of the resonance calculation, many studies have clarified that the subdivision of a fuel pellet into multiple annular regions does not have a major impact on the accuracy of the resonance calculation, even if the spatial distribution of the number density due to burnup is taken into account. This means that the average treatment of resonance nuclides can be justified for a fuel pellet, at least from the viewpoint of the resonance calculation. A more detailed discussion of this will be offered in [3.11.3](#).

Though the major objective of a lattice physics computation is to provide cross section sets for a core calculation code, the calculation results are also used in mechanical design and safety analyses (e.g., decay heat is dominated by the number densities of heavy and fission product nuclides, which are calculated by a lattice physics code).

Let us now assume that an isolated fuel pellet is annularly subdivided into multiple annular rings, as shown in [Fig. 28](#). The final objective of the Stoker-Weiss method is to derive an expression of the energy dependence of a neutron spectrum for an annular region i with the N -term rational approximation.

When the macroscopic cross section is assumed to be spatially constant inside a pellet region, and the NR approximation is applied to calculate the slowing down source, the neutron flux in region i is expressed as

$$\phi_i(E) = \frac{1}{E} \left((1 - P_{i \rightarrow m}(E)) \frac{\Sigma_{p,f}}{\Sigma_{t,f}(E)} + P_{i \rightarrow m}(E) \right) \quad (252)$$

where i is a region in a pellet ($i \in f$); a detailed derivation of the above equation is given in [\(139\)](#).

In the Stoker-Weiss method, the escape probability from region i to the moderator region m , $P_{i \rightarrow m}(E)$ is assumed to be expressed as

$$P_{i \rightarrow m}(E) = DP_{e,i}(E) \quad (253)$$

where $P_{e,i}(E)$ is the escape probability of a neutron from a fuel, which includes region i , and D is the Dancoff factor (which is unity for isolated fuel). When the number of annular regions in a pellet is one, (253) is reduced into the conventional equivalence theory with the Dancoff factor.

Theoretically, the Dancoff factor should be an energy-dependent parameter in (253). However, the energy dependence of the Dancoff factor is neglected in the derivation of this method.

In order to evaluate $P_{e,i}(E)$, we start from the escape probability for an isolated lump, that is, (106):

$$P_e(E) = \frac{1}{\Sigma_{t,f}(E)\bar{l}} \int_0^\infty dl f(l) \{1 - \exp(-\Sigma_{t,f}(E)l)\} \quad (254)$$

In (254), $\exp(-\Sigma_{t,f}(E)l)$ denotes the transmission probability of a fuel lump, and thus $1 - \exp(-\Sigma_{t,f}(E)l)$ is the probability that a neutron entering from the surface of a fuel lump will suffer a collision in the fuel lump. Consequently, $\int_0^\infty dl f(l) \{1 - \exp(-\Sigma_{t,f}(E)l)\}$ gives the expected value of the collision probability in a fuel lump.

When a neutron entering a fuel pellet has its first collision in region i (in the fuel pellet) with the probability of $\gamma_i(E)$, the escape probability from region i can be expressed as

$$P_{e,i}(E) = \frac{1}{\Sigma_{t,f}(E)\bar{l}_i} \int_0^\infty dl f(l) \{1 - \exp(-\Sigma_{t,f}(E)l)\} = \frac{\gamma_i(E)}{\Sigma_{t,f}(E)\bar{l}_i} \quad (255)$$

where

$\bar{l}_i = 4V_i/S_f$, which is the “average chord length” of region i , expressed by the volume of region i (V_i) and the surface of a fuel pellet (S_f). Note that the definition of the average chord length in this derivation (\bar{l}_i) is different from the conventional one, which is defined by $\bar{l}_i = 4V_i/S_i$. In (255), a neutron that enters from the pellet surface (S_f) collides at region $i(V_i)$. However, in the conventional definition, a neutron that enters from region $i(S_i)$ collides at region $i(V_i)$.

In (255), $\gamma_i(E)$ is also considered as the blackness of region i . The blackness of a solid cylinder that includes region i (ABC in Fig. 29) is approximated by

$$\gamma_{i,ABC}(E) = (\gamma_{i,OBC}(E) - \gamma_{i,OAB}(E)) \quad (256)$$

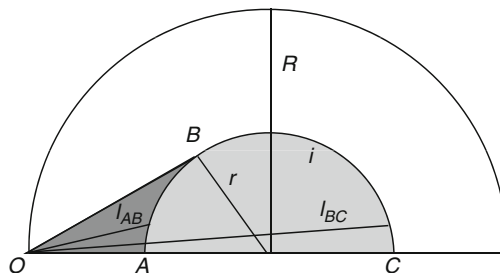


Figure 29
Calculation geometry of blackness for a cylinder

A similar expression for the solid cylinder that includes region $i - 1$ is given by

$$\gamma_{i-1,ABC}(E) = (\gamma_{i-1,OBC}(E) - \gamma_{i-1,OAB}(E)) \quad (257)$$

Equations (256) and (257) assume that the blackness of each region can be synthesized by the subtraction that is shown in Fig. 29.

Finally, in the Stoker–Weiss method, the blackness of region i is evaluated by (258), since the blackness of ring i can be approximated by subtraction of the blackness for the solid cylinders, including regions i and $i - 1$:

$$\gamma_i(E) = (\gamma_{i,OBC}(E) - \gamma_{i,OAB}(E)) - (\gamma_{i-1,OBC}(E) - \gamma_{i-1,OAB}(E)) \quad (258)$$

Next, we will try to estimate each component on the right-hand side of (258). Recalling (254), the collision probability in a region can be expressed by the product of the optical length of a region ($\Sigma_{t,f}(E)\bar{l}$) and the escape probability $P_e(E)$:

$$\int_0^\infty dl f(l) \{1 - \exp(-\Sigma_{t,f}(E)l)\} = \Sigma_{t,f}(E)\bar{l} \times P_e(E) \quad (259)$$

Using the above observation, the blackness for solid region OBC can be evaluated by the following:

$$\begin{aligned} \gamma_{i,OBC}(E) &= (\text{Entering probability to the region } OBC \text{ for a neutron entering the fuel}) \\ &\quad \times (\text{Collision probability in the solid region } OBC) \\ &= (\text{Entering probability to the region } OBC \text{ for a neutron entering the fuel}) \\ &\quad \times (\text{Optical length of the solid region } OBC) \\ &\quad \times (\text{Escape probability from the solid region } OBC) \\ &= \rho_i \times \Sigma_{t,f}(E)\bar{l}_{i,BC} \times \sum_{n=1}^N \frac{b_n a_n}{\Sigma_{t,f}(E)\bar{l}_{i,BC} + a_n} \end{aligned} \quad (260)$$

The entering probability into region OBC is given by

$$\rho_i = r_i/R \quad (261)$$

where r_i and R are the radii of region i , and the fuel pellet, respectively, and the escape probability from the solid region OBC is approximated by the N -term rational approximation.

The average chord length from O (origin of a neutron entering a fuel pellet) to arc BC , is analytically derived through some algebra, and given by

$$\bar{l}_{i,BC} = \frac{2R}{\pi} \left(\sqrt{1 - \rho_i^2} + \frac{1}{\rho_i} \sin^{-1} \rho_i + \frac{\pi}{2} \rho_i \right) \quad (262)$$

Similarly, the average chord length from O to arc AB is

$$\bar{l}_{i,AB} = \frac{2R}{\pi} \left(\sqrt{1 - \rho_i^2} + \frac{1}{\rho_i} \sin^{-1} \rho_i - \frac{\pi}{2} \rho_i \right) \quad (263)$$

By applying the above derivation to the other terms in (258), we have the following relationship for the blackness of ring i :

$$\begin{aligned}\gamma_i(E) &= (\gamma_{i,OBC}(E) - \gamma_{i,OAB}(E)) - (\gamma_{i-1,OBC}(E) - \gamma_{i-1,OAB}(E)) \\ &= \rho_i \Sigma_{t,f}(E) \overline{l_{i,BC}} \sum_{n=1}^N \frac{b_n a_n}{\Sigma_{t,f}(E) \overline{l_{i,BC}} + a_n} - \rho_i \Sigma_{t,f}(E) \overline{l_{i,AB}} \sum_{n=1}^N \frac{b_n a_n}{\Sigma_{t,f}(E) \overline{l_{i,AB}} + a_n} \\ &\quad - \rho_{i-1} \Sigma_{t,f}(E) \overline{l_{i-1,BC}} \sum_{n=1}^N \frac{b_n a_n}{\Sigma_{t,f}(E) \overline{l_{i-1,BC}} + a_n} \\ &\quad + \rho_{i-1} \Sigma_{t,f}(E) \overline{l_{i-1,AB}} \sum_{n=1}^N \frac{b_n a_n}{\Sigma_{t,f}(E) \overline{l_{i-1,AB}} + a_n}\end{aligned}\tag{264}$$

By substituting (264) into (255), we obtain

$$\begin{aligned}P_{e,i}(E) &= \frac{\gamma_i(E)}{\Sigma_{t,f}(E) \overline{l_i}} \\ &= \frac{1}{\Sigma_{t,f}(E) \overline{l_i}} \left[\begin{array}{l} \rho_i \Sigma_{t,f}(E) \overline{l_{i,BC}} \sum_{n=1}^N \frac{b_n a_n}{\Sigma_{t,f}(E) \overline{l_{i,BC}} + a_n} \\ - \rho_i \Sigma_{t,f}(E) \overline{l_{i,AB}} \sum_{n=1}^N \frac{b_n a_n}{\Sigma_{t,f}(E) \overline{l_{i,AB}} + a_n} \\ - \rho_{i-1} \Sigma_{t,f}(E) \overline{l_{i-1,BC}} \sum_{n=1}^N \frac{b_n a_n}{\Sigma_{t,f}(E) \overline{l_{i-1,BC}} + a_n} \\ + \rho_{i-1} \Sigma_{t,f}(E) \overline{l_{i-1,AB}} \sum_{n=1}^N \frac{b_n a_n}{\Sigma_{t,f}(E) \overline{l_{i-1,AB}} + a_n} \end{array} \right] \\ &= \frac{\rho_i \overline{l_{i,BC}}}{\overline{l_i}} \sum_{n=1}^N \frac{b_n a_n}{\Sigma_{t,f}(E) \overline{l_{i,BC}} + a_n} - \frac{\rho_i \overline{l_{i,AB}}}{\overline{l_i}} \sum_{n=1}^N \frac{b_n a_n}{\Sigma_{t,f}(E) \overline{l_{i,AB}} + a_n} \\ &\quad - \frac{\rho_{i-1} \overline{l_{i-1,BC}}}{\overline{l_i}} \sum_{n=1}^N \frac{b_n a_n}{\Sigma_{t,f}(E) \overline{l_{i-1,BC}} + a_n} + \frac{\rho_{i-1} \overline{l_{i-1,AB}}}{\overline{l_i}} \sum_{n=1}^N \frac{b_n a_n}{\Sigma_{t,f}(E) \overline{l_{i-1,AB}} + a_n} \\ &= \sum_{m=1}^4 c_m \sum_{n=1}^N \frac{b_n a_n}{\Sigma_{t,f}(E) \overline{l_m} + a_n}\end{aligned}\tag{265}$$

The coefficients c_m and average chord length $\overline{l_m}$ that appear in (265) are summarized in  [Table 14](#).

The coefficient c_m satisfies the following relationship:

$$\sum_{m=1}^4 c_m = 1\tag{266}$$

Table 14

Coefficients and average chord length used in (265) of the Stoker–Weiss method

M	c_m	\bar{l}_m
1	$\rho_i \bar{l}_m / l_i$	$\bar{l}_{i,BC}$
2	$-\rho_i \bar{l}_m / l_i$	$\bar{l}_{i,AB}$
3	$\rho_{i-1} \bar{l}_m / l_i$	$\bar{l}_{i-1,BC}$
4	$-\rho_{i-1} \bar{l}_m / l_i$	$\bar{l}_{i-1,AB}$

With (253) and (265), $1 - P_{i \rightarrow m}(E)$ can be expressed as

$$\begin{aligned} 1 - P_{i \rightarrow m}(E) &= \sum_{m=1}^4 c_m \sum_{n=1}^N b_n - D \sum_{m=1}^4 c_m \sum_{n=1}^N \frac{b_n a_n}{\Sigma_{t,f}(E) \bar{l}_m + a_n} \\ &= \sum_{m=1}^4 c_m \sum_{n=1}^N b_n \left(1 - D \frac{a_n}{\Sigma_{t,f}(E) \bar{l}_m + a_n} \right) \\ &= \sum_{m=1}^4 c_m \sum_{n=1}^N b_n \frac{\Sigma_{t,f}(E) \bar{l}_m + (1 - D) a_n}{\Sigma_{t,f}(E) \bar{l}_m + a_n} \end{aligned} \quad (267)$$

where $\sum_{n=1}^N b_n = 1$ is used by recalling (121).

Finally, by substituting (267) into (252), the energy dependence of the neutron flux in region i is given by

$$\begin{aligned} \phi_i(E) &= \frac{1}{E} \left((1 - P_{i \rightarrow m}(E)) \frac{\Sigma_{p,f}}{\Sigma_{t,f}(E)} + P_{i \rightarrow m}(E) \right) \\ &= \frac{1}{E} \frac{\Sigma_{p,f}}{\Sigma_{t,f}(E)} \sum_{m=1}^4 c_m \sum_{n=1}^N b_n \frac{\Sigma_{t,f}(E) \bar{l}_m + (1 - D) a_n}{\Sigma_{t,f}(E) \bar{l}_m + a_n} \\ &\quad + D \frac{1}{E} \sum_{m=1}^4 c_m \sum_{n=1}^N \frac{b_n a_n}{\Sigma_{t,f}(E) \bar{l}_m + a_n} \end{aligned} \quad (268)$$

When the macroscopic total cross section is very large, the energy dependence of the neutron flux can be approximated as follows:

$$\begin{aligned} \phi_i(E) &= \frac{1}{E} \frac{\Sigma_{p,f}}{\Sigma_{t,f}(E)} \sum_{m=1}^4 c_m \sum_{n=1}^N b_n \frac{\Sigma_{t,f}(E) \bar{l}_m + (1 - D) a_n}{\Sigma_{t,f}(E) \bar{l}_m + a_n} + \frac{1}{E} D \sum_{m=1}^4 c_m \sum_{n=1}^N \frac{b_n a_n}{\Sigma_{t,f}(E) \bar{l}_m + a_n} \\ &\approx (1 - D) \frac{1}{E} \sum_{m=1}^4 c_m \sum_{n=1}^N b_n \frac{\Sigma_{p,f} \bar{l}_m}{\Sigma_{t,f}(E) \bar{l}_m} + D \frac{1}{E} \sum_{m=1}^4 c_m \sum_{n=1}^N b_n \frac{\Sigma_{p,f} \bar{l}_m + a_n}{\Sigma_{t,f}(E) \bar{l}_m + a_n} \\ &= (1 - D) \frac{1}{E} \sum_{m=1}^4 c_m \sum_{n=1}^N b_n \frac{\sigma_0}{\sigma_{a,r}(E) + \sigma_0} + D \frac{1}{E} \sum_{m=1}^4 c_m \sum_{n=1}^N b_n \frac{\sigma_{0,mn}}{\sigma_{a,r}(E) + \sigma_{0,mn}} \end{aligned} \quad (269)$$

where

$$\begin{aligned}\sigma_0 &= \Sigma_{p,f}/N_r \\ \sigma_{0,mn} &= (\Sigma_{p,f} + a_n/\bar{l}_m)/N_r\end{aligned}$$

In the above derivation, the following approximations are used:

$$\begin{aligned}\frac{1}{E} \frac{\Sigma_{p,f}}{\Sigma_{t,f}(E)} \sum_{m=1}^4 c_m \sum_{n=1}^N b_n \frac{(1-D)a_n}{\Sigma_{t,f}(E)\bar{l}_m + a_n} &\approx 0 \\ \frac{1}{E} \sum_{m=1}^4 c_m \sum_{n=1}^N b_n \frac{\Sigma_{p,f}\bar{l}_m}{\Sigma_{t,f}(E)\bar{l}_m + a_n} &\approx \frac{1}{E} \sum_{m=1}^4 c_m \sum_{n=1}^N b_n \frac{\Sigma_{p,f}\bar{l}_m}{\Sigma_{t,f}(E)\bar{l}_m}\end{aligned}$$

In (125) and (132) we derived a formula for the effective cross section when the energy dependence of the neutron flux is given by the N -term rational approximation. Considering the similarity between (125) and (269), and by applying (132), we can derive the following formula for the effective cross section:

$$\begin{aligned}\sigma_{g,x,i} &= \frac{\int_{E_g}^{E_{g-1}} dE \sigma_x(E) \lim_{\Sigma_{t,f}(E) \rightarrow \infty} \phi_i(E)}{\int_{E_g}^{E_{g-1}} dE \lim_{\Sigma_{t,f}(E) \rightarrow \infty} \phi_i(E)} \\ &= \frac{(1-D)I_{g,x}(\sigma_0) + D \sum_{m=1}^4 c_m \sum_{n=1}^N b_n I_{g,x}(\sigma_{0,mn})}{1 - (1-D)I_{g,a}/\sigma_0 - D \sum_{m=1}^4 c_m \sum_{n=1}^N b_n I_{g,a}(\sigma_{0,mn})/\sigma_{0,mn}}\end{aligned}\quad (270)$$

Once the Dancoff factor D is evaluated, the effective cross section in each annular ring can be evaluated by (270). Since the background cross section for each annular ring is evaluated by the potential scattering cross section and the geometry information of an annularly divided fuel pellet, the application and implementation of the Stoker–Weiss method for common lattice physics codes are easy.

Space-Dependent Dancoff Method (SDDM)

The above method can be modified by incorporating Stamm’ler’s method for the evaluation of blackness, as described in [3.5.6](#) (Matsumoto et al. 2005; Matsumoto et al. 2006). The improved approach is called the spatially dependent Dancoff method, or SDDM. Recalling (173), we have the following relationship between the fuel-to-fuel collision probability in isolated and lattice systems in Stamm’ler’s method:

$$p_{FF} = p_{ff} + \frac{x(1-p_{ff})^2}{x(1-p_{ff}) + A + B}\quad (271)$$

Recalling (255), the blackness for the fuel regions in the isolated and the lattice systems are given by

$$\gamma_F = \frac{4V_f}{S_f} \Sigma_{t,f}(1 - p_{FF}) = x(1 - p_{FF})\quad (272)$$

and

$$\gamma_f = \frac{4V_f}{S_f} \Sigma_{t,f}(1 - p_{ff}) = x(1 - p_{ff}) \quad (273)$$

respectively. By substituting (272) and (273) into (271), we obtain

$$\gamma_F = \frac{\gamma_f C}{\gamma_f + C} \quad (274)$$

where

$$C = A + B \quad (A \text{ and } B \text{ is given in (173)}).$$

Care should be taken that C in (274) is different from the Dancoff correction. The term expressed by C represents the effect of a finite fuel assembly. In SDDM, this term is assumed to be proportional to the fractional radius of region i , that is, $\rho_i = r_i/R$.

By utilizing (274) and considering the above discussion, (258) can be written as

$$\gamma_i^{lat} = \left(\frac{\rho_i C \gamma_{i,OBC}}{\gamma_{i,OBC} + \rho_i C} - \frac{\rho_i C \gamma_{i,OAB}}{\gamma_{i,OAB} + \rho_i C} \right) - \left(\frac{\rho_{i-1} C \gamma_{i-1,OBC}}{\gamma_{i-1,OBC} + \rho_{i-1} C} - \frac{\rho_{i-1} C \gamma_{i-1,OAB}}{\gamma_{i-1,OAB} + \rho_{i-1} C} \right) \quad (275)$$

By applying Carlvik's two-term rational approximation for $\gamma_{i,OBC}$, $\gamma_{i,OAB}$, $\gamma_{i-1,OBC}$, $\gamma_{i-1,OAB}$, we have the following formula for escape probability based on SDDM:

$$P_{e,i}(E) = \sum_{m=1}^4 c_m \sum_{n=1}^2 \frac{\beta_n \alpha_n}{\Sigma_{t,f}(E) \bar{l}_m + \alpha_n} \quad (276)$$

where

$$\alpha_{1,2} = \frac{(5C + 6) \mp \sqrt{C^2 + 36C + 36}}{2(C + 1)}$$

$$\beta_1 = \frac{C' - \alpha_1}{\alpha_2 - \alpha_1}$$

$$\beta_2 = 1 - \beta_1$$

$$C' = \frac{4C + 6}{C + 1}$$

$$C = A + B \quad (A \text{ and } B \text{ is given in (173)}).$$

Therefore, the energy dependence of the neutron flux is

$$\phi_i(E) = \frac{1}{E} \sum_{m=1}^4 c_m \sum_{n=1}^2 \beta_n \frac{\sigma_{0,mn}}{\sigma_{t,r}(E) + \sigma_{0,mn}} \quad (277)$$

where

$$\begin{aligned}\sigma_{0,mn} &= \sigma_{0,f} + \alpha_n \Sigma_e / N_r = \sigma_{0,f} + \alpha_n / N_r / \bar{l}_m \text{ and} \\ \sigma_{0,f} &= \sum_{k \neq r} N_k \sigma_{s,k} / N_r\end{aligned}$$

Finally, the effective cross section can be obtained by

$$\sigma_{g,x,i} = \frac{\sum_{m=1}^4 c_m \sum_{n=1}^2 \beta_n I_{g,x}(\sigma_{0,mn})}{1 - \sum_{m=1}^4 c_m \sum_{n=1}^2 \beta_n I_{g,a}(\sigma_{0,mn}) / \sigma_{0,mn}} \quad (278)$$

When (270) and (278) are compared, (278), that is, SDDM, gives a more consistent formula than the original Stoker–Weiss method.

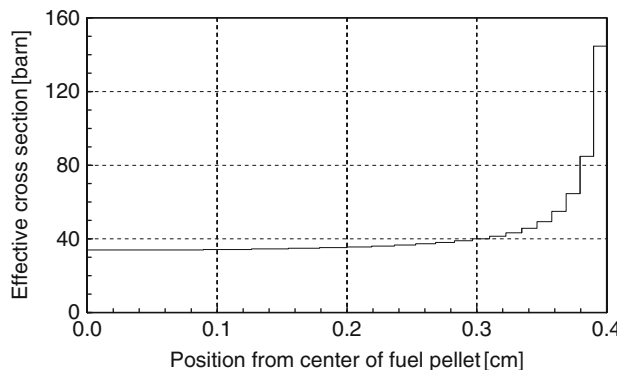
The advantages and disadvantages of the Stoker–Weiss method (or SDDM method) are summarized as follows:

- It is an extension of the equivalence method and can be easily implemented in conventional lattice physics codes.
- The calculation procedure for the background cross section in each region is simple.
- Since the derivation of the background cross section is based on the analytic approach for a cylinder with annular divisions, its extension to a general geometry is impossible.
- The NR approximation is used.
- The Dancoff factor is used to incorporate the shadowing effect of other fuel rods. In the case of SDDM, Stamm’ler’s method is used.
- The macroscopic total cross section is assumed to be spatially constant in a fuel pellet, which means no variations in the temperature and/or number density distribution in a pellet.

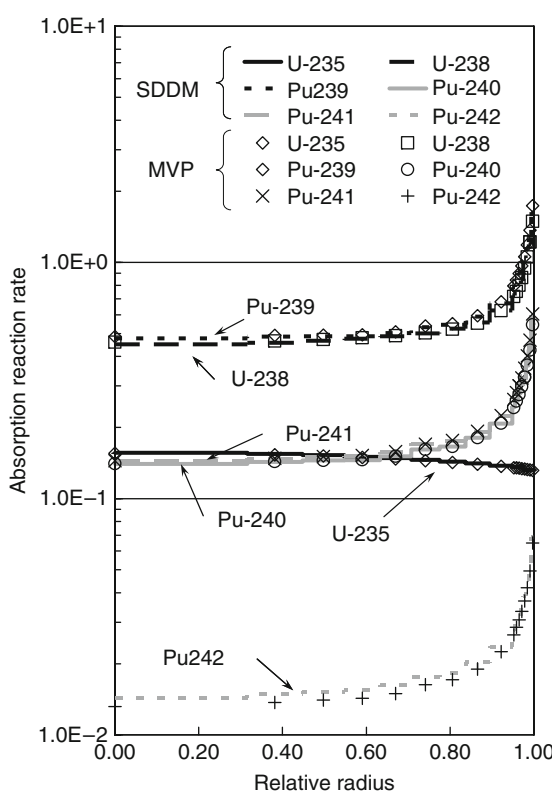
Previous studies have revealed that the spatial variation of the number density of a resonance nuclide does not have a significant impact on the calculation accuracy of the effective cross section. Thus, the Stoker–Weiss method can be applied to a resonance calculation in which the distribution of the number density in a pellet exists. On the contrary, when the temperature profile in a pellet is taken into account, the Stoker–Weiss method will not be very accurate. In such a case, particular considerations need to be incorporated (Matsumoto et al. 2006).

➤ *Figure 30* shows the space-dependent effective cross section in a UO₂ fuel pellet that was obtained by the Stoker–Weiss method. In the outer region, the effective cross section is larger than that in the inner regions, due to neutron inflow from the moderator region. Thus, this method reproduces the trend intuited for the space-dependent effective cross sections.

➤ *Figure 31* shows a comparison of the number density distributions obtained by SDDM and by the continuous-energy Monte Carlo method. SDDM well produces the plutonium buildup on the pellet surface, which is referred to as the rim effect. This comparison clarifies that SDDM can be applied to evaluate not only the space-dependent effective cross sections, but also the number density distribution in a pellet. Therefore, the power depression inside a pellet, which is an important factor in the mechanical design of a fuel rod, can also be evaluated by this method. Burnup calculation by the continuous-energy Monte Carlo method can also provide such results, but the Stoker–Weiss and SDDM methods are more suitable for production calculations, due to the short computation time they require.

**Figure 30**

Example of space dependency of the effective cross section of ^{238}U in a fuel pellet calculated by the Stoker-Weiss method (293 K, typical PWR cell, pellet radius is 0.4 cm) (Matsumoto et al. 2005)

**Figure 31**

Comparison of absorption reaction rates obtained by SDDM and continuous-energy Monte Carlo code MVP, at the end of life of UO_2 fuel (Matsumoto et al. 2005)

3.10 Resonance Overlap Effect

3.10.1 Overview

Various resonance calculation methods have been discussed in this section thus far. These resonance calculation methods (except for the ultrafine group method) assume just one resonance nuclide in a system – no interference of the resonance peaks of different nuclides is considered. In reality, however, a fuel pellet contains many resonance nuclides, especially in burnt fuels. Consequently, a discrepancy arises between the calculation model (i.e., resonance theory) and the actual situation regarding prediction error of the effective cross section. This discrepancy is referred to as the resonance overlap (or interference) effect (Hébert 2004).

From the viewpoint of the “gross” neutronics characteristics of a fuel assembly, the impact of the resonance overlap effect is, fortunately, not very large. However, if more detailed information is necessary, such as the nuclide number densities of burnt fuel or the reaction rate of a particular nuclide, then the resonance overlap effect might play a very important role. Consideration of the resonance overlap effect, therefore, should not be neglected in the resonance calculation of a lattice physics code.

For example, let us consider the effective cross section of ^{151}Sm at 6.16–7.524 eV (88th group of the 172 XMAS groups). In this energy range, ^{238}U has a large resonance peak at 6.7 eV, as shown in Fig. 32. Therefore, the typical neutron spectrum in the fuel shows a significant depression in this energy range due to the resonance absorption of ^{238}U . The neutron slowing down source in this energy range is also far from the asymptotic one (which is typically constant in the NR approximation).

^{151}Sm also has large resonance in this energy range. When the resonance overlap between ^{151}Sm and ^{238}U is not taken into account, the effective cross section for ^{151}Sm at 6.16–7.524 eV

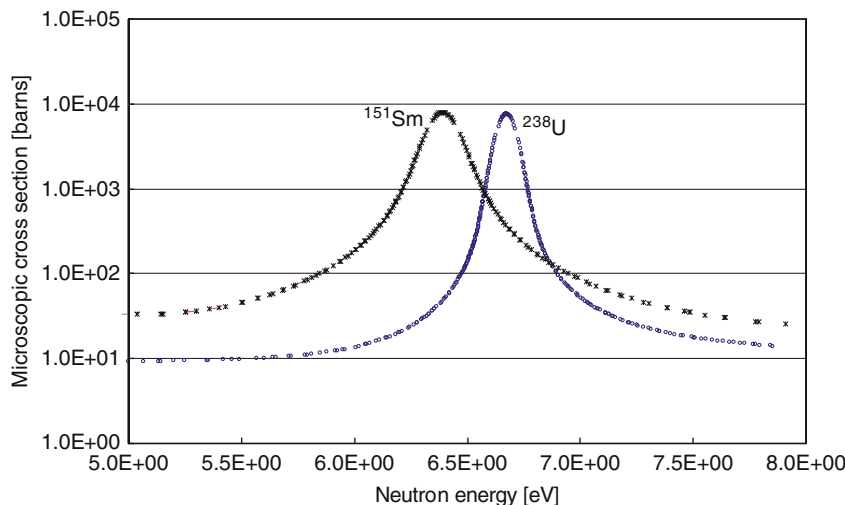


Figure 32

Resonance overlap between ^{238}U and ^{151}Sm (microscopic absorption cross section at 300 K)

with a low number density (nearly the infinite-dilution condition) is 1,185 barn, while it becomes 898 barn when distortion of the neutron spectrum due to the presence of ^{238}U is taken into account. The resulting difference in the effective cross sections is approximately 25%, which has a significant impact on the absorption reaction rate of ^{151}Sm . Though the impact on the k -infinity of a fuel assembly is limited due to the low contribution of ^{151}Sm , the number density of ^{151}Sm during burnup is significantly mispredicted if the resonance interference effect is not taken into account.

We can see similar observations for more important nuclides, for example, ^{235}U . Since there are coincident resonance overlaps between ^{238}U and ^{235}U , the accuracy of the effective cross section of ^{235}U in some energy groups becomes lower if the overlap effect is neglected. A previous study suggests that the resonance overlap effect between ^{235}U and ^{238}U is approximately 0.2% dk/k on k -infinity for a typical UO_2 LWR fuel assembly. In MOX fuel, similar resonance interference is observed between ^{239}Pu and ^{238}U . The effect is reported to be approximately 0.2% dk/k , which is close to that between ^{235}U and ^{238}U .

In the following subsection, a countermeasure for the resonance overlap effect will be discussed.

3.10.2 Resonance Interference Factor (RIF) Table

In principle, the resonance overlap effect can occur between any two resonance nuclides. However, in the typical situation of LWR lattices, the resonance overlap effect between ^{238}U and other resonance nuclides is dominant, and the interferences among other resonance nuclides can be considered as a second-order effect. This can be justified by the fact that the number density of ^{238}U is usually much larger than that of other resonance nuclides, so that the neutron spectrum in a fuel pellet is dominated by the resonance absorption of ^{238}U . Thus, from an engineering perspective, the treatment of the resonance overlap effect can be simplified to those between ^{238}U and other resonance nuclides.

Since the effective cross section is affected by the resonance overlap effect, it can be corrected by the resonance interference (overlap) factor, which is prepared in advance of lattice physics computations. In more detail, the resonance interference factors defined by the following equation are evaluated and tabulated in a cross section library:

$$\text{RIF}_{k,g,N_{^{238}\text{U}}} = \frac{\sigma_{\text{eff},k,g}(N_{^{238}\text{U}})}{\sigma_{\text{eff},k,g}(0)} \quad (279)$$

where

$\text{RIF}_{k,g,N_{^{238}\text{U}}}$: resonance interference factor for nuclide k and energy group g , when the number density of ^{238}U is $N_{^{238}\text{U}}$;

$\sigma_{\text{eff},k,g}(N_{^{238}\text{U}})$: effective cross section for nuclide k and energy group g , when the number density of ^{238}U is $N_{^{238}\text{U}}$; and

$\sigma_{\text{eff},k,g}(0)$: effective cross section for nuclide k and energy group g , when the number density of ^{238}U is zero, that is, no resonance overlap effect is considered.

In the resonance calculation, the effective cross section without consideration of the resonance overlap is evaluated first, then the RIF is multiplied by the obtained effective cross section in order to capture the resonance overlap effect.

The RIF table can be prepared by the NJOY code or by utilization of the ultrafine group spectrum calculations. In the usual spectrum calculation based on the NR approximation, a typical asymptotic neutron spectrum with $1/E$ (or similar shape) is used as a starting point, then the actual neutron spectrum with the depression due to a resonance peak is evaluated by

$$\phi(E) = \phi_{\text{asymptotic}}(E) \frac{\sigma_0}{\sigma_t(E) + \sigma_0} \quad (280)$$

The neutron spectrum obtained by (280) is then used to collapse the cross section to obtain a group averaged effective cross section. The NJOY code also has the following option:

$$\phi(E) = \phi_{\text{input}}(E) \frac{\sigma_0}{\sigma_t(E) + \sigma_0} \quad (281)$$

where

$\phi_{\text{input}}(E)$: user-specified neutron spectrum.

In order to consider the resonance overlap effect, the following procedure can be followed:

1. Perform the spectrum calculation for ^{238}U using (280).
2. Use the spectrum obtained in (1) as the user-specified spectrum in (281).
3. Collapse the cross section to obtain the effective cross section using the neutron spectrum obtained in (2).

The effective cross section obtained in (3) includes the resonance overlap effect with ^{238}U . It can therefore be used as the numerator in (279). Since the neutron spectrum obtained in (1) depends on the background cross section (number density) of ^{238}U , several calculations with different shielding conditions (different background cross sections and/or number densities of ^{238}U) should be carried out. The evaluated RIFs are edited as a table for the utilization of resonance calculations in lattice physics codes.

3.10.3 Utilization of an Ultrafine Energy Group Cross Section

We can also use an ultrafine energy group cross section to correct the resonance overlap effect. The ultrafine energy group spectrum calculation discussed in 3.7 can precisely capture any resonance overlap effect, so it can be used to incorporate the effect. However, as previously discussed in 3.7, direct application of the ultrafine energy group calculation for a whole fuel assembly still requires an impractical amount of computation time, so the appropriate combination with other methods would be required. For example, an ultrafine energy group calculation is carried out in simple pin cell geometry, and the position-dependence of the effective cross section due to the shadowing effect of other fuel rods is evaluated through the Dancoff correction (Sugimura and Yamamoto 2007).

Since a neutron spectrum calculation for an ultrafine energy group requires some computation time, a more simplified approach can be used to capture the resonance interference effect. Since an approximate neutron spectrum can be obtained by the NR (or IR)

approximation, the following procedures can be used to evaluate the resonance overlap factor “on the fly”:

1. By recalling (108), evaluate the neutron spectrum using the NR approximation with one resonance nuclide,

$$\begin{aligned}\phi_{f,\text{no-RI}}(E) &= \frac{1}{E} \frac{\Sigma_{p,f} + \Sigma_e}{\Sigma_{t,f}(E) + \Sigma_e} \\ &= \frac{1}{E} \frac{N_r(\sigma_{p,r} + \sigma_{0,f}) + \Sigma_e}{N_r(\sigma_{t,r}(E) + \sigma_{0,f}) + \Sigma_e}\end{aligned}\quad (282)$$

where

Σ_e : macroscopic escape cross section,

$$\sigma_{0,f} = \sum_{k \neq r} N_k \sigma_{p,k} / N_r.$$

2. Evaluate the neutron spectrum using the NR approximation with multiple resonance nuclides,

$$\begin{aligned}\phi_{f,\text{with-RI}}(E) &= \frac{1}{E} \frac{\Sigma_{p,f} + \Sigma_e}{\Sigma_{t,f}(E) + \Sigma_e} \\ &= \frac{1}{E} \frac{\sum_k N_k \sigma_{p,k} + \Sigma_e}{\sum_k N_k \sigma_{t,k}(E) + \Sigma_e}\end{aligned}\quad (283)$$

3. The resonance interference factor is evaluated by

$$\begin{aligned}\text{RIF}_g &= \frac{\sigma_{k,g,\text{with-RI}}(\vec{r})}{\sigma_{k,g,\text{no-RI}}(\vec{r})} = \frac{\int_{E_g}^{E_{g-1}} dE \sigma_k(E) \phi_{f,\text{with-RI}}(\vec{r}, E)}{\int_{E_g}^{E_{g-1}} dE \phi_{\text{with-RI}}(\vec{r}, E)} \\ &\times \frac{\int_{E_g}^{E_{g-1}} dE \phi_{f,\text{no-RI}}(\vec{r}, E)}{\int_{E_g}^{E_{g-1}} dE \sigma_k(E) \phi_{\text{no-RI}}(\vec{r}, E)}\end{aligned}\quad (284)$$

Note that the IR approximation can be also used in the above procedure.

The advantages and disadvantages of this method are summarized as follows:

- The resonance interference factor can be evaluated with the actual composition of the resonance material. Therefore, the resonance interference not only for ^{238}U , but also for other nuclides can be taken into account.
- Since the resonance interference factor is evaluated “on the fly”, additional computation time is necessary. The ultrafine energy group calculation, particularly, requires some computation time, though it is accurate. The second approach with the NR (or IR) approximation could yield a solution that offers a compromise between calculation accuracy and computation time.
- The ultrafine energy group calculation is applied to the resolved resonance energy range, which is $\sim 10 \text{ keV}$ for heavy resonance isotopes. In order to accurately cover this energy range,

a few to several tens of thousand energy group is necessary. If the number of nuclides considered in the evaluation of the resonance interference factor increases, these cross sections with fine energy resolution require considerable memory storage.

Some of the most recent lattice physics codes adopt this approach to capture the resonance interference effect (Wehlage et al. 2005; Sugimura and Yamamoto 2007).

3.11 Other Topics in Resonance Calculations

3.11.1 Effective Temperature Used in Resonance Calculation

The effective cross section depends not only on the background cross section, but also on the temperature, due to the Doppler broadening of the cross section. The temperature of a fuel pellet varies across its volume during power generation. The shape of the temperature distribution is approximately parabolic in a pellet during steady-state operation. In lattice physics computations, a fuel pellet is commonly treated as a single region, since equivalence theory is widely used. In this case, the choice of “average temperature” is very important in resonance calculations.

Resonance absorption generally takes place on the surface of a resonance lump, due to neutron injection from the moderator. Thus, the surface region should assume more importance than the center region.

Several estimation methods have been developed to date:

- Simple volume average model

$$T_{f,eff} = \frac{1}{V_f} \int_{V_f} T_f(\vec{r}) d\vec{r} \quad (285)$$

- Rowland's model (for parabolic temperature distribution) (Rowlands 1962)

$$T_{f,eff} = T_s + \frac{4}{9}(T_c - T_s) \quad (286)$$

where

T_s : surface temperature, and

T_c : centerline temperature

- Arnold and Dannels's model (for parabolic temperature distribution) (Arnold and Dannels 1960)

$$T_{f,eff} = T_s + 0.35(T_c - T_s) \quad (287)$$

- Chord average model (Kruijf 1994; Kruijf and Jansen 1996)

$$T_{f,eff} = \int_S \int_{\vec{n} \bullet \vec{\Omega} > 0} d\vec{\Omega} g(\vec{r}_s, \vec{\Omega}) \frac{\int_0^L(\vec{r}_s, \vec{\Omega}) T(l) dl}{L(\vec{r}_s, \vec{\Omega})} \quad (288)$$

Table 15

Weight factors of temperature for the chord average model (10 equi-volumes in an annularly divided cylindrical pellet). Regions 1 and 10 indicate the center and surface, respectively

Region	Weight
1	0.079560
2	0.081776
3	0.084304
4	0.087240
5	0.090726
6	0.094994
7	0.100461
8	0.107987
9	0.119917
10	0.153034

Source: Matsumoto et al. (2006).

where

$L(\vec{r}_s, \vec{\Omega})$: chord length at position \vec{r}_s on surface S and in direction $\vec{\Omega}$,

$g(\vec{r}_s, \vec{\Omega})$: probability distribution of a chord, which is given by $g(\vec{r}_s, \vec{\Omega}) = n \cdot \vec{\Omega} / (\pi S)$ in the case of isotropic and uniform incident incoming neutrons.

From the viewpoint of integrated parameters such as k-infinity, the above definitions do not yield a considerable discrepancy. However, with respect to the temperature coefficients of a fuel pellet (i.e., the Doppler coefficient), the chord average model more accurately reproduces reference results obtained using a continuous-energy Monte Carlo method. Under transient conditions, the temperature distribution inside a pellet may not have a parabolic shape. For example, during very fast transitions such as a reactivity initiated accident (RIA), which occurs as a rapid increase in reactivity on control rod ejection for LWRs, the temperature distribution may be proportional to the power distribution inside a pellet because of the adiabatic variation of the temperature. The power density is greater on the pellet surface than in the center, so the maximum temperature may appear near the surface in a rapid transition. Both the Rowland and the Arnold and Dannells models assume a parabolic temperature distribution, which is appropriate for the steady state, but which might not be applicable in transient cases. Therefore, the chord average model becomes useful in such a case.

When a fuel pellet is divided into ten annularly equi-volume regions, the weight factors used in the chord average model are those given in [Table 15](#).

3.11.2 Temperature Distribution in a Resonance Region

Several resonance calculation methods that can handle the spatial resonance self-shielding effect were discussed in [3.7–3.9](#). When a fuel pellet is subdivided into annular regions, it

is straightforward to consider the temperature distribution in each annular region. However, direct utilization of space-dependent resonance shielding methods with a temperature profile may go beyond the assumptions used in the resonance calculation model.

Since the ultrafine energy group calculation is based on the “first principle,” it can handle the temperature distribution in a fuel lump, and gives a reliable result even with the temperature profile.

The subgroup parameters are generated by the fitting or the moment methods, which assume a certain temperature. Since the probability (weight) of each subgroup and of the subgroup cross section are temperature-dependent, they cannot be directly applied to a space-dependent self-shielding calculation with a temperature profile. Let us consider a subgroup. This subgroup has a certain probability, which “physically” corresponds to the ratio of the energy range in an energy group. This probability depends on the temperature, and takes on another value for a different temperature. This means that the ratio of the energy range for a particular subgroup in an energy group changes due to temperature. Subgroup parameters with different temperatures have different and inconsistent “energy group structures,” so they cannot be used in the same calculation. On the contrary, when a subgroup parameter is generated through the direct method with a fixed energy group structure, it can be applied to a temperature distribution problem because there is no inconsistency in the subgroup parameters for different temperatures. Several studies have been carried out to address this inconsistency in the probability table approach to a temperature-dependent problem (Joo et al. 2005).

The Tone method and the Stoker–Weiss method (or SDDM) also assume a constant macroscopic cross section throughout a fuel lump. Thus, the direct application of these methods to a temperature distribution problem would result in misprediction, and particular considerations would be necessary (Matsumoto et al. 2006).

3.11.3 Treatment of Number Density Distribution in a Pellet

Resonance capture by ^{238}U mainly occurs on the pellet surface due to the spatial self-shielding effect. As a result, plutonium buildup in the surface region becomes dominant, as shown in

Fig. 31.

Resonance calculation methods based on the equivalence theory (including Tone, Stoker–Weiss, SDDM) assumes a constant macroscopic cross section in a fuel lump. Strictly speaking, then, the spatial distributions of resonance nuclides cannot be taken into account and are neglected. Fortunately, previous studies have clarified that the distribution of number density in a pellet has a small impact on the calculation results, so it can be treated as a constant throughout the fuel region in common lattice physics computations (Stoker and Weiss 1996). Therefore, the simple average of number density can be applied to a fuel region in the resonance calculation. Such treatment greatly simplifies the resonance treatment in actual calculations. Note that the subgroup method and the ultrafine energy group calculation method accurately handle these effects, since no assumption regarding the constant cross section is taken into account.

As will be discussed in Sect. 6, a gadolinia-bearing fuel pellet is subdivided into several annular regions in order to capture the depletion characteristics of gadolinia (the onion skin effect). In this case, we can apply the space-dependent self-shielding method to evaluate the space-dependent effective cross section in each ring. However, in common lattice physics computation such detailed treatment is not necessary, that is, a pellet’s average number density can be used in the resonance calculation, and the same effective cross section can be used in all regions inside a pellet. Note that the number densities in each region are independently

tracked through the burnup calculation, since the reaction rates in each region are different due to spatial variations in the neutron spectrum (even if an identical effective cross section is used in all regions).

3.11.4 Resonance Calculation for Non-Heavy Nuclides

➤ Section 3 mainly considers the resonance calculation for heavy nuclides, for example, ^{238}U . However, a resonance treatment for other nuclides also has important role.

In LWR fuel, gadolinia is commonly used as a burnable absorber. Since the major isotopes of Gd have large resonances and are used with high-content, the self-shielding effect should be taken into account. As described in ➤ Sect. 3.11.3, the spatial dependence of the number densities of Gd isotopes can be handled through the simple average over a pellet in the resonance treatment.

The absorbers used in LWRs also have large resonances, that is, Ag, In, and Cd for PWR, and Hf for BWR. Since the number densities of these resonance nuclides in the absorber are high, the resonance treatment is important in order to accurately predict the reactivity value of the control rod. When an infinite-dilute cross section is used for absorber nuclides, the reactivity value of a control rod will be significantly over-predicted.

Zircaloy is used not only as a cladding material, but also as a structural material such as a water rod, channel box, and grid spacer. Because zirconium isotopes have resonances in the medium energy range, the self-shielding effect of these isotopes would be taken into account, even though absorption by zirconium isotopes is low. In a typical LWR cell, the self-shielding effect of the zirconium isotopes reaches $0.1\%\Delta k/k$, which is considerable. The number densities of the zirconium isotopes in Zircaloy are almost constant, and the shapes of Zircaloy are limited (e.g., cladding and channel box). Pre-tabulation of these isotopes for a particular background cross section might therefore be efficient in practical applications.

Structural material such as Fe, Ni, and Cr have many sharp resonances in the medium energy range. These materials are used for the reflector material in APWR/EPR, and the resonance shielding effect should be taken into account in the reflector calculations. Since the angular dependency of the neutron flux is very large in the reflector, particular care becomes necessary in the resonance calculation for the reflector material. A similar situation can be found in the blanket calculation for a fast breeder reactor. In this case, application of the subgroup method is effective (Yamamoto and Takeda 2000).

3.11.5 Verification and Validation of Resonance Calculation Model

Since many assumptions and approximations are used in resonance calculation models, the verification and validation of these models is very important. Since the verification and validation of a resonance calculation model can be carried out in a small geometry, utilization of a continuous-energy Monte Carlo code is very useful.

In comparison with the results achieved using Monte Carlo code, the effective cross section is usually considered as a benchmark quantity. We must remember, however, that the effective cross sections in lattice physics computations are just intermediate products. Our final objective is the evaluation of neutronics characteristics such as k -infinity and fission rate distribution. In

this sense, the microscopic reaction rates are rather more important than the effective cross sections. Indeed, even if the effective cross sections show excellent agreement in their Monte Carlo and the resonance calculation results, this does not necessarily mean that the resonance calculation model has given accurate reaction rates (Sugimura and Yamamoto 2007). When the effective cross section obtained by a resonance calculation model exactly reproduces the Monte Carlo result, they would still produce inconsistent reaction rates, due to the energy collapsing process that is inevitably included in a resonance calculation model (Rothenstein et al. 1988; Sugimura and Yamamoto 2007). This consideration should not be neglected in the validation and verification process.

3.12 Summary

In [Sect. 3](#), resonance calculation methods to estimate the effective cross section for successive pin cell and/or assembly calculations are described. Since a direct numerical solution to the neutron slowing down equation in a general heterogeneous geometry is still time consuming for practical applications, various calculation models, for example, the equivalence theory, the subgroup method, ultrafine group calculation in small geometry, the Tone method, the Stoker-Weiss (or SDDM) method, have been developed, and are applied in current lattice physics codes.

These models adopt various approximations that could be valid under certain conditions. One should therefore carefully consider the limitations of resonance calculation models and the potential prediction errors associated with the approximations. In this context, the current major resonance methods are still an approximate science, as opposed to the science of approximation, in which prediction errors associated with approximations are well controlled. Therefore, validation and verification of a resonance calculation model in a lattice physics code is quite important.

4 Energy Condensation Scheme

4.1 Introduction

Energy condensation refers to the generation of a unique flux spectrum in each material region of the problem that can be used to condense cross sections from the energy group structure of the cross section library (e.g., hundreds of energy groups) to a smaller energy group structure in preparation for the fine-mesh assembly transport solution (e.g., at most, a couple dozen energy groups). The scheme that will be discussed in this section was used in CASMO-4 and LANCER02 and consists of a series of one-dimensional pin-cell calculations followed by a two-dimensional coupling calculation. This section develops the theory behind the scheme and describes the numerics used to solve the system of equations.

Note that not all lattice physics codes use a condensation scheme. Those that do not use a condensation scheme perform the fine-mesh assembly transport calculation in the energy group structure of the cross section library. For the major fuel vendors who design dozens of reload cores each year requiring the need to design and analyze hundreds of different bundles on their way to finding the best fit for their cores, the need to perform millions of lattice calculations annually almost necessitates the need for a condensation scheme. For small fuel vendors or

utilities that may analyze a very limited number of reload core designs annually, the need for a condensation scheme in the lattice physics code is not so great.

It is important to keep in mind that, at this point in our lattice physics computational scheme, we are only concerned with generating a good condensation flux with which to collapse cross sections. We are allowed to sacrifice accuracy – especially spatial accuracy – for execution speed. However, the number of energy groups required for the fine-mesh assembly transport solution is directly proportional to the accuracy of the condensation spectra, so it is in our best interest to produce a reasonably accurate condensation flux.

4.2 Pin-Cell Spectral Calculations

Our condensation scheme begins with a series of one-dimensional pin-cell spectral calculations. The pin-cell spectral calculations are used to generate a flux spectrum in each region of each pin cell in the lattice, where the term *pin cell* implies a system consisting of a fuel rod plus the coolant in the immediate vicinity. It is also meant to include each of the inert rods present in the assembly, such as water rods and any absorber pins. The flux spectra in each region of the cell are generated in the energy group structure of the cross section library. During the pin-cell spectral calculations, each pin cell in the lattice is isolated from the influence of all other cells. Once all the pin-cell spectral calculations have been completed, we will perform a two-dimensional coupling calculation to modify the flux spectrum in each region of each cell to account for the influence of the surroundings.

For each pin cell, the square coolant region is approximated by a cylinder, preserving the volume of the outer coolant region and allowing for a purely one-dimensional analysis to be performed. White boundary conditions are applied to the outer edge of the cell to simulate perfect reflection in the true square geometry.

To help drive the flux across each pin cell, a buffer zone of average fuel material may be placed on the outside of the coolant zone. The pin-cell analysis is a fixed source calculation, where the neutron fission spectrum is used as the neutron source and may be placed in the buffer zone, exclusively, or in both the buffer zone and the fuel pellet. Either approach works equally well. The use of a fixed source helps to speed up convergence of the solution to the transport equation without adversely affecting the accuracy of the solution.

Because the pin-cell calculation is a purely one-dimensional problem, any solution technique to the transport equation is a viable choice. We can choose to solve the integrodifferential form of the transport equation using discrete ordinates, or we can choose to solve the integral form of the transport equation using the method of collision probabilities. Our choice is to use the method of collision probabilities because of its superior performance on physically small problems containing only a few mesh. ➤ [Sections 4.2.1](#) and ➤ [4.2.2](#) will be devoted to the method of collision probabilities as applied to the pin-cell spectral calculations in a lattice physics code. The contents of this section have been taken from lectures given to postgraduate students in a course on computational reactor analysis at The Pennsylvania State University in 1990 (Knott 1990). Citations are absent from the bulk of the text because the material has been derived from first principles. The interested reader is directed to Lewis and Miller (1984) and Stamm’ler and Abbate (1983), from which much of the material have been culled. For an excellent discussion on the method of collision probabilities, the interested reader is directed to the seven publications that comprise Ingvar Carlvik’s Ph.D. thesis (Carlvik 1967a, b, c, d, 1965,

1966a, b; Carlvik and Pershagen 1959) along with one additional publication that did not appear in his thesis (Carlvik 1966c).

4.2.1 General Theory

The spectral calculation determines the neutron flux distribution across the pin cell by solving the integral form of the transport equation using the method of collision probabilities. The integral equation is derived from the integrodifferential form of the Boltzmann transport equation

$$\frac{1}{|\nu|} \frac{\partial \Phi(\vec{r}, E, \hat{\Omega}, t)}{\partial t} = Q(\vec{r}, E, \hat{\Omega}, t) - \Omega \cdot \nabla \Phi(\vec{r}, E, \hat{\Omega}, t) - \Sigma_t(\vec{r}, E) \Phi(\vec{r}, E, \hat{\Omega}, t) \quad (289)$$

where the source term, $Q(\vec{r}, E, \hat{\Omega}, t)$, is the total source of neutrons at location \vec{r} , with energy E , traveling in direction $\hat{\Omega}$, at time t , and is given by

$$Q(\vec{r}, E, \hat{\Omega}, t) = \iint \Sigma_s(\vec{r}, E' \rightarrow E, \hat{\Omega}' \rightarrow \hat{\Omega}) \Phi(\vec{r}, E', \hat{\Omega}', t) dE' d\hat{\Omega}' + S(\vec{r}, E, \hat{\Omega}, t) \quad (290)$$

In the above expressions, $\Phi(\vec{r}, E, \hat{\Omega}, t)$ is the angular flux, $\Sigma_t(\vec{r}, E)$ is the total macroscopic cross section, and $\Sigma_s(\vec{r}, E' \rightarrow E, \hat{\Omega}' \rightarrow \hat{\Omega})$ is the macroscopic scattering cross section. $S(\vec{r}, E, \hat{\Omega}, t)$ is the source of neutrons at location \vec{r} , either internal (i.e., due to fission) or external.

In lattice physics calculations, only time-independent problems are considered and the steady state Boltzmann equation to be solved is expressed as

$$\Omega \cdot \nabla \Phi(\vec{r}, E, \hat{\Omega}) + \Sigma_t(\vec{r}, E) \Phi(\vec{r}, E, \hat{\Omega}) = Q(\vec{r}, E, \hat{\Omega}) \quad (291)$$

[Equation \(291\)](#) describes neutron motion as viewed from a fixed reference point, giving rise to the partial derivative in the streaming term. If neutron motion were viewed from the neutron's frame of reference, the partial derivative in the streaming term reduces to a total derivative along the path of motion of the neutron

$$\frac{d\Phi(\vec{r}, E, \hat{\Omega})}{ds} + \Sigma_t(\vec{r}, E) \Phi(\vec{r}, E, \hat{\Omega}) = Q(\vec{r}, E, \hat{\Omega}) \quad (292)$$

where s is the track along which the neutron is traveling across the region at location \vec{r} .

[Equation \(292\)](#) may be solved to obtain an expression for the angular flux. We first solve the homogeneous portion of the equation, where the source term, $Q(\vec{r}, E, \hat{\Omega})$, is set to zero. The homogeneous solution is

$$\Phi^h(\vec{r}, E, \hat{\Omega}) = C e^{-\int_0^s \Sigma_t(s', E) ds'} \quad (293)$$

where s is measured along the streaming path from the differential volume element dV' to the differential volume element of interest, dV , as illustrated in [Fig. 33](#).

Next Lagrange's method of varying the constant is used, where the integration constant in [\(293\)](#), C , is assumed to be a function of the streaming length, $C(s)$. This solution is back-substituted into [\(292\)](#) and the entire differential equation is integrated along s from $-\infty$

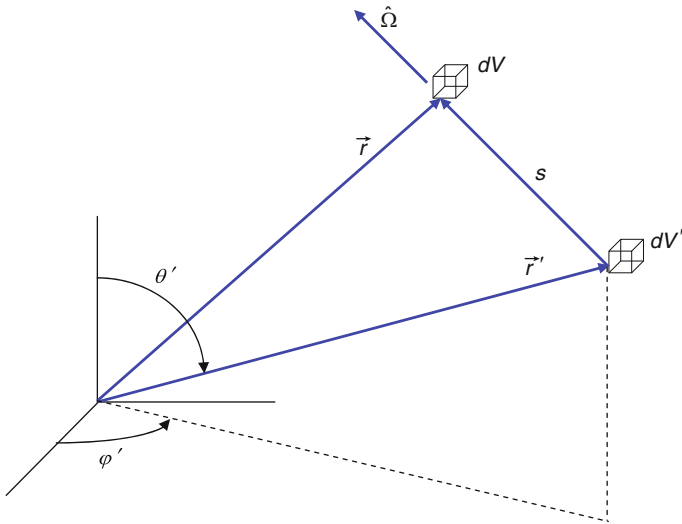


Figure 33
Coordinate system for the integral transport equation

to the differential volume of interest, dV . The final expression for the integrating constant is given by

$$\int_{-\infty}^s dC(s') ds' = \int_{-\infty}^s Q(s', E, \hat{\Omega}) \cdot e^{\int_0^{s'} \Sigma_t(s'', E) ds''} ds' \quad (294)$$

$$C(s) = C(-\infty) + \int_{-\infty}^s Q(s', E, \hat{\Omega}) \cdot e^{\int_0^{s'} \Sigma_t(s'', E) ds''} ds' \quad (295)$$

Back-substituting (295) into (293) gives the general form of the integral equation for the angular flux at location \vec{r} ,

$$\Phi(\vec{r}, E, \hat{\Omega}) = \int_{-\infty}^s Q(s', E, \hat{\Omega}) \cdot e^{-\int_{s'}^s \Sigma_t(s'', E) ds''} ds' \quad (296)$$

where the $C(-\infty)$ term in (295) has been taken to be zero since it would take a neutron, infinitely far away, an infinite length of time to travel along the streaming path in order to reach the volume element located at \vec{r} and, infinitely long ago, there were no neutrons.

To visualize the integral equation, imagine standing at a point in space. If you wished to calculate the neutron flux at that point, you would look around yourself in all directions and count up all the neutrons that are streaming toward you along lines that originate from the location of each neutron's most recent collision (i.e., birth). The angular fluxes would be the number of neutrons streaming toward you along each specific line. Each time you moved your head to look in a different direction, you would be viewing a different angular flux. To calculate a scalar flux, you would simply count up all neutrons moving toward you from all directions.

The energy dependence in (296) is represented by neutrons that are moving at different speeds along each of those lines. As we move to Sect. 5, we will refer to these lines as *characteristics* and we will view our system from the neutron's point of view as it moves along the line, instead of viewing our system while standing still and watching the neutron move toward us.

If we assume that all self-scattering and total cross sections in the library have been transport corrected, then scattering can be modeled, mathematically, in the same way as an isotropic source is modeled. In addition, the only source of neutrons are those due to fission, which is inherently isotropic, and the angular source term, $Q(\vec{r}, E, \hat{\Omega})$, may be expressed in terms of the total source term, $q(\vec{r}, E)$, as

$$Q(\vec{r}, E, \hat{\Omega}) = \frac{q(\vec{r}, E)}{4\pi} = \int \frac{\Sigma_s(\vec{r}, E' \rightarrow E)}{4\pi} \int_{4\pi} \Phi(\vec{r}, E', \hat{\Omega}') d\hat{\Omega}' dE' + \frac{s(\vec{r}, E)}{4\pi} \quad (297)$$

where the fixed scalar source term, $s(\vec{r}, E)$, can be due to fission or may be a constant external source. The angular source due to fission has the following appearance:

$$S(\vec{r}, E, \hat{\Omega}) = \frac{s(\vec{r}, E)}{4\pi} = \frac{\chi(E)}{k^\infty} \int \frac{v\Sigma_f(\vec{r}, E')}{4\pi} \int_{4\pi} \Phi(\vec{r}, E', \hat{\Omega}') d\hat{\Omega}' dE' \quad (298)$$

Here, k^∞ is the infinite multiplication factor, which assumes no leakage of neutrons from the system, and is calculated as

$$k^\infty = \frac{\iint v\Sigma_f(\vec{r}, E) \phi(\vec{r}, E) \cdot d^3\vec{r} \cdot dE}{\iint \Sigma_a(\vec{r}, E) \phi(\vec{r}, E) \cdot d^3\vec{r} \cdot dE} \quad (299)$$

and the scalar flux at location \vec{r} in (299) is the integration of the angular flux over all directions,

$$\phi(\vec{r}, E) = \int_{4\pi} \Phi(\vec{r}, E, \hat{\Omega}) d\hat{\Omega} \quad (300)$$

Using (300), the source term in (297) may be expressed in terms of the scalar flux alone, as

$$\begin{aligned} Q(\vec{r}, E, \hat{\Omega}) &= \frac{q(\vec{r}, E)}{4\pi} \\ &= \frac{1}{4\pi} \left[\int \Sigma_s(\vec{r}, E' \rightarrow E) \phi(\vec{r}, E') dE' + \frac{\chi(E)}{k^\infty} \int v\Sigma_f(\vec{r}, E') \phi(\vec{r}, E') dE' \right] \end{aligned} \quad (301)$$

Substituting (301) into (296) yields

$$\Phi(\vec{r}, E, \hat{\Omega}) = \int_{-\infty}^s \frac{q(s', E)}{4\pi} \cdot e^{-\int_{s'}^s \Sigma_t(s'', E) ds''} ds' \quad (302)$$

Equation (302) is the integral equation for the angular flux, where all sources are considered to be isotropic (using transport-corrected cross sections to account for anisotropic effects). The

integral equation may be formulated directly for the scalar flux by using (300) and integrating (302) over all angles. Hence,

$$\phi(\vec{r}, E) = \int_{4\pi} \Phi(\vec{r}, E, \hat{\Omega}) \cdot d\hat{\Omega} = \int_{4\pi} \int_{-\infty}^s \frac{q(s', E)}{4\pi} \cdot e^{-\int_{s'}^s \Sigma_t(s'', E) ds''} ds' \cdot d\hat{\Omega} \quad (303)$$

Since the path of integration over s' stretches to infinity in all directions, all space is included in the integral $ds' d\hat{\Omega}$. As such, the line integral in (303) may be converted to a volume integral by the following change of variables:

$$\vec{r}' = \vec{r} - s' \cdot \hat{\Omega} \quad (304)$$

Rearranging (304)

$$s' = |\vec{r} - \vec{r}'| \quad (305)$$

Multiplying and dividing the integrand in (303) by s'^2 we get

$$\phi(\vec{r}, E) = \int_{4\pi} d\hat{\Omega} \int_0^\infty s'^2 \frac{q(\vec{r}', E) e^{-\tau(\vec{r}' \rightarrow \vec{r}, E)}}{|\vec{r} - \vec{r}'|^2} ds' \quad (306)$$

where $\tau(\vec{r} \rightarrow \vec{r}', E)$ is the distance between points \vec{r}' and \vec{r} in mean free paths (i.e., the optical distance), represented by

$$\tau(\vec{r}' \rightarrow \vec{r}, E) = \int_{r'}^r \Sigma_{tr}(s', E) ds' \quad (307)$$

If we now take a spherical coordinate system with \vec{r} at the origin, as illustrated in Fig. 34, the incremental volume centered about \vec{r}' is

$$dV' = 4\pi \cdot d\hat{\Omega} \cdot ds' \cdot s'^2 \quad (308)$$

where we have made use of the definition for the incremental solid angle $d\hat{\Omega} = d\varphi \cdot \sin\theta \cdot d\theta/4\pi$. Combining (308) with (306), we obtain our new expression of the integral equation for the scalar flux with isotropic sources,

$$\phi(\vec{r}, E) = \int q(\vec{r}', E) \cdot \frac{e^{-\tau(\vec{r}' \rightarrow \vec{r}, E)}}{4\pi |\vec{r} - \vec{r}'|^2} \cdot dV' \quad (309)$$

The exponential term in (309) represents the non-collision probability along a streaming path, which may intersect regions of different material properties (i.e., cross sections). We may write (309) in a more compact form as

$$\phi(\vec{r}, E) = \int_{-\infty}^0 dV' \cdot T(\vec{r}' \rightarrow \vec{r}, E) \cdot q(\vec{r}', E) \quad (310)$$

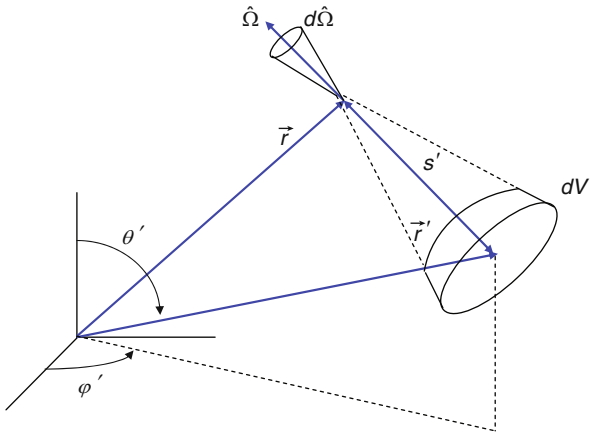


Figure 34
Spherical coordinate system centered at \vec{r}

where $T(\vec{r}' \rightarrow \vec{r}, E)$ is referred to as the transport matrix between \vec{r}' and \vec{r} for neutrons at energy E ,

$$T(\vec{r}' \rightarrow \vec{r}, E) = \frac{1}{4\pi |\vec{r} - \vec{r}'|^2} \cdot \exp \left\{ - \int_{\vec{r}'}^{\vec{r}} \Sigma_{tr}(s, E) ds \right\} \quad (311)$$

To convert (310) into a form that is amenable for computations, we split the problem geometry into regions where the flux is considered to be flat and, therefore, the source distribution will be constant across the region. The discretized form of the integral equation becomes

$$\phi_i^g = \sum_{i'} T_{i' \rightarrow i}^g \cdot q_{i'}^g \cdot V_{i'} \quad (312)$$

where i is the mesh in which the flux is being calculated and the summation is over all mesh in the problem, including the mesh i itself; g is the energy group. The solution to the integral equation reduces to determining the transport matrix for the geometry of the system.

4.2.2 The Method of Collision Probabilities in Slab Geometry

In all solutions to the transport equation, we must solve for the motion of neutrons in all three dimensions. This is true regardless of the dimensionality of the problem. The dimensionality of the problem merely reflects the number of axes along which material boundaries exist. For example, a one-dimensional problem contains material boundaries along one axis and is infinite along the other two axes. Similarly, a two-dimensional problem contains material boundaries along two axes and is infinite along the third axis. Regardless of the dimensionality of the problem, we must always model neutron motion in all three dimensions. In most transport solution techniques, such as the method of characteristics or discrete ordinates, we must model neutron motion explicitly in all directions through the use of a quadrature set. In the method of collision

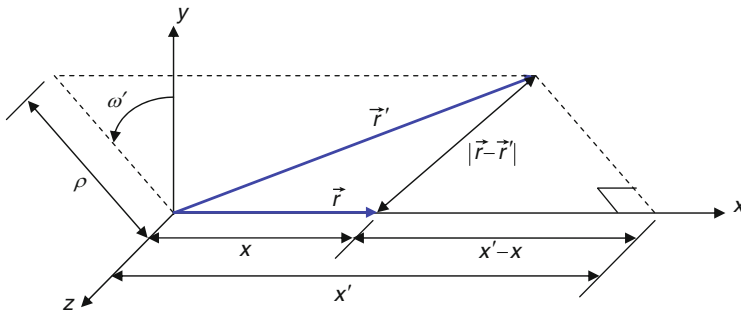


Figure 35

Cylindrical coordinate system for slab geometry

probabilities with isotropic sources, though, it is possible to integrate over all polar directions of motion analytically. This removes a great deal of the computational burden. Once we do this, we need only compute neutron motion numerically in the plane of the problem.

We begin our derivation for the method of collision probabilities in slab geometry. We will then move into cylindrical geometry, which is our desired geometry for the pin-cell calculation. In slab geometry, to perform the polar integration, we begin by expressing the volume element in cylindrical coordinates,

$$dV' = \rho \cdot d\rho \cdot d\omega' \cdot dx' \quad (313)$$

The coordinates to (313) are illustrated in Fig. 35. Using the cylindrical coordinate system, the integral equation can be expressed as

$$\phi(x, E) = \int_{-\infty}^{\infty} dx' \cdot q(x', E) \int_0^{\infty} \rho \cdot d\rho \int_0^{2\pi} \frac{e^{-\tau(\vec{r}' \rightarrow \vec{r}, E)}}{4\pi |\vec{r}' - \vec{r}|^2} \cdot d\omega' \quad (314)$$

where $\tau(\vec{r}' \rightarrow \vec{r}, E)$ now represents the distance, in mean free paths, between \vec{r}' and \vec{r} at some energy, E .

Integrating over $d\omega'$, we get 2π , and (314) becomes

$$\phi(x, E) = 2\pi \int_{-\infty}^{\infty} dx' \cdot q(x', E) \int_0^{\infty} \rho \cdot d\rho \cdot \frac{e^{-\tau(\vec{r}' \rightarrow \vec{r}, E)}}{4\pi |\vec{r}' - \vec{r}|^2} \quad (315)$$

Since the cross sections change only in the x -direction of motion, the optical path between \vec{r}' and \vec{r} , $\tau(\vec{r}' \rightarrow \vec{r}, E)$, may be expressed in terms of the projected length onto the x -axis. Here, we let γ be the projected ratio,

$$\gamma = \frac{|\vec{r}' - \vec{r}|}{|x' - x|} = \frac{\text{true}}{\text{projected}} \quad (316)$$

Then, $\tau(\vec{r}' \rightarrow \vec{r}) = \gamma \cdot \tau(x' - x)$. Using the right triangle illustrated in Fig. 35

$$|\vec{r}' - \vec{r}|^2 = \rho^2 + |x' - x|^2 \quad (317)$$

and, therefore, we can rearrange (317) to get an expression for $\rho \cdot d\rho$,

$$\begin{aligned}\rho^2 &= |\vec{r}' - \vec{r}|^2 - |x' - x|^2 \\ &= \gamma^2 \cdot |x' - x|^2 - |x' - x|^2 \\ &= (\gamma^2 - 1) \cdot |x' - x|^2 \\ \rho &= \sqrt{(\gamma^2 - 1)} \cdot |x' - x| \\ d\rho &= \frac{1}{2\sqrt{(\gamma^2 - 1)}} \cdot 2\gamma \cdot d\gamma \cdot |x' - x| \\ &= \frac{1}{\sqrt{(\gamma^2 - 1)}} \cdot \gamma \cdot d\gamma \cdot |x' - x|\end{aligned}\tag{318}$$

Now, we may express the integral in ρ in terms of the projected ratio, γ ,

$$\rho \cdot d\rho = \gamma \cdot d\gamma \cdot |x' - x|^2\tag{319}$$

Substituting (319) into (315) we get the equation for the flux expressed in terms of the projected ratio

$$\begin{aligned}\phi(x, E) &= 2\pi \int_{-\infty}^{\infty} dx' \cdot q(x', E) \int_0^{\infty} \rho \cdot d\rho \cdot \frac{e^{-\tau(\vec{r}' \rightarrow \vec{r}, E)}}{4\pi |\vec{r}' - \vec{r}|^2} \\ &= \int_{-\infty}^{\infty} dx' \cdot q(x', E) \int_1^{\infty} \gamma \cdot d\gamma \cdot |x' - x|^2 \cdot \frac{e^{-\gamma\tau(x' \rightarrow x, E)}}{2\gamma^2 \cdot |x' - x|^2} \\ &= \int_{-\infty}^{\infty} dx' \cdot q(x', E) \int_1^{\infty} \frac{d\gamma}{2\gamma} \cdot e^{-\gamma\tau(x' \rightarrow x, E)}\end{aligned}\tag{320}$$

Although the above transformation may seem pointless, it actually simplifies things because the integral over γ may be expressed in terms of the exponential integral, $E_n(\tau)$,

$$E_n(\tau) = \int_1^{\infty} \frac{dy}{y^n} e^{-y\tau}\tag{321}$$

Our integral equation for the scalar flux with isotropic sources now becomes much more compact,

$$\phi(x, E) = \int_{-\infty}^{\infty} dx' \cdot q(x', E) \cdot \frac{1}{2} E_1 \tau [(x' \rightarrow x, E)]\tag{322}$$

Numerical recipes for exponential integrals are widely available in the literature. The interested reader is directed to the Appendix contained in citation (Stamm'ler and Abbate 1983).

For our slab, we divide the interval between the left boundary and the right boundary of the slab into I number of mesh, where the scalar flux is constant (flat) across each mesh. The width of mesh i is $\Delta_i = x_i - x_{i-1}$.

The scalar flux in mesh i is calculated as

$$\phi_i^g = \frac{1}{\Delta_i} \int_{x_{i-1}}^{x_i} dx \cdot \phi(x, E) = \frac{1}{\Delta_i} \int_{x_{i-1}}^{x_i} dx \int_1^\infty dx' \cdot \frac{1}{2} E_1 [\tau(x' \rightarrow x, E)] \cdot q(x', E) \quad (323)$$

where the flat flux approximation leads to the following expression for the source:

$$q(x, E) = q_i^g = \sum_{g'} \Sigma_{s,i}^{g' \rightarrow g} \phi_i^{g'} + \frac{\chi_\infty^g}{k^\infty} \sum_{g'} v \Sigma_{f,i}^{g'} \phi_i^{g'} \quad (324)$$

Multiplying (323) through by $\Sigma_{tr,i}^g \cdot \Delta_i$, we get

$$\Sigma_{tr,i}^g \cdot \Delta_i \cdot \phi_i^g = \sum_{i'=1}^I P_{i' \rightarrow i}^g \cdot \Delta_{i'} \cdot q_{i'}^g \quad (325)$$

The left-hand side of (325) represents the total number of interactions in mesh i . On the right-hand side of the equation, $\Delta_{i'} \cdot q_{i'}^g$ represents the total number of neutrons born in mesh i' , and $P_{i' \rightarrow i}^g$ represents the probability that a neutron travels undisturbed from mesh i' to mesh i , where it suffers its first collision. In this context, $P_{i' \rightarrow i}^g$ is a true probability in the sense that $\sum_i P_{i' \rightarrow i}^g = 1$. That is, the neutron must eventually interact with something, somewhere.

Comparing (323) against (325), the collision probability can be expressed as

$$P_{i' \rightarrow i}^g = \frac{\Sigma_{tr,i'}^g}{\Delta_{i'}} \int_{x_{i-1}}^{x_i} dx \int_{x_{i'-1}}^{x_{i'}} dx' \cdot \frac{1}{2} E_1 [\tau(x' \rightarrow x, E)] \quad (326)$$

Integrating, we get the following expression for the collision probability between mesh i' and i :

$$P_{i' \rightarrow i}^g = \frac{1}{2 \Sigma_{tr,i'}^g \cdot \Delta_{i'}} \begin{bmatrix} E_3(\tau_{i' \rightarrow i}^g) \\ -E_3(\tau_{i' \rightarrow i}^g + \Sigma_{tr,i}^g \cdot \Delta_i) \\ -E_3(\tau_{i' \rightarrow i}^g + \Sigma_{tr,i'}^g \cdot \Delta_{i'}) \\ +E_3(\tau_{i' \rightarrow i}^g + \Sigma_{tr,i}^g \cdot \Delta_i + \Sigma_{tr,i'}^g \cdot \Delta_{i'}) \end{bmatrix} \quad (327)$$

and the collision probability within mesh i ,

$$P_{i \rightarrow i}^g = 1 - \frac{1}{2 \Sigma_{tr,i}^g \cdot \Delta_i} [1 - 2E_3(\Sigma_{tr,i}^g \cdot \Delta_i)] \quad (328)$$

where $\tau_{i' \rightarrow i}^g$ is the optical path between mesh i' and i along the x -axis, in energy group g . Note that the optical path does not rely on the direction of motion of the neutron. In other words, $\tau_{i' \rightarrow i}^g = \tau_{i \rightarrow i'}^g$, which is the *optical reciprocity relationship*. In arriving at our final expression in (327) and (328), we have made use of the relationship $E_n(\tau) = \int_\tau^\infty E_{n-1}(x) dx$.

For a slab with vacuum boundary conditions, a neutron can only make it from mesh i' to mesh i if it starts off streaming in the direction of mesh i . If it streams in the opposite direction, it will have a collision or leak through the vacuum boundary without ever reaching mesh i . The

collision probabilities represented by (327) are referred to as *black body* CP's since, should a neutron reach the system boundary, it is lost forever. In this way, the boundary acts as a perfect absorber (i.e., black).

For reflective boundary conditions, all neutrons have some chance of reaching mesh i from mesh i' . To account for this, we can take one of two approaches to correct our black body CP's. We may extend the calculation of $P_{i' \rightarrow i}^g$ to include the reflection off each surface to the slab. Usually, the calculation of collision probabilities will proceed until $\tau_{i' \rightarrow i}^g$ is beyond a preset value, typically between 6 and 10 mean free paths. A neutron that is born 6 mean free paths from mesh i has an e^{-6} chance of reaching the mesh without suffering a collision. This probability is only 1 in 400, which can usually be ignored without impacting the results. The trouble with this approach is the sheer amount of bookkeeping required, especially in the fast energy groups where the mean free paths can be very large. Neutrons may bounce from boundary to boundary many times before reaching the preset limit on mean free path.

An alternative approach would be to calculate the total current on both boundaries caused by the flux in each mesh. Once the surface currents are known, the contribution to the flux in each mesh caused by the current on each surface can be calculated. To do this, we need to calculate the collision probability from mesh i to surface j , which ends up appearing as

$$\begin{aligned} P_{i \rightarrow j}^g &= \int_{S_j} dS \int_{A_i} dA \cdot \hat{n} \cdot |\vec{r} - \vec{r}'| \frac{E_2[\tau(\vec{r} \rightarrow \vec{r}')] }{|\vec{r} - \vec{r}'|^2} \\ &= \left[E_3(\tau_{i \rightarrow j}^g) - E_3(\tau_{i \rightarrow j}^g + \Sigma_{tr,i}^g \Delta_i) \right] \end{aligned} \quad (329)$$

Then the current on surface j is the sum of all neutrons arriving on the surface from all mesh in the problem and also from the other surface to the slab. The contribution from each mesh can be expressed as

$$J_j^g = \sum_{i=1}^I P_{i \rightarrow j}^g \cdot q_i^g \cdot \Delta_i \quad (330)$$

The contribution from the other surface of the slab will be addressed shortly.

The τ values in (327) and (329) are measured as the shortest distance between two mesh, or between a mesh and a surface. For mesh that share a common surface (i.e., mesh that neighbor each other), $\tau_{i' \rightarrow i}^g = 0$ and $E_3(0) = 1/2$. Similarly, for mesh that neighbor a slab boundary, $\tau_{i \rightarrow j}^g = 0$.

To represent the boundary condition ideally, we would need to know the angular distribution of the flux as it reaches the surface. Since we are solving directly for the scalar flux, we do not know the angular flux distribution. Therefore, we must make some sort of assumption. For illustrative purposes, we will say that the angular flux is distributed isotropically as it reaches the surface. Then, for example, the current along the west surface of the slab is given by

$$J_{\text{west}}^g = \int_{\hat{\Omega} \cdot \hat{n} < 0} d\hat{\Omega} |\hat{\Omega} \cdot \hat{n}| \Phi_{\text{west}}^g(\hat{\Omega}) = \int_{\hat{\Omega} \cdot \hat{n} < 0} d\hat{\Omega} |\hat{\Omega} \cdot \hat{n}| \frac{\phi_i^g}{4\pi} = \frac{1}{4} \phi_{\text{west}}^g \quad (331)$$

where we are only concerned with neutrons traveling to the west. Rearranging (331) we get an expression for the flux along the west surface of the slab,

$$\phi_{\text{west}}^g = 4J_{\text{west}}^g \quad (332)$$

The expression for the scalar flux can now include the contribution from the surface currents (assuming an isotropic angular flux distribution)

$$\phi_i^g = \sum_{i'=1}^I T_{i' \rightarrow i}^g \cdot \Delta_{i'} \cdot q_{i'}^g + 4 \sum_{j=1}^J T_{j \rightarrow i}^g \cdot J_j^g \quad (333)$$

where the transport matrices are given by

$$T_{i' \rightarrow i}^g = \frac{1}{\Sigma_{tr,i}^g \cdot \Delta_i} P_{i' \rightarrow i}^g$$

$$T_{j \rightarrow i}^g = \frac{1}{2\Sigma_{tr,i}^g \cdot \Delta_i} P_{j \rightarrow i}^g$$

and the currents are calculated from

$$J_j^g = \sum_{i=1}^I T_{i \rightarrow j}^g \cdot q_i^g \cdot \Delta_i \quad (334)$$

Note that the transport matrices are insensitive to the direction of motion of the neutron,

$$T_{i' \rightarrow i}^g = T_{i \rightarrow i'}^g \quad (335)$$

(335) is the optical reciprocity relationship, where the transport matrices are diagonally symmetric and only the diagonal elements and upper triangle elements need to be calculated; the lower triangle elements of the matrix can be filled in with the values from the upper triangle.

4.2.3 The Method of Collision Probabilities in Cylindrical Geometry

In slab geometry, we are able to represent neutron streaming in all directions through the slab by using the exponential integral in the streaming term during the calculation of collision probabilities. This is extremely efficient because we now need only know the width of each mesh in order to determine all the first flight collision probabilities. We are able to express the collision probability this way because the neutron's angle of motion with respect to the slab normal is constant. As a result, the track length of the neutron through the slab is the same regardless of the point at which the neutron enters the slab. This is illustrated schematically in ➤ Fig. 36, where the angle of motion with respect to the x -axis is referred to as ω .

We cannot do the same thing in cylindrical geometry because the face of the cylinder is not flat, as the face of the slab is. In cylindrical geometry, we can only perform the integration analytically over all polar directions. To perform the integration over azimuthal directions of motion, we must use streaming tracks.

For cylindrical geometry, infinite in the z -direction, the integration over the polar angle, θ , is equivalent to determining the flux at a point caused by a line source. If the line source is isotropic, and the point at which the flux is to be determined is a distance t from the line source, then the flux may be calculated by integrating along the line source

$$\phi(P) = \int_{-\infty}^{\infty} \frac{e^{-\Sigma R}}{4\pi R^2} dz = \int_{-\infty}^{\infty} \frac{e^{-\rho}}{4\pi R^2} dz \quad (336)$$

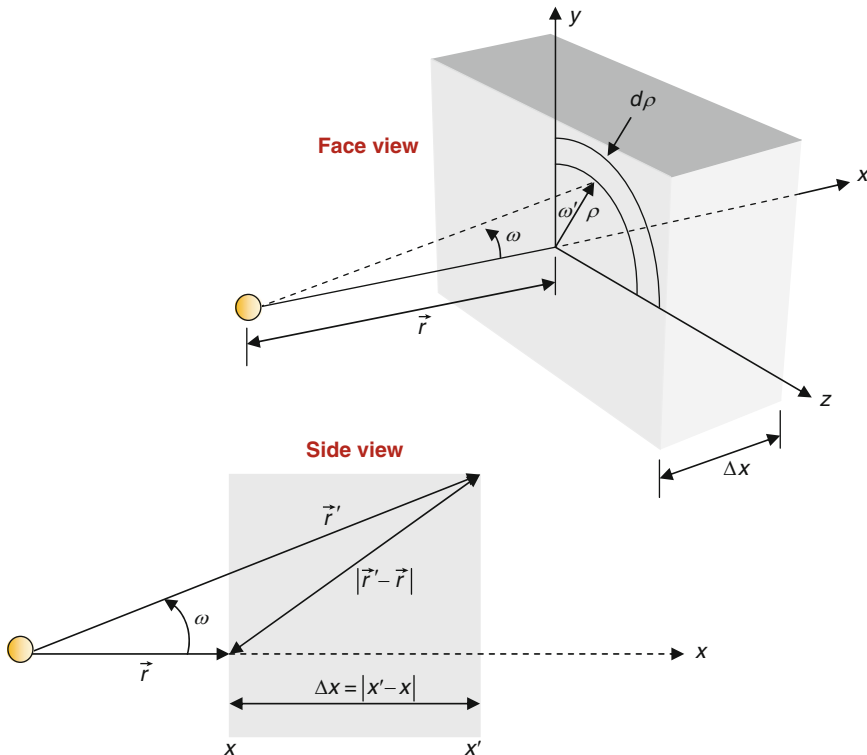


Figure 36
A neutron streaming through a slab

where we have defined $\rho = \Sigma_{tr}R$ to be the optical distance from a point on the line source to the point at which the flux is to be calculated. And the length of R can be expressed as $R = t/\cos\theta$, where t is the closest distance of point P to the line source. The coordinates for this system are illustrated in [Figs. 37](#) and [38](#).

If we define $\tau = \Sigma_{tr}t$, then $\rho = \tau/\cos\theta$, where τ is in mean free paths. Then (336) becomes

$$\phi(P) = \int_{-\infty}^{\infty} \frac{e^{-(\tau/\cos\theta)}}{4\pi(t^2/\cos^2\theta)} dz = \int_0^{\infty} \frac{e^{-(\tau/\cos\theta)}}{2\pi(t^2/\cos^2\theta)} dz \quad (337)$$

where we have made use of the symmetry of the system about the plane of the problem.

Using [Fig. 38](#), we make the following change of variables:

$$\begin{aligned} dz &= \frac{R \cdot d\theta}{\cos\theta} \\ &= \frac{t \cdot d\theta}{\cos^2\theta} \end{aligned} \quad (338)$$

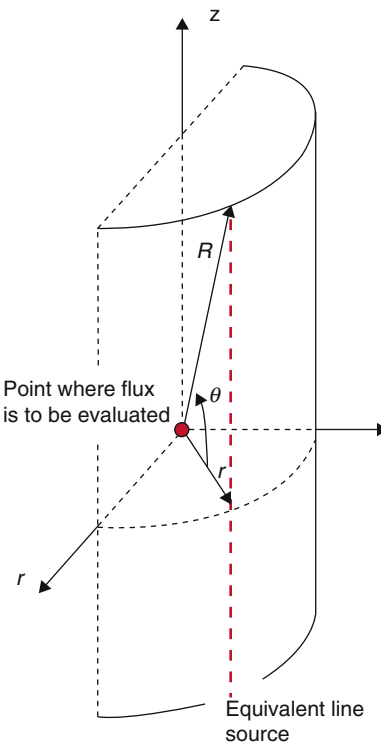


Figure 37
Coordinate system for calculating the flux at a point

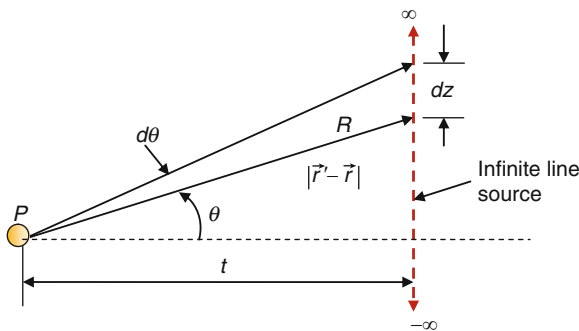


Figure 38
Variables in cylindrical geometry

Substituting (338) into (337) we get

$$\begin{aligned}\phi(P) &= \int_0^{\pi/2} \frac{e^{-(\tau/\cos\theta)}}{2\pi t} d\theta \\ &= \frac{Ki_1(\tau)}{2\pi t}\end{aligned}\quad (339)$$

where $Ki_1(\tau)$ is the first order Bickley–Naylor function, defined as

$$Ki_n(\tau) = \int_0^{\pi/2} \exp\left\{-\frac{\tau}{\cos\theta}\right\} \cos^{n-1}\theta \cdot d\theta \quad (340)$$

The probability of a neutron actually traveling the projected distance, $\tau = \Sigma_{tr}t$, is given by

$$p(\tau) = \int_{\tau}^{\infty} Ki_1(\tau') \cdot d\tau' = Ki_2(\tau) \quad (341)$$

In cylindrical geometry, the Bickley–Naylor functions serve the same purpose as the exponential integral serves in slab geometry. The main difference is that the exponential integral accounts for motion in all directions, whereas the Bickley–Naylor function accounts for motion only out of the plane of the problem. However, by using the Bickley–Naylor functions, we need now only account for neutron streaming in the plane of the problem. This is much more efficient than having to numerically account for streaming in three dimensions and helps to simplify our analysis. This is the great benefit of using the method of collision probabilities over other transport solution techniques. As with the exponential functions, numerical recipes for Bickley–Naylor functions are contained in the Appendix in citation (Stamm’ler and Abbate 1983).

The coordinate system for the azimuthal and spatial integration is shown in Fig. 39, where φ represents the azimuthal angle, and h represents the spatial dimension. For this particular geometry, the azimuthal integration can be rolled into the spatial integration. Also, due to symmetry in the azimuthal plane, we need only model 1/4 of the cylinder – applying perfect reflection along the x - and y -axes and a vacuum boundary condition along the outer edge of the cylinder. The resulting coordinate system is shown in Fig. 40, where each track drawn at a different h value represents a different φ angle. Collision probabilities will be integrated along these tracks in order to calculate the corresponding transport matrix.

Going through the same exercise for the scalar flux as was followed for slab geometry, we come out with the following expressions for the collision probabilities in cylindrical geometry:

$$\begin{aligned}P_{i' \rightarrow i}^g &= Ki_3(\tau_{i' \rightarrow i}^g) - Ki_3(\tau_{i' \rightarrow i}^g + \tau_{i' \rightarrow i'}^g) - Ki_3(\tau_{i' \rightarrow i}^g + \tau_{i' \rightarrow i'}^g) \\ &\quad + Ki_3(\tau_{i' \rightarrow i}^g + \tau_{i \rightarrow i}^g + \tau_{i' \rightarrow i'}^g) \\ P_{i \rightarrow i}^g &= \Sigma_{tr,i}^g V_i - \left[\frac{\pi}{4} - Ki_3(\tau_{i \rightarrow i}^g) \right] \\ P_{s \rightarrow i}^g &= Ki_3(\tau_{s \rightarrow i}^g) - Ki_3(\tau_{s \rightarrow i}^g + \tau_{i \rightarrow i}^g) \\ P_{s' \rightarrow s}^g &= Ki_3(\tau_{s' \rightarrow s}^g)\end{aligned}\quad (342)$$

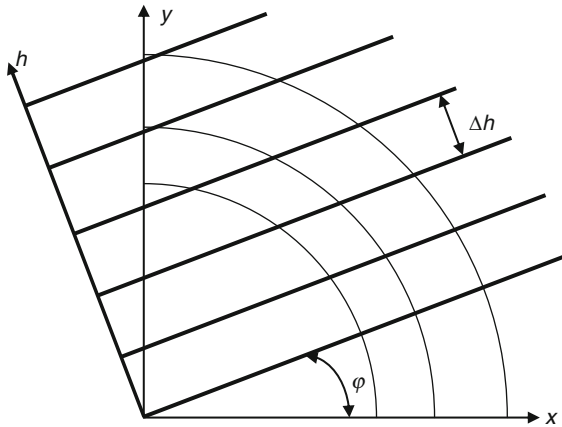


Figure 39
Spatial and angular variables for cylindrical geometry

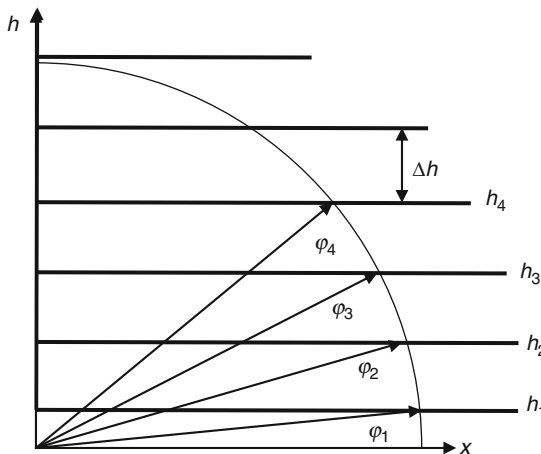


Figure 40
Angular variable combined with spatial variable

where i and i' represent mesh in the problem; and s and s' represent surfaces in the problem. The elements of the transport matrix are given by

$$\begin{aligned}
 T_{i' \rightarrow i}^g &= \frac{1}{\Sigma_{tr,i}^g V_i \Sigma_{tr,i'}^g V_{i'}} \int P_{i' \rightarrow i}^g(h) \cdot dh = \frac{1}{\Sigma_{tr,i}^g V_i \Sigma_{tr,i'}^g V_{i'}} \sum_m P_{i' \rightarrow i}^g(h_m) \cdot \Delta h \\
 T_{i \rightarrow i}^g &= \frac{1}{(\Sigma_{tr,i}^g V_i)^2} \int P_{i \rightarrow i}^g(h) \cdot dh = \frac{1}{(\Sigma_{tr,i}^g V_i)^2} \sum_m P_{i \rightarrow i}^g(h_m) \cdot \Delta h \\
 T_{s' \rightarrow i}^g &= \frac{1}{\Sigma_{tr,i}^g V_i A_{s'}} \int P_{s' \rightarrow i}^g(h) \cdot dh = \frac{1}{\Sigma_{tr,i}^g V_i A_{s'}} \sum_m P_{s' \rightarrow i}^g(h_m) \cdot \Delta h \\
 T_{s' \rightarrow s}^g &= \frac{1}{A_s A_{s'}} \int P_{s' \rightarrow s}^g(h) \cdot dh = \frac{1}{A_s A_{s'}} \sum_m P_{s' \rightarrow s}^g(h_m) \cdot \Delta h
 \end{aligned} \tag{343}$$

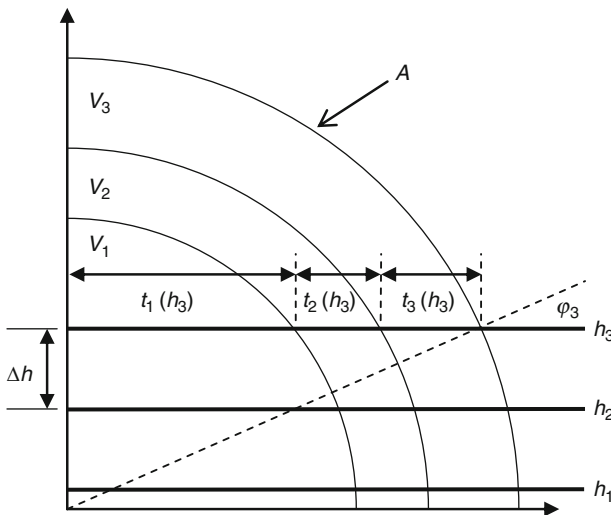


Figure 41
Integration variables associated with annular geometry

where V_i represents the volume of a mesh, which in our one-dimensional cylinder is actually the area of the mesh; and A_s represents the surface area of each outer surface of the cylinder, which in our one-dimensional cylinder is actually the outer perimeter of the cylinder. This is shown in [Fig. 41](#). The figure also contains an example of the track distances across the different mesh of the cylinder. These are the track lengths used to calculate the τ values in [\(342\)](#).

To apply the method of collision probabilities, the cylindrical problem is subdivided into a number of small annular mesh. The scalar flux and, hence, the source across each mesh is assumed to be constant. To obtain an accurate solution to the integral equation, the size of each mesh must be small enough such that the flat source approximation is valid. If the source exhibits large variations across a given mesh, the mesh in question would need to be subdivided into smaller mesh where the source variations were not so extreme.

For cylindrical geometry, the equation for the scalar flux is given by

$$\phi_i^g = T_{i \rightarrow i}^g \cdot q_i^g \cdot V_i + \sum_{i' \neq i} q_{i'}^g \cdot V_{i'} \cdot T_{i' \rightarrow i}^g \quad (344)$$

In this formulation, the surface of the cylinder is considered to be non reentrant. That is, if a neutron reaches the surface of the cylinder, it leaks out of the system and does not return. In this respect, the collision probabilities represented in [\(342\)](#) are for a black boundary. We will correct these accordingly in [Sect. 4.2.4](#) to account for reflection along the edge of the cylinder.

4.2.4 White Boundary Conditions

As mentioned earlier, the spectral calculation takes the true geometry of each pin cell – cylindrical fuel and clad regions imbedded in a square coolant zone – and cylindricalizes the coolant

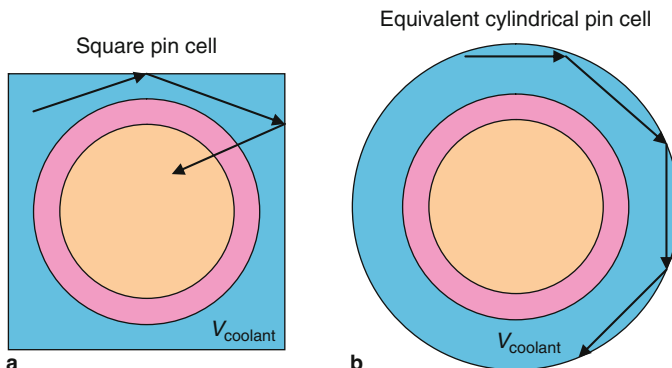


Figure 42
Neutron streaming effects in a cylindrical cell

region of the cell, preserving the coolant volume, in order to allow for a one-dimensional calculation to be performed on the cell. To isolate the cell from its assembly surroundings, the surfaces along the square coolant region are assumed to be perfectly reflecting. In this way, the spectral calculation generates an infinite spectrum for each pin cell.

Once the pin cell has been cylindricalized, the boundary conditions applied to the equivalent cylindrical coolant region must be consistent with those that would be applied to the square coolant region. Applying perfect reflection along the outer surface of the cylindrical cell will not, however, produce results equivalent to the results generated from a two-dimensional pin-cell calculation. The reason for this is best illustrated in [Fig. 42](#). Here, [Fig. 42a](#) illustrates a neutron streaming across a square coolant region of the true pin-cell geometry at a rather shallow angle relative to the top surface of the cell. Following a few reflections off the boundary of the cell, the neutron streams into the fuel region and is potentially absorbed. [Figure 42b](#) illustrates the same neutron streaming across the coolant region of the cylindrical cell geometry at the same shallow angle relative to the boundary of the cell. Regardless of the number of times the neutron reaches the boundary of the cell, it will never be reflected through the fuel region unless it suffers a scattering collision. As a result, the flux in the coolant region of the cylindrical cell will be overestimated and the cylindrical cell geometry will produce results that are not entirely representative of the results generated in the true geometry of the cell. In even simpler terms, perfect reflection imposes the constraint that a neutron will forever stream back and forth along the same ray trace shown in [Fig. 41](#) unless it suffers a scattering collision. It is easy to see from [Fig. 42a](#) that this is not the case for a square boundary.

To provide a more accurate estimate of the flux in the coolant region of the equivalent cylindrical cell, a “white” boundary condition is applied at the outer surface of the one-dimensional pin-cell geometry, rather than perfect reflection. Here, a neutron reaching the boundary of the system is reflected back into the system with a cosine distribution. In this way, neutrons moving at steep angles relative to the surface of the cylinder are weighed more heavily than neutrons that move at shallow angles relative to the surface of the cylinder, thereby minimizing the streaming effect illustrated in [Fig. 42](#). By using the white boundary condition, most results from the equivalent cell geometry agree nicely with results from the true cell geometry that uses perfect reflection.

Carlvik's method is used to update all collision probabilities from a black boundary to a white boundary (Carlvik 1967a). Here, the vector R_i^g is determined following the calculation of the black boundary $P_{i' \rightarrow i}^g$,

$$R_i^g = \Sigma_{tr,i}^g V_i - \sum_{i'} \Sigma_{tr,i'}^g V_{i'} P_{i' \rightarrow i}^g \quad (345)$$

The black boundary collision probabilities are all updated using the relationship

$$\Sigma_{tr,i}^g V_i \hat{P}_{i' \rightarrow i}^g = \Sigma_{tr,i}^g V_i P_{i' \rightarrow i}^g - \frac{R_{i'} R_i}{\sum_j R_j} \quad (346)$$

where $P_{i' \rightarrow i}^g$ is a black boundary collision probability, and $\hat{P}_{i' \rightarrow i}^g$ is a white boundary collision probability. Once the collision probabilities have been updated, (344) may be solved directly for the scalar flux. (344) should be rewritten to reflect the fact that we have modified the collision probabilities in (342). Our new expression for the scalar flux is

$$\phi_i^g = \hat{T}_{i \rightarrow i}^g \cdot q_i^g \cdot V_i + \sum_{i' \neq i} q_{i'}^g \cdot V_{i'} \cdot \hat{T}_{i' \rightarrow i}^g \quad (347)$$

where the modified transport matrix elements are given by

$$\begin{aligned} \hat{T}_{i' \rightarrow i}^g &= \frac{1}{\Sigma_{tr,i}^g V_i \Sigma_{tr,i'}^g V_{i'}} \sum_m \hat{P}_{i' \rightarrow i}^g(h_m) \cdot \Delta h \\ \hat{T}_{i \rightarrow i}^g &= \frac{1}{(\Sigma_{tr,i}^g V_i)^2} \sum_m \hat{P}_{i \rightarrow i}^g(h_m) \cdot \Delta h \\ \hat{T}_{s' \rightarrow i}^g &= \frac{1}{\Sigma_{tr,i}^g V_i A_{s'}} \sum_m \hat{P}_{s' \rightarrow i}^g(h_m) \cdot \Delta h \\ \hat{T}_{s' \rightarrow s}^g &= \frac{1}{A_s A_{s'}} \sum_m \hat{P}_{s' \rightarrow s}^g(h_m) \cdot \Delta h \end{aligned} \quad (348)$$

4.2.5 Buffer Zone

For normal fuel pin cells, the fuel pellet itself produces neutrons via the fission process and the cell can sustain its own chain reaction for the pin-cell spectral calculation. For inert cells, such as water rods, control rods, or vanish portions of part length rods, there is no neutron source within the pin cell and, hence, there is no way of generating a solution to the integral transport equation. Similarly for fuel pins containing Gadolinium, the Gd cross sections are so large at energies below 1 eV that it becomes difficult to produce a realistic thermal flux spectrum within the pin cell without an external source of neutrons.

In an effort to impose consistency between different pin-cell spectral calculations, all pin cells can be modeled with an outer buffer zone comprised of a representative amount of fuel, cladding, and water. For normal fuel pins, the buffer zone is slightly detrimental because it places fuel material too close to the coolant region. But for inert rods and rods containing Gadolinium, the buffer zone helps to drive the neutron flux across the problem. The size of the buffer zone is somewhat irrelevant to the solution of the problem. For application in most lattice physics codes, the buffer zone can be chosen to be equivalent in size to eight pin cells.

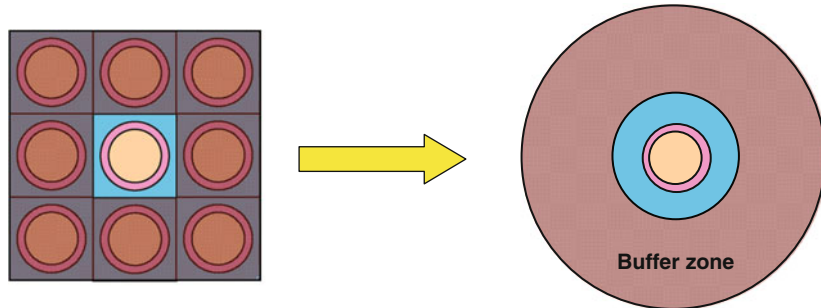


Figure 43
Geometry of a pin cell with a buffer zone attached

The buffer zone is placed on the outside of each pin cell, as illustrated in [Fig. 43](#), and the white boundary condition described in [4.2.4](#) is applied at the outer surface of the buffer zone.

The cross sections for the buffer zone can be created in many different ways. The results to the analysis are highly insensitive to the method used. The easiest way to create cross sections for the buffer zone is to simply volume-average all materials in the problem into a single, homogenized material. When applying this simple averaging technique, one should ensure that none of the strong absorbers in the assembly are included in the buffer material. That is, materials for the control blade, control rods, absorber pins, and any fuel pins containing Erbium or Gadolinium should be left out of the average. Inclusion of the strong absorbers into the material will produce a spectrum that is too hard. Another alternative for creating the cross sections for the buffer zone material is to perform a single pin-cell calculation on a representative pin cell (that does not contain a buffer zone) and use the flux from that calculation to flux- and volume-weight the cross sections into a homogenized material. Either approach is perfectly acceptable.

4.2.6 Numerics of the Pin-Cell Spectral Calculation

The pin-cell spectral calculations can be treated as fixed source problems. The fission cross sections of all fuel regions are set to zero and a fixed source of neutrons is defined to exist in the buffer zone only, using the fission spectrum as the neutron source. This is done to help speed up convergence of the solution without adversely affecting the final neutron distribution.

The routine begins by calculating the collision probabilities between all mesh in the problem, using [\(342\)](#). The surface terms are dropped from consideration because they are now rolled into the white boundary correction,

$$\begin{aligned}
 P_{i' \rightarrow i}^g(h) &= K i_3(\tau_{i' \rightarrow i}^g) - K i_3(\tau_{i' \rightarrow i}^g + \tau_{i' \rightarrow i'}^g) - K i_3(\tau_{i' \rightarrow i}^g + \tau_{i \rightarrow i}^g) \\
 &\quad + K i_3(\tau_{i' \rightarrow i}^g + \tau_{i \rightarrow i}^g + \tau_{i' \rightarrow i'}^g) \\
 P_{i \rightarrow i}^g(h) &= \Sigma_{tr,i}^g V_i - \left[\frac{\pi}{4} - K i_3(\tau_{i \rightarrow i}^g) \right]
 \end{aligned} \tag{349}$$

The black boundary collision probabilities are then modified for a white boundary condition using (346). Next, the transport kernel is calculated using (343), where a Gaussian quadrature is used to perform the integration over angle. Once again, the surface terms are dropped from the explicit calculation because they are implicit in the modified collision probability terms,

$$\begin{aligned}\hat{T}_{i' \rightarrow i}^g &= \frac{1}{\Sigma_{tr,i}^g V_i \Sigma_{tr,i'}^g V_{i'}} \sum_m \hat{P}_{i' \rightarrow i}^g(h_m) \cdot \Delta h \\ \hat{T}_{i \rightarrow i}^g &= \frac{1}{(\Sigma_{tr,i}^g V_i)^2} \sum_m \hat{P}_{i \rightarrow i}^g(h_m) \cdot \Delta h\end{aligned}\quad (350)$$

Once the transport kernel has been calculated for the system, the iteration scheme begins. The one-group expression for the flux can be written from (312) as

$$\phi_i = \sum_{i'} q'_{i'} V_{i'} \hat{T}_{i' \rightarrow i} + \sum_{i' \neq i} \Sigma_{s,i'} \phi_{i'} V_{i'} \hat{T}_{i' \rightarrow i} + \Sigma_{s,i} \phi_i V_i \hat{T}_{i \rightarrow i} \quad (351)$$

where the superscript representing the energy group has been dropped and the self-scattering portion of the source has been isolated from the in-scattering and the fixed source, $q'_{i'}$. Rearranging (351) to isolate the in-scattering source term, we get

$$\phi_i - \Sigma_{s,i} \phi_i V_i \hat{T}_{i \rightarrow i} - \sum_{i' \neq i} \Sigma_{s,i'} \phi_{i'} V_{i'} \hat{T}_{i' \rightarrow i} = \sum_{i'} q'_{i'} V_{i'} \hat{T}_{i' \rightarrow i} \quad (352)$$

$$\sum_{i'} \phi_{i'} (\delta_{i,i'} - \Sigma_{s,i'} V_{i'} \hat{T}_{i' \rightarrow i}) = \sum_{i'} q'_{i'} V_{i'} \hat{T}_{i' \rightarrow i} \quad (353)$$

where the in-scattering and fixed source term is given by

$$q'^g_{i'} = \sum_{g' \neq g} \Sigma_{s,i'}^{g' \rightarrow g} \phi_{i'}^{g'} + \chi_{i'}^g \quad (354)$$

recalling that the fixed source is zero everywhere other than in the buffer zone.

(352) may be expressed in one-group matrix notation as

$$\underline{\underline{A}}_{ii'} \underline{\phi}_i = \underline{B}_i \quad (355)$$

where

$$\begin{aligned}\underline{\underline{A}}_{ii'} &= \delta_{i,i'} - \Sigma_{s,i'} V_{i'} \hat{T}_{i' \rightarrow i} \\ \underline{B}_i &= \sum_{i'} q'_{i'} V_{i'} \hat{T}_{i' \rightarrow i}\end{aligned}\quad (356)$$

The solution to (355) is of the form

$$\underline{\phi}_i = \underline{\underline{A}}_{ii'}^{-1} \underline{B}_i \quad (357)$$

where the $\underline{\underline{A}}$ matrix is inverted only once, prior to beginning the iteration process, using Gaussian elimination.

The iteration scheme consists of a series of inner iterations that are used to converge the scalar flux in each energy group. The inner iterations are contained within outer iterations that

are used to converge the source distribution. Since the pin-cell spectral calculations are treated as a fixed source problem, the flux in the fast energy groups can be solved directly without the need for an outer iteration. The outer iterations are used only to treat up-scattering in the thermal energy groups below ~ 2 eV.

The calculation begins by initializing all scalar flux values in all groups, all mesh, to unity. This represents the flux distribution from the 0 outer iteration. Using this flux initialization, the total (scalar) source in each region of the problem is calculated as

$$q_{i,iter}^g = \sum_{g' < g} \Sigma_{s,i}^{g' \rightarrow g} \phi_{i,iter}^{g'} + \sum_{g' > g} \Sigma_{s,i}^{g' \rightarrow g} \phi_{i,iter-1}^{g'} + \chi_i^g \quad (358)$$

where *iter* refers to the current outer iteration. The first summation in (358) is over all energy groups above the current group, *g*. The second summation in (358) is over all energy groups below the current group, *g*. The value χ_i^g is the fixed source and is present only in the buffer zone. For energy groups above the thermal up-scattering threshold, the second summation in (358) is always zero and (357) can be solved directly to obtain the fast flux distribution across the pin cell. For thermal energy groups, the flux distribution in lower energies influences the flux distribution in higher energies via thermal up-scattering and the outer iterations are used to drive the flux distribution to a converged solution.

Following the completion of an outer iteration, a fundamental mode rebalancing of the group flux distribution is performed in order to properly normalize the flux and ensure neutron conservation in the thermal groups. The fundamental mode calculation is performed on an equivalent homogeneous system using flux and volume weighted cross sections from the pin-cell calculation

$$\bar{\Sigma}_x^g = \frac{\sum_i \Sigma_{x,i}^g \phi_i^g V_i}{\sum_i \phi_i^g V_i} \quad (359)$$

The fundamental mode equation to be solved is a simple balance equation

$$\begin{aligned} \bar{\Sigma}_{tr}^g \psi^g &= \sum_{g' \neq g} \bar{\Sigma}_s^{g' \rightarrow g} \psi^{g'} + \bar{\Sigma}_s^{g \rightarrow g} \psi^g + \bar{\chi}^g \\ (\bar{\Sigma}_{tr}^g - \bar{\Sigma}_s^{g \rightarrow g}) \psi^g &= \sum_{g' \neq g} \bar{\Sigma}_s^{g' \rightarrow g} \psi^{g'} + \bar{\chi}^g \\ \psi^g &= \frac{\bar{\chi}^g}{\bar{\Sigma}_r^g} \end{aligned} \quad (360)$$

where the source term does not contain self-scattering and $\bar{\Sigma}_r^g$ is the removal cross section, given by $\bar{\Sigma}_r^g = \bar{\Sigma}_{tr}^g - \bar{\Sigma}_s^{g \rightarrow g}$.

Following the solution to (360), the scalar flux distribution is scaled using

$$\hat{\phi}_i^g = \phi_i^g \cdot \frac{\psi^g}{\sum_i \phi_i^g V_i} \quad (361)$$

Once the flux has converged, the infinite multiplication factor for the pin cell can be calculated from

$$k^\infty = \frac{\sum_g v \bar{\Sigma}_f^g \psi^g}{\sum_g \bar{\Sigma}_a^g \psi^g} \quad (362)$$

4.3 Coupling Calculation

The flux from the pin-cell calculations can be used, directly, as a condensation spectrum to generate broad-group cross sections for the fine-mesh transport solution. Since each pin-cell calculation was performed by isolating the pin from the rest of the assembly, the spectra are only a fair approximation of the actual distribution of neutrons in energy in the various regions of the pin cell (fuel pellet, cladding, and coolant region). If we choose to use these spectra to condense cross sections, we will end up having to carry a lot of broad energy groups in order to preserve accuracy at the fine-mesh assembly level. We will also run into a dilemma with respect to condensing cross sections in the outer regions of the assembly. For example, we have no specific flux spectrum from the series of pin-cell calculations with which to condense the outer water gaps of a BWR fuel assembly, the channel shroud, or regions of the control blade. We will need to use either the spectrum from one of the pin-cell regions, or possibly from the buffer zone – neither of which is an adequate choice. By performing a two-dimensional coupling calculation, we can avoid this dilemma.

The coupling calculation is used to adjust the energy distribution of neutrons from the pin-cell spectral calculations to account for the effects of the true surroundings. Once the energy distribution from the series of pin-cell calculations is adjusted, the resulting flux spectra are used to condense macroscopic cross sections in each material region of the problem from the energy group structure of the cross section library to a smaller, broad-group energy structure in preparation for the fine-mesh transport calculation. The coupling calculation is performed on the entire lattice using homogenized pin-cell cross sections. As such, the solution may be obtained in a straightforward Cartesian geometry and any solution technique to the transport equation is a viable candidate for the coupling calculation.

The solution techniques considered for the coupling calculation include the explicit transport techniques of discrete ordinates, collision probabilities, and the method of characteristics. Approximate techniques considered for the coupling calculation include transmission probabilities (TP) and diffusion theory. Obviously, the explicit transport techniques offer the greatest accuracy. Their main deficiency is execution speed, especially for the large number of energy groups we are considering. In addition, one might wonder why we would bother performing a coupling calculation at all if we are going to use an explicit transport technique to do it. That is, we should simply perform the fine-mesh assembly transport calculation in the energy group structure of the cross section library and be done with it. So, our only real choices for the coupling calculation are the two approximate techniques – TP and diffusion theory. The major assumption used in the derivation of the diffusion approximation is that scattering is the dominant process taking place in the problem. For normal fuel regions and water regions, this assumption is true. For strongly absorbing regions, however, such as control blades, control rods, absorber pins, and fuel pins containing Erbium or Gadolinium, this assumption is very

poor and the use of diffusion theory becomes questionable. Around highly absorbing regions, diffusion theory underestimates the gradient of the flux dip across the absorber and calculates a much flatter flux profile than other solution techniques. The result is too many neutrons being placed directly in, and around, the absorber region and a resulting flux spectrum that is too hard. This is highly undesirable from the point of view of producing a condensation spectrum. As a result, in this section we will focus on a coupling scheme based on a response matrix formulation that uses a simplified transmission probabilities method. The method is accurate in terms of distributing neutrons in energy, and is extremely fast.

4.3.1 The Method of Transmission Probabilities

As in the pin-cell spectral calculations, the transmission probabilities method solves the integral form of the transport equation. In collision probabilities, (347) represent contributions to the scalar flux in mesh i from all other mesh in the system, as well as from the system boundary. The number of solutions to (347) required to calculate a new flux distribution for each energy group is equal to the square of the number of mesh in the problem. If the system being analyzed has many mesh and many energy groups, the number of times (347) must be solved may become very large indeed. In addition, the amount of memory needed to store the transport matrix, (348), for large problems with hundreds of energy groups is excessive, and it may become necessary to store only portions of the matrix in memory at any given time.

This burden on the computer system renders the collision probabilities technique, in its present form, a rather poor choice for large problems such as a whole fuel assembly. The burden on the computer system can be relaxed significantly by coupling mesh together via their surface currents, rather than via their scalar fluxes.

In the transmission probabilities technique, an outgoing current is calculated along each surface of each mesh. The outgoing current will become the incoming current to the neighboring mesh. This eliminates the first summation in (347) for the scalar flux and leaves only the contribution to the scalar flux from neutrons born within a particular mesh, and from the incoming currents along all surfaces to the mesh. The equations to be solved are then reduced to

$$\phi_i^g = T_{i \rightarrow i}^g \cdot q_i^g \cdot V_i + 4 \sum_{s'_i} T_{s'_i \rightarrow i}^g \cdot J_{s'_i, in}^g \cdot A_{s'_i} \quad (363)$$

$$J_{s_i, out}^g = q_{i'}^g \cdot V_{i'} \cdot T_{i' \rightarrow s_i}^g + 4 \sum_{s'_i \neq s_i} T_{s'_i \rightarrow s_i}^g \cdot J_{s'_i, in}^g \cdot A_{s'_i} \quad (364)$$

where $J_{s_i, out}^g$ becomes $J_{s'_i, in}^g$ to the subsequent mesh. All summations in (363) and (364) are over surfaces to mesh i only. It should be remembered that, in the derivation of these equations, the source – and hence the scalar flux – was assumed to be constant across a mesh.

The average neutron current crossing a mesh surface is calculated from the outward directed angular flux distribution along the surface as

$$J_{s_i}^g = \int |\hat{n} \cdot \hat{\Omega}_m| \cdot \Phi_{m, i}^g \cdot d\hat{\Omega}_m = \sum_m \sin \varphi_m \cdot \cos \theta_m \cdot \Phi_{m, i}^g \cdot \omega_m \quad (365)$$

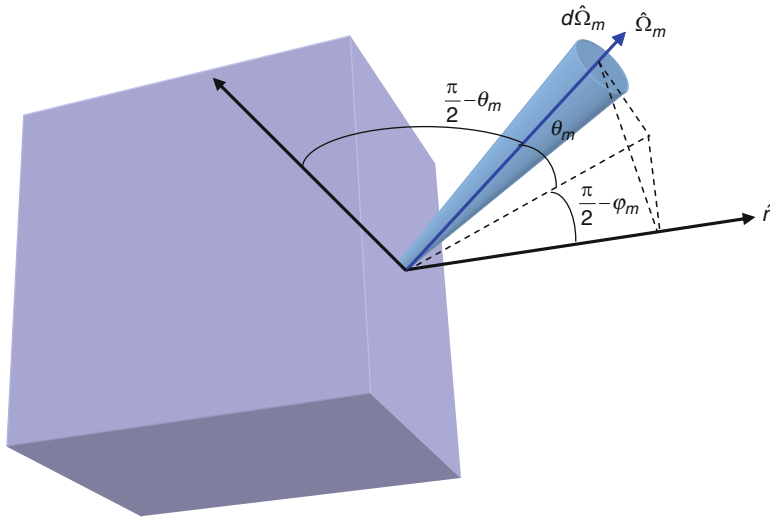


Figure 44

Variables for calculating the surface current leaving a mesh

where the current is normal to the mesh surface. The meanings of the variables used in (365) are illustrated in [Fig. 44](#).

In methods that solve the integrodifferential form of the Boltzmann transport equation, such as the discrete ordinates method, the equations are formulated in terms of the angular flux and the current can be easily calculated, if desired. In integral transport theory, though, the angular dependency of the flux is integrated out of the equation prior to formulating the numerical solution. By doing so, the integral equation is solved directly in terms of the scalar flux, which is usually the desired quantity. The one drawback to this process, in relation to transmission probabilities, is that the angular flux is needed in order to determine the current.

To calculate a current passing through each surface of each mesh, the angular flux must now be approximated in some manner. In the response matrix technique that uses a simplified transmission probabilities method, the angular flux crossing each surface of each mesh is assumed to be distributed isotropically in angle and uniformly in space along the surface

$$\Phi_{m,i}^g = \frac{\phi_i^g}{4\pi} \quad (366)$$

where m represents a specific direction of motion, of which there are a total of 4π radian. (366) leads to the following expression for the current crossing a surface:

$$J_{s_i}^g = \int_{\hat{\Omega} \cdot \hat{n} > 0} d\hat{\Omega} |\hat{\Omega} \cdot \hat{n}| \Phi(\vec{r}, \hat{\Omega}) = \frac{\phi_i^g}{4} \quad (367)$$

From (367), the relationship between the scalar flux and the current is given by

$$4J_{s_i}^g = \phi_i^g \quad (368)$$

where s is a surface to mesh i .

In the coupling calculation routine, the current crossing any boundary is assumed to be isotropically distributed in angle. For a very detailed calculation in space, this would be a very poor approximation. For homogenized pin cells, however, this is actually a better approximation than one might think and allows the simplified transmission probabilities method to be used successfully to generate a reasonably accurate condensation flux. Remember that, at this stage of the calculational scheme, we are focusing on obtaining an accurate energy distribution of neutrons and not so much an accurate spatial distribution.

4.3.2 Numerics of the Coupling Calculation

As in the method of collision probabilities, the transmission probabilities technique reduces to calculating reasonably accurate transport probabilities between all surfaces of a mesh. The equations to be solved here are similar to those introduced for the collision probabilities method

$$\begin{aligned} T_{i \rightarrow i}^g &= \frac{1}{(\Sigma_{tr,i}^g V_i)^2} \int \frac{d\varphi}{2\pi} \int P_{i \rightarrow i}^g(\varphi, h) dh \\ T_{s \rightarrow i}^g &= \frac{1}{\Sigma_{tr,i}^g V_i A_s} \int \frac{d\varphi}{2\pi} \int P_{s \rightarrow i}^g(\varphi, h) dh \\ T_{s' \rightarrow s}^g &= \frac{1}{A_s A_{s'}} \int \frac{d\varphi}{2\pi} \int P_{s' \rightarrow s}^g(\varphi, h) dh \end{aligned} \quad (369)$$

where the $P_{i \rightarrow i}^g(\varphi, h)$'s represent the collision probabilities, given by

$$\begin{aligned} P_{i \rightarrow i}^g(\varphi, h) &= \Sigma_{tr,i}^g V_i - \left[\frac{\pi}{4} - K_{i3}(\tau_{i \rightarrow i}^g) \right] \\ P_{s \rightarrow i}^g(\varphi, h) &= \frac{1}{2} \left[\frac{\pi}{4} - K_{i3}(\tau_{s \rightarrow i}^g) \right] \\ P_{s' \rightarrow s}^g(\varphi, h) &= K_{i3}(\tau_{s' \rightarrow s}^g) \end{aligned} \quad (370)$$

In the above equation, the A_s 's represent the surface areas of a mesh, and the $\tau_{i \rightarrow i}^g$'s represent the optical distances between surfaces of a mesh, in mean free paths, in the xy -plane of the problem. The $K_{i3}(\tau_{i \rightarrow i}^g)$ values are the Bickley–Naylor functions arising from the integration over polar angle performed analytically, as discussed previously. Note that collision probabilities for the coupling calculation are calculated on a mesh by mesh basis and are, therefore, much simpler than the collision probabilities calculated for the pin-cell spectral calculations.

The integrations in (369) are performed numerically using sets of parallel, equidistant tracks (separated by a distance dh), which are traced over each mesh individually at several evenly spaced angles (distributed every $\Delta\varphi$ radians). The collision probabilities between the various surfaces are then calculated along these tracks.

The numerics of the coupling calculation are very similar to those of the pin-cell spectral calculations. Here, though, streaming tracks are traced over each mesh in the system individually in order to obtain the optical distances, τ , needed to solve (370) and to perform the integrations over angle and space contained in (369).

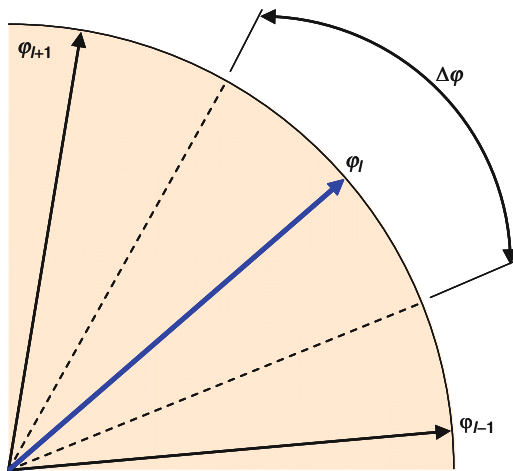


Figure 45
Area between different angles of motion

For a specified number of azimuthal angles, L , the azimuthal boundaries are evenly spaced and the direction of the streaming tracks are distributed according to

$$\varphi_l = \left(l - \frac{1}{2} \right) \cdot \Delta\varphi \quad (371)$$

The weight associated with each direction, $d\varphi = \Delta\varphi$, is then given by

$$\Delta\varphi = \frac{2\pi}{L} \quad (372)$$

The weight represents the area between different directions, as illustrated in [Fig. 45](#). Since the integration over polar angles was performed analytically, giving rise to the Bickley–Naylor functions, polar angles of motion out of the plane of the problem need not be specified.

Tracks are traced across each mesh individually and the distance of each track is calculated by determining the intersection of each track with each surface of the mesh, as illustrated in [Fig. 46](#). The optical distance along each track is then calculated as

$$\tau_{k,l,i}^g = \sum_{tr,i}^g s_{k,l,i} \quad (373)$$

where k is a specific track number; l is a specific angle of motion; and i is a specific mesh in the system.

The total length of the line segment across the mesh is calculated as

$$\begin{aligned} s_{k,l,i} &= \frac{\Delta x - x_0}{\cos \varphi_l}, & \text{for } \varphi_l < \frac{\pi}{2} \\ s_{k,l,i} &= \frac{x_0}{\cos \varphi_l}, & \text{for } \varphi_l > \frac{\pi}{2} \end{aligned} \quad (374)$$

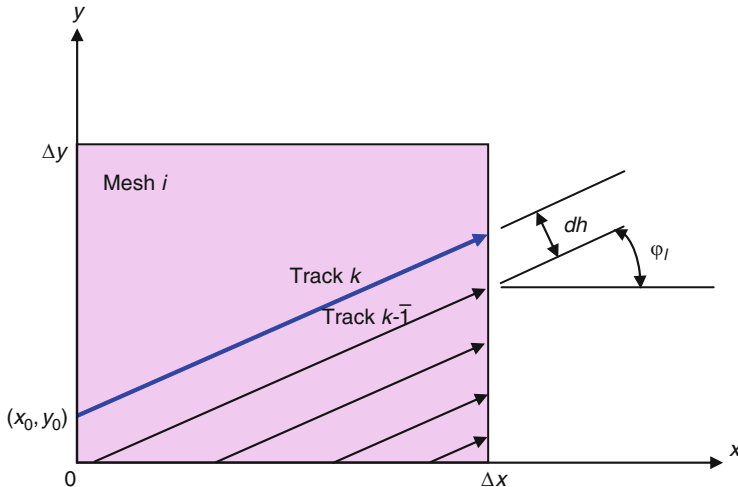


Figure 46
Streaming rays traced across a mesh at a specific angle

The exiting point of the line segment along the y-axis is calculated as

$$y_{\text{out}} = y_0 + s_{k,l,i} \cdot \sin \varphi_l \quad (375)$$

If $y_{\text{out}} > \Delta y$, then the track exits along the top of the mesh and the track length is re-calculated as

$$s_{k,l,i} = \frac{\Delta y - y_0}{\sin \varphi_l} \quad (376)$$

During the ray tracing, the code keeps track of the surface along which the segment enters and leaves the mesh. These surfaces will be used in the calculation of volume-to-surface and surface-to-surface transmission probabilities.

Rays are traced over each individual mesh at azimuthal angles from 0 to π and neutrons are assumed to flow in both directions along a single segment, thus integration for all azimuthal angles (2π) is not necessary.

The transport matrices, (369), are then calculated as

$$\begin{aligned} T_{i \rightarrow i}^g &= \frac{1}{(\Sigma_{tr,i}^g V_i)^2} \sum_l \frac{\Delta \varphi}{2\pi} \sum_k dh \cdot \left\{ \Sigma_{tr,i}^g V_i - \left[\frac{\pi}{4} - K_{i3}(\tau_{k,l,i}^g) \right] \right\} \\ T_{i,s \rightarrow i}^g &= \frac{1}{2\Sigma_{tr,i}^g V_i A_{i,s}} \sum_l \frac{\Delta \varphi_l}{2\pi} \sum_k dh \cdot \left[\frac{\pi}{4} - K_{i3}(\tau_{k,l,i}^g) \right] \\ T_{i,s' \rightarrow i,s}^g &= \frac{1}{A_{i,s} A_{i,s'}} \sum_l \frac{\Delta \varphi_l}{2\pi} \sum_k K_{i3}(\tau_{k,l,i}^g) \end{aligned} \quad (377)$$

where the surface areas and volumes in (377) are those that are approximated by the ray tracing,

$$\begin{aligned} V_i &= \sum_l \sum_k dh \cdot \frac{\Delta\varphi_l}{2\pi} \cdot s_{k,l,i} \\ A_{i,s} &= \sum_l \sum_k dh \cdot \frac{\Delta\varphi_l}{2\pi} \end{aligned} \quad (378)$$

Note that the surface summations in (377) and (378) include only those tracks, k , that actually intersect the specific surface, whereas the volume summations include all tracks, k , traced at each azimuthal angle, l .

4.3.3 Solution to the Response Matrix Equations

For the coupling calculation, the scalar flux in all groups, all mesh, is initialized to unity prior to the start of the first iteration. All inward directed currents along the boundaries of the problem, in all energy groups, are initialized to 1/4, from (367). This initialization supplies an initial guess to the solution technique and the iterative algorithm may begin.

Inner Iterations

The inner iterations are used to converge the scalar flux distribution throughout the entire problem domain in a single energy group. The inner iterations will also drive the current along the system boundaries to converge. These are the solutions to (363) and (364).

The scalar flux distribution is considered converged when the following criterion is met within each mesh of the problem:

$$\frac{|\phi_{i,iter}^g - \phi_{i,iter-1}^g|}{\phi_{i,iter}^g} < \varepsilon \quad (379)$$

where ε is the convergence criterion on the scalar flux, which can be loosely set to 10^{-4} .

The outward directed current coming in contact with the boundary of the system is considered converged when the following criterion is met within each mesh along the problem boundary:

$$\frac{|J_{s,i,out,iter}^g - J_{s,i,out,iter-1}^g|}{J_{s,i,out,iter}^g} < \varepsilon \quad (380)$$

where ε is the convergence criterion on the current, which can be loosely set to 10^{-4} . The subscripts in (380) represent only the mesh, and surfaces of those mesh, which lie along the system boundary.

During an inner iteration, the source term of neutrons born into the energy group of interest, g , is constantly being updated using the scalar flux from inner iterations in higher energy groups. In this way the source takes on the appearance

$$q_i^g = \sum_{g' < g} \Sigma_{s,i}^{g' \rightarrow g} \phi_{i,iter}^{g'} + \sum_{g' \geq g} \Sigma_{s,i}^{g' \rightarrow g} \phi_{i,iter-1}^{g'} + \frac{\chi_i^g}{k^\infty} \left[\sum_{g'} \nu \Sigma_{f,i}^{g'} \phi_{i,iter-1}^{g'} \right] \quad (381)$$

where group 1 is the highest energy group of the cross section library. This defines a Gauss-Seidel scheme for the inner iterations.

In lattice physics computations, the fission source can be represented as a production kernel, similar to the way in which the scattering source is represented as a kernel, and the fission source term may be rolled up into the scattering source term as

$$q_i^g = \sum_{g' < g} \Sigma_{s,i}^{g' \rightarrow g} \phi_{i,iter}^{g'} + \sum_{g' \geq g} \Sigma_{s,i}^{g' \rightarrow g} \phi_{i,iter-1}^{g'} + \frac{1}{k^\infty} \sum_{g'} \Sigma_{p,i}^{g' \rightarrow g} \phi_{i,iter-1}^{g'} \quad (382)$$

where the production kernel is defined as

$$\Sigma_{p,i}^{g' \rightarrow g} = \chi_i^g v \Sigma_{f,i}^{g'} \quad (383)$$

Outer Iterations

Just as mesh are coupled together via their surface currents, energy groups are coupled together via the scattering and fission sources. The outer iterations are used to converge the source distribution and, hence, the eigenvalue to the problem. The outer iterations redistribute the source neutrons resulting from the updated scalar flux distribution generated during the sweep through the inner iterations. A complete sweep of inner iterations through all energy groups of the problem defines one outer iteration.

The source is considered to be converged when the following criterion is met during two successive iterations,

$$\frac{|k_{iter}^\infty - k_{iter-1}^\infty|}{k_{iter}^\infty} < \varepsilon \quad (384)$$

where ε is the convergence criterion on the eigenvalue, which can be loosely set to 10^{-4} .

During an outer iteration, the fission source distribution is held constant and the scattering distribution is updated continuously using results from the most recent inner iteration.

Fundamental Mode Rebalance

Following completion of an outer iteration, a fundamental mode rebalancing of the group flux distribution is performed in order to properly normalize the flux and ensure neutron conservation. The fundamental mode calculation is performed on an equivalent homogeneous system using flux and volume weighted cross sections from the heterogeneous calculation. The resulting group flux values from the homogeneous calculation are then used to rebalance the magnitude of the heterogeneous group flux values.

The equation to be solved here is equivalent to (360)

$$\phi_{FM}^g = \frac{\bar{q}^g}{\bar{\Sigma}_r^g} \quad (385)$$

where the source term does not include self scattering and the fission source is normalized to unity by the multiplication factor. Hence,

$$\bar{q}^g = \sum_{g' \neq g} \bar{\Sigma}_s^{g' \rightarrow g} \phi_{FM}^{g'} + \frac{\bar{\chi}^g}{k^\infty} \sum_{g'} v \bar{\Sigma}_f^{g'} \phi_{FM}^{g'} \quad (386)$$

where the flux and volume weighted cross sections for the fundamental mode calculation are calculated from

$$\bar{\Sigma}_x^g = \frac{\sum_i \Sigma_{x,i}^g \phi_i^g V_i}{\sum_i \phi_i^g V_i} \quad (387)$$

In (387), x represents the desired reaction (e.g., fission, absorption, etc.).

Since there are no neutron leakage effects across the boundaries of the problem (i.e., perfect reflection is assumed along all boundaries), the multiplication factor in (387) can be calculated directly as the ratio of neutron production in the system to neutron destruction

$$k^\infty = \frac{\sum_{g'} v \bar{\Sigma}_f^{g'} \phi_{FM}^{g'}}{\sum_{g'} \bar{\Sigma}_a^{g'} \phi_{FM}^{g'}} \quad (388)$$

If we normalize the flux in such a way that there is only one neutron being absorbed in the entire problem, then the denominator to (388) becomes unity and the multiplication factor is simply the sum of all neutrons born through fission

$$k^\infty = \sum_{g'} v \bar{\Sigma}_f^{g'} \phi_{FM}^{g'} \quad (389)$$

Plugging (389) into (386) yields the final expression for the fundamental mode homogeneous source

$$\bar{q}^g = \sum_{g'} \bar{\Sigma}_s^{g' \rightarrow g} \phi_{FM}^{g'} + \bar{\chi}^g \quad (390)$$

Due to up-scattering in the thermal energy groups, the solution to (385) defines an iterative process and the fundamental mode equation is solved directly with no acceleration. Following the solution to (385), the scalar flux distribution from the solution to (363) is scaled using the solution from the fundamental mode calculation

$$\hat{\phi}_{i,iter}^g = \phi_{i,iter}^g \cdot \frac{\phi_{FM}^g}{\sum_i \phi_{i,iter}^g V_i} \quad (391)$$

4.3.4 Geometry of the Coupling Calculation

The coupling calculation takes the true geometry of the lattice and homogenizes all non-rectangular regions into an equivalent rectangular geometry and an equivalent set of material cross sections. Homogenization of the material sets is done using a straightforward flux and volume weighting of the heterogeneous material sets. The flux used in the homogenization process is obtained from the pin-cell spectral calculations. If there exists no flux from the pin-cell spectral calculations for regions that are to be homogenized, then the homogenization is done in a straightforward volume weighting process.

For a typical LWR lattice, all pin cells are homogenized into a single equivalent material set

$$\bar{\Sigma}_{x,I}^g = \frac{\sum_{i \in I} \Sigma_{x,i}^g \phi_i^g V_i}{\sum_{i \in I} \phi_i^g V_i} \quad (392)$$

where i represents a region of the pin cell (fuel, clad, and coolant), and I represents the homogenized square.

For the inner regions of the fuel bundle, most cells take part in the pin-cell spectral calculations and, therefore, there exist flux spectrums for each of the various regions of the cell. In rare circumstances, there may not exist a flux spectrum for the various regions of a cell. In such cases, the materials are volume weighted into a single homogeneous set

$$\bar{\Sigma}_{x,I}^g = \frac{\sum_{i \in I} \Sigma_{x,i}^g V_i}{\sum_{i \in I} V_i} \quad (393)$$

For BWR lattices, (393) is also used to homogenize the inner water gap, along the inside wall of the channel, with the channel wall itself. For absorber pins of a cruciform control blade, fluxes can be obtained from a special series of pin-cell spectral calculations performed on each absorber tube and (392) can be used to homogenize all absorber tubes into a single homogeneous material set. The final geometry of the coupling calculation appears as in [Fig. 47](#), where the red mesh lines represent the geometry of the coupling calculation.

For regions containing strong absorbers, such as control blades, control rods, burnable absorber pins, or fuel pins containing Gadolinium or Erbium, the homogenized cross sections will grossly overestimate the actual absorption rate in the heterogeneous cell. One way of accounting for this is to calculate correction factors for the homogenized material. The correction factors are determined by performing one additional pin-cell calculation on the absorber cell that uses the homogenized cross sections in all regions of the cell – fuel, clad, and coolant.

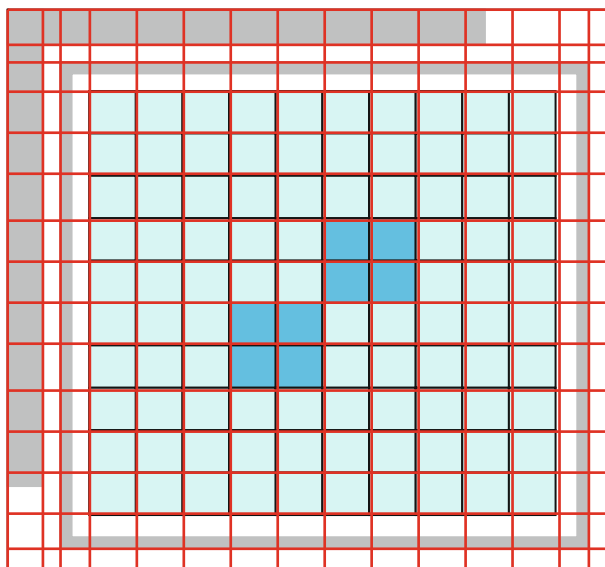


Figure 47
Typical geometry of coupling calculation

The cross sections for the buffer zone are the same as those used in the heterogeneous pin-cell calculation.

The reaction rate in the homogenized cell is then compared against the averaged reaction rate in the combined regions of the heterogeneous cell. Correction factors are determined that, when applied to the homogenized cross sections, produce equivalent reaction rates in the homogenized cell. This involves an iterative process, where the correction factors are estimated using the results from the first homogenized pin-cell analysis,

$$R^g = \frac{\sum_i \Sigma_{tr,i}^g \phi_i^g V_i}{\bar{\Sigma}_{tr}^g \bar{\phi}^g \bar{V}} \quad (394)$$

The new homogenized cross sections are estimated to be $\bar{\Sigma}_{x,new}^g = R^g \cdot \bar{\Sigma}_{x,old}^g$. Using these new homogenized cross sections, the homogenized pin-cell calculation is re-performed. This process continues until the reaction rates using the homogenized cross sections match those from the heterogeneous pin cell. Note that there is a unique correction factor for each energy group.

For normal fuel pins, the correction factors will be unity or close enough to unity that no correction needs to be applied to the homogenized cross section set. For strong absorber pins, such as fuel pins containing Gadolinium, the correction factors will be far from unity in the thermal energy groups. They will be close to unity above the thermal energy cut-off of 0.625 eV.

Use of the correction factors will produce a slightly better condensation spectrum, depending on the number of strong absorber pins present in the fuel assembly. For problems containing a cruciform control blade, the use of correction factors is almost a necessity in order to obtain meaningful results.

Once the homogenized materials have been constructed, the material layout has been assigned, and the transmission matrices have been calculated, the code can proceed to solve for the flux and current in each mesh by the use of a red–black iteration scheme. The layout for this scheme is illustrated in Fig. 48, where each mesh is assigned either a “red” or “black” declaration. Here, the flux and outward directed currents for all red mesh are solved first. The inward currents to all black mesh are set equal to the newly calculated outward currents from the corresponding red mesh. The flux and outward directed currents for all black mesh are then solved. The inward currents to all red mesh are then set equal to the outward currents from the corresponding black mesh. And so on and so forth. An inner iteration is complete when the outward currents and mesh fluxes have converged for a given source distribution in a given energy group.

4.4 Cross Section Condensation

The energy distribution of neutrons from the series of one-dimensional pin-cell calculations are updated with the flux spectra from the two-dimensional response matrix calculation

$$\tilde{\phi}_i^g = \phi_i^g \cdot \frac{\phi_I^g V_I}{\sum_{i \in I} \phi_i^g V_i} \quad (395)$$

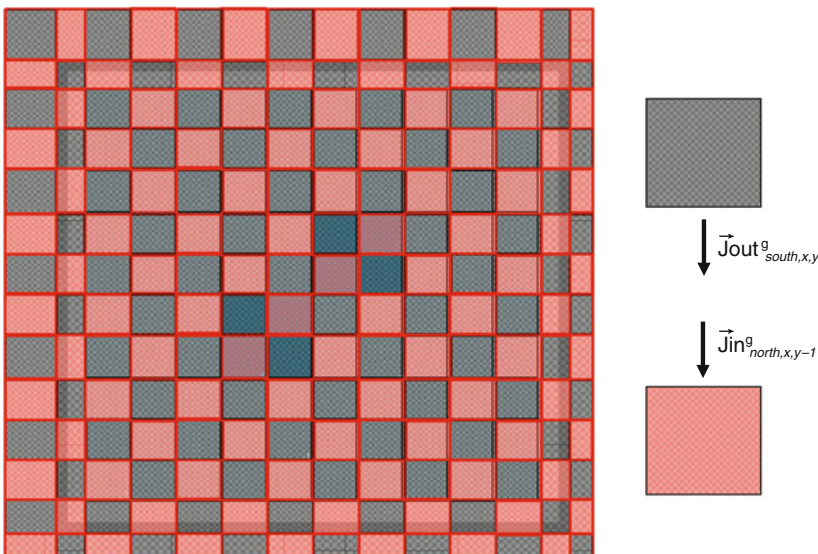


Figure 48
Red–black iteration scheme

where i represents a region of the pin cell (fuel, clad, and coolant), and I represents the homogenized rectangle from the coupling calculation.

Fluxes for the surrounding regions of the lattice – channel box wall, water gaps, etc. – are obtained directly from the response matrix solution. Fluxes for the absorber tubes of a control blade are obtained from the special series of pin-cell calculations performed on each absorber tube and updated with the flux from the response matrix solution. Equation (395) represents the flux for each material region of the problem that will be used to condense the macroscopic cross sections. The final energy group structure for the fine-mesh transport calculation depends on the accuracy of the condensation scheme, the energy group boundaries in the original cross section library, and the types of problems to be analyzed by the lattice physics code. The broad-group cross sections are created using the following expression:

$$\Sigma_{x,i}^G = \frac{\sum_{g \in G} \Sigma_{x,i}^g \tilde{\phi}_i^g}{\sum_{g \in G} \tilde{\phi}_i^g} \quad (396)$$

where g represents the fine-group energy structure of the cross section library, and G represents the broad-group energy structure of the condensed cross sections. The summations in (396) are performed for all fine-groups within a broad-group.

The primary assumptions used in the derivation of the response matrix method are as follows: the scalar flux is flat across each mesh; the angular flux is distributed isotropically across the surface of each mesh; and the angular flux is spatially constant along the surface of each mesh. For normal fuel cells and water regions, these assumptions are not entirely bad. In fact,

when grouped together for such situations, the errors associated with each assumption tend to balance and one is left with a surprisingly better-than-expected solution to the transport equation. For strongly absorbing, relatively thin regions, though, the angular flux emerging from a mesh is highly anisotropic. This is most noticeable in mesh used to model the presence of the cruciform control blade. Under such conditions, neutrons that strike the blade surface head-on, have a much greater chance of streaming across the blade without interacting than do neutrons that strike the blade surface at a steep angle. The assumption of an isotropic current, however, tends to suppress the transmission probability of the neutrons that strike the blade head-on. This results in an excess of absorptions taking place in the black regions of the model, including Gadolinium pins. The increased strength of the control blade will tend to cause the flux to be pushed away from the control blade corner of the problem, across the lattice to the corner where the detector resides. The increased strength of Gadolinium pins will tend to push neutrons away from Gd pins, to pins along the edge of the bundle.

4.5 Sundries

Due to the limitations mentioned above, there is a lower limit to the number of energy groups that must be maintained for the broad-group, fine-mesh transport calculation in order to preserve the accuracy of the fine-group library structure. It is up to the developer to determine the appropriate energy boundaries for the broad-group cross section set.

The most direct way of determining the broad-group energy structure is via trial and error. To do this, the lattice physics code must be developed in such a way as to ensure that the fine-mesh transport calculation is capable of providing a solution in the energy group structure of the cross section library. This provides the code with the ability to generate a reference solution for any condensed group structure. Once a fine-group reference solution exists, groups can be combined to determine which boundaries are necessary for the broad-group solution and which groups can be combined. In general, the more energy groups that exist in the fine-group cross section library, the more groups are needed in the broad-group structure to maintain a desired accuracy.

The energy boundaries required for a desired accuracy will depend on the problem being analyzed and the materials present in the bundle design. Fuel designs containing Gadolinium as an absorber require more thermal energy groups for a desired accuracy than do fuel designs containing, say, Erbium or Boron as an absorber. Fuel designs containing a cruciform control blade require more fast energy groups for a desired accuracy than do fuel designs, which contain pin-sized control fingers inserted directly into the assembly. Fuel designs containing mixed-oxide fuel require more thermal and epithermal energy groups for a desired accuracy than do fuel designs containing, say, uranium-oxide fuel.

In general, it is perfectly acceptable to determine unique broad-group energy structures for different types of problems, so long as the lattice physics code is capable of accurately determining the type of problem being analyzed. Alternatively, the lattice physics code may contain a single broad-group energy structure that is applicable to all problems. This single group structure will likely contain more detail than needed for most problems being analyzed, but will remove the chance that the code will accidentally use the wrong group structure on a certain type of problem.

5 Fine-Mesh Assembly Calculation

5.1 Introduction

Once the cross sections have been condensed to the broad-group structure (if, indeed, there exists a cross section condensation scheme to the specific lattice physics code), we are ready to perform the fine-mesh, two-dimensional heterogeneous transport calculation on the entire lattice. Since we are interested in modeling the lattice in its exact geometry, we are limited to techniques that solve the integral form of the transport equation. Due to the overwhelming benefits associated with the method of characteristics (MoC), as discussed in [Sect. 1](#), we will dedicate this section to developing that method and not discuss other alternatives any further.

Unless otherwise indicated, the content of this section is based on unpublished lectures given to postgraduate students in a course on computational reactor analysis at The Pennsylvania State University in 1990 (Knott 1990). The interested reader is directed to the original paper by Askew (Askew 1972), or the follow-up paper by Halsall (Halsall 1980), for a brief introduction to the MoC. Similar information can be found in Knott (1991), Knott and Edenius (1993), Goldgberg et al. (1995), Cho and Hong (1996), Roy (1998), Postma and Vujic (1999), Kosaka and Saji (2000), Kim et al. (2002), Jevremovic et al. (2002). This section presents a much broader description of the method of characteristics than is found in any of the references.

5.2 General Theory of the Method of Characteristics

5.2.1 Introduction

The characteristics form of the steady state Boltzmann transport equation is derived from the integrodifferential form of the equation

$$\frac{1}{|v|} \frac{\partial \Phi(\vec{r}, E, \hat{\Omega}, t)}{\partial t} = Q(\vec{r}, E, \hat{\Omega}, t) - \Omega \cdot \nabla \Phi(\vec{r}, E, \hat{\Omega}, t) - \Sigma_t(\vec{r}, E) \Phi(\vec{r}, E, \hat{\Omega}, t) \quad (397)$$

Which, after rearranging for steady state applications, becomes

$$\Omega \cdot \nabla \Phi(\vec{r}, E, \hat{\Omega}) - \Sigma_t(\vec{r}, E) \Phi(\vec{r}, E, \hat{\Omega}) = Q(\vec{r}, E, \hat{\Omega}) \quad (398)$$

where the source term, $Q(\vec{r}, E, \hat{\Omega})$, is the total angular source of neutrons at location \vec{r} , with energy E , traveling in direction $\hat{\Omega}$, and is expressed as

$$Q(\vec{r}, E, \hat{\Omega}) = \iint \Sigma_s(\vec{r}, E' \rightarrow E, \hat{\Omega}' \rightarrow \hat{\Omega}) \Phi(\vec{r}, E', \hat{\Omega}') dE' d\hat{\Omega}' + S(\vec{r}, E, \hat{\Omega}) \quad (399)$$

In the above expressions, $\Phi(\vec{r}, E, \hat{\Omega})$ is the angular flux, $\Sigma_t(\vec{r}, E)$ is the total macroscopic cross section, and $\Sigma_s(\vec{r}, E' \rightarrow E, \hat{\Omega}' \rightarrow \hat{\Omega})$ is the macroscopic scattering cross section. $S(\vec{r}, E, \hat{\Omega})$ is the angular source of neutrons at location \vec{r} , either internal (i.e., due to fission) or external.

[Equation \(398\)](#) describes neutron motion as viewed from a fixed reference point, giving rise to the partial derivative in the streaming term. If neutron motion is viewed from the neutron's

frame of reference, the partial derivative in the streaming term reduces to a total derivative along the path of motion of the neutron and (398) becomes

$$\frac{d\Phi(\vec{r}, E, \hat{\Omega})}{ds} + \Sigma_t(\vec{r}, E)\Phi(\vec{r}, E, \hat{\Omega}) = Q(\vec{r}, E, \hat{\Omega}) \quad (400)$$

where s is the track along which the neutron is traveling across the region at location \vec{r} (i.e., the location relative to the fixed reference point).

[Equation \(400\)](#) is the characteristics form of the transport equation and describes neutron motion as viewed through the eyes of the neutron – if, indeed, neutrons do have eyes.

5.2.2 Solution to the Characteristics Form of the Transport Equation

At this point in our derivation of the MoC, we will focus exclusively on one-dimensional slab problems. A little later in this section, we will move into one-dimensional cylindrical geometry, which is a prelude to moving into two-dimensional geometries for orthogonal systems. We choose to start with one-dimensional slab geometry because many of the most important features of the method of characteristics can be described easily for such a system. We will use slab geometry to introduce all features of the MoC, including simple quadrature sets, flat source regions, a simple iteration scheme, and a simple acceleration technique. Once we get into two-dimensional geometry, we will describe the more complicated features used in modern lattice physics codes.

To make things as simple as possible, we will assume that all scattering and all sources (fission and fixed) are isotropic. That is, there are no preferred angles of emission. Anisotropic effects can easily be represented using transport-corrected cross sections, which were briefly alluded to in [Sect. 1](#).

For an isotropic scalar source of total strength q , the isotropic angular source in each direction of travel will be $Q = q/4\pi$ and the transport equation becomes

$$\frac{d\Phi}{ds} + \Sigma_{tr}\Phi = \frac{q}{4\pi} \quad (401)$$

where Σ_{tr} is the transport cross section and the arguments associated with each variable have been dropped to simplify the equation. [Equation \(401\)](#) has the solution

$$\Phi(s) = \Phi(0)e^{-\Sigma_{tr}s} + \frac{q}{4\pi\Sigma_{tr}}(1 - e^{-\Sigma_{tr}s}) \quad (402)$$

where s is the characteristic along which the neutron is traveling and $s = 0$ is the location of the neutron at time $t = 0$, as illustrated in [Fig. 49](#).

[Equation \(402\)](#) is only applicable if we can assume that the source of neutrons inside the region of interest is constant. In such cases, the scalar flux will also be constant and we can solve directly for the value of the angular flux exiting the mesh, based on the value of the angular flux entering the mesh,

$$\Phi_{out} = \Phi_{in}e^{-\Sigma_{tr}t/\cos\varphi} + \frac{q}{4\pi\Sigma_{tr}}(1 - e^{-\Sigma_{tr}t/\cos\varphi}) \quad (403)$$



Figure 49
Coordinate system for the characteristics equation

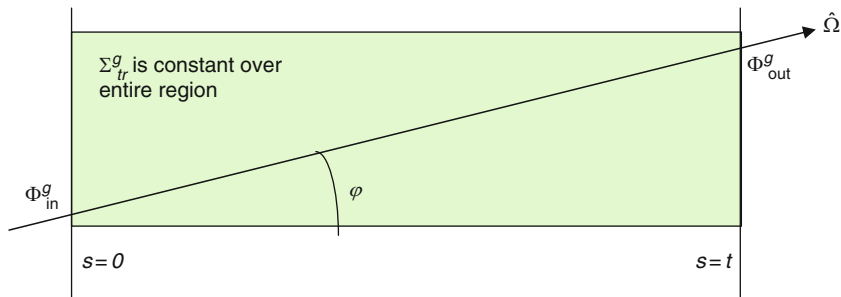


Figure 50
Angular flux across a region of constant material properties

The variables in (403) are illustrated in [Fig. 50](#).

The average value of the angular flux, $\bar{\Phi}$, along any track segment is calculated by integrating the value of the angular flux along the entire length of the track segment and dividing by the length of the segment,

$$\bar{\Phi} = \frac{\int_0^{t/\cos\varphi} \Phi(s) ds}{\int_0^{t/\cos\varphi} ds} = \frac{\int_0^{t/\cos\varphi} \left\{ \Phi(0)e^{-\Sigma s} + \frac{q}{4\pi\Sigma} (1 - e^{-\Sigma s}) \right\} ds}{t/\cos\varphi} \quad (404)$$

After carrying out the integration in the numerator of (404), we are left with the following expression for the average value of the angular flux along a track segment

$$\bar{\Phi} = \frac{\frac{1}{\Sigma} \left\{ \Phi(0) - \Phi(0)e^{-\Sigma t/\cos\varphi} + \frac{qt}{4\pi\cos\varphi} - \frac{q}{4\pi\Sigma} (1 - e^{-\Sigma t/\cos\varphi}) \right\}}{t/\cos\varphi} \quad (405)$$

Combining the second and fourth terms in the numerator, we can express the average value of the angular flux along a track segment in a more compact form

$$\bar{\Phi} = \frac{q}{4\pi\Sigma} + \frac{\Phi(0) - \Phi(t)}{\Sigma t/\cos\varphi} = \frac{q}{4\pi\Sigma} + \frac{\Delta}{\Sigma t'} \quad (406)$$

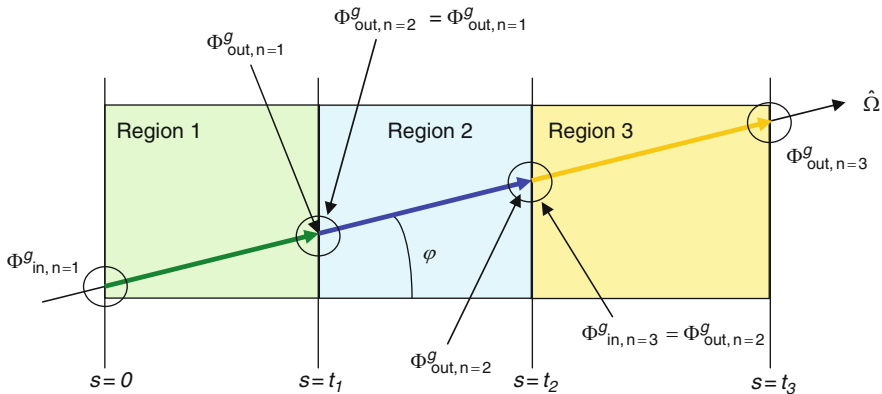


Figure 51
Angular flux across multiple regions

where $\Delta = \Phi(0) - \Phi(t)$ is the change in the angular flux along the track segment; and $t' = t / \cos \varphi$ is the true length of the segment in the xy -plane of the problem across the mesh. Note that the average angular flux in (406) is the value along a specific track segment, across a specific mesh, at a specific angle, in a specific energy group. There will be many such values crossing each slab at different angles, in different energy groups.

If we have multiple slabs, the angular flux exiting each successive slab can be calculated as

$$\begin{aligned}\Phi(t_1) &= \Phi(0)e^{-\Sigma_1 t'_1} + \frac{q_1}{4\pi\Sigma_1}(1 - e^{-\Sigma_1 t'_1}) \\ \Phi(t_2) &= \Phi(t_1)e^{-\Sigma_2 t'_2} + \frac{q_2}{4\pi\Sigma_2}(1 - e^{-\Sigma_2 t'_2}) \\ \Phi(t_3) &= \Phi(t_2)e^{-\Sigma_3 t'_3} + \frac{q_3}{4\pi\Sigma_3}(1 - e^{-\Sigma_3 t'_3}) \\ \Phi(t_n) &= \Phi(t_{n-1})e^{-\Sigma_n t'_n} + \frac{q_n}{4\pi\Sigma_n}(1 - e^{-\Sigma_n t'_n})\end{aligned}\quad (407)$$

where the calculation of the angular flux exiting one slab is a cascading effect into the next slab, as illustrated in [Fig. 51](#). Note that the energy dependence has been omitted from (407) and that the parameter Σ is understood to represent the transport-corrected total cross section of each material region.

If we apply this principle to a number of different directions, L , then the scalar flux in each slab can be calculated from the average angular flux across each slab at each of the different angles,

$$\phi_n^g = \int_{\hat{\Omega}} \bar{\Phi}_n^g(\hat{\Omega}) d\hat{\Omega} = \sum_i \bar{\Phi}_n^g(\varphi_i) \cdot \Delta\varphi_i \quad (408)$$

where $\Delta\varphi_i$ is the solid angle subtended by the direction φ_i (i.e., the weight associated with direction φ_i), and is illustrated in [Fig. 52](#).

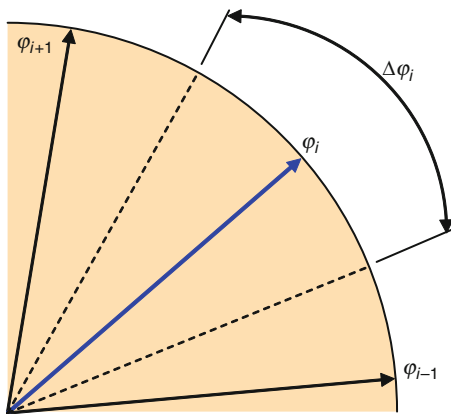


Figure 52
Weight associated with angular direction

Equation (408) can be rewritten as

$$\phi_n^g = \sum_m \bar{\Phi}_{m,n}^g \omega_m = \sum_m \left(\frac{q_n^g}{4\pi \Sigma_{tr,n}^g} + \frac{\Delta_{m,n}^g}{\Sigma_{tr,n}^g t'_{m,n}} \right) \omega_m \quad (409)$$

where $\sum_m \omega_m = 4\pi$, noting that the directions cover polar angles out of the xy -plane of the problem as well as azimuthal angles in the xy -plane of the problem.

For our isotropic source and transport-corrected cross sections

$$\sum_m \frac{q_n^g}{4\pi \Sigma_{tr,n}^g} \omega_m = \frac{q_n^g}{\Sigma_{tr,n}^g} \quad (410)$$

and we arrive at our final expression for the scalar flux in each slab

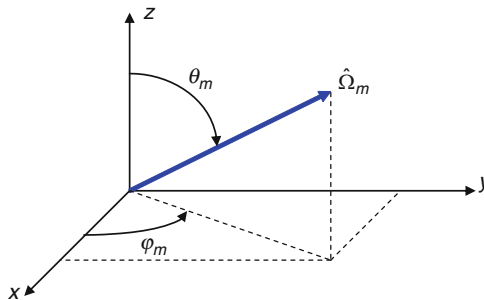
$$\phi_n^g = \frac{q_n^g}{\Sigma_{tr,n}^g} + \frac{1}{\Sigma_{tr,n}^g} \sum_m \frac{\Delta_{m,n}^g}{t'_{m,n}} \cdot \omega_m \quad (411)$$

The flux in (411) is assumed to be a constant value within a given mesh (i.e., the flat flux approximation).

5.3 Quadrature Sets

5.3.1 Introduction

The $d\hat{\Omega}$ in (408) represents the weight associated with each particular direction, $\hat{\Omega}$, which together make up the quadrature set. Here it should be pointed out that neutrons always travel in three dimensions. The problem being studied may be a one- or two-dimensional problem, but

**Figure 53**

Coordinates describing the direction of motion of a neutron

neutrons are always moving in all directions. The only detail that separates a one-dimensional problem from a two-dimensional or three-dimensional problem is the fact that there are material boundaries along only one axis of the coordinate system – the material regions all stretching to infinity along the remaining axes. Neutrons, however, are traveling at every imaginable angle to the one finite dimension. Therefore, we must model neutron motion in all three dimensions regardless of the dimensionality of the problem.

The direction of a neutron may be described using an azimuthal angle, φ , and a polar angle, θ . For all of our discussions, the azimuthal angle is measured from the positive x direction in the xy -plane of the problem. The polar angle is measured down from the positive z-direction, as illustrated in [Fig. 53](#).

To model neutron transport, we need to trace streaming paths (i.e., characteristics) across the system in a number of directions. We then solve for $\bar{\Phi}_n^g(\hat{\Omega}_m)$ along each characteristic, across each slab, n , in each direction, $\hat{\Omega}_m$, using [\(406\)](#), and calculate ϕ_n^g using [\(411\)](#). This is done best by choosing a set of azimuthal angles and a set of polar angles, which together will determine each unique direction of motion, as illustrated by the quadrature ball contained in [Fig. 54](#).

5.3.2 Azimuthal Angles

For lattice physics calculations, the azimuthal angles in the characteristics method are evenly spaced in the xy -plane of the problem. If we wish to model four azimuthal directions of motion, say, we would split the directions up evenly in the xy -plane such that the *boundaries* of motion occur at intervals calculated from the following expression:

$$\Delta\varphi = \frac{2\pi}{I} = \frac{2\pi}{4} = \frac{\pi}{2} \quad (412)$$

In this way, the azimuthal *boundaries* are located at angles: $\varphi_0 = 0$, $\varphi_1 = \pi/2$, $\varphi_2 = \pi$, $\varphi_3 = 3\pi/2$, and $\varphi_4 = 2\pi (= 0)$. The azimuthal *direction of motion* takes place through the center of two neighboring *boundaries*,

$$\bar{\varphi}_i = \frac{1}{2}(\varphi_{i-1} + \varphi_i) \quad (413)$$

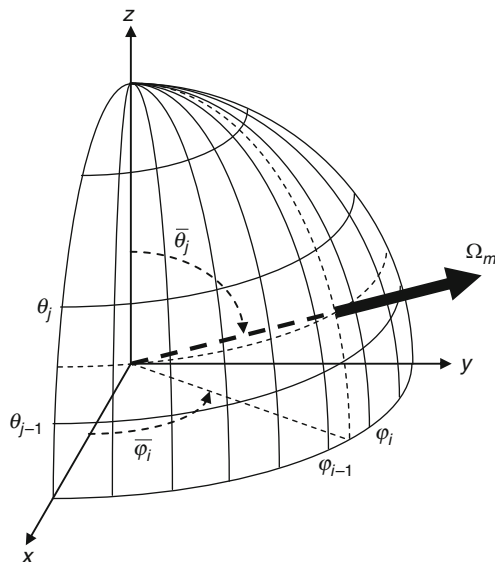


Figure 54
Typical quadrature ball

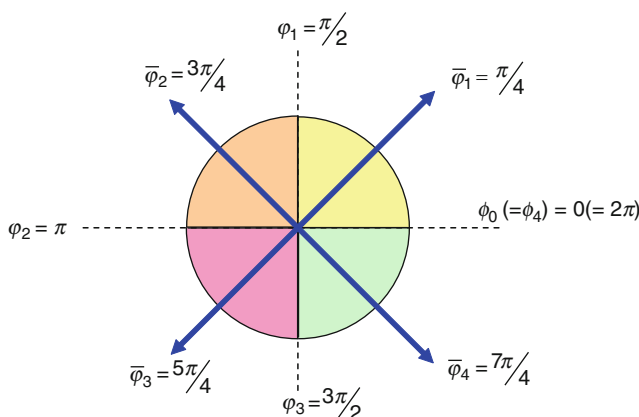


Figure 55
Azimuthal boundaries and angles of motion for $l = 4$

Each azimuthal direction of motion represents neutrons that travel at all angles in between the two surrounding azimuthal boundaries, as illustrated in Fig. 55. The neutrons that are modeled as traveling along the $\bar{\varphi}_1 = \pi/4$ characteristic, for instance, actually represent all neutrons traveling at angles between $\varphi_0 = 0$ and $\varphi_1 = \pi/2$. The neutrons that are modeled as traveling along the $\bar{\varphi}_2 = 3\pi/4$ characteristic represent all neutrons traveling at angles between $\varphi_1 = \pi/2$ and $\varphi_2 = \pi$. And so on, and so forth.

The weight associated with each azimuthal direction of motion is then given by

$$\omega_i = \frac{2\pi}{I} \quad (414)$$

where I is the total number of azimuthal directions of motion in the quadrature set.

5.3.3 Polar Angles

Choosing polar directions of motion is somewhat more complicated than choosing azimuthal directions of motion and is open to one of several different methods. We will discuss a couple of very simple methods and then make mention of the more complicated, more accurate methods, that are used in most lattice physics codes. The two methods to be discussed in this section are those associated with *equal weights* and *equal angles*.

Equal Weights Quadrature Set

To generate an *equal weights* quadrature set, we choose polar directions of motion that will result in all directions having equal polar weights (and, hence, equal weights in all directions of motion). The weights associated with each direction are calculated from the differential area on a unit sphere subtended by all boundaries for a given direction of motion, such as that illustrated in [Fig. 54](#). To calculate *equal weights* for all directions of motion, we proceed in the following manner: The differential area on a unit sphere associated with each direction, $\hat{\Omega}_m$, is given by

$$dA = \hat{\Omega}_m^2 \sin \bar{\theta}_m d\theta d\varphi \quad (415)$$

where the variables are defined in [Fig. 56](#). For a unit sphere, $|\hat{\Omega}| = 1$, and (415) can be expressed as

$$dA = \sin \bar{\theta}_m \cdot d\theta \cdot d\varphi \quad (416)$$

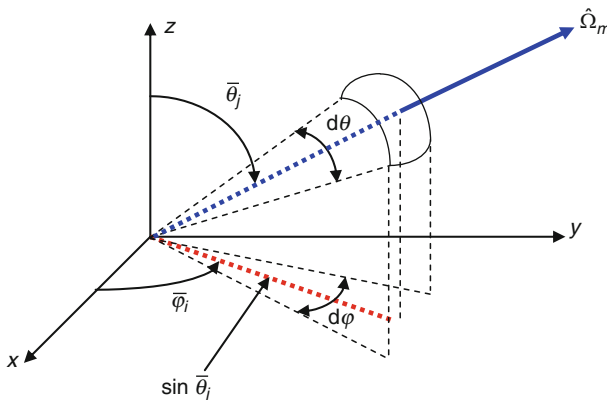


Figure 56

Differential surface area on a unit sphere

The total area associated with each direction, $\hat{\Omega}_m$, subtended on the unit sphere is then calculated as

$$A = \int_{\theta_{j-1}}^{\theta_j} \int_{\phi_{i-1}}^{\phi_i} dA = \int_{\theta_{j-1}}^{\theta_j} \int_{\phi_{i-1}}^{\phi_i} \sin \bar{\theta} \cdot d\theta \cdot d\phi = (\phi_i - \phi_{i-1})(\cos \theta_{j-1} - \cos \theta_j) \quad (417)$$

Since the spacing between azimuthal angles is $\Delta\varphi = \phi_i - \phi_{i-1}$, equal areas on the unit sphere require

$$A = \frac{4\pi}{I \cdot J} \quad (418)$$

where I is the total number of azimuthal angles, and J is the total number of polar angles. Rearranging (417) and setting it equal to (418) yields

$$(\cos \theta_{j-1} - \cos \theta_j) = \frac{4\pi}{I \cdot J \cdot \Delta\varphi} \quad (419)$$

From (412), $\Delta\varphi = 2\pi/I$ so the boundaries to the polar directions can be expressed as

$$\theta_j = \cos^{-1} \left\{ \cos \theta_{j-1} - \frac{2}{J} \right\} \quad (420)$$

where $\theta_0 = 0$.

We would like the polar direction of motion to pass through the centroid of the surface area subtended by the polar boundaries. Therefore, the polar directions of motion are calculated as

$$\bar{\theta}_j = \cos^{-1} \left\{ \frac{1}{2} (\cos \theta_j + \cos \theta_{j-1}) \right\} \quad (421)$$

The corresponding polar weights associated with the polar directions are the differential areas on the surface of the unit sphere created by the polar boundaries

$$\omega_j = \cos \theta_j - \cos \theta_{j-1} \quad (422)$$

Equal Angles Quadrature Set

For the *equal angles* quadrature set, we run through exactly the same scenario as we went through to generate the *equal weights* quadrature set. For the *equal angles* quadrature set, we are interested in distributing the angles uniformly in the polar direction, just as we have done with the azimuthal angles in the xy -plane of the problem. Without actually showing the mathematics associated with the derivation, the *equal angles* requirement leads us to make the following choices for the polar boundaries, polar directions of motion, and associated weights, respectively,

$$\Delta\theta = \frac{\pi}{J} \quad (423)$$

$$\bar{\theta}_j = \cos^{-1} \left\{ \frac{1}{2} (\cos \theta_j + \cos \theta_{j-1}) \right\} \quad (424)$$

$$\omega_j = \cos \theta_j - \cos \theta_{j-1} \quad (425)$$

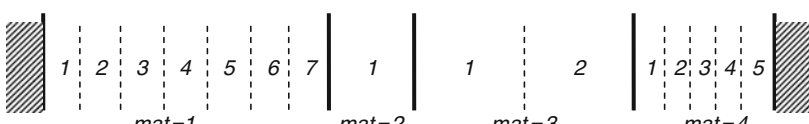
where the polar boundaries are distributed from $\theta_0 = 0$ to $\theta_J = \pi$. Note that, in the *equal weights* quadrature set, only the distribution of polar *boundaries* is different from that in the *equal areas* distribution. The equations used to calculate the angles of motion and associated weights are the same for the *equal angles* quadrature as they are for the *equal weights* quadrature.

This section has described the generation of two slightly different quadrature sets – *equal weights* and *equal angles*. Both of these quadrature sets are perfectly acceptable for use with the method of characteristics. Different quadrature sets will require a different number of polar angles to obtain the same accuracy. That is, the *equal weights* quadrature set places more emphasis on neutrons that stream at angles close to the plane of the problem. In contrast, the *equal angles* quadrature set places the same emphasis on neutrons streaming in any direction out of the plane of the problem. The *equal angles* quadrature set is preferable for three-dimensional transport problems because it distributes the angles symmetrically in all directions, similar to the way in which our azimuthal directions are distributed symmetrically in the xy -plane of the problem. The *equal weights* quadrature set is preferable for one- and two-dimensional problems because angles are weighted toward the plane of motion.

For one- and two-dimensional problems, better distributions of angles are generated using Legendre and Gaussian quadratures. These quadrature sets will be discussed later in this section, once we reach the subject of two-dimensional applications. For now, we can say that the MoC problem reduces to tracing characteristics across the system at several angles, along each of which we will solve the transport equation. For the cases being described presently, we will focus solely on systems where all sources are isotropic and all cross sections have been transport-corrected such that scattering can be treated mathematically as being isotropic.

5.4 Geometry Routine

5.4.1 Introduction

The first step we take in writing a computer code to solve the characteristics form of the transport equation is to lay down the streaming paths along which our neutrons will travel. In order to do this, we must first assign material IDs to each region of the problem and then subdivide each material region into a suitable number of mesh that represent the flat source regions. This is illustrated in  Fig. 57.

In an arrangement such as this, we might hold data in arrays structured by both mesh and region. That is, the array that holds the scalar flux in each mesh of the problem, say, might be structured as flux (mesh, region). Alternatively, mesh could be numbered sequentially beginning from the left side of the problem and moving to the right. This approach is depicted in

 **Figure 57**
Example of flat source mesh and material numbers

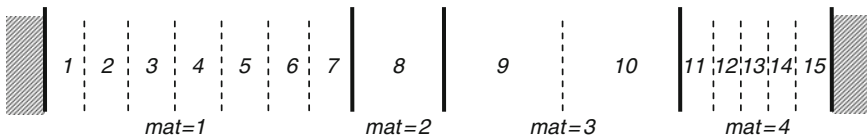


Figure 58
Alternative example of flat source mesh and material numbers

► *Fig. 58.* The scalar flux in each mesh would be held in an array such as flux (mesh). Then we would need another array, material (mesh), which defined the material for each mesh. Either approach is acceptable. At one time, when memory was scarce, we would choose the most economical approach, that is, the one that used the least amount of memory. Nowadays, though, memory is plentiful and it is more important to choose the most intuitive approach, that is, the one that provides the most clarity to the programmer and especially to subsequent programmers who need to decipher the original programmer's work.

To begin our application of the MoC, we first lay down the paths in the azimuthal direction only (i.e., in the xy -plane of the problem). Once we calculate all the t' s in (411) – through all mesh of the system, at all azimuthal angles of motion – we can ratio each of the path lengths with the sine of the various polar angles to obtain the true track length at each of the directions of motion, $\hat{\Omega}_m$.

So, we have some system of slabs (i.e., mesh) with boundaries at $\{x_0, x_1, x_2, \dots, x_N\}$, where N is the total number of slabs in the problem. In each of these regions we have a set of constant cross sections and, possibly, an external source that is also spatially constant across the slab region.

Now we choose the number of azimuthal angles and polar angles at which we would like to solve the transport equation. Let I be the total number of azimuthal angles we choose and let J be the total number of polar angles we choose. We calculate the azimuthal boundaries, φ_i 's, to the quadrature set using (412), and we calculate the azimuthal directions of motion, $\bar{\varphi}_i$'s, using (413). The weights associated with each azimuthal direction of motion, w_i 's, are calculated using (414).

5.4.2 Neutron Streaming and Symmetry in Slab Geometry

There are a couple of points that can be made here regarding neutron motion in the xy -plane of the problem and out of the xy -plane of the problem.

To begin with, when we lay down tracks for the neutrons to stream along, we lay them down such that each track has a counter-track in the opposite direction. This is a requirement in order to model perfectly reflecting (i.e., mirror symmetric) boundary conditions. For instance, if we choose to lay four tracks down in the azimuthal direction, we have tracks at $\bar{\varphi}_1 = \pi/4$, $\bar{\varphi}_2 = 3\pi/4$, $\bar{\varphi}_3 = 5\pi/4$, and $\bar{\varphi}_4 = 7\pi/4$. The $\bar{\varphi}_3 = 5\pi/4$ track is in the opposite direction to the $\bar{\varphi}_1 = \pi/4$ track, and the $\bar{\varphi}_4 = 7\pi/4$ track is in the opposite direction to the $\bar{\varphi}_2 = 3\pi/4$ track. Since neutrons are indifferent to the direction at which they stream along a given track, we may – if we so desire – lay down tracks only between $0 \leq \bar{\varphi} \leq \pi$ in the problem and allow neutrons to travel in both directions along each track. This will help simplify our ray-tracing routine.

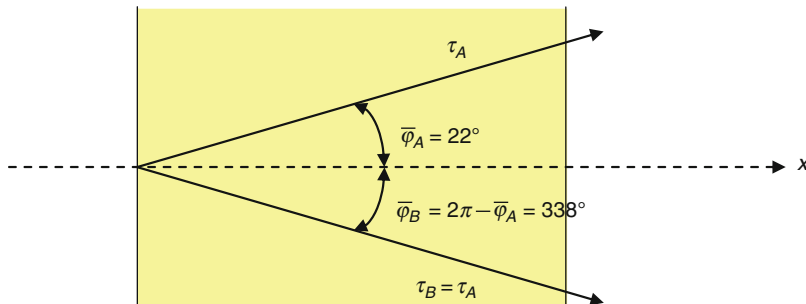


Figure 59
Neutrons moving at equivalent azimuthal angles

Secondly, in a one-dimensional problem such as a slab problem, neutrons travel at azimuthal angles between $0 \leq \bar{\varphi} \leq \pi$ in an identical fashion to the way in which they travel at azimuthal angles between $\pi \leq \bar{\varphi} \leq 2\pi$, as illustrated in [Fig. 59](#).

We may take advantage of these observations within our geometry routine, if we care to, by only having to trace tracks over our slab system at azimuthal angles between $0 \leq \bar{\varphi} \leq \pi$. If we choose to do this, we must compensate for the neglected directions by modifying our azimuthal weights, to wit,

$$\omega_i = 2 \times \frac{2\pi}{I} = \frac{4\pi}{I} \quad (426)$$

where I still represents the number of azimuthal directions of motion distributed between $0 \leq \bar{\varphi} \leq 2\pi$.

Lastly, in one- and two-dimensional geometries, neutrons travel at polar angles between $0 \leq \bar{\theta} \leq \pi/2$ in an identical fashion to the way in which they travel at polar angles between $\pi/2 \leq \bar{\theta} \leq \pi$. We may take advantage of this point in a manner similar to the azimuthal symmetry condition described for slab geometry. That is, we can trace tracks in the upper hemisphere of the problem, only, and modify the polar weights to account for symmetry in the lower hemisphere of the problem

$$\omega_j = 2(\cos \theta_j + \cos \theta_{j-1}) \quad (427)$$

where J now represents the total number of polar directions between $0 \leq \bar{\theta} \leq \pi/2$.

5.4.3 Ray Tracing in Slab Geometry

We now have a set of azimuthal angles, $\{\bar{\varphi}_1, \bar{\varphi}_2, \bar{\varphi}_3, \dots, \bar{\varphi}_I\}$, which are distributed between $0 \leq \bar{\varphi} \leq 2\pi$ (although we will only trace rays between $0 \leq \bar{\varphi} \leq \pi$), and associated weights, $\{\omega_1, \omega_2, \omega_3, \dots, \omega_I\}$, which are all equal and sum to 2π . We know, from the problem definition, the widths of all N slabs in the system, $\{\Delta x_1, \Delta x_2, \Delta x_3, \dots, \Delta x_N\}$. We may determine the track lengths through each slab, at each azimuthal angle, in the xy -plane of the problem,

$$t_{i,n} = \frac{\Delta x_n}{\cos \bar{\varphi}_i} \quad (428)$$

where each direction carries with it a weight of ω_i .

Once we have all the track lengths traced through all the slabs at all the desired azimuthal angles, and we have a weight associated with each of the azimuthal directions of motion, we can generate the polar angles of neutron motion, which will complete our quadrature set. Once again, as with the generation of the azimuthal angles, we take advantage of the symmetry of the problem and generate angles only between $0 \leq \bar{\theta} \leq \pi/2$. Each direction represents neutrons moving in both the upper and lower hemispheres of the problem. We generate our set of polar angles, $\{\bar{\theta}_1, \bar{\theta}_2, \bar{\theta}_3, \dots, \bar{\theta}_J\}$, and associated weights, $\{\omega_1, \omega_2, \omega_3, \dots, \omega_J\}$, based on either the *equal weights or equal angles* equations – or perhaps from a Legendre or Gaussian quadrature. The polar weights sum to 2.

With our polar angles of motion, we can ratio the track lengths from the plane of the problem into the upper hemisphere

$$t_{i,j,n} = \frac{t_{i,n}}{\sin \bar{\theta}_j} \quad (429)$$

We now have our quadrature set and our track lengths, which have been measured in the xy -plane of the problem and ratioed to their proper lengths in the polar direction. Now we can begin to solve the transport equation for the flux distribution.

5.5 Solution to the Characteristics Equation

5.5.1 Introduction

We have, really, only one equation to solve, namely,

$$\Phi_{\text{out}} = \Phi_{\text{in}} e^{-\Sigma_{tr} t} + \frac{q}{4\pi\Sigma_{tr}} (1 - e^{-\Sigma_{tr} t}) \quad (430)$$

which is to be solved using the assumptions mentioned before and restated below:

1. All scattering is transport corrected and can be modeled as isotropic
2. All sources are inherently isotropic
3. The source and, hence, scalar flux is constant within a mesh (i.e., flat flux approximation).

[Equation \(430\)](#) represents two physical processes: $\Phi_{\text{in}} e^{-\Sigma_{tr} t}$ are the number of neutrons that stream across the mesh without suffering a collision; and $q \cdot (1 - e^{-\Sigma_{tr} t}) / 4\pi\Sigma_{tr}$ are the number of neutrons that are picked up along the track from scatterings and sources as the track crosses the mesh. Together, these two processes determine the number of neutrons that reach the end of the track on the other side of the mesh.

[Equation \(430\)](#) is very simple to solve. For any problem we analyze, we will always know the cross sections beforehand. These will be the cross sections that are created from the energy condensation scheme (i.e., if one exists for the lattice physics code). In our geometry routine, we have already calculated the ratioed track lengths crossing every mesh, $t_{i,j,n}$. All we need to know in order to solve [\(430\)](#) is the angular flux entering the mesh at the beginning of the track, and the total source term within the mesh – Φ_{in} and q , respectively.

5.5.2 Initialization of the Flux

The need to know Φ_{in} and q brings us to the flux initialization. For lack of a better choice, we may simply guess at what Φ_{in} and q are everywhere. This constitutes our initial flux guess that will be used to start solving (430). We set $\phi = 1.0$ in every energy group, every mesh of the problem. For the Φ_{in} 's, we only need to guess these values along one boundary of the slab problem since Φ_{out} will become Φ_{in} as we move along each track. So, a good guess for Φ_{in} is to set it equal to $\Phi_{in} = 1/4\pi$ in all groups, in all directions, along one edge of the slab problem.

Now we may calculate the $\Phi_{in} e^{-\Sigma_{ir} t}$ part of the Φ_{out} equation, leaving us to determine the q part.

5.5.3 Calculating the Source Term

The total angular source term is a combination of three separate sources:

1. Scattering: $Q_s(\vec{r}, E, \hat{\Omega}) = \int \int \Sigma_s(\vec{r}, E' \rightarrow E, \hat{\Omega}' \rightarrow \hat{\Omega}) \Phi(\vec{r}, E', \hat{\Omega}') dE' d\hat{\Omega}'$
2. Fission: $Q_f(\vec{r}, E, \hat{\Omega}) = \chi(\vec{r}, E) \int v \Sigma_f(\vec{r}, E', \hat{\Omega}) \phi(\vec{r}, E') dE'$
3. Fixed external: $Q_{ext}(\vec{r}, E, \hat{\Omega}) = S(\vec{r}, E, \hat{\Omega})$

Scattering Source

As mentioned earlier, all scattering is assumed isotropic for our purposes. Anisotropic scattering effects are accounted for by transport-correcting the self scattering and total cross sections. By doing so, we can express the scattering cross section as

$$\Sigma_s(\vec{r}, E' \rightarrow E, \hat{\Omega}' \rightarrow \hat{\Omega}) = \frac{1}{4\pi} \Sigma_s(\vec{r}, E' \rightarrow E) \quad (431)$$

Then the integral over angle in the scattering source term becomes

$$\begin{aligned} Q_s(\vec{r}, E, \hat{\Omega}) &= \int \int \Sigma_s(\vec{r}, E' \rightarrow E, \hat{\Omega}' \rightarrow \hat{\Omega}) \Phi(\vec{r}, E', \hat{\Omega}') dE' d\hat{\Omega}' \\ &= \frac{1}{4\pi} \int \Sigma_s(\vec{r}, E' \rightarrow E) \phi(\vec{r}, E') dE' \end{aligned} \quad (432)$$

In multigroup theory, where the entire range of energies is discretized into a number of energy groups, the scattering kernel is defined as elements which make up a matrix

$$Q_{s,n}^g = \frac{1}{4\pi} \int \Sigma_s(\vec{r}, E' \rightarrow E) \phi(\vec{r}, E') dE' = \frac{1}{4\pi} \sum_{g'} \Sigma_{s,n}^{g' \rightarrow g} \phi_n^{g'} \quad (433)$$

Here, the quantity $\Sigma_{s,n}^{g' \rightarrow g} \phi_n^{g'}$ defines the total number of neutrons within the mesh n , within energy group g' , which have scattering collisions and are scattered into an energy within group g – our energy of interest. Out of all the neutrons that are scattered into energy group g , only $1/4\pi$ of them are traveling in direction Ω – our direction of interest.

Fission Source

For criticality problems, the only source of fresh neutrons are those born into the fast energy groups of the problem via fission. Neutrons born via fission are assumed to be distributed

isotropically (a good assumption) and integration of the angular fission source over all angles reduces to

$$\begin{aligned} Q_f(\vec{r}, E, \hat{\Omega}) &= \chi(\vec{r}, E) \int v \Sigma_f(\vec{r}, E', \hat{\Omega}) \phi(\vec{r}, E') dE' \\ &= \chi(\vec{r}, E) \int \frac{v \Sigma_f(\vec{r}, E')}{4\pi} \phi(\vec{r}, E') dE' \end{aligned} \quad (434)$$

In multigroup form,

$$Q_{f,n}^g = \chi(\vec{r}, E) \int \frac{v \Sigma_f(\vec{r}, E')}{4\pi} \phi(\vec{r}, E') dE' = \chi_n^g \sum_{g'} \frac{v \Sigma_{f,n}^{g'}}{4\pi} \phi_n^{g'} \quad (435)$$

Here, we sum up all the fissions that occur in mesh n per unit volume,

$$\sum_{g'} v \Sigma_{f,n}^{g'} \phi_n^{g'} \quad (436)$$

and distribute those neutrons within the various fast energy groups using the fission spectrum, χ_n^g , which can be unique for each fuel material in the problem. The fission spectrum is normalized to unity,

$$\sum_{g'} \chi_n^{g'} = 1.0 \quad (437)$$

The fission neutrons are then distributed isotropically by dividing the total scalar fission source by 4π . [Equation \(435\)](#) can be expressed as a production kernel, $\Sigma_{p,n}^{g' \rightarrow g}$, in a manner similar to the scattering kernel,

$$Q_{f,n}^g = \chi_n^g \sum_{g'} \frac{v \Sigma_{f,n}^{g'}}{4\pi} \phi_n^{g'} = \sum_{g'} \frac{\Sigma_{p,n}^{g' \rightarrow g}}{4\pi} \phi_n^{g'} \quad (438)$$

where

$$\Sigma_{p,n}^{g' \rightarrow g} = \chi_n^g \sum_{g'} v \Sigma_{f,n}^{g'} \quad (439)$$

External Source

For an external source of neutrons with energy E , located at position \vec{r} , with total (scalar) strength $s(\vec{r}, E)$, we distribute the neutrons isotropically such that

$$Q_{ext}(\vec{r}, E, \hat{\Omega}) = \frac{s(\vec{r}, E)}{4\pi} \quad (440)$$

or in multigroup form

$$Q_{ext,n}^g = \frac{s_n^g}{4\pi} \quad (441)$$

Total Source for a Non-Multiplying System

For a non-multiplying system, there is no source due to fission. For such a system, we are interested only in the flux distribution and not the multiplication factor. This is the type of problem solved when determining a gamma distribution. The external source in such instances is the gamma source resulting from the neutron flux distribution and contains contributions from neutron slowing down (scattering), from the fission process, and from the decay of fission products from an excited state to a more stable state. The final total (scalar) source distribution for a non-multiplying system would be expressed as

$$q_n^g = q_{s,n}^g + q_{ext,n}^g = \sum_{g'} \Sigma_{s,n}^{g' \rightarrow g} \phi_n^{g'} + s_n^g \quad (442)$$

Total Source for a Multiplying System

For a multiplying system, we may or may not have an external source. If we have an external source, then we are concerned with a subcritical system where the total source term is expressed as

$$q_n^g = q_{s,n}^g + q_{f,n}^g + q_{ext,n}^g = \sum_{g'} \left(\Sigma_{s,n}^{g' \rightarrow g} + \Sigma_{p,n}^{g' \rightarrow g} \right) \phi_n^{g'} + s_n^g \quad (443)$$

Lattice physics applications consist of multiplying systems with no external sources. For these types of problems the total scalar source is expressed as

$$q_n^g = q_{s,n}^g + q_{f,n}^g = \sum_{g'} \left(\Sigma_{s,n}^{g' \rightarrow g} + \frac{\Sigma_{p,n}^{g' \rightarrow g}}{k^\infty} \right) \phi_n^{g'} \quad (444)$$

which is similar to the expression of the source in (443) with the external source having been removed from the equation. The parameter k^∞ in (444) is the infinite multiplication factor and, for a system with no neutron leakage, is equal to the volume integrated number of neutrons born through fission divided by the volume integrated number of neutrons absorbed in the system,

$$k^\infty = \frac{\sum_n \sum_g \nu \Sigma_{f,n}^g \phi_n^g V_n}{\sum_n \sum_g \Sigma_{a,n}^g \phi_n^g V_n} \quad (445)$$

where V_n is the volume of each mesh in the system.

Physically, (445) describes a mesh, n , where there are $\sum_g \nu \Sigma_{f,n}^g \phi_n^g$ fission neutrons being born *per unit volume*. To calculate the total number of fission neutrons born in mesh n , we simply multiply by the volume of the mesh. This is only possible because we have assumed that the scalar flux is constant across mesh n , as are the cross sections. In a similar manner, there are $\sum_g \Sigma_{a,n}^g \phi_n^g$ neutrons absorbed in mesh n *per unit volume*. To calculate the total number of neutrons absorbed in mesh n , we once again multiply by the volume of the mesh. As before, this is possible because we have assumed that the scalar flux and the cross sections are constant across the volume. Mathematically, k^∞ is used to stabilize the source of neutrons from one flux iteration to the next.

So, now we can calculate q for each slab in the problem and we have all the information we need to solve the transport equation

$$\Phi_{\text{out}} = \Phi_{\text{in}} e^{-\Sigma_{tr} t} + \frac{q}{4\pi\Sigma_{tr}} (1 - e^{-\Sigma_{tr} t}) \quad (446)$$

5.5.4 Boundary Conditions

Boundary conditions in the characteristics method are applied to the angular flux only. There are two types of boundary conditions we will examine for slab geometry – periodic and reflective. Each of these will be discussed below. We will not examine vacuum boundary conditions because they are not applied in single assembly lattice physics analysis, although they can be applied when generating nodal discontinuity factors for water reflector regions. Such applications, however, are beyond the scope of this chapter.

Periodic Boundary Conditions

Periodic boundary conditions require the value of the angular flux in group g , in direction $(\bar{\varphi}_i, \bar{\theta}_j)$, entering the western-most surface of the system of slabs ($n = 1$) to be equal to the value of the angular flux in group g , moving in direction $(\bar{\varphi}_i, \bar{\theta}_j)$, leaving the eastern-most surface of the system of slabs ($n = N$). This is illustrated in [Fig. 60](#) and expressed mathematically as

$$\begin{aligned} \Phi_{\text{in},n=1}^g(\bar{\varphi}_i, \bar{\theta}_j) &= \Phi_{\text{out},n=N}^g(\bar{\varphi}_i, \bar{\theta}_j) && \text{for } 0 \leq \bar{\varphi}_i \leq \pi/2 \\ \Phi_{\text{in},n=N}^g(\bar{\varphi}_i, \bar{\theta}_j) &= \Phi_{\text{out},n=1}^g(\bar{\varphi}_i, \bar{\theta}_j) && \text{for } \pi/2 \leq \bar{\varphi}_i \leq \pi \end{aligned} \quad (447)$$

Reflective Boundary Conditions

Reflective boundary conditions require a fraction, α , of the value of the angular flux hitting the boundary of the system along the characteristic traveling in direction $\bar{\varphi}_i$ to be reflected back along the companion characteristic traveling in direction $\pi - \bar{\varphi}_i$. This is illustrated in [Fig. 61](#) and expressed mathematically as

$$\Phi_{\text{in},n=N}^g(\bar{\varphi}'_i, \bar{\theta}'_j) = \alpha \cdot \Phi_{\text{out},n=N}^g(\bar{\varphi}_i, \bar{\theta}_j) \quad (448)$$

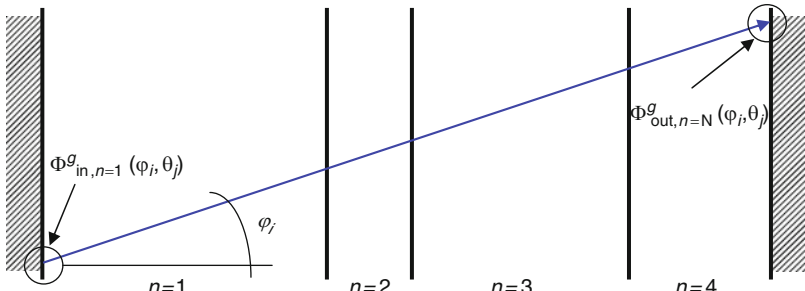


Figure 60

Periodic boundary condition in slab geometry

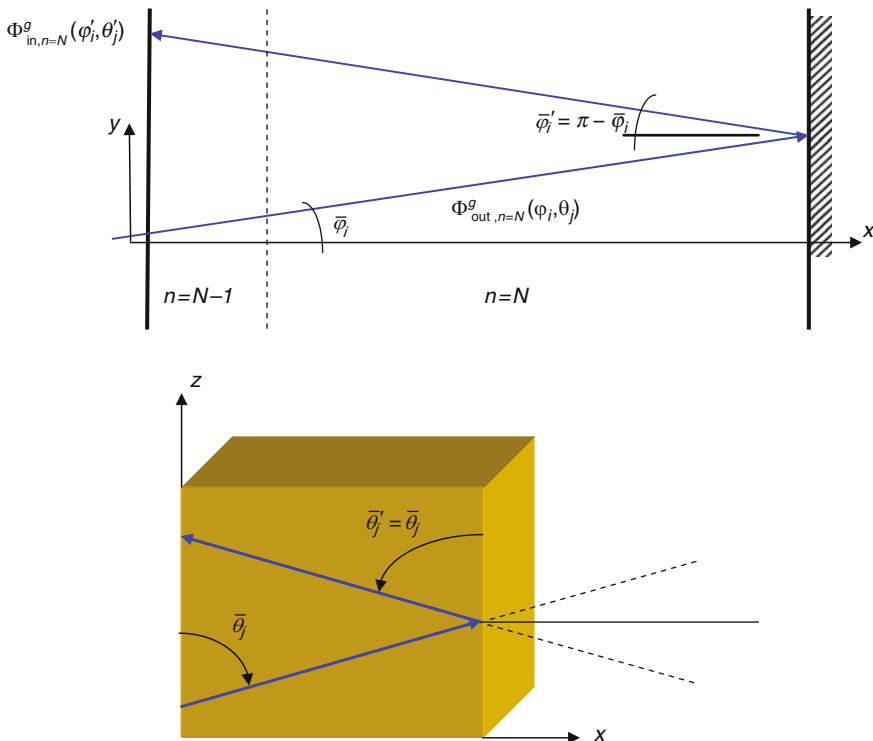


Figure 61
Reflective boundary condition in slab geometry

where the primes on the azimuthal and polar angles represent the reflective counterparts to the incident angles. For $\alpha = 1.0$, we have perfect reflexion. For $\alpha = 0.0$, we have a perfect vacuum condition.

For the reflective boundary condition, we must make sure we have distributed the azimuthal angles in such a way that there exists a reflective counterpart for each incident direction. For the equally distributed set of azimuthal angles we use in our implementation of the method of characteristics, this criterion is satisfied automatically. For I azimuthal directions distributed evenly between $0 \leq \bar{\varphi}_i \leq \pi$, the reflected counterpart to angle i' is angle $i' = I - i + 1$.

5.5.5 Convergence

Convergence of the Angular Flux

For each energy group, g , we have an initial value for the inward flux along the surface of the problem, in azimuthal direction i , polar direction j , which is represented by $\Phi_{\text{in},n=1}^g(\bar{\varphi}_i, \bar{\theta}_j)$. We march along the track until we reach the opposite boundary of the slab system, at which point we have an outwardly directed angular flux, $\Phi_{\text{out},n=N}^g(\bar{\varphi}_i, \bar{\theta}_j)$. This then becomes the inward value for the angular flux in the reflected (or periodic) direction, using (448). This replaces the

previous value for the inward directed angular flux in direction $(\bar{\varphi}'_i, \bar{\theta}'_j)$. The difference in the two values – the value of the angular flux at the end of the previous iteration, and the value of the angular flux at the end of the present iteration – is a measure of how close we are to the true solution to the problem. When the difference between the two angular flux values is within a certain criterion, ε , for all inward directions, along both surfaces of the slab system, the angular flux for that particular energy group is assumed to be converged,

$$\left| \frac{\Phi_{\text{new,in},n}^g(\bar{\varphi}_i, \bar{\theta}_j) - \Phi_{\text{old,in},n}^g(\bar{\varphi}_i, \bar{\theta}_j)}{\Phi_{\text{new,in},n}^g(\bar{\varphi}_i, \bar{\theta}_j)} \right| < \varepsilon \quad (449)$$

where $n = 1$ represents the western-most surface to the slab system and $n = N$ represents the eastern-most surface to the slab system. (449) must hold true for all i 's and j 's in order to satisfy a fully converged solution to the problem in a given energy group.

Convergence of the Scalar Flux

At the end of each inner iteration, in addition to testing for convergence of the angular flux, the scalar flux is also tested for convergence. The same principle applies here as for the angular flux.

We begin the iteration with some value for the scalar flux in group g , $\phi_n^g(\text{old})$. This value for the scalar flux is used to calculate the source term prior to solving for the new flux distribution. With the source distribution frozen, we solve for a new scalar flux distribution, $\phi_n^g(\text{new})$. The new scalar flux is calculated by solving the equation

$$\phi_n^g(\text{new}) = \frac{q_n^g}{\Sigma_{tr,n}^g} + F_n^g \quad (450)$$

where

$$q_n^g = \sum_{g' < g} \left(\Sigma_{s,n}^{g' \rightarrow g} + \frac{\Sigma_{p,n}^{g' \rightarrow g}}{k^\infty} \right) \phi_n^{g'}(\text{new}) + \sum_{g' \geq g} \left(\Sigma_{s,n}^{g' \rightarrow g} + \frac{\Sigma_{p,n}^{g' \rightarrow g}}{k^\infty} \right) \phi_n^{g'}(\text{old}) \quad (451)$$

$$F_n^g = \sum_j \sum_i \frac{\Delta_{i,j,n}^g \cdot \omega_i \cdot \omega_j}{\Sigma_{tr,n}^g t_{i,j,n}} \quad (452)$$

In (452), $\Delta_{i,j,n}^g = \Phi_{\text{in},n}^g(\bar{\varphi}_i, \bar{\theta}_j) - \Phi_{\text{out},n}^g(\bar{\varphi}_i, \bar{\theta}_j)$ is the change in the angular flux value along the characteristic as it passes through a mesh.

The difference between the old and new value of the scalar flux will approach zero as the solution converges. Typically, as in the case of the angular flux, convergence is declared when the following statement is satisfied in every mesh:

$$\left| \frac{\phi_n^g(\text{new}) - \phi_n^g(\text{old})}{\phi_n^g(\text{new})} \right| < \varepsilon \quad (453)$$

Convergence of the Multiplication Factor

Prior to starting an outer iteration, the multiplication factor for the old flux distribution is calculated, k^∞ . As the fission source distribution converges, so too will the multiplication factor.

From one iteration to the next, we check for convergence of the multiplication factor

$$\left| \frac{k^\infty(\text{new}) - k^\infty(\text{old})}{k^\infty(\text{new})} \right| < \varepsilon \quad (454)$$

Equation (454) will always be satisfied if both (449) and (453) are satisfied. That is, the multiplication factor will always be converged if the flux distribution is converged. For this reason, satisfying (454) is relatively irrelevant.

5.5.6 Accelerating the Flux Convergence

For large problems, the number of iterations needed for convergence may become extreme if the initial flux guess is far from the converged solution. In order to reduce the number of iterations needed to satisfy convergence requirements, we would like to accelerate the convergence rate. We wish to accelerate the energy convergence as well as the spatial convergence. This section presents two methods that can be applied to accelerate the convergence of the scalar flux.

Energy Acceleration

Following completion of an outer iteration, a fundamental mode rebalancing of the group flux distribution is performed in order to properly normalize the flux and ensure neutron conservation. The fundamental mode calculation is performed on an equivalent homogeneous system using flux and volume weighted cross sections from the heterogeneous calculation. The resulting group flux values from the homogeneous calculation are then used to rebalance the magnitude of the heterogeneous group flux values. The description of the fundamental mode rebalances calculation for the MoC is identical to that found in  Sect. 4 for the rebalance applied to the coupling calculation.

The equation to be solved here is equivalent to (310),

$$\phi_{\text{FM}}^g = \frac{\bar{q}^g}{\bar{\Sigma}_r^g} \quad (455)$$

where the source term does not include self scattering and the fission source is normalized to unity by the eigenvalue. Hence,

$$\bar{q}^g = \sum_{g' \neq g} \bar{\Sigma}_s^{g' \rightarrow g} \phi_{\text{FM}}^{g'} + \frac{\bar{\chi}^g}{k^\infty} \sum_{g'} v \bar{\Sigma}_f^{g'} \phi_{\text{FM}}^{g'} \quad (456)$$

The flux and volume weighted cross sections for the fundamental mode calculation are calculated from

$$\bar{\Sigma}_x^g = \frac{\sum_i \Sigma_{x,i}^g \phi_i^g V_i}{\sum_i \phi_i^g V_i} \quad (457)$$

where x represents the desired reaction.

For problems exhibiting no neutron leakage across the boundaries (i.e., perfect reflection along all boundaries), the multiplication factor in (457) can be calculated directly as the ratio of neutron production in the system to neutron destruction, as in (445),

$$k^\infty = \frac{\sum_{g'} v \bar{\Sigma}_f^{g'} \phi_{\text{FM}}^{g'}}{\sum_{g'} \bar{\Sigma}_a^{g'} \phi_{\text{FM}}^{g'}} \quad (458)$$

If we normalize the flux in such a way that there is only one neutron being absorbed in the entire problem, then the denominator to (458) becomes unity and the multiplication factor is simply the sum of all neutrons born through fission,

$$k^\infty = \sum_{g'} v \bar{\Sigma}_f^{g'} \phi_{\text{FM}}^{g'} \quad (459)$$

Plugging (459) into (456) yields the final expression for the fundamental mode homogeneous source

$$\bar{q}^g = \sum_{g'} \bar{\Sigma}_s^{g' \rightarrow g} \phi_{\text{FM}}^{g'} + \bar{\chi}^g \quad (460)$$

Due to up-scattering in the thermal energy groups, the solution to (455) defines an iterative process and the fundamental mode equation is solved directly, with no acceleration. Following the solution to (455), the scalar flux distribution from the solution to (411) is scaled using the rebalance factors,

$$\hat{\phi}_n^g = \phi_n^g \cdot \frac{\phi_{\text{FM}}^g}{\sum_n \phi_n^g V_n} \quad (461)$$

where the summation in (461) is over all mesh in the problem.

Spatial Acceleration

The scalar flux can be accelerated spatially using a simple coarse mesh rebalance (CMR) throughout the system. This is especially important since the characteristics equations are not based on a neutron balance and solution to the equations does not necessarily conserve neutrons from one iteration to the next. Coarse mesh are determined by material region. Each material region may be subdivided into smaller mesh to improve the accuracy of the flat flux approximation. The CMR is performed to ensure neutron conservation within each material region – or coarse mesh – of the problem.

The balance equation to be solved in each coarse mesh is defined as

$$\left[\sum_{m \in n} \Sigma_{r,m}^g \phi_m^g V_m + \sum_{s \in n} J_{\text{out},s,n}^g \right] \cdot f_n^g = \sum_{m \in n} q_m^g V_m + \sum_{s' \in n'} J_{\text{in},s',n'}^g \cdot f_{n'}^g \quad (462)$$

where m represents the mesh subdivisions within a coarse mesh material region, n ; s represents the surfaces to the coarse mesh, n ; s' represents the surfaces to the neighboring coarse mesh, n' . The variables in (462) are illustrated in  Fig. 62.

The currents must be accumulated as the inner iterations are performed. The contribution to the outgoing current along a coarse mesh surface is calculated as

$$J_{\text{out},s,n}^g = \sum_j \sum_i \sum_{k_m} \Phi_{k_m, i, j}^g \cdot \omega_i \cdot \omega_j \cdot |\cos \varphi_i \cdot \sin \theta_j| \quad (463)$$

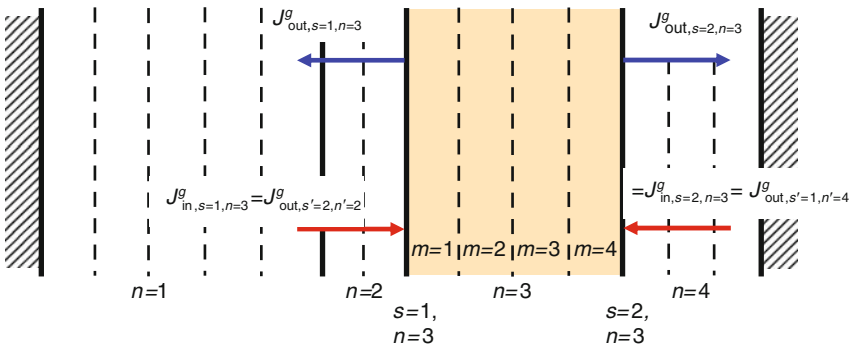


Figure 62
Variables for the coarse mesh rebalance calculation

where k_m represents a track segment crossing mesh m , and the accumulation is only performed if mesh m is along the edge of coarse mesh n .

Equation (462) is solved iteratively for the balance factors, f_n^g . Once the balance factors are determined, the scalar flux is updated,

$$\phi_m^g = \phi_m^g \cdot f_n^g \quad (464)$$

for all mesh subdivisions, m , within coarse mesh region n . The CMR calculation is performed at the end of each inner iteration. Note that the CMR method is not inherently stable and the acceleration scheme can diverge or oscillate when mesh become optically very thin or very thick. The interested reader is directed to refer to, for instance, Reed (1971), Yamamoto et al. (2004), Cefus and Larsen (1990), Adams and Larsen (2002), Cho and Park (2003), and Lee and Downar (2003) for more information on convergence issues associated with acceleration techniques.

5.6 Cylindrical Geometry

5.6.1 Introduction

So far, only slab geometry has been discussed. The remaining one-dimensional geometries are cylindrical and spherical. For the characteristics method, spherical geometry is a special case of cylindrical geometry. Cylindrical geometry also forms the basis for moving on to complex geometries in two dimensions. Therefore, cylindrical geometry will be discussed in this section as a prelude to the discussion of two-dimensional analysis.

For our one-dimensional geometry, we consider a cylinder that is infinite in the z -direction and may contain many annular regions. If we use the coordinate system shown in Fig. 63, then the azimuthal angles of motion are constructed from the radius vector, \vec{R} , and a track parallel with the x -axis and perpendicular to the y -axis. The two lines are located such that the radius vector intersects the track at the outer radius of the cylinder.

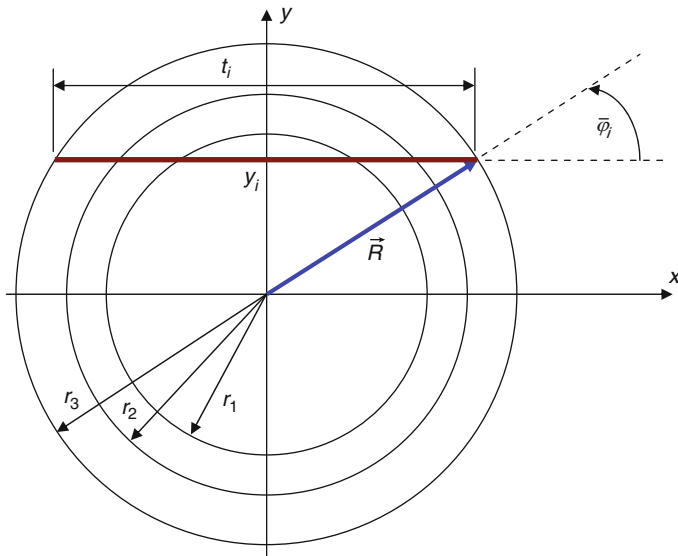


Figure 63
Coordinates used for MoC cylindrical geometry

The intersection of the track occurs at some height along the y -axis. This height, or y -intersection, may be calculated by equating the equations of the two lines

$$\vec{R}^2 = x_i^2 + y_i^2 \text{ radius of outer annulus} \quad (465)$$

$$t_i = 2\vec{R} \cos \bar{\varphi}_i \quad (466)$$

where t_i is the track length spanned across the cylinder by the characteristic associated with azimuthal angle $\bar{\varphi}_i$.

We know \vec{R} from the problem definition, and we have chosen $\bar{\varphi}_i$ from our quadrature set. The value of x_i is the point along the x -axis at which the track intersects the outer radius of the cylinder and is easily calculated as

$$x_i = \vec{R} \cos \bar{\varphi}_i = \frac{1}{2} t_i \quad (467)$$

and the y -intercept is calculated as

$$y_i = \vec{R} \sin \bar{\varphi}_i \quad (468)$$

From (468), if $r_n > y_i$, then track t_i passes through annulus n , where r_n is the radius of annulus n .

$$r_n^2 = x_n^2 + y_i^2 \quad \text{or} \quad x_n = \sqrt{r_n^2 - y_i^2} \quad (469)$$

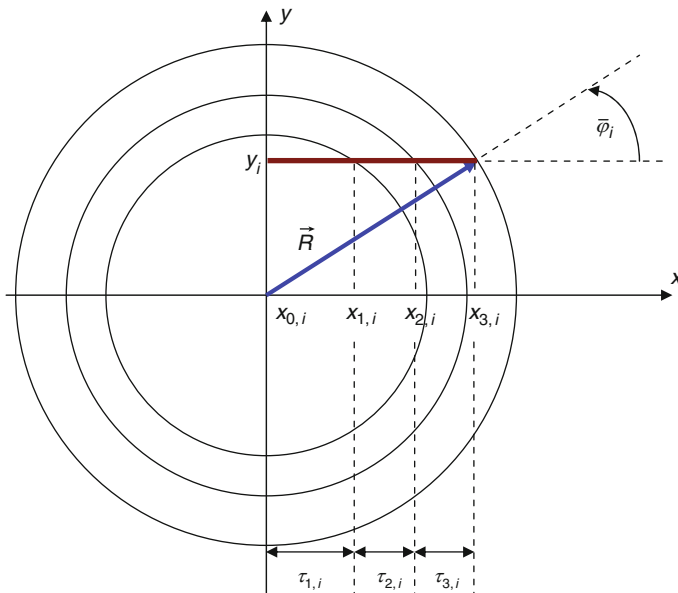


Figure 64
Track segments along a single characteristic

and track segment $\tau_{n,i}$ at azimuthal angle i , passing through region n , may be calculated as

$$\tau_{n,i} = x_n - x_{n-1} \quad (470)$$

This is illustrated in [Fig. 64](#).

5.6.2 Choosing the Azimuthal Angles of Motion

Even Angle Distribution

As in the case of slab geometry, we wish to model neutron motion in the azimuthal plane of the problem in several unique directions. We could stick with our original choice of an evenly spaced set of azimuthal directions and boundaries, φ_i and $\bar{\varphi}_i$, respectively. To this end, we would have tracks crossing the system as shown in [Fig. 65](#).

The above choice of four unique directions evenly distributed between $0 \leq \bar{\varphi}_i \leq \pi/2$ generates the boundaries, directions, and associated weights on a unit cylinder listed in [Table 16](#). Note that the weight associated with each direction of motion is equivalent to the distance between parallel lines.

It can be seen from the table that, for our *equal angle* quadrature set, we will have more characteristics concentrated toward the top of the cylinder than we have near the center of the cylinder. This distribution is highly undesirable.

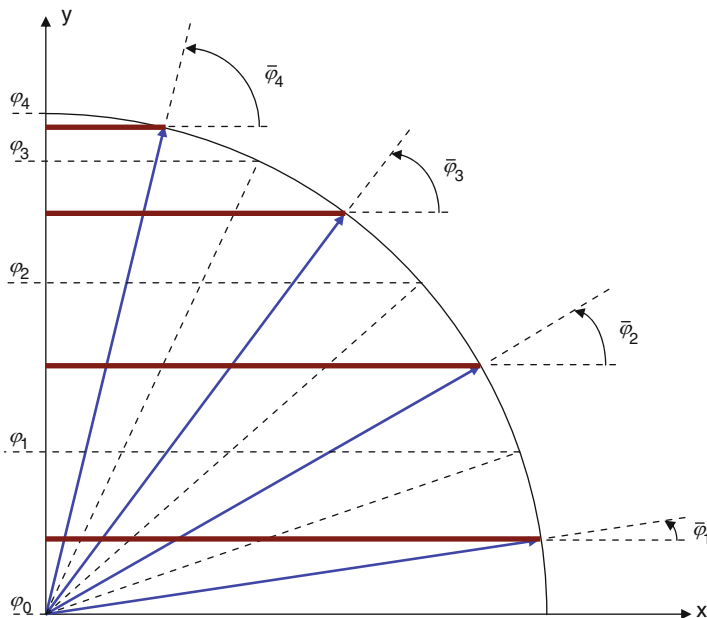


Figure 65
Evenly distributed angles in the azimuthal plane of a cylinder

Table 16
Evenly distributed angles in azimuthal plane of unit cylinder

i	φ_i	$\bar{\varphi}_i$	y_i	\bar{y}_i	ω_i
0	0°	—	0.00000	—	—
1	22.5°	11.25°	0.38268	0.19509	0.38268
2	45°	33.75°	0.70711	0.55557	0.32443
3	67.5°	56.25°	0.92388	0.83147	0.21677
4	90°	78.75°	1.00000	0.98079	0.07612

To correct for this skewed distribution, we wish to distribute the characteristics evenly, or more precisely we wish to produce azimuthal angles with the same weights, which requires the characteristic boundaries to be distributed evenly.

Even Boundary Distribution

From our previous example, if we wish to distribute the four characteristic boundaries evenly, we choose to enforce the following constraint:

$$\Delta y = \frac{R}{I} \quad (471)$$

where R is the outer radius of the cylinder and I is the total number of azimuthal angles. Then the y -intercepts of the boundaries are calculated as

$$y_i = R \sin \varphi_i \quad (472)$$

and the angles of motion are defined by rearranging (472)

$$\varphi_i = \sin^{-1} \left(\frac{y_i}{R} \right) \quad (473)$$

The location of the characteristic passing between the boundaries should be chosen to preserve the mean chord length of the prism being intersected. In the xy -plane, the mean chord length of a circle is simply the ratio of the area to the diameter,

$$\frac{A}{D} = \frac{\pi R^2}{2R} = \frac{\pi R}{2} \quad (474)$$

To convert this to the mean chord of a cylinder, we multiply by the mean secant of the azimuthal angle, where the mean secant is calculated as

$$\sec \bar{\varphi} = \frac{\int_0^{\pi/2} \sec \varphi \cdot \cos^2 \varphi \cdot d\varphi}{\int_0^{\pi/2} \cos^2 \varphi \cdot d\varphi} = \frac{4}{\pi} \quad (475)$$

and the mean chord length for a complete cylinder then becomes $2R$.

The mean chord length for a horizontal slice through a cylinder can be calculated in a similar manner. This calculation results in an expression for the angle of travel for the characteristic passing through the slice

$$\begin{aligned} \sec \bar{\varphi}_i &= \frac{\omega_i}{\frac{1}{2}(\varphi_i - \varphi_{i-1}) + \frac{1}{4}(\sin 2\varphi_i - \sin 2\varphi_{i-1})} \\ &= \frac{\sin \varphi_i - \sin \varphi_{i-1}}{\frac{1}{2}(\varphi_i - \varphi_{i-1}) + \frac{1}{4}(\sin 2\varphi_i - \sin 2\varphi_{i-1})} \end{aligned} \quad (476)$$

Inverting (476) gives

$$\cos \bar{\varphi}_i = \frac{\frac{1}{2}(\varphi_i - \varphi_{i-1}) + \frac{1}{4}(\sin 2\varphi_i - \sin 2\varphi_{i-1})}{\sin \varphi_i - \sin \varphi_{i-1}} \quad (477)$$

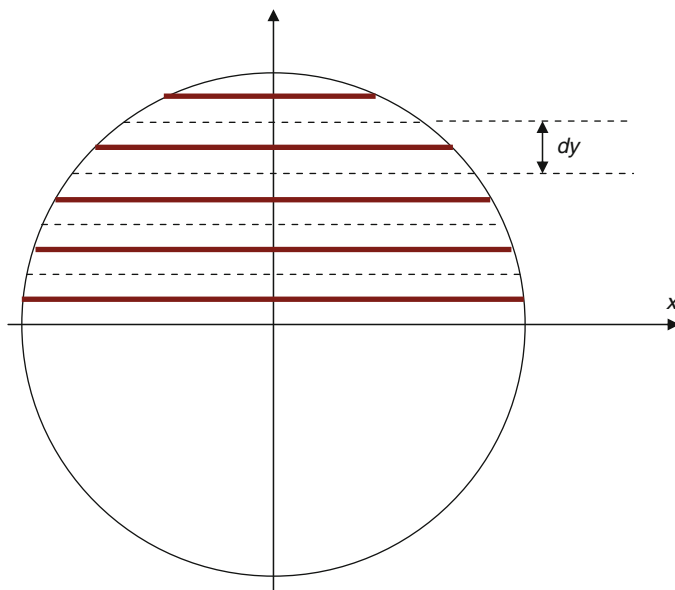
From (477), the expression for the angle of travel for the characteristic passing through the centroid of the horizontal slice in the xy -plane of the problem is

$$\begin{aligned} \bar{\varphi}_i &= \cos^{-1} \left\{ \frac{\frac{1}{2}(\varphi_i - \varphi_{i-1}) + \frac{1}{4}(\sin 2\varphi_i - \sin 2\varphi_{i-1})}{\sin \varphi_i - \sin \varphi_{i-1}} \right\} \\ &= \cos^{-1} \left\{ \frac{\frac{1}{2}(\varphi_i - \varphi_{i-1}) + \frac{1}{4}(\sin 2\varphi_i - \sin 2\varphi_{i-1})}{\omega_i} \right\} \end{aligned} \quad (478)$$

For our previous example of four azimuthal directions of motion between $0 \leq \bar{\varphi}_i \leq \pi/2$, the new angles and weights using the *equal weights* quadrature will be those listed in [Table 17](#).

Table 17**Evenly distributed boundaries in azimuthal plane of unit cylinder**

i	φ_i	$\bar{\varphi}_i$	y_i	\bar{y}_i	ω_i
0	0°	–	0.00	–	–
1	14.4775°	8.3168°	0.25	0.19509	0.25
2	30°	22.5209°	0.50	0.55557	0.25
3	48.5904°	39.1897°	0.75	0.83147	0.25
4	90°	63.0437°	1.00	0.98079	0.25

**Figure 66****Evenly distributed characteristics in the azimuthal plane of a cylinder**

5.6.3 An Alternative Tracking Approach

General Theory

Rather than concerning ourselves with the azimuthal boundaries and positioning of the azimuthal angle of motion, there is a somewhat simpler, more direct way to track across our cylindrical system. We may lay tracks across the system, evenly spaced at increments of dy , as shown in [Fig. 66](#). Each characteristic has associated with it a “width,” which extends from the characteristic, half the way to the next characteristic on either side, as illustrated in [Fig. 67](#). The weight that is associated with each characteristic is then equal to the width of the characteristic, dy . The width of each characteristic is easily calculated by dividing the radius of the cylinder by the number of azimuthal directions of motion (i.e., the number of characteristics),

$$dy = \frac{R}{I} \quad (479)$$

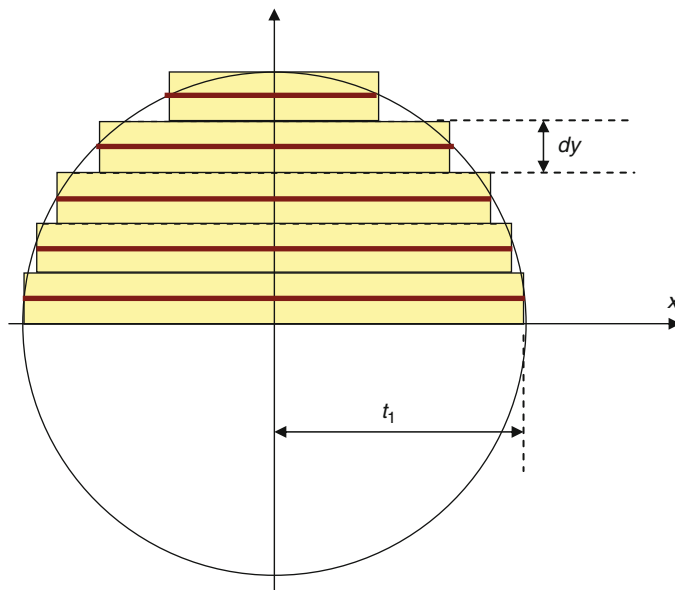


Figure 67
Characteristic “widths”

Here, I is the number of characteristics in the NE quadrant of the cylinder and dy is the spacing between tracks and also between boundaries.

For one-dimensional cylinders, which exhibit azimuthal symmetry, we need only trace in the NE quadrant of the problem, since all other quadrants would be reflections of the NE quadrant. Since each characteristic has associated with it a width, we have two cylinder areas – (1) the *true* area of the NE quadrant $A_{\text{true}} = \pi R^2 / 4$, and (2) the area *approximated* by the characteristic widths,

$$A_{\text{approx}} = \sum_i t_i \cdot dy \quad (480)$$

where t_i is the length of the i th characteristic across the NE quadrant of the cylinder in the xy -plane of the problem.

Example

If we have many annular rings, but only a few characteristics, then we may end up with A_{approx} being much different from the A_{true} value. To illustrate this, let us suppose we have the system contained in [Fig. 68](#).

If we look at the innermost ring – region 1 – then the true area of that region is

$$A_{\text{true}} = \frac{\pi r_1^2}{4} = \frac{\pi (0.74'')^2}{4} = 0.43 \text{ in}^2$$

and the x -intercept of the first characteristic with the radius of region 1 occurs at

$$\tau_{1,1} = \sqrt{r_1^2 - y_1^2} = \sqrt{(0.74'')^2 - (0.45'')^2} = 0.58745''$$

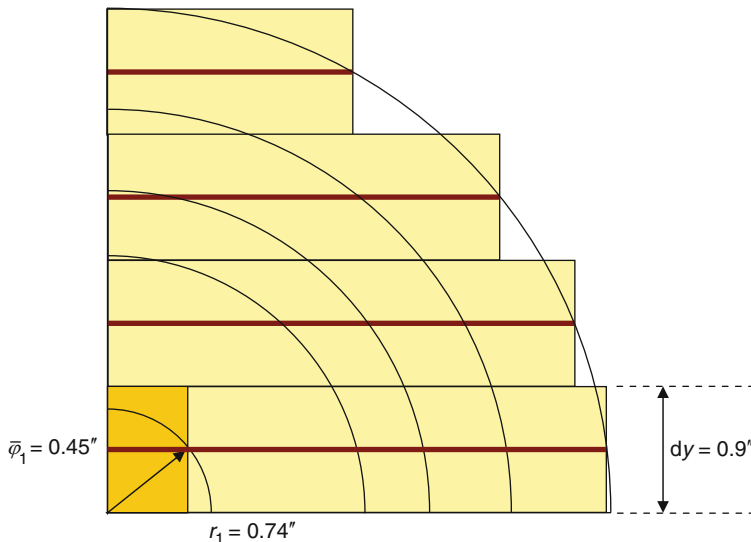


Figure 68
System with many annular rings and few characteristics

The approximated area of region 1 is calculated using (480)

$$A_{\text{approx}} = \tau_{1,1} \cdot dy = 0.58745'' \times 0.9'' = 0.52871 \text{ in}^2$$

In this example, the approximated area through region 1 is overestimated by

$$\% \text{diff} = \frac{|A_{\text{approx}} - A_{\text{true}}|}{A_{\text{true}}} \times 100\% = \frac{|0.52871 \text{ in}^2 - 0.43 \text{ in}^2|}{0.43 \text{ in}^2} \times 100\% = 23\%$$

Therefore, $\tau_{1,1}$ is really 23% longer than it should be and we will get too few neutrons being passed from region 1 to region 2 along this track segment if we leave it to remain as it is.

Track Adjustments

To correct for the poor estimation of the region area, we can adjust the track length until $A_{\text{approx}} = A_{\text{true}}$. We do this using the ratio below,

$$\tau'_{1,1} = \tau_{1,1} \cdot \frac{A_{\text{true}}}{A_{\text{approx}}} \quad (481)$$

For our example above, we would perform the following ratio:

$$\tau'_{1,1} = 0.58745'' \times \frac{0.43 \text{ in}^2}{0.52871 \text{ in}^2} = 0.47777''$$

In this way, we have reduced the true track length by 23% to ensure that the approximated area is correct. This will help to ensure that a proper number of neutrons are passed through region 1 to region 2, and vice versa.

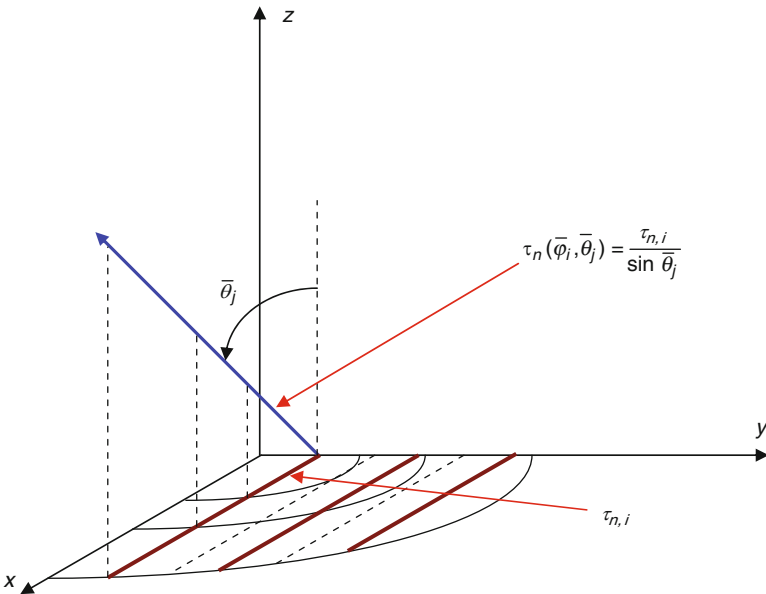


Figure 69
Definition of track segments in MoC cylindrical coordinates

In general, then, we keep a running tally of the approximated area in each region using (480) and ratio all track segments following the completion of the tracking routine

$$\tau'_{n,i} = \tau_{n,i} \cdot \frac{A_{\text{true}}}{A_{\text{approx}}} = \tau_{n,i} \cdot \frac{\pi(r_n^2 - r_{n-1}^2)}{\sum_{\tau_{n,i} \cdot dy}} \quad (482)$$

where the parameters in (482) are illustrated in **Fig. 69**. The transport equation may then be solved using the ratioed track lengths

$$\Phi_{\text{out},n}^g(\bar{\varphi}_i, \bar{\theta}_j) = \Phi_{\text{in},n}^g(\bar{\varphi}_i, \bar{\theta}_j) e^{-\Sigma_n^g \tau'_n(\bar{\varphi}_i, \bar{\theta}_j)} + \frac{q_n^g}{4\pi \Sigma_n^g} \left(1 - e^{-\Sigma_n^g \tau'_n(\bar{\varphi}_i, \bar{\theta}_j)} \right) \quad (483)$$

5.6.4 Modification to the Characteristics Equation

The solution to the transport equation must now be modified in order to apply our new tracking approach. In slab geometry, our ray tracing was precise and we kept track of the following summation in (411):

$$\sum_j \sum_i \frac{\Delta_n^g(\bar{\varphi}_i, \bar{\theta}_j) \cdot \omega_i \cdot \omega_j}{\tau_n(\bar{\varphi}_i, \bar{\theta}_j)} \quad (484)$$

where $\Delta_n^g(\bar{\varphi}_i, \bar{\theta}_j)$ is the change in the value of the angular flux across a mesh, moving in azimuthal direction $\bar{\varphi}_i$ and polar direction $\bar{\theta}_j$; and $\tau_n(\bar{\varphi}_i, \bar{\theta}_j)$ is the length of the track segment crossing the mesh. These lengths are always precise in slab geometry and all characteristics cross all slab regions in the problem.

In cylindrical geometry, the situation is different because not all characteristics cross each of the annular cylindrical regions and the characteristics do not preserve the true volume of each annular region. We can modify the summation in (484) to compensate for this. First, we rewrite (484) in a form that includes the length of the track segment projected onto the xy -plane of the problem

$$\sum_j \sum_i \frac{\Delta_n^g(\bar{\varphi}_i, \bar{\theta}_j) \cdot \omega_i \cdot \omega_j}{\tau'_{n,i} / \sin \bar{\theta}_j} = \sum_j \sum_i \frac{\Delta_n^g(\bar{\varphi}_i, \bar{\theta}_j) \cdot \omega_i \cdot \omega_j \cdot \sin \bar{\theta}_j}{\tau'_{n,i}} \quad (485)$$

Now we can substitute our expression for the approximated volume into (485) to replace the length of the projected track segment

$$\sum_j \sum_i \frac{\Delta_n^g(\bar{\varphi}_i, \bar{\theta}_j) \cdot \omega_i \cdot \omega_j \cdot \sin \bar{\theta}_j}{\tau_{n,i} \cdot \frac{A_{\text{true}}}{A_{\text{approx}}}} = \frac{1}{A_{\text{true}}} \sum_j \sum_i \Delta_n^g(\bar{\varphi}_i, \bar{\theta}_j) \cdot \omega_i \cdot \omega_j \cdot \sin \bar{\theta}_j \cdot dy \quad (486)$$

Substituting (486) into (411) gives us our modified expression for the scalar flux in cylindrical geometry,

$$\phi_n^g = \frac{q_n^g}{4\pi \Sigma_{tr,n}^g A_{\text{true}}} + \frac{dy}{\Sigma_{tr,n}^g A_{\text{true}}} \sum_j \left(\omega_j \cdot \sin \bar{\theta}_j \sum_i \Delta_n^g(\bar{\varphi}_i, \bar{\theta}_j) \cdot \omega_i \right) \quad (487)$$

5.7 Two-Dimensional Geometry

For two-dimensional characteristics calculations, we take an approach similar to the approach we took for the one-dimensional cylindrical geometry. We assign a width to each characteristic and trace characteristics across the entire system at several azimuthal angles between $0 \leq \bar{\varphi} \leq 2\pi$. In one dimension, neutrons traveled at angles between $0 \leq \bar{\varphi} \leq \pi$ in an identical fashion to the way in which they traveled at angles between $\pi \leq \bar{\varphi} \leq 2\pi$. Therefore, we needed only to model neutron motion between $0 \leq \bar{\varphi} \leq \pi$ and account for the remaining azimuthal angles by doubling the associated weight, ω_i . Similarly, neutrons traveled at polar angles between $0 \leq \bar{\theta} \leq \pi/2$ in an identical fashion to the way in which they traveled at angles between $\pi/2 \leq \bar{\theta} \leq \pi$ and we accounted for this symmetry by modeling neutron motion only between $0 \leq \bar{\theta} \leq \pi/2$ and doubling the associated polar weight, ω_j .

In two dimensions, neutron motion in the polar direction is still symmetric about the xy -plane of the problem. That is, neutron motion above the plane is symmetric to neutron motion below the plane. Neutron motion within the xy -plane, though, is not symmetric about either the x -axis or y -axis and we must model neutron motion explicitly at all azimuthal angles between $0 \leq \bar{\varphi} \leq 2\pi$. The tracking routine may be eased somewhat by tracing across the system at angles between $0 \leq \bar{\varphi} \leq \pi$ only, and allowing neutrons to travel in both directions along each track during the characteristics solution.

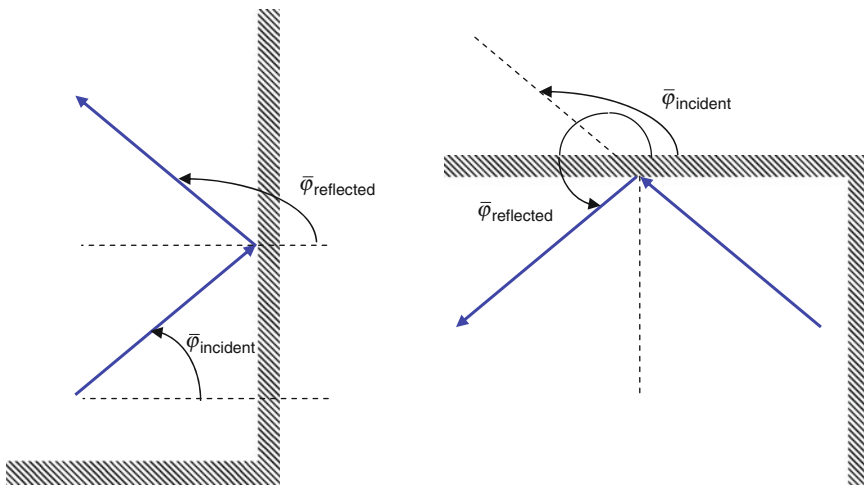


Figure 70

Reflected tracks off different boundaries to the two-dimensional problem

As in the one-dimensional case for reflective boundary conditions, we have a set of unique characteristics, which are distributed between $0 \leq \bar{\varphi} \leq \pi/2$. In one-dimension, we had the associated reflected tracks distributed between $\pi/2 \leq \bar{\varphi} \leq \pi$. In two-dimensional problems, we have tracks reflecting off the top and bottom boundaries of the problem, as well as off the side boundaries to the problem, as illustrated in Fig. 70. This leads to three reflected angles between $\pi/2 \leq \bar{\varphi} \leq 2\pi$ – one reflected angle in each directional quadrant of the problem. To this end, then, we must make sure that the end of each incident characteristic aligns precisely with the beginning of its reflected counterpart.

To ensure perfect reflection in two dimensions, track separations and streaming angles in the xy -plane of the problem must be altered based on the overall dimensions of the problem. We specify the number of azimuthal angles of motion that are to be used to model neutron streaming, I , and the separation of the set of parallel, equidistantly spaced tracks, d , at each azimuthal angle. The unadjusted set of azimuthal angles will be evenly spaced at angles defined by the following expressions:

$$\bar{\varphi}_i = \frac{1}{2}(\varphi_i + \varphi_{i-1}), \quad \text{where } \varphi_0 = 0^\circ \quad (488)$$

$$\varphi_i - \varphi_{i-1} = \frac{2\pi}{I} \quad (489)$$

where I is the number of azimuthal angles distributed between $0 \leq \varphi_i \leq 2\pi$.

If the system is of total width X and total height Y , then the total number of system widths spanned by a characteristic moving in the azimuthal direction of motion i , with a characteristic separation of distance d , is

$$nx = \frac{X \sin \bar{\varphi}_i}{d} \quad (490)$$

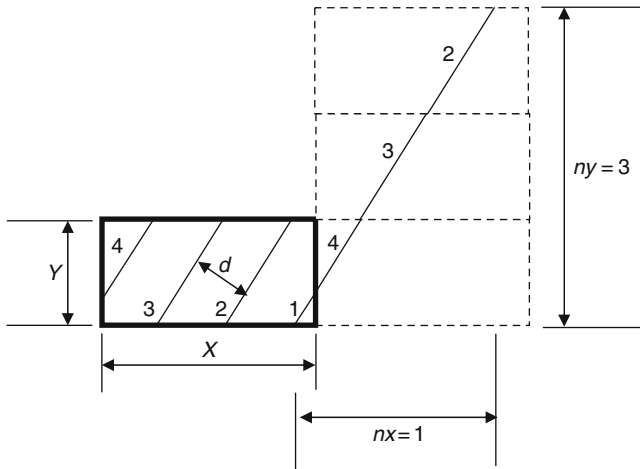


Figure 71
System heights and widths spanned by characteristic

and the total number of system heights spanned is

$$ny = \frac{X \cos \bar{\varphi}_i}{d} \quad (491)$$

This is illustrated in Fig. 71.

In order to ensure that all tracks in direction $\bar{\varphi}_i$ align themselves with their reflective counterparts at the boundaries of the system, nx and ny are rounded up to the nearest integer values and the updated angle of streaming is then calculated as

$$\bar{\varphi}'_i = \tan^{-1} \left(\frac{ny_i}{nx_i} \right) \quad (492)$$

along with the updated separation distance

$$d'_i = \frac{X}{\sqrt{ny_i^2 + nx_i^2}} \quad (493)$$

Using these angles and separations, the azimuthal set of parallel, equidistantly spaced tracks are traced across the system at angles between $0 \leq \bar{\varphi}'_i \leq \pi$. For the angles between $\pi \leq \bar{\varphi}'_i \leq 2\pi$, the previous tracks are used, allowing neutrons to travel in the opposite direction.

For reflection cases, we have a separate reflected angle for each boundary of the system – north, south, east, and west.

For two-dimensional cases, the solution to the characteristics form of the transport equation is slightly different from the slab geometry case, since now each characteristic has associated

with it a width, d'_i . The average angular flux through mesh n at angle $(\bar{\phi}'_i, \bar{\theta}_j)$ is equivalent to the cylindrical geometry case and is calculated by averaging the contribution from all tracks that pass through mesh n at angle i ,

$$\overline{\Phi}_n^g(\bar{\phi}'_i, \bar{\theta}_j) = \frac{\sum_k \overline{\Phi}_{k,n}^g(\bar{\phi}'_i, \bar{\theta}_j) \cdot t_{k,n}(\bar{\phi}'_i, \bar{\theta}_j) \cdot d'_i}{\sum_k t_{k,n}(\bar{\phi}'_i, \bar{\theta}_j) \cdot d'_i} \quad (494)$$

where the sum over k are the tracks at azimuthal angle $\bar{\phi}'_i$, polar angle $\bar{\theta}_j$, which pass through mesh n .

As before, the scalar flux is considered flat across mesh n and is given by

$$\begin{aligned} \phi_n^g &= \sum_j \sum_i \overline{\Phi}_n^g(\bar{\phi}'_i, \bar{\theta}_j) \cdot \omega_i \cdot \omega_j \\ \varphi_n^g &= \frac{q_n^g}{4\pi \Sigma_{tr,n}^g} + \sum_j \sum_i \frac{\sum_k \frac{\Delta_{k,n}^g(\bar{\phi}'_i, \bar{\theta}_j)}{\Sigma_{tr,n}^g \cdot t_{k,n}(\bar{\phi}'_i, \bar{\theta}_j)} \cdot t_{k,n}(\bar{\phi}'_i, \bar{\theta}_j) \cdot d'_i}{\sum_k t_{k,n}(\bar{\phi}'_i, \bar{\theta}_j) \cdot d'_i} \cdot \omega_i \cdot \omega_j \\ \phi_n^g &= \frac{q_n^g}{4\pi \Sigma_{tr,n}^g} + \frac{1}{\Sigma_{tr,n}^g} \sum_j \sum_i \sum_k \frac{\Delta_{k,n}^g(\bar{\phi}'_i, \bar{\theta}_j)}{t_{k,n}(\bar{\phi}'_i, \bar{\theta}_j)} \cdot \omega_i \cdot \omega_j \end{aligned} \quad (495)$$

where the expression for the average angular flux along track segment k , crossing mesh n , in azimuthal direction $\bar{\phi}'_i$, polar direction $\bar{\theta}_j$, represented by the variable $\overline{\Phi}_{k,n}^g(\bar{\phi}'_i, \bar{\theta}_j)$, has been expanded using (406).

As with the cylindrical geometry calculation, each track length should be ratioed with the quotient of the approximated-to-true area of the mesh being subtended by the characteristic. This leads to an expression equivalent to (482),

$$t'_{k,n}(\bar{\phi}_i, \bar{\theta}_j) = t_{k,n}(\bar{\phi}_i, \bar{\theta}_j) \cdot \frac{A_{\text{approx}}}{A_{\text{true}}} \quad (496)$$

This, in turn, leads to an expression for the scalar flux equivalent to (487),

$$\phi_n^g = \frac{q_n^g}{4\pi \Sigma_{tr,n}^g} + \frac{1}{\Sigma_{tr,n}^g \cdot A_{\text{true},n}} \sum_j \sum_i \omega_i \cdot \omega_j \cdot d_i \cdot \sin \bar{\theta}_j \cdot \sum_k \Delta_{k,n}^g(\bar{\phi}'_i, \bar{\theta}_j) \quad (497)$$

where

$$\Delta_{k,n}^g = \Phi_{k,n}^g(s=0) - \Phi_{k,n}^g(s=t'_{k,n}), \text{ in direction } \bar{\phi}'_i, \bar{\theta}_j \quad (498)$$

The angular fluxes are calculated along each characteristic in the same manner as before,

$$\begin{aligned} \Phi_{\text{out},k,n}^g(\bar{\phi}'_i, \bar{\theta}_j) &= \Phi_{\text{in},k,n}^g(\bar{\phi}'_i, \bar{\theta}_j) \cdot \exp \left\{ -\Sigma_{tr,n}^g \cdot t'_{k,n}(\bar{\phi}'_i, \bar{\theta}_j) \right\} \\ &\quad + \frac{q_n^g}{4\pi \Sigma_{tr,n}^g} \left[1 - \exp \left\{ -\Sigma_{tr,n}^g \cdot t'_{k,n}(\bar{\phi}'_i, \bar{\theta}_j) \right\} \right] \end{aligned} \quad (499)$$

The main difference between the slab geometry calculation and the two-dimensional calculation is that, in slab geometry, there was one characteristic per azimuthal angle and each characteristic passed through all regions of the problem. In two-dimensions, there are many characteristics per azimuthal angle (the k subscript in the summations) and no single characteristic passes through all regions of the problem. We must, therefore, keep track of the region through which each characteristic, k , in azimuthal direction i , passes.

5.8 Mesh Subdivisions for Two-Dimensional Problems

The ray-tracing routine is the most complex module associated with the MoC. Ray tracing, itself, is not all that complicated. However, the calculation of true areas for all the complicated mesh shapes requires a great effort and is fairly cumbersome to implement. The true area of each mesh is required to accurately solve (496) and (497). Alternatively, one could make the assumption that enough ray-tracing detail will be used that the approximated area will be close enough to the true area to remove the need to ratio the track lengths. Such an assumption would simplify the ray-tracing module significantly, hopefully without overly penalizing the accuracy of the solution.

There are different approaches to ray tracing. The details that will be described in this section are based on the approach used in CASMO-4 and LANCER02. This approach has been shown to be extremely advantageous, in terms of execution speed. It uses predefined cell types that are commonly found in all LWR lattice designs and is preferred because it simplifies the calculation of true mesh areas. Alternative approaches include generalized geometry routines, such as those routinely used in Monte Carlo codes, and factorial geometry, such as that used in AEGIS. For such routines, the calculation of true mesh areas can become complicated and the correction in (496) might need to be abandoned. The other benefit of using predefined cell types is that meshing can be predetermined by the programmer and, therefore, is guaranteed to be adequate. For generalized ray-tracing routines, the meshing is typically left to the user, who may or may not have an adequate feel for the meshing needs of the problem being solved. The accuracy of the MoC depends on the size of the flat source mesh – especially those used in the thermal energy range – so inadequate meshing can produce misleading results. The interested reader is directed to refer Jevremovic et al. (2001), Yamamoto et al. (2005), Sugimura et al. (2007), West and Emmet (1980), and Weiss and Ball (1991).

5.8.1 Assigning Material Regions

Before we begin to ray trace, we first define the various material regions of the problem and then split each material region into an adequate number of flat source/flat flux mesh. The materials are the broad-group macroscopic cross section sets from the condensation scheme (if one exists).

To do this, we must first assign *cell* numbers to the problem. We define a *cell* to be a large region of the lattice that may contain multiple material regions, such as a whole pin cell or a portion of a control blade that contains one or more absorber pins and sheathing. All *cells* are rectangular, as illustrated in Fig. 72, and are part of a Cartesian grid. The *cells* are numbered sequentially starting, for example, in the upper left-hand corner of the problem and working across the row and then down the columns. Note that the oversized water rod in the center

1	2	3	4	5	6	7	8	9	10
11	(12)	(13)	(14)	(15)	(16)	(17)	(18)	(19)	20
21	(22)	(23)	(24)	(25)	(26)	(27)	(28)	(29)	30
31	(32)	(33)	(34)	(35)	(36)	(37)	(38)	(39)	40
41	(42)	(43)	(44)	45	46	(47)	(48)	(49)	50
51	(52)	(53)	(54)	55	56	(57)	(58)	(59)	60
61	(62)	(63)	(64)	(65)	(66)	(67)	(68)	(69)	70
71	(72)	(73)	(74)	(75)	(76)	(77)	(78)	(79)	80
81	(82)	(83)	(84)	(85)	(86)	(87)	(88)	(89)	90
91	92	93	94	95	96	97	98	99	100

■ **Figure 72**
Definition of *cells*

of the lattice in ➤ Fig. 72 has been divided into four *cells* by our Cartesian grid. This will be addressed by four separate ray-tracing routines.

The cell numbers are held by a two-dimensional array, such as “CellNumber(maxx,maxy),” where “maxx” is the number of *cells* along the *x*-axis of our lattice, and “maxy” is the number of *cells* along the *y*-axis of our lattice, which in ➤ Fig. 72 would be 10×10 .

Within each *cell*, there may be multiple material *regions*, each one representing a different material type. For instance, within a pin *cell*, there is a coolant *region*, a cladding *region*, possibly an air gap *region* between the fuel pellet and the cladding, and a fuel pellet *region*. If the fuel pellet contains Gadolinium, there may be multiple pellet *regions* defined in order to accurately model the spatial self-shielding nature of the Gadolinium. Each of the pellet *regions* is its own unique material type. The *regions* within a *cell* can be thought of as levels in our lattice physics code, where the base level is the outermost material in the *cell* and you add levels as you move further into the *cell*. This is illustrated for a simple pin cell in ➤ Fig. 73, where the coolant material forms the base *region* and the *region* numbers (i.e., levels) increase as the cylinders become smaller.

From a programming point of view, we would represent this using a two-dimensional array. For instance, we may define material sets for each *region* of each *cell* using an array

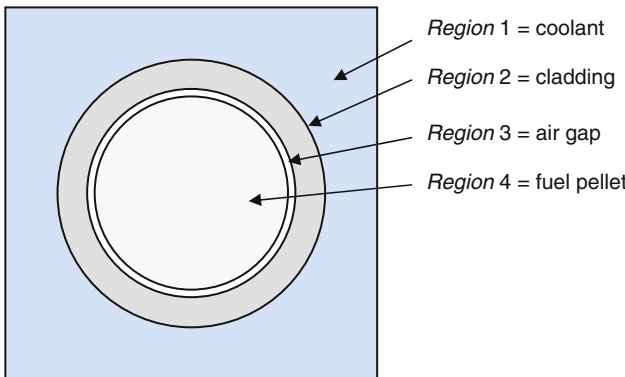


Figure 73
Definition of *regions* within a *cell*

such as “MaterialPerRegion(*regions,cells*).” Then we would need a one-dimensional array that described the number of *regions* per *cell*, such as “RegionsPerCell(*cells*).” The value of “*cells*” in the two arrays would come from our “CellNumber(*maxx,maxy*)” variable.

5.8.2 Meshing

Each *cell* in the problem needs to be broken into a number of *mesh* that are small enough to accurately represent the source and the flux as being perfectly flat within the *mesh*. In an LWR lattice, the *regions* within each *cell* are usually small enough to accurately be used as flat source *mesh* without further subdivision for neutron energies in the epithermal and fast range. That is, for neutron energies above roughly 2 eV, the cross sections are small enough and consistent enough from one material region to the next to use a *mesh* such as that illustrated in [Fig. 72](#) to represent the flux and the source as being perfectly flat. In the thermal energy range below 2 eV, though, some cross sections can be very large indeed and the size of the cross sections may vary wildly from one material region to the next. This is especially true for regions containing strong thermal absorbers, such as the B4C or hafnium absorber pins in a control blade, or fuel pellets containing Gadolinium. In such cases, the flux will change rapidly across a material *region* and the material *region* will need to be subdivided into much smaller *mesh* in order to produce an accurate solution to the characteristics equation.

During the initial development of CASMO-4 (early 1990s), computer memory was at a premium and it was necessary to devise clever schemes to save memory wherever possible. One way of minimizing the memory required by the MoC solution was by using two separate mesh – a coarse mesh for all energy groups above 2 eV, and a fine mesh for all energy groups below 2 eV. This was acceptable for all lattice calculations except BWRs containing a cruciform control blade in one corner of the problem. For those cases, it was necessary to apply the fine mesh to all energy groups in order to properly model the steep flux gradient across the bundle that was created by the presence of the control blade. The use of the dual mesh system allowed the MoC to be applied on machines with small memory, but at a price. Accuracy – primarily at cold

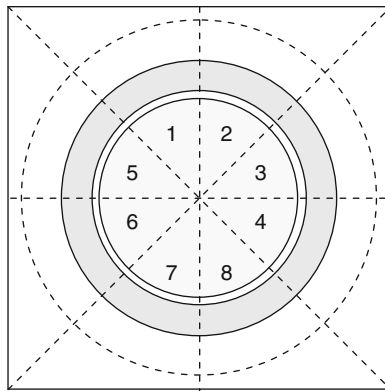


Figure 74
Example of *mesh* ordering

conditions – was somewhat compromised. Also, since the mesh changed for different energy groups, there had to be a way of superimposing the fine mesh onto the coarse mesh and vice versa. This complicated bookkeeping within the code. Today, memory is plentiful and there is no need to micro-manage memory on a scale like that, so the fine mesh is always used for all energy groups. This makes bookkeeping within the code much simpler.

Figure 74 contains an example of a pin cell that has been subdivided into octants of equal areas. The cell has been subdivided in this way because it lends itself to an easy calculation of true areas for each *mesh*. The figure contains an example of a numbering scheme used for the *mesh* layout. Any numbering scheme is valid – the important point being that a consistent scheme exists that allows the ray-tracing routine to determine the *mesh* through which the characteristic passes. In this scheme, we might have a three-dimensional array to hold the flux or area of each mesh, such as “`MeshArea(mesh,regions,cells)`.”

5.8.3 Defining Various Cell Types

The different types of *cells* are distinguished by their contents. Figure 75 contains examples of some of the *cells* that might be defined internally by the MoC ray-tracing module. The most common *cell* found in a typical problem is a square or rectangular cell that may or may not contain imbedded cylinders. The origin of the imbedded annular cylinders is typically centered in the cell, although this is not necessarily a requirement and is sometimes modified by the code internally, as will be explained later in this section. Other *cells* may contain imbedded slabs at different angles. A collection of *cells* can be created to handle pins along the edge of the bundle that abut the channel shroud of a BWR. Unique *cells* exist along each different face of the channel and in each corner of the channel. The corner *cells* are created to handle the specific intricacies of the rounded channel corners and the thick–thin nature of channel walls on modern BWR assembly designs. Additional *cells* can be created to handle the oversized water rods and water boxes found in designs from the various fuel vendors.

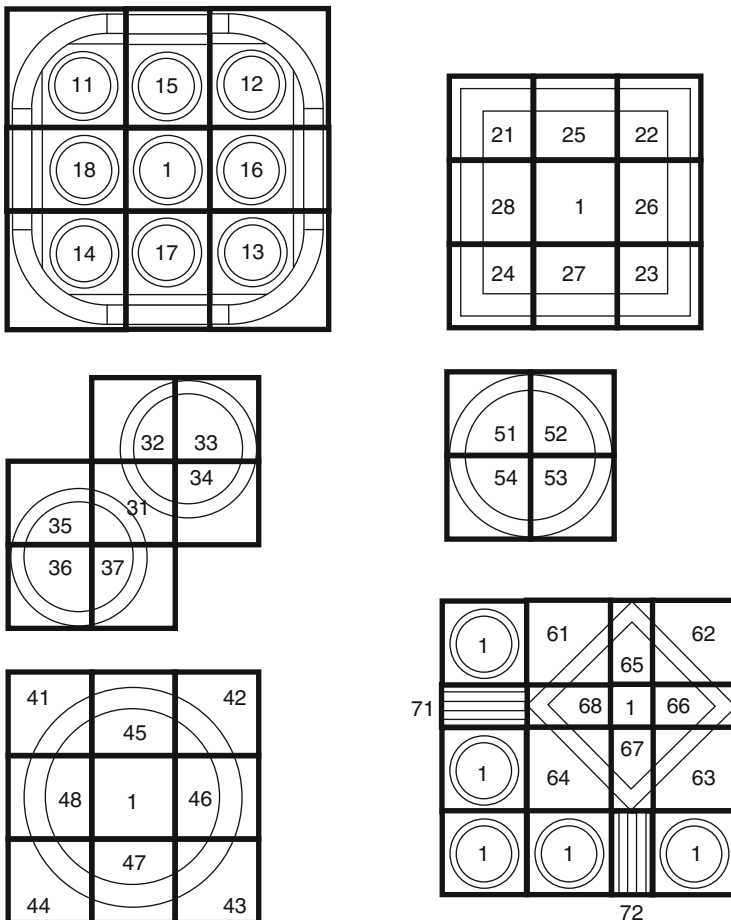


Figure 75
Examples of different type of *cells*

For such a scheme, we should define a two-dimensional array to carry the type of each *cell* in the lattice, such as “CellType(maxx,maxy).” For each *cell* type, we create a unique ray-tracing routine that is specific for the contents of that *cell*, that is, imbedded cylinders, or orthogonal slabs, or whatever. Then, for any characteristic we trace across the geometry of the problem, we will know what type of *cell* we are traversing at any point in the lattice and we will enter the appropriate ray-tracing routine, which has been written specifically for the type of geometry contained within the *cell*. If the lattice physics code is being developed for a specific application, such as analyzing BWR or PWR fuel designs, this is the preferred approach, in terms of execution speed and ease of use. The major drawback is that the code requires modifications if a new geometry is introduced into a fuel design. But that rarely happens. The different geometries that exist in fuel designs today have remained unchanged for decades.

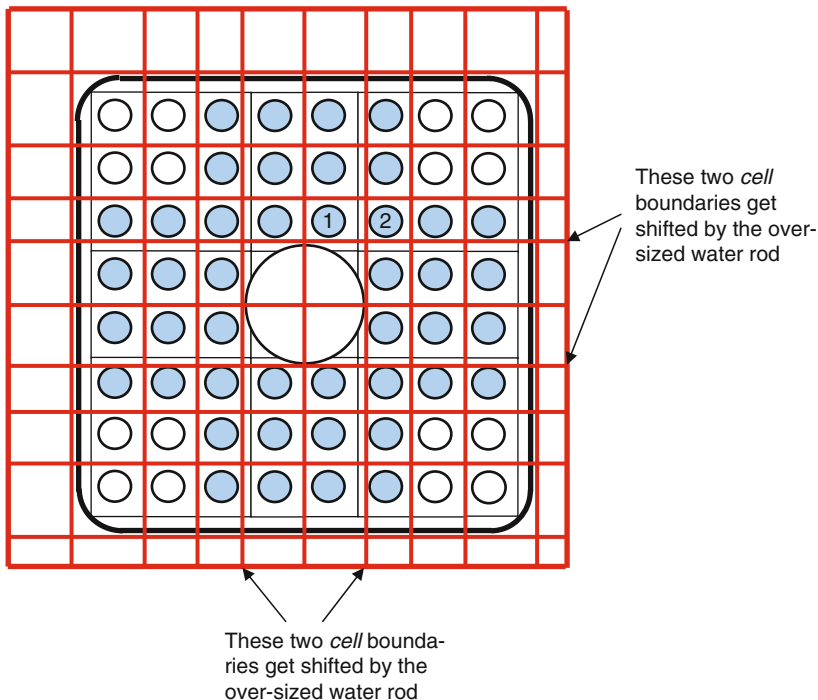
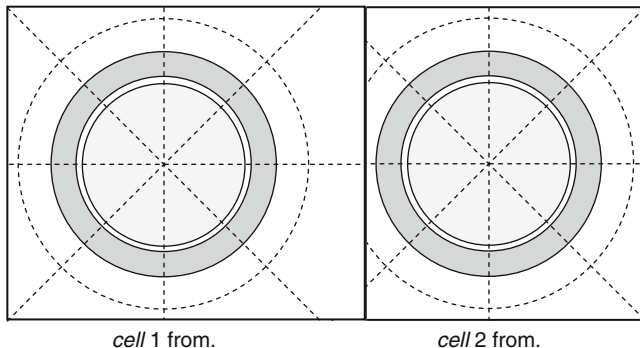


Figure 76
Modifying *cell* boundaries to accommodate oversize rods

For most LWR applications, the MoC ray-tracing routine can be limited to dealing with imbedded cylinders that have a common origin within the *cell* of interest. A special exception to this rule-of-thumb is made for some legacy BWR fuel designs that contained water rods whose center of origin was located in a neighboring *cell*. This situation is illustrated in [Fig. 75](#) as *cell* types 31 through 37, where the two water rods were centered in cells 33 and 36, respectively, and cell 31 contained contributions from each. But for most *cells*, the physical dimensions of the rod can safely be prohibited from crossing the *cell* boundaries. For bundles containing water rods that occupy multiple *cell* locations, for example, *cells* 51 through 54 in [Fig. 75](#), the MoC ray-tracing routine can be written to modify the Cartesian grid boundaries in such a way that the water rods fit entirely within four *cells*. When this happens, the pins in rows of *cells* neighboring the water rod will be shifted from their *cell* centers and the *cells* themselves will be modified from a square to a rectangular shape, as illustrated in [Fig. 76](#). In the figure, all pins shaded in blue are those whose origins have been shifted from the center of the *cell* by the new grid boundaries.

[Fig. 77](#) contains details of two *cells* taken from [Fig. 76](#). These are the two *cells* labeled "1" and "2" in [Fig. 76](#). Both *cells* have had a grid boundary adjusted by the presence of the oversized water rod in the center of the lattice. *Cell* "1" has had its east boundary moved further to the east, increasing the area of the *cell*. *Cell* "2" has had its west boundary moved to the east, reducing the area of the *cell*. Mesh subdivisions are always centered in the

**Figure 77**

Mesh subdivisions centered in annular regions

middle of the annular cylinders. This is done to simplify the ray-tracing logic. Unfortunately, this action results in somewhat uncommon mesh shapes and complicates the calculation of the true area of some mesh subdivisions. In contrast, if no imbedded annular cylinders exist in the mesh, the azimuthal subdivisions can be drawn between diagonal corners of the mesh. Note that annular *mesh* subdivisions are allowed to intersect with the *cell* boundaries, whereas annular *material boundaries* are not allowed to intersect with the *cell* boundaries. The coding must be capable of distinguishing between *mesh boundaries* and *material boundaries* when imposing this limitation.

5.8.4 Meshing of Control Blade Cells

The presence of the control blade presents its own challenge, in terms of the *cells* that are created by the Cartesian grid, not only for the ray tracing, but especially for the calculation of the true area for each mesh subdivision in the control blade. In essence, the same Cartesian grid as that illustrated in [Fig. 76](#) is placed over the geometry of the bundle with or without the control blade being present. In instances when the control blade is present, the interior of some of the *cells* take on more complicated geometries, as illustrated in [Fig. 78](#). Each *cell* of the control blade will contain multiple absorber tubes and it is possible that each absorber tube can be made up of a unique material (B_4C , Hafnium, etc.). The Cartesian grid boundaries can intersect the control blade at any point, which complicates the calculation of the true areas of the mesh subdivisions in each *cell*.

5.8.5 Final Mesh Layout

The final geometry layout consists of a mesh that resembles that illustrated in [Figs. 77](#) and [78](#). That is, the fine mesh are very small and are used to model the steep flux gradients present primarily in the thermal energy groups. The mesh layout for a typical BWR assembly is illustrated in [Fig. 79](#). The lavender colored pins in the figure represent pellets containing Gd_2O_3 .

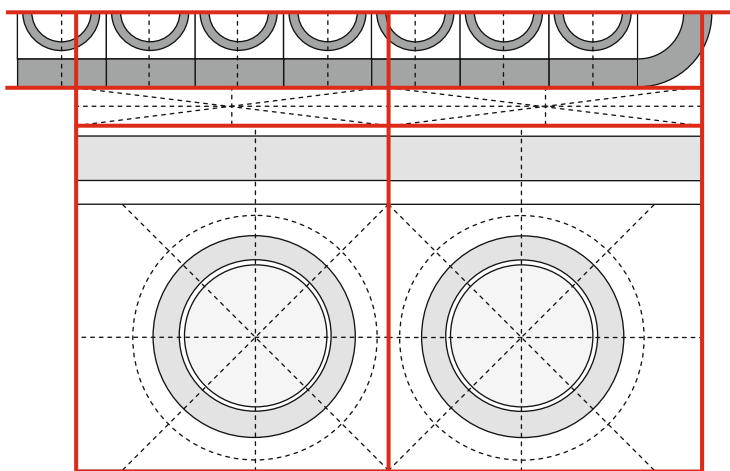


Figure 78
An example of control blade *cells*

For such locations, the pellets will be subdivided annularly into multiple concentric rings. Each ring in the pellet is represented by a set of unique material cross sections. This allows for an accurate modeling of the Gadolinium radial depletion rate.

For a typical modern fuel design, the fine-mesh layout will contain approximately 5,000 flat source/flat flux mesh. The water gaps should be subdivided vertically and horizontally such that no gap mesh is wider than 0.5 cm. After the outer gaps have been subdivided, additional azimuthal mesh should be applied to further subdivide each gap mesh into octants, as illustrated in  Fig. 79. Large water rods should be subdivided annularly into smaller fine-mesh sizes to better model thermal flux gradients across the rod.

5.9 Two-Dimensional Ray Tracing

5.9.1 The Cyclic Tracking Approach

Once the problem has been segmented into various *cell* types, the MoC routine is ready to begin ray tracing across the problem. Ray tracing takes place only for the azimuthal directions of motion. The resulting track lengths are raised out of the plane of the problem to each of the various polar angles and the track lengths are adjusted accordingly. For any given azimuthal angle of motion, $\bar{\varphi}_i'$, the ray-tracing routine will first determine the number of characteristics that begin along the x -axis and the y -axis and will then determine the coordinates of the origin of each characteristics. The separation of the characteristics along the x and y axes is calculated as

$$\delta x_i = \frac{d_i}{|\sin \varphi'_i|} \quad (500)$$

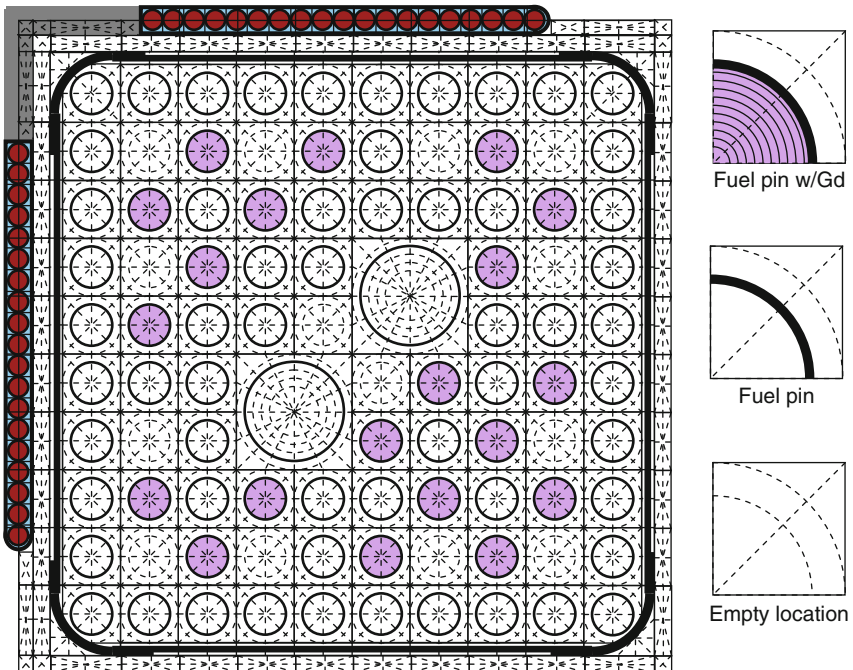


Figure 79
Typical *mesh layout* for a BWR assembly calculation

and

$$\delta y_i = \frac{d_i}{|\cos \bar{\varphi}'_i|} \quad (501)$$

as illustrated in [Fig. 80](#).

As described in [Fig. 5.7](#), the azimuthal angle has been slightly modified to ensure that each characteristic aligns with its reflective counterpart along each boundary of the problem, and the separation between parallel characteristics has been slightly adjusted to ensure that there are a perfect integral number of characteristics covering the problem geometry. To avoid a characteristic originating in a corner of the problem, the entire set of characteristics is centered along the axes. This results in the first characteristic along each axis being shifted by an amount equal to half the separation distance along that particular axis,

$$\delta x_{i,0} = \frac{\delta x_i}{2} \quad (502)$$

and

$$\delta y_{i,0} = \frac{\delta y_i}{2} \quad (503)$$

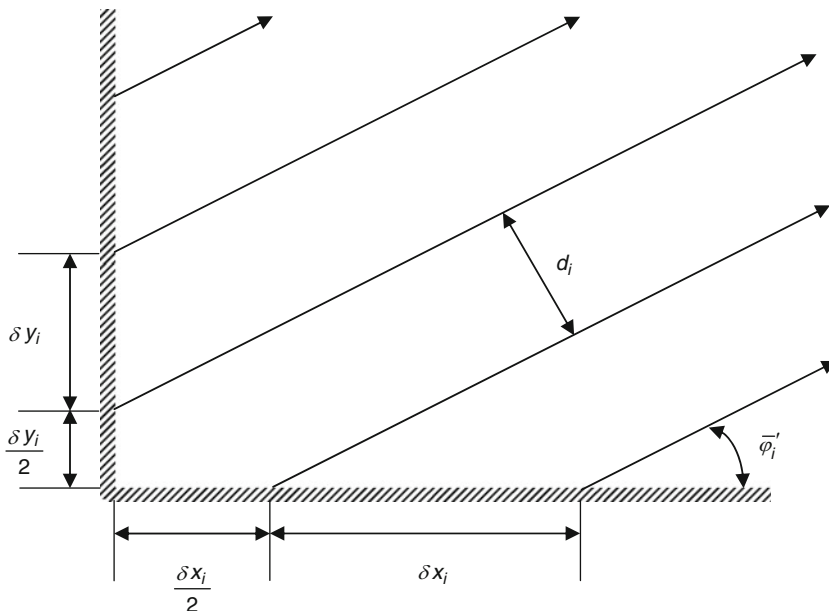


Figure 80
Origin of each characteristic at a given angle

Once the origin of each track is determined, the code may begin to trace the characteristics across the geometry of the problem. The module first determines the *cell* being crossed by the characteristic. Based on the specific *cell* type, the module will enter the appropriate ray-tracing routine and proceed to determine all intersections of *mesh* lines with the crossing characteristic. The basic principles of each ray-tracing routine are illustrated in [Fig. 81](#).

Within any *cell* containing imbedded cylinders, the origin of the *cell* is placed at the center of the annular rings. The fine-*mesh* subdivisions are also centered in the middle of the annular cylinders. This simplifies the ray-tracing routine for *cells* that contain imbedded cylinders whose origin is not located in the center of the *cell*. The entrance point to the *cell*, $(x_{\text{in}}, y_{\text{in}})$, is known either from the exit point from the neighboring *cell*, or from the origin of the characteristic along one of the outer problem boundaries. The width of the *cell* in the *x* and *y* directions is also known, x_{dim} and y_{dim} , respectively. The total length of the characteristic across the *cell* can then be calculated as

$$l = \frac{x_e - x_{\text{in}}}{\cos \bar{\varphi}'_i}, \quad \text{if } \bar{\varphi}'_i < \pi/2 \quad (504)$$

or

$$l = \frac{x_w - x_{\text{in}}}{\cos \bar{\varphi}'_i}, \quad \text{if } \bar{\varphi}'_i > \pi/2 \quad (505)$$

The exiting point of the characteristic along the *y*-axis is calculated as

$$y_{\text{out}} = y_{\text{in}} + l \cdot \sin \bar{y}\varphi'_i \quad (506)$$

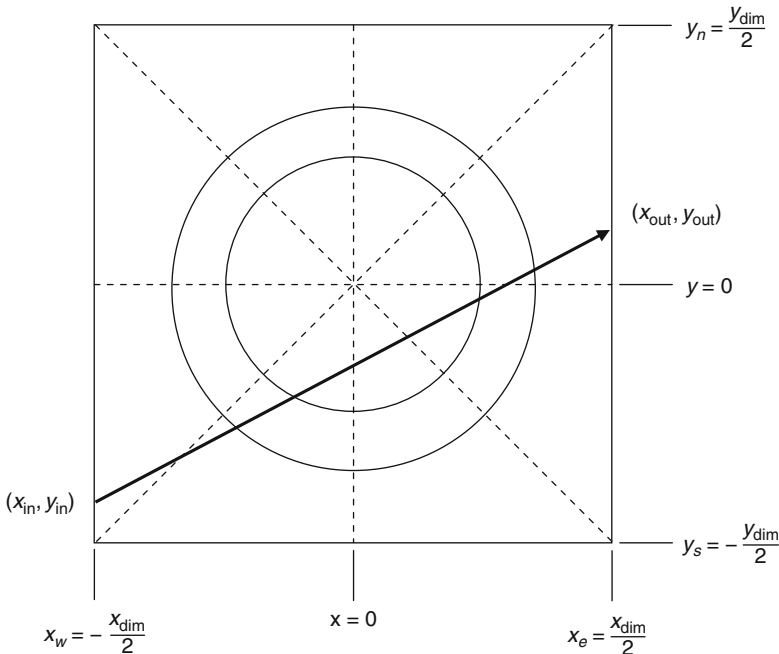


Figure 81
Intersections of *mesh* with a passing characteristic

If y_{out} is determined to lie outside the boundaries of the *cell*, then the track length is recalculated as

$$l = \frac{y_n - y_{\text{in}}}{\sin \bar{\varphi}'_i} \quad (507)$$

y_{out} is then equal to y_n and x_{out} is calculated as

$$x_{\text{out}} = x_{\text{in}} + l \cdot \cos \bar{\varphi}'_i \quad (508)$$

The ray-tracing routine keeps track of the surface of the *cell* that is crossed when the characteristic enters and exits the *cell*. This information is later used during the coarse mesh rebalance acceleration scheme, described later in this section.

Once the entrance and exit points are known, all intersections within the *cell* may be determined. This is done by equating the equation of the line for the characteristic with the equation of the line/arc for each *mesh* or material *region* in the *cell*. The equation of the line for the characteristic is expressed as

$$y = m_c x + b_c \quad (509)$$

where m_c is the slope of the line of the characteristic, calculated as $\tan \bar{\varphi}'_i$; and b_c is the point at which the characteristic intersects the y -axis, as illustrated in Fig. 82.

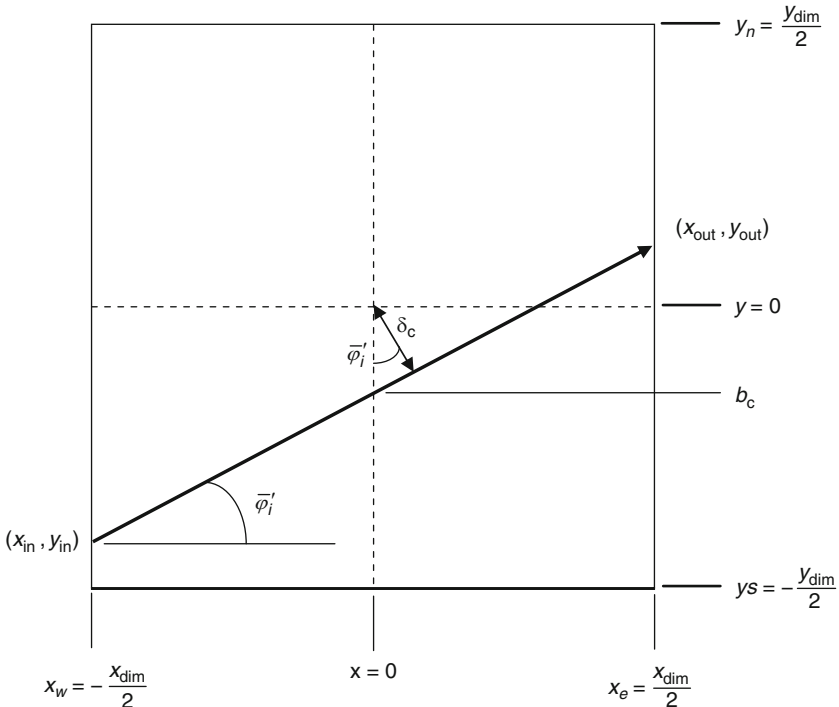


Figure 82
Variables associated with the equation of the characteristic

The y -axis intercept is calculated as

$$b_c = y_{in} - \left(x_{in} \cdot \tan \bar{\varphi}'_i \right) \quad (510)$$

And the closest the characteristic approaches to the origin of the *cell* is

$$\delta_c = |b_c \cdot \cos \bar{\varphi}'_i| \quad (511)$$

The equation for any annular cylinder in the *cell* is given by

$$r_{cyl}^2 = x^2 + y^2 \quad (512)$$

or

$$y = \sqrt{r_{cyl}^2 - x^2} \quad (513)$$

Equating (513) with (509) produces the two values for the x -intercept of the characteristic with the cylinder,

$$x = \frac{-m_c b_c \pm \sqrt{m_c^2 r_{cyl}^2 + r_{cyl}^2 - b_c^2}}{m_c^2 + 1} \quad (514)$$

The corresponding y -intercept values can be obtained by plugging the x -intercept values into (513) or (509). These intercepts are only calculated if $\delta_c < r_{\text{cyl}}$, otherwise, the characteristic cannot cross the boundary of the cylinder. After determining the coordinate intercepts of the characteristic with the cylinder, the routine checks to make sure that the intercepts lie within the *cell* boundaries. This is necessary because the cylindrical fine-*mesh* subdivision in the coolant is allowed to cross the *cell* boundaries.

Similar logic is used to determine the intercept of the characteristic with a slab imbedded in a *cell*. Slabs are typically vertical or horizontal and the equation of the line representing the slab is then of the form

$$x = \text{const} \quad (515)$$

or

$$y = \text{const} \quad (516)$$

The constants that represent the equation of the line for the various vertical slabs may be plugged directly into (509) to determine the corresponding y -intercepts. For horizontal slabs, (509) is rearranged prior to plugging in the constants and is subsequently solved for the corresponding x -intercept. After determining the intercepts, the routine checks to make sure the intercepts lie within the *cell* boundaries. If not, the characteristic cannot cross the slab within the *cell* and the intercepts are discarded. Intersections of the characteristic with the fine-*mesh* subdivisions are determined in a similar manner.

The number of intersections resulting from ray tracing over a typical LWR lattice is usually on the order of one million. That is, we will end up having to solve the transport equation approximately one million times for each inner iteration we perform. Even on today's computers, this is a rather daunting task. The solution to our problem will go much faster if we hold the ray-tracing results in tightly packed one-dimensional arrays. In the early days, this was also necessary in order to manage memory properly. However, that is no longer a consideration for single assembly calculations.

In any event, we wish to hold the ray-tracing data in tightly packed, one-dimensional arrays. One way to do this is to simply allocate enough space that we could not possibly surpass it. That is, we could allocate an array, such as "TrackLengths(2000000)." A more economical approach is the one taken in CASMO-4 and LANCER02. In this approach, the ray-tracing routine is entered twice in a row. The first time the routine is entered, none of the information is retained except for the total number of track lengths traced. Using this one value, all ray-tracing arrays are dimensioned to the minimum size needed and the ray-tracing routine is entered for the second time through, all information is retained.

From the ray-tracing routine, we need only save: the track lengths; the *mesh*, *region*, and *cell* through which each track passes; and the *cell* surface across which each track crosses (if, indeed, it does cross a *cell* surface). The last bit of information is used for the acceleration scheme.

Once we have the tracking information, our best approach is to calculate all mean free paths in all energy groups and hold them in memory in preparation for the iteration scheme. That is, we calculate the following portion of (499):

$$\exp \left\{ -\Sigma_{tr,n}^g \cdot t'_{k,n} (\bar{\varphi}'_i) / \sin \bar{\theta}_j \right\} \quad (517)$$

If there are one million track segments, three polar angles of motion in the quadrature set, and 20 energy groups, the entire size of the array needed to hold (517) will be 60 million words, or

240 Mb. A sizeable amount of memory, but worth every bit of it (pun intended) based on the amount of execution time it saves during the iteration process. The alternative is to evaluate the exponential for every track segment in the problem, for every iteration we perform. This is a very expensive proposition, in terms of computation time.

To employ (517), (499) should be rearranged in a simplified form

$$\Phi_{k,n,\text{out}}^g(\bar{\varphi}_i, \bar{\theta}_j) = \hat{Q}_n^g + \exp[-\Sigma_{tr,n}^g \tau_{k,n}(\bar{\varphi}_i, \bar{\theta}_j)] \cdot (\Phi_{k,n,in}^g(\bar{\varphi}_i, \bar{\theta}_j) - \hat{Q}_n^g) \quad (518)$$

where $\tau_{k,n}(\bar{\varphi}_i, \bar{\theta}_j) = t'_{k,n}(\bar{\varphi}_i)/\sin \bar{\theta}_j$ is the modified track length after being lifted out of the xy -plane of the problem to the appropriate polar angle; and $\hat{Q}_n^g = q_n^g/4\pi\Sigma_{tr,n}^g$ is the term containing the angular source. The scalar source term concealed in (518) is expressed as

$$q_n^g = \sum_{g'} \left(\Sigma_{s,n}^{g' \rightarrow g} + \frac{\Sigma_{p,n}^{g' \rightarrow g}}{k^\infty} \right) \phi_n^{g'} \quad (519)$$

where the production cross section is defined as $\Sigma_{p,n}^{g' \rightarrow g} = \chi_n^g \sum_{g'} v \Sigma_{f,n}^{g'}$.

The scalar flux in (519) – for any given *mesh*, n – is obtained using (497).

5.9.2 The Macro-Band Approach

In the cyclic tracking approach, all characteristics were traced across the entire width of the problem and the end of each characteristic aligned precisely with the beginning of its reflective counterpart along the problem boundaries. An alternative approach to the cyclic tracking method is to employ a macro-band method. In this method, ray tracing takes place on an individual *cell* basis only and characteristics are not forced to align along the boundaries of each *cell*. Instead, angular fluxes at the beginning of a track segment are inferred from the interpolation of the two closest track segments exiting the neighboring *cell*. This is illustrated in Fig. 83 where the ends of the red characteristics do not align precisely with the beginning of the blue

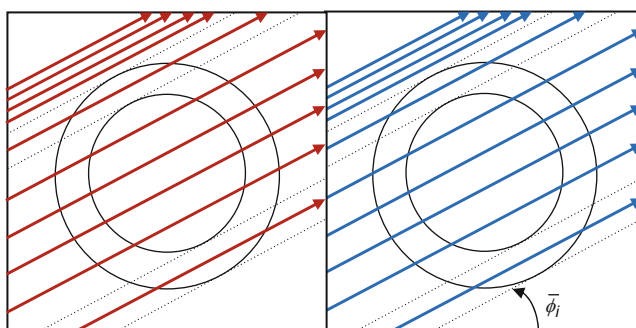


Figure 83
Macro-bands and characteristics

characteristics. To get the value of the angular flux entering a *cell*, the angular flux exiting the neighboring *cell* is linearly interpolated.

The macro-bands are the dotted lines in the pin cells in [Fig. 83](#). They bound the singularities that arise from the intercept of the mesh in the *cell* with the characteristic at angle $\bar{\varphi}_i$. The macro-bands ensure that no characteristic ever passes through a singularity. In our cyclic tracking routine, this was ensured by continuously nudging the track away from a local singularity. We want to avoid singularities because, in such cases, it is unclear which mesh is being intersected. By nudging the characteristic in one direction or another, we force the track to pass through one of the multiple mesh that are part of the singularity.

In the macro-band method, which was first implemented commercially in the HELIOS CCCP method, characteristics are distributed evenly between macro-bands. If desired, characteristics can take on different spacing between different macro-bands, as illustrated in the figure. In subsequent implementations of the concept, such as in the AEGIS lattice physics code, the bands are distributed according to a Gauss–Legendre quadrature set, which improves the accuracy of integration (Yamamoto et al. [2005](#)).

The macro-band method is superior to the cyclic tracking method at treating singularities, but at the price of having to estimate the angular flux at the cell boundaries. Either ray-tracing approach is perfectly adequate for an LWR lattice physics code. The choice is up to the programmer's own preference.

5.10 Quadrature Sets for Two-Dimensional LWR Lattice Calculations

5.10.1 Quadratures for Modeling Polar Motion

The quadrature sets described previously in this section were based on simple formulas that either forced all weights to be equal, or forced all angle increments to be equal. These types of quadratures serve as very good examples for developing the theory of the MoC, but are rather inefficient when used to represent neutron streaming out of the plane of the problem, resulting in the need to model many angles of motion in order to arrive at an accurate solution to the transport equation. The integration can be performed much more efficiently with the use of other quadrature sets that will be discussed in this section.

The use of a Legendre quadrature set is far more efficient for two-dimensional transport problems than either the equal weights or equal angles quadrature sets described in [5.3.3](#). An adequate set of Legendre quadratures are given in [Table 18](#) (Lewis and Miller [1984](#)). There are six separate Legendre quadratures contained in the table from which to choose. For the majority of production analyses, the $N = 6$ quadrature set should be sufficient. This set of angles and weights models neutron motion out of the plane of the problem in three unique polar directions. Solutions using the $N = 6$ quadrature set are virtually saturated and there is little measurable improvement in results by going to a quadrature set that contains more polar directions of motion. The μ values in [Table 18](#) represent the cosine of the polar angle of motion, that is, $\mu_j = \cos \theta_j$. For problems containing mixed-oxide pellets, more polar angles are usually needed in order to account for changes in the flux out of the plane of the problem due to the much larger thermal absorption cross sections.

An even more efficient set of angles and weights can be obtained by minimizing the error involved in numerically integrating the Bickley functions of the collision probability method.

Table 18

Legendre quadratures for modeling polar motion

$P_N(\mu_j)$	j	$\pm\mu_j$	ω_j
$N = 2$	1	0.57735 02691	1.00000 00000
$N = 4$	1	0.33998 10435	0.65214 51549
	2	0.86113 63115	0.34785 48451
$N = 6$	1	0.23861 91860	0.46791 39346
	2	0.66120 93864	0.36076 15730
	3	0.93246 95142	0.17132 44924
$N = 8$	1	0.18343 46424	0.36268 37834
	2	0.52553 24099	0.31370 66459
	3	0.79666 64774	0.22238 10344
	4	0.96028 98564	0.10122 85363
$N = 10$	1	0.14887 43387	0.29552 42247
	2	0.43339 53941	0.26926 67193
	3	0.67940 95682	0.21908 63625
	4	0.86506 33666	0.14945 13492
	5	0.97390 65285	0.06667 13443
$N = 12$	1	0.12523 34085	0.24914 70458
	2	0.36783 14989	0.23349 25365
	3	0.58731 79542	0.20316 74267
	4	0.76990 26741	0.16007 83286
	5	0.90411 72563	0.10693 93260
	6	0.98156 06342	0.04717 53364

This approach leads to the set of angles and weights contained in [Table 19](#) (Yamamoto et al. 2007). Using this quadrature set, an accurate solution to the transport equation can usually be obtained from $N = 2$ for typical uranium-oxide problems. As with all other quadrature sets, more detail may be necessary for problems containing mixed-oxide pellets. Note that the values in the table are the $\mu_j = \sin \theta_j$, not the $\mu_j = \cos \theta_j$.

Alternative polar angle quadrature sets are available in Leonard and McDaniel (1995) and Sanchez et al. (2002).

5.10.2 Quadratures for Modeling Azimuthal Motion

Azimuthal angles of motion are distributed evenly throughout the plane of the problem. There is really no other reasonable choice for distributing the angles in the azimuthal direction for LWR lattice physics calculations. The same set of angles can be used for all energy groups or different quadratures can be used for different energy ranges. In general, the energy ranges that are of interest in lattice physics problems can be split into three separate distributions. This is

Table 19

Tabuchi–Yamamoto quadratures for modeling polar motion

$P_N(\mu_j)$	j	$\pm\mu_j$	ω_j
$N = 2$	1	0.798184	1.000000
$N = 4$	1	0.363900	0.212854
	2	0.899900	0.787146
$N = 6$	1	0.166648	0.046233
	2	0.537707	0.283619
	3	0.932954	0.670148

done in an effort to accurately capture the distinct features of neutron motion as the neutrons lose energy via scattering collisions.

A very large number of angles are required to accurately model neutron motion above 500 keV in order to capture the streaming effect exhibited between isolated fuel pellets. The streaming effect occurs as a result of the neutrons being born in the isolated fuel pellets at very high energies. As the neutrons stream away from the pellets, they suffer very few collisions, and those collisions that do take place tend to result in the neutron losing a substantial amount of energy and slowing down below the 500 keV threshold. Because of this, the angular flux is highly anisotropic and many azimuthal angles are needed in order to properly model the phenomenon. Below the 500 keV threshold, many collisions are taking place in the coolant and, to a lesser extent, in the oxide pellet itself and the angular flux becomes more isotropic such that fewer azimuthal angles are needed to capture the physics of the problem. To produce accurate results, as many as 128 evenly spaced azimuthal angles of motion should be used in all energy groups above 500 keV and 64 evenly spaced azimuthal angles of motion should be used in all energy groups below 500 keV.

In addition to using a different number of directions to model neutron streaming over different energy ranges, a different track spacing between parallel characteristics can be used over different energy ranges. The track spacing is dictated by the variation in cross sections from one material region of the problem to another. Above the up-scatter cut-off point of ~ 2 eV most material cross sections are of a similar size and flux gradients are considered to be relatively mild across the problem. This is true even across the resonance energy range. For energy ranges exhibiting a relatively flat flux profile, the characteristics can be widely spread apart without affecting the accuracy of the solution. As the flux begins to exhibit larger gradients, though, the characteristics must be much closer together in order to accurately capture the physics of the problem. Typical values for track separation are 1 to 2 mm in all groups above the up-scatter cut-off energy of 2 eV and 0.5 to 1 mm in all groups below the up-scatter cut-off energy.

The combination of variations in the number of azimuthal angles and the spacing of parallel characteristics typically produces three separate quadratures for the MoC solution. The three quadrature sets are listed in [Table 20](#). Note that a single quadrature set can be used, but should include the maximum detail from each of the three sets listed in [Table 20](#). That is, 128 azimuthal angles, two polar angles, and a characteristic separation of between 0.05 and 0.1 cm.

Table 20**Typical quadrature sets for different energy ranges**

Range	Upper energy	Lower energy	J^\dagger	$J^{\dagger\dagger}$	d_i [cm]
Fast	20 MeV	500 keV	128	2	0.1–0.2
Epithermal	500 keV	2 eV	64	2	0.1–0.2
Thermal	2 eV	10^{-5} eV	64	2	0.05–0.1

[†] Number of azimuthal angles distributed over 2π rad.^{††} Number of polar angles distributed over $\pi/2$ rad.

This will increase execution time with no improvement in accuracy, but will ease some of the bookkeeping within the code.

5.11 Acceleration Schemes for Two-Dimensional Calculations

The method of characteristics is notoriously slow to converge. Thankfully, this is not much of a problem for lattice physics calculations, for a couple of reasons. First, there exist a couple of sufficient acceleration schemes to speed up convergence. Second, there almost always exists a very good flux guess from which to begin the iteration process for a new calculation. Because of this second reason, the flux is rarely far from a converged solution and the acceleration scheme becomes less important. This is a consequence of the sheer number of state points that must be analyzed by the lattice physics code in order to provide the needed data to the three-dimensional nodal code. Each state point differs little from the previous point analyzed and the flux from one point is an excellent starting guess for the following point.

In this section, we will discuss two very reasonable and easily implemented acceleration schemes for the MoC. Both schemes are equally acceptable for single assembly lattice physics calculation. The CMFD scheme is superior for very large problems that contain multiple assemblies. Such calculations, though, are outside the scope of providing cross section data to three-dimensional nodal codes.

5.11.1 Coarse Mesh Rebalance

Coarse mesh rebalance, discussed in “Spatial acceleration” for one-dimensional slabs, is an adequate scheme for accelerating the spatial convergence rate of the two-dimensional characteristics solution. Once again, we want to solve the balance equation given in (462) and reproduced below,

$$\left[\sum_{m \in n} \Sigma_{r,m}^g \phi_m^g V_m + \sum_{s \in n} J_{\text{out},s,n}^g \right] \cdot f_n^g = \sum_{m \in n} q_m^g V_m + \sum_{s' \in n'} J_{\text{in},s',n'}^g \cdot f_{n'}^g \quad (520)$$

where m represents the *fine mesh* within a *cell*, n ; s represents the surfaces to the *cell*; and s' represents the surfaces to neighboring *cell*, n' . The coarse mesh are the *cells* of the problem, such as those illustrated in  Fig. 72. The solutions to the coupled balance equations are the

f_n^g values – one for each coarse mesh in the problem. Once the f_n^g values are known, the scalar flux can be modified as

$$\phi_m'^g = \phi_m^g \cdot f_n^g \quad (521)$$

for all *fine mesh*, m , within *cell* n . The angular flux along the cell boundaries can also be modified,

$$\Phi_{k,i,j,m}'^g = \Phi_{k,i,j,m}^g \cdot f_n^g \quad (522)$$

[Equation \(520\)](#) is solved using a red–black iteration scheme, just as was done for the two-dimensional coupling calculation in [Sect. 4](#). All values of f_n^g are initialized to unity to begin the iterations. With these initial values, a sweep is performed across the entire problem, solving the balance equation for the f_n^g values in all red *cells*. Following this, a second sweep is performed across the entire problem, solving the balance equation for the f_n^g values in all black *cells* – using the newly calculated f_n^g values in all red *cells* from the previous sweep. This process continues, un-accelerated, until the f_n^g value in all *cells* converge. The currents in [\(520\)](#) are calculated as

$$J_{\text{out},s,n}^g = \sum_j \sum_i \sum_k \Phi_{k,i,j,m}^g \cdot \omega_i \cdot \omega_j \cdot |\cos \varphi_i \cdot \sin \theta_j| \quad (523)$$

where i is an azimuthal angle; j is a polar angle; and k is a specific characteristic crossing the *cell*. The inward-directed current across a surface is calculated in the same way, but for the opposite azimuthal angles. For instance, along the east face of a *cell*, the outward-directed angles of motion extend from $-\pi/2$ to $\pi/2$, whereas the inward-directed angles of motion extend from $\pi/2$ to $3\pi/2$. Along the west surface to the cell, the situation is exactly the opposite.

The acceleration is performed following each inner iteration. For this acceleration scheme, there should only be one inner iteration performed per energy group. This scheme is not guaranteed to converge, so it is prudent to include a check for oscillations or divergence between applications. It is very rare that the scheme not converge for typical LWR lattice physics calculations. However, for somewhat extreme cases, such as 100% voided coolant cases at hot conditions, it is possible for the scheme to fail. If it appears that the scheme is diverging or oscillating, the scheme can simply be disengaged for the problem and the MoC iterations can continue un-accelerated. A more rigorous formulation can be found in Yamamoto ([2005](#)) as applied to generalized geometries, not just LWRs. In Yamamoto ([2005](#)), the CMR is applied to accelerate the solution both spectrally and spatially.

5.11.2 Coarse Mesh Finite Difference

A slightly different approach that can be used to accelerate both the spatial and spectral convergence rate simultaneously is the coarse mesh finite difference scheme (CMFD) that has been applied very successfully to nodal iterations ([Smith 1983](#)). Here, we are solving the diffusion equation using a diffusion coefficient that preserves the details from the MoC solution. The information needed to apply the CMFD scheme is similar to that needed to apply the CMR.

For lattice physics calculations, the CMFD acceleration technique is applied on a cell basis, just like the CMR technique ([Smith and Rhodes 2000](#); [Cho 2002](#); [Joo et al. 2002](#); [Smith and](#)

Rhodes 2002; Clarno 2007). For a given energy group, the contents of a cell are homogenized using the typical formula (we have dropped the broad energy group symbol from the following variables for conciseness)

$$\bar{\Sigma}_{x,I} = \frac{\sum_{i \in I} \Sigma_{x,i} \phi_i V_i}{\bar{\phi}_I V_I} \quad (524)$$

where the average scalar flux in the cell is given by

$$\bar{\phi}_I = \frac{\sum_{i \in I} \phi_i V_i}{V_I} \quad (525)$$

and V_I is just the total volume of the cell.

To solve the diffusion equation, we make reference to the variables depicted in Fig. 84. We want to solve for the flux in a given coarse mesh (i.e., cell), namely $\bar{\psi}_I$. Within each coarse mesh, the diffusion equation is given by

$$\frac{\partial J_I}{\partial u} + \bar{\Sigma}_{r,I} \bar{\psi}_I = S_I \quad (526)$$

where, along the surface of each coarse mesh, the current is defined as

$$J_I = -D_I \frac{\partial \psi(u)}{\partial u} \quad (527)$$

Here, u is the direction either along the x -axis or the y -axis; and $\bar{\Sigma}_{r,I}$ is the removal cross section, $\bar{\Sigma}_{r,I} = \bar{\Sigma}_{tr,I} - \bar{\Sigma}_{s,I}^{g \rightarrow g}$. The total source, S_I , is defined in the usual way (i.e., scatterings plus fissions).

Using the current from our MoC solution, that is, (523), we can define a diffusion coefficient along each surface of each cell that preserves the details from the fine-mesh calculation. For the u_I^+ surface we would have

$$\hat{D}(u_I^+) = -\frac{\hat{J}(u_I^+) + \tilde{D}(u_I^+) \{\bar{\phi}_{I+1} - \bar{\phi}_I\}}{\bar{\phi}_{I+1} + \bar{\phi}_I} \quad (528)$$

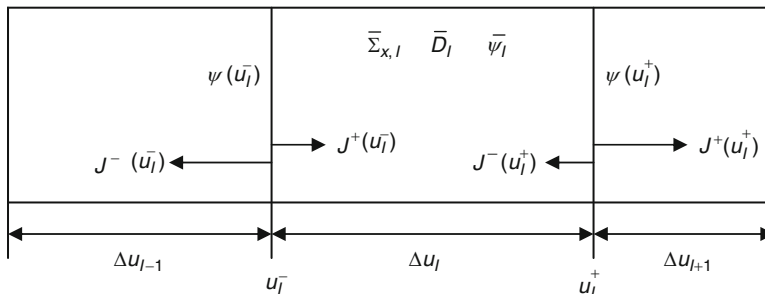


Figure 84
Parameters for the CMFD scheme

where

$$\tilde{D}(u_I^+) = \frac{2\bar{D}_{I+1}\bar{D}_I}{\bar{D}_{I+1}\Delta u_I + \bar{D}_I\Delta u_{I+1}} \quad (529)$$

The current in (528) is the net current from the MoC solution. It is defined as $\hat{J}(u_I^+) = J_{\text{out}}(u_I^+) - J_{\text{in}}(u_I^+)$ along the east surface to the *cell*, and as $\hat{J}(u_I^-) = J_{\text{in}}(u_I^-) - J_{\text{out}}(u_I^-)$ along the west surface to the *cell*. That is, it is the net current moving in the positive u direction. The *cell*-averaged diffusion coefficient is calculated in the usual way, $\bar{D}_I = (3\bar{\Sigma}_{tr,I})^{-1}$. The surface current can be expressed by rearranging (529), to wit,

$$\hat{J}(u_I^+) = -\tilde{D}(u_I^+) \{\bar{\phi}_{I+1} - \bar{\phi}_I\} - \hat{D}(u_I^+) \{\bar{\phi}_{I+1} + \bar{\phi}_I\}.$$

Using these parameters, we solve the diffusion equation for the average flux in each cell,

$$\left\{ \hat{J}(x_I^-) - \hat{J}(x_I^+) \right\} - \left\{ \hat{J}(y_I^-) - \hat{J}(y_I^+) \right\} + \bar{\Sigma}_{r,I} \bar{\psi}_I V_I = S_I V_I \quad (530)$$

$$S_I = S_I^g = \sum_{g' \neq g} \bar{\Sigma}_{s,I}^{g' \rightarrow g} \psi_I^{g'} + \frac{\chi_I^g}{k_\infty} \sum_{g'} v \Sigma_{f,I}^{g'} \psi_i^{g'} \quad (531)$$

More information on acceleration techniques for the MoC can be found in Yamamoto (2005), Smith and Rhodes (2000), Cho (2002), Joo et al. (2002), Smith and Rhodes (2002), and Clarno (2007).

5.12 Treating Very Thin Cylindrical Regions

One of the few drawbacks with the method of characteristics is in its treatment of very thin, highly absorbing cylindrical regions. Unfortunately, these regions are very common in certain PWR fuel designs, where they arise in the form of a very thin layer of ZrB₂ sprayed onto the outside of fuel pellets as a burnable absorber, referred to as IFBA pellets. The layer is, on average, no thicker than 0.002 cm.

The issue is depicted in Fig. 85, where three rays are illustrated to bisect the fuel pellet and the absorber coating. The rectangles depicted in the figure represent the area associated with the track lengths that bisect the absorber coating. In the case on the left, the characteristics are arranged in such a way that one of the tracks just happens to skim along the edge of the thin absorber region. In the case on the right, the characteristics are shifted ever so slightly and no track skims the edge of the thin absorber region. Because the region is so strongly absorbent, the solution is very sensitive to the length of track that bisects it and we will get two very different solutions to the situation depicted in the figure. This is highly undesirable. With our cyclic tracking method, the only way to truly avoid this sensitivity is to distribute characteristics with a spacing equal to the width of the region – 0.002 cm – which is out of the question.

An alternative solution to our dilemma is to homogenize the thin coating with the fuel pellet. If we have performed a pin-cell spectral calculation on this pin to generate a spectrum with which to condense cross sections, then we have a good flux distribution to use for the homogenization. Assuming that our flux from the pin-cell spectral calculation is represented

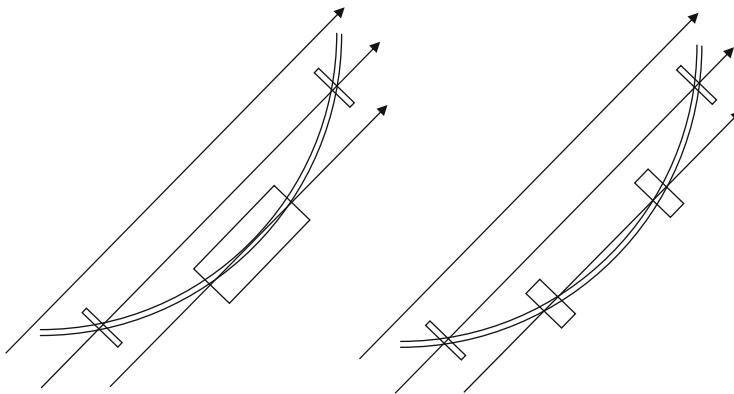


Figure 85
Characteristics skimming a thin, strongly absorbent region

as ϕ_{fuel}^g in the fuel pellet and ϕ_{absorber}^g in the absorber coating, where g is our fine-group energy structure, we first collapse the individual cross sections using the typical formula

$$\begin{aligned}\Sigma_{x,\text{fuel}}^G &= \frac{\sum_{g \in G} \Sigma_{x,\text{fuel}}^g \phi_{\text{fuel}}^g}{\sum_{g \in G} \phi_{\text{fuel}}^g} \\ \Sigma_{x,\text{absorber}}^G &= \frac{\sum_{g \in G} \Sigma_{x,\text{absorber}}^g \phi_{\text{absorber}}^g}{\sum_{g \in G} \phi_{\text{absorber}}^g}\end{aligned}\quad (532)$$

where G represents the broad-group energy structure. While we are collapsing cross sections, we must also collapse the flux in the two regions since we will need the flux to homogenize the broad-group cross sections of the two regions, to wit,

$$\begin{aligned}\psi_{x,\text{fuel}}^G &= \sum_{g \in G} \phi_{\text{fuel}}^g \\ \psi_{x,\text{absorber}}^G &= \sum_{g \in G} \phi_{\text{absorber}}^g\end{aligned}\quad (533)$$

Now we homogenize the two regions using flux and volume weighting to preserve the reaction rates

$$\bar{\Sigma}_x^G = \frac{\Sigma_{x,\text{fuel}}^G \psi_{\text{fuel}}^G V_{\text{fuel}} + \Sigma_{x,\text{absorber}}^G \psi_{\text{absorber}}^G V_{\text{absorber}}}{\psi_{\text{fuel}}^G V_{\text{fuel}} + \psi_{\text{absorber}}^G V_{\text{absorber}}}\quad (534)$$

After homogenizing the regions, we still want to maintain the true geometry of the pellet and the coating during the MoC solution in order to simplify the bookkeeping in the code. To account for this, the cross sections represented by (534) are applied to both the fuel pellet and the absorber coating.

Following the MoC solution, we must back out the true flux in the absorber coating and the fuel pellet. To do this, we first average the MoC flux in the fuel pellet and the absorber coating using a straightforward volume weighting

$$\bar{\phi}_{\text{fuel}}^G = \frac{\phi_{\text{fuel}}^G V_{\text{fuel}} + \phi_{\text{absorber}}^G V_{\text{absorber}}}{V_{\text{fuel}} + V_{\text{absorber}}} \quad (535)$$

With this average flux, we can superimpose the condensed flux from the pin-cell spectral calculation and obtain the true flux for each region,

$$\begin{aligned} \phi_{\text{fuel}}^G &= \frac{\psi_{\text{fuel}}^G}{\bar{\phi}_{\text{fuel}}^G} \cdot \left\{ \frac{\psi_{\text{fuel}}^G V_{\text{fuel}} + \psi_{\text{absorber}}^G V_{\text{absorber}}}{V_{\text{fuel}} + V_{\text{absorber}}} \right\} \\ \phi_{\text{absorber}}^G &= \frac{\psi_{\text{absorber}}^G}{\bar{\phi}_{\text{fuel}}^G} \cdot \left\{ \frac{\psi_{\text{fuel}}^G V_{\text{fuel}} + \psi_{\text{absorber}}^G V_{\text{absorber}}}{V_{\text{fuel}} + V_{\text{absorber}}} \right\} \end{aligned} \quad (536)$$

This approach works remarkably well to provide consistently accurate results when extremely thin cylindrical regions are present in the fuel design. Alternatively, this entire issue can be avoided by moving to a ray-tracing method based on macro-bands.

5.13 Final Comments

This section has presented a very detailed derivation of the method of characteristics, in its most fundamental, simplistic form. Within this derivation, it was assumed that scattering effects could be treated as being isotropic, with transport-corrected cross sections accounting for the majority of effects caused by anisotropic scattering. When analyzing a single lattice employing perfectly reflective or periodic boundaries, such an assumption is quite adequate – especially for neutron calculations, but even for gamma calculations. If particles are allowed to leak out of the system through the boundaries, though, this assumption may be invalidated.

It was also assumed that the use of a flat flux/flat source approximation was valid and would produce accurate results, so long as the fine-mesh were small enough to capture all flux gradient effects in the thermal groups. Once again, when analyzing a single lattice employing perfectly reflective or periodic boundaries, such an assumption is quite adequate. If multiple bundles are to be analyzed, or if large areas of water are to be included in the problem, such an assumption may be invalidated.

In any case, the fundamental concepts described in this section are contained in many of today's lattice physics codes and an understanding of this section should provide the reader with a reasonably good grasp of current lattice physics transport methods.

It is interesting to note that, in the not too distant past, the fine-mesh transport solution in a lattice physics code accounted for the overwhelming majority of computer resources (memory use and execution time). Back in the day, when it was common – almost necessary – for cross section libraries to be limited to 100 energy groups and 100 different isotopes, and when burnup chains were linearized, the fine-mesh transport solution could easily account for two-thirds of the total execution time, or more. In some current lattice physics codes employing a cross section condensation scheme, the fine-mesh transport solution accounts for less than one-third of the total execution time and is, by no means, limiting on memory requirements. The biggest

burden on computer resources in these lattice physics codes is in constructing the macroscopic scattering matrices from the microscopic data contained in the cross section library. Here, we are referring to the construction of a matrix containing possibly 600×600 elements from as many as 200 isotopes (if the contribution from fission products is included). This has to be done in every fuel region in the lattice. An equal amount of execution time can be spent solving the burnup chains in their matrix form. Like the calculation of the macroscopic scattering matrix, this has to be done in every fuel region of the lattice, which can easily exceed 200 unique regions in a BWR lattice containing 20 or so Gadolinium pins, each split into 10 or 12 multiple depletion rings. These two pieces of the lattice physics code – constructing macroscopic scattering matrices and solving the burnup matrix – can easily account for two-thirds of the total execution time of a modern lattice physics code.

6 Burnup Calculation

6.1 Objective

Nuclear fission is one of the principal mechanisms in the generation of energy from nuclear fuels. The composition of fuels varies during irradiation in a nuclear reactor core. In the vocabulary of reactor physics, the change in fuel composition due to nuclear fission, neutron capture, radioactive decay, and other factors, is referred to as “burnup.” The burnup of a nuclear fuel is different from the conventional concept of burnup, which is based on chemical reactions. Therefore, when uranium “burns” in a nuclear reactor core, there is no emission of CO₂ since the burnup of a nuclear fuel is based on nuclear reactions. While energy is released by changes in the chemical bonding states of materials in conventional burnup, in nuclear burnup, energy is generated by the changes in nuclear binding. If burnup is viewed as a “process of energy generation through changes in a material,” then nuclear fission can quite naturally be considered a burnup phenomenon. In this sense, the technical term burnup seems quite aptly and carefully chosen.

The properties of nuclear fuels depend on the composition of the fuel. The characteristics of the reactor core therefore undergo changes during burnup. In practice, precise prediction of core lifetime and reactor behavior during burnup is an essential part of reactor core analysis. In fact, the prediction accuracy of burnup calculations is a critical factor in the reactor analysis sequence.

In this section, the physics of the burnup of nuclear fuel is discussed. The fundamental theoretical basis for burnup phenomena will first be discussed, and then the major numerical solution schemes for solving the burnup equation will be presented. The burnup behavior of gadolinium, a burnable poison in nuclear fuel, is quite important in actual core analysis, but its behavior is somewhat complicated, requiring special treatment in numerical modeling and calculations. ➤ 6.4 will therefore be devoted to the treatment of gadolinium-bearing fuels. Finally, some discussion will be presented on power normalization, which plays an inevitable role in burnup calculations.

In reactor core analysis, there are two levels of burnup calculation, that is, burnup in lattice physics analysis, and burnup in core analysis. This section focuses on the former, that is, burnup calculation in lattice physics computations.

6.2 The Physics of Burnup and its Modeling

6.2.1 Phenomena during Burnup

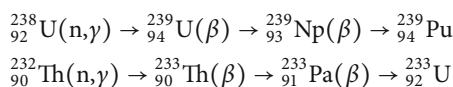
During burnup in a nuclear reactor, the following phenomena occur in nuclear fuels:

Depletion of Fissile Nuclides (a)

The fissile nuclides (e.g., ^{235}U , ^{239}Pu) deplete during burnup due to fission reactions. This effect has a negative impact on fuel reactivity since the number of fissile nuclides decreases during burnup.

Conversion from Fertile Nuclide to Fissile Nuclide (b)

Fertile nuclides become fissile nuclides through neutron capture and beta decay, for example,



The conversion effect increases the number of fissile nuclides, and thus has a positive impact on fuel reactivity during burnup.

Production of Fission Products (c)

The fissions of fissionable nuclides yield various fission products. Since these fission products are neutron absorbers, they have a negative impact on fuel reactivity.

The above three phenomena, that is, (a)–(c), take place simultaneously in nuclear fuel during burnup. In thermal reactors (e.g., light water reactors), the conversion effect is rather small, and the absorption by fission products is large, due to the thermal neutron spectrum. Note that this conversion takes place by means of the resonance capture of fertile material in the epithermal energy region; thus, the conversion is generally small in thermal reactors.

Absorption cross sections of some fission products are large in the thermal energy region. Therefore, since the negative effects on reactivity ((a) and (c)) are large, and the positive effect (b) is small in thermal reactors, the multiplication factor of nuclear fuel decreases as burnup proceeds.

The above dynamic is different in typical fast reactors. Since fast neutrons dominate nuclear reactions in a fast reactor core, the conversion effect is much larger than it is in thermal reactors. Furthermore, the absorption by fission products is small due to the absence of thermal neutrons. Consequently, due to greater conversion (the positive reactivity effect) and smaller absorption by fission products (negative reactivity effect), the reduction of the multiplication factor of nuclear fuel during burnup becomes smaller than that in thermal reactors.

In addition to the above effects, which have a major impact on fuel reactivity, the following phenomena must also be considered as contributors to fuel reactivity:

Decay

Various nuclides are produced during burnup but many of them are unstable, so they are transformed into other nuclides through α - $,$ β -decay, spontaneous fission, and other processes. This decay has a considerable impact on fuel reactivity, as will be described later.

Transmutation of Nuclides due to Neutron Absorption

Conversion is included in this category. During burnup, various reactions due to neutron absorption take place as follows:

- (n, 2n): neutron absorption followed by emission of two neutrons
- (n, 3n): neutron absorption followed by emission of three neutrons
- (n, 4n): neutron absorption followed by emission of four neutrons
- (n, γ): neutron absorption followed by emission of gamma radiation
- (n, p): neutron absorption followed by emission of a proton
- (n, d): neutron absorption followed by emission of a deuteron
- (n, t): neutron absorption followed by emission of a triton
- (n, α): neutron absorption followed by emission of an alpha particle
- Other

The transmutation of nuclides due to neutron absorption is very important, especially for burnup calculations of burnable poison in a light water reactor analysis. Burnable poison is used to flatten out the variations in reactivity during burnup and to improve the characteristics of the core neutronics. The burnable absorber nuclides loaded in a reactor core at the beginning of cycle (BOC) are depleted and converted to other nuclides during burnup through neutron capture. Thus, the negative reactivity of the burnable poison diminishes or disappears at the end of cycle (EOC); that is, the burnable poison is “burnt-out” at EOC.

The flattening of variations in reactivity provides several merits in actual core design. In the case of PWR, a higher reactivity of fresh fuel assemblies at BOC requires a higher boron concentration to suppress excess reactivity in the core. However, a high boron concentration may create problems related to water chemistry, for example, excess deposition of crud on the cladding. A high boron concentration may also have a negative impact on core safety, since the moderator temperature coefficient tends to be positive, and reactivity insertion during a boron dilution accident tend to be large. In the case of BWR, higher core reactivity may reduce the shutdown margin, making core design difficult. The above discussion clearly indicates the important role of burnable poison in light water reactor core design. In fact, a burnable poison is almost always used in light water reactor core designs, with a few exceptions (e.g., no burnable poison is used in the short operating cycle).

Boron, gadolinium, and erbium are the major burnable absorber materials in light water reactor designs. The actual implementation and design of these burnable poisons in a fuel assembly is a key topic in fuel design for which lattice physics computation is used.

6.2.2 Burnup Chain

Design and Setup of Burnup Chain

As described in the previous section, various transmutations of nuclides occur during burnup in a reactor core. In a burnup analysis, a series of nuclide changes is treated by the concept of a “chain,” since the transmutations of nuclides occur successively. In reactor physics calculations, this chain is known as the burnup chain. For example, the conversion from a fertile to a fissile nuclide, $^{238}\text{U} \rightarrow ^{239}\text{U} \rightarrow ^{239}\text{Np} \rightarrow ^{239}\text{Pu}$, is a typical burnup chain that appears in reactor analysis.

In general, burnup chains are classified in terms of the following nuclides:

- Heavy nuclides (Th, U, Pu, Am, Cm, etc.)
- Fission products (Xe, Sm, Pm, etc.)
- Burnable absorber or burnable poison nuclides (B, Gd, Er, etc.)

The actual nuclide transmutations in nuclear fuels are highly complicated, with several thousands of nuclides being produced and disappearing through various nuclear reactions. Since the direct modeling of such complex nuclide behavior is not feasible, lattice physics computation treats the specific nuclides that have significant or considerable impact on the characteristics of neutronics.

From the viewpoint of calculation accuracy, of course, detailed modeling is desirable; that is, the treatment of as many nuclides as possible. However, many cross section libraries for these nuclides must be prepared, and their effective cross sections must be evaluated in resonance calculations in order to treat the many nuclides. Since such detailed treatment is quite burdensome in terms of memory storage and computation time, the number of nuclides used in a burnup calculation must be selectively limited. In the case of a burnup calculation in a small configuration, for example, single pin-cell geometry or a fuel assembly, a very detailed burnup chain can be used. In actual reactor core calculations, however, the scale of the calculation configuration must be carefully assessed, as discussed below.

Let us assume that a set of burnup chains, which includes 300 nuclides, is used for a reactor core analysis. Note that a set of burnup chains with 300 nuclides is a detailed one in current burnup analysis. When the variations in nuclide number densities are tracked in each fuel pin, the required memory storage for a three-dimensional PWR whole-core analysis is evaluated as follows:

$$1[\text{byte}/\text{nuclide}] \times 300[\text{nuclides}/\text{burnup region}] \times 300[\text{burnup regions}/\text{fuel assembly(radial)}] \\ \times 193[\text{fuel assemblies}/\text{core}] \times 60[\text{meshes}/\text{fuel assembly(axial)}] = 10^9[\text{byte}].$$

The above rough estimate suggests that 1 GB of memory storage is necessary to hold the nuclide number densities when 300 nuclides are tracked in pin-by-pin whole-core analysis.

In order to reduce the computational burden, the number of nuclides explicitly (independently) treated in burnup calculations may be limited to the major nuclides that have a considerable impact on the neutronics characteristics. Those that have a lesser impact would be gathered and treated in an approximate manner as one or several groups. Fission products, in particular, are often modeled as several groups of pseudo fission product nuclides that comprise multiple fission products. The modeling of pseudo fission products depends on the burnup chain, and there are variations on this, ranging from a very simple one-group model (combine all fission products that are not explicitly treated), to a complicated model (which considers dependency on fissile nuclide, saturation, and the non-saturation behaviors of number density during burnup). For example, the MVP-BURN code, which is a continuous energy Monte Carlo code with burnup capability, has several burnup chains, as shown in [Table 21](#).

The burnup chain used in the MVP-BURN code is depicted in [Figs. 86–88](#).

In the case of a Monte Carlo burnup calculation, since continuous energy (point-wise) cross section data for each nuclide are stored in memory, utilization of a detailed burnup chain requires a larger amount of memory. Furthermore, the reaction rate estimate (tally) of each nuclide, which is inevitable in a burnup calculation, requires a longer computation time when

Table 21
Burnup chains implemented in the MVP-BURN code

Name	Number of heavy nuclides	Number of FPs	Number of pseudo FPs	Note
Standard	21 (^{234}U to ^{246}Cm)	49	1	Conventional UO ₂ /MOX analysis
General	21 (^{234}U to ^{246}Cm)	103	1	PIE analysis, etc.
Developer	28 (^{232}Th to ^{246}Cm)	193	0	Verification of a burnup chain
Simplified	19 (^{235}U to ^{245}Cm)	30	4	Conventional UO ₂ /MOX analysis

Source: Okumura et al. (2000, 2007).

the number of nuclides in a calculation configuration is large. In general, therefore, the utilization of a simple burnup chain model that satisfies the purpose and accuracy requirements of the analysis is desirable. Note that “pseudo” treatment, which is sometimes used for fission products, is not usually applied to heavy nuclides; the less important heavy nuclides are simply omitted from the burnup chain.

Our discussion thus far has focused particularly on the neutronics characteristics, which is major objective of lattice physics computing. In high burnup and MOX fuels, however, evaluation of the source term, that is, the neutron/gamma source intensities and heat generation rate, becomes important for fuel storage and reprocessing. These source terms depend on the isotopic composition of the fuel. For example, the neutron source intensity and heat generation rate are generally dominated by ^{242}Cm , ^{244}Cm , and ^{238}Pu , respectively.

A dedicated code that has an extensive burnup chain, for example, ORIGEN2, is commonly used to estimate the source term, since the important nuclides may not be included in the burnup chain of a common lattice physics code, in which nuclides are selected from the point of view of neutronics. A detailed burnup analysis code such as ORIGEN2, however, applies an approximate treatment to the cross section of each nuclide. For example, ORIGEN2 has one-group cross section libraries that are generated and collapsed under the neutron spectra of several typical reactor types. Users can select a cross section library that is suitable for their analysis. Though various cross section libraries are provided, the neutron spectrum assumed for library generation may not well reproduce that of the analysis configuration. As a consequence, dedicated burnup analysis codes are not superior to lattice physics codes in terms prediction accuracy for nuclide number density.

The above discussion suggests that any new burnup chain developed for lattice physics computations might have capability of source term estimation. In fact, instead of pseudo fission products, most recent lattice physics codes adopt detailed burnup chains in which 20–30 heavy and 200–300 fission-product nuclides that are explicitly considered.

Evaluation of Fission-Product Yield

One of the most troublesome tasks in the design of a burnup chain is the evaluation of fission-product yields. The fission-product yield is given in a nuclear data file (e.g., the ENDF

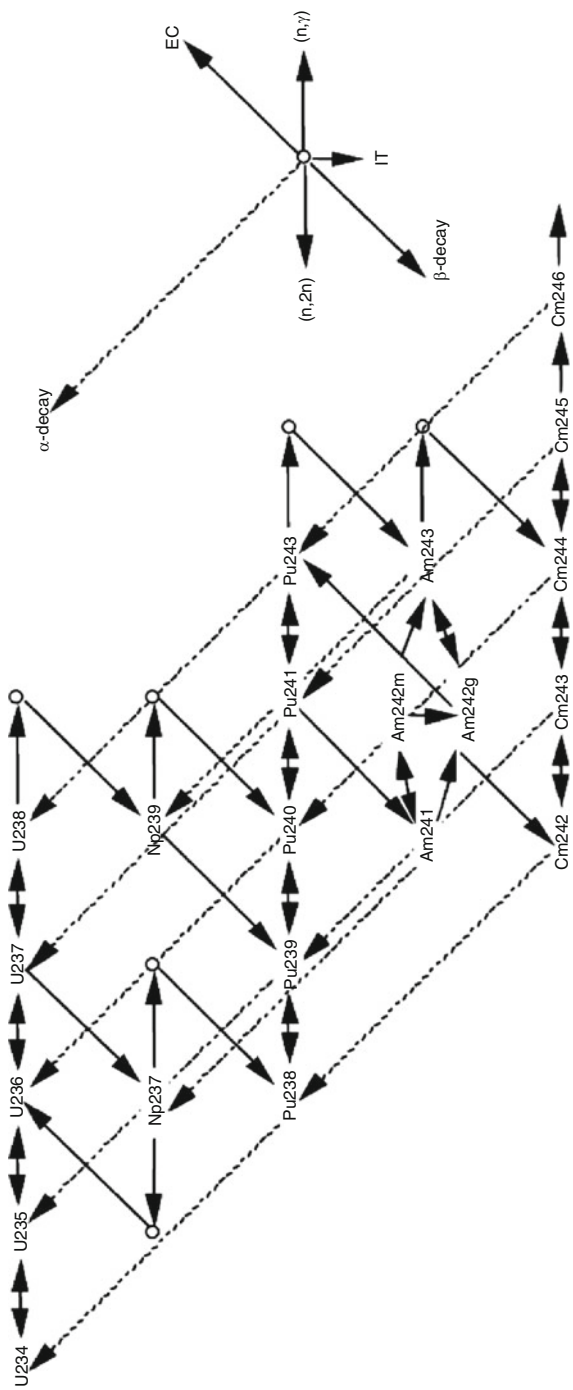


Figure 86
Burnup chain of MVP-BURN code for heavy nuclides (Standard burnup chain) (Okumura et al. 2000, 2007)

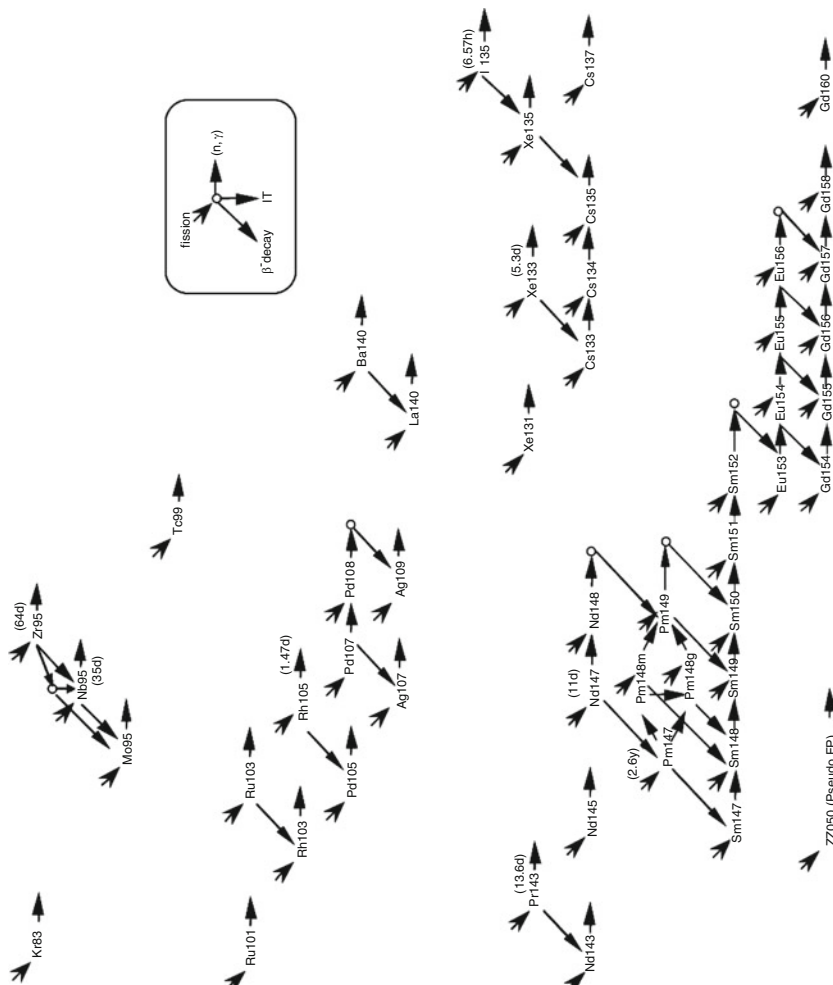
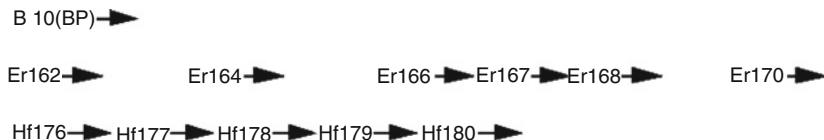
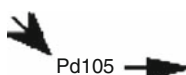


Figure 87
Burnup chain of MVP-BURN code for fission product nuclides (Standard burnup chain) (Okumura et al. 2000, 2007)

**Figure 88**

Burnup chain of MVP-BURN code for burnable poison nuclides (Standard burnup chain) (Okumura et al. 2000, 2007)

**Figure 89**

Simplified chain for ^{105}Pd in the MVP-BURN code

fission-product data or the JNDC nuclear data library of fission products), in which the yield values for more than 1,000 fission products are given (McLane 2001; Ihara 1989). In contrast, just a few dozen to a few hundred fission products are independently treated in lattice physics codes. This difference (more than a thousand versus a few hundred) should be carefully taken into account when the fission-product yield is being set. A simple treatment that neglects the yields of nuclides not included in the burnup chain is not appropriate.

For example, let us consider the part of the burnup chain in [Fig. 87](#), namely $^{105}\text{Rh} \rightarrow ^{105}\text{Pd}$. This part of the burnup chain is expressed somewhat differently in the Simplified and the Developer chains of the MVP-BURN code, as shown in [Figs. 89](#) and [90](#).

In the Simplified chain, ^{105}Pd is produced directly from a fission reaction. But in the Standard chain shown in [Fig. 87](#), ^{105}Pd is partly produced from the beta decay of ^{105}Rh , and the rest is produced from a fission reaction. Finally, in the Developer chain, the production of ^{105}Pd has three paths: a neutron capture of ^{104}Pd , a beta decay of ^{105}Rh , and a fission reaction. The fission-product yields for these chains are compared in [Table 22](#).

[Table 22](#) clearly indicates that the yields of ^{105}Rh and ^{105}Pd are very different in the different burnup chains. In the Developer chain, the yields for ^{105}Rh and ^{105}Pd are very small (effectively zero). These are the independent yields, that is, the number of fission products directly produced from a fission reaction. In the Standard chain, though the yield for ^{105}Pd is the same as that from the Developer chain, ^{105}Rh has a larger yield of 9.63844×10^{-3} . This is the cumulative yield, which is obtained by summing the yields of the “upstream” fission products of ^{105}Rh , for example, ^{104}Ru and ^{105}Ru . In other words, the “upstream” fission products of ^{105}Rh are assumed to be immediately transformed into ^{105}Rh along the burnup chain. The cumulative yield is estimated based upon this consideration. A similar assumption is used for the Simplified chain, in which the upstream fission products of ^{105}Pd are immediately transformed into ^{105}Pd after a fission reaction.

The above discussion suggests that the estimation of fission yields (whether independent or cumulative) depends on the design of a burnup chain, and is a very complicated task. A common practice today is to adopt an ad hoc approach, that is, the utilization of small ad hoc codes that calculate the independent and cumulative yield.

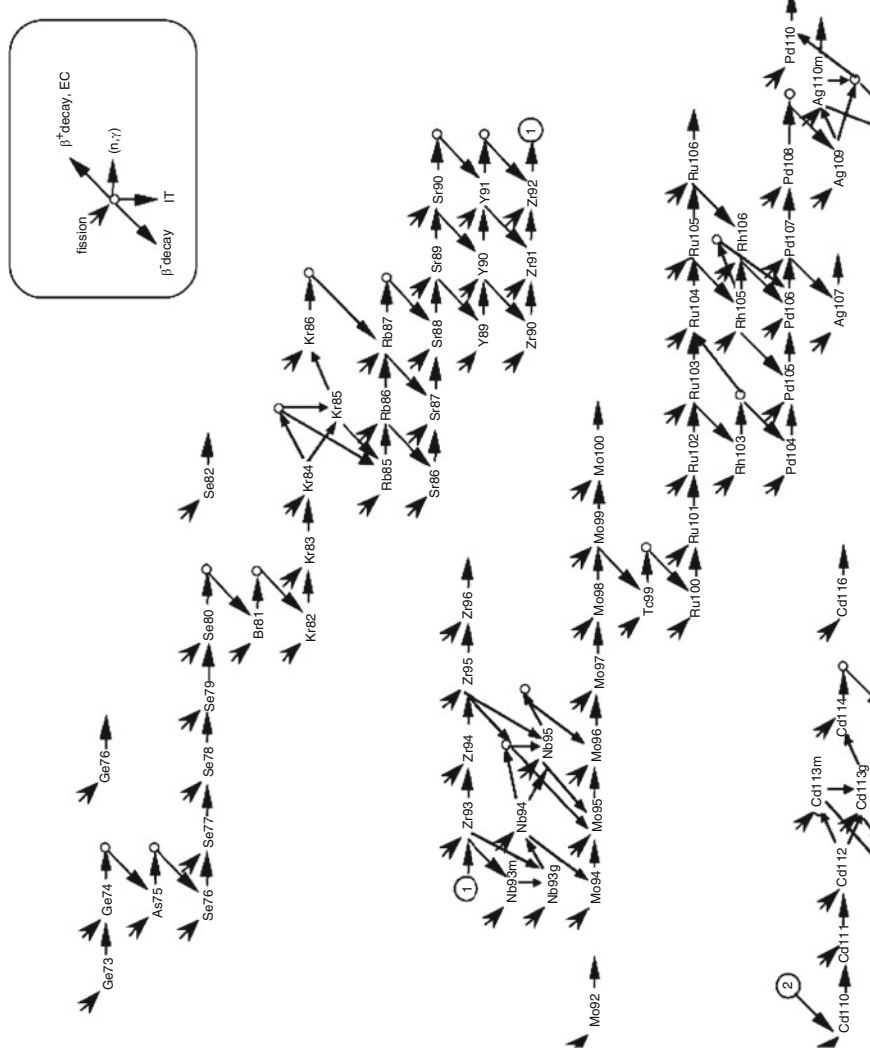


Figure 90
Developer chain including ^{105}Rh and ^{105}Pd in the MVP-BURN code (Okumura et al. 2000, 2007)

Table 22

Yields of ^{105}Rh and ^{105}Pd in the burnup chains of the MVP-BURN code

Name	^{105}Rh	^{105}Pd
Developer	1.70062E-08	9.99776E-13
Standard	9.63844E-03	9.99776E-13
Simplified	–	9.63844E-03

Estimation of Cross Sections and Yields for Pseudo Fission Products

When the number of fission products in a burnup chain is small, the pseudo fission products should be used in order to maintain the prediction accuracy of the burnup dependency of fuel reactivity (Garrison and Roos 1962; Iijima and Yoshida 1982; Ikehara et al. 1998). The cross sections and yields of the pseudo fission products are evaluated and adjusted with the calculation results of a detailed burnup chain, for example, the Developer chain in the MVP-BURN code. Therefore, in a strict sense, the cross section and yield of pseudo fission products depend on the reactor types being analyzed. Different pseudo fission–product nuclides may therefore need to be prepared for different reactor types.

The utilization of a detailed burnup chain with many independent fission products reduces the importance of the pseudo fission products. For example, when 112 fission products are independently considered in a BWR burnup analysis, we can capture more than 98% of the neutron absorption by the fission products. In this case, the reactivity discrepancy caused by the utilization of pseudo fission products is less than 0.1% $\Delta k/k$ up to 100 GW d/t (Ikehara et al. 1998). Utilization of a more detailed burnup chain, such as the Developer chain of the MVP-BURN code, allows for the elimination of the pseudo fission product. If we take into account the ongoing improvements in computer platforms, the incorporation of a detailed burnup chain is recommended.

Branching Ratio

Some nuclides can produce different daughter nuclides after the decay of the neutron capture reaction. For example, ^{241}Am can be transformed into $^{242\text{m}}\text{Am}$ or ^{242}Am after the capture of a neutron. The ratio of branch (branching ratio) is inherent to the reaction and the nuclide. Though the branching ratio depends on the neutron energy, there are not many experimental results on this relationship. The branching ratio can therefore be a source of error in burnup calculations. Though the major sources of error in burnup calculations are sometimes considered to be the accuracy of the effective cross section and neutron spectrum, etc., the branching ratio can also be an important factor.

6.2.3 Burnup Equation

Burnup of a Fissile Nuclide

As a first step, a very simple burnup model is discussed here. The variation of the number density of ^{235}U number is treated as an example.

The variation of ^{235}U during burnup can be described by (537).

$$\frac{dN^{235}\text{U}(t)}{dt} = -N^{235}\text{U}(t) \times \sigma_a(t) \times \phi(t) \quad (537)$$

where

- $N^{235}\text{U}(t)$: number density of ^{235}U [cm^{-3}],
- $\sigma_a(t)$: microscopic absorption cross section of ^{235}U (= capture + fission) [cm^2],
- $\phi(t)$: neutron flux [$\text{cm}^{-2} \text{s}^{-1}$].

Equation (537) indicates that the reduction rate of the fissile (i.e. ^{235}U) number density is given by the absorption reaction rate. Note that the absorption includes not only the fission reaction but also the capture reaction. In an actual situation, the production of ^{235}U (e.g., by the neutron capture of ^{234}U) and its decay may be considered, but they are omitted here for the sake of simplicity. Note that the reaction rate is given by (538).

$$R = N \times \sigma \times \phi \quad (538)$$

where

- R : reaction rate (e.g., [$\text{cm}^{-3} \text{s}^{-1}$]),
- N : number density (e.g., [cm^{-3}]),
- σ : microscopic cross section (e.g., [cm^2]),
- ϕ : neutron flux (e.g., [$\text{cm}^{-2} \text{s}^{-1}$]).

When the neutron flux and microscopic absorption cross section are assumed to be constant, (537) can be written as follows:

$$\frac{dN^{235}\text{U}(t)}{dt} = -N^{235}\text{U}(t) \times \sigma_a \times \phi \quad (539)$$

Equation (539) is a basic differential equation and its solution is analytically expressed by

$$N^{235}\text{U}(t) = N^{235}\text{U}(0) \exp(-\sigma_a \phi t) \quad (540)$$

In common burnup analyses, the initial number density, the microscopic cross section, and neutron flux are given as input data. Therefore, the number density of ^{235}U is expressed as a function of burnup time. For example, when the microscopic absorption cross section of ^{235}U and the neutron flux are approximately given by 1,000 [barn] ($=1,000 \times 10^{-24} [\text{cm}^2]$) and $10^{13} [\text{cm}^{-2} \text{s}^{-1}]$, respectively, the variation of the number density of ^{235}U is expressed by

$$N^{235}\text{U}(t) = N^{235}\text{U}(0) \exp(-10^{-8} t) \quad (541)$$

where unit of t is [s].

In the above derivation, the microscopic cross section and neutron flux are assumed to be constant. However, these parameters generally depend on the burnup time, so (540) cannot be directly applied to a reactor core analysis. In actual burnup analyses, the microscopic cross section and neutron flux are assumed to be constant during a short period Δt , and number density is evaluated by

$$N^{235}\text{U}(t + \Delta t) = N^{235}\text{U}(t) \exp(-\sigma_a \phi \Delta t) \quad (542)$$

This is the fundamental temporal discretization in burnup calculation. Further discussion will be provided in [\(6.3\)](#).

Burnup Equation with Multiple Nuclides

In the previous section, we focused on a simple burnup equation with a nuclide. In our next step, more complicated burnup equations with multiple nuclides ($^{238}\text{U} \sim ^{241}\text{Pu}$) will be discussed. These burnup equations are important in common reactor analyses as conversion reactions. The burnup equations for these nuclides are as follows:

$$^{238}\text{U} : \frac{dN^{238\text{U}}(t)}{dt} = -N^{238\text{U}}(t) \times \sigma_a^{238\text{U}} \times \phi \quad (543)$$

$$^{239}\text{Pu} : \frac{dN^{239\text{Pu}}(t)}{dt} = -N^{239\text{Pu}}(t) \times \sigma_a^{239\text{Pu}} \times \phi + N^{238\text{U}}(t) \times \sigma_c^{238\text{U}} \times \phi \quad (544)$$

$$^{240}\text{Pu} : \frac{dN^{240\text{Pu}}(t)}{dt} = -N^{240\text{Pu}}(t) \times \sigma_a^{240\text{Pu}} \times \phi + N^{239\text{Pu}}(t) \times \sigma_c^{239\text{Pu}} \times \phi \quad (545)$$

$$^{241}\text{Pu} : \frac{dN^{241\text{Pu}}(t)}{dt} = -N^{241\text{Pu}}(t) \times \sigma_a^{241\text{Pu}} \times \phi + N^{240\text{Pu}}(t) \times \sigma_c^{240\text{Pu}} \times \phi \quad (546)$$

Note that decays are omitted for the sake of simplicity. Though ^{239}Pu is generated from ^{238}U through ^{239}U and ^{239}Np , it is assumed to be produced directly from ^{238}U .

Care should be taken that both the absorption and capture cross sections are used in [\(543\)–\(546\)](#). The vanishing rate of a nuclide is given by its absorption rate, but the conversion rate of a nuclide, for example, transmutation from ^{238}U to ^{239}Pu , is given by the capture rate. Therefore, the absorption cross section is used for the vanishing term and the capture cross section is used for the production term, which corresponds to a conversion from an ancestor nuclide.

As described previously, since microscopic cross sections, neutron flux, and initial number densities are given as input parameters, variations in the number densities of $^{238}\text{U} - ^{241}\text{Pu}$ can be evaluated by the analytical solutions in [\(543\)–\(546\)](#). Though this example treats only four nuclides, the analytical solutions are highly complicated. In an actual burnup analysis, the number of nuclides is much larger than in the above example.

Burnup Equation in General Form

Based on the discussion in this section so far, we will now derive a general burnup equation in which the production and disintegration of nuclides are considered. In general, the production or disintegration of a nuclide is described by [\(547\)](#)

$$\frac{dN_i}{dt} = \text{production rate} - \text{absorption rate} - \text{decay rate} \quad (547)$$

[Equation \(547\)](#) is written in the form of a burnup equation as follows:

$$\frac{dN_i}{dt} = \sum_j \gamma_{ji} \sigma_{f,j} N_j \phi + \sigma_{c,i-1} N_{i-1} \phi + \sum_k \lambda_{ki} N_k - \sigma_{a,i} N_i \phi - \lambda_i N_i \quad (548)$$

where

N_i : number density of nuclide i [cm^{-3}],

γ_{ji} : yield of nuclide j from a fission of nuclide i [–],

- $\sigma_{f,j}$: microscopic fission cross section of nuclide j [cm^2],
 ϕ : neutron flux [$\text{cm}^{-2} \text{s}^{-1}$],
 $\sigma_{c,i-1}$: capture cross section of nuclide $i - 1$ [cm^2],
 λ_{ki} : decay constant of nuclide k to nuclide i [s^{-1}],
 λ_i : decay constant of nuclide i [s^{-1}],
 $\sigma_{a,i}$: absorption cross section of nuclide i [cm^2].

The first term on the right side of (548) shows the direct production from a fission. When the nuclide i is not a fission product, this term is zero. The second term is the production due to neutron capture, that is, (n, γ) reaction. The third term is the production due to decay of other nuclides, which considers α - and β -decays. The fourth and last terms are the disintegration by the neutron absorption, and the decay, respectively. Note that (548) is not truly rigorous since some nuclear reactions have been omitted. For example, $(n, 2n)$, $(n, 3n)$, and (n, p) reactions are not taken into account. If these reactions are important, they would be also considered as additional terms in (548).

Equation (548) is an extension of the burnup equation, as discussed in this section so far, and is a differential equation of the first order (Bateman 1910). When the number densities of nuclides are considered as a vector, (548) can be written in a more general form:

$$\frac{d\vec{N}}{dt} = \mathbf{A}\vec{N} \quad (549)$$

where

\vec{N} : vector of nuclide number density,

\mathbf{A} : the burnup matrix.

When the nuclides in a vector \vec{N} are arranged in order of atomic mass (light fission products appear first, then heavy fission products, and finally heavy nuclides), the typical structure of the burnup matrix \mathbf{A} is that shown in Fig. 91.

The analytical solution of (549) is formally given by the following formula, when the element of the burnup matrix is constant.

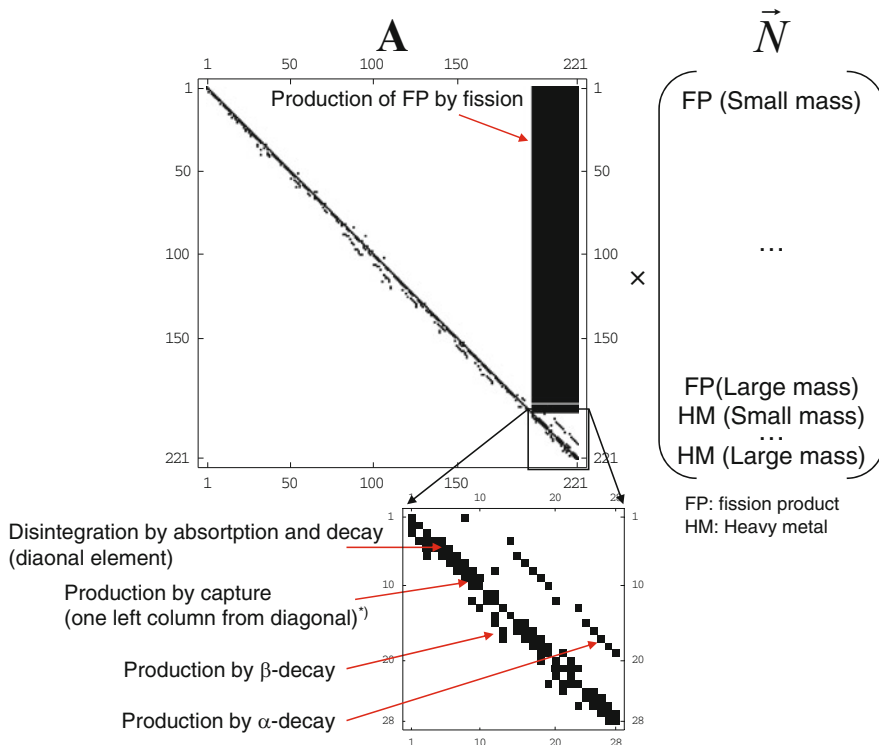
$$\vec{N}(t) = \exp(\mathbf{A}t)\vec{N}(0) \quad (550)$$

Equation (550) is a natural extension of (540), which is derived for a single nuclide. The term $\exp(\mathbf{A}t)$ is called the matrix exponential, but its analytical expression for a general case cannot, unfortunately, be obtained. For example, when the rank of matrix \mathbf{A} is two, $\exp(\mathbf{A})$ is given as follows:

$$\text{MatrixExp} \left[\begin{pmatrix} a & b \\ c & d \end{pmatrix} \right] = \begin{pmatrix} \frac{e^{\frac{a+d}{2}} \left(\alpha \cosh\left(\frac{\alpha}{2}\right) + (a-d) \sinh\left(\frac{\alpha}{2}\right) \right)}{\alpha} & \frac{2be^{\frac{a+d}{2}} \sinh\left(\frac{\alpha}{2}\right)}{\alpha} \\ \frac{2ce^{\frac{a+d}{2}} \sinh\left(\frac{\alpha}{2}\right)}{\alpha} & \frac{e^{\frac{a+d}{2}} \left(\alpha \cosh\left(\frac{\alpha}{2}\right) + (d-a) \sinh\left(\frac{\alpha}{2}\right) \right)}{\alpha} \end{pmatrix}$$

where $\alpha = \sqrt{(a-d)^2 + 4bc}$.

The above result suggests that when the number of nuclides is from several dozen to a few hundred, it is impractical to seek a direct solution through the analytical approach; some approximations should be used in order to practically obtain the analytical solution, as will be discussed later. Therefore, in an actual burnup calculation, the numerical solution of (550) is necessary.



*) May be appeared more than two columns to the left depending on the order of nuclides in the vector

Figure 91
Typical structure of a burnup matrix

6.2.4 Burnup, Burnup Time, and Normalization of Neutron Flux

Burnup and Burnup Time

Burnup is expressed as the cumulative energy output per unit weight of the initial heavy metal loading. Since the cumulative energy release from a nuclear fuel is very large, MWd/t or GWd/t is commonly used as the unit of burnup. ISO states that “M” (mega, 10⁶), “G” (giga, 10⁹), and “W” (Watt) must be written in upper case letters, while “d” (day) and “t” (ton) must be written in the lower case. The value of 1MWd/t indicates that 1t of heavy metal sustains 1MW energy production for 1d, and that a value of 1GWd/t shows that 1t of heavy metal sustains 1GW energy production for 1d.

One must be careful when defining the weight of the heavy metal used in burnup. Since the weight of heavy metal diminishes during burnup due to fission reactions, the weight of the heavy metal at initial loading (i.e., beginning of life) is used for the definition of a burnup unit.

In burnup calculations, not only burnup (e.g., MWd/t) but also burnup time (e.g., in second) is important. In actual in-core fuel management calculations, the planned cycle length is given

as burnup time (days or months). The conversion of these two parameters (burnup and burnup time) is therefore quite important. The conversion of units can be carried out as follows:

- Conversion from Burnup Time (e.g., Day) to Burnup (e.g., MWd/t)

$$\text{Burnup (MWd/t)} = \text{Thermal output (MW)} \times \text{duration (day)} \div \text{heavy metal weight (t)}$$

Note that the initial (beginning of life) value of the heavy metal weight should be used in the above relationship. The thermal output and the initial heavy metal weight of a fuel assembly for unit axial length are usually used in lattice physics computations, while those for the entire core are used in core calculations.

- Conversion from Burnup to Burnup Time

$$\text{Duration (day)} = \text{Burnup (MWd/t)} \div \text{Thermal output (MW)} \times \text{Heavy metal weight (t)}$$

Normalization of Neutron Flux

The neutron transport calculation in a lattice physics computation is carried out as an eigenvalue calculation; thus, the neutron flux is obtained as a relative value. However, the absolute value of the neutron flux is necessary in order to perform the burnup calculation. Normalization of the neutron flux to an absolute value is performed as follows:

- Integrate the thermal output by fission reaction over the entire configuration.
- Evaluate the normalization factor by (input thermal output)/(integrated thermal output).
- Normalize the neutron flux by the normalization factor obtained in (2).

Normalization of the neutron flux and the conversion between burnup time and burnup can be sources of error. Furthermore, since errors related to these calculations are often not apparent, care must be taken in actual lattice physics/in-core fuel management calculations. The following points in the analyses should be checked:

- Unit of thermal output (W/kW/MW)

The input unit of thermal output depends on the codes used in the calculation. Some lattice physics/core calculation codes may use non-SI units.

- Specification of power normalization (whole core, an assembly, an assembly per unit axial height, power density, etc.)

Care must be taken with the power normalization input of a lattice physics code. The power normalization input greatly depends on the lattice physics codes, and various specifications are possible, that is, thermal output for a whole assembly, power linear density for fuel assembly or fuel pin, power density per unit heavy metal weight (W/gHM), and power density per unit volume (W/cm³). One should be careful regarding the specification used in the lattice physics code for the analysis.

- Specification of Heavy Metal Weight

In the USA, a non-SI unit, for example, short ton (st) may be used instead of ton (t). Since the difference between the two is not very large (1 st = 0.907 t), it is quite difficult to find out their discrepancy in a burnup calculation. However, when the conversion from MWd/t to d, or d to MWd/t is carried out with an incorrect weight unit, a difference of approximately 10% takes place, which is completely unacceptable in actual in-core fuel management calculations.

Furthermore, in lattice physics and core calculations, the precise value of the total heavy metal weight is necessary in order to estimate burnup. We would again emphasize

here that the initial heavy metal weight is used for burnup calculations. In the evaluation of heavy metal weight, detailed specifications of the fuel assembly should be taken into account. For example, a gadolinia-bearing fuel rod contains less heavy metal than an ordinary fuel rod without burnable poison. Fuel assemblies from different fuel vendors may have different heavy metal weights. Since heavy metal weight has a direct impact on the value of a burnup, it should be accurately calculated with this in mind.

d. Lattice/Core Volume

Since the total thermal output is calculated through the integration of power density over configuration, the volume of the calculation configuration is important. If an inaccurate volume is given, the normalized power will reflect that discrepancy.

As discussed above, there can be various reasons for wrong power normalization, that is, an inaccurate estimate of the absolute value of the neutron flux. Since common lattice physics codes internally use both burnup and burnup time, they are both printed in the output list. Therefore, when the specification for burnup is given in MWd/t or GWd/t, the burnup time (day) should be confirmed. The inverse, of course, is also true: when the burnup time is used in the input data, the burnup in units of MWd/t or GWd/t should be checked. This double checking is very useful for preventing errors related to burnup specifications.

6.3 Numerical Scheme

6.3.1 Potential Causes of Error in a Numerical Solution

As discussed in the previous subsections, a general solution for the burnup equation is given by (550). However, it is difficult to obtain a general analytic solution of (550) that can be used for numerical calculations. A numerical solution is therefore inevitable in practical burnup calculations. Before we present a detailed discussion of a numerical solution, potential causes of error in a numerical solution for the burnup equation are discussed below.

Error in Reaction Rate (Production, Absorption, and Decay Rates)

The microscopic reaction rate (e.g., $\sigma_a(t)\phi(t)$) is given as the product of a microscopic cross section and the neutron flux. In order to accurately evaluate microscopic reaction rates, effective microscopic cross sections and the neutron fluxes in burnup regions must be precisely evaluated. However, since precise evaluation of these parameters is still a major research topic in reactor physics, some errors are still inevitable when present calculation methods are used. This is especially true for nuclides with resonances, in which the resonance interference effect and other factors can become a source of error. Furthermore, the number densities of resonant nuclides (especially fission products and higher heavy nuclides) vary during burnup, so the magnitude of the self-shielding effect also changes. In the beginning of life, their self-shielding effect is very small, and infinite-dilute treatment is appropriate. But the self-shielding effect gradually becomes larger as the burnup proceeds, so it must be accurately taken into account.

Temporal Discretization Error of the Differential Equation of Burnup Equation

In order to numerically solve the differential equation, temporal discretization may be necessary, which introduces some error. This issue will be discussed later in more detail.

Temporal Discretization Error in Reaction Rates of Burnup Equation

The reaction rates that appear in the burnup equation depend on the burnup time, since both the microscopic cross section and neutron flux vary during burnup. They are usually assumed to be constant, however, within a particular time-step in the numerical solution of the burnup equation. This assumption introduces some error in the reaction rates used in the burnup equation. The discrepancy could be large when the temporal variation of the reaction rate is large. A detailed discussion of this point will be offered in the latter part of this section.

Normalization Error of Thermal Output

As described previously, the neutron flux used in a burnup calculation should be an absolute value rather than the relative one obtained in the eigenvalue calculation. The absolute value of the neutron flux is normalized with the thermal output of a reactor. The thermal output of an actual reactor is estimated by the heat balance of the primary cooling system. Since it requires measurement values for the inlet/outlet temperatures, the flow rate of the primary coolant and so on, these measured values contain errors. Therefore, the thermal output of a reactor core based on the measured value may also include some uncertainty. Consequently, the absolute neutron flux evaluated from the measured core thermal output may also be in error. Generally speaking, though the error in the core thermal output is not very large, it is nonetheless a potential cause of error in the burnup analysis.

Error in Initial Composition of Fuel

The initial composition of the fuel can be a source of error in burnup calculation and is often overlooked. Actual fuels inevitably have fluctuations in their properties, for example, ^{235}U enrichment and heavy metal loading. The tolerances of these fluctuations in the manufacturing process are set based on their impact upon the neutronics properties. Therefore, they have a limited impact on core behavior, for example, core k -effective. That said, fluctuations in the initial fuel composition may not be negligible in regard to the calculation of nuclide number densities, which are often required in the post-irradiation examination (PIE) of fuel assemblies. An error in initial number density has an especially large impact on nuclides whose number density is small. In any case, the nominal value of the fuel's isotopic composition should not be used without cross-checking the mill-sheet.

6.3.2 General Remarks on Numerical Solutions for the Burnup Equation

The general form of the burnup equation is (549) and its solution is formally given by (550). Solution methods for the burnup equation have long been the subject of investigation (England 1962; Ball and Adams 1967; Lapidus and Luus 1967; Vondy 1962; Bell 1973; Tasaka 1977), and the major results of this inquiry are implemented in the ORIGEN2 code, which is a dedicated burnup analysis code for general purposes (Croat 1980). The reference manual of the ORIGEN2 code well summarizes the numerical solution methods for the burnup equation, and also provides useful information. Since the numerical methods used in the ORIGEN2 code are sophisticated, many burnup calculation codes adopt the one used in the ORIGEN2 code.

In fact, this type of burnup equation, that is, the first-order differential equation, has frequently appeared not only in the field of reactor physics, but also in the fields of physics, chemistry, economics, and systems analysis. Studies of this type of equation have also been independently carried out in the field of applied mathematics. Moler and Loan (2003) summarizes the results of the investigations in this field, and reviews various methods used to solve the matrix exponential, that is, (550). Though more than 20 methods are described by Moler and Loan (2003), only 3~4 of them have been applied in the field of reactor physics.

In the following sections, a fundamental method to solve the differential equation (the Euler method), and typical numerical solutions used in burnup analysis (the Runge–Kutta method, the matrix exponential method, the matrix decomposition method, the Bateman method) are described. Furthermore, the Padé approximation, which is a general numerical method used to solve the matrix exponential, and the Krylov subspace method, which is suitable for estimating the matrix exponential of a sparse matrix, are also explained.

Note that the microscopic reaction rate ($\sigma\phi$) is assumed to be constant throughout a particular burnup step. In other words, the elements of burnup matrix \mathbf{A} remain constant during a burnup step. A consideration of variations in the microscopic reaction rate will be presented in [6.3.11](#).

6.3.3 The Euler Method

The Euler method is a quite simple numerical method based on the finite-difference scheme. When (549) is differentiated with respect to the temporal variable, we obtain (551):

$$\frac{d\vec{N}}{dt} \approx \frac{\vec{N}^{l+1} - \vec{N}^l}{\Delta t} = \mathbf{A}\vec{N}^l \quad (551)$$

where l shows the number of burnup steps. Equation (551) can be transformed into the following:

$$\vec{N}^{l+1} = (\mathbf{I} + \mathbf{A}\Delta t)\vec{N}^l \quad (552)$$

where \mathbf{I} shows the unit matrix. Since the value of \vec{N}^l is known (input values), the nuclide number densities at $l + 1$ step can be obtained by (552).

Equation (549) can be also differentiated as (553):

$$\frac{d\vec{N}}{dt} \approx \frac{\vec{N}^{l+1} - \vec{N}^l}{\Delta t} = \mathbf{A}\vec{N}^{l+1} \quad (553)$$

Equation (553) can be transformed into (554)

$$\vec{N}^{l+1} = (\mathbf{I} - \mathbf{A}\Delta t)^{-1}\vec{N}^l \quad (554)$$

The nuclide number densities at step $l + 1$ can be obtained by (554).

The numerical method shown in (551) and (552) is an explicit method, and that of (553) and (554) is an implicit method. Though the computation time for a burnup step is short in the explicit method, the time-step size must be fine in order for a reliable result to be obtained. When a coarser burnup step is used in the explicit method, we often encounter numerical instability. In the case of the implicit method, the inverse of the matrix, that is, $(\mathbf{I} - \mathbf{A}\Delta t)^{-1}$, is

necessary, so that a longer computation time is required for a complicated burnup chain. However, the numerical stability of the implicit method for a coarse burnup step is much higher than that of the explicit method.

Temporal discretization errors from both methods diminish as finer burnup step sizes are used in calculations. However, since the number of burnup steps to achieve a particular burnup is increased with a finer burnup step, there can be a considerable accumulation of round-off errors in the numerical solution. Furthermore, the computation time naturally increases with an increasing number of burnup steps. The appropriate burnup step should be chosen with consideration for these observations. Note that though the Euler method is a simple numerical method, it does not offer a high degree of accuracy under practical calculation conditions. For this reason it is not usually used for actual lattice physics computations.

6.3.4 The Runge–Kutta Method

The Runge–Kutta method is one of the most widely used numerical methods applied to differential equations, and is frequently offered as illustrative material for lectures on numerical methods. Though there are several formulations for the Runge–Kutta method, the second- or fourth-order Runge–Kutta methods are commonly used for numerical calculations.

In the second-order Runge–Kutta method, (555)–(557) are used:

$$\vec{d}_1 = \frac{d\vec{N}}{dt}(t^l, \vec{N}^l) \Delta t = \mathbf{A} \vec{N}^l \Delta t \quad (555)$$

$$\vec{d}_2 = \frac{d\vec{N}}{dt} \left(t^l + \frac{\Delta t}{2}, \vec{N}^l + \frac{\vec{d}_1}{2} \right) \Delta t = \mathbf{A} \left(\vec{N}^l + \frac{\vec{d}_1}{2} \right) \Delta t \quad (556)$$

$$\vec{N}^{l+1} = \vec{N}^l + \vec{d}_2 \quad (557)$$

where $\frac{d\vec{N}}{dt}(t^l, \vec{N}^l)$ shows $\frac{d\vec{N}}{dt}$ at time t^l and number density \vec{N}^l .

The governing concept of the Runge–Kutta method is shown in Fig. 92: the gradient at the midpoint of burnup steps is estimated by (556), and is used to obtain the number density

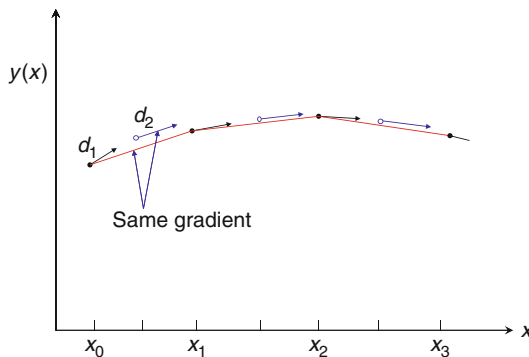


Figure 92
Concept of the second-order Runge–Kutta method

at the next step. Since the gradient at the midpoint of a burnup step gives better accuracy than that at the beginning, the calculation accuracy exceeds that of the Euler method, which uses the gradient at the beginning of the burnup step.

The fourth-order Runge–Kutta method utilizes the following equations:

$$\vec{d}_1 = \frac{d\vec{N}}{dt}(t^l, \vec{N}^l) \Delta t = \mathbf{A} \vec{N}^l \Delta t \quad (558)$$

$$\vec{d}_2 = \frac{d\vec{N}}{dt} \left(t^l + \frac{\Delta t}{2}, \vec{N}^l + \frac{\vec{d}_1}{2} \right) \Delta t = \mathbf{A} \left(\vec{N}^l + \frac{\vec{d}_1}{2} \right) \Delta t \quad (559)$$

$$\vec{d}_3 = \frac{d\vec{N}}{dt} \left(t^l + \frac{\Delta t}{2}, \vec{N}^l + \frac{\vec{d}_2}{2} \right) \Delta t = \mathbf{A} \left(\vec{N}^l + \frac{\vec{d}_2}{2} \right) \Delta t \quad (560)$$

$$\vec{d}_4 = \frac{d\vec{N}}{dt} \left(t^l + \Delta t, \vec{N}^l + \vec{d}_3 \right) \Delta t = \mathbf{A} \left(\vec{N}^l + \vec{d}_3 \right) \Delta t \quad (561)$$

$$\vec{N}^{l+1} = \vec{N}^l + \frac{\vec{d}_1 + 2\vec{d}_2 + 2\vec{d}_3 + \vec{d}_4}{6} \quad (562)$$

Though the governing concept of the fourth-order Runge–Kutta method is similar to that of the second-order method, the “average gradient” between burnup steps is estimated in a more sophisticated manner, as shown in Fig. 93.

The accuracy of the fourth-order Runge–Kutta method is high and its computation time is short. Furthermore, since it can handle any form of burnup matrix, it can be applied to very complicated burnup chains. The above features make the fourth-order Runge–Kutta method a practical numerical method for the burnup equation, which is adopted by some lattice physics codes (Morimoto et al. 1989).

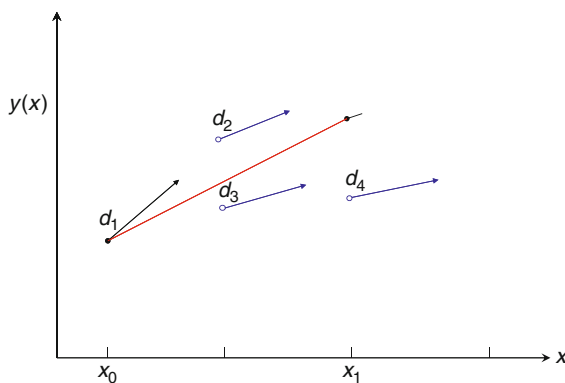


Figure 93
Concept of the fourth-order Runge–Kutta method

6.3.5 The Matrix Exponential Method

The matrix exponential method directly performs the numerical calculation of (550), which is a general solution of the burnup equation. The matrix exponential can be evaluated by the Taylor series expansion as follows:

$$\exp(\mathbf{A}\Delta t) = \mathbf{I} + (\mathbf{A}\Delta t) + \frac{(\mathbf{A}\Delta t)^2}{2!} + \frac{(\mathbf{A}\Delta t)^3}{3!} + \dots \quad (563)$$

Since the evaluation of (563) directly gives a general numerical solution to the burnup equation, the matrix exponential method seems to be an ideal numerical method. In actual computation, however, the convergence of the expansion series given in (563) can pose a numerical problem. For example, let us numerically estimate the value of $\exp(-100)$ by applying the Taylor series expansion:

$$\exp(-100) = 1 + (-100) + \frac{(-100)^2}{2!} + \frac{(-100)^3}{3!} + \dots \quad (564)$$

Note that the value of $\exp(-100)$ is approximately 4×10^{-44} . The salient point is whether or not the present value can be obtained through the numerical computation of (564). The actual numerical computation shows that the maximum value of a term on the right side of (564) appears to be approximately $n = 100$, that is, $(-100)^{100}/100! \sim 1 \times 10^{42}$. Therefore, in order to estimate $\exp(-100)$ with five significant digits, at least $42 + 44 + 5 = 92$ significant digits will be necessary during computation, due to the severe round-off error. The number of digits in double-precision calculations in common computer languages (e.g., Fortran, C, C++) is 16, and so 92 significant digits is for all purposes impractical.

A similar consideration becomes relevant in the evaluation of (563). Roughly speaking, the diagonal elements, that is, absolute value of the disintegration term due to absorption and decay, are largest in matrix \mathbf{A} . When a burnup matrix is a diagonal matrix, its matrix exponential can be obtained through exponentials of the diagonal elements. Therefore, the convergence of (563) is dominated by the largest diagonal elements. In other words, when short-lived nuclides exist in the burnup chain, the absolute values of these disintegration terms ($-\lambda - \sigma_a \phi$) in the diagonal position of the burnup matrix become large, so that the convergence of the Taylor series expansion becomes slower. Note that a higher absorption reaction could have a similar impact on a numerical calculation, but a large decay constant is far more important in actual burnup calculations.

To address this more precisely, the maximum norm of burnup matrix \mathbf{A} must be considered. When the norm of a matrix is defined by (565), the maximum (absolute) term that appears in the Taylor series expansion of (563) does not exceed $(|\mathbf{A}| \Delta t)^n / n!$, where n is the largest integer that does not exceed $|\mathbf{A}| \Delta t$ (Lapidus and Luus 1967).

$$|\mathbf{A}| = \min \left\{ \max \sum_i |a_{ij}|, \max \sum_j |a_{ij}| \right\} \quad (565)$$

In the ORIGEN2 code, (566) is used to limit the value of $|\mathbf{A}| \Delta t$ (Cropp 1980):

$$|\mathbf{A}| \Delta t \leq -2 \ln(0.001) \leq 13.855 \quad (566)$$

In this case, the maximum value of $(|\mathbf{A}| \Delta t)^n / n!$ is obtained at $n = 13$, which is approximately 1.1×10^5 . When double-precision calculations (16 significant digits) are used for the numerical

computation of (563), the elements of the matrix exponential for the burnup matrix have significant digits up to 10^{-11} . Therefore, when five significant digits are required in calculation results, a value as small as 10^{-6} can be treated by applying the above limitation.

The limitation of (566) can be satisfied by forcing $\exp(-d\Delta t) < 0.001$, where d is the maximum (absolute) value of the diagonal elements. Since d is the disintegration rate (= absorption rate + decay rate), the value of $|\mathbf{A}|$ does not exceed $2d$. For example, in the case of ^{135}Xe , it transforms into ^{136}Xe due to neutron capture or into ^{135}Cs due to decay. Let us assume that the diagonal element of a burnup matrix for ^{135}Xe is -1.0 , and the transformation ratio to ^{136}Xe , and the decay ratio to ^{135}Cs , are 0.4 and 0.6 , respectively. In this case, the summation of absolute values of the row elements for ^{135}Xe is $| -1.0 | + | 0.4 | + | 0.6 | = 2.0$, which corresponds to twice the absolute value of the diagonal element (-1.0). Consequently, we have the following relationship:

$$|\mathbf{A}| \Delta t \leq 2d\Delta t \leq -2 \ln(\exp(-d\Delta t)) \leq -2 \ln(0.001) \quad (567)$$

In the case of actual burnup calculations, the above relationship can be satisfied by limiting d or Δt . The most direct approach is to limit Δt as follows:

$$\Delta t \leq \frac{-2 \ln(0.001)}{2d} \quad (568)$$

The apparent drawback of this method is that an impractically small Δt may be obtained for a large d . For example, in the case of the “Developer” burnup chain of the MVP-BURN code, the maximum value of d is given by ^{106}Rh , whose half-life is 29.8 s:

$$d = \ln(2)/29.8 \approx 0.0233[\text{s}^{-1}] \quad (569)$$

By substituting (569) into (568), we obtain Δt in order to satisfy (567) as follows:

$$\Delta t \leq \frac{-2 \ln(0.001)}{2 \times 0.0233} \approx 297[\text{s}] \quad (570)$$

A typical burnup step in lattice physics computations is 100–1,000 MWd/t. When a typical power density for a PWR is used, these burnup steps correspond to 3–30 d. Since this burnup step (3–30 d) is much larger than that in (570), some compensatory measures become necessary.

There are two possible ways to resolve this issue. The first is to utilize the scaling and squaring method, which utilizes the following nature of a matrix:

$$\exp(\mathbf{A}\Delta t) = \exp\left(m \frac{\mathbf{A}\Delta t}{m}\right) = \left[\exp\left(\frac{\mathbf{A}\Delta t}{m}\right)\right]^m = \left[\exp\left(\mathbf{A}\frac{\Delta t}{m}\right)\right]^m \quad (571)$$

By using (571), an integer m is defined to satisfy $\Delta t/m \leq \frac{-2 \ln(0.001)}{2d}$. The scaling and squaring method is a very effective way to compute a matrix exponential. This is especially true when $m = 2^n$. In the above case, however, m would be approximately 1,000, so the round-off error and computational cost would be considerable.

The second approach is the modification of the burnup chain, which eliminates nuclides with a high disintegration rate (d) and treats them independently. Nuclides with a high disintegration rate attain a radiation equilibrium state with precursors in a short time. Therefore, an

equilibrium solution that is obtained by ignoring the temporal differentiation on the left side of (548) can be used:

$$0 = \sum_j \gamma_{ji} \sigma_{f,j} N_j \phi + \sigma_{c,i-1} N_{i-1} \phi + \sum_k \lambda_{ki} N_k - \sigma_{a,i} N_i \phi - \lambda_i N_i \quad (572)$$

Equation (572) yields the following solution:

$$N_i = \frac{\sum_j \gamma_{ji} \sigma_{f,j} N_j \phi + \sigma_{c,i-1} N_{i-1} \phi + \sum_k \lambda_{ki} N_k}{\sigma_{a,i} \phi + \lambda_i} \quad (573)$$

A nuclide with a very high disintegration rate may be treated by the Bateman method, as described in  Sect. 8.3.7, since neither the matrix exponential method nor application of the equilibrium solution yields appropriate results. The equilibrium solution, the Bateman method, and the matrix exponential method are used in the ORIGEN2 code in order to compensate for the weakness of each method.

Finally, we will discuss an important relationship among the matrix exponential method, the Euler method and the Runge–Kutta method. In many textbooks on numerical computation, these methods are explained independently. The Euler method, however, is an approximation that considers up to the second terms (i.e., up to the first order) in the Taylor series expansion shown in (563). This becomes obvious when (552) and (563) are compared.

When the elements of the burnup matrix are constant in a burnup step, the Runge–Kutta method of the second order considers up to the third terms (i.e., up to the second order) in the Taylor series expansion. This can be confirmed by substituting (555) and (556) into (557), then comparing the result with (563). Similarly, the Runge–Kutta method of the fourth order considers up to the fifth terms (i.e., up to the fourth order) in the Taylor series expansion, which can be confirmed by substituting (558)–(561) into (562), then comparing the result with (563).

To sum up, in the Taylor series expansion of the burnup matrix:

Consideration up to the second terms (the first order): the Euler method.

Consideration up to the third terms (the second order): the Runge–Kutta method of the second order.

Consideration up to the fifth terms (the fourth order): the Runge–Kutta method of the fourth order.

From the above viewpoint, both the Euler and Runge–Kutta methods can be considered as variations of the matrix exponential method. Furthermore, the above discussion also suggests the limitation of the Euler and Runge–Kutta methods for nuclides with a high disintegration rate. Since both methods truncate the Taylor series expansion, the limitations of the burnup step in these methods are expected to be smaller than that shown in (568).

6.3.6 The Matrix Decomposition Method

Let us assume that a burnup matrix \mathbf{A} can be decomposed by two matrixes \mathbf{L} and \mathbf{D} :

$$\mathbf{A} = \mathbf{LDL}^{-1} \quad (574)$$

The substitution of (574) into (563) yields

$$\begin{aligned}
 \exp(\mathbf{A}\Delta t) &= \mathbf{I} + (\mathbf{LDL}^{-1}\Delta t) + \frac{(\mathbf{LDL}^{-1}\Delta t)^2}{2!} + \dots \\
 &= \mathbf{LL}^{-1} + \mathbf{L}(\mathbf{D}\Delta t)\mathbf{L}^{-1} + \frac{(\mathbf{LDL}^{-1}\mathbf{LDL}^{-1}\Delta t^2)}{2!} + \dots \\
 &= \mathbf{LL}^{-1} + \mathbf{L}(\mathbf{D}\Delta t)\mathbf{L}^{-1} + \frac{(\mathbf{LD}^2\mathbf{L}^{-1}\Delta t^2)}{2!} + \dots \\
 &= \mathbf{LL}^{-1} + \mathbf{L}(\mathbf{D}\Delta t)\mathbf{L}^{-1} + \mathbf{L}\frac{(\mathbf{D}\Delta t)^2}{2!}\mathbf{L}^{-1} + \dots \\
 &= \mathbf{L}\left(\mathbf{I} + (\mathbf{D}\Delta t) + \frac{(\mathbf{D}\Delta t)^2}{2!}\dots\right)\mathbf{L}^{-1} \\
 &= \mathbf{L}\exp(\mathbf{D}\Delta t)\mathbf{L}^{-1}
 \end{aligned} \tag{575}$$

Equation (575) indicates that the matrix exponential of \mathbf{A} can be replaced by that of \mathbf{D} . When \mathbf{D} is a matrix with a general form, the transformation shown in (575) is not of value, though it requires a computational cost similar to that of $\exp(\mathbf{D}\Delta t)$. However, if \mathbf{D} is a diagonal matrix, which has nonzero elements only at diagonal positions, then the above formulation has practical merit

$$\mathbf{D} = \begin{bmatrix} \alpha_1 & & & 0 \\ & \alpha_2 & & \\ & & \ddots & \\ 0 & & & \alpha_n \end{bmatrix}. \tag{576}$$

In this case, the matrix exponential of \mathbf{D} is expressed by

$$\exp(\mathbf{D}\Delta t) = \begin{bmatrix} \exp(\alpha_1\Delta t) & & & 0 \\ & \exp(\alpha_2\Delta t) & & \\ & & \ddots & \\ 0 & & & \exp(\alpha_n\Delta t) \end{bmatrix}, \tag{577}$$

thus $\exp(\mathbf{A}\Delta t)$ can be easily obtained by (575). In this method, once a matrix is decomposed, then the matrix exponential is evaluated by the decomposed matrixes; this is called the matrix decomposition method.

Next, we should consider a numerical procedure that evaluates the matrixes of \mathbf{D} and \mathbf{L} . Such a procedure is common in the field of linear algebra, that is, the diagonalization of a matrix, which is equivalent to evaluate all eigenvalues and eigenvectors of matrix \mathbf{A} . Note that the diagonal elements of matrix \mathbf{D} correspond to the eigenvalues, and the matrix \mathbf{L} is composed of eigenvectors. In general, the calculation of eigenvalues and eigenvectors requires computation time, so that matrix decomposition is inevitably time consuming. However, the diagonal matrix \mathbf{D} can be obtained easily when the burnup equation is approximated as follows:

$$\begin{aligned}
 \frac{dN_i}{dt} &= \sum_j \gamma_{ji} \sigma_{f,j} N_j \phi + \sigma_{c,i-1} N_{i-1} \phi + \lambda_{i-1} N_{i-1} - \sigma_{a,i} N_i \phi - \lambda_i N_i \\
 &= F_i + (\sigma_{c,i-1} \phi + \lambda_{i-1}) N_{i-1} - (\sigma_{a,i} \phi + \lambda_i) N_i
 \end{aligned} \tag{578}$$

Equation (578) is different from (548) in the following points:

- The production rate from a fission is assumed to be constant.
- The production from a “previous” nuclide, only, is taken into account.

By incorporating the above assumptions, the burnup equation and the burnup matrix become as follows:

$$\frac{d\vec{N}}{dt} = A\vec{N} + \vec{F} \quad (579)$$

$$A = \begin{bmatrix} -\sigma_{a,1} - \lambda_1 & 0 & 0 & \dots & 0 \\ \sigma_{c,1} + \lambda_1 & -\sigma_{a,2} - \lambda_2 & \dots & \dots & \dots \\ 0 & \dots & \dots & \dots & \dots \\ \dots & 0 & \dots & -\sigma_{a,n-1} - \lambda_{n-1} & 0 \\ 0 & \dots & 0 & \sigma_{c,n-1} + \lambda_{n-1} & -\sigma_{a,n} - \lambda_n \end{bmatrix} \quad (580)$$

The diagonalization of matrix A given by (580) is easy. The matrixes of L and D are assumed as follows:

$$L = \begin{bmatrix} l_{1,1} & l_{2,1} & \dots & \dots & l_{n,1} \\ l_{1,2} & l_{2,2} & \dots & \dots & \dots \\ \dots & \dots & \dots & \dots & \dots \\ \dots & \dots & \dots & l_{n-1,n-1} & \dots \\ l_{1,n} & \dots & \dots & \dots & l_{n,n} \end{bmatrix}, \quad D = \begin{bmatrix} \alpha_1 & 0 & \dots & \dots & 0 \\ 0 & \alpha_2 & \dots & \dots & \dots \\ \dots & \dots & \dots & \dots & \dots \\ \dots & \dots & \dots & \alpha_{n-1} & 0 \\ 0 & \dots & \dots & 0 & \alpha_n \end{bmatrix} \quad (581)$$

Equation (574) can be transformed into

$$AL = LD \quad (582)$$

Therefore, by comparing each element of the matrixes in (582), the following relationship can be obtained:

$$(-\sigma_{a,1} - \lambda_1)l_{1,1} = l_{1,1}\alpha_1 \quad (583)$$

$$(\sigma_{c,1} + \lambda_1)l_{1,1} + (-\sigma_{a,2} - \lambda_2)l_{1,2} = l_{1,2}\alpha_1 \quad (584)$$

Since (583) and (584) are the recurrence relationships, the elements in matrixes L and D can be easily obtained. Here, column vector of matrix L is eigenvector thus they can be normalized arbitrary. The analytical solution of (579) is

$$\begin{aligned} \vec{N}^{l+1} &= \exp(-A\Delta t) \left[\vec{N}^l - A^{-1}\vec{F} \right] + A^{-1}\vec{F} \\ &= L \exp(D\Delta t) L^{-1} \left[\vec{N}^l - A^{-1}\vec{F}^l \right] + A^{-1}\vec{F}^l \end{aligned} \quad (585)$$

The inverse of matrix A is given as follows:

$$A^{-1} = LD^{-1}L^{-1} \quad (586)$$

since

$$AA^{-1} = I \quad (587)$$

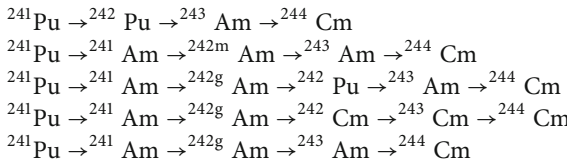
The matrix decomposition method can estimate an accurate solution but has the following drawbacks:

- A complicated burnup chain that includes the neutron capture, α -, β -decay, and (n, 2n) reactions cannot be directly treated

As shown in (578), the production of a nuclide is limited by a fission and the “previous” nuclide, that is, there are only two paths. Therefore, even if there are multiple production paths, for example, ^{239}Pu is produced from α -, β -decay and (n, 2n) reactions, direct treatment of these production paths is not possible; the “linearization” of the burnup chain is necessary.

- All burnup chains must be linearized

For example, let us consider the production of ^{244}Cm from ^{241}Pu in the burnup chains shown in Fig. 86. In order to linearize a burnup chain, all production paths should be treated independently. Therefore, the following five linearized burnup chains need to be solved.



Once the solutions for these five burnup equations are obtained, the final solution can be reconstructed through the summation of these solutions. This is a somewhat complicated treatment in the actual implementation of a numerical solution.

The above discussion suggests that number of burnup equations significantly increases when linearization is carried out for a complicated burnup chain.

- A numerical difficulty (divide by zero) appears when two nuclides have identical disintegration rates (= absorption + decay rate)
- A burnup chain with a “circuit shape” cannot be treated

For example, the burnup chain of ${}^{241}\text{Pu} \rightarrow {}^{242}\text{Pu} \rightarrow {}^{243}\text{Am} \rightarrow {}^{244}\text{Cm} \rightarrow {}^{240}\text{Pu} \rightarrow {}^{241}\text{Pu}$ is an example of a circuit-shaped chain.

The matrix decomposition method is a numerically efficient method (Knott and Edenius 1993). However, it is not very suitable for treating very complicated burnup chains.

6.3.7 Bateman Method

The Bateman method utilizes an analytic solution for first-order linear differential equations (Okumura et al. 2007; Bateman 1910; Tasaka 1977; Villarino et al. 1992). The general solution for the linearized burnup equation shown in (578) is given as follows:

$$N_i(t + \Delta t) = N_i(t) \exp(-d_i \Delta t) + \sum_{k=1}^{i-1} N_k(t) \left[\sum_{j=k}^{i-1} \frac{\exp(-d_j \Delta t) - \exp(-d_i \Delta t)}{d_i - d_j} a_{j+1,j} \prod_{\substack{n=k \\ n \neq j}}^{i-1} \frac{a_{n+1,n}}{d_n - d_j} \right] \quad (588)$$

where $a_{i,j}$ is the element of matrix \mathbf{A} and $d_i = -a_{i,i}$. Note that F_i is assumed to be zero in the above derivation. [Equation \(588\)](#) has a very complicated form that includes several summation and multiplication operations.

The matrix decomposition method and the Bateman method solve the identical equation since both methods treat the same linearized burnup chain. The difference between these methods is the actual solution method: numerical calculation for a matrix is used in the matrix decomposition method, and the analytic solution is used in the Bateman method.

Though the accuracy of the Bateman method is superior due to its utilization of the analytic solution, it presents several problems that are identical to those of the matrix decomposition method:

- Since linearization of the burnup chain is necessary, some approximations may be necessary for a complicated burnup chain.
- Numerical difficulty arises when two nuclides have identical disintegration rates. In this case, the denominator in [\(588\)](#) becomes zero.
- A circulating burnup chain cannot be directly treated.

The issue of (b) can be avoided by deriving the analytical solution with the assumption of an identical disintegration rate (i.e., $d_i = d_j$ or $d_n = d_j$). Issue (c) can be approximately treated by terminating and cutting the circuit burnup chain at a certain point. Note that the degree of error due to the approximation of terminating the burnup chain is negligible when the number of burnup steps is sufficiently large.

The Bateman method is used in the ORIGEN2 code for short-lived nuclides, as described [6.3.5](#). The MVP-BURN code (Okumura et al. 2000) also utilizes the Bateman method, whose burnup module is based on the DCHAIN code developed by JAERI (former JAEA) (Tasaka 1977).

6.3.8 The Padé Approximation

The Padé approximation of (p, q) -order for the exponential function is given as follows:

$$\exp(x) \cong \frac{N_{pq}(x)}{D_{pq}(x)} \quad (589)$$

where

$$N_{pq}(x) = \sum_{k=0}^p \frac{(p+q-k)!p!}{(p+q)!k!(p-k)!} x^k$$

$$D_{pq}(x) = \sum_{k=0}^q \frac{(p+q-k)!q!}{(p+q)!k!(q-k)!} (-x)^k$$

[Equation \(589\)](#) can be reduced into the Taylor series expansion when $q = 0$:

$$\frac{N_{p0}(x)}{D_{p0}(x)} = 1 + x + \frac{x^2}{2!} + \cdots + \frac{x^p}{p!} \quad (590)$$

The Padé approximation for the matrix exponential utilizes (589) rather than the conventional Taylor series expansion, that is,

$$\exp(A\Delta t) \cong \frac{N_{pq}(A\Delta t)}{D_{pq}(A\Delta t)} \quad (591)$$

In general, convergence of the Padé approximation is faster than that of the Taylor series expansion. The Padé approximation with $p = q$ (the diagonal Padé approximation) is frequently used due to the special advantages it offers in computation time and numerical stability.

The Padé approximation is, of course, a series of expansion, so the problems of slower convergence and round-off error manifest when the norm of $A\Delta t$ is large. For this reason, the scaling and squaring method is also used to efficiently estimate for a matrix exponential with a large norm.

The Padé approximation is widely used as the numerical solution of the matrix exponential method (Moler and Loan 2003). For example, Mathematica and Matlab adopt the Padé approximation and the scaling and squaring method to evaluate a matrix exponential.

The Padé approximation has also been successfully applied to the burnup calculation for a complicated burnup chain (Yamamoto et al. 2007). However, since the Padé approximation is best suited to calculation for a dense-matrix, the Krylov subspace method is more suitable for a burnup calculation when the burnup matrix is very sparse, as shown in Fig. 91.

6.3.9 The Krylov Subspace Method

The matrix exponential method and the Padé approximation offer a general numerical scheme to evaluate the matrix exponential. Burnup calculations in lattice physics computing, however, have the following features:

- Only the number densities are necessary as calculation results, that is, the matrix exponential itself is not necessary.
- The burnup matrix is a sparse matrix with many zero elements.

The Krylov subspace method is a new numerical method that utilizes the above features and is being applied in the fields of molecular dynamics and computational finance (Moler and Loan 2003). By using the Krylov subspace method, stiff burnup calculations with short-lived nuclides, which are difficult to treat by conventional methods, for example, the matrix exponential and the Runge–Kutta methods, have been successfully carried out in short computation time (Yamamoto et al. 2007). A detailed theoretical description of this method is shown by Yamamoto et al. (2007). A theoretical outline of the Krylov subspace method is offered as follows.

When (563) is truncated by m -th order, we have the following polynomial:

$$\vec{N}(t+\Delta t) \cong c_0 \vec{N}(t) + c_1 (\mathbf{A}\Delta t)^1 \vec{N}(t) + c_2 (\mathbf{A}\Delta t)^2 \times \vec{N}(t) + \cdots + c_{m-1} (\mathbf{A}\Delta t)^{m-1} \times \vec{N}(t) \quad (592)$$

where

$$c_k = \frac{1}{k!}$$

The group of the vectors appearing in (592) is known as the Krylov subspace, which is defined as follows:

$$\mathbf{K}_m(\mathbf{A}\Delta t, \vec{N}(t)) = \text{Span} \left\{ \vec{N}(t), (\mathbf{A}\Delta t)\vec{N}(t), (\mathbf{A}\Delta t)^2\vec{N}(t), \dots, (\mathbf{A}\Delta t)^{m-1}\vec{N}(t) \right\}$$

Equation (592) is an example of a polynomial that approximately estimates $\vec{N}(t + \Delta t)$ with the m th order Krylov subspace. Therefore, when the appropriate coefficients, that is, c_k , can be chosen, a better estimate of $\vec{N}(t + \Delta t)$ may become possible. In the Krylov subspace method, c_k are chosen to minimize the square residual of the prediction error for $\vec{N}(t + \Delta t)$. Roughly speaking, appropriate c_k , which depend on matrix \mathbf{A} , are chosen by the least square fitting in the Krylov subspace method, while the conventional method (e.g., the matrix exponential method) utilizes $c_k = \frac{1}{k!}$ regardless of the burnup matrix.

The above explanation suggests that the Krylov subspace method offers an advantage in the choice of expansion coefficients, and is thus different from conventional methods. Since the matrix exponential method and the Runge–Kutta method also utilize a part of the Krylov subspace, they might be classified as a variation of the Krylov subspace method with fixed expansion coefficients.

6.3.10 Numerical Example

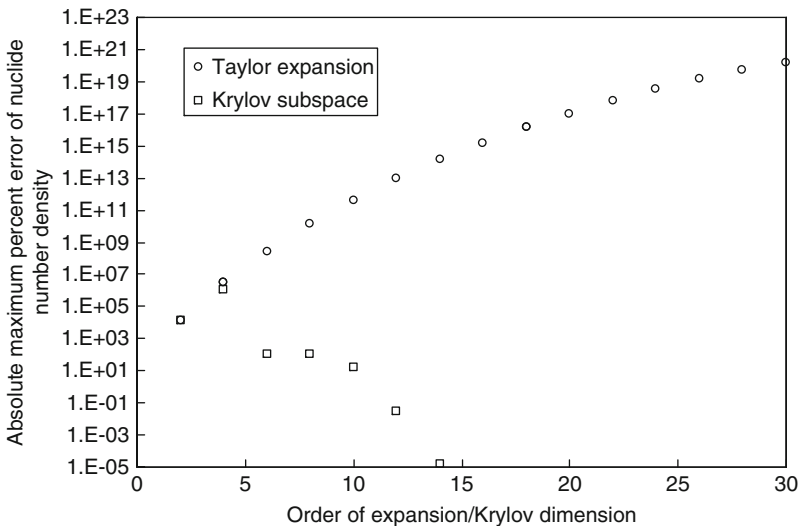
Test calculations to confirm the validity of the Krylov subspace method are offered and explained below. The calculation configuration is the pin-cell geometry of UO₂ fuel in PWR whose enrichment is 4.1 wt%. The initial number densities and geometry of this configuration are shown in  [Table 23](#).

The linear power density is set at 179 W/cm. The burnup calculation up to 1MWd/t (~2,300 s) is carried out by the matrix exponential method (the Taylor series expansion) and the

 **Table 23**
Specifications of a pin cell for test calculation

	Pellet	Clad	Moderator
Radius [cm]	0.4095	0.4750	0.6300*)
Temperature [K]	900	600	559
Number density [1/cm ³]			
²³⁴ U	7.6551E+18		
²³⁵ U	9.5264E+20		
²³⁸ U	2.1994E+22		
¹⁶ O	4.5888E+22		
Nat-Zr		3.7375E+22	
¹ H			4.9848E+22
¹⁶ O			2.4926E+22

Square cell with 1.26 cm pitch is used in this analysis.

**Figure 94**

Maximum absolute error of number densities versus order of Taylor series expansions or dimensions of Krylov subspace

Krylov subspace method. The burnup chain used in this calculation is the “Developer” burnup chain of the MVP-BURN code, which consists of 28 heavy nuclides and 193 fission products (a total of 221 nuclides). The nuclide with the shortest half-life in this burnup chain is ^{106}Rh (29.8 s), and the norm of the burnup matrix ($\mathbf{A}\Delta t$) is $\ln(2)/29.8 \times 2,300 = 0.0233 \times 2,300 = 53.6$, which is quite large. The reference solution is obtained by Mathematica, in which evaluation of the matrix exponential is performed by the Padé approximation.

The maximum (absolute) error of number densities at 1 MW d/t is shown in Fig. 94. In the case of Taylor series expansion, the maximum absolute error increases as the order of Taylor series expansion increases, which suggests that a very large expansion order will be necessary to obtain the converged result. Even if such Taylor series expansion is numerically evaluated, the reliability of the result is doubtful because of the severe numerical round-off error, as discussed in 6.3.5. In the Krylov subspace method, on the other hand, the maximum absolute error of nuclide number densities rapidly decreases with an increasing order of expansion (i.e., the order of Krylov subspace dimensions), and sufficient accuracy is obtained when the order of dimension is 14. The number densities of the nuclides and their associated errors are presented in Figs. 95–99.

Next, burnup calculations up to 100, 1,000, 10,000 and 100,000 MW d/t are carried out by the fourth-order Runge–Kutta, Padé (order $p = 2, 4, 6, 8$) and Krylov subspace (order of dimension = 5, 10, 20, 30, 40, 50, 60) methods, and the accuracy of their calculations are compared. Note that three different time-steps, that is, 0.0001, 0.001, and 0.002 d are used in the fourth-order Runge–Kutta method. In the Padé and Krylov subspace methods, burnup steps are automatically adjusted in order to keep the error of nuclide number densities sufficiently small. Once again, the burnup chain used in the calculation is the “Developer” chain of the MVP-BURN code. The reference solution is obtained by the Mathematica.

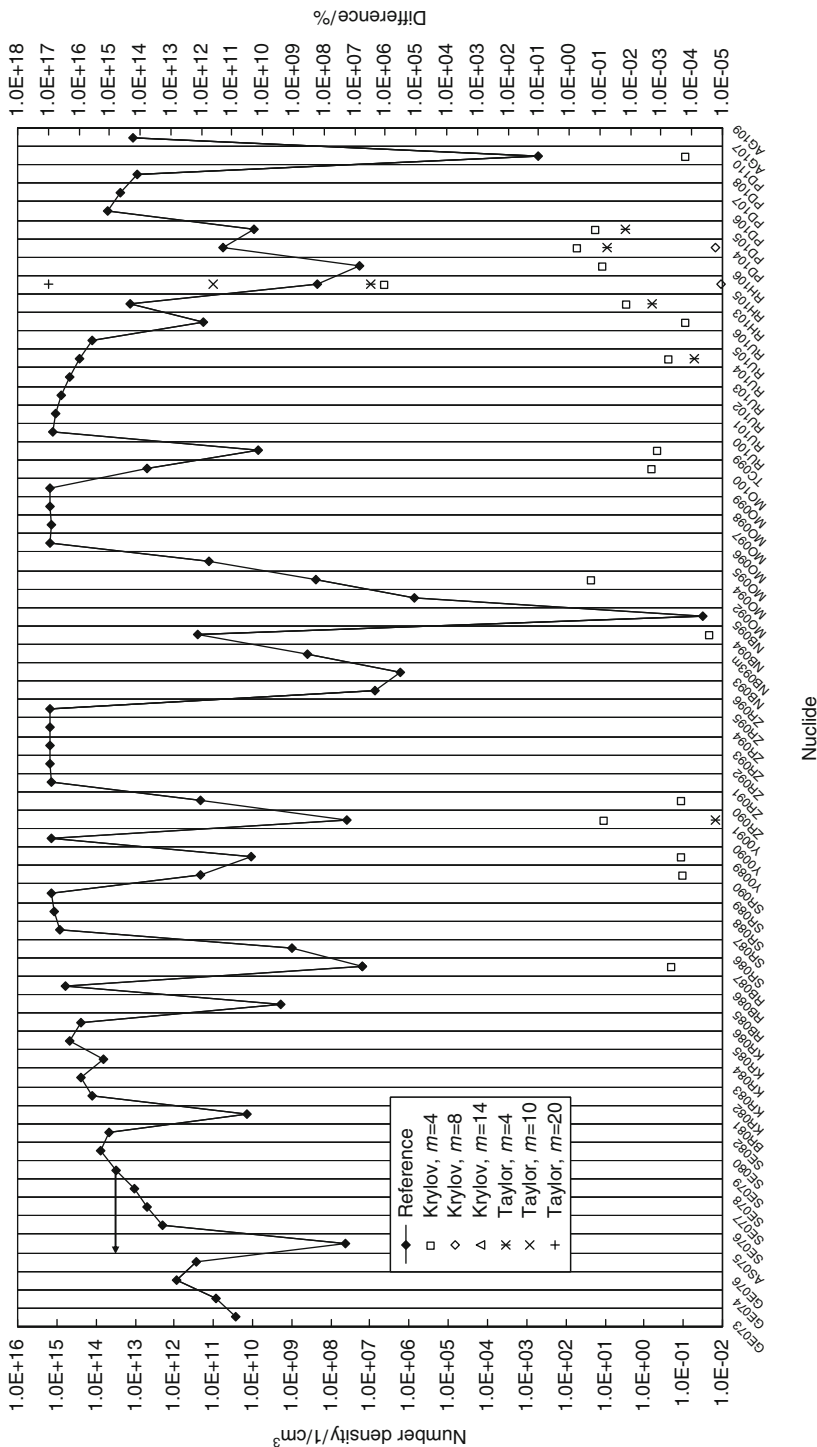


Figure 95 Number densities and their errors at 1 MW d/t. (^{73}Ge - ^{109}Ag) Note that errors less than $10^{-5}\%$ are not shown

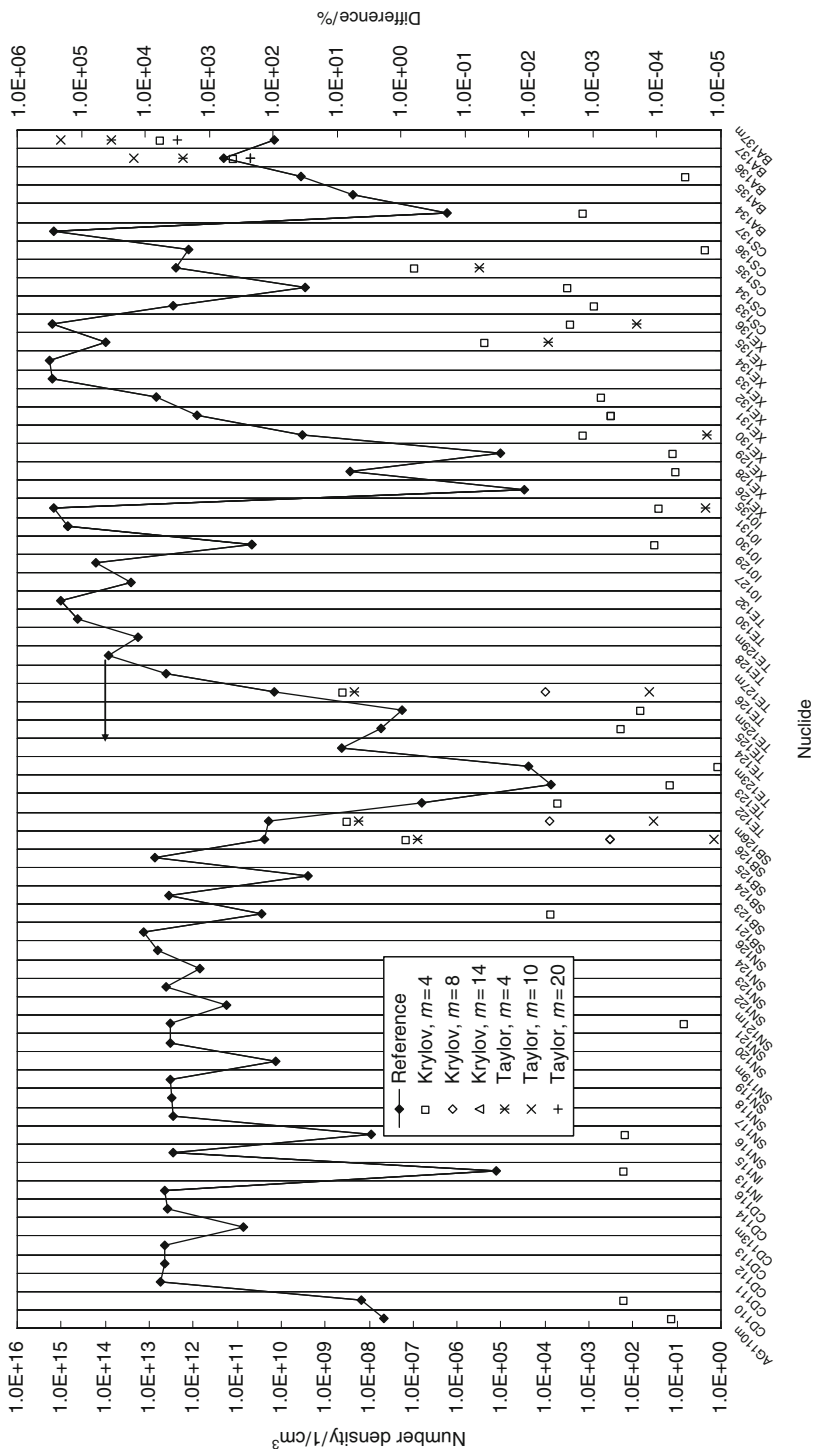


Figure 96 Number densities and their errors at 1 MW d/t. (^{109}Ag - ^{137}mBa) Note that errors less than $10^{-5}\%$ are not shown

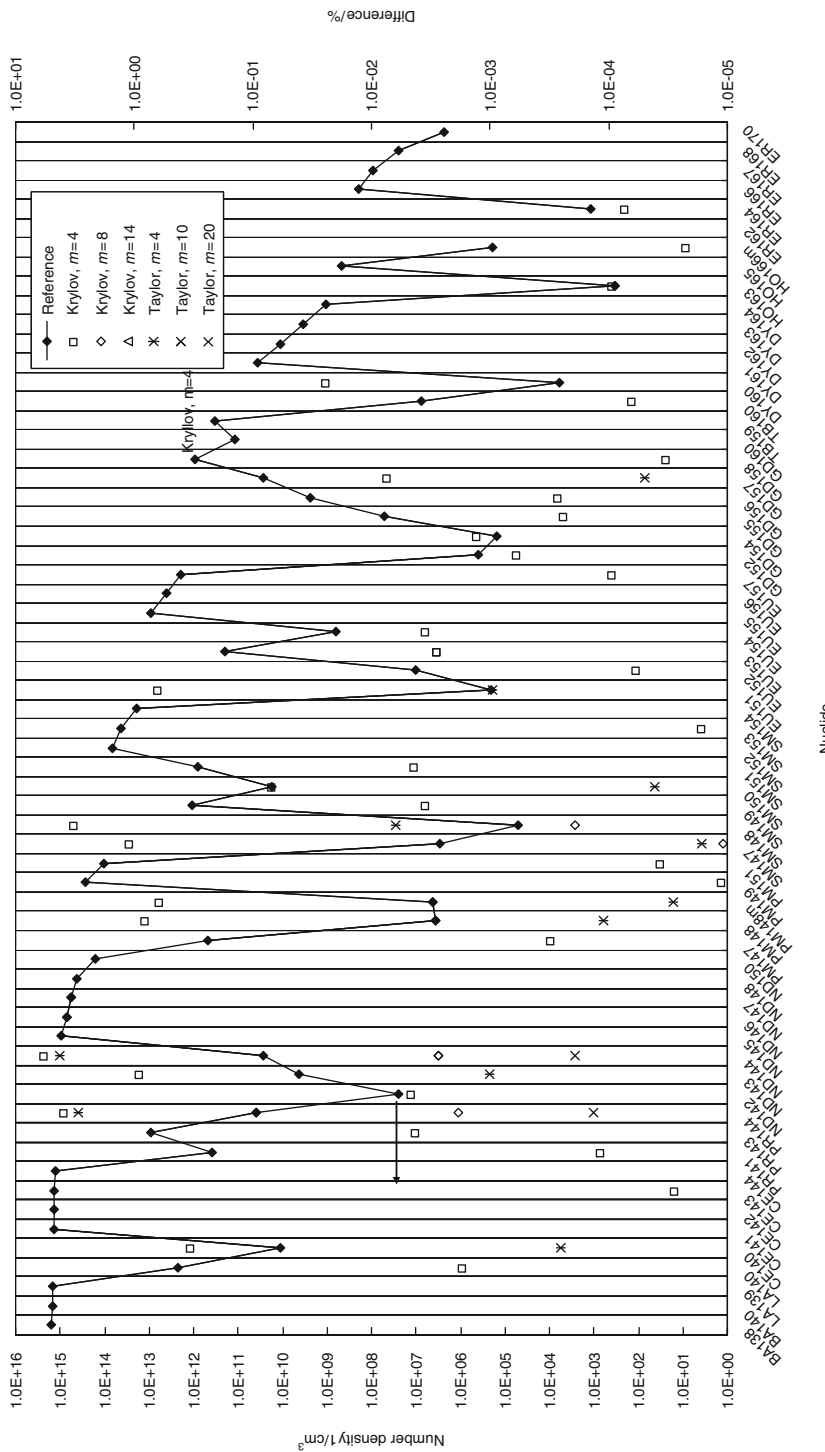


Figure 97
Number densities and their errors at 1MW d/t. (^{138}Ba - ^{170}Er) Note that errors less than $10^{-5}\%$ are not shown

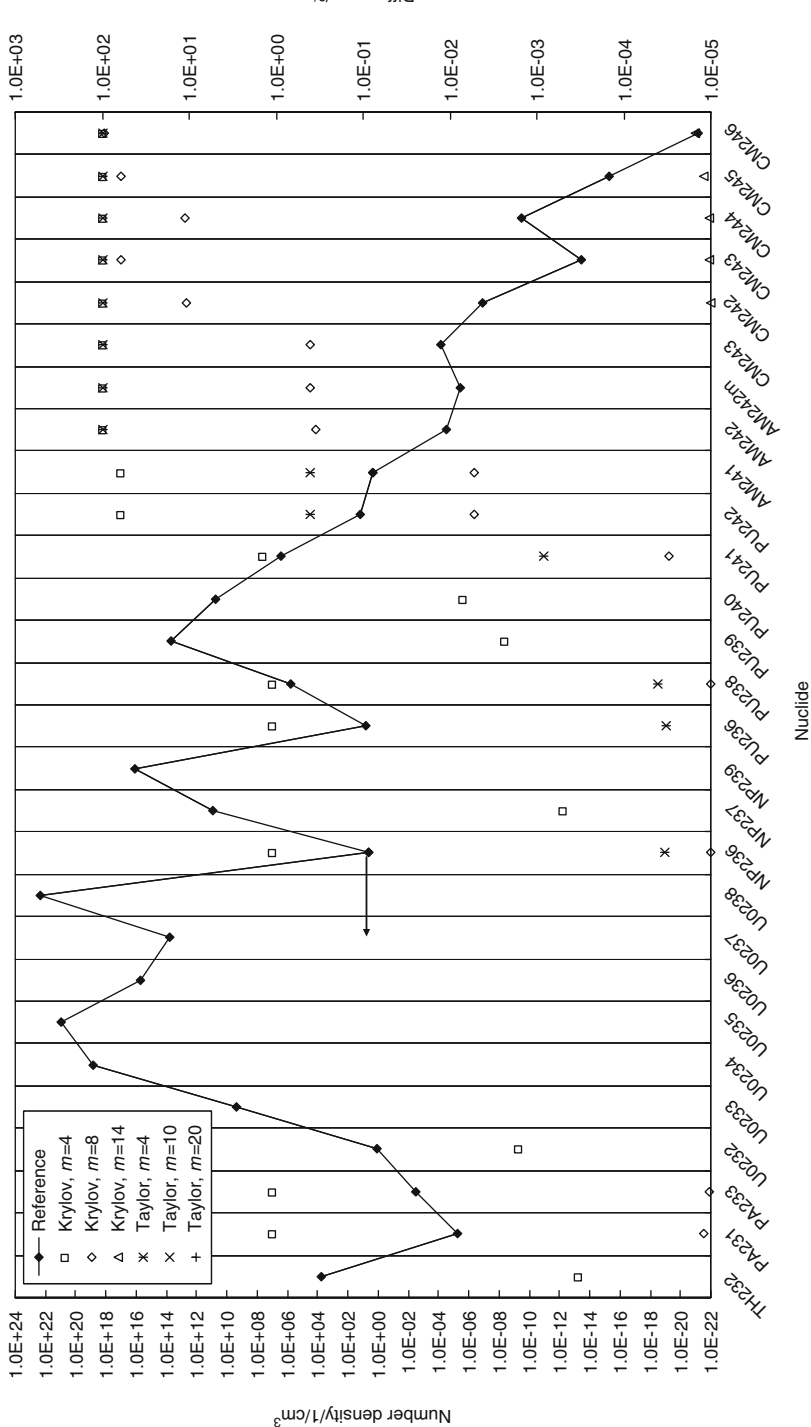


Figure 98
Number densities and their errors at 1MW d/t. (^{232}Th - ^{246}Cm) Note that errors less than 10⁻⁹% are not shown

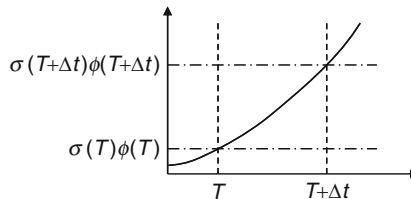


Figure 99
Example of microscopic absorption rate during burnup

The maximum errors of nuclide number densities after burnup, and calculation times, are summarized in [Tables 24](#) and [25](#). From these tables we can make the following observations:

- In the Runge–Kutta method, a very fine burnup step is necessary in order to obtain the appropriate result. The burnup step should be set at less than 0.001 d (~90 s) in the present burnup calculation, due to the presence of a short-lived nuclide (^{106}Rh). Consequently, the computation time becomes impractically long.
- Both the Padé and Krylov subspace methods give accurate results from a practical point of view.
- The Krylov subspace method is between several and several hundred times faster than the Padé method.
- When the dimension of subspace is increased, the accuracy of the expansion by the subspace increases; thus, the width of the burnup step can be reduced in order to achieve sufficient accuracy. The computation time for matrix manipulations, however, then becomes longer. On the contrary, when the dimension of subspace is decreased, the accuracy of the expansion decreases; thus, the burnup step must be increased. The computation time for matrix manipulations, however, then becomes shorter. Consequently, in terms of computation time, there is an adequate dimension of the Krylov subspace.

The above observations suggest that the Krylov subspace method can provide an accurate solution in a short computation time for a complicated burnup chain with short-lived nuclides.

In the actual implementation of the Krylov subspace method, a well-established package such as EXPOKIT can be used (Sidje 1998). The utilization of such sophisticated software reduces the work of implementation.

6.3.11 Predictor–Corrector Method

There are two sources of error in the numerical simulation of a burnup calculation, that is, temporal discretization errors in the sections so far, and the reaction rate. The former topic has been addressed in the previous subsections. The latter topic, the temporal discretization error in the reaction rate, is treated in this section.

First, we consider a very simple burnup equation for an absorber nuclide:

$$\frac{dN}{dt} = -\sigma_a(t)\phi(t)N \quad (593)$$

Table 24**Maximum error of nuclide number densities (unit: %)**

Method	Burnup time			
	10^2 MWd/t (2.67 days)	10^3 MWd/t (26.7 days)	10^4 MWd/t (267 days)	10^5 MWd/t (2,670 days)
Reference (Mathematica)	0.0E+00	0.0E+00	0.0E+00	0.0E+00
Runge-Kutta				
Substep = 0.0001 day	8.3E-01	—**	—	—
Substep = 0.001 day	8.3E-01	—	—	—
Substep = 0.002 day	NA*	—	—	—
Pade				
Order = 2	3.8E-05	3.7E-05	4.9E-05	4.9E-05
Order = 4	3.8E-05	3.7E-05	4.9E-05	4.9E-05
Order = 6	3.8E-05	3.7E-05	4.9E-05	4.9E-05
Order = 8	3.8E-05	3.7E-05	4.9E-05	4.9E-05
Krylov				
Dimension = 5	1.0E+02	1.0E+02	1.0E+02	1.8E+03
Dimension = 10	7.5E-06	4.6E-06	1.0E+02	1.7E+03
Dimension = 20	7.5E-06	4.6E-06	1.2E-05	4.9E-06
Dimension = 30	1.0E-05	4.6E-06	1.2E-05	4.9E-06
Dimension = 40	7.5E-06	4.6E-06	1.2E-05	4.9E-06
Dimension = 50	7.5E-06	3.3E-04	1.2E-05	4.9E-06
Dimension = 60	7.5E-06	3.3E-04	1.2E-05	4.9E-06

* Diverged.

** Not evaluated.

The analytic solution of (593) is given as follows:

$$N(T + \Delta t) = N(T) \exp\left(- \int_T^{T+\Delta t} \sigma_a(t) \phi(t) dt\right) \quad (594)$$

In a common burnup calculation, the absorption cross section and the neutron flux are given as constants at the discrete burnup step (T). Thus (594) can be written as

$$N(T + \Delta t) = N(T) \exp\left(- \int_T^{T+\Delta t} \sigma_a(t) \phi(t) dt\right) \cong N(T) \exp(-\sigma_a(T) \phi(T) \Delta t) \quad (595)$$

When the absorption cross section and neutron flux is fairly constant throughout a burnup step, the accuracy of (595) is high. However, when the behavior of the absorption rate is not constant, as shown in  Fig. 99, the integrated absorption rate during $T \sim T + \Delta t$ is underestimated. The number density of a nuclide is therefore overestimated; that is, a nuclide appears to have burned more slowly than it actually did.

Table 25

Computation time (unit: s)

Method	Burnup time			
	10^2 MWd/t (2.67 days)	10^3 MWd/t (26.7 days)	10^4 MWd/t (267 days)	10^5 MWd/t (2,670 days)
Reference (Mathematica)	1.24	1.47	14.38	30.41
Runge-Kutta				
Substep = 0.001 day	>1,000*	—***	—	—
Substep = 0.001 day	>100	—	—	—
Substep = 0.002 day	NA**	—	—	—
Padé				
Order = 2	1.29	1.49	1.63	1.64
Order = 4	1.31	1.50	1.63	1.65
Order = 6	1.29	1.50	1.64	1.65
Order = 8	1.30	1.50	1.65	1.65
Krylov				
Dimension = 5	1.03	1.05	0.97	0.82
Dimension = 10	0.61	1.50	1.71	1.64
Dimension = 20	0.01	0.07	0.31	1.51
Dimension = 30	0.01	0.03	0.11	0.58
Dimension = 40	0.02	0.04	0.09	0.36
Dimension = 50	0.04	0.05	0.09	0.33
Dimension = 60	0.11	0.12	0.18	0.48

*Precise measurement was not carried out since the code was not optimized for computation speed.

**Diverged.

***Not evaluated.

Variations in the reaction rate, such as those shown in Fig. 99, frequently occur in actual burnup calculations. Such a trend is especially apparent when a burnable absorber, for example, gadolinium, is used in a fuel. The number density of a burnable absorber decreases as burnup proceeds. Consequently, the neutron flux in the burnable absorber becomes higher since the macroscopic absorption cross section of the absorber becomes smaller. Furthermore, the neutron spectrum shifts to a lower energy region (becomes “softer”) since the macroscopic thermal absorption cross section of the burnable absorber becomes smaller. A multigroup (energy-averaged) microscopic cross section becomes larger during burnup due to its softer neutron spectrum. Consequently, the microscopic reaction rate ($\sigma\phi$) becomes larger during burnup.

The temporal discretization error due to (595) can be suppressed by reducing the time-step in a burnup calculation. In other words, utilization of a finer burnup step can limit the temporal

discretization error. However, evaluation of the reaction rate, that is, evaluations of an effective microscopic cross section and neutron flux, is the most time-consuming part of actual burnup calculations. Therefore, the number of reaction rate calculations (i.e., those of an effective microscopic cross section and neutron flux) should be minimized in terms of computation time.

One way to resolve the above conflict is the predictor–corrector (PC) method. Roughly speaking, the PC method performs burnup calculation using a time-averaged absorption reaction rate during a time-step, through pre-evaluation of the absorption rate at $T + \Delta t$.

The actual calculation procedure of the PC method is as follows (Method 1):

- a. Evaluate the microscopic reaction rate with the number density of burnup step n .
- b. Perform the burnup calculation to burnup step $n + 1$ using the reaction rate obtained in (a). This calculation step is called the predictor step.
- c. The number density of burnup step $n + 1$ is estimated using the calculation result of (b). The microscopic reaction rates at this point (burnup step $n + 1$) are then evaluated.
- d. Again perform the burnup calculation using the average microscopic reaction rates of (a) and (c). This step is called the corrector step.

The following alternative method (Method 2) can also be used:

- a. Evaluate the microscopic reaction rate with the number density of burnup step n .
- b. Perform burnup calculation to burnup step $n + 1$ using the reaction rate obtained in (a). This calculation step is called the predictor step.
- c. The number density of burnup step $n + 1$ is estimated using the calculation result of (b). The microscopic reaction rates at this point (burnup step $n + 1$) are then evaluated.
- d. Again perform burnup calculation using the microscopic reaction rates of (c). This step is called the corrector step.
- e. Average the number densities obtained in (b) and (d) to obtain the final results.

Because two reaction rate calculations (predictor and corrector) are necessary for a burnup step in the PC method, it would seem to require longer computation time. However, since the PC method enables the width of the burnup step to be increased by a factor of 10, the computational efficiency of the PC method is actually much greater than that of the conventional method. Therefore, the PC method is the inevitable choice for production lattice physics and core simulation codes.

6.3.12 Sub-Step Method

As described in [6.3.11](#), reaction rate calculations dominate the computation time of a lattice physics computation. Therefore, the time-step size for reaction rate calculations can be longer than that for temporal discretization of the burnup equation, as shown in [Fig. 100](#). Such “double” time-step setting is called the sub-stepping method.

In common lattice physics codes, the burnup steps for reaction rate evaluations are given as input data. Since the sub-step is automatically (and internally) set by the lattice physics codes, users are usually not aware of this. For example, the MVP-BURN code subdivides an input burnup step into 20 sub-steps to which the numerical solution of the burnup calculation is applied, using the Bateman method.

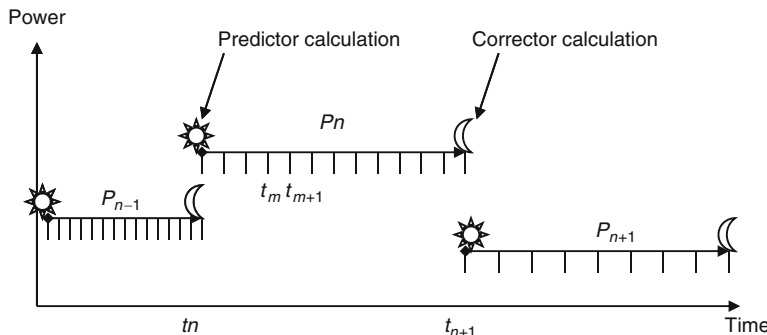


Figure 100
Concept of sub-stepping method for burnup calculation

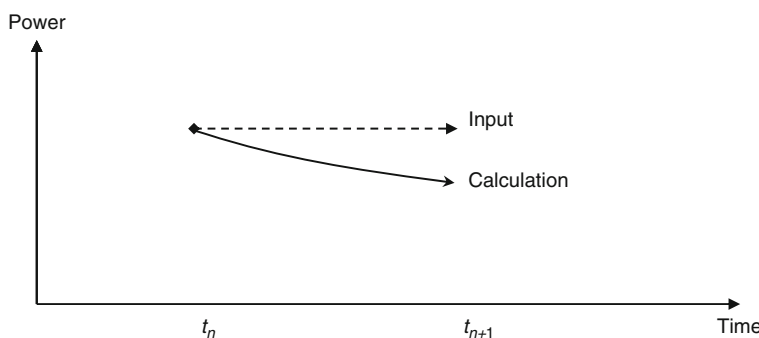


Figure 101
Variation of power density during a time-step

There are two objectives to incorporating the sub-stepping method:

Reduction of Temporal Discretization Error

Temporal discretization error inevitably occurs in a numerical solution by the Euler, Runge-Kutta, matrix exponential, Padé, and Krylov subspace methods, all of which contain a degree of error due to truncation of the expansion series of a matrix exponential. The temporal discretization error can be reduced by the sub-stepping method (though the discretization error from the reaction rate cannot be reduced). Since the matrix decomposition and Bateman methods utilize the “analytic solution” for the burnup equation, temporal discretization error might not be produced by these methods. However, they still suffer from temporal discretization error since in actual calculations, the burnup chain is approximated (e.g., cut the “circuit chain”). Therefore, the sub-stepping method is also useful for these methods.

Power Normalization during Burnup Step

In light water reactor calculations, fissile nuclides are depleted during burnup. Since the neutron flux is normalized at the beginning of the time-step, power density gradually decreases during burnup, as shown in Fig. 101.

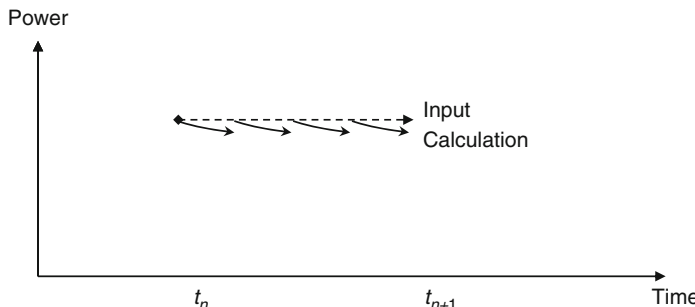


Figure 102
Variation of power with power normalization at sub-step during burnup step

Since burnup is evaluated by the time integration of power, the calculated burnup will be underestimated in [Fig. 101](#). Therefore, the following power normalization is carried out at sub-step m , that is, the normalized factor Norm_m is multiplied by the reaction rate.

$$P = \text{Norm}_m \sum_i \left(\sum_k \kappa_k \sigma_{f,k,i} N_{k,i} \right) \phi_i V_i \quad (596)$$

where

P : power (input data) [J s^{-1}],

κ_k : released energy per fission of nuclide k [J],

$\sigma_{f,k,i}$: microscopic fission cross section of nuclide k in region i [cm^2],

$N_{k,i}$: number density of nuclide k in region i [cm^{-3}],

ϕ_i : neutron flux [$\text{cm}^{-2} \text{s}^{-1}$],

V_i : region volume [cm^3].

By using the above power normalization, the underestimation of burnup can be avoided, as shown in [Fig. 102](#).

6.3.13 Cooling Calculation

The composition of fuels varies during shutdown due to the decay of nuclides. This variation of fuel composition during shutdown has a considerable impact on core characteristics, so this effect must be taken into account in actual in-core fuel management calculations.

In light water reactor analyses, the following decays are important:



This decay has an impact on criticality during the immediate return to power after a scram. It is also a cause of Xe oscillation. Since the half-life of ^{135}Xe is also short (9 h), in a startup analysis after refueling, all Xe is assumed to have decayed (no Xe).

$^{149}\text{Pm} \rightarrow (\text{Half-Life } 54 \text{ h}) \rightarrow ^{149}\text{Sm}$

This has an impact on the core characteristics during the startup operation. Since ^{149}Sm is a stable isotope, all ^{149}Pm is assumed to have decayed into ^{149}Sm (peak condition of Sm) in the startup analysis.

 $^{239}\text{Np} \rightarrow (\text{Half-Life } 2.4 \text{ days}) \rightarrow ^{239}\text{Pu}$

This has an impact on the criticality during return to power after a scram. The positive reactivity effect of this decay is partly canceled out by the negative reactivity effect of $^{149}\text{Pm} \rightarrow ^{149}\text{Sm}$, whose half-life is similar to that of ^{239}Np . Therefore, in an analysis of return to power during a few days after a shutdown, the decay of both $^{149}\text{Pm} \rightarrow ^{149}\text{Sm}$ and $^{239}\text{Np} \rightarrow ^{239}\text{Pu}$ should either be taken into account, or not considered at all.

 $^{148\text{m}}\text{Pm} \rightarrow (\text{Half-Life } 41 \text{ days}) \rightarrow ^{148}\text{Sm}$

This has an impact on the core characteristics of a startup physics test after a normal periodic inspection and refueling that requires a few months.

 $^{148}\text{Pm} \rightarrow (\text{Half-Life } 2.6 \text{ years}) \rightarrow ^{148}\text{Sm}$

Since the half-life of this decay is quite long, it has an impact on the reactivity of reinserted fuels, which were irradiated during a cycle then temporarily stored in the spent fuel pool for future use. When reinserted fuels with long-term cooling are used, the present decay will affect the core characteristics.

 $^{155}\text{Eu} \rightarrow (\text{Half-Life } 4.7 \text{ years}) \rightarrow ^{155}\text{Gd}$

This also has an impact on the reactivity of reinserted fuels. It is a major cause of reactivity variations in reinserted fuels that have been stored for a long time.

 $^{241}\text{Pu} \rightarrow (\text{Half-Life } 14.4 \text{ years}) \rightarrow ^{241}\text{Am}$

This has a major impact on the reactivity of reinserted fuels. This decay reaction is especially important for MOX fuels, since a considerable amount of ^{241}Pu is initially loaded in them. In a core design loaded with MOX fuels, this cooling effect should be taken into account not only for spent MOX fuels, but also for fresh MOX fuels. In order to estimate the decay amount, an accurate cooling time (the span of time from fuel composition characterization to fuel loading) is necessary.

A cooling calculation can be carried out as a burnup calculation with a very low power density. Note that zero power density might cause numerical problems, so the utilization of a very low power density might be appropriate in actual cooling calculations.

6.4 Burnup in Gadolinia-Bearing Fuel

Gadolinia (Gd_2O_3) is a common burnable absorber used in light water reactors. A comparison of the microscopic absorption cross sections of major nuclides used as burnable absorber is shown in ➤ Fig. 103. This figure indicates that the absorption cross section of gadolinium (^{155}Gd , ^{157}Gd) is considerably larger than those of other nuclides. This blackness, that is, the

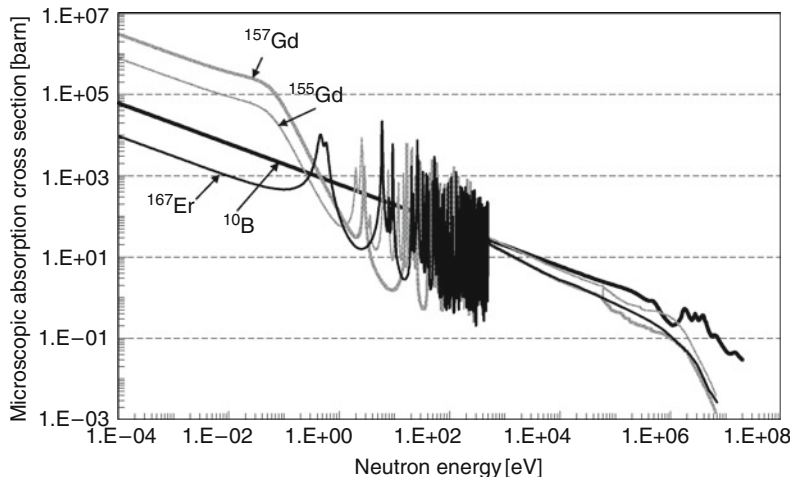


Figure 103
Comparison of microscopic absorption cross sections of major burnable absorber nuclides

strong neutron absorption property of gadolinia, requires some particular consideration in a burnup analysis.

First, since the absorption cross section of gadolinium is very large, gadolinia-bearing fuel rods are generally sparsely located (scattered) in fuel assemblies. Therefore, a gadolinia-bearing fuel assembly has a higher neutronics heterogeneity due to the presence of the “black” regions. Such “black” regions should be handled through sophisticated calculation methods, for example, a neutron transport calculation with explicit geometry treatment. Otherwise, the prediction error will be greater than that of conventional fuel assemblies without gadolinia-bearing fuel rods.

The second point is the unique burnup properties of a gadolinia-bearing fuel rod. This point will be discussed in detail in the next section.

In the following sections, modeling considerations in the accurate handling of a gadolinia-bearing fuel assembly are discussed.

6.4.1 Onion-Skin Effect

The mean free path of thermal neutrons in a gadolinia-bearing fuel pellet is very short, due to the large absorption cross section of gadolinia isotopes. At the beginning of life, thermal neutrons entering from a moderator into a pellet are immediately absorbed by gadolinium nuclides at the surface. Therefore, gadolinium nuclides are depleted from the pellet surface like the layered skins of an onion. This particular burnup behavior of gadolinium isotopes is called the “onion-skin” effect.

In the numerical modeling of a gadolinia-bearing fuel pellet, the onion-skin effect should be carefully treated since it has a significant impact on the neutronics characteristics of a gadolinia-bearing fuel assembly. To accurately capture the onion-skin effect, a gadolinia-bearing fuel pellet

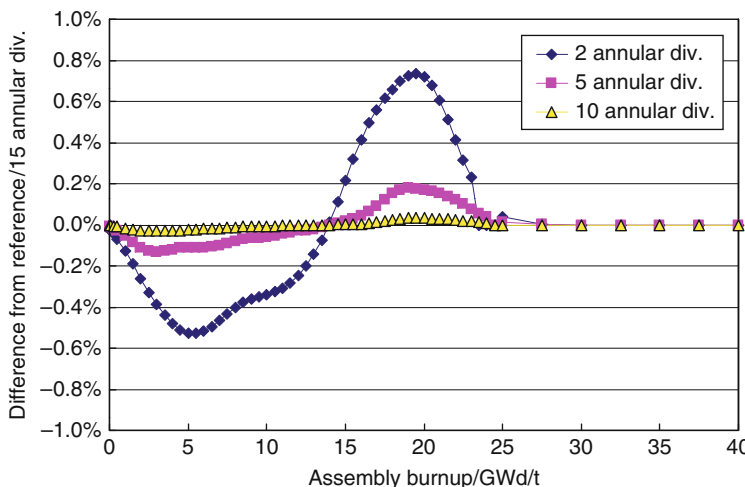


Figure 104

Effect of annular division of gadolinia-bearing fuel pellet (17×17 PWR fuel assembly with 24 Gd-bearing fuel rods of 10 wt% Gd_2O_3)

is annularly divided into regions ranging in number from several to more than a dozen, and the depletion of gadolinium isotopes is explicitly tracked in each annular region. Note that ordinary UO_2 fuel usually has one spatial region in a pellet.

The effect of the annular divisions of a gadolinia-bearing fuel pellet on fuel assembly k-infinity is shown in Fig. 104. This figure shows that the annular division of a gadolinia-bearing fuel pellet has a significant impact on the k-infinity of a fuel assembly, and more than several annular regions are necessary to obtain an accurate result.

The onion-skin effect requires detailed spatial modeling of the gadolinia-bearing fuel pellet. Such modeling, however, requires a very burdensome calculation, which is why various numerical techniques have been used in practical lattice physics computations. Previously, the “off-line” depletion calculation for a gadolinia-bearing fuel pellet was used in conventional lattice physics codes. In this approach, a gadolinia-bearing fuel pellet is depleted in one-dimensional cylindrical geometry, which consists of an annularly divided pellet, clad, moderator, and buffer regions. The buffer region simulates the spectrum environment of adjacent fuel cells in order to reproduce the neutron spectrum in a gadolinia-bearing fuel pellet. The depletion calculation in one-dimensional geometry is carried out prior to the assembly calculation, and spatially homogenized and energetically collapsed cross sections for a gadolinia-bearing fuel pellet or fuel cell are provided in the subsequent assembly calculation. Since the “off-line” depletion calculation is carried out in one-dimensional geometry, detailed spatial discretization (annular divisions) of a gadolinia-bearing fuel pellet can be used within a short computation time.

Though the off-line approach has merit in terms of computation time, its accuracy depends on the calculation conditions used in the one-dimensional transport calculation. Since the actual assembly configuration in two-dimensional geometry is approximated by one-dimensional geometry, there is some ambiguity in the setting of the buffer region. In fact, the difference between the neutron spectrum obtained by one-dimensional geometry and that

obtained by explicit two-dimensional geometry sometimes becomes considerable, and can be a major cause of error in the burnup calculation of a gadolinia-bearing fuel assembly.

Ongoing progress in the computational environment and the requirement of increased accuracy strongly promote the utilization of more advanced and sophisticated treatment of a gadolinia-bearing fuel assembly. As described in [Sect. 5](#), the latest lattice physics codes explicitly treat the heterogeneous geometry of the entire fuel assembly in the spectrum calculation, in which annular divisions of the gadolinia-bearing fuel pellet are also explicitly and directly taken into account. Such detailed modeling of fuel assembly improves the prediction accuracy of burnup behavior of a gadolinia-bearing fuel assembly, since the neutron spectrum in a gadolinia-bearing fuel pellet (and thus the absorption reaction rate of gadolinium isotopes) is more accurately evaluated than it is by the conventional model that utilizes the buffer region.

6.4.2 Asymmetry Effect in Gadolinium Depletion

The previous section describes the necessity of the annular division of a gadolinia-bearing fuel pellet due to the onion-skin effect. Such modeling is appropriate when the adjacent fuel cells are similar from the viewpoint of the neutron spectrum. In other words, when the neutron spectra entering into a gadolinia-bearing fuel pellet are fairly uniform in azimuthal direction, the annular division (without azimuthal division) of a pellet is adequate, since the depletion rate of gadolinium isotopes is azimuthally uniform.

However, in actual situations, especially in a BWR fuel assembly, the neutron spectrum is highly space-dependent due to the presence of gap water and large water holes. Therefore, the azimuthal dependence of the gadolinium depletion rate (asymmetry effect in gadolinium depletion) should be taken into account for an accurate prediction of the burnup behavior of a gadolinia-bearing fuel assembly.

In order to capture the asymmetry effect, a gadolinia-bearing fuel pellet should be azimuthally divided, in addition to the annular division. The magnitude of the asymmetry effect is evaluated in an 8×8 BWR fuel assembly with gadolinia-bearing fuel rods (Tohjoh et al. 2006). A continuous energy Monte Carlo calculation code is used to evaluate the asymmetry effect in this calculation, since detailed spatial discretization in the azimuthal direction cannot be directly modeled by many lattice physics codes.

Calculation geometries are shown in [Fig. 105](#). The left model is an ordinary spatial (material) discretization used in lattice physics computations. Unlike this, the right model has an azimuthal division in addition to the discretization used in the left one. These two calculation models are used for burnup calculation by the continuous energy Monte Carlo burnup code. The difference of the k -infinity at 40% voided condition is shown in [Fig. 106](#). This figure indicates that the asymmetry effect reaches $0.15\%\Delta k/k$ at 10,000 MW d/t, where gadolinium is almost burned out. When the gadolinia-bearing fuel pellet is azimuthally divided, the depletion of gadolinium isotopes is independently tracked in each azimuthal region. Consequently, the k -infinity of the Gd-bearing fuel assembly changes, due to variations in the burnup behavior of gadolinium isotopes.

Though the asymmetry depletion effect is not very large in this case, it could be larger when the azimuthal variation of the neutron spectrum becomes more significant. For example, in a conventionally designed fuel assembly, the gadolinia-bearing fuel rods are sparsely located,

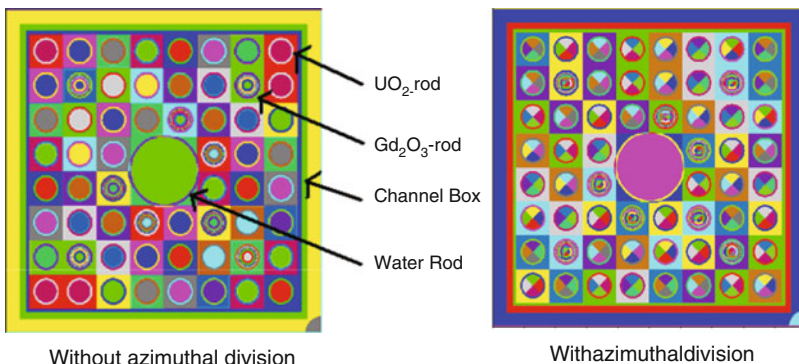


Figure 105
Calculation geometries used for asymmetry effect of gadolinium depletion

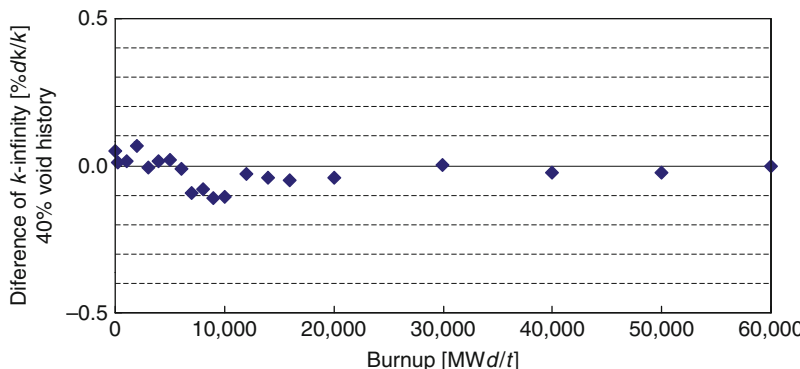


Figure 106
Difference of assembly k -infinity with and without azimuthal division in 8×8 BWR assembly.
Difference is defined by (without – with)/with

but they may be placed side-by-side in order to improve their performance. In such a case, the asymmetry depletion effect should be carefully investigated and its impact should be estimated.

6.4.3 Various Numerical Techniques for Gadolinium Depletion

The predictor–corrector method to reduce the effect of the constant reaction rate approximation in a burnup step is discussed in 6.3.11. However, even if the PC method is used, the typical time-step size used for a Gd-bearing fuel assembly is 0.2 GW d/t (Knott and Wehlage 2007), since the absorption reaction rate of gadolinium isotopes changes rapidly during burnup. Since gadolinium typically burns out at 10–20 GW d/t, from several dozen to a hundred burnup steps are still necessary to accurately deplete a Gd-bearing fuel assembly with the PC method.

In order to reduce this computational burden, some numerical techniques have been developed. One of these is the dual-time depletion method (Rhodes et al. 2006; Knott and Wehlage 2007). In this approach, only the pin-cell calculation for the Gd-bearing fuel rods is performed at a fine time-step size, and the time-consuming assembly calculation is executed at a coarser time-step. By synthesizing these two different calculations (i.e., pin cell and assembly), we can obtain the assembly calculation results that are equivalent to a fine time-step analysis. The reference suggests that the time-step size for assembly calculations can be increased to five times larger than that of the conventional burnup method, without dual-time stepping.

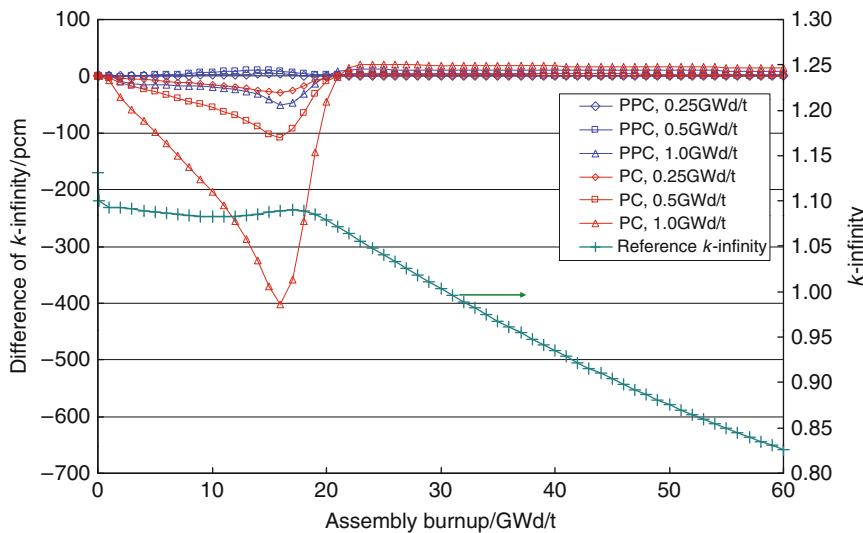
Another approach is the consideration of reaction rate variation during a time-step. In the conventional approach, the coefficients of the burnup equation (i.e., the reaction rates) are assumed to be constant during a time-step. This assumption is used for both the predictor and corrector burnup calculations. The final results are obtained by averaging the predictor and corrector burnup calculation results in order to cancel out the discretization error caused by the assumption of a constant reaction rate. In order to more accurately capture the depletion of each nuclide, the variation of reaction rates within a burnup step can be taken into account. These variations are incorporated by using the linear (Knott and Wehlage 2007) or the quadratic (Rhodes et al. 2006) function of the burnup time.

One of the problems with the conventional PC method is the error in the estimate of reaction rates in a corrector step. The reaction rates of a corrector step are estimated based on the number density obtained by a predictor step. Therefore, when the calculation accuracy of the predictor step is not sufficient, the number densities used in the corrector step may contain some error. Thus, the estimated corrector reaction rates might not be predicted accurately. This is especially true for a Gd-bearing fuel assembly, since the neutron flux in a Gd-bearing fuel rod rapidly increases before the burnout of gadolinia. In this case, the reaction rates in Gd-bearing fuel rods at a predictor step are smaller than the “true” (or the average during the time-step) values, so that the depletion of gadolinium isotopes will be smaller. Since the gadolinia content will be higher than the appropriate (or “true”) value in the corrector calculation, the reaction rates in the Gd-bearing fuel rod are also underestimated. Consequently, the reaction rates in the Gd-bearing fuel rod will be underestimated, since both the predictor and the corrector reaction rates are underestimated. This, in fact, is one of the dominant errors in the conventional PC method.

The traditional countermeasure for this problem is the iteration of the corrector calculations. That is, corrector calculations are carried out until the corrector reaction rates are converged with the best-estimated number densities (obtained by the average of the predictor and updated corrector results). The apparent drawback of this approach is the computation time it requires. Since the corrector calculations need to be repeated, the computation time per time-step will increase.

Another approach is to utilize the relationship between gadolinium number density and the microscopic reaction rate of gadolinium isotopes. In fact, the microscopic reaction rates (i.e., reaction rate per atom) of gadolinium isotopes are approximately proportional to their number densities, at least within a moderate burnup step-size. By using this relationship, improved corrector reaction rates are estimated by the projection (or extrapolation) of the conventional PC results. This approach does not require additional corrector calculation; it is computationally efficient (Yamamoto et al. 2009).

A comparison of the accuracy achieved with the conventional PC and the “projected” PC (PPC) methods is presented in  Fig. 107. Apparently, the PPC method gives better accuracy than the conventional PC method. By using the PPC method, the width of the burnup step-size



■ Figure 107

Comparison of k -infinity for Gd-bearing fuel assembly (17 × 17 PWR fuel, 4.1 wt% enrichment, 10 wt% Gd_2O_3)

can be increased (less than doubled), that is, the number of the burnup step can be reduced (by less than half). Note that we can apply higher-order polynomials to represent the relationship between the number densities of gadolinium and their microscopic reaction rates. The drawback of the higher-order method is the amount of memory it requires. For example, in order to use the second-order polynomial, additional memory storage to maintain the microscopic reaction rates at three burnup points is necessary.

6.5 Summary

In this section, various aspects of the burnup calculations used in lattice physics computation, that is, physics, modeling, numerical methods, and other topics are summarized. Since the burnup calculation is one of the dominant factors contributing to the overall accuracy of calculations, its treatment is important. Though the burnup calculation is a major part of a lattice physics code, a detailed description of this issue can be hardly be found in common textbooks. This subsection would be helpful for both the users and developers of lattice physics codes.

7 Case Matrix

7.1 Introduction

All the individual state points that need to be analyzed by the lattice physics code to fully characterize the fuel design for use in a specific three-dimensional nodal code are referred to as

the *case matrix*. The case matrix will vary between different nodal codes and between different reactor types (i.e., between BWRs and PWRs). The necessity for a case matrix arises from our need to condense and homogenize cross sections over the entire lattice in order to generate two-group nodal data. To perform the condensation and homogenization, we need a very detailed flux distribution. The flux distribution changes as the conditions in the core change, and as the isotopics of the fuel change. This requires us to analyze the lattice every time the isotopics change substantially (i.e., burnup calculation) or every time a core parameter changes substantially (i.e., branch calculation), giving rise to a large collection of different cases. In this section, we will describe the approach used to build cross sections for use in a nodal code such as SIMULATE-3 (Dean et al. 2005). This is by no means an exhaustive discussion on case matrices and the reader should be aware that there are other ways of designing a case matrix to support a nodal code.

7.2 Cross Section Dependencies in BWRs

In general, macroscopic nodal cross sections for a specific reactor condition (e.g., exposure, fuel temperature, and moderator density) can be pieced together as the sum of a base cross section and a collection of partial cross sections, where each partial cross section is used to account for changes in the base cross section due to perturbations in various reactor conditions. To a good approximation, this can be expressed for BWRs as

$$\Sigma_x^g = \Sigma_{x,V}^g(E, U) + \delta\Sigma_{x,TF}^g(E, V) + \delta\Sigma_{x,TM}^g(E, V) + \delta\Sigma_{x,CR}^g(E, V) \\ + \delta\Sigma_{x,HCR}^g(E) + \delta\Sigma_{x,HTF}^g(E) + \delta\Sigma_{x,SDC}^g(E) \quad (597)$$

where x is a reaction type (e.g., absorption and fission); g is one of the two energy groups (either fast or thermal). The various cross sections have the following definitions:

- $\Sigma_{x,V}^g(E, U)$ is the base cross section as a function of instantaneous void content in the coolant, V ; exposure, E ; and historical void content, U (to be explained soon).
- $\delta\Sigma_{x,TF}^g(E, V)$ is the change in the base cross section at different exposures and different void conditions due to a change in fuel temperature, TF .
- $\delta\Sigma_{x,TM}^g(E, V)$ is the change in the base cross section at different exposures and different void conditions due to a change in the moderator temperature, TM .
- $\delta\Sigma_{x,CR}^g(E, V)$ is the change in the base cross section at different exposures and different void conditions due to the insertion of a control blade, CR .
- $\delta\Sigma_{x,HCR}^g(E)$ is the change in the base cross section at different exposures due to the removal of a control blade following a period of time during which the blade was inserted, HCR . This is referred to as the *control blade history* effect.
- $\delta\Sigma_{x,HTF}^g(E)$ is the change in the base cross section at different exposures due to extended operation at a fuel temperature other than the average fuel temperature, HTF . This is referred to as the *fuel temperature history* effect.
- $\delta\Sigma_{x,SDC}^g(E)$ is the change in the base cross section at different exposures following an extended period of inactivity, SDC . This is referred to as the *shutdown cooling* effect.

Historical Void

In (597), the *historical* void content in the coolant, U , is the void level at which the fuel has been depleted. In contrast, the *instantaneous* void content, V , is the amount of void currently in the coolant. To illustrate, a node may deplete for the first 6 months of operation with a void content of 50% (i.e., half vapor, half liquid). This 50% represents the *historical* void content, which is a function of time. It is also the instantaneous void content because it is the void level at which the node is currently operating. If, after 6 months of operation, the conditions in the core change and the void redistributes itself such that the node is filled with 35% void (i.e., 35% vapor, 65% liquid), we would say that our *instantaneous* void content is now 35%, but our *historical* void content remains 50% until we begin to deplete the node at this new void level. Then, assuming the void content remains at 35% for the foreseeable future, the new historical void content will slowly change from 50 to 35% over time.

The *historical* void content determines the isotopics of the fuel with time: higher void content produces a harder spectrum, which produces more Plutonium through U^{238} capture and depletes less U^{235} due to less thermal fission. When the node changes void instantaneously, the effect of the change is determined by the isotopes present in the fuel, which are determined by the historical void content. So, a node at an exposure of 20 GWd/ST that instantaneously changes from $U = 50\%$, $V = 50\%$ to $U = 50\%$, $V = 35\%$ will differ in reactivity from a node at an exposure of 20 GWd/ST that instantaneously changes from $U = 60\%$, $V = 60\%$ to $U = 60\%$, $V = 35\%$, simply because the isotopes will have built up differently over time in the two nodes. Although the two nodes currently contain the same void at the same exposure, their reactivities are different because their operating histories have been different.

The relationship between *instantaneous* void and *historical* void is illustrated in ➤ Fig. 108. In the figure, the saw tooth green line represents the void level over time, which is constant for long periods, but changes abruptly as core conditions change (e.g., adjustment of control blades, changes in core flow rate). In the graph, the abscissa is burnup, expressed in GWd/ST, and the ordinate is water density, expressed in g/cc, which is inverse to void content. That is, as void content increases, the water density decreases. The blue line in the graph represents a straightforward averaging of the void over time using the relationship

$$U = \frac{\sum V_i \cdot \Delta E_i}{\sum \Delta E_i} \quad (598)$$

This would be considered a crude estimate of void history. The orange line in the graph represents the true historical void content, defined by the reactivity worth of the node at any point in time. It can be closely approximated by the expression

$$U = \frac{\sum \exp\{0.08 \cdot \Delta E_i\} \cdot V_i \cdot \Delta E_i}{\sum \exp\{0.08 \cdot \Delta E_i\} \cdot \Delta E_i} \quad (599)$$

In (599), the exponential term is a weighting function that describes the decay of spectral effects from past void levels. In (598), the weighting function was set to unity for the straightforward averaging with time. The graph in ➤ Fig. 108 should be interpreted as follows: At any point in time, the reactivity of a node that has operated with the void levels represented by the V curve, is equivalent to having depleted the node at a constant void level defined by the U (*exact*) curve and then branching to the instantaneous void level represented by V . So, for example, the reactivity of the node at an exposure of 30 GWd/ST and an instantaneous water density of 0.742 g/cc in the figure (i.e., 0% void at hot operating conditions), can be determined by depleting the node

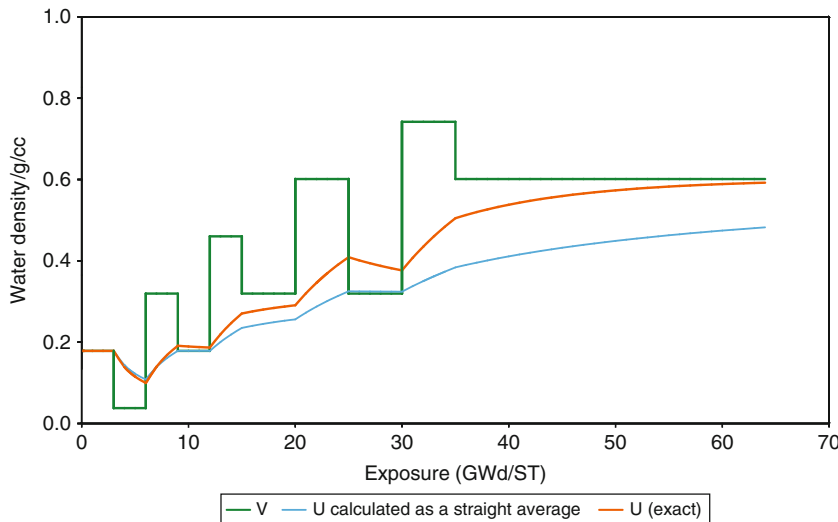


Figure 108
Relationship between instantaneous and historical void

at a constant water density of 0.377 g/cc (i.e., approximately 50% void at hot operating conditions) for 30 GWd/ST and then instantaneously branching to a water density of 0.742 g/cc. In this way, the lattice physics code does not have to follow the exact operating history of a node in order to supply cross sections to the nodal code. We simply need to deplete each lattice at several different historical void levels and perform back branch calculations periodically to different instantaneous void levels in order to generate sufficient cross section information for the nodal code. The nodal code can then interpolate between the explicit points analyzed by the lattice physics code in order to obtain cross sections for a specific core condition.

We now need to determine the number of different historical void levels that need to be analyzed by the lattice physics code in order to supply the nodal code with sufficient information to achieve the accuracy we desire. This number can be ascertained by inspecting Fig. 109, which contains a graph of the fast group macroscopic cross section as a function of void fraction in the coolant (void fraction is defined as void percentage divided by 100, so a void fraction of 0.1 is 10% void, and so on). In the figure, there are two separate curves represented. The first curve is the magenta line, which is the fast group absorption cross section for the node. It has been generated by performing a detailed analysis of the lattice at void fraction increments of 0.1 (i.e., 10% void increments). This is the reference solution. The second curve is the black line that has been generated by fitting a quadratic through the explicit points at void fractions of 0, 0.4, and 0.8 (highlighted by the blue squares on the graph). Here, it can be seen that the cross section can be accurately represented as a quadratic between void fractions of 0 and 0.8. However, beyond a void fraction of 0.8, the cross section no longer behaves as a quadratic and the extrapolated points beyond a void fraction of 0.8 deviate significantly from the reference solution.

The implications of Fig. 109 are rather significant. Years ago, when power densities at most BWRs were consistently at or below 50 kW/L, exit void fractions from fuel bundles were within the 0.8 range. From the quadratic fit in Fig. 109, it can be seen that very little error

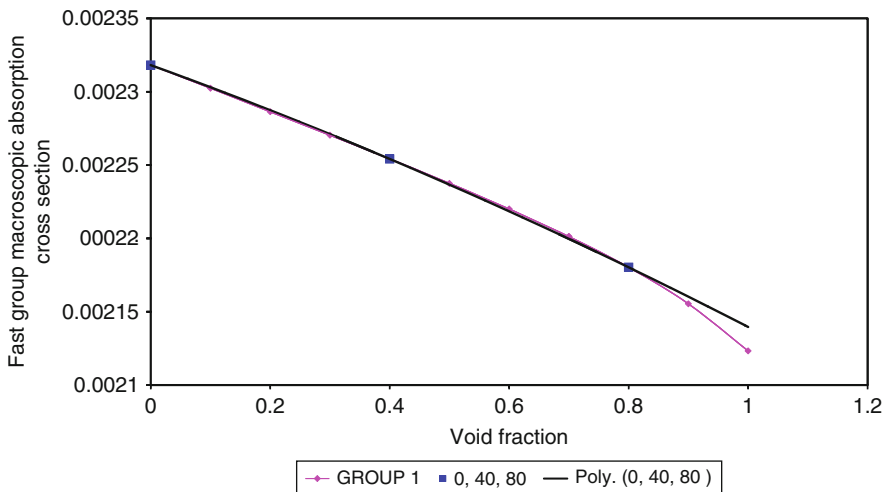


Figure 109
Behaviour of cross section as a function of void fraction

would be incurred by producing explicit data at void fractions of 0, 0.4, and 0.8 and then fitting a quadratic through the three points. Today, after years of power up-rates at many BWRs, the exit void fraction is close to 1.0. If the nodal code uses data from the lattice code that has been generated at explicit void fractions of 0, 0.4, and 0.8, the reactivity at the top of the core will be underestimated and the nodal code will model the axial power shape as being too bottom-peaked early in the cycle. This will result in the nodal code depleting the fuel in the bottom of the core too rapidly, causing the power shape to become too top-peaked during the second half of the cycle.

In order for the nodal code to provide us with the accuracy we desire, the lattice physics code will have to provide cross section data at four different void levels and then the nodal code can use a polynomial to interpolate between explicit data points. This is illustrated in [Fig. 110](#), where a polynomial has been fit through explicit data points at void fractions of 0, 0.4, 0.8, and 1. Note that there will be an inherent error in our cross sections from our polynomial interpolation scheme. That is, the black polynomial trend does not lie precisely on the magenta line. This is the error we will have to live with if we choose to implement this particular case matrix scheme.

The lattice physics code must supply the nodal code with tables of all the cross sections needed to solve the nodal diffusion equation. This includes fast and thermal group data for absorption and production cross sections, as well as the diffusion coefficient. In addition, the nodal code requires data for the fast group removal cross section, energy release values (κ), and a few parameters needed for modeling Xenon transients. If there are 15,000 nodes in the reactor model, then the nodal code has to perform approximately $12 \times 15,000$ interpolations for every analysis, or nearly 200,000 interpolations. This number does not include all the other tables of data that need to be interpolated, such as pin power form functions. If we want the nodal code to use a third-order polynomial fit to interpolate between points in our tables of cross sections, this could become very time consuming.

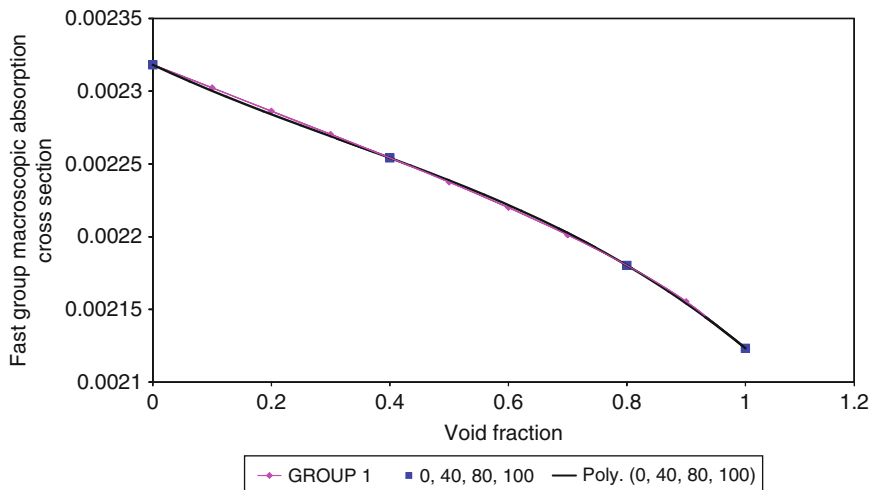


Figure 110
Polynomial fit to cross section data

A more economical approach is to allow the nodal code to interpolate linearly between explicit points in the cross section tables. But interpolating linearly between the four explicit data points is not going to provide us with the accuracy we desire. So we break the process into two steps. Our first step is to gather the explicit data points from the lattice physics code with a processing code that fits the data with a polynomial and creates intermediate points in our tables. That is, we gather the data points at void fractions of 0, 0.4, 0.8, and 1 from the lattice physics code and then allow the processing code to create additional points at void fractions of, say, 0.2 and 0.6 using a polynomial interpolation. The processing code creates tables for the nodal code that include data at void fractions of 0, 0.2, 0.4, 0.6, 0.8, and 1. Then the nodal code can interpolate linearly between all points in the table. This saves us a great deal of time during the nodal analysis without appreciably affecting our accuracy. It also saves us from having to analyze six explicit void fractions with the lattice physics code, which also saves us a great deal of time.

We will return to the topic of void in a later section.

Exposure

➤ *Figure 111* contains several graphs of reactivity from the depletion of a BWR lattice at various void fractions. The graph can be broken into three distinct regions. The first region consists of exposures between 0 and 0.25 GWd/ST. To help put these numbers in perspective, a single day of full power operation at a typical BWR accounts for approximately 0.025 GWd/ST of exposure, so the first region on the graph accounts for roughly 10 days of full power operation. During this period, the fuel is building in fission products, which account for a drop in reactivity of roughly 2% (i.e., $-0.02 \Delta\rho$ of reactivity).

The second region on the graph encompasses the rise in reactivity from an exposure of 0.25 GWd/ST to approximately 20 GWd/ST. During this period of time, the Gadolinium in the fuel design, which is used to hold down reactivity during the bundle's first cycle of operation, is

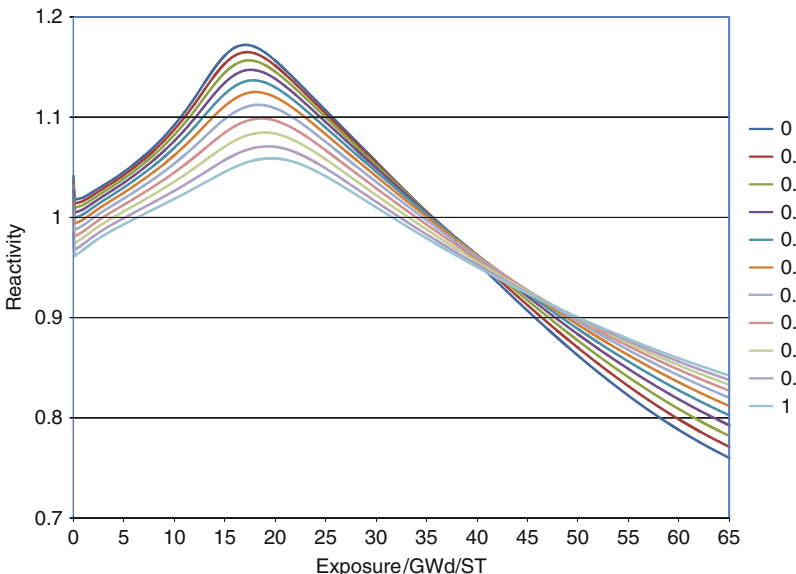


Figure 111
Reactivity as a function of exposure and void fraction

being depleted. The rise in reactivity, and the length of time that the rise lasts, is proportional to the Gadolinium loading. Different designs will have different rises and also different slopes to that rise. However, the point that is being made here is that there will be such a rise whenever Gadolinium is present. The reactivity peak is reached when the Gadolinium has been completely depleted from the bundle.

The third region of the curve consists of all data beyond the reactivity peak – in this case from an exposure of approximately 20 to 65 GWd/ST. This represents the typical reactivity let-down as the U^{235} depletes. It is not linear because there is Pu^{239} being bred due to U^{238} capture, and the Pu^{239} is producing energy during the depletion. Note that the reactivity letdown curve has a steeper slope for the smaller void fractions. As the void fraction increases, the flux spectrum hardens and more U^{238} capture takes place. As a result, there is more Pu available at the higher void fractions and the bundle's energy is consumed more slowly.

It is very important for the lattice physics code – and the nodal code – to accurately capture the detail of the bundle depletion around the reactivity peak. Since we never know exactly where this peak will occur until after the fuel design has been analyzed, the lattice physics code must be able to track the Gadolinium isotopes in the fuel and automatically take time-steps small enough to capture the details of this depletion. As a rule of thumb, time-step sizes for BWR fuel designs should probably not exceed 0.5 GWd/ST until the bundle has surpassed the reactivity peak. This ensures that the onion-skin style of depletion of the Gadolinium pins will be modeled with sufficient accuracy. Once the Gadolinium has been exhausted, it is customary to take time-steps that can range in size from 2.5 to 5 GWd/ST. When the lattice physics results are tabularized for use in the nodal code, it is crucial to ensure that enough exposure detail is maintained such that the reactivity peak is explicitly captured.

Void Coefficient

$\Sigma_{x,V}^g(E, U)$ in (597) represents the base cross section, which accounts for changes in reactivity due to changes in void content. These are the tables of cross sections alluded to in “Historical void” of this section, when we discussed depleting the lattice at several different void levels (i.e., void histories) and then performing a series of back branches at various exposures to various instantaneous void levels. In practice, we would choose our four base void fractions – 0, 0.4, 0.8, and 1 – and, for each void fraction, perform lattice depletions to a final exposure that is guaranteed to encompass the entire operating lifetime of the bundle (e.g., 65 GWD/ST). During the depletion analysis, we save the pin-by-pin isotopic concentrations at each depletion step in a binary file that we will refer to as a *restart file*. The restart file allows us to go back to any point during the depletion of the lattice and perturb one of the system parameters, such as void, and re-perform the step to determine the change in cross sections due to the perturbed parameter.

For the base cross sections, we would like to generate a full three-dimensional table as a function of exposure, historical void, and instantaneous void. To do this, we deplete the lattice at our first void fraction – 0 – and then go back and perform branch calculations to the other three void fractions – 0.4, 0.8, and 1 – at various exposures. Next, we deplete the lattice at our second void fraction – 0.4 – and then go back and perform back branches to the other three void fractions – 0, 0.8, and 1 – at various exposures. And so on with the remaining two void fractions. This will create our three-dimensional table of base cross sections.

For BWRs, the instantaneous void coefficient is more than an order of magnitude larger (i.e., more negative) than any of the other reactivity coefficients.

Fuel Temperature Coefficient

$\delta\Sigma_{x,TF}^g(E, V)$ in (597) represents changes in the cross sections due to changes in fuel temperature. This is referred to as the Doppler coefficient, which varies linearly with the square root of the fuel temperature, $\sqrt{T_f}$, and changes as the composition of the fuel changes. That is, the Doppler coefficient is dependent upon the amount of Uranium, Plutonium, and Gadolinium in the fuel. The cases performed with the lattice physics code to generate the Doppler coefficient consist of back branches at various exposures to a different fuel temperature from each of the uncontrolled depletions. Since the Doppler coefficient is linear, it makes no difference what fuel temperature is chosen for the back branches, so long as the change in reactivity is large enough to be captured by the lattice physics code. Often times, users prefer to branch from the full power fuel temperature used for the base depletions at the four different void fractions, to the hot zero power fuel temperature of 561 K (550 °F).

Moderator Temperature Coefficient

$\delta\Sigma_{x,TM}^g(E, V)$ in (597) represents changes in the cross sections due to changes in the moderator temperature. In BWRs at hot operating conditions, the coolant enters the reactor at a slightly subcooled temperature, but reaches saturation conditions within the first foot or so of the bottom of the core. Once the temperature reaches saturation conditions, it does not change and all heat from the fuel goes into boiling the water. As a result, there really is no cross section dependence on moderator temperature at operating conditions. The moderator temperature dependence comes into play at shutdown conditions. Unlike PWRs, which warm the reactor vessel up to hot zero power conditions before going critical, BWRs can go critical at any zero power temperature. Consequently, the lattice physics code needs to generate enough cross section data so as to enable the nodal code to accurately model criticality conditions at any

temperature below hot zero power conditions. This can usually be accomplished by performing back branches at various exposures from each of the uncontrolled depletions to three separate temperatures between cold conditions (293 K, 68 °F) and hot zero power (approximately 561 K, 550 °F). The back branches have to be performed at both uncontrolled and controlled conditions. The nodal code can then use a straightforward quadratic fit through the cross sections to obtain data at any cold temperature.

Control Blade Coefficient

$\delta\Sigma_{x,CR}^g(E, V)$ in (597) represents changes in the cross sections due to the presence of the control blade. This is perhaps the most direct dependency in (597). The data for this coefficient is generated by performing back branches at various exposures from each of the uncontrolled depletions to an identical condition with the control blade inserted.

Control Blade History Coefficient

$\delta\Sigma_{x,HCR}^g(E)$ in (597) is usually referred to as the *control blade history* effect. When a control blade is present next to a fuel bundle, the blade hardens the spectrum by removing thermal neutrons from the surroundings. The hardened spectrum enhances neutron capture in U²³⁸ and promotes the build-up of Plutonium in the controlled bundle – primarily in the fuel pins along the edge of the bundle closest to the control blade. If the control blade is present for several weeks of full power operation, the Pu build-up can be substantial. When the blade is removed, the bundle will have a different isotopic composition from its composition prior to being controlled and its reactivity may have actually increased over the controlled period of time. If the bundle is now operated uncontrolled for a long period of time, the Pu will eventually be exhausted. This effect is usually modeled at the lattice physics level by depleting the fuel segment with the control blade present and then performing uncontrolled back branches at various exposures. The uncontrolled back branches are compared against uncontrolled depletions of the fuel segment and the appropriate adjustments are made to the cross sections to capture the effect. The control blade history effect is typically modeled at the nominal void level (e.g., 40% void).

Fuel Temperature History Coefficient

$\delta\Sigma_{x,HTF}^g(E)$ in (597) represents changes in the cross sections due to extended periods of operation at a fuel temperature other than the nominal fuel temperature. The fuel temperature is directly proportional to the power level. Higher fuel temperatures represent higher power levels and harden the flux spectrum. Lower fuel temperatures represent lower power levels and soften the flux spectrum. Operating a fuel segment at a higher or lower fuel temperature, relative to the nominal temperature, for an extended period of time will change the isotopic concentration of the fuel and, hence, its reactivity. The data for this effect is generated by depleting the fuel at either an elevated or diminished fuel temperature and then performing back branches to the nominal fuel temperature at various exposures. The depletion at the elevated fuel temperature can be performed at a single void fraction – say the nominal value of 0.4 – and applied to all void levels. The partial cross sections are determined by comparing the back branches against results from the base depletion for the nominal void fraction. In a BWR, fuel temperature history is a very minor effect compared to the other reactivity coefficients and can be ignored without significantly affecting the accuracy of the cross sections.

Shutdown Cooling Coefficient

$\delta\Sigma_{x,SDC}^g(E)$ in (597) represents the decay of certain important isotopes as the bundle cools during a period of inactivity – often referred to as *shutdown cooling*. For short periods of inactivity (i.e., days), the isotopes that are of most interest are the fission products Promethium and Iodine, which decay to Samarium and Xenon, respectively. These decays are important because the Sm¹⁴⁹ and Xe¹³⁵ absorption cross sections are very large in the thermal energy range and have a profound effect on the reactivity of the fuel. The Xe¹³⁵ is also an unstable isotope and will eventually decay to Cs¹³⁵, which is neutronically inert. For long periods of inactivity (i.e., years), we are most interested in the decay of Pu²⁴¹ to Am²⁴¹ and, to a lesser extent, the decay of Eu¹⁵⁵ to Gd¹⁵⁵.

To model shutdown cooling effects, the lattice physics code can perform back branches at various exposures from one of the voided depletions – say the nominal value of 40%. Several shutdown cooling times are analyzed at each exposure point. These cooling times are usually spaced to cover a wide range of periods of inactivity. For example, 1 day, 10 days, 30 days, 1 year, and 4 years. This is usually adequate to cover all bundles that would be discharged from the core at the end of a given cycle and possibly be reinserted into the core at the beginning of a future cycle. The partial cross sections are created by comparing the values from the branch cases against values for the base set at the nominal void.

Our final set of BWR cross section tables will consist of a three-dimensional table of base cross sections augmented by a combination of two-dimensional and three-dimensional tables of various partial cross sections. For the case matrix described in this section, we will have a total of five depletions: four uncontrolled depletions at void fractions of 0, 0.4, 0.8, and 1; and one controlled depletion at a void fraction of 0.4. We will then have a very large series of back branches needed to generate the partial cross sections to (597). A generic CASMO-4 case matrix for generating a BWR cross section model at hot operating conditions is shown in

➤ [Table 26](#). The case matrix for generating a corresponding BWR cross section model at cold shutdown conditions is shown in ➤ [Table 27](#). In the tables: U represents the historical void level; V represent the instantaneous void level; CR represents the presence of the control blade; TFU represents the fuel temperature; TMO represents the moderator temperature; SDC represents shutdown cooling time; and BOR represents the boron concentration in the coolant, which is included only to analyze the effectiveness of the standby liquid control system (SLCS). All cases in the hot case matrix are performed at hot saturation conditions (i.e., an average coolant temperature of approximately 550 °F at a vessel dome pressure of 1,040 psi). The hot, full power fuel temperature of 900 K contained in the two tables is meant for illustration purposes only. The true value for the fuel temperature is typically obtained from a fuel-mechanical analysis of the fuel rod.

The exposure vector for depletion cases consists of time-step sizes of 0.5 GWd/MTU up to an exposure of 20 GWd/MTU, which can be considered at or beyond the Gadolinium burnout point. Beyond the Gadolinium burnout point, time-step sizes of 2.5 GWd/MTU are taken. In general, branch cases are performed at exposure increments of 2.5 GWd/MTU up to an exposure of 20 GWd/MTU. Beyond that, branch cases are performed at exposure increments of 10 GWd/MTU. Note that it is important for the lattice physics code to be able to determine the Gadolinium burnout point because the point will change as a function of void content in the coolant. At very high void fractions, such as 0.8 and 1, the Gadolinium depletes extremely slowly due to the diminished number of thermal neutrons present and the burnout point can be several GWd/MTU beyond the equivalent point at lower void fractions. For the depletion case with the control blade present, the Gadolinium will take a very long time to deplete.

Table 26**An example of a BWR hot case matrix**

Case#	DEPL#	Branch from DEPL#	U [%]	V [%]	CR	TFU [K]	SDC [days]
1	1		0	0	No	900	0
2	2		40	40	No	900	0
3	3		80	80	No	900	0
4	4		100	100	No	900	0
5	5		40	40	Yes	900	0
6		1	0	40	No	900	0
7		1	0	80	No	900	0
8		1	0	100	No	900	0
9		2	40	0	No	900	0
10		2	40	80	No	900	0
11		2	40	100	No	900	0
12		3	80	0	No	900	0
13		3	80	40	No	900	0
14		3	80	100	No	900	0
15		4	100	0	No	900	0
16		4	100	40	No	900	0
17		4	100	80	No	900	0
18		1	0	0	No	561	0
19		2	40	40	No	561	0
20		3	80	80	No	561	0
21		4	100	100	No	561	0
22		2	40	40	No	900	1
23		2	40	40	No	900	10
24		2	40	40	No	900	30
25		2	40	40	No	900	365
26		2	40	40	No	900	1,460
27		1	0	0	Yes	900	0
28		2	40	40	Yes	900	0
29		3	80	80	Yes	900	0
30		4	100	100	Yes	900	0
31		5	40	40	No	900	0

Table 27**An example of a BWR cold case matrix**

Case#	Branch from DEPL#	U [%]	V [%]	CR	TMO [K]	SDC [days]	BOR [ppm]
32	1	0	0	No	293	0	0
33	2	40	0	No	293	0	0
34	3	80	0	No	293	0	0
35	4	100	0	No	293	0	0
36	1	0	0	Yes	293	0	0
37	2	40	0	Yes	293	0	0
38	3	80	0	Yes	293	0	0
39	4	100	0	Yes	293	0	0
40	3	80	0	No	353	0	0
41	3	80	0	No	475	0	0
42	3	80	0	Yes	353	0	0
43	3	80	0	Yes	475	0	0
44	3	80	0	No	293	0	1,000
45	3	80	0	No	475	0	1,000
46	3	80	0	No	293	1	0
47	3	80	0	No	293	10	0
48	3	80	0	No	293	30	0
49	3	80	0	No	293	365	0
50	3	80	0	No	293	1,460	0

7.3 Cross Section Dependencies in PWRs

To a good approximation, the macroscopic cross section for a PWR can be expressed as

$$\Sigma_x^g = \Sigma_{x,HTM}^g(E) + \delta\Sigma_{x,HBOR}^g(E) + \delta\Sigma_{x,TF}^g(E) + \delta\Sigma_{x,TM}^g(E) \\ + \delta\Sigma_{x,BOR}^g(E) + \delta\Sigma_{x,CRD}^g(E) + \delta\Sigma_{x,HTF}^g(E) + \delta\Sigma_{x,SDC}^g(E) \quad (600)$$

where x and g are as previously defined in (597). The various cross sections have the following definitions:

- $\Sigma_{x,HTM}^g(E)$ is the base cross section as a function of exposure and historical moderator temperature, HTM .
- $\delta\Sigma_{x,HBOR}^g(E)$ is the change in the base cross section at different exposures due to changes in the historical boron concentration, $HBOR$.
- $\delta\Sigma_{x,TF}^g(E)$ is the change in the base cross section at different exposures due to a change in fuel temperature, TF .

- $\delta\Sigma_{x,TM}^g(E)$ is the change in the base cross section at different exposures due to a change in the instantaneous moderator temperature, TM .
- $\delta\Sigma_{x,BOR}^g(E)$ is the change in the base cross section at different exposures due to a change in the instantaneous boron concentration, BOR .
- $\delta\Sigma_{x,CR}^g(E)$ is the change in the base cross section at different exposures due to the insertion of a control rod cluster, CR .
- $\delta\Sigma_{x,HTF}^g(E)$ and $\delta\Sigma_{x,SDC}^g(E)$ are as previously defined in (597).

Historical Moderator Temperature

In (600), the *instantaneous* and *historical* moderator temperatures fill a role similar to the role filled by the instantaneous and historical void concentrations in the BWR cross section model. In a PWR, the vessel is pressurized to approximately 2,250 psi and the coolant is not meant to boil. As the liquid coolant flows up the assembly, it picks up heat from the fuel rods and the temperature of the coolant steadily rises with elevation. As a result, the coolant is relatively cool at the bottom of the fuel and is relatively hot at the top of the fuel, with a difference in temperature of approximately 75 °F (i.e., approximately 40 K) between the inlet to and exit from the core. The fuel at the bottom of the core consistently experiences a softer spectrum (i.e., higher water density) compared to the fuel at the top of the core, which consistently experiences a harder spectrum (i.e., lower water density). As time goes by, this difference in the flux spectrum produces a difference in isotopic concentrations between the bottom of a fuel rod and the top of the rod.

In order to model the effect this axial variation in the flux spectrum has on the fuel, the nodal code applies an *historical moderator temperature* model that is similar to the historical void model applied for BWRs. However, since it is rare for the axial moderator temperature profile to change appreciably during PWR operation, there is no real need to perform back branches off the historical moderator temperature depletions the way we performed back branches off the historical void depletions for BWRs. Therefore, it is acceptable to use a two-dimensional table for the base set of cross sections as opposed to the three-dimensional table we used for our BWR model. To generate the cross sections, the lattice is depleted at multiple moderator temperatures, using a nominal fuel temperature and a nominal boron concentration in the coolant. The instantaneous moderator temperature is assumed to be equal to the historical moderator temperature.

Historical Boron Concentration

By now, the reader should be developing a fairly good understanding behind historical parameters. These parameters change the isotopic concentrations of the fuel during extended operation, caused by changes in the flux spectrum – either a hardening or softening effect. The instantaneous parameters are those that have an instantaneous effect on reactivity, but no effect on isotopic concentrations. In (600), the *historical* boron concentration is used to account for changes in the fuel isotopics caused by extended periods of operation at boron concentrations in the coolant, which are different from the nominal value used to generate the base set of cross sections.

The presence of soluble boron in the coolant has a hardening effect on the flux spectrum by removing thermal neutrons. To properly model the dependency of the cross sections on boron, we can simply re-deplete the lattice with multiple boron concentrations, at the nominal moderator temperature and the nominal fuel temperature. The partial cross sections, $\delta\Sigma_{x,HBOR}^g(E)$,

are then calculated simply as the difference between the depletion using the perturbed boron concentrations and the depletion using the nominal boron concentration. The instantaneous boron concentration is assumed to be equal to the historical boron concentration (i.e., no back branches).

Moderator Temperature Coefficient

$\delta\Sigma_{x,TM}^g(E)$ in (600) represents changes in the cross sections due to instantaneous changes in the moderator temperature. The data for this effect is generated by performing back branches at various exposures to a different moderator temperature from the nominal historical moderator temperature. This accounts for spectrum softening effects caused by a drop in moderator temperature (i.e., an increase in moderator density) or spectrum hardening effects caused by a rise in moderator temperature (i.e., a decrease in moderator density). The cross sections behave as a quadratic versus moderator temperature, so data should be generated at three separate moderator temperatures (e.g., 560, 580, and 600 K). The nominal level is typically the middle level (i.e., core mid-plane temperature at full power conditions).

Boron Coefficient

$\delta\Sigma_{x,BOR}^g(E)$ in (600) represents changes in the cross sections due to instantaneous changes in the soluble boron concentration in the coolant. The data for this effect are generated by performing back branches at various exposures to different boron concentrations from the nominal historical boron concentration. This accounts for spectrum softening effects caused by a reduction in boron concentration or spectrum hardening effects caused by an increase in boron concentration. The absorption cross sections behave as a quadratic versus boron concentration, so data should be generated at three separate boron levels (e.g., 0, 800, and 1,600 ppm). The nominal level is typically the middle level (i.e., middle of cycle level).

The remainder of the partial cross sections contained in (600) has been discussed in [Table 7.2](#), so we will not revisit them here. All PWR reactivity coefficients are of a similar magnitude, so they are all equally important to the overall accuracy of the nodal cross section sets. This includes the historical fuel temperature coefficient, which was considered somewhat insignificant in the BWR cross section model because it was so much smaller than all the other effects.

For the case matrix described in this section, we will have a total of four depletions: the base depletion; a depletion at a perturbed moderator temperature; a depletion at a perturbed boron condition; and a depletion at a perturbed fuel temperature condition. A generic CASMO-4 case matrix for generating a PWR cross section model at hot operating conditions is contained in [Table 28](#). The case matrix for generating a corresponding PWR cross section model at cold shutdown conditions is contained in [Table 29](#). In the tables: *HTMO* represents the historical moderator temperature; *TMO* represent the instantaneous moderator temperature; *CR* represents the presence of the control blade; *HTFU* represents the historical fuel temperature; *TFU* represents the instantaneous fuel temperature; *HBOR* represents the historical boron concentration; *BOR* represents the instantaneous boron concentration; and *SDC* represents shutdown cooling times.

The exposure vector for PWR depletion cases consists of time-step sizes of 1 GWd/MTU up to an exposure of 15 GWD/MTU (assuming Gadolinium is not being used as a burnable absorber in the fuel design). Beyond that, time-step sizes of 2.5 GWd/MTU are taken. In general, branch cases are performed at exposure increments of 2 GWd/MTU up to an

Table 28

An example of a PWR hot case matrix

Case#	DEPL#	Branch from DEPL#	HTMO [K]	TMO [K]	CR	HTFU [K]	TFU [K]	HBOR [ppm]	BOR [ppm]	SDC [days]
1	1		580	580	No	900	900	800	800	0
2	2		560	560	No	900	900	800	800	0
3	3		580	580	No	900	900	1,600	1,600	0
4	4		580	580	No	560	560	800	800	0
5		1	580	580	No	900	900	800	0	0
6		1	580	580	No	900	900	800	1,600	0
7		1	580	580	No	900	900	800	2,400	0
8		1	580	560	No	900	900	800	800	0
9		1	580	600	No	900	900	800	800	0
10		1	580	580	No	900	560	800	800	0
11		1	580	580	Yes	900	900	800	800	0
12		1	580	580	No	900	900	800	800	1
13		1	580	580	No	900	900	800	800	10
14		1	580	580	No	900	900	800	800	30
15		1	580	580	No	900	900	800	800	365
16		1	580	580	No	900	900	800	800	1,460

exposure of 20 GWd/MTU. Beyond that, branch cases are performed at exposure increments of 10 GWd/MTU.

7.4 Summary

This section has provided a description of one possible way of constructing a case matrix for a nodal code. The models described in this section are by no means exhaustive and are meant only to provide the reader with a glimpse at the types of analyses performed using a lattice physics code to support a nodal code. There are other ways of designing a case matrix for a nodal code. The main premise, though, is to provide the reader with an appreciation for the number of cases needed to be performed by the lattice physics code in order to accurately capture the behavior of the fuel over its anticipated lifetime in the core. For BWRs, the case matrix we have described will require approximately 1,200 state points per lattice. If the fuel design contains 8 lattices, it will take approximately 10,000 lattice physics state point calculations to fully functionalize the behavior of the fuel. The PWR case matrix we described contains substantially less – approximately 800 state points, 300 of which are needed to model hot

Table 29

An example of a PWR cold case matrix

Case#	DEPL#	Branch from DEPL#	HTMO [K]	TMO [K]	CR	HTFU [K]	TFU [K]	HBOR [ppm]	BOR [ppm]	SDC [days]
17		1	580	293	No	900	293	800	0	0
18		1	560	293	No	900	293	800	800	0
19		1	580	293	No	900	293	800	1,600	0
20		1	580	425	No	900	425	800	0	0
21		1	580	425	No	900	425	800	800	0
22		1	580	425	No	900	425	800	1,600	0
23		1	580	560	No	900	560	800	0	0
24		1	580	560	No	900	560	800	800	0
25		1	580	560	No	900	560	800	1,600	0
26		1	580	560	No	900	560	800	2,400	0
27		1	580	293	Yes	900	293	800	1,600	0
28		1	580	475	Yes	900	475	800	1,600	0
29		1	580	560	Yes	900	560	800	1,600	0
30		1	580	293	No	900	293	800	1,600	1
31		1	580	293	No	900	293	800	1,600	10
32		1	580	293	No	900	293	800	1,600	30
33		1	580	293	No	900	293	800	1,600	365
34		1	580	293	No	900	293	800	1,600	1,460
35		2	560	293	No	900	293	800	1,600	0
36		3	580	293	No	900	293	1,600	1,600	0

operating conditions. With this knowledge, the reader can begin to appreciate the effort required to accurately model the fuel in the core of a nuclear power plant.

8 Edits

This section presents some of the more common data passed from a lattice physics code to a nodal code. It is by no means an exhaustive list and there are often times more than one way of calculating a parameter. A perfect example of this would be the diffusion coefficient, which has no precise definition at the lattice physics level. Nevertheless, this section should provide the reader with an understanding of some of the back-end calculations performed by the lattice physics code.

The contents of this section have been taken from various information edited from LANCER02 (Knott and Wehlage 2007) for use in the nodal codes PANACEA (Moore et al. 1999) and AETNA (Iwamoto et al. 2003), and from various information edited from CASMO-4 (Knott et al. 1995) for use in the nodal code SIMULATE-3 (Dean 2005).

8.1 Nomenclature

g = energy group structure of the nodal code (typically two groups)

r = material region (e.g., fuel, clad, and coolant)

s = surface length of a particular mesh (cm)

S = surface length of an entire side of the lattice (cm)

h = six-group delayed neutron structure

i = energy group structure of the lattice physics code's neutron cross section library

j = energy group structure of the lattice physics code's gamma library

dr = volume of material region r per unit height (cm³/cm)

$V(r) = dr$

V_{ass} = volume of entire lattice per unit height (cm³/cm)

V_{fuel} = total volume of all fuel pellets per unit height (cm³/cm)

$N_m(r)$ = atomic number density for nuclide m ; at position r

A_m = atomic mass of nuclide m

ρ_m = density for nuclide m , in (g/cm³)

$\sigma_{xm}(g, r)$ = microscopic cross section for reaction type x ; of nuclide m ; in energy group g ; at position r .

$\phi(g, r)$ = neutron flux in energy group g ; at position r

$\psi(g, s)$ = neutron surface flux in energy group g ; at surface position s

$\chi_m(i, h)$ = delayed neutron fission spectrum of nuclide m ; for neutrons born in energy group i ; to be deposited in delayed group h

$\Psi(i)$ = neutron flux in group i from fundamental mode calculation

$\Psi^\dagger(i)$ = adjoint flux in group i from fundamental mode calculation

8.2 Various Edits

Parameters that need to be edited by the lattice physics code for use in the accompanying nodal code may include some of the following:

Lattice-averaged atomic number densities of nuclide m

$$\bar{N}_m = \frac{\int_{V_{ass}} N_m(r) dr}{\int_{V_{ass}} dr} \quad (601)$$

Fuel-averaged atomic number density of heavy isotope m

$$\tilde{N}_m = \frac{\int_{V_{fuel}} N_m(r) dr}{\int_{V_{fuel}} dr} \quad (602)$$

Decay constant of delayed neutrons in delayed group h

$$\bar{\lambda}(h) = \frac{\sum_m \lambda_m(h) \cdot \beta_m(h) \cdot \sum_g N_m v \sigma_{f,m}(g) \phi(g)}{\bar{\beta}(h) \cdot \sum_g v \bar{\Sigma}_f(g) \phi(g)} \quad (603)$$

where $\beta_m(h)$ is the delayed neutron fraction for nuclide m , in delayed group h ; and $\lambda_m(h)$ is its decay constant. The summation over m is performed over all fissile isotopes. The averaged delayed neutron fraction, $\bar{\beta}(h)$, is calculated as

$$\bar{\beta}(h) = \frac{\sum_m \beta_m(h) \cdot \sum_g N_m v \sigma_{f,m}(g) \phi(g)}{\sum_g v \bar{\Sigma}_f(g) \phi(g)} \quad (604)$$

Lattice-averaged flux per nodal group

$$\bar{\phi}(g) = \frac{\int_{V_{ass}} \phi(g, r) dr}{\int_{V_{ass}} dr} \quad (605)$$

where the fine-mesh flux in the nodal-group energy structure, $\phi(g, r)$, is calculated by a straightforward condensation

$$\phi(g, r) = \sum_{i \in g} \phi(i, r) \quad (606)$$

Boundary diffusion coefficient per nodal group for each assembly surface

$$\bar{D}_S(g) = \frac{\int_{S_{ass}} D(g, r) \psi(g, r) dS}{\int_{S_{ass}} dS} \quad (607)$$

where the integral is performed over one assembly surface only. There are four $\bar{D}_S(g)$ values edited: (1) north; (2) east; (3) south; and (4) west.

Effective delayed neutron fraction for delayed group h

The effective delayed neutron fraction accounts for the fact that delayed neutrons are born at energies lower than those of prompt neutrons and, hence, do not contribute to fast fission and have smaller leakage rates into (or out of) the system than prompt neutrons. The effective delayed neutron fraction is calculated as

$$\beta(h) = \frac{\sum_m \left[\sum_i \beta_m(h) \bar{\chi}_{d,m}(i, h) \Psi^\dagger(i) \cdot \sum_i v \bar{\sigma}_{f,m}(i) \bar{N}_m \Psi(i) \right]}{\sum_m \left\{ \left(1 - \sum_h \beta_m(h) \right) \left(\sum_i \bar{\chi}_{p,m}(i) \Psi^\dagger(i) \right) + \sum_h \beta_m(h) \left(\sum_i \bar{\chi}_{d,m}(i, h) \Psi^\dagger(i) \right) \right\} \cdot \sum_i v \bar{\Sigma}_f(i) \Psi(i)} \quad (608)$$

$$\begin{aligned}
&\approx \frac{\sum_m \left[\sum_i \beta_m(h) \bar{\chi}_{d,m}(i, h) \Psi^\dagger(i) \cdot \sum_i v \bar{\sigma}_{f,m}(i) \bar{N}_m \Psi(i) \right]}{\sum_i \bar{\chi}(i) \Psi^\dagger(i) \cdot \sum_i v \bar{\Sigma}_f(i) \Psi(i)} \\
&\approx \frac{\sum_m \left[\sum_i \beta_m(h) \bar{\chi}_{d,m}(i, h) \Psi^\dagger(i) \cdot \sum_i v \bar{\sigma}_{f,m}(i) \bar{N}_m \Psi(i) \right]}{k^\dagger \sum_i v \bar{\Sigma}_f(i) \Psi(i)}
\end{aligned} \tag{608}$$

where the summation over m includes the isotopes: Th²³², U²³³, U²³⁴, U²³⁵, U²³⁶, U²³⁸, Pu²³⁹, Pu²⁴⁰, Pu²⁴¹, and Pu²⁴²; $\bar{\chi}_{d,m}(i, h)$ is the delayed neutron fission spectrum from energy group i to delayed group h , for isotope m ; $\bar{\chi}_{p,m}(i)$ is the prompt neutron fission spectrum for isotope m ; and $\bar{\chi}(i)$ is the total fission spectrum for the homogeneous system. The adjoint flux, $\Psi^\dagger(i)$, can be obtained by solving the non-leakage adjoint form of the fundamental mode equation

$$\bar{\Sigma}_{tr}(i) \cdot \Psi^\dagger(i) = \sum_{i'} \left[\bar{\Sigma}_s(i \rightarrow i') + \frac{v \bar{\Sigma}_f(i)}{k^\dagger} \cdot \bar{\chi}(i') \right] \Psi^\dagger(i') \tag{609}$$

where the adjoint multiplication factor is given by

$$k^\dagger = \sum_{i'} \bar{\chi}(i') \Psi^\dagger(i') \tag{610}$$

All cross sections are flux-volume weighted over the entire assembly using the forward flux from the MoC solution after expanding it to the energy group structure of the cross section library (i.e., the fine-group structure). In this formulation, it is assumed that the flux-volume weighted assembly-averaged cross sections using the forward flux are not significantly different from the equivalent cross sections that would be created using a spatial adjoint flux distribution. This assumption is perfectly adequate when non-leakage boundary conditions are used (either perfect reflexion or periodic).

The effective delayed neutron fraction can be calculated a slightly different way by considering neutron leakage effects. The adjoint flux, $\Psi^\dagger(i)$, is obtained by solving the adjoint form of the fundamental mode equation that includes neutron leakage effects

$$[\bar{\Sigma}_{tr}(i) + \bar{D}(i)B^2] \cdot \Psi^\dagger(i) = \sum_{i'} \left[\bar{\Sigma}_s(i \rightarrow i') + \frac{v \bar{\Sigma}_f(i)}{k^\dagger} \cdot \bar{\chi}(i') \right] \Psi^\dagger(i') \tag{611}$$

where B^2 is the value of the material buckling from the solution to the forward form of the fundamental mode calculation, (29). The value of $\beta(h)$ should be more accurate when including leakage effects into the adjoint flux spectrum, since neutron leakage out of the system occurs predominately in the fast energy groups.

Total effective delayed neutron fraction

$$\beta_{\text{total}} = \sum_{h=1}^6 \beta(h) \tag{612}$$

Lattice-averaged diffusion coefficient per nodal group

$$D(g) = \sum_{i \in g} \left\{ \frac{1/3}{\int_{V_{ass}} \Sigma_{tr}(i, r) \phi(i, r) dr} \right\} \quad (613)$$

where the lattice-averaged diffusion coefficient is calculated in the fine-group energy structure and collapsed directly to the nodal-group energy structure. Note that it is important that the spatial homogenization be performed on the transport cross section, not the diffusion coefficient. If the spatial homogenization is performed on the diffusion coefficient, any vacuum regions in the lattice (e.g., air gaps between fuel pellet and cladding) will skew the value of the coefficient.

In the context of (613), the lattice-averaged diffusion coefficient in each energy group is being condensed. That is, we calculate a diffusion coefficient in the fine-group energy structure of the cross section library and condense it to the nodal-group structure. An alternative approach would be to condense the transport cross section to the nodal-group structure and calculate a diffusion coefficient from that. The equation would then take the form

$$D(g) = \frac{1/3}{\sum_{i \in g} \left\{ \int_{V_{ass}} \Sigma_{tr}(i, r) \phi(i, r) dr \right\}} \quad (614)$$

Equations (613) and (614) will give different values for the diffusion coefficients, especially in the fast energy group. Neither approach is incorrect – nor correct. Most nodal methods modify the diffusion coefficient during the iteration process, so the choice is somewhat irrelevant. Nodal results should be somewhat insensitive to the method chosen in the lattice physics code.

Absorption reaction rates per isotope m

$$\Sigma_{a,m} = \sum_g \int_{V_{ass}} N_m(r) \sigma_{a,m}(g) \phi_g(r) dr \quad (615)$$

Effective energy release per fission, per fuel rod

$$\kappa(r) = \frac{E_{kinetic}(r) + E_\gamma(r) + E_\beta(r) + E_s(r)}{\sum_g \Sigma_f(g, r) \phi(g, r) V(r)} \quad (616)$$

where the energy terms are defined in (45)–(48).

Flux discontinuity factor per nodal group

$$DF_S(g) = \frac{\int_S \psi(g, s) ds}{\int_{V_{ass}} \phi(g, r) dr} \quad (617)$$

Lattice-averaged fast flux (above 1 MeV)

$$\overline{\Psi}_{fast} = \sum_{E_i \geq 1 \text{ MeV}} \Psi(i) \quad (618)$$

where the summation over energy group runs from 20 MeV (group 1) to the energy boundary closest to 1 MeV.

Relative fission rate per fuel rod

$$\text{FRR}(r) = \frac{\sum_g \int_{V_{x,y}} \Sigma_f(g, r) \phi(g, r) dr}{\left\{ \frac{\sum_g \int_{V_{\text{fuel}}} \Sigma_f(g, r) \phi(g, r) dr}{\int_{V_{\text{fuel}}} dr} \right\}} \quad (619)$$

Relative gamma energy deposition per fuel rod

$$\text{GRR}(r) = \frac{\sum_j \int_{V_{x,y}} \Sigma_e(j, r) \phi(j, r) dr}{\left\{ \frac{\sum_j \int_{V_{\text{fuel}}} \Sigma_e(j, r) \phi(j, r) dr}{\int_{V_{\text{fuel}}} dr} \right\}} \quad (620)$$

where $\Sigma_e(j, r)$ is the macroscopic energy deposition cross section for material region r in the energy group structure of the gamma library, j .

Gamma detector response

$$D^\gamma = \left(\frac{1}{P} \right) \sum_j \sigma_{e,m}(j) \phi(j, r) \quad (621)$$

where $\phi(j, r)$ is the gamma flux in the narrow–narrow corner of the problem for BWRs, or in the location of the instrument thimble for PWRs; and $\sigma_{e,m}(j)$ is the microscopic energy deposition cross section for some nuclide of choice (e.g., Fe). P is the lattice power level, in MeV.

Fission detector response

$$D^n = \left(\frac{1}{P} \right) \sum_i \sigma_{f,\text{U}^{235}}(i) \phi(i, r) \quad (622)$$

where $\phi(i, r)$ is the fine-group flux in the narrow–narrow corner of the problem for BWRs, or in the location of the instrument thimble for PWRs; and $\sigma_{f,\text{U}^{235}}(i)$ is the fine-group microscopic fission cross section for U^{235} . P is the lattice power level, in MeV.

Nodal infinite multiplication factor

This is the multiplication factor obtained from the two-group cross sections. The two-group cross sections are created using the fine-group critical flux spectrum following the fundamental mode calculation. Since the cross sections are collapsed using the critical spectrum, the two-group multiplication factor will not be precisely equal to the multiplication factor from the fine-mesh assembly transport calculation unless the multiplication factor for the system just happens to be 1.0.

$$k = \frac{v\bar{\Sigma}_f(1) + v\bar{\Sigma}_f(2) \cdot \frac{\bar{\Sigma}_{\text{rem}}}{\bar{\Sigma}_a(2)}}{\bar{\Sigma}_a(1) + \bar{\Sigma}_{\text{rem}}} \quad (623)$$

Lattice-averaged microscopic cross section per isotope

$$\bar{\sigma}_x(g) = \frac{\int_{V_{ass}} N_m(r) \sigma_{x,m}(g, r) \phi(g, r) dr}{\int_{V_{ass}} N_m(r) \phi(g, r) dr} \quad (624)$$

where x is a reaction type, such as absorption, capture, fission, or production.

Average nodal-group neutron velocity

$$\bar{v}(g) = \frac{\sum_{i \in g} \Psi^\dagger(i)}{\sum_{i \in g} \frac{\Psi^\dagger(i)}{v(i)}} \quad (625)$$

where $v(i)$ is the neutron velocity in the fine-group energy structure (i.e., velocity at the mid-point of the energy group); and $\Psi^\dagger(i)$ is the adjoint flux from the fundamental mode solution, including leakage. The value can also be calculated using the forward flux if the adjoint flux is not available.

$$\bar{v}(g) = \frac{\sum_{i \in g} \Psi(i)}{\sum_{i \in g} \frac{\Psi(i)}{v(i)}} \quad (626)$$

where $\Psi(i)$ is the critical forward flux from the fundamental mode solution.

Lattice-averaged macroscopic cross section per nodal group

$$\bar{\Sigma}_a(g) = \frac{\sum_{i \in g} \int_{V_{ass}} \Sigma_a(i, r) \phi(i, r) dr}{\sum_{i \in g} \int_{V_{ass}} \phi(i, r) dr} \quad (627)$$

where x is a reaction type, such as absorption, fission, or production.

Lattice-averaged macroscopic scattering kernel per nodal group

$$\bar{\Sigma}_s(g' \rightarrow g) = \frac{\sum_{i \in g} \sum_{i' \in g'} \int_{V_{ass}} \Sigma_s(i' \rightarrow i, r) \phi(i', r) dr}{\sum_{i \in g} \sum_{i' \in g'} \int_{V_{ass}} \phi(i', r) dr} \quad (628)$$

Lattice-averaged macroscopic removal cross section per nodal group

$$\bar{\Sigma}_{rem}(1) = \bar{\Sigma}(1 \rightarrow 2) - \frac{\bar{\phi}(2)}{\bar{\phi}(1)} \bar{\Sigma}(2 \rightarrow 1) \quad (629)$$

[Equation \(629\)](#) represents the value for a two-group energy structure, where there is a nonzero removal cross section only for the fast group (i.e., group 1). For a three-group energy structure, the expressions for the various group-dependent removal cross sections become

$$\begin{aligned}\bar{\Sigma}_{\text{rem}}(1) &= \frac{v\bar{\Sigma}_f(1) + v\bar{\Sigma}_f(2) \cdot \frac{\bar{\phi}(2)}{\bar{\phi}(1)} + v\bar{\Sigma}_f(3) \cdot \frac{\bar{\phi}(3)}{\bar{\phi}(1)}}{k^\infty} - \bar{\Sigma}_a(1) \\ \bar{\Sigma}_{\text{rem}}(2) &= \bar{\Sigma}_{\text{rem}}(1) \cdot \frac{\bar{\phi}(1)}{\bar{\phi}(2)} - \bar{\Sigma}_a(2) \\ \bar{\Sigma}_{\text{rem}}(3) &= 0\end{aligned}\quad (630)$$

In the expression for the fast group removal cross section, $\bar{\Sigma}_{\text{rem}}(1)$, the infinite multiplication factor is calculated as

$$k^\infty = \frac{v\bar{\Sigma}_f(1) \cdot \bar{\phi}(1) + v\bar{\Sigma}_f(2) \cdot \bar{\phi}(2) + v\bar{\Sigma}_f(3) \cdot \bar{\phi}(3)}{\bar{\Sigma}_a(1) \cdot \bar{\phi}(1) + \bar{\Sigma}_a(2) \cdot \bar{\phi}(2) + \bar{\Sigma}_a(3) \cdot \bar{\phi}(3)} \quad (631)$$

The above formulations closely preserve the reactivity from the fine-mesh assembly calculation. The reactivity will not be preserved precisely because the flux used to condense cross sections from the fine-group structure to the nodal-group structure is the critical spectrum, not the infinite spectrum.

Microscopic fission cross section at TIP location

$$\sigma_f(g, r') = \frac{\sum_{i \in g} \sigma_{f, \text{U}^{235}}(i) \phi(i, r')}{\sum_{i \in g} \phi(i, r')} \quad (632)$$

where r' is the location of the TIP tube in the narrow–narrow water gap corner of a BWR problem. The microscopic fission cross section is the unshielded (i.e., infinitely dilute) value.

Lattice-averaged fission yield of various isotopes

$$Y_m = \frac{\sum_{m' \in V_{\text{fuel}}} \int Y_{m', m} N_{m'}(r) \sigma_{f, m'}(g, r) \phi(g, r) dr}{\int_{V_{\text{fuel}}} N_{m'}(r) \sigma_{f, m'}(g, r) \phi(g, r) dr} \quad (633)$$

where $Y_{m', m}$ is the yield from actinide m' to isotope m ; and the summation is performed over all actinides Th²²⁸ through Cm²⁴⁶. The isotopes, m , of interest are typically La¹⁴⁰, Ba¹⁴⁰, Ce¹⁴⁴, I¹³⁵, Xe¹³⁵, Pm¹⁴⁹, and Sm¹⁴⁹.

Thermal–hydraulic data

In addition to cross section data, the lattice physics code usually edits thermal–hydraulic related data to the nodal code, which may include some or all of the following:

- In-channel flow area (not including water rods) (cm^2).
- Out-channel flow area (not including control blade) (cm^2).
- Water rod flow area (cm^2).
- Control blade flow area (cm^2).
- Total flow area (cm^2).

- Density of in-channel water (g/cm^3).
- Density of out-channel water (g/cm^3).
- Density of water in water rods (g/cm^3).
- Density of water in control blade (g/cm^3).
- Lattice-averaged water density (g/cm^3).
- Heated perimeter of all fuel rods (cm).
- Wetted perimeter of in-channel coolant (cm).
- Wetted perimeter of out-channel coolant (cm).
- Hydraulic diameter of in-channel coolant (cm).
- Number of heated pins.

8.3 Neutron Balance

Neutron balances typically include the following definitions:

Region integrated flux

$$\text{RIF}(g, r) = \sum_{r' \in r} \bar{\phi}(g, r') \cdot V(r') \quad (634)$$

In this nomenclature, the neutron balance is being performed over all the mesh included in the region of choice, r . They could be all the mesh in the lattice, or a subset defined by the user.

Region averaged flux

$$\text{RAF}(g, r) = \frac{\text{RIF}(g, r)}{\sum_{r' \in r} V(r')} \quad (635)$$

Integrated absorptions

$$\text{ABS}(g, r) = \text{RIF}(g, r) \cdot \bar{\Sigma}_a(g, r) \quad (636)$$

Integrated fissions

$$\text{FISS}(g, r) = \text{RIF}(g, r) \cdot \bar{\Sigma}_f(g, r) \quad (637)$$

Integrated neutron production

$$\text{NUFISS}(g, r) = \text{RIF}(g, r) \cdot \bar{\nu}\bar{\Sigma}_f(g, r) \quad (638)$$

Integrated neutron leakage

$$\text{LEAK}(g, r) = \text{RIF}(g, r) \cdot \bar{D}(g) \cdot B^2 \quad (639)$$

Integrated out-scattering

$$\text{OUTSC}(g, r) = \text{RIF}(g, r) \cdot \sum_{g' \neq g} \bar{\Sigma}_s(g \rightarrow g', r') \quad (640)$$

Integrated in-scattering

$$\text{INSC}(g, r) = \sum_{g' \neq g} \text{RIF}(g', r) \cdot \bar{\Sigma}_s(g' \rightarrow g, r') \quad (641)$$

Integrated neutron source

$$\text{SOURCE}(g, r) = \bar{\chi}(g) \sum_{g'} \frac{\text{RIF}(g', r) \cdot v\bar{\Sigma}_f(g, r)}{k_{eff}} \quad (642)$$

Net neutron in-current

$$\begin{aligned} \text{INCURR}(g, r) = & \text{ABS}(g, r) + \text{EAK}(g, r) + \text{OUTSC}(g, r) \\ & - \text{INSC}(g, r) - \text{SOURCE}(g, r) \end{aligned} \quad (643)$$

All cross sections in (636)–(642) are region-averaged, using the following expression:

$$\bar{\Sigma}_x(g, r) = \frac{\sum_{r' \in r} \Sigma_x(g, r') \cdot \phi(g, r') \cdot V(r')}{\sum_{r' \in r} \phi(g, r') \cdot V(r')} \quad (644)$$

The fluxes and cross sections have been condensed directly from the fine-group energy structure to the nodal-group energy structure

$$\Sigma_x(g, r') = \frac{\sum_{i \in g} \Sigma_x(i, r') \cdot \phi(i, r')}{\sum_{i \in g} \phi(i, r')} \quad (645)$$

$$\phi(g, r') = \sum_{i \in g} \phi(i, r') \quad (646)$$

9 Concluding Remarks

In this chapter, we have presented a rather verbose treatise on current lattice physics methodology. The salient features of a lattice physics code include the following:

- The generation of energy group-dependent neutron and gamma cross section libraries;
- A resonance calculation used to obtain cross sections from the neutron cross section library for resonance absorbers;
- A means of combining energy groups in order to accelerate the solution to the Boltzmann transport equation;
- A detailed solution to the Boltzmann transport equation to determine the spectral and spatial distribution of neutrons throughout the exact planar geometry of the fuel design;
- A fundamental mode calculation to account for neutron leakage effects in an ad hoc manner;
- The calculation of gamma sources and a detailed solution to the fixed-source Boltzmann transport equation to determine the spectral and spatial distribution of gamma particles throughout the exact planar geometry of the fuel design;
- Editing of nodal constants and various form functions;
- The saving of isotopic data to some sort of a restart file;
- And the solution to the burnup chains, assuming the analysis involves a time-step.

For some of these topics, there may exist multiple approaches that are equally well suited to solving the problem at hand. In such cases, we have tried to provide a broad description of the

various techniques. This is most notable in ➤ Sects. 3 and ➤ 6, which cover the resonance calculation and the solution to the burnup chains, respectively. In both sections, many different techniques have been presented. For other topics – most notably those concerned with solving the Boltzmann transport equation – there is one approach that is so vastly superior to all other approaches that we have simply concentrated on describing that one method in great detail such that the reader can fully appreciate its intricacies. This includes ➤ Sects. 4 and ➤ 5, which cover the group condensation scheme and the fine-mesh lattice transport calculation, respectively.

The accuracy of current state-of-the-art lattice physics codes for light water reactor analysis has now approached the level of accuracy of the Monte Carlo codes that are being used to generate reference solutions for benchmarking. As such, potential improvements stand to gain little in the way of accuracy and are little more than minor tweaks to the current methods. As computers become more powerful, the most significant improvements may be realized by adding more energy groups to the lower resonance region of the cross section library (i.e., below 100 eV), creating unshielded cross section groups and minimizing the importance of the resonance calculation described in ➤ Sect. 3. Beyond that, improvements in accuracy will most likely come from improvements to the raw cross section data and the processing of the data (e.g., the NJOY methodology), both of which are beyond the scope of the lattice physics code.

Recent developments in lattice physics are almost universally related to expanding the analysis to a collection of bundles, as opposed to analyzing a single bundle. Such two-dimensional multi-bundle analyses are not needed in order to generate cross sections for use in nodal codes, but rather are used as reference solutions for comparison to equivalent nodal calculations. These comparisons can sometimes serve to help uncover modeling deficiencies at the nodal level. This type of development really falls outside the traditional definition of a lattice physics code and could be thought of more appropriately as a convenient way of replacing the Monte Carlo analysis as a reference solution, since such analyses can be cumbersome to implement and time consuming to execute. In any event, this seems to be an area that is experiencing a great deal of attention at the moment with the promise that, at some point in the future, it will translate into a full three-dimensional modeling capability with thermal–hydraulic feedback and include an explicit thermal–mechanical treatment of the stresses experienced by the fuel cladding. Once again, such calculations would serve to provide reference solutions against which the nodal production code could be benchmarked.

References

- Abagyan LN, Bazazyants NO, Nikoleav MN, Tsibulya AM (1980) A new system of group constants for the calculation of fast reactors. Sov At Energy 48:117
- Adams ML, Larsen EW (2002) Fast iterative methods for discrete-ordinates particle transport calculations. Prog Nucl Energy 40:3
- Ahlin A, Edenius M (1977) CASMO – a fast transport theory assembly depletion code for LWR analysis. Trans Am Nucl Soc 26:604
- Ahlin A, Edenius M (1978) The collision probability module EPRI-CPM, Pt II, Chap 6. EPRI CCM-1, Electric Power Research Institute
- Amster HJ, Suarez R (1957) The calculation of thermal constants averaged over a Wigner-Wilkins flux spectrum: description of the SOFOCATE code. U.S. AEC Report WAPD-TM-39
- Arnold WH, Dannels RA (1960) The Doppler coefficient of $U^{238}O_2$. Trans Am Nucl Soc 3:229
- Askew JR (1972) A characteristics formulation of the neutron transport equation in complicated geometries. AEEW-M 1108
- Askew JR, Fayers FJ, Kemshell PB (1966) A general description of the lattice code WIMS. J Brit Nucl Ener Soc 5:564

- Azekura K, Maruyama H, Ikebara T, Yamamoto M, Mills V, Marcille T (2003) Development of a BWR lattice analysis code LANCER based on an improved CCCP method. In: Advances in nuclear fuel management III, Hilton Head Island
- Ball SJ, Adams RK (1967) MATEXP: a general purpose digital computer program for solving ordinary differential equations by the matrix exponential method, ORNL/TM-1933, Union Carbide Corporation, Nuclear Division, Oak Ridge National Laboratory
- Barry FR (1963) LEOPARD – a spectrum dependent non-spatial depletion code for the IBM-7094. U.S. AEC Report WCAP-3741
- Bateman H (1910) The solution of differential equations occurring in the theory of radioactive transformations. Proc Cambridge Phil Soc 15:423
- Bell MJ (1973) ORIGEN – the ORNL isotope depletion and generation code, ORNL-4628
- Bitelli G, Salvatores M, Cecchini G (1970) Heterogeneity effects on neutron self-shielding factors for fast reactors. Nucl Sci Eng 40:138
- Bohl H Jr, Gelbard EM, Ryan GH (1957) MUFT-4, fast neutron spectrum code for the IBM-704. U.S. AEC Report WAPD-TM-72
- Carlvik I (1965) A method for calculating collision probabilities in general cylindrical geometry and applications to flux distributions and Dancoff factors. In: U.N. international conference on the peaceful uses of atomic energy, vol 2. Geneva, p 225
- Carlvik I (1966a) Integral transport theory in one-dimensional geometries. AB Atomenergi, Stockholm, Sweden, AE-227
- Carlvik I (1966b) The Dancoff correction in square and hexagonal lattices. Part of Carlvik's PhD thesis, Chalmers University, Göteborg, Sweden, AE-257
- Carlvik I (1966c) On the use of integral transport theory for the calculation of the neutron flux distribution in a Wigner-Seitz cell, vol 8. Nukleonik, p 226
- Carlvik I (1967a) Studies of integral neutron transport methods for nuclear reactor calculations, Ph.D. thesis, Chalmers University, Göteborg, Sweden
- Carlvik I (1967b) Calculations of neutron flux distributions by means of integral transport methods. AB Atomenergi, Stockholm, Sweden, AE-279
- Carlvik I (1967c) Collision probabilities for finite cylinders and cuboids. AB Atomenergi, Stockholm, Sweden, AE-281
- Carlvik I (1967d) Monoenergetic critical parameters and decay constants for small spheres and thin slabs. AB Atomenergi, Stockholm, Sweden, AE-273
- Carlvik I, Pershagen B (1959) The Dancoff correction in various geometries. AB Atomenergi, Stockholm, Sweden, AE-16
- Casal JJ, Stamm'ler RJ, Villarino E, Ferri A (1991) HELIOS: geometric capabilities of a new fuel assembly program. In: Proceedings of the international topical meeting on advances in mathematics, computations, and reactor physics, Pittsburgh
- Cefus CR, Larsen EW (1990) Stability analysis of coarse-mesh rebalance. Nucl Sci Eng 105:31
- Cho NZ, Hong SG (1996) CRX: a transport theory code for cell and assembly calculations based on the characteristics method. In: Proceedings of the international conference on physics of reactors, PHYSOR96, vol 1, September 16–20, 1996, Mito, Japan, p A-80
- Chao YA, Martinez AS (1978) On approximations to the neutron escape probability from an absorbing body. Nucl Sci Eng 66:254
- Chao YA, Yarbrough MB, Martinez AS (1981) Approximations to neutron escape probability and Dancoff corrections. Nucl Sci Eng 78:89
- Chiarella C, Keane A (1969) Equivalence relation based on an improved rational approximation. J Nucl Sci Technol 6:273
- Chiba G (2003) A combined method to evaluate the resonance self shielding effect in power fast reactor fuel assembly calculation. J Nucl Sci Technol 40:537
- Chiba G, Unesaki H (2006) Improvement of moment-based probability table for resonance self-shielding calculation. Ann Nucl Energy 33:1141
- Cho NZ, Park CJ (2003) A comparison of coarse mesh rebalance and coarse mesh finite difference accelerations for the neutron transport calculations. In: Proceedings of the nuclear mathematical and computational sciences: a century in review, April 6–11, 2003, American Nuclear Society, Gatlinburg [CD-ROM]
- Cho JY et al (2002) Cell based CMFD formulation for acceleration of whole-core method of characteristics calculations. J Korean Nucl Soc 34(3):250
- Croff AG (1980) ORIGEN2 – a revised and updated version of the Oak Ridge isotope generation and depletion code, ORNL-5621, 22
- Clarno K (2007) Implementation of generalized coarse-mesh rebalance in NEWTRNX for acceleration of parallel block-Jacobi transport. Trans Am Nucl Soc 97:498
- Cullen DE (1974) Application of the probability table method to multi-group calculations of neutron transport. Nucl Sci Eng 55:387
- Cullen DE (1986) Nuclear cross section preparation. In: CRC handbook of nuclear reactor calculations I. CRC Press, Boca Raton

- Dean D, Rempe K, Umbarger J (2005) SIMULATE-3 – an advanced three-dimensional two-group reactor analysis code, User's Manual. STUDSVIK/ SOA-95/15, rev. 3, Studsvik of America
- Dirac PAM (1943) Approximate rate of neutron multiplication for a solid of arbitrary shape and uniform density. British Report MS-D-5, Part I
- Dresner L (1960) Resonance absorption in nuclear reactors. Pergamon Press, Elmsford
- England TR (1962) CINDER – a one-point depletion and fission product program, WAPD-TM-334, Bettis Atomic Power Laboratory
- Fayers FJ, Davidson W, George CH, Halsall MJ (1972) LWRWIMS, a modular computer code for the evaluation of light water reactor lattices – part I: description of methods. UKAEA Report AEEW-R 785, Winfrith
- Garrison JD, Roos BW (1962) Fission-product capture cross sections, a compilation of yields for U233T, U235T, and PU239T. Nucl Sci Eng 12:115
- Goldberg L, Vujic J, Leonard A (1995) The method of characteristics in general geometry. Trans Am Nucl Soc 73:173
- Goldstein R (1967) Intermediate resonance absorption including interference scattering and Doppler broadening. Trans Am Nucl Soc 6:161
- Goldstein R, Cohen ER (1962) Theory of resonance absorption of neutrons. Nucl Sci Eng 13:132
- Halsall MJ (1980) CACTUS, a characteristics solution to the neutron transport equation in complicated geometries. AEEW-R 1291, Atomic Energy Establishment, Winfrith, Dorchester, Dorset, UK
- Halsall MJ (1995) The WIMS subgroup method for resonance absorption. Trans Am Nucl Soc 72:354
- Hazama T, Chiba G, Sugino K (2006) Development of a fine and ultra-fine group cell calculation Code SLAROM-UF for fast reactor analyses. J Nucl Sci Technol 43:908
- Hébert A (1998) A comparison of three methods for computing probability tables. In: Proceedings Of the international conference on physics of nuclear science and technology, October 5–8, 1998, Hauppauge
- Hébert A (2004) A mutual resonance self-shielding model consistent with subgroup equations. In: Proceedings of the international meeting on physics of fuel cycles and advanced nuclear systems: global developments, PHYSOR2004, April 25–29, 2004, Chicago
- Hébert A (2005a) The ribbon extended self-shielding model. Nucl Sci Eng 151:1
- Hébert A (2005b) A review of legacy and advanced self-shielding models for lattice calculations. In: Proceedings of the mathematics and computation, supercomputing, reactor physics and nuclear and biological applications (M&C2005), September 12–15, 2005, Avignon, France
- Hébert A, Coste M (2002) Computing moment-based probability tables for self-shielding calculations in lattice codes. Nucl Sci Eng 142:245
- Hébert A, Marleau G (1991) Generalization of the Stamm'ler method for the self-shielding of resonant isotopes in arbitrary geometries. Nucl Sci Eng 108:230
- Hébert A, Marleau G, Roy R (2000) A description of the DRAGON data structures. Version DRAGON_000331 Release 3.04, Report IGE-232 Rev. 3, Institut de génie nucléaire, École Polytechnique de Montréal, Montréal, Québec
- Hébert A, Santamarina A (2008) Refinement of the Santamarina-Hfaiedh energy mesh between 22.5 eV and 11.4 keV. In: Proceedings international conference on reactor physics, nuclear power: a sustainable resource (Physor2008), September 2008, Interlaken, Switzerland [CD-ROM]
- Hfaiedh N, Santamarina A (2005) Determination of the optimized SHEM mesh for neutron transport calculations. In: Proceedings of the mathematics and computation, supercomputing, reactor physics and nuclear and biological applications (MC&SNA2007), September 2005, Avignon, France [CD-ROM]
- Hoffmann A et al (1973) APOLLO: code Multigroupe de résolution de l'équation du transport pour les neutrons thermiques et rapides. Note CEA-N-1610, Commissariat à l'énergie Atomique, France
- Honeck HC (1961) THERMOS, a thermalization transport code for reactor lattice calculations. U.S. AEC Report BNL-5826
- Huria H, Ouislomen M (2008) An optimized ultra-fine energy group structure for neutron transport calculations. In: Proceedings of the international conference on the physics of reactors (PHYSOR2008), September 2008, Interlaken, Switzerland [CD-ROM]
- Hwang RN (2003) Resonance theory in reactor applications. In: Review lecture in topical meeting nuclear mathematical and computational sciences: a century in review – a century anew (M&C 2003), Gatlinburg, April 6–10, 2003, American Nuclear Society, LaGrange Park, pp 1–15
- Ihara H (ed) (1989) Tables and figures from JNDC nuclear data library of fission products, version 2, JAERI-M 89–204
- Iijima S, Yoshida T (1982) Fission product model for BWR lattice calculation code. J Nucl Sci Technol 19:96

- Ikehara T, Ando Y, Yamamoto M (1998) Fission product model for BWR analysis with improved accuracy in high burnup. *J Nucl Sci Technol* 35:527
- Ishiguro Y (1968) Exact treatment of the resonance absorption of neutrons of intermediate energy. *Nucl Sci Eng* 32:422
- Ishiguro Y (1974) PEACO-II: a code for calculation of effective cross sections in heterogeneous systems, JAERI-M 5527
- Ishiguro Y (1985) Generalized Dancoff factor in complex lattice arrangement. *J Nucl Sci Technol* 22:853
- Ishiguro Y, Takano K (1969) Intermediate neutron resonance absorption with interference scattering in heterogeneous systems. *J Nucl Sci Technol* 6:380
- Iwamoto T, Tamitani M, Moore B (2003) Methods, benchmarking, and applications of the BWR core simulator code AETNA. In: Proceedings of the International Conference on Advances in Nuclear Fuel Management III (ANFM 2003), CD-ROM, American Nuclear Society, Hilton Head Island
- Jevremovic T, Ito T, Inaba Y (2002) ANEMONA: multiassembly neutron transport modelling. *Ann Nucl Energy* 29:2105
- Jevremovic T, Vujic J, Tsuda K (2001) ANEMONA-a neutron transport code for general geometry reactor assemblies based on the method of characteristics and R-function solid modeller. *Ann Nucl Energy* 28:125
- Jonsson A, Loretz RA (1991) Historical and recent developments, applications, and performance of the DIT assembly lattice code. In: Proceedings of the international topical meeting on advances in mathematics, computations, and reactor physics, Pittsburgh
- Joo HG, Cho JY, Kim HY et al (2002) Dynamic implementation of the equivalence theory in the heterogeneous whole core transport calculation. In: Proceedings of the international conference on the new frontiers of nuclear technology: reactor physics, safety and high-performance computing (PHYSOR2002), October 7–10, 2002, Seoul, Korea, p 13A-02 [CD-ROM]
- Joo HG, Han BS, Kim CH (2005) Implementation of subgroup method in direct whole core transport calculation involving non-uniform temperature distribution. In: Proceedings of the mathematics and computation, supercomputing, reactor physics and nuclear and biological applications (M&C2005), September 12–15, 2005, Avignon, France [CD-ROM]
- Joo HG, Kim GY, Pogosbekyan L (2009) Subgroup weight generation based on shielded pin-cell cross section conservation. *Ann Nucl Energy* 36:859
- Karthikeyan R, Hébert A (2008) Performance of advanced self-shielding models in DRAGON version 4 on analysis of high conversion light water reactor lattice. *Ann Nucl Energy* 35:396
- Kidmon RB (1975) The shielding factor method for generating multigroup cross sections for fast reactor analysis. *Nucl Sci Eng* 44:189
- Kim KS, Kim HY, Zee SQ (2002) Benchmark calculations of DENT-2D code for PWR fuel assemblies. In: Proceedings of the international conference on the new frontiers of nuclear technology: reactor physics, safety and high-performance computing, vol 14, October 7–10, 2002, Seoul, Korea, p A-05
- Knott D (1990) NUC ENG 521, computational methods in steady state neutron transport theory. Department of Nuclear Engineering, The Pennsylvania State University
- Knott D (1991) KRAM, a lattice physics code for modelling the detailed depletion of Gadolinia isotopes from BWR fuel designs. PhD thesis, The Pennsylvania State University, University Park
- Knott D, Edenius M (1993) Validation of CASMO-4 transport solution. In: Proceedings of the international meeting mathematical methods and supercomputing in nuclear applications, vol 2, April 19–23, 1993, Karlsruhe, Germany, p 547
- Knott D, Forssen B-H, Edenius M (1995) CASMO-4 – a fuel assembly burnup program, methodology. STUDSVIK/SOA-95/2, Studsvik of America
- Knott D, Wehlage E (2007) Description of the LANCER02 lattice physics code for single-assembly and multibundle analysis. *Nucl Sci Eng* 155:331
- Kobayashi K (1995) Genshiro Butsuri (Reactor Physics). Corona, Tokyo [in Japanese]
- Koike H, Yamaji K, Sato D et al (2010) A resonance calculation method based on the multi-terms rational approximation for general geometry with gray resonance absorbers, Proc. PHYSOR2010, Pittsburgh
- Kosaka S, Saji E (2000) Transport theory calculation for heterogeneous multi-assembly problem by the characteristics method with direct path linking technique. *J Nucl Sci Technol*, 37:1015
- Kruif WJ (1994) Reactor physics analysis of the pin-cell Doppler effect in a thermal nuclear reactor, Ph.D. thesis, Delft University
- Kruif W, Jansen A (1996) The effective fuel temperature to be used for calculating resonance

- absorption in a $^{238}\text{UO}_2$ lump with a nonuniform temperature profile. *Nucl Sci Eng* 123:121
- Lamarche JR (1972) Introduction to nuclear reactor theory. Addison-Wesley, Reading, ISBN 0-201-04120-X
- Lapidus L, Luus R (1967) Optimal control of engineering processes. Blaisdell, Waltham
- Lee D, Downar TJ (2003) Convergence analysis of the nonlinear coarse mesh finite difference method. In: Proceedings of the nuclear mathematical and computational sciences: a century in review, April 6–11, 2003, American Nuclear Society, Gatlinburg [CD-ROM]
- Lee D, Smith K, Rhodes J (2009) The impact of ^{238}U resonance elastic scattering approximations on thermal reactor Doppler reactivity. *Ann Nucl Energy* 36:274
- Leonard A, McDaniel CT (1995) Optimal polar angles and weights. *Trans Am Nucl Soc* 73:171
- Levine M (1963) Resonance integral calculations for ^{238}U lattices. *Nucl Sci Eng* 18:271
- Levitt LB (1972) The probability table method for treating unresolved neutron resonances in Monte Carlo calculations. *Nucl Sci Eng* 49:450
- Lewis EE, Miller WF (1984) Computational methods of neutron transport. Wiley, New York, ISBN 0-471-09245-2
- Loubiere S, Sanchez R, Coste M et al (1999) APOLLO2 twelve years later. In: Proceedings Of the international conference on mathematics and computation, reactor physics and environmental analysis in nuclear applications, September 27–30, 1999, Madrid
- MacFarlane RE, Muir DW (1994a) The NJOY nuclear data processing system, Version 91. LA-12740-M, Los Alamos National Laboratory, Los Alamos
- MacFarlane RE, Muir DW (1994b) The NJOY nuclear data processing system, Version 91, LA-17740-M, Los Alamos National Laboratory, Los Alamos
- Marcille TF, Mills VW (2003) An automated multi-group cross section processing technique using NJOY. In: Proceedings of the advances in nuclear fuel management III, October 5–8, 2003, Hilton Head Island [CD-ROM]
- Marleau G, Hébert A, Roy R (2000) A user guide for DRAGON. Version DRAGON_000331 Release 3.04, Report IGE-174 Rev. 5, Institut de génie nucléaire, École Polytechnique de Montréal, Montréal, Québec
- Marleau G, Roy R, Hébert A (1994) DRAGON: a collision probability transport code for cell and supercell calculations. Report IGE-157, Institut de génie nucléaire, École Polytechnique de Montréal, Montréal, Québec
- Masiello E, Sanchez R, Zmijarevic I (2009) New numerical solution with the method of short characteristics for 2-D heterogeneous Cartesian cells in the APOLLO2 code: numerical analysis and tests. *Nucl Sci Eng* 161:257
- Matsumoto H, Ouisloumen M, Takeda T (2005) Development of spatially dependent resonance shielding method. *J Nucl Sci Technol* 42:688
- Matsumoto H, Ouisloumen M, Takeda T (2006) Spatially dependent self-shielding method with temperature distribution for the two-dimensional transport code PARAGON. *J Nucl Sci Technol* 43:1311
- MC**2-2 (1999) Multigroup neutron spectra, slowing-down calculation using ENDF/B, P1 and B1 approximation, NESC0355, NEA/OECD (last updated November 1999)
- McLane V (ed) (2001) ENDF-102 data formats and procedures for the evaluated nuclear data file ENDF-6, BNL-NCS-44945-01/04-Rev
- Mertyurek U (2007) Gamma flux calculations in lattice physics code LANCER02. *Trans Am Nucl Soc* 97:580
- Mizuta H (1970) Accuracy of approximations used in resonance integral calculation. *J Nucl Sci Technol* 7:264
- Moler C, Loan CV (2003) Nineteen dubious ways to compute the exponential of a matrix, twenty-five years later. *SIAM Rev* 45:3
- Moore B, Zhang H, Congdon S (1999) Comparison of methods for BWR prediction accuracy as applied to a small BWR/4. In: Proceedings of the mathematical and computational reactor physics, and environmental analysis in nuclear Applications, Madrid, Spain, p 679
- Morimoto Y, Maruyama H, Ishii K et al (1989) Neutronic analysis code for fuel assembly using a vectorized Monte Carlo method. *Nucl Sci Eng* 103:351
- Nikolaev MN (1976) Comments on the probability table method. *Nucl Sci Eng* 61:286
- Nikoleav MN, Ignatcv AA, Isaev NV, Khokhlov VF (1971) The method of subgroups for considering the resonance structure of cross sections in neutron calculations. *Sov At Energy* 5:426
- Nikoleav MN, Germogenova TA, Isaev NV, Khokhlov VF (1973) Computations of neutron propagation, allowing for the resonance structure of the cross sections. *Sov At Energy* 35:29
- Okumura K, Kugo T, Kaneko K, Tsuchihashi K (2007) SRAC2006: a comprehensive neutronics calculation code system, JAEA-Data/Code 2007-004
- Okumura K, Mori T, Nakagawa M, Kanako K (2000) Validation of a continuous-energy Monte Carlo burn-up code MVP-BURN and its application to

- analysis of post irradiation experiment. *J Nucl Sci Technol* 37:128
- Ouisloumen M et al (2001) PARAGON: the New Westinghouse assembly lattice code. In: ANS international topical meeting on mathematical methods for Nuclear Applications, Salt Lake City
- Postma T, Vujic J (1999) The method of characteristics in general geometry with anisotropic scattering. In: Proceedings of the international conference on mathematics and computation, reactor physics and environmental analysis in nuclear applications, vol 2, September 27–30, 1999, Madrid, Spain, p 1215
- Reed WH (1971) The effectiveness of acceleration techniques for iterative methods in transport theory. *Nucl Sci Eng* 45:245
- Reuss P, Coste-Delclaux M (2003) Development of computational models used in France for neutron resonance absorption in light water lattices. *Prog Nucl Energy* 42:237
- Rhodes JD III (2009) ENDF/B-VII.0 586 group neutron data library for CASMO-5 and CASMO-5M. SSP-07/402, rev. 5, Studsvik Scandpower, Inc
- Rhodes J, Smith K, Lee D (2006) CASMO-5 development and applications. In: Proceedings of the PHYSOR-2006, ANS topical meeting on reactor physics, September 2006, Vancouver, Canada
- Ribon P (1986) Probability tables and Gauss quadrature application to neutron cross-sections in the unresolved energy range. In: Proceedings of the topical meeting on advances in reactor physics and safety, September 17–19, 1986, vol 1. Saratoga Springs, p 280
- Rosenstein W (1960) Collision probabilities and resonance integrals for lattice. *Nucl Sci Eng* 7:162
- Rothenstein W (1980) Resonance absorption calculations in thermal reactors. *Prog Nucl Energy* 5:95
- Rothenstein W, de Oliveira CRE, Brandman N (1988) Accurate resonance absorption calculations including 2-D effects and their representation in multigroup lattice physics codes. *Ann Nucl Energy* 15:293
- Rothenstein W, Segev M (1986) Unit cell calculations. In: CRC handbook of nuclear reactor calculations I. CRC Press, Boca Raton
- Rowlands G (1962) Resonance absorption and non-uniform temperature distributions. *J Nucl Energy Parts A/B* 16:235
- Roy R (1998) The cyclic characteristics method. In: Proceedings of the international topical meeting on the physics of nuclear science and technology, vol 1, October 5–8, 1998, Long Island, p 407
- Sanchez R, Mao L, Santandrea S (2002) Treatment of boundary conditions in trajectory-based deterministic transport methods. *Nucl Sci Eng* 140:23
- Sanchez R, Mondot J, Stancovski Z, Cosic A, Zmijarevic I (1988) APOLLO II: a user-oriented, portable, modular code for multi-group transport assembly calculations. *Nucl Sci Eng* 100:352
- Santamarina A, Collignon C, Garat A (2004) French calculation schemes for light water reactor analysis. In: Proceedings of the International Conference on PHYSOR2004-The physics of fuel cycles and advanced nuclear systems, April, 2004, Chicago [CD-ROM]
- Sartori E (1990) OECD/NEA Data Bank, Standard energy group structures of cross section libraries for reactor shielding, reactor cell and fusion neutronics applications: VITAMIN-J, ECCO-33, ECCO-2000 and XMAS, JEF/DOC-315 Revision 3 – DRAFT (December 11, 1990)
- Sauer A (1963) Approximate escape probabilities. *Nucl Sci Eng* 16:329
- Segev M (1975) A theory of resonance group self-shielding. *Nucl Sci Eng* 56:72
- Segev M (1981) Interpolation of resonance integrals. *Nucl Sci Eng* 79:113
- Sehgal BR, Goldstein R (1966) Intermediate resonance absorption in heterogeneous media. *Nucl Sci Eng* 25:174
- Sidje RB (1998) EXPOKIT: software package for computing matrix exponentials. *ACM Trans Math Software* 24:130
- Sinitsa VV, Nikoleav MN (1973) Analytic determination of subgroup parameters. *Sov At Energy* 35:429
- Smith KS (1983) Nodal method storage reduction by nonlinear iteration. *Trans Am Nucl Soc* 44:265
- Smith KS, Rhodes JD (2000) CASMO-4 characteristics method for two-dimensional PWR and BWR core calculations. *Trans Am Nucl Soc* 83:292
- Smith KS, Rhodes JD III (2002) Full-core, 2-D, LWR core calculation with CASMO-4E. In: Proceedings of the international conference on the new frontiers of nuclear technology: reactor physics, safety and high-performance computing (PHYSOR2002), October 7–10, 2002, Seoul, Korea, p 13A-04 [CD-ROM]
- Stacy WM (2001) Nuclear reactor physics. Wiley, New York
- Stamm'ler RJ (1992) PHOENIX – User's guide. ABB-Atom AB Report UR 92-054, Rev. 5
- Stamm'ler RJ, Abbate MJ (1983) Methods of steady state reactor physics in nuclear design. Academic, London, New York, ISBN 0-12-663320-7
- Stamm'ler RJ, Blomstrand J, Weiss ZJ (1973) Equivalence relations for resonance integral calculations. *J Nucl Energy* 27:885

- Stoker CC, Weiss ZJ (1996) Spatially dependent resonance cross sections in a fuel rod. *Ann Nucl Energy* 23:765
- Sublet J, Ribon P (2002) A probability table based cross section processing system: CALENDF-2001. *J Nucl Sci Technol* 2(Suppl):856
- Sugimura N, Yamamoto A (2006) Evaluation of Dancoff factors in complicated geometry using the method of characteristics. *J Nucl Sci Technol* 43:1182
- Sugimura N, Yamamoto A (2007) Resonance treatment based on ultra-fine-group spectrum calculation in the AEGIS code. *J Nucl Sci Technol* 44:958
- Sugimura N, Yamamoto A, Ushio T, Mori M, Tabuchi M, Endo T (2007) Neutron transport models of AEGIS: an advanced next-generation neutronics design system. *Nucl Sci Eng* 155:276
- Tasaka K (1977) DCHAIN: code for analysis of buildup and decay of nuclides, JAERI 1250, Japan Atomic Energy Research Institute [in Japanese]
- Taubman CJ (1975) The WIMS 69-group library tape 166259. Report AEEW-M1324, U.K. Atomic Energy Authority, Winfrith
- Tohjoh M, Watanabe M, Yamamoto A (2006) Study on spatial discretization and temperature distribution approximation effects on BWR assembly calculations. *Ann Nucl Energy* 33:242
- Tone T (1975) A numerical study of heterogeneity effects in fast reactor critical assemblies. *J Nucl Sci Technol* 12:467
- Tsuchihashi K, Takano H, Horikami K et al (1982) SRAC: JAERI thermal reactor standard code system for reactor design and analysis, JAERI-1302, Japan Atomic Energy Research Institute
- Villarino EA, Stamm'ler RJ, Ferri AA, Casal JJ (1992) HELIOS: angularly dependent collision probabilities. *Nucl Sci Eng* 112:16
- Vondy DR (1962) Development of a general method of explicit solution to the nuclide chain equations for digital machine calculations, ORNL/TM-361, Union Carbide Corporation, Nuclear Division, Oak Ridge National Laboratory
- Wehlage EM (2005) Modeling resonance interference effects in the LANCER02 lattice physics code. MSc thesis, The Ohio State University, Columbus
- Wehlage E, Knott D, Mills VW (2005) Modeling resonance interference effects in the lattice physics code LANCER02. In: Proceedings of the mathematics and computation, supercomputing, reactor physics and nuclear and biological applications (M&C2005), September 12–15, 2005, Avignon, France [CD-ROM]
- Weinberg AM, Wigner EP (1958) The physical theory of neutron chain reactors. University of Chicago Press, Chicago
- Weiss Z, Ball G (1991) Ray-tracing in complicated geometries. *Ann Nucl Energy* 18:483
- Wemple CA, Gheorghiu H-NM, Stamm'ler RJ, Villarino EA (2008) Recent advances in the HELIOS-2 lattice physics code. In: Proceedings of the international conference on the physics of reactors (PHYSOR2008), September 2008, Interlaken, Switzerland [CD-ROM]
- Wemple CA, Stamm'ler RJ, Ferri AA (2007) Improved temperature-dependent resonance treatment in HELIOS-1.9. *Trans Am Nucl Soc* 96:657
- West JT, Emmet MB (1980) MARS: a multiple array system using combinatorial geometry. Oak Ridge National Laboratory, Radiation Shielding Information Center
- Wigner EP, Creutz E, Jupnik H, Snyder T (1955) Resonance absorption of neutrons by spheres. *J Appl Phys* 26:260
- Williams ML (1983) Correction of multigroup cross sections for resolved resonance interference in mixed absorbers. *Nucl Sci Eng* 83:37
- Williams ML, Asgari M, Hollenbach DF (2005) CENTRM: a one-dimensional neutron transport code for computing pointwise energy spectra. Sect. F18 of SCALE: a modular code system for performing standardized computer analyses for licensing evaluations, ORNL/TM-2005/39, Version 5, vols I–III, April 2005. Available from Radiation Safety Information Computational Center at Oak Ridge National Laboratory as CCC-725
- WIMS-D/4 (2000) Multi-group reactor lattice calculation for thermal reactor and fast reactor, NEA-0329, NEA/OECD (last updated March, 2000)
- Yamamoto A (2005) Generalized coarse-mesh rebalance method for acceleration of neutron transport calculations. *Nucl Sci Eng* 151:274
- Yamamoto A (2008) Evaluation of background cross-section for heterogeneous and complicated geometry by the enhanced neutron current method. *J Nucl Sci Technol* 45:1287
- Yamamoto A (2009) Applicability of the enhanced neutron current method for non-convex fuel shapes. *Ann Nucl Energy* 36:193
- Yamamoto T (2003) Background-cross-section-dependent subgroup parameters. *J Nucl Sci Technol* 40:370
- Yamamoto T (2004) Generalized approach to optimize subgroup parameters. *J Nucl Sci Technol* 41:425

- Yamamoto M et al (1984) Development and validation of TGBLA lattice physics methods. In: Proceedings of the topical meeting on reactor physics and shielding, Chicago
- Yamamoto A, Kitamura Y, Ushio T, Sugimura N (2004) Convergence improvement of coarse mesh rebalance method for neutron transport calculations. *J Nucl Sci Technol* 41:781
- Yamamoto A, Koike H, Yamane Y (2009a) A new framework of resonance calculation method based on the sub-group method (1); theory. *Trans Am Nucl Soc* 100:647
- Yamamoto A, Koike H, Yamane Y (2009b) A new framework of resonance calculation method based on the sub-group method (2); calculation. *Trans Am Nucl Soc* 100:650
- Yamamoto A, Sugimura N (2006) Improvement on multi-group scattering matrix in thermal energy range generated by NJOY. *Ann Nucl Energy* 33:555
- Yamamoto A, Tabushi M, Sugimura N, Ushio T, Mori M (2007) Derivation of optimum polar angle quadrature set for the method of characteristics based on approximation error for the Bickley function. *J Nucl Sci Technol* 44:129
- Yamamoto A, Tabuchi M, Sugimura N et al (2005) Non-equidistant ray tracing for the method of characteristics. In: Proceedings of the international topical meeting on mathematics and computation, super-computing, reactor physics and nuclear and biological applications (M&C2005), Sept. 12–15, 2005, Avignon, France [CD-ROM]
- Yamamoto A, Tada K, Sugimura N, Ushio T, Mori M (2006) Generation of cross section library for lattice physics code, AEGIS. In: Proceedings of the Physor-2006, September 10–14, 2006, Vancouver, Canada [CD-ROM]
- Yamamoto T, Takeda T (2000) Reaction rate calculation in fast reactor blanket using multiband Sn theory. *J Nucl Sci Technol* 37:428
- Yamamoto T, Takeda T (2006) A complement proposal for optimization of subgroup parameters. *J Nucl Sci Technol* 43:765
- Yamamoto A, Tatsumi M, Sugimura N (2007) Numerical solution of stiff burnup equation with short half lived nuclides by the Krylov subspace method. *J Nucl Sci Technol* 44:147
- Yamamoto A, Tatsumi M, Sugimura N (2009) Projected predictor-corrector method for lattice physics burnup calculations. *Nucl Sci Eng* 163:144

